Cable-Driven Pantographs

Thèse

Simon Perreault

Doctorat en génie mécanique
Philosophiæ doctor (Ph.D.)

Québec, Canada

Cable-Driven Pantographs

Thèse

Simon Perreault

Sous la direction de:

Philippe Cardou, directeur de recherche
Clément Gosselin, codirecteur de recherche

Résumé

Cette thèse propose une nouvelle famille de pantographes, les pantographes à transmission par câbles (PTC). Les PTC sont définis comme des mécanismes permettant la reproduction, selon un facteur d'échelle préétabli, de mouvements imposés à l'effecteur maître vers l'effecteur esclave en se servant de câbles comme moyen de transmission des forces. Ils peuvent être aussi présentés comme étant la communion entre les pantographes conventionnels, mécanismes constitués de membrures rigides, et les mécanismes parallèles entraînés par câbles (MPEC).

L'objectif de cette thèse étant la conception de PTC combinant fiabilité d'utilisation, sécurité et faible coût de fabrication, nous avons choisi de développer des outils permettant la conception de PTC purement mécaniques, c'est-à-dire qu'aucune composante électrique n'est nécessaire afin de transmettre les efforts entre les parties maître et esclave. Plusieurs applications peuvent être d'ailleurs envisagées pour ce type de mécanismes, soient, par exemple, la télémanipulation d'objets à l'intérieur d'environnements sensibles aux perturbations électromagnétiques causées par l'activation de moteurs électriques ou tout simplement lorsque l'accès à des sources d'énergie électrique est limité.

L'utilisation exclusive de câbles entre les deux parties du pantographe apporte plusieurs avantages, mais aussi quelques inconvénients qui leurs sont inhérents. Le principal désavantage des PTC est sans contredit l'unilatéralité de la transmission des forces dans les mécanismes à entraînement par câbles. Ce dernier impose une disposition réfléchie des câbles, c'est-à-dire que ceux-ci doivent supporter l'effecteur selon toutes les directions, et un niveau minimum de tension afin de conserver la géométrie du système. En général, pour les MPEC, les moteurs électriques doivent fournir un couple et une puissance constants afin de maintenir cette tension. Nous proposons donc, dans cette thèse, l'utilisation de ressorts dans l'objectif de produire cette tension sans actionneur, laissant ainsi à l'utilisateur l'application de toute charge additionnelle (par exemple, pour vaincre la friction, l'inertie ou des forces extérieures appliquées à l'effecteur). Ce concept est validé par la conception mécanique du premier prototype de PTC plan à deux degrés de liberté (DDL) et entraîné par trois câbles.

Dans le but de restreindre au minimum la dépense énergétique de l'utilisateur, nous suggérons ensuite la conception et l'utilisation de ressorts non-linéaires. Une méthodologie est ainsi développée afin de déterminer le comportement idéal de ces ressorts pour à la fois maintenir

les câbles en tension et approximer l'équilibrage statique du mécanisme sur son espace de travail. Ces ressorts non-linéaires sont en fait constitués de mécanismes à quatre barres et de ressorts à couples constants. À titre d'exemple, cette technique est appliquée à la conception mécanique d'une nouvelle version du PTC plan à deux DDL et entraîné par trois câbles.

Lors de la conception de tout PTC (et particulièrement pour les PTC comportant un espace de travail tridimensionnel), un second inconvénient doit être pris en compte. Ce sont les interférences mécaniques entre les différents câbles reliant un même effecteur à sa base correspondante (autant pour l'effecteur maître que l'effecteur esclave) lors de déplacements en translation, en rotation ou combinés. Par conséquent, nous proposons dans cette thèse une méthode permettant de déterminer de manière géométrique les régions d'interférences entre une paire de câbles et aussi entre un câble et une arête de l'effecteur à l'intérieur de l'espace de travail du PTC pour une orientation constante de ce dernier. Il est entre autres démontré que, pour une orientation constante de l'effecteur, ces zones d'interférences sont définies par des segments de plans et de lignes à l'intérieur de l'espace de travail. Cette méthode permet alors de prévoir, de manière exacte et très rapide, les lieux d'interférences pour un PTC donné et elle fournit un puissant outil lors de l'optimisation géométrique de ce type de systèmes. Cette technique est aussi directement applicable lors de la conception de tout MPEC tridimensionnel.

Finalement, afin de déterminer une géométrie adéquate pour une application donnée, la dernière partie de cette thèse se concentre sur la conception d'un algorithme d'optimisation géométrique pour les PTC ou MPEC basé sur trois critères principaux. Le premier critère est la maximisation du volume de l'espace des poses polyvalentes (EPP) (critère bien connu dans la litérature scientifique). Les second et troisième critères sont basés sur l'espace libre de toute interférence mécanique (théorie développée dans la partie précédente de cette thèse) et ces espaces doivent être aussi maximisés. À titre d'exemple, les paramètres géométriques d'un MPEC comportant six DDL, étant entraîné par sept câbles et comportant neuf arêtes sont optimisés pour illustrer cette technique. Par la suite, une application médicale est utilisée comme deuxième exemple, soit la synthèse dimensionnelle d'un PTC à six DDL, entraîné par huit câbles et comportant dix-sept arêtes, prévu pour être utilisé à l'intérieur d'un système conventionnel d'imagerie par résonance magnétique (IRM) cylindrique permettant ainsi d'effectuer des biopsies simples sous guidage visuel.

Abstract

This thesis reports the first steps toward the development of a new family of telemanipulators: cable-driven pantographs (CDPs). We define CDPs as mechanisms designed to reproduce trajectories induced from a master (input) to a slave (output) with a chosen scale factor and using cables in order to transmit corresponding forces or moments. They can also be presented as the combination of conventional pantographs, devices where rigid links are used to transmit forces between the master and the slave, and cable-driven parallel mechanisms (CDPMs).

Given that the purpose of this thesis is the design of CDPs which combine reliability, safety and a low manufacturing cost, we have chosen to develop tools that allow the design of purely mechanical CDPs, i.e., no electrical component is necessary to transmit forces between the master and the slave. Several applications can be considered for this new family of pantographs, e.g., the telemanipulation of objects inside environments that are sensitive to electromagnetic disturbances, or simply where electrical energy access is limited.

The strict use of cables between the two main components of the pantograph leads to many advantages but also to some inherent drawbacks. The main disadvantage of CDPs is without any doubt the unilaterality of force transmission in the CDPM's cables. It imposes a reflected cables distribution, i.e., cables must support the end effector in all directions, and a minimum level of tension in order to preserve the system geometry. In general, for a CDPM, the driving electrical motors are used to produce continuous torque (and power) to maintain the cable tensions. In this thesis, we propose a methodology which relies on springs in order to produce these tensions in a purely mechanical manner, leaving to the user the application of the additional forces, i.e., those forces needed to overcome friction, produce accelerations and balance external forces applied at the end effector. This conceptual idea is validated through the design of the prototype of the first planar three-cable two-degree-of-freedom (DoF) CDP.

Then, with the objective of minimizing the energy expenditure required by the user, we also suggest to compute nonlinear springs behaviours that maintain the cable tensions to a minimum level, while approximating the static equilibrium of the mechanism over its workspace. The nonlinear springs are in fact embodied as four-bar mechanisms coupled with constant-torque springs. This methodology is illustrated by its application to a modified version of the

three-cable two-DoF planar CDP.

When designing any CDP (in particular for CDPs with tridimensional workspace), a second drawback must be taken into account. This drawback is the possible occurrence of mechanical interferences between the different cables used to constrain the pose of the end effector from its respective base (this applies to both the master and the slave effectors) when moving in translation, in rotation or both. Thence, in this thesis, we propose a methodology for determining, in a geometrical manner, the interference regions between a pair of cables and between a cable and an end-effector edge for a given orientation within its workspace. It is shown that, for a constant end-effector orientation, these interference regions are defined by plane and line segments belonging to the CDP workspace. Then, this technique allows to determine—exactly and rapidly—the interference regions for a given CDP, and thus provides a powerful tool for optimizing the geometry of this kind of mechanisms. This methodology can also be directly applied to the design of any tridimensional CDPMs.

Finally, in order to generate a suitable geometry for a given application, the last part of this thesis details an algorithm to synthesize CDP or CDPM geometries based on three main criteria. The first criterion is based on the wrench-closure workspace (WCW) (which criterion is well known in the literature), whose volume should be maximized. The second and the third ones are based on the free-interference workspace, methodology developed in the previous part of the thesis, whose volumes should also be maximized. As an example, the geometric parameters of a seven-cable nine-edge six-DoF CDPM are optimized to illustrate the relevance of the technique. Then, a medical application is used as a second example, i.e., the dimensional synthesis of an eight-cable seventeen-edge six-DoF CDP intended to be used inside a standard cylindrical magnetic-resonance-imaging (MRI) system for performing simple image-guided biopsies.

Contents

List of Tables

List of Figures

À tous ceux et toutes celles
qui m'ont accompagné durant
ces magnifiques années

"Everything around you that you call life was made up by people that were no smarter than you, and you can change it, you can influence it, you can build your own things that other people can use."

Steve Jobs

Foreword

"It matters if you just
don't give up."
- Stephen Hawking

☑ Thèse de doctorat rédigée ... Checked (!)

Ces quelques mots, bien simples à première vue, ont une très grande signification. Ce banal crochet indique la fin d'une étape de vie, la fin de cette aventure qu'auront été mes études universitaires: baccalauréat, projet parascolaire, stage en entreprise, maîtrise, doctorat, conférences canadiennes et internationales, stage d'études, cours à l'étranger, assistance à l'enseignement, bénévolat, emplois ... et ça de l'automne 2000 à l'automne 2017. Toutes ces expériences inoubliables auront sans aucun doute aidé à forger la personne que je suis aujourd'hui.

En cours de rédaction, lorsque je suis tombé par hasard sur cette citation du célèbre physicien Stephen Hawking, je me suis brièvement remémoré tous les efforts qui ont été nécessaires à la complétion de ces études, de cette thèse et bien entendu des travaux sous-jacents, mais surtout, et en toute honnêteté, les quelques fois durant lesquelles il aurait été tellement plus simple de tout laisser tomber car la combinaison travail-étude n'a pas toujours été un mélange que je qualifierais d'agréable. Cependant, l'être humain peut être très tenace lorsqu'il se fixe un objectif et le mien était assurément de terminer cette thèse, mais surtout d'en être fier... peu importe les efforts et le temps nécessaires afin d'atteindre ce but. D'ailleurs, je me permets d'ouvrir une petite paranthèse afin de lever mon chapeau aux personnes qui ont rédigé une partie ou la totalité de leur thèse de doctorat tout en travaillant en parallèle car la détermination et la volonté sont plus souvent qu'à leur tour mises à rude épreuve.

Tout au long de l'écriture du premier jet de cette thèse, qui, vu les circonstances, s'est étendue sur un peu plus de six ans, je m'étais promis d'écrire petit à petit cette partie plus personnelle. Plusieurs idées me sont venues à l'esprit et se sont bousculées afin de se retrouver en premières

lignes sur ces pages initialement blanches. Cependant, j'ai finalement décidé d'y aller selon les convenances et de me limiter au plus important, c'est-à-dire les remerciements.

Ainsi, mes premiers remerciements se dirigent tout d'abord vers mon directeur de thèse, le professeur Philippe Cardou, qui s'est avéré pour moi une ressource inépuisable de connaissances dans chacune des sphères de mes travaux, mais aussi une véritable source de motivation. Je lui serai toujours très reconnaissant pour ses nombreux encouragements tout au long de mon cheminement, pour ses commentaires sans l'ombre d'un doute des plus pertinents, pour sa patience exemplaire et pour son soutien financier aux moments opportuns. J'ai assurément beaucoup appris lors de ces années et la réalisation de ces travaux n'auraient jamais été possibles sans son aide précieuse.

Dans un même ordre d'idées, je tiens à remercier mon co-directeur de thèse, le professeur Clément Gosselin, pour la justesse et l'élégance de ses conseils, qui auront été un phare tout au long de mes études graduées. Il aura été pour moi un honneur de cotoyer une telle sommité internationale du domaine de la robotique et une personne d'une intégrité sans égal. Bien entendu, je dois aussi remercier le professeur Gosselin pour son soutien financier afin de supporter mes travaux de maîtrise et de doctorat tout comme je me dois de mentionner la contribution des Fonds Québécois de Recherche sur la Nature et les Technologies (FQRNT) pour mes travaux de doctorat. Ces différentes aides auront été fort utiles et appréciées.

Ensuite, j'aimerais spécialement remercier les membres au sein de mon comité de thèse, soit le chercheur Marc Gouttefarde, le professeur Marc J. Richard et le professeur Alain Curodeau. Ces derniers, malgré un horaire chargé, ont, tout comme les professeurs Cardou et Gosselin, accepté et pris le temps nécessaire afin d'évaluer mes travaux. Leurs commentaires ont indubitablement permis d'améliorer la présentation et la qualité de cette thèse.

J'offre aussi mes plus sincères remerciements à tous les membres du Laboratoire de robotique de l'Université Laval. Je ne veux pas tous les nommer ici, par crainte d'en oublier, et aussi que la liste serait très longue, vu le nombre d'années durant lesquelles j'ai fréquenté ce laboratoire (!). Une chose est sûre, c'est qu'au cours des nombreuses années pendant lesquelles j'ai établi mon bureau de travail en ces murs, j'ai eu la chance de côtoyer des gens extraordinaires et brillants, qui ont été collègues de travail, partenaires de voyages, coéquipiers dans la pratique de sports (une petite note spéciale pour le hockey) et qui sont ainsi devenus des amis(ies). Je tiens particulièrement à remercier les professionnels de recherche du laboratoire, soient Thierry Laliberté, Simon Foucault et anciennement Boris Mayer St-Onge, pour leur disponibilité et leur aide inestimable afin de faciliter l'avancement des travaux de tous et de toutes au laboratoire. De plus, je me dois de remercier Mathieu Lepage, Coralie Germain et Dany Dubé pour l'aide apportée à mes travaux de recherche au cours de leur stage d'études respectif. Finalement, j'aimerais aussi remercier les professeurs Rajni Patel et Ana Luisa Trejos, ainsi que les membres du groupe CSTAR (Canadian Surgical Technologies & Advanced

Robotics), pour leur accueil chaleureux et leur collaboration lors de mon stage d'études au Western Ontario University, London, ON, à l'automne 2009.

Lors de projets se déroulant sur plusieurs années, différentes épreuves de vie risquent de survenir et elles font partie de notre formation personnelle aussi bien que les études font partie de notre formation professionnelle. Ainsi, je me dois de saluer tous les gens qui me sont chers, parents et amis(ies), vous m'avez accompagné pendant toutes ces années dans mes moments joyeux, mais aussi supporté dans mes moments plus difficiles, je ne peux que me considérer choyé d'être entouré de gens de votre trempe. Je tiens d'ailleurs à remercier spécialement mon père Ghislain Perreault et ma mère Michèle Bérubé, qui même lors de périodes difficiles, ont su montrer, à leur manière, supports, encouragements et fierté vis-à-vis mes études. On dit que les enfants sont le reflet de leurs parents, et bien je remercie les miens d'être les personnes qu'ils sont et de m'avoir inculqué de belles valeurs de vie. Enfin, je désire remercier tendrement ma conjointe Anne-Marie Champoux pour son soutien moral constant et la patience dont elle a fait preuve tout au long de l'écriture de cette thèse. Sans toi, mes multiples fins de semaine de travail auraient sans aucun doute été beaucoup moins agréables ☺.

Finalement, de vrais amis ne craignent pas de nous dire le fond de leur pensée, ainsi, après avoir entendu mille et une fois la question que tout doctorant craint: "quand crois-tu terminer ton doctorat?", on sait qu'il est plus que le temps d'achever la rédaction et de se consacrer—entièrement—à l'étape suivante, soit la poursuite de la fameuse carrière professionnelle; ce monde tant mystérieux que terrifiant si l'on se fie aux divertissantes bandes dessinées "Ph.D. Comics".

Mais tout d'abord, passons aux choses sérieuses ...

En toute humilité,
je vous souhaite,

Bonne lecture !

Introduction

"I can't define a robot,
but I know one when I see one."
- Joseph F. Engelberger

Context

The first use of the word *robot* is reported to be in the play called "Rossum's Universal Robots", for which the premiere was held at the National Theatre in Prague on January 25, 1921 [1, 2]. It was a science-fiction theatrical piece created by the Czech Karel Capek and *robot* was associated to a biological humanlike-in-appearance system that can do the work of two-and-a-half human labourers. This play was an enormous success in Europe and later in the United-States. Consequently, the word *robot* officially entered the English language in 1922 [3]. At this time, robotic systems as we know them today could only be conceived by people with a high level of imagination and they strictly belonged to the realm of science fiction.

Four decades later, the inventor and entrepreneur George C. Devol Jr. and the engineer Joseph F. Engelberger founded Unimation Corp. (for *Universal Automation*) in Danbury, CT, United-States, the world's first robotics company, based on Mr. Devol's patent [4]. Their system was called *Unimate* and was the first programmable industrial robot in the market. It was hydraulically powered and designed to learn a trajectory by storing the angles involved, enabling the robot to repeatedly perform tasks (see Fig. 0.1). This new invention was perfect to execute labours such as spot welding and spray painting in cars assembly lines of the 60s. It was so spectacular that *Unimate* even appeared on "The Tonight Show"[1], in 1966, in order to perform human tasks such as knocking a golf ball into a cup, pouring a beer and leading the orchestra. Without any doubt, from the work of Mr. Devol and Mr. Engelberger, a new era was beginning and what were only belonging to science fiction until now started to slowly become reality—a *robot* was able to perform tasks by itself.

Despite this breakthrough, more than 50 years of technological progress later, we are not yet

[1] "The Tonight Show" is a popular American late-night talk show that has aired since 1954.

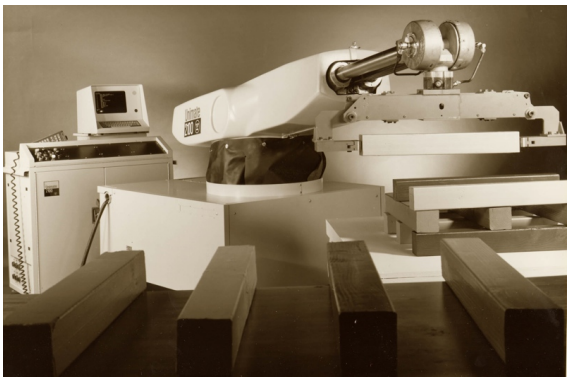

Figure 0.1 – First programmable industrial robot: *Unimate*.

sharing our daily tasks with electromechanical entities having a really high level of artificial intelligence, as per Mr. Capek's theatrical piece. In fact, before we truly live in his science-fiction world, plenty of work still remains to be done in order to fill the gap [5, 6]. But the robotics world is maturing very fast with the increasing number of new worldwide research groups and the large projects diversity which lead it, without any doubt, to a promising bright future. Currently, researchers from all around the world work at designing systems that can extend our capabilities, can assist us to become more efficient or can easily execute tasks in environments where the human being is not very welcomed. We can think of dangerous conditions such as those found under water, in fires, inside nuclear plants, etc. In fact, the lack of oxygen, the high pressure, the extreme temperatures, the high level of radioactivity and the limited access to some environments are sufficient reasons that lead to the use of articulated electromechanical systems to perform these tasks instead of humans.

Nowadays, a human is generally always involved into the control loop of current designed robots. In general, three different approaches are followed by designers. One is to define and program optimal trajectories to perform accurate, fast and repetitive tasks at the system end-effector under known external parameters, as for the robot *Unimate*. The second, mostly used when external parameters are unknown or unpredictable, is to move the end effector by direct manual control from a human. This type of system can be named an assisting device. The last method is mainly similar to the second one, but the human input is provided remotely, using a second system to indirectly control the end effector. This approach corresponds to systems called *telemanipulators* or *teleoperators*, which are defined as "*any remote-controlled machine which mimics or responds to the actions of a human controller at a distance*" [3]. This branch of mechanisms is also known as master-slave architectures because of the motion relationship between their two main parts. One part, the master, contains an end effector on which displacements are imposed by the user, and the second part, the slave, contains an end effector that mimics the master's displacements and interacts with objects inside its workspace. The distance between the master and the slave can vary from millimetres to kilometres and different scaling factors can be applied between their respective ranges of

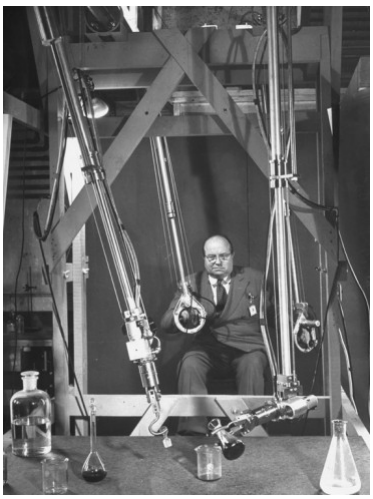

(a) Mr. Payne's design

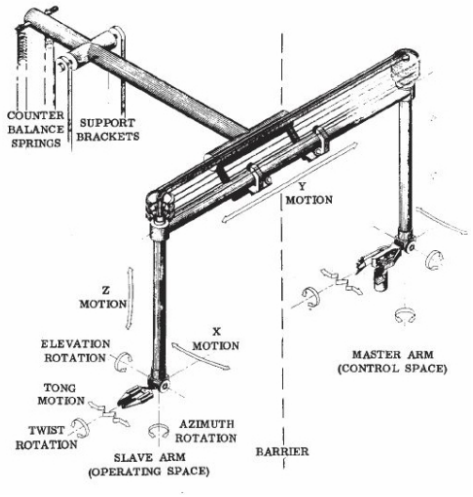

(b) Mr. Goertz's design

Figure 0.2 – First master-slave mechanisms.

motions.

From our research in the scientific literature, the first telemanipulators or teleoperators, which were purely-mechanical systems, seem to have been designed by two separate groups in the late $40s$, i.e., approximately 20 years before the invention of the programmable robot *Unimate*. One group was led by John H. Payne while he was a designer for General Electric [7]. The second was directed by Raymond C. Goertz while working as an associate director for the Atomic Energy Commission at Argonne National Laboratory in the United-States [8, 9, 10]. Their master-slave systems were both used to remotely handle radioactive material through a large protective wall in a nuclear plant. Their designs presented seven degrees of freedom in order to facilitate the grasping of multiple objects. Clearly, the purpose of these mechanisms was to eliminate human exposure to high levels of radioactivity while performing experiments. Figures 0.2a and 0.2b show the designs of Mr. Payne and Mr. Goertz, respectively.

During the following years, many researchers have developed and patented similar master-slave mechanisms, but using different approaches in order to improve their capabilities. As examples, we may cite the work of Wiesener [11], Germond *et al.* [12], François *et al.* [13], Glachet *et al.* [14] and Reboulet [15]. These works aimed at improving the accuracy of reproduced movements (between the master and the slave parts), at increasing the range of motion for each degree of freedom and at statically balancing these master-slave mechanisms. However, in return, most of these enhanced system capabilities involve higher complexity of their internal mechanics and the working distance between the master and the slave is still constrained by the rigid links which are required to transmit forces and motions.

In parallel, with the technological progress in electromechanics, researchers decided to trade

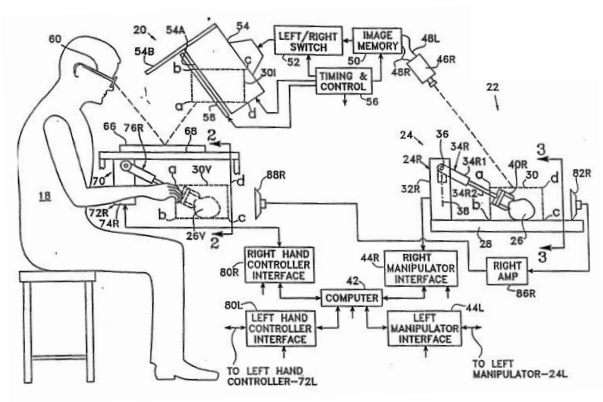

Figure 0.3 – Philip S. Green's Canadian patent 2,632,123: schematic drawing.

rigid links that were used to transmit forces and motions, with actuators and electronic components. See for instance the work of Goertz *et al.* [16] in the late 50*s*, Green [17] in the 90*s*, and more recently Brock *et al.* [18]. These US and Canadian patents present systems that use electronics and actuators in order to generate the required forces and motions. Indeed, master and slave parts that were initially mechanically connected with rigid linkages are then electrically connected with wires and driven by motors. These modifications lead to the decrease of the system's size and the internal mechanics complexity and allow a much larger potential distance between the two workstations, which brings us to the essence of the word *telemanipulator*. Moreover, research in this direction has led to the creation of another term, the word *telepresence*, which is defined as *the use of remote control and the feedback of sensory information to produce the impression of being at another location; a sensation of being elsewhere created in this way* [3]. In Green's work [17], from the Stanford Research Institute (SRI), the use of two cameras with different viewing angles for the production of stereoscopic signal provides the operator with the sensation of directly controlling the end effectors with his or her hands, regardless of the distance between the master and the slave parts (see Fig. 0.3).

All these developments on telemanipulators, during the last decades, opened the door to new applications such as telesurgery in the medical field. Indeed, since the mid 80*s*, the health-care system gradually takes advantage of new technologies in order to increase the quality of diagnoses, to improve the accuracy of surgical procedures and to facilitate the training of medical staff. The appearance of robotics in the medical field is mostly explained by the increasing precision of surgical procedures to be performed by surgeons; indeed, the actions to be taken are often at the limit of dexterity and endurance of man. Then, with the advantages inherent to these new telemanipulators, researchers were interested in investigating the possibility of developing robots for medical applications. The potential increase of dexterity, accuracy (exact reproduction of movements with different scaling factors) and stability of the end effector (no fatigue and human hand tremors filtering) were sufficient incentives to begin

(a) neuromate®

(b) neuroArm

Figure 0.4 – Assisting and master-slave neurosurgical systems.

the evaluation of their practicability.

Hence, in the last three decades, four surgical specialties have seen the major developments regarding medical robotic technologies: neurosurgery, orthopaedic surgery, laparoscopic surgery and radiosurgery. In the literature, several papers describe the history of medical robotics and provide an overview of the features and applications of the different systems designed for research and also those available on the market [19, 20, 21, 22, 23, 24]. One of the first surgical robots, which has been designed in 1985, is called neuromate® [25] (see Fig. 0.4a). This assisting device is designed to aim at a specific target inside the human brain with a very high level of accuracy. It is qualified of semi-active because it only constrains the motion of the instrument which is inserted by the surgeon. In 1989, the first robotic neurosurgical procedure was performed on a patient and neuromate® was used to place a needle for a brain biopsy using computed tomography (CT)[2] guidance.

In the same surgical field, and approximately fifteen years later, a research group has worked on the design of a robotic system compatible with magnetic-resonance-imaging (MRI)[3] to perform neurosurgery (see Fig. 0.4b). This project, which involved important financial and human resources, is called neuroArm [27, 28, 29]. The system is based on a master-slave architecture and power is electrically transmitted between the two parts of the telemanipulator. In 2008, the neuroArm system was used to perform, for the first time, an image-guided MRI-compatible robotic neurosurgical procedure on a patient. This technology was then acquired by the company IMRIS Inc. (a Deerfield Imaging Brand) and it was planned to be commercially available under the name SYMBIS Surgical System [30].

[2]Computed tomography (CT) scanning, also called computerized axial tomography (CAT) scanning, is a medical imaging procedure that uses x-rays to show cross-sectional images of the body [26].

[3]Magnetic resonance imaging (MRI) is a medical imaging procedure that uses strong magnetic fields and radio waves to produce cross-sectional images of organs and internal structures in the body. Because the signal detected by an MRI machine varies depending on the water content and local magnetic properties of a particular area of the body, different tissues or substances can be distinguished from one another in the study image [26].

(a) ROBODOC® (b) MAKOplasty®

Figure 0.5 – Assisting orthopaedic surgical systems.

In orthopaedics, the first robotic system was called ROBODOC® [31] (see Fig. 0.5a). This device was designed for total hip and knee replacements. For the hip, the robot was developed to mill a cavity in the femur for the placement of a prosthetic implant. The accurate shaping of the cavity for a precise fit and positioning of the implants for optimum biomechanics allowed for better outcomes for the patient. For the knee, the robot was able to plane the knee surfaces on the femur and tibia to achieve a precise fit of the implant. In 1992, the first human hip replacement surgery with the ROBODOC® system was successfully completed [32]. More recently, another orthopaedic robotic system has been launched in the medical market and has received the Food and Drug Administration (FDA) [26] approval for total hip and partial knee replacements, this system is called MAKOplasty® [33] (see Fig. 0.5b). It is interesting to note that these two medical robots are assisting devices for the orthopaedic surgeon to perform more precise surgical procedures (tremors filtering and limiting hand motions to within virtual boundaries) and are not telemanipulators (master-slave architectures) such as the design of Mr. Payne, Mr. Goertz and the neuroArm.

In laparoscopic surgery, three well-known telemanipulators have been mainly used in the operating rooms worldwide: the AESOP® Endoscope Positioner, the ZEUS® Surgical System and the da Vinci® Surgical System. The AESOP® (see Fig. 0.6a) is a voice-activated robotic system for endoscopic surgery created by the company Computer Motion Inc. In 1993, this became the first robot approved by the FDA for laparoscopic surgery. The system allows to steadily maneuver the endoscopic camera inside the patient's body during surgery through voice commands by the surgeon. Then, surgeon's hands are free for controlling conventional laparoscopic tools in order to perform the surgical procedure in a minimally-invasive[4] man-

[4]Minimally invasive is designating or relating to therapeutic and diagnostic techniques and procedures that minimize the extent of surgical intervention, such as laparoscopic surgery or percutaneous—through the skin—needle biopsy [3].

(a) AESOP®

(b) ZEUS®

Figure 0.6 – Voice-controlled assisting and master-slave laparoscopic surgical systems.

ner. Another system, designed by the same company was the ZEUS® Surgical System (see Fig. 0.6b), this robot consists of three table-mounted arms, one of them uses AESOP® technology while the two others are used as the surgeon's right and left hands. Then, surgeons can give voice commands to adjust their view while controlling the other two robotic arms by sitting at a console, where a tridimensional image of the surgery is provided. The ZEUS® was a more complete surgical system than the AESOP® and it has then been used to perform the first complete telesurgery in 2001 [34]. The operating surgeon was in Manhattan, NY, United-States, and the patient (a porcine specimen) was in Strasbourg, France, with more than 6 000 km of distance between each site.

In addition to laparoscopic surgery, a competitive system has been designed by the company Intuitive Surgical Inc [35]. They redesigned the telepresence surgery system created by Green (see Fig. 0.3) and developed the da Vinci® Surgical System [36, 37]. This system proposes a master-slave architecture with a console containing two master controllers, a high-definition (HD) stereo viewer and foot pedals in order to control the four anthropomorphic robotic arms belonging to the slave part. The patient cart (slave side component) contains four arms, one arm to hold a two-channel HD endoscopic camera and three additional arms to constrain the motion of different laparoscopic wristed-design tools. This system was approved by the FDA in 2000 for general laparoscopic surgery. This was followed with FDA clearings for thoracoscopic, cardiac, gynaecology, paediatric, transoral and urology procedures [38]. The system's medical-market growth is attributed to the numerous benefits inherent to its use for the patient (more significant for patients with difficult conditions) compared with open and conventional laparoscopic surgery such as smaller incisions (less scars), less blood loss, less trauma and pain due to the intuitive motion, the fixed pivot-point for the laparoscopic instruments and the improved vision and dexterity for the surgeon. All of these normally leads to a shorter recovery time and a faster return to normal activities for the patient. Until today, four generations of the da Vinci® Surgical System have been launched: the da Vinci® Standard in 1999, the da Vinci® S in 2006, the da Vinci® Si in 2009, and recently the da

Figure 0.7 – The well-known master-slave da Vinci® Si Surgical System (laparoscopic surgery).

Figure 0.8 – The image-guided CyberKnife® Robotic Radiosurgery System.

Vinci® Xi in 2014 (see Fig. 0.7, which shows the third generation–da Vinci® Si Surgical System–with dual console). In 2003, the two companies, Computer Motion Inc. and Intuitive Surgical Inc., have merged together and as of October 2017, more than 4 270 da Vinci® Surgical System robots have been installed worldwide.

Finally, in radiosurgery, a well-known system is the image-guided CyberKnife® Robotic Radiosurgery System [39] (see Fig. 0.8) which is commercialized by Accuray Inc. This system is a method of delivering radiotherapy, with the intention of targeting treatment more accurately than standard radiotherapy. The two main elements of the CyberKnife® are: (1) the delivery of beams of high dose radiation produced from a small linear particle accelerator and (2) a robotic arm which allows the energy to be directed at any part of the body from any direction. This is a non-invasive alternative to surgery for the treatment of both cancerous and non-cancerous tumours, including the prostate, lung, brain, spine, liver, pancreas and kidney. This system is based on a serial architecture, it is guided by an x-ray imaging system and it was cleared by the FDA in 2001 to treat tumours anywhere in the body.

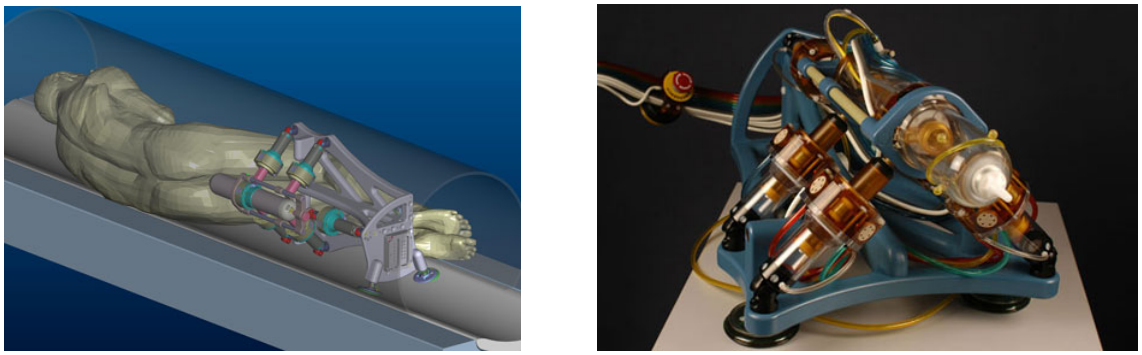

(a) CAD model (b) Prototype

Figure 0.9 – The Johns Hopkins University fully-actuated MRI robot.

Without need to say, the surgical devices discussed above are only a few among a wide range of research and industrial projects that could have been presented here. But, from the viewpoint of the author, they represent the major commercially-available robotic systems applied to neurosurgery, orthopaedic surgery, laparoscopic surgery and radiosurgery.

Similar to the progress of robotics in medicine, the imaging technologies have seen significant growth in the past years. Indeed, they have received strong interests from scientists, which have strived to improve images quality and decrease the associated computing time, which potentially leads to earlier diagnoses of diseases such as cancers. Among the different types of imaging, magnetic resonance imaging has been involved in several research projects, since this technology allows discerning different types of soft human tissues. This is useful when performing biopsies, as it allows to accurately reach the desired target in the human body [40, 41]. With these two parallel growths in the medical field, robotics and imaging, it is tempting to take advantage and merge their technologies to create complete and versatile systems, as it is clearly possible based on the achievements of the neuroArm project [27, 28].

From our research of the literature, in the last fifteen years, several robots have been designed to be totally or partially MRI compatible [41, 42, 43, 44, 45, 46]. Among those, we may cite the work of the Johns Hopkins University (JHU) team that has designed the system called *MrBot* [46, 47, 48]. This MRI-compatible five-degree-of-freedom (DoF) robot is pneumatically actuated for image-guided access of the prostate gland and can be used for fully automated brachytherapy[5] seed placement (see Fig. 0.9a for a computer-aided design (CAD) model of the device installed inside the gantry of a MRI cylindrical scanner and Fig. 0.9b for a prototype photography). Another project, based on the work of Christoforou *et al.* [44, 49], aims at developing a seven-DoF remotely controlled MRI-compatible manipulator to perform minimally-invasive interventions inside clinical cylindrical scanners. This master-

[5]Brachytherapy is a form of radiotherapy where a radiation source is placed inside or next to the area requiring treatment.

slave architecture is based on two serial kinematic chains (one for each part) and they use electrical motors and wires in order to transmit the system inputs. Then, in order to minimize the inevitable MRI image alteration, they move all electronic components in a Faraday cage. Finally, a research team from the Massachusetts Institute of Technology (MIT), DeVita *et al.*, has designed a system to perform biopsy interventions and treatments for prostate cancer therapy within the bore of a MRI system [43]. This project proposes a parallel mechanism actuated by bistable components in order to generate discrete movements to the tool. Except for some of them, including the neuroArm, a majority of the MRI-compatible systems found in the literature only have few degrees of freedom and a limited workspace.

The manufacturing of MRI-compatible robots, which requires particular attentions from designers because of the numerous constraints associated to the use of this type of imagers [41, 42, 49], can easily lead to the increase of the project cost. Among those, we can point to the use of non-magnetic and non-conductive materials (such as plastic, ceramic, fibreglass, carbon fibre and other composite materials) and of non-electromagnetic motors (as per examples: manual, hydraulic and pneumatic actuation or ultrasonic and piezoelectric actuators). These constraints stem from the necessity of controlling the robotic system even when subjected to the strong electromagnetic fields, inherent to MRI scanners. Conversely, the chosen materials and driving components must not alter the images quality. Finally, the use of the system, in combination with the scanner, must not present any additional risk to the patient (it must be MRI-safe). If these constraints are satisfied, then the physician will have high-quality real-time images feedback while doing the surgical procedure and will be allowed to stay outside of the MRI environment during the operation, thus minimizing his or her exposure time to the strong magnetic fields.

Having this in mind, the Laboratoire de robotique de l'Université Laval has proposed to design a new type of mechanism that will be based on a purely mechanical master-slave architecture. This concept, that will be manually actuated, can be placed in the same category that the telemanipulators designed by Mr. Payne and Mr. Goertz in the late 40*s* (Figs. 0.2a and 0.2b) and, consequently, may be seen as a step backward when comparing to all of the technological improvements done in robotics over the past decades. But in fact, the long-term objective here is to develop a more-affordable alternative system, i.e., a low-cost and relatively low-complexity device with a six-DoF workspace and reasonable performances. Moreover, as per the recent works presented in the previous paragraphs, this type of systems would be ultimately compatible to be used in a MRI environment. However, compared to a project as the neuroArm, which is intended to high-precision human-brain neurosurgery and involves considerable financial support, the expected design here will be rather intended to surgical procedures such as simple image-guided biopsies performed inside the bore of a conventional MRI cylindrical scanner, as it is the case for other projects such as at the MIT [43] and JHU [46].

Figure 0.10 – Example of a MRI scanner: the MAGNETOM® Skyra three-tesla MRI system from Siemens.

Objectives and Contributions

With the technical enhancements of MRI scanners over the past years, numerous medical interventions now take advantage of this type of imaging devices. However, one of the most restricting problems is the fact that MRI devices (for an illustrated example, see Fig. 0.10 for a three-tesla MRI device designed by Siemens [50]) and the majority of current medical robotic systems cannot be used within a common work area due to the constraints inherent to this type of imagers. As presented in the previous section, several projects aim at developing robotic systems that are MRI-compatible. But most of them show a high level of complexity and entail high manufacturing costs. Hence, it would be interesting to develop a new class of telemanipulators, fully compatible with MRI systems, that have sufficient performances for simple telesurgery applications, that allow a surgeon to minimize his or her time of exposure to the high-level electromagnetic field, and which present a low manufacturing cost when compared to currently commercialized medical robotic systems, i.e., a good compromise between performances and costs.

Moreover, the development of surgical robots is highly demanding when compared to other fields of applications. This is due to the restrictions associated with surgery, such as the necessity to clean and sterilize the various tools, the generally limited space where the system has to fit, the required level of ergonomics, the proximity of humans sharing the same workspace, and the direct contacts with the patient's body [19, 21]. Thence, the focus of this project will be placed on the reliability of the telemanipulator, i.e., the impossibility of an unintended loss of control, which is ensured by a manual actuation. In fact, this type of applications requires an absolute surgeon's confidence as this aspect is one of the main decisive points when choosing any medical devices. In addition, the system must allow a reduction of the surgeon's motions by a given scaling factor, and, if possible, elimination of his or her hand tremor and transmission of the forces applied at the end effector to the hand of the operator. The design must also present a fast and easy installation process and an intuitive control.

Following these requirements, the current thesis presents the first steps towards the development of a new family of mechanisms called *cable-driven pantographs* (CDPs). The main objective here is to develop relevant tools required to determine a suitable design, optimize the geometry and enhance the capabilities of these new mechanisms. They are expected to entail a low cost, to be safe, reliable and to consume little energy due to a purely-mechanical design (no electrical components will be involved in the design). To the best knowledge of the author, no mechanisms similar to the one proposed in this thesis, i.e., CDPs, have been previously reported in the scientific literature. This project will ultimately lead to the design of a six-DoF CDP, which will be conceptually optimized to manipulate needles inside an MRI scanner in order to perform image-guided punctions or simple biopsies on patients.

As it will be described in this thesis, the design of purely-mechanical telemanipulators actuated by cables brings up significant difficulties. Indeed, many constraints must be taken into account to produce a telemanipulator that shows reasonable performances [8] and to overcome drawbacks inherent to relying on cables to transmit forces between the master and the slave [51, 52]. One of these difficulties is the fact that a minimal tension must be constantly kept in cables in order to preserve the mechanism geometry. A second difficulty is that a neutral static equilibrium should be reached and guaranteed over the system workspace in order to minimize the energy input required from the operator to move the end effector. A third challenge is that the multiple-cable-actuated mechanisms must be designed in a way to minimize or avoid any cable interferences (cable contacts) within its own workspace to ensure a suitable control of the end-effector pose.

Then, in summary, the work proposed in this thesis should contribute to scientific progress by the following innovations:

- The development of a new family of telemanipulators, i.e., the CDPs;
- The development of the kinematic and kinetostatic models associated to the n-DoF CDPs;
- The development and evaluation of a methodology allowing an approximate static equilibrium of the CDPs, i.e., to minimize its potential energy fluctuations over a given workspace;
- The development of a general method to geometrically determine the occurrence of mechanical interferences involving the cables used to constrain the pose of the CDP end-effector;
- The development of a global methodology to dimensionally synthesize the geometry of CDPs that fulfill application-based requirements.

Finally, all of these contributions put together represent a significant step towards the design of a six-DoF CDP-type telemanipulator to be installed inside a conventional MRI scanner.

Nomenclature and Organization

First, in order to facilitate the reading of this thesis, it is necessary to define the chosen nomenclature. Then, in general, a lower-case italized letter such as "x" represents a scalar, while a capital italized letter such as "X" is associated to a point or a line. The use of bold font is reserved to objects having more than one component such as "$\mathbf{x}$" for a vector (lower-case letter) and "$\mathbf{X}$" for a matrix (capital letter). Calligraphic letters such as "$\mathcal{X}$" are used to identify reference frames, subspaces or sets such as a line segment.

The system of measurement units used throughout this thesis corresponds to the modern form of the metric system, i.e., the International System of Units [53]. The length, mass and time units are the metre m, the kilogram kg and the second s, respectively. As for the derived units of the SI system such as the plane angle, the force and the torque, they are represented by the radian rad (and, when specified, by the degree $^\circ$), the newton N and the newton-metre N·m. Finally, the positive direction of a rotation along a given axis follows the right-hand rule.

The current work is divided in four main chapters, the order of which is not chronological but rather logical. This choice is made to ease the overall understanding of the reader. It goes without saying that by nature, research follows a path strewn with successes and failures and, as a result, the order in which the work has been done is not necessarily always the order in which it has to be presented.

Chapter 1 defines the new class of telemanipulators, i.e., the CDPs, which are a blend of conventional pantographs with the cable-driven parallel mechanisms (CDPMs). The working principle of CDPs is then demonstrated by describing the one-DoF fundamental component of a CDP, the architecture of a general n-DoF CDP, the input-output displacement and load relationships inherent to this family of telemanipulators and their kinetostatic modelling. As a proof of concept, the design of a three-cable two-DoF CDP prototype is then presented as well as a verification of its performances.

Chapter 2 describes a methodology aimed at improving the CDP performances by the introduction of nonlinear springs to maintain minimum cable tensions while approximating the static equilibrium over the mechanism workspace. We first present the definition of an approximate static equilibrium, a concept that is then applied to a three-cable two-DoF CDP. The minimum cable tensions are first determined in order to approach as much as possible the static equilibrium and, based on the resulting tension profiles, the nonlinear spring parameters are determined using an optimization technique. This method is implemented on the prototype presented in Chapter 1 in order to validate the results.

Chapter 3 reports an exhaustive analysis of the mechanical interferences phenomenon that can occur between a pair of cables constraining the pose of the end effector of a CDP as well as between a cable and an edge of the same end effector. This methodology, first created to facilitate the development of CDPs, is directly applicable to any CDPM. In this chapter, the definition of a mechanical interference is initially presented with its application to planar CDPMs. Then, this analysis is extended in order to geometrically determine the mechanical interferences loci within the constant-orientation end-effector workspace of any generic spatial CDPMs. The technique is first applied to the determination of the interference regions for a pair of cables and secondly applied to the determination of the interference regions for a cable and an end-effector edge. The technique is validated through its use on a six-cable six-edge six-DoF CDPM and then an eight-cable 31-edge six-DoF CDPM.

Chapter 4 then demonstrates a dimensional synthesis method to determine the geometric parameters of a CDP (or a general CDPM) for a specific application, e.g., for a particular prescribed workspace. The three criteria on which this optimization technique is based are first defined: the constant-orientation wrench-closure workspace (COWCW), the constant-orientation cable-cable interference (COCCI) and the constant-orientation cable-edge interference (COCEI). In order to validate the proposed synthesis technique, the resulting method is applied to the synthesis of a seven-cable nine-edge six-DoF CDPM with an arbitrarily-chosen prescribed workspace. Finally, the same methodology is applied to optimize the geometric parameters of a novel eight-cable seventeen-edge six-DoF spatial CDP which would be applied to the coveted medical application, i.e., to manipulate needles inside the bore of a MRI system in order to perform simple image-guided punctions or biopsies on a patient.

Finally, this thesis is concluded with a summary of its main scientific contributions. Since the current work presents the first steps towards the development of a new family of mechanisms called cable-driven pantographs, a complete list of propositions for future work and research lines is then provided. These guidelines could serve as a source of inspirations for future researchers in order to lead this project to its coveted goal, i.e., the design and prototyping of a MRI-compatible six-DoF CDP aimed to perform simple image-guided biopsies inside the bore of cylindrical MRI scanners.

Chapter 1

Cable-Driven Pantographs and Their Working Principle

"Necessity ... the mother of invention."
- Plato

This chapter unveils the premise of the work presented in this thesis, i.e., the development of a new class of pantographs, a type of mechanisms that allow the reproduction of the displacements of an input link, the master, at an output link, the slave. The application we envision for these devices is the telemanipulation of objects from small distances, at low cost, where magnetic fields or other design constraints prohibit the use of electromechanical systems. Despite the long history of pantographs, which were invented between the 15^{th} and the 17^{th} century, the class of pantographs proposed here is new, as it relies on cable-driven parallel mechanisms (CDPMs) to transmit the motion. This allows the reproduction of rigid-body displacements, while the majority of previous pantographs were limited to point displacements, in order to copy and scale diagrams and writings.

Since this new type of mechanisms, called *cable-driven pantographs* (CDPs), lies in the middle between conventional pantographs and CDPMs, these two distinct families of devices are first defined for the reader in Sections 1.1 and 1.2, respectively. The working principle of CDPs is then presented in Section 1.3. More specifically, Sub-sections 1.3.1 and 1.3.2 describe their basic geometry, for a one-DoF and a n-DoF CDP, respectively, and Sub-section 1.3.3 contains the derivation of the input-output displacement relationship associated to CDPs with its validation by means of numerical simulation. Moreover, Sub-section 1.3.4 presents the input-output load relationship inherent to CDPs while Sub-section 1.3.5 proposes the formulation of their kinetostatic model. From Section 1.3, it is shown that one important challenge in the design of the proposed systems is that the cables must remain taut at all times. We address this issue by adding springs that passively maintain a minimum tension in the ca-

bles. As a preliminary validation, the behaviour of this conceptual design is experimentally tested by building the first three-cable two-DoF planar CDP in Section 1.4. Sub-section 1.4.1 shows the prototype of this apparatus and Sub-section 1.4.2 reports the experimental evaluation of its performances, results that demonstrate the practicability of this new class of pantographs. Finally, a brief summary that highlights the main results obtained from this chapter is presented in Section 1.5.

1.1 Pantographs

The word *pantograph* may be decomposed into its Greek roots *panto* and *graph*, which respectively mean *all* and *writing*. In the literature, it is commonly used to represent three different kinds of mechanisms. The first meaning of the word *pantograph* according to the Oxford English Dictionary [3] is *an instrument for the mechanical copying of a plan, diagram, pattern, etc., especially on a different scale, typically with two drawing points connected by an adjustable parallelogram of jointed rods. Also: any of various similar mechanisms for automatically guiding or scaling the motion of a cutter, stylus, etc.*

According to this definition, the first pantograph seems to have been constructed in 1603 by Christoph Scheiner[1], who only gave a written account of his invention in 1631 [54]. This device allowed the reproduction of the displacements of a point in the plane, and was intended for copying drawings. As shown in Fig. 1.1, this first pantograph was designed with rigid planar links, which were connected with passive revolute joints. Two pencils were fixed to this mechanism, one handled by the user to follow the contours of the original drawing and the second constrained to follow the same motion but at a distance. The mechanism is based on a parallelogram geometry, the scaling ratio between the original and the copied drawings being determined by the ratio of the lengths of the segments within the linkage. Indeed, and as we can observe in Fig. 1.1, the scaling factor is defined by the ratio between the lengths of segments $\overline{KS}$ and $\overline{IR}$, i.e., $\overline{KS}/\overline{IR}$. It should also be noted that, in order to have the exact original image proportion applied to the resulting image, $\overline{IM} = \overline{KL}$ and $\overline{IK} = \overline{ML}$ must be true, i.e., these segments must form a parallelogram geometry.

Since Scheiner's device, researchers have published and patented different versions of the original two-DoF pantograph. We may cite some relatively recent work such as the patent of Plumbley [55], who designed a system that automatically cuts metal sheets by following the irregular lines of the original shapes; The patent of Plese [56], who designed a purely mechanical pantograph based on a new shape of metallic links; The patent of Valois [57], who created a pantograph with a linkage geometry that is perpendicular to the working plane instead of being parallel as in previous designs; And the patent of Blain [58], who proposed a

[1]Note: Even if some report that Leonardo da Vinci, Michelangelo and various ancient Greeks may have used a pantographic device as early as in the 15^{th} century, no archived and clear evidence has been found by the author.

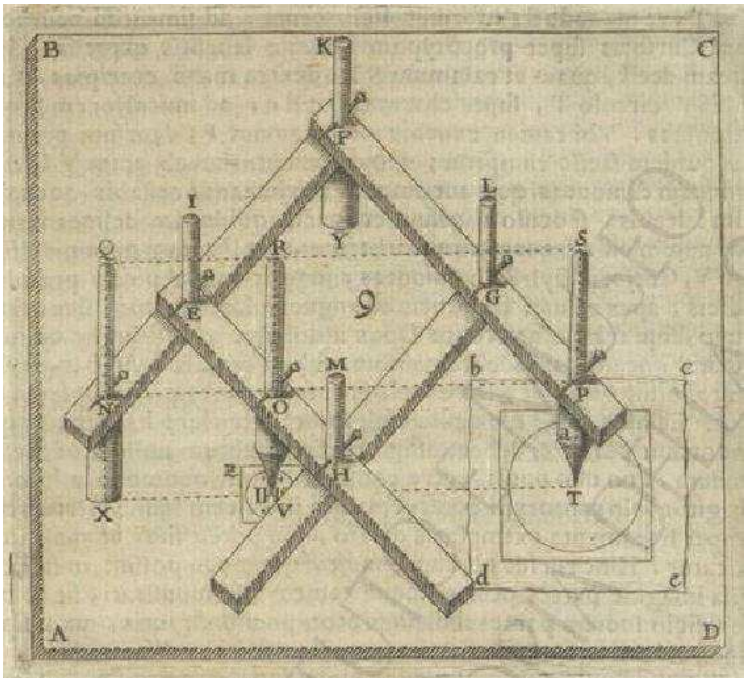

Figure 1.1 – First definition of *pantograph*: Scheiner's pantograph.

new architecture based on a transmission of motion built from gears and a worm screw in order to increase the reproduction quality. Other interesting reports include a new design that can modify the scaling factors independently along two mutually perpendicular directions [59], a family of feasible geometries to generate the pantograph behaviour [60] and the design of pantographs based on compliant mechanisms [61].

Moreover, work has also been done on three-DoF pantographs (see Fig. 1.2a for a three-DoF pantograph that was patented in England by Benjamin Cheverton in 1844 [62]). Such mechanisms have been extensively used for sculpting, machining and engraving applications, when an existing part or feature is to be reproduced [63, 64]. Still today, several companies sell three-dimensional pantographs, which reproduce the displacements of a point in space (for example, see Fig. 1.2b [65]). In contrast with these pure-translational mechanisms, a three-DoF pantograph that transmits pure rotations was also patented by Reboulet [66]. This patent enumerates different possible assemblies of mechanical and electromechanical components in order to produce the intended behaviour. It should be noted that all of these purely-rotational mechanisms present the particularity to have a rigid link that supports their end effectors and contains a spherical joint at its extremity to allow for rotations about a fixed point.

A second definition for the word *pantograph* is: *a jointed, self-adjusting framework on the top of an electric vehicle for conveying the current from overhead wires* [3]. This class of pantographs has been widely used in the design of the electrification system for high-speed

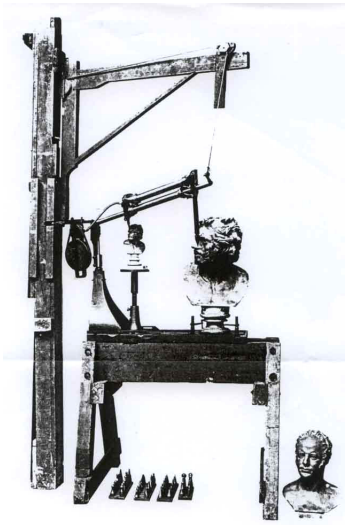

(a) The Cheverton's sculpturing machine

(b) A market-available three-DoF pantograph

Figure 1.2 – First definition of *pantograph*: two examples.

(a)

(b)

Figure 1.3 – Second definition of *pantograph*: two different designs of pantographic mechanisms installed on electrical trains.

trains (see Fig. 1.3 for two examples). We can easily find in the literature work done on these mechanisms such as, for examples, papers reporting on their design and dynamics analysis [67, 68, 69].

Finally, a third definition for *pantograph* is *any of various other adjustable supporting or extending mechanisms in the form of a diamond-shaped trellis or lazy tongs* [3]. This class of pantographs has been widely used in the design of commercialized products such as lazy-tong riveters (Fig. 1.4a), extendable shaving mirrors (Fig. 1.4b) and scissor-lift systems (Fig. 1.4c). Moreover, some researchers have used this kind of mechanisms for the design of deployable structures [70, 71, 72, 73, 74] and others for the development of haptic instruments [75, 76].

(a) A lazy-tong reviter

(b) An extendable mirror

(c) A scissor lift

Figure 1.4 – Third definition of *pantograph*: three examples.

For the purpose of this thesis, the word *pantograph* will be referring to the first definition, i.e., a mechanism that allows the reproduction of displacements according to a constant scaling factor between its master and its slave parts. Based on this definition, we note that pantographs can also be seen as a type of *telemanipulator* or *teleoperator*. Moreover, since the end effectors of our pantograph—one for the master and one for the slave—will be driven by cables attached in parallel, the *cable-driven pantograph* will show a behaviour similar to that of conventional cable-driven parallel mechanisms.

1.2 Cable-Driven Parallel Mechanisms

Cable-driven parallel mechanisms are now well-known architectures within the robotics community. In general, these systems rely on four main components: a base frame, servo-actuated winch assemblies, cables and an end effector (also called a moving platform). Figure 1.5a shows a schematic model of an arbitrary four-cable three-DoF planar CDPM. The winch assemblies serve to wind the cables, i.e., to control their lengths and tensions. Normally, these anchor points, noted A_i, here $i = 1, \ldots, 4$, are fixed to a base frame. The end effector, which in the example of Fig. 1.5a has three DoFs, i.e., two translations of the reference point P $\{x, y\}$ and one rotation $\{\phi\}$, is constrained to move in the workspace defined by the points A_i (here the workspace is a section of a plane) and contains the attachment points B_i. Finally, the cables $\overline{B_iA_i}$ connect points B_i to their respective points A_i and modifying their lengths simultaneously allows the generation of controlled trajectories and wrenches at the end effector.

The growth in popularity of CDPMs, which can be observed by the increasing number of related papers in the literature during the past years [77], is due to the many advantages held by these mechanisms over conventional robots, where rigid links are used to control the end-effector pose in space. Scientists generally agree on the following:

- Light weight of the moving parts;

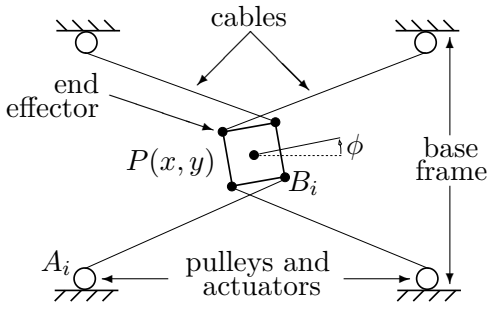

(a) An arbitrary four-cable three-DoF planar CDPM

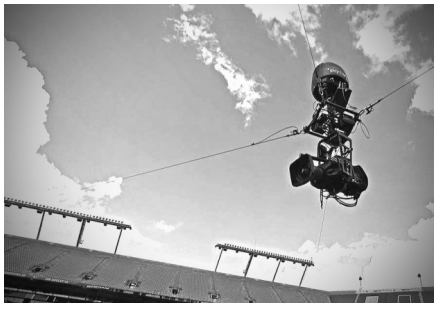

(b) The commercialized SKYCAM system

Figure 1.5 – Two examples of CDPMs.

- Higher accelerations due to a better ratio payload/weight of the moving parts;
- Larger workspace than conventional manipulators;
- Higher stiffness than serial manipulators;
- Modularity and portability;
- Low cost.

Due to the use of cables instead of rigid links, moving parts have lower inertias, which allows for larger accelerations for a similar payload (cables generally have a negligible mass compared to the payload). Also, the fact that cables are wound on reels leads to the possibility of covering a larger workspace because of the theoretical non-existence of a length limit [78, 79, 80]. Based on their parallel architecture, and depending on the chosen cables elasticity and actuators backlash, CDPMs generally show a higher stiffness at their end effector than serial robots [81]. The modularity and the potential portability of this kind of mechanisms are additional benefits inherent to their use. In general, it is easy to modify the workspace of a CDPM only by adjusting the position of one or a few pulley-actuator assemblies. Finally, the cost related to the purchase of cables is considered to be less than that involved when rigid parts need to be designed, machined and assembled.

Because of these non-negligible advantages over conventional robots, many designs and prototypes have been developed by worldwide researchers and these systems were applied to a wide range of applications. For example, CDPMs have been used to design cable-driven haptic interfaces [82, 83, 84, 85, 86, 87, 88, 89, 90, 91, 92, 93], a virtual swimming interface [94], upper-limb neuro-rehabilitation systems [95, 96], a wire-driven leg rehabilitation system [97, 98], a locomotion interface [99, 100, 101, 102, 103, 104], an active suspension for wind tunnels [105, 106, 107], an air vehicle simulator [108, 109], a sports simulator [110], a safety-related system for land demining [111], systems for the research and aid after natural

disasters [112, 113, 114], a mechanism for capturing object appearance [115] and some very large radiotelescope concepts [78, 79, 116, 117]. In addition, other groups have focused on industrial applications such as high-speed manipulators [118, 119], a waste storage tank remediation system [120] and a welding device for environments hostile to human workers [121]. Another team of researchers has developed a family of CDPMs particularly designed for medium and large-scale industrial handling and assembly tasks [122]. More recently, a group has worked on the design of a MRI-compatible CDPM [52, 123, 124]. Finally, CDPMs are now also available on the market for some specific applications. For example, a well-known commercial system is the SKYCAM [125] (see Fig. 1.5b), which is used for live video shootings during sport events held in large stadiums. It goes without saying that all of these projects represent only a small part of the research done on CDPMs, but they clearly demonstrate the wide range of potential applications of this class of mechanisms.

Other than their applications, CDPMs have also been the topic of many studies in order to understand, describe and improve their behaviour. We may cite some of the work done on their inverse and forward kinematics [126, 127, 128, 129, 130, 131], their kinematic sensitivity [132], their dexterity [133], their singularity analysis [134, 135, 136] and their workspace analysis [137, 138, 139, 140, 141, 142, 143, 144, 145, 146]. More specifically, some have evaluated their wrench-closure workspace (WCW) [147, 148, 149, 150], and some others, their wrench-feasible workspace (WFW) [151, 152, 153, 154]. These workspaces may be roughly defined as the reachable CDPM workspace where all or a set of the possible wrenches can be generated at its end effector by tightening a combination of its cables. In addition, other work has focused on the performance of under-constrained CDPMs [155, 156, 157, 158, 159, 160, 161, 162], the force distribution of over-constrained CDPMs [101, 102, 163, 164, 165, 166], different tools for their kinematic synthesis [99, 100, 167, 168, 169, 170, 171, 172, 173], and finally, some researchers have published papers on their dynamic analysis, their control and their calibration [174, 175, 176, 177, 178, 179, 180, 181, 182, 183, 184, 185, 186].

However, even if CDPMs have been extensively used and studied by many groups of researchers worldwide, one must be also aware of the drawbacks inherent to their use:

- Unilaterality of the force transmission through cables;
- Necessity of having $n+1$ cables to fully constrain a n-DoF CDPM;
- Possibility of mechanical interferences between two cables and between a cable and an object inside the workspace (such as the CDPM end-effector's geometry itself);
- Lower stiffness than conventional parallel manipulators (possible vibrations of the moving parts).

In fact, by their nature, cables cannot push on an object; They can only pull. This unilaterality of force transmission with cables leads to the need of having at least two cables when one desires to design a fully-constrained one-DoF CDPM, i.e., two different cables are necessary to pull on the end effector in order to move it towards both directions of this DoF. By extending this reasoning fact to n-DoF CDPMs, we obtain a minimum of $n + 1$ cables to suitably constrain n DoFs [82, 148]. Therefore, having more cables than degrees of freedom also leads to a higher risk of collisions between these cables [99, 101, 103, 187, 188]. Indeed, these cables are all attached in parallel to the same end effector, which, when moved, can easily induce interferences. Finally, if the cable tension is not sufficiently high and the material properties of the cables are not suitable for the application, the system stiffness is reduced and vibrations of the moving parts can be observed, which can decrease the accuracy of the CDPM [81, 189].

It is also interesting to note that another indirect drawback is the necessity to keep the cables taut at all times to preserve the geometry of the mechanism. As a result, even when no external wrench is applied on the moving platform, continuous power is needed from an external input system (most of the time from electrical motors) in order to ensure a minimal cable tension. This can be seen as a lack of safety (e.g., during a power failure) and an unnecessary expenditure of energy, which is a long-term drawback for the use of CDPMs.

1.3 Cable-Driven Pantographs: Working Principle

Until today, and to our best knowledge, current pantographs—more specifically, those corresponding to the first definition as given in Section 1.1—are generally designed to either reproduce the displacement of a point on a plane or in tridimensional space or to transmit pure rotations. When it comes to reproducing arbitrary rigid-body displacements in space, i.e., both translations and rotations, all existing solutions require the introduction of actuators. Such solutions are applicable in many cases, but in some others, cost, reliability, or compatibility reasons prohibit the use of electricity or of other sources of energy.

In this thesis, we propose to replace these active devices with a passive one, namely, a purely mechanical device that transmits a part of the applied forces. We call this mechanism a *cable-driven pantograph*, since it relies on cables to reproduce the rigid-body displacements of a master end-effector at a slave end-effector. Basically, a cable-driven pantograph (CDP) contains two CDPMs with a linkage system that connects both mechanisms together. One CDPM—the master—is manipulated by the user and the second one—the slave—reproduces the displacements generated at the master following a chosen scale factor κ_s.

Such mechanisms offer several advantages over conventional telemanipulators, due to two main characteristics: (*i*) they are purely mechanical and (*ii*) they are formed with cable-driven parallel mechanisms.

The first characteristic (*i*) makes cable-driven pantographs suitable for low-cost applications, which preclude the use of servomotors, electric drives and controllers. Moreover, these purely mechanical devices may be regarded as more reliable, since they involve fewer components than other electrically actuated machines, and do not rely on software. Such a characteristic is thought to be important when one needs to manipulate hazardous material from a distance, for instance. CDPs are also interesting for applications where conventional actuators are incompatible with the work environment. Such incompatibilities may occur because of intense magnetic fields, for example, or the unavailability of electrical power.

The second characteristic (*ii*) calls for the same advantages as those of cable-driven parallel mechanisms over conventional robots. As described in Section 1.2, the robotics community generally acknowledges six main advantages. First of all, because the end effector and cables are the only moving parts, the inertia of the mechanism is extremely low. This fact, that leads to the second advantage, generally allows CDPMs to reach higher accelerations than other robotic manipulators [190]. Thirdly, cable-driven parallel mechanisms can have very large workspaces [191], since their cables can extend over long distances. Fourthly, CDPMs can show higher stiffness than serial manipulators due to their parallel architecture [81]. Fifthly, these mechanisms are modular, because the reels on which the cables are wound can be easily dismounted and reconfigured to accommodate a new workspace, and the parts of the mechanism are light and easily disassembled, then the mechanism is portable [192]. And sixthly, the manufacturing cost of CDPMs is normally lower than that of conventional robots because less parts have to be machined. In the context of the reported cable-driven pantographs, the reader should note that a lower inertia of the pantograph implies a smaller difference between the inertia controlled by the user and the inertia he would control if he was directly manipulating the payload without the mechanism, i.e., moving the CDPM's end-effector of the slave instead of the master.

One of the applications envisioned for cable-driven pantographs is simple MRI-guided surgery. Indeed, as briefly discussed in the Introduction, compatibility problems arise when designing a telemanipulator that is to operate inside an MRI device [41, 42, 49, 193]. In such a case, conventional electric motors cannot operate in the same room as the scanner. In order to resolve this problem, one can place the electric motors in a different room and transmit the mechanical power to the scanner through a mechanism [194]. Another approach is to use ultrasonic motors, which rely on piezoelectricity instead of electromagnetism in order to produce mechanical power from electricity [195]. However, ultrasonic motors need to be located outside of the scanner bore, since the high voltages they require degrade the MRI measurements. These facts push in favour of cable-driven pantographs as an alternative to conventional telemanipulators that is perfectly compatible with an MRI environment.

Because of the potentially large workspace of CDPs, they could also be used to scan large objects [115]. By using a scaling factor greater than one between the master and the slave, the

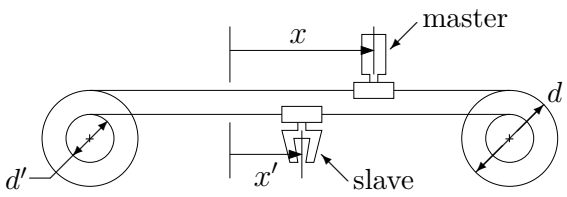

Figure 1.6 – Fundamental component of the proposed n-DoF CDP.

operator could theoretically scan a volume of tridimensional space larger than that he could normally reach. He could then quickly perform scans for applications such as inspection, reverse-engineering, and tridimensional animation, for example.

Having as goal, in this thesis, to develop tools to facilitate the design of a low-cost, high-reliability telemanipulator that would allow the manipulation of objects from small distances, the simple principle on which our proposed design is based on is described in the following sub-section.

1.3.1 Fundamental Component

The fundamental component of cable-driven pantographs is presented in Fig. 1.6, where it is shown as a generator of pure translations with one degree of freedom. In this design, the *master* is in direct contact with the user, while the *slave* performs the task as the end effector of a robot, i.e., that its displacements are prescribed. It must be noticed that cables ends are attached to their respective pulleys. Also, this architecture preserves the similitude between the manipulators for any end-effector position. In fact, the slave translations are in proportion with those of the master, namely,

$$x' = \kappa_s x, \tag{1.1}$$

where κ_s is simply the ratio of the diameters of two pulleys, i.e., $\kappa_s = d'/d$. We use cables for the transmission of forces between the master and the slave, which ensures a low inertia of the telemanipulator and generally suits well the transmission of forces over a few metres. Moreover, here the reader should note that we make the hypothesis that cables are perfect line segments without mass, which was proven a suitable assumption for this size of mechanisms, based on the work of dit Sandretto *et al.* [196].

The architecture presented in Fig. 1.6, however, has a problem regarding its forces equilibrium. Indeed, this current version cannot maintain the necessary tension in the cables at all times, and then fulfill our previous hypothesis regarding the straightness of cables. Thus, this mechanism cannot keep its geometry, i.e., it is not in equilibrium.

In order to ensure a minimum tension $t_{\min}$ in the cables while avoiding any electronics, we resort to springs. Another solution could be the use of counterweights, but, for practical

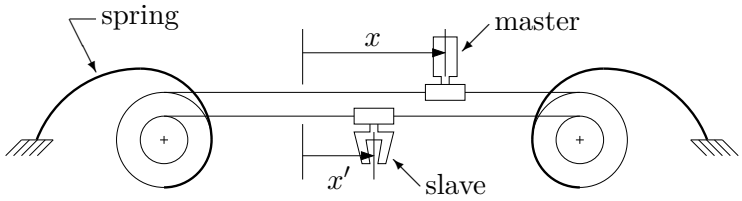

Figure 1.7 – Fundamental component of the proposed n-DoF CDP with springs.

reasons such as the preservation of a low inertia of the moving parts and compactness, we prefer springs. In the case of the linear one-degree-of-freedom pantograph of Fig. 1.6, the natural choice would be springs that apply constant forces, regardless of the displacement. Such springs, which are available on the market (see, for example, the *Neg'ator Springs*, from the SDP/SI company [197]), maintain the system in a neutral equilibrium while the cables remain in tension. Figure 1.7 presents the fundamental component of CDPs with springs attached to pulleys in order to provide the required passive forces to keep the cables taut at all times. In general, notice that neutral equilibrium cannot be reproduced with simple springs for mechanisms with $n > 1$ degrees of freedom, at least, not exactly, since the positions of the eyelets or pulleys are usually fixed in the workspace and non-zero resulting forces are generally encountered.

1.3.2 General Description

Based on the fundamental component of cable-driven pantographs shown in the previous subsection, a CDP with multiple degrees of freedom can be constructed by assembling several instances of the elementary concept shown in Fig. 1.7. As a result, a generic cable-driven pantograph with six DoFs and actuated by m cables is schematized in Fig. 1.8. The master and the slave are two cable-driven parallel manipulators whose geometries are the same, up to a scaling factor κ_s. The user controls the moving platform of the master, and the task is accomplished at the moving platform of the slave. Cable i, $i = 1, \ldots, m$, of the master, which is attached to point B_i on the master end-effector, passes through a base-fixed eyelet A_i, and reaches pulley i, which consists of two drums and a spring. The cable winds on one of the two drums, and is kept in tension by the spring between the pulley and the base. The second drum winds the corresponding cable i', $i' = 1, \ldots, m$, of the slave, which runs through an eyelet A'_i and connects to the moving platform of the slave through point B'_i. Notice that the ratio of the diameter of the two drums of the i^{th} pulley must be equal to the ratio κ_s of any corresponding lengths on the master and the slave. As a result, we call the device of Fig. 1.8 a *cable-driven pantograph*.

1.3.3 Input-Output Displacement Relationship

In order to elaborate the input-output displacement relationship of generic cable-driven pantographs with n degrees of freedom, we can, in a general manner, schematize this mechanism

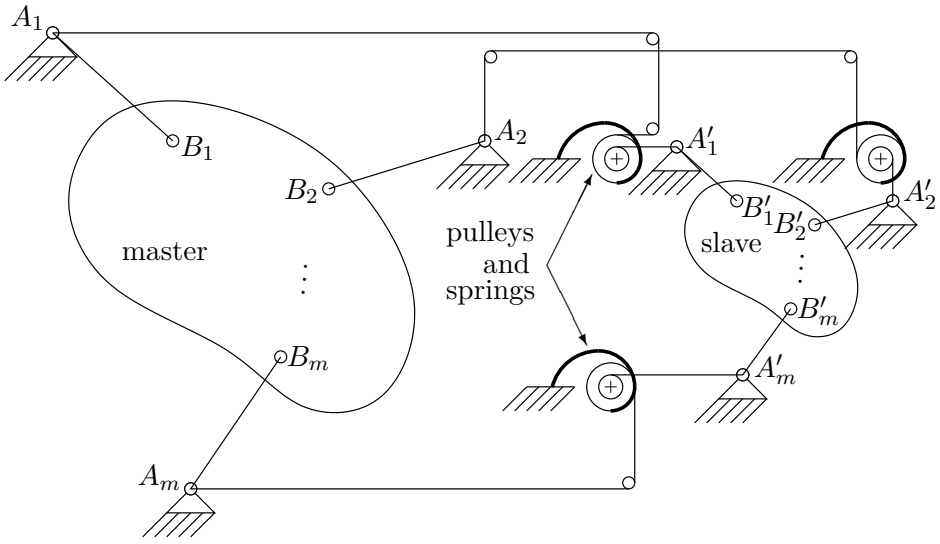

Figure 1.8 – A generic six-DoF cable-driven pantograph.

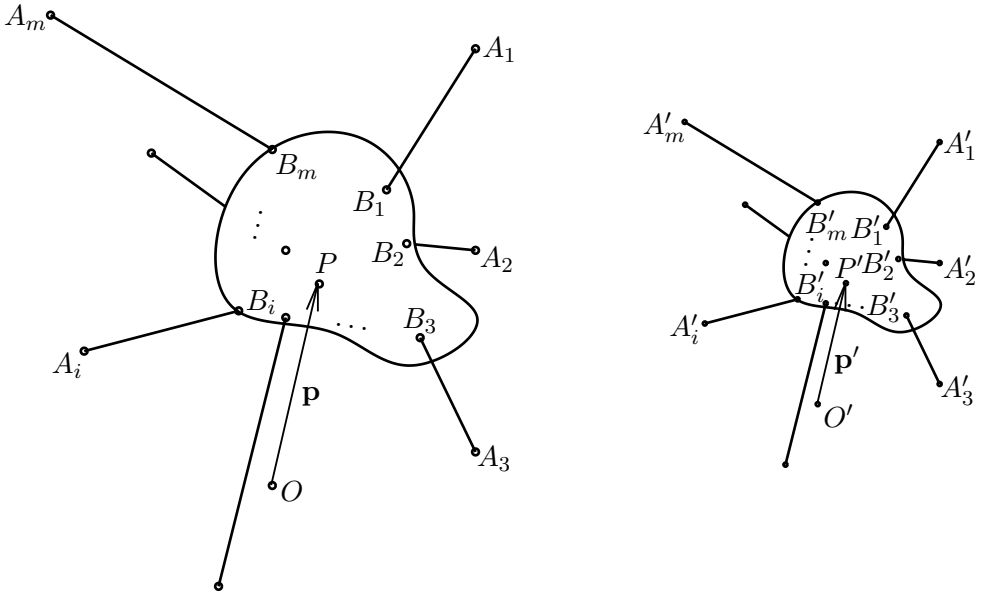

(a) The master (b) The slave

Figure 1.9 – Schematic representation of a CDP.

as shown in Fig. 1.9. As specified in Sub-section 1.3.2, the master and the slave CDPMs are similar regarding their respective geometry, i.e., their counterpart lengths follow a constant ratio κ_s. Then, the transmission ratio (winding and unwinding ratio of the cables between the master and the slave) is chosen equivalent to this same ratio κ_s. Moreover, $\mathbf{p}$ represents the position vector of the master's reference point P relative to the origin point O on the base and $\mathbf{p}'$ is the position of the slave's reference point P' from the origin point O'.

In Fig. 1.9a, points A_i and B_i represent respectively the attachment points of cable i on the base and the end effector of the master part, while in Fig. 1.9b, points A'_i and B'_i represent the attachment points of the cable i' on the base and the end effector of the slave mechanism, respectively.

These two CDPMs are mechanically connected by their counterpart cables, which wind following the constant ratio κ_s. Therefore, any displacement of the master end-effector generates a variation Δc_i of the length c_i of the i^{th} cable of the master in its reference pose. These length variations result in variations $\Delta c'_i = \kappa_s \Delta c_i$ of the lengths c'_i of the cables of the slave mechanism. The resulting cables lengths of the two sub-systems are then $c_i + \Delta c_i$ and $c'_i + \Delta c'_i = \kappa_s(c_i + \Delta c_i)$. This similitude ratio is therefore kept, which allows us to conclude that this mechanism is a CDP.

Then, based on Fig. 1.9 and on the fact that the slave is related to the master by a proportional transformation, it is possible to establish these following rules:

- The geometric dimensions of the slave correspond by a scaling factor to those of the master;
- The slave point-displacements also correspond to a scaling ratio from those of the master;
- The slave rotations correspond exactly to those of the master.

The last two rules can be mathematically demonstrated, assuming the first to be true. If one focuses on the schematic representation of the master CDPM (see Fig. 1.9a) and the slave CDPM (see Fig. 1.9b), and assuming that $c'_i = \kappa_s c_i$, the following relationship can be derived:

$$(c'_i)^2 = ||\mathbf{a}'_i - \mathbf{p}' - \mathbf{Q}'\mathbf{b}'_i||_2^2 = \kappa_s^2 ||\mathbf{a}_i - \mathbf{p} - \mathbf{Q}\mathbf{b}_i||_2^2 = (\kappa_s c_i)^2, \tag{1.2}$$

where $\mathbf{a}_i$ is the vector pointing from the origin point O to the attachment point A_i, $\mathbf{b}_i$ is the vector pointing from the reference point P to the attachment point B_i, $\mathbf{Q}$ is the 3×3 matrix representing the end-effector attitude of the master CDPM and $\mathbf{a}'_i$, $\mathbf{b}'_i$ and $\mathbf{Q}'$ are their corresponding counterparts for the slave CDPM.

First, if we consider a constant orientation on both mechanisms, i.e., $\mathbf{Q}$ and $\mathbf{Q}'$ are constants, we can reformulate Eq. (1.2) as follows:

$$(\mathbf{a}'_i - \mathbf{p}' - \mathbf{b}'_i)^T(\mathbf{a}'_i - \mathbf{p}' - \mathbf{b}'_i) = \kappa_s^2(\mathbf{a}_i - \mathbf{p} - \mathbf{b}_i)^T(\mathbf{a}_i - \mathbf{p} - \mathbf{b}_i). \tag{1.3}$$

From the first rule, we know that $\mathbf{a}'_i = \kappa_s \mathbf{a}_i$ and $\mathbf{b}'_i = \kappa_s \mathbf{b}_i$, and consequently $(\mathbf{a}'_i - \mathbf{b}'_i) = \kappa_s(\mathbf{a}_i - \mathbf{b}_i)$, we can simplify this equation by defining $\mathbf{u} \equiv (\mathbf{a}'_i - \mathbf{b}'_i) = \kappa_s(\mathbf{a}_i - \mathbf{b}_i)$, which leads to

$$(\mathbf{p}' - \mathbf{u})^T(\mathbf{p}' - \mathbf{u}) = (\kappa_s \mathbf{p} - \mathbf{u})^T(\kappa_s \mathbf{p} - \mathbf{u}), \tag{1.4}$$

and for this relation to be true, we must have

$$\mathbf{p}' = \kappa_s \mathbf{p}, \tag{1.5}$$

which demonstrates that the slave point-displacements correspond to a scaling ratio from those of the master.

From this result, and now when $\mathbf{Q}$ and $\mathbf{Q}'$ are variables, we can express the Eq. (1.2) as follows:

$$(\mathbf{a}'_i - \mathbf{p}' - \mathbf{Q}'\mathbf{b}'_i)^T(\mathbf{a}'_i - \mathbf{p}' - \mathbf{Q}'\mathbf{b}'_i) = \kappa_s^2(\mathbf{a}_i - \mathbf{p} - \mathbf{Q}\mathbf{b}_i)^T(\mathbf{a}_i - \mathbf{p} - \mathbf{Q}\mathbf{b}_i). \tag{1.6}$$

Similar to the previous case, here, we know that $\mathbf{a}'_i = \kappa_s \mathbf{a}_i$, $\mathbf{p}' = \kappa_s \mathbf{p}$, and consequently we can define a vector $\mathbf{v}$ such as $\mathbf{v} \equiv (\mathbf{a}'_i - \mathbf{p}') = \kappa_s(\mathbf{a}_i - \mathbf{p})$. This variable change leads to

$$(\mathbf{Q}'\mathbf{b}'_i - \mathbf{v})^T(\mathbf{Q}'\mathbf{b}'_i - \mathbf{v}) = (\kappa_s \mathbf{Q}\mathbf{b}_i - \mathbf{v})^T(\kappa_s \mathbf{Q}\mathbf{b}_i - \mathbf{v}), \tag{1.7}$$

and for this relation to be true, knowing that $\mathbf{b}'_i = \kappa_s \mathbf{b}_i$, we must have

$$\mathbf{Q}' = \mathbf{Q}. \tag{1.8}$$

In conclusion, this mathematical development demonstrates that the slave rotations correspond exactly to those of the master.

Moreover, it is possible to extend the point-displacement relationships as follows:

$$\mathbf{p}' = \kappa_s \mathbf{p}, \tag{1.9}$$

$$\dot{\mathbf{p}}' = \kappa_s \dot{\mathbf{p}}, \tag{1.10}$$

$$\ddot{\mathbf{p}}' = \kappa_s \ddot{\mathbf{p}}, \tag{1.11}$$

where $\dot{\mathbf{p}}$ and $\ddot{\mathbf{p}}$ are respectively the velocity vector and the acceleration vector of point P on the end effector relative to point O on the base of the master CDPM. Vectors $\dot{\mathbf{p}}'$ and $\ddot{\mathbf{p}}'$ are similarly defined for the slave CDPM. As previously written, κ_s represents the scaling factor or the scaling ratio.

On the other hand, the rotations of both CDPMs—the master and the slave—are equal, as should their time derivatives. This characteristic, which applies to all CDPs, can be expressed by the following general relations:

$$\mathbf{Q}' = \mathbf{Q}, \ \dot{\mathbf{Q}}' = \dot{\mathbf{Q}} \text{ and } \ddot{\mathbf{Q}}' = \ddot{\mathbf{Q}}. \tag{1.12}$$

Validation of the Displacement Relationship by Simulation

The validation of a theoretical concept is always an important intermediate step prior to the manufacturing of prototypes, which have inherent costs and are time consuming. Then, in

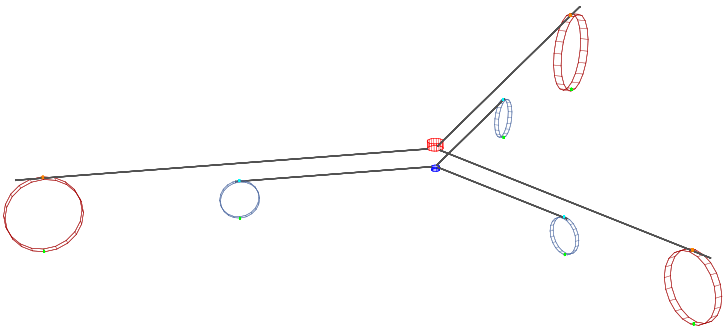

Figure 1.10 – Simulation with the software ADAMS®: a two-DoF planar CDP.

this work, we decided to perform software simulations in order to confirm the displacement behaviours of this new type of mechanisms. The software application ADAMS® [198] has been used to this end and cables are defined as rigid cylindrical bars (we assume that cables are always in tension).

Previously in this sub-section, it has been shown that $\mathbf{p}' = \kappa_s \mathbf{p}$ and $\mathbf{Q}' = \mathbf{Q}$ for cable-driven pantographs (and similarly for their time derivatives) for a chosen scaling factor κ_s. Then, this preliminary validation focuses on the resulting similitude ratio of translational displacements for a two-DoF CDP and of both translational and rotational displacements for a six-DoF CDP. The results obtained from this study aim at confirming the fact that keeping the same ratio κ_s between the master and the slave mechanisms at all levels, i.e., between the geometry of both bases (attachment points A_i and A'_i), the geometry of both moving platforms (attachment points B_i and B'_i) and between both winding drums diameter (d and d'), ensures having the exact same angular displacements as well as the exact same similitude ratio between the displacement in translation of both CDPMs' end-effector.

Looking at Figs. 1.10 and 1.11, one can observe that for a generic three-cable two-DoF planar CDP, when a chosen similitude ratio of $\kappa_s = 1/2$ is applied to all components of the cable-driven pantograph, i.e., to the base and end-effector geometries and to the drum diameters, this same ratio is preserved between the master and slave end-effector displacements. It should be noted that the end-effector motions here are dependent on their respective pulley positions (points A_i and A'_i) and their end-effector attachment points (points B_i and B'_i), which would not be necessarily the case for a two-cable one-DoF CDP because of its linear behaviour (see Figs. 1.6 and 1.7).

For the simulation of the three-cable two-DoF CDP, the following planar trajectory has been imposed to the master end-effector:

$$P_x(t) = 0.3\sin(2\pi t),\ P_y(t) = 0.4\sin(4\pi t),\ t = 0,\ldots,3 \text{ s}, \tag{1.13}$$

and the resulting master and slave end-effector displacements are shown in Fig. 1.11. Here, the upper-graph and lower-graph solid red lines with circles are respectively associated to

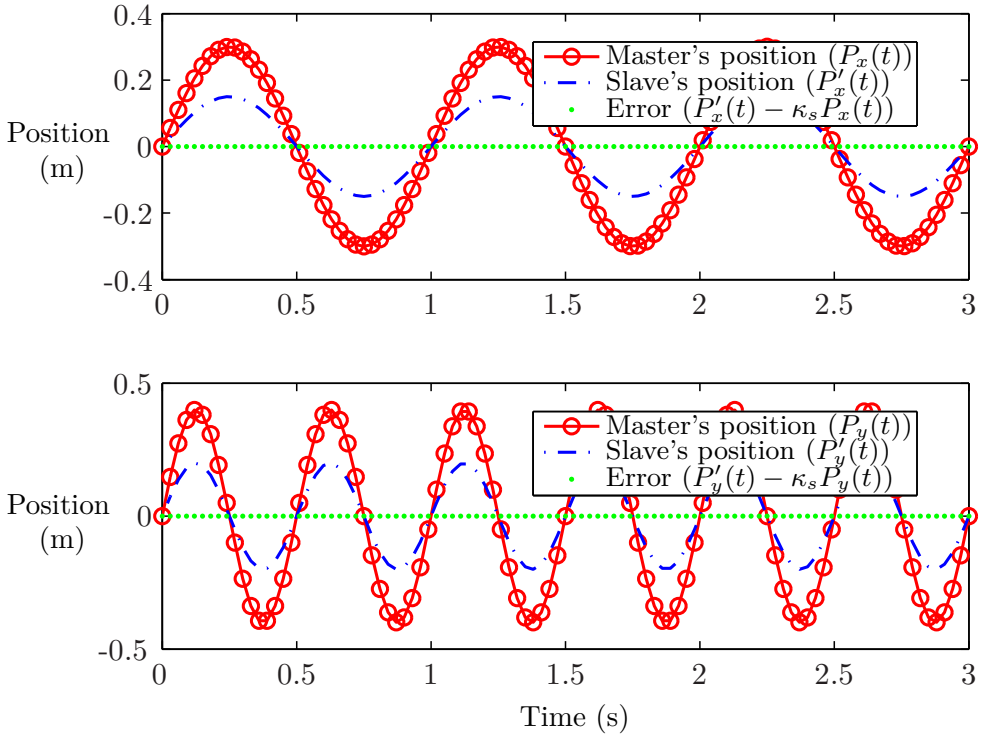

Figure 1.11 – Simulation of a two-DoF planar CDP: comparison of motion plots.

the motion in the X and Y directions of the master end-effector, while the dashed blue lines (upper and lower graphs) are associated to the motion in the X and Y directions of the slave end-effector. Based on their in-phase displacements and their respective magnitude (half of the master magnitude for the slave), it is obvious that the resulting ratio is $\kappa_s = 1/2$. One can also notice the magnitude difference for the two directions, i.e., following X and Y directions, which is zero along the full trajectory ($P'_x(t) - \kappa_s P_x(t) = 0$ and $P'_y(t) - \kappa_s P_y(t) = 0$, where $t = 0, \ldots, 3$ s).

Finally, in order to validate the translation and rotation relationships together, a simulation has been performed with a generic eight-cable six-DoF CDP (see Fig. 1.12). As for the previous two-DoF planar CDP, the scaling factor $\kappa_s = 1/2$ was applied to all mechanical components. Then, as expected, similar results were obtained when performing the following tridimensional trajectory in translation (see Fig. 1.13a):

$$P_x(t) = 0.6 \sin(2\pi t), \tag{1.14}$$

$$P_y(t) = 0.4 \sin(4\pi t), \tag{1.15}$$

$$P_z(t) = 0.5 \sin(2\pi t), \ t = 0, \ldots, 3 \text{ s}, \tag{1.16}$$

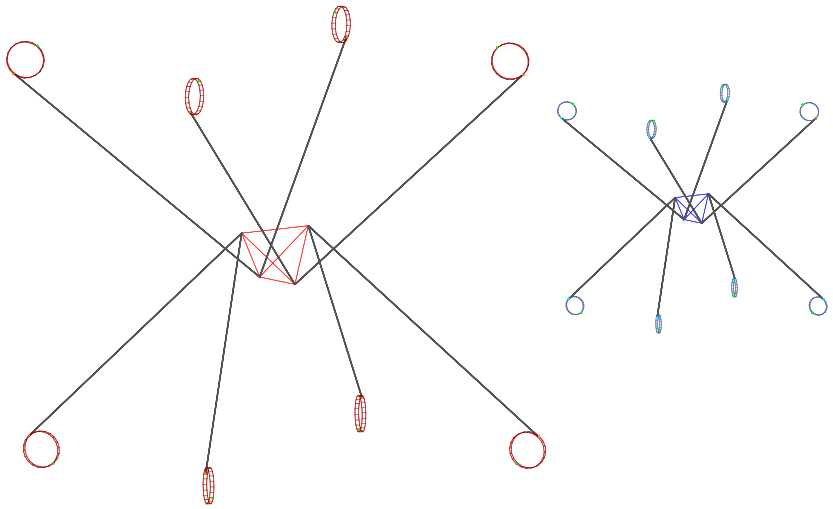

Figure 1.12 – Simulation with the software ADAMS®: a six-DoF CDP.

and in rotation (see Fig. 1.13b):

$$\theta_x(t) = (\pi/4)\sin(2\pi t), \tag{1.17}$$

$$\theta_{y^{\mathrm{I}}}(t) = (\pi/8)\sin(2\pi t), \tag{1.18}$$

$$\theta_{z^{\mathrm{II}}}(t) = (\pi/6)\sin(2\pi t),\ t = 0,\ldots,3\text{ s}. \tag{1.19}$$

In Fig. 1.13a, the first graph, the second graph and the third one are respectively associated to the translational motion in the X direction, in the Y direction and in the Z direction of the master (red curve with circles) and the slave (blue dashed line) end-effectors. In Fig. 1.13b, the first, the second and the third graphs are respectively associated to the three rotations $\{\theta_x,\ \theta_{y^{\mathrm{I}}},\ \theta_{z^{\mathrm{II}}}\}$, which are the three angles defining the orientation $\mathbf{Q}$ of the CDPM end-effector (see Eq. (A.17) from Appendix A), following the Euler angles convention XYZ (three successive pure rotations along the axes X, Y^{I} (the new axis Y after one rotation along axis X) and Z^{II} (the new axis Z after one rotation along axis X and then one rotation along Y^{I}), of the master end-effector (red curve with circles) and $\{\theta'_x,\ \theta'_{y^{\mathrm{I}}},\ \theta'_{z^{\mathrm{II}}}\}$ defining $\mathbf{Q}'$ for the slave end-effector (blue dashed line). In translation, the motion of the slave end-effector is in phase with the motion of its master counterpart and magnitudes follow a scaling factor of $\kappa_s = 1/2$ (all magnitude errors are zero). Moreover, in rotation, it is easily observed from Fig. 1.13b that angular displacements of both the master and the slave moving platforms are identical.

In summary, these two numerical simulations and their corresponding results have corroborated our theoretical input-output displacement relationships derived in this sub-section. Then, based on this validation, our analysis can be now continued to the input-output load relationship inherent to the cable-driven pantographs.

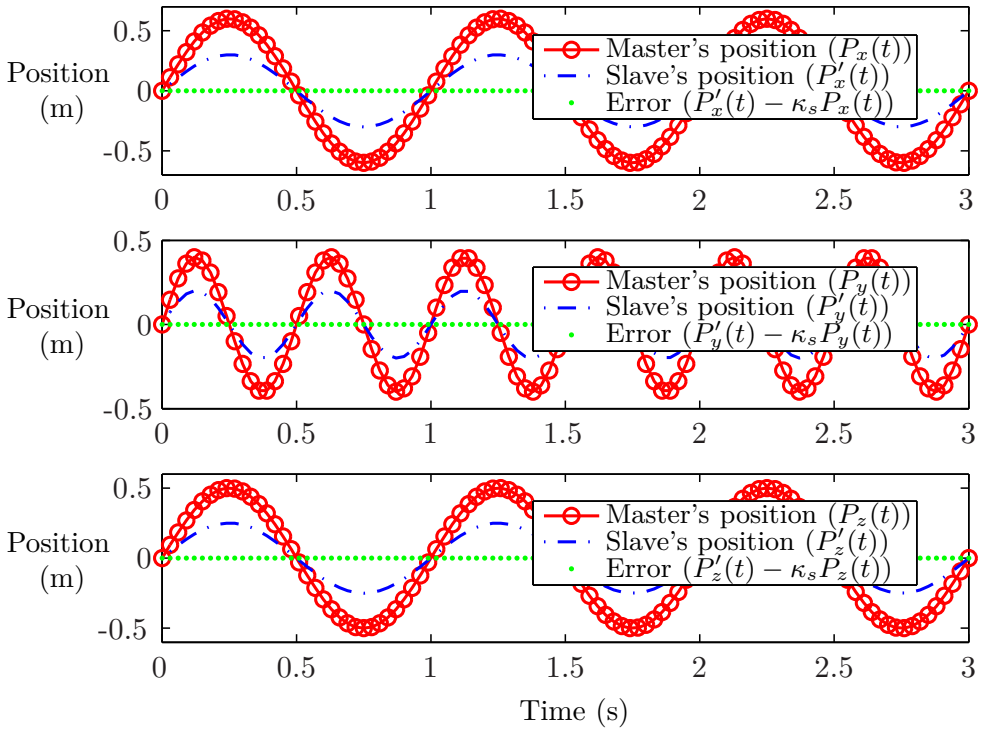

(a) The motion in translation

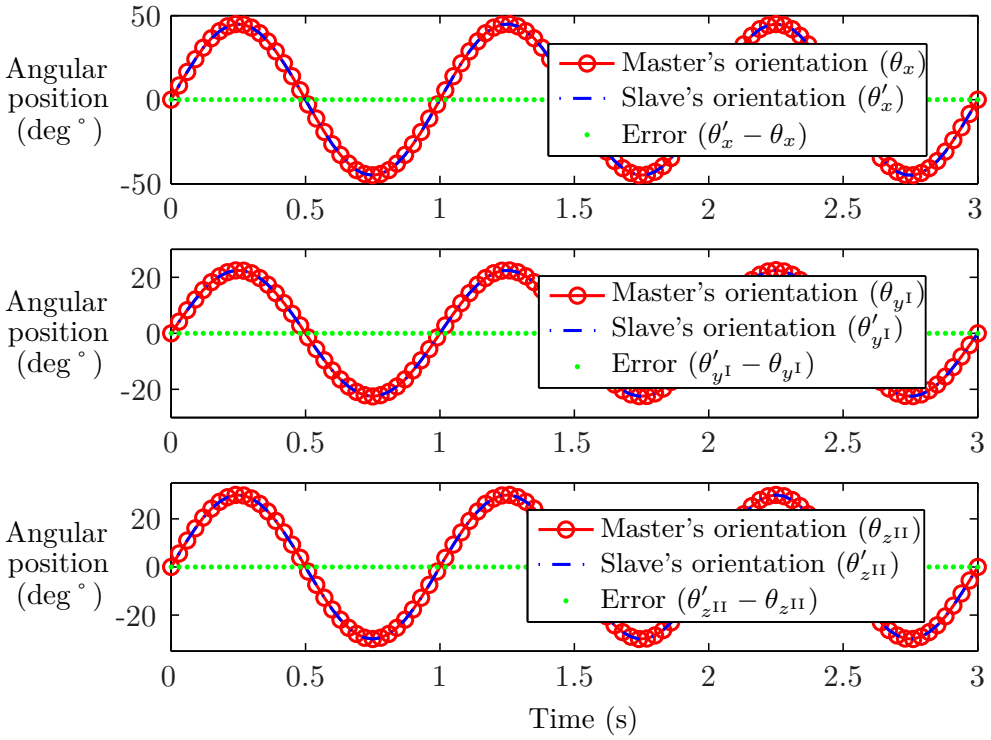

(b) The motion in rotation

Figure 1.13 – Simulation of a six-DoF CDP: comparison of motion plots.

1.3.4 Input-Output Load Relationship

Knowing the relation between the input and output displacements—both in translation and rotation—we can now determine the relation between an input wrench applied at the master moving platform, and the corresponding output wrench applied at the slave moving platform. For a first approximate relation, let us make two assumptions, which are never exactly true:

1. There is no friction acting on the cables connecting the master and slave moving platforms;

2. The springs maintain a perfect neutral equilibrium of the pantograph over its workspace.

The friction can be decreased by using a small number of pulleys between the master and the slave and by selecting the appropriate journal bearings to support them and suitable eyelets at points A_i and A'_i. On the other hand, maintaining a minimum level of cable tensions while preserving a neutral equilibrium of the two moving platforms is a challenging problem, which will be addressed in Chapter 2.

For now, if we assume that these variations in the potential energy are negligible, then we may apply the principle of virtual work as follows. Let us first define the force $\mathbf{f}$ at an arbitrary point P and the torque $\mathbf{n}$, both acting on the moving platform of the master (see Fig. 1.14a), while the force $\mathbf{f}'$ applied at the homologous point P' of P and the moment $\mathbf{n}'$ both act on the slave (see Fig. 1.14b). Let $\delta\mathbf{p}$ be a small virtual displacement of P, $\delta\mathbf{Q}$, a small virtual rotation of the master moving platform, and, likewise, $\delta\mathbf{p}'$ a small virtual displacement of P', and $\delta\mathbf{Q}'$, a small virtual rotation of the slave moving platform. Then, the virtual work done by $\mathbf{f}$ and $\mathbf{n}$ is

$$\delta U = \mathbf{f}^T \delta\mathbf{p} + \mathbf{n}^T(\mathbf{e}\delta\theta), \tag{1.20}$$

and, similarly, the virtual work done by $\mathbf{f}'$ and $\mathbf{n}'$ is

$$\delta U' = \mathbf{f}'^T \delta\mathbf{p}' + \mathbf{n}'^T(\mathbf{e}'\delta\theta'), \tag{1.21}$$

where $\mathbf{e}$ and $\mathbf{e}'$ are the unit vectors giving the directions of the rotation axes corresponding to $\delta\mathbf{Q}$ and $\delta\mathbf{Q}'$, respectively, and $\delta\theta$ and $\delta\theta'$ are the corresponding small virtual angles of rotation about $\mathbf{e}$ and $\mathbf{e}'$, respectively. The relationship with $\delta\mathbf{Q}$ and $\delta\mathbf{Q}'$ can be expressed by the following:

$$\delta\mathbf{Q} \equiv \mathbf{1}_{3\times 3} + \mathrm{cpm}(\mathbf{e})\delta\theta, \tag{1.22}$$

and,

$$\delta\mathbf{Q}' \equiv \mathbf{1}_{3\times 3} + \mathrm{cpm}(\mathbf{e}')\delta\theta', \tag{1.23}$$

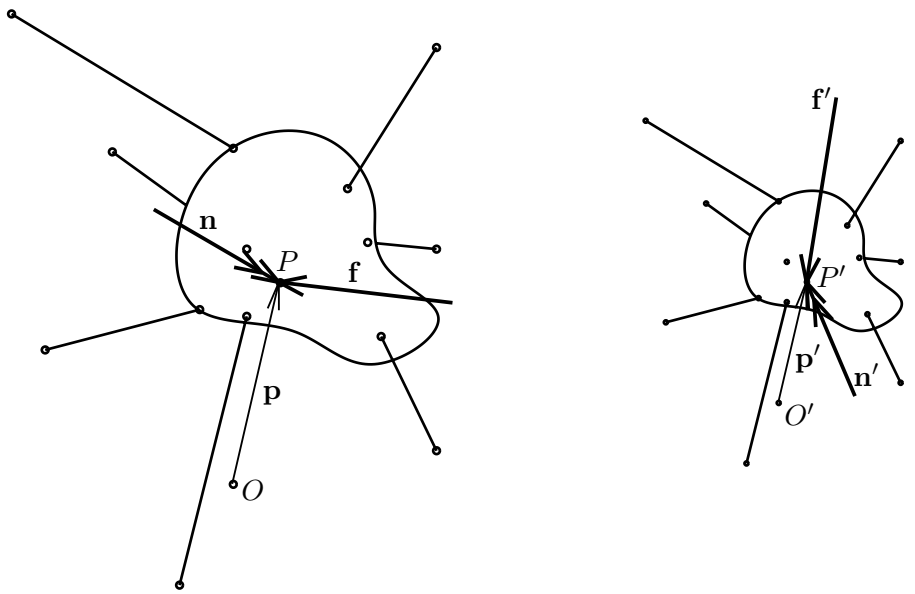

(a) The master (b) The slave

Figure 1.14 – Schematic representation of the applied wrench.

and where $\mathbf{1}_{3\times3}$ is the 3×3 identity matrix and cpm() returns the cross-product matrix[2] of its vector argument.

According to the principle of virtual work, the equilibrium equation of this system can be written as

$$\delta U + \delta U' = 0, \tag{1.24}$$

or

$$\mathbf{f}^T \delta\mathbf{p} + \mathbf{n}^T(\mathbf{e}\delta\theta) + \mathbf{f'}^T \delta\mathbf{p'} + \mathbf{n'}^T(\mathbf{e'}\delta\theta') = 0. \tag{1.25}$$

Because of the behaviour of a cable-driven pantograph, we know that $\delta\mathbf{p'} = \kappa_s \delta\mathbf{p}$ and $\mathbf{e'}\delta\theta' = \mathbf{e}\delta\theta$, and the equilibrium equation becomes

$$(\mathbf{f} + \kappa_s \mathbf{f'})^T \delta\mathbf{p} + (\mathbf{n} + \mathbf{n'})^T(\mathbf{e}\delta\theta) = 0. \tag{1.26}$$

Since $\{\delta\mathbf{p}, \mathbf{e}\delta\theta\}$ are arbitrary small virtual displacements, their vector coefficients must vanish, which leads to

$$\mathbf{f'} = -\frac{1}{\kappa_s}\mathbf{f} \qquad \text{and} \qquad \mathbf{n'} = -\mathbf{n}. \tag{1.27}$$

Therefore, in theory, when no friction acts on the cables and a perfect neutral equilibrium is reached over the CDP's workspace, a force applied at the moving platform of the master must be balanced by another force applied to the slave moving platform, in an opposite direction and of magnitude inversely proportional to κ_s, while a torque acting on the master must be

[2]The cross-product matrix $\mathbf{X}$ of $\mathbf{x} \in \mathbb{R}^3$ is defined as $\mathbf{X} \equiv \partial(\mathbf{x} \times \mathbf{y})/\partial\mathbf{y},\ \mathbf{y} \in \mathbb{R}^3$.

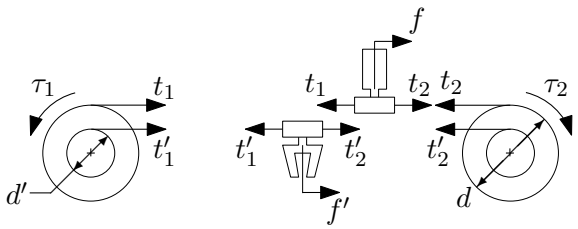

Figure 1.15 – Free-body diagram of the proposed one-DoF CDP with springs.

balanced by a torque of the same magnitude but in the opposite direction on the slave moving platform. It is important to note that, in practice, however, since our concept of CDPs is based on the use of springs with given torsion coefficients, the magnitudes of $\mathbf{f}'$ and $\mathbf{n}'$ will be limited.

1.3.5 Kinetostatic Modelling

When aiming at designing a cable-driven pantograph, one should have an idea not only of the system input-output behaviours but also of its internal behaviours. Here, a kinetostatic analysis of a two-cable one-DoF CDP and then a three-cable two-DoF CDP is presented.

Two-Cable One-DoF Cable-Driven Pantograph

From a cursory inspection of the system presented in Fig. 1.7, it is clear that this mechanism can be qualified as statically indeterminate[3] (or hyperstatic). Indeed, for a given position x of the master, it is impossible to determine the individual tension in each cable of the system, unless one accounts for the deformation in all cables. By looking at the corresponding general free-body diagrams shown in Fig. 1.15, one can infer the following relations:

$$f = t_1 - t_2, \tag{1.28}$$

$$\tau_1 = \frac{d}{2}(t_1 + \kappa_s t'_1), \tag{1.29}$$

$$f' = t'_1 - t'_2, \tag{1.30}$$

and

$$\tau_2 = \frac{d}{2}(t_2 + \kappa_s t'_2), \tag{1.31}$$

where t_1 and t'_1 represent the tensions of the two cables attached to the left spring (its torque being noted τ_1), which belong to the master and the slave, respectively. Similarly, t_2 and t'_2 represent the tension of the two cables attached to the right spring (its torque being noted τ_2). Only with this system of four linear equations, however, it is not possible to find a unique

[3] A statically indeterminate problem occurs when the conventional static equilibrium equations are insufficient for determining the reactions acting on a body.

solution for $\{t_1, t_2, t'_1, t'_2\}$. This system of linear equations can be reformulated as:

$$\mathbf{P}_{4,4}\mathbf{t}_4 = \mathbf{c}_4, \tag{1.32}$$

where

$$\mathbf{P}_{4,4} = \begin{bmatrix} 1 & -1 & 0 & 0 \\ 0 & 0 & 1 & -1 \\ 1 & 0 & \kappa_s & 0 \\ 0 & 1 & 0 & \kappa_s \end{bmatrix}, \ \mathbf{t}_4 = \begin{bmatrix} t_1 \\ t_2 \\ t'_1 \\ t'_2 \end{bmatrix}, \text{ and } \mathbf{c}_4 = \begin{bmatrix} f \\ f' \\ 2\tau_1/d \\ 2\tau_2/d \end{bmatrix}. \tag{1.33}$$

These equations are not linearly independent, i.e., the 4×4 matrix $\mathbf{P}_{4,4}$ is singular, its rank being 3. Therefore, Eq. 1.32 admits an infinite number of solutions $\mathbf{t}_4$. Hence, an additional independent equation is required, which is generally called the *compatibility equation*.

This compatibility equation is based on the internal length-variation behaviour that occurs within our CDP's fundamental component. Since we chose to rigidly fix each winding pulley of the master to its counterpart winding pulley of the slave, we know that their respective small angular displacements, $\delta\phi_i$ and $\delta\phi'_i$, have to be the same, and consequently,

$$\delta\phi_i = \frac{2\delta c_{\phi_i}}{d} = \frac{2\delta c'_{\phi'_i}}{d'} = \delta\phi'_i, \tag{1.34}$$

where δc_{ϕ_i} is the variation of the length c_i of the i^{th} cable of the master due to its unwinding and winding on its corresponding drum and, similarly, $\delta c'_{\phi'_i}$ the small variation of the length of its counterpart cable at the slave. We also set $\delta c_i \equiv \delta c_{\phi_i} + \delta c_{e_i}$ and $\delta c'_i \equiv \delta c'_{\phi'_i} + \delta c'_{e'_i}$, knowing that the elastic deformation δc_e of a cable can be approximated by $(tl)/(EA)$, where t is its tension, l is the original total length of the cable, A is the cross-sectional area of the cable and E is its modulus of elasticity. Here, we assume that the total length of the cable is the winded and unwinded lengths. This implies that the winded length of the cable can deform or slip on the pulley while the tension is applied. Moreover, we can assume, for our problem, that if δc is set to be the sum of all cables length variations at the master and $\delta c'$ the sum of all cables length variations at the slave, $\delta c = \delta c_1 + \delta c_2$ and $\delta c' = \delta c'_1 + \delta c'_2$, respectively. Finally, taking into account that A and E are constants for all cables, that $\delta c' = \kappa_s \delta c$ and $l' = \kappa_s l$, we obtain the following compatibility equation:

$$t_1 l + t_2 l = \frac{1}{\kappa_s}(t'_1 l' + t'_2 l') = t'_1 l + t'_2 l. \tag{1.35}$$

This equation provides the sufficient condition in order to determine a unique solution for $\mathbf{t}_4$ based on the system of linear equations of Eq. (1.32). The new system of equations becomes

$$\mathbf{P}_{5,4}\mathbf{t}_4 = \mathbf{c}_5, \tag{1.36}$$

where

$$\mathbf{P}_{5,4} = \begin{bmatrix} 1 & -1 & 0 & 0 \\ 0 & 0 & 1 & -1 \\ 1 & 0 & \kappa_s & 0 \\ 0 & 1 & 0 & \kappa_s \\ 1 & 1 & -1 & -1 \end{bmatrix}, \text{ and } \mathbf{c}_5 = \begin{bmatrix} f \\ f' \\ 2\tau_1/d \\ 2\tau_2/d \\ 0 \end{bmatrix}. \tag{1.37}$$

One should note that this system of equations is fully-determined, and therefore has only one solution, which, after solving the problem using the Gaussian elimination method, can be expressed as follows:

$$t_1 = \frac{4\tau_2 + (2+\kappa_s)df + \kappa_s df'}{2d(1+\kappa_s)}, \tag{1.38}$$

$$t_2 = \frac{4\tau_2 - \kappa_s d(f - f')}{2d(1+\kappa_s)}, \tag{1.39}$$

$$t'_1 = \frac{4\tau_2 + df + (1+2\kappa_s)df'}{2d(1+\kappa_s)}, \tag{1.40}$$

and

$$t'_2 = \frac{4\tau_2 + d(f - f')}{2d(1+\kappa_s)}. \tag{1.41}$$

One should note that for the previous solution to hold, the following relationship must be satisfied:

$$\frac{2\tau_2}{d} = \frac{2\tau_1}{d} - f - \kappa_s f', \tag{1.42}$$

which can be easily validated from Fig. 1.15.

In the case where we choose the *Neg'ator Springs* in order to balance out our two-cable one-DoF CDP, the two constant torques would be equivalent at each winding pulley ($\tau_1 = \tau_2$). This would lead to the solution $t_1 = t_2 = t'_1 = t'_2$, when f and f' are null. Hence, when the CDP is in static equilibrium (no external force required), we assume that torques generated by the slave sub-system τ'_{ss} are proportional to torques generated by the master sub-system τ_{ss}, for their respective cables, following the scaling factor κ_s, i.e., $\tau'_{ss} = \kappa_s \tau_{ss}$. Then, their respective sum balances the corresponding spring torque τ as follows:

$$\tau_i = \tau_{ss,i} + \tau'_{ss,i} = (1+\kappa_s)\tau_{ss,i}. \tag{1.43}$$

It is important to note that this relation is true if and only if the CDP is in static equilibrium, i.e., if the vector sum of the tensions in the cables attached to the master's end-effector is null, and, similarly, if the vector sum of the vector tensions in the cables attached to the slave's end-effector are null.

If we prefer choosing springs with a non-constant torque-rotation relationship, an applied force f would be required by the user on the master end-effector in order to maintain a

position outside an equilibrium position. From Eq. (1.32), we can formulate this new problem with five unknowns instead of four:

$$\mathbf{P}_{5,5}\mathbf{t}_5 = \mathbf{c}_5, \tag{1.44}$$

where

$$\mathbf{P}_{5,5} = \begin{bmatrix} -1 & 1 & -1 & 0 & 0 \\ 0 & 0 & 0 & 1 & -1 \\ 0 & 1 & 0 & \kappa_s & 0 \\ 0 & 0 & 1 & 0 & \kappa_s \\ 0 & 1 & 1 & -1 & -1 \end{bmatrix}, \ \mathbf{t}_5 = \begin{bmatrix} f \\ t_1 \\ t_2 \\ t'_1 \\ t'_2 \end{bmatrix}, \text{ and } \mathbf{c}_5 = \begin{bmatrix} 0 \\ f' \\ 2\tau_1/d \\ 2\tau_2/d \\ 0 \end{bmatrix}. \tag{1.45}$$

For this problem, where matrix $\mathbf{P}_{5,5}$ is full rank, when it is assumed that f' is known and $\tau_i = k_{sp}(\phi_{sp,i} - \phi_{sp,i,0})$, where k_{sp} is the spring constant in N·m/rad, $\phi_{sp,i}$ is the angular position of the spring corresponding to the displacement of the cables on the pulley, and $\phi_{sp,i,0}$ is the free angular position of the chosen spring in torsion, i.e., when $\tau_i = 0$ N·m, the solution can be easily obtained by resolving the corresponding system of linear equations. The set of solutions is represented by the following relations:

$$f = \frac{2(\tau_1 - \tau_2)}{d} - \kappa_s f', \tag{1.46}$$

$$t_1 = \frac{2(2\tau_1 + \kappa_s\tau_1 - \kappa_s\tau_2) - \kappa_s(1+\kappa_s)df'}{2d(1+\kappa_s)}, \tag{1.47}$$

$$t_2 = \frac{2(2\tau_2 + \kappa_s\tau_2 - \kappa_s\tau_1) + \kappa_s(1+\kappa_s)df'}{2d(1+\kappa_s)}, \tag{1.48}$$

$$t'_1 = \frac{2(\tau_1 + \tau_2) + (1+\kappa_s)df'}{2d(1+\kappa_s)}, \tag{1.49}$$

and

$$t'_2 = \frac{2(\tau_1 + \tau_2) - (1+\kappa_s)df'}{2d(1+\kappa_s)}. \tag{1.50}$$

This solution is valid for any linear two-cable one-DoF CDP that includes springs, or an equivalent torque-generator system, at its winding pulleys in order to preserve the cables taut. From these results, it is easily seen that, when the CDP does not present a perfect static equilibrium over its workspace, here Δx, the force f that a user must provide to hold a given position of the end effector of the master mechanism is proportional to the difference between the torques generated by the two springs and to the force applied at the slave end-effector. Moreover, it should be noted that a designer can choose suitable values of k_{sp} and $\phi_{sp,\min}$ in order to ensure a minimum tension $t_{\min}$ in the CDP cables since $\{t_1, t_2, t'_1, t'_2\}$ are strongly dependent, as one can expect, on τ_1 and τ_2.

From the description of the kinetostatic behaviour of a two-cable one-DoF CDP, it is now possible to extend this analysis to a three-cable two-DoF CDP.

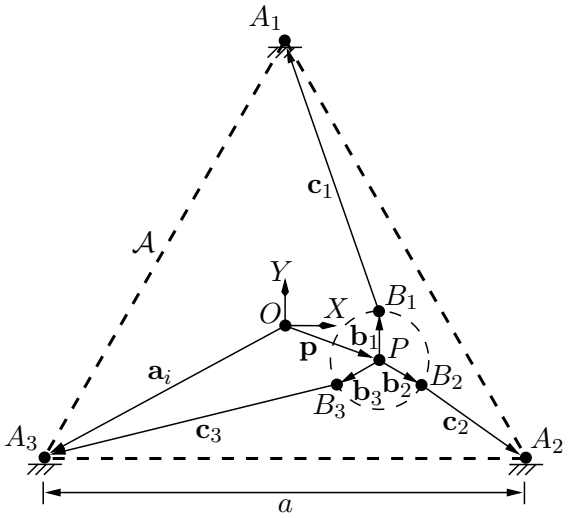

Figure 1.16 – Kinematic model of the three-cable two-DoF planar CDP (master part).

Three-Cable Two-DoF Cable-Driven Pantograph

The modelling of a planar two-DoF cable-driven pantograph constrained by three cables is more difficult than that of the simple one-DoF component. To do so, the kinematic modelling of the master geometry is presented with Fig. 1.16. In this figure, the vector $\mathbf{a}_i$ represents the position of the base-fixed eyelet A_i of cable i in the base frame, the vector $\mathbf{p}$ represents the position of the reference point P of the end effector from the origin point O, the vector $\mathbf{b}_i$ represents the position of the attachment point B_i on the end effector from point P and expressed in the base frame. Then, the vector $\mathbf{c}_i \equiv \mathbf{a}_i - \mathbf{p} - \mathbf{b}_i$ points from B_i to A_i, its magnitude c_i being the length of the i^{th} cable. Finally, the workspace of the planar CDPM is $\mathcal{A}$, an equilateral triangle, and the length of its bounding edges is a. On the other hand, the slave geometry is the exact image of the master but following the scaling factor κ_s, its planar workspace being $\mathcal{A}'$, an equilateral triangle geometry, and the length of its bounding edges is $a' = \kappa_s a$.

As the reader may notice from Fig. 1.16, this geometry's purpose is to translate a point inside a two-DoF workspace. In practice, however, the end effector is chosen to be a rigid body instead of a single point in order to better represent a potential experimental testbed (for instance, if measuring tools such as force sensors need to be attached). Then, since the end-effector geometry is not a point, it should be noted that the mechanism has potentially three DoFs—two point coordinates and one orientation—instead of only two. However, with the chosen equilateral triangle architecture, only small rotations along the Z axis can be observed. Hence, for simplicity reasons, it can be assumed that the system has two degrees of freedom.

In order to support this two-degree-of-freedom hypothesis, the author has computed the exact rotations relative to the point displacements of the end effector over the mechanism's workspace and the results are shown in Fig. 1.17a. It can be seen that, except for the regions

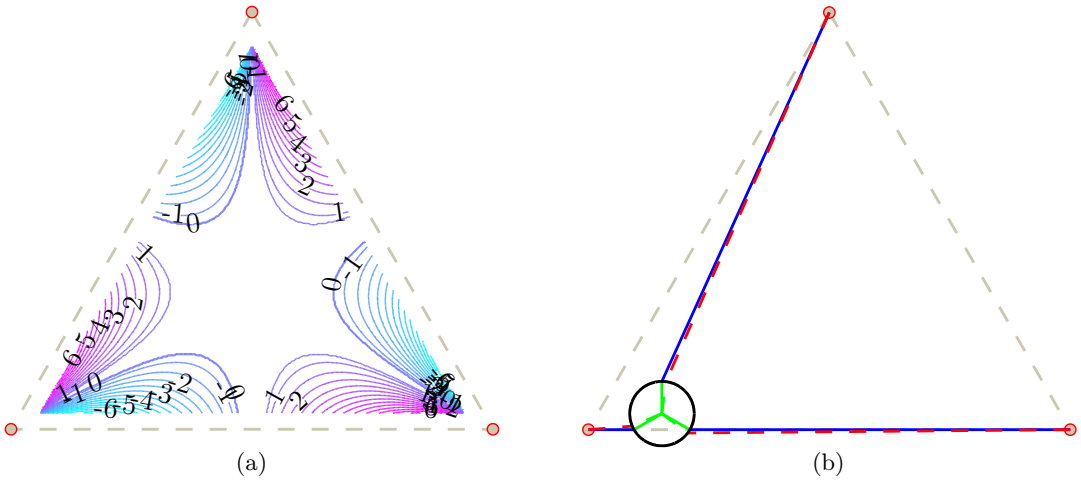

(a) (b)

Figure 1.17 – Graphical demonstration of the two-DoF hypothesis: (a) Rotations in degrees ($^\circ$) of the planar CDP's end-effector (master) relative to its point displacements over its workspace $\mathcal{A}$ and (b) Difference between the direction of the cables attached to the planar CDP's end-effector with and without rotations (worst configuration: rotation of -7.1487°).

close to the three vertices of the equilateral triangle formed by the workspace, the rotations at the end effector are either null or very small (only a few degrees). Moreover, in Fig. 1.17b, the author shows the direction of the three cables attached to the end effector with (dashed red lines) and without (solid blue lines) rotations for the worst-case configuration, i.e., when the absolute value of the relative rotation is maximum (-7.1487°). It can be observed, since the end-effector's geometry is small compared to the base's geometry, that the error on the direction of the cables is very small, even for the worst configuration. If the end effector is kept away from the triangle's vertices, then the initial assumption is verified, i.e., the author can neglect the rotation of the mechanism's end-effector relative to its linear displacements. Thence, the three-DoF planar CDP can be considered as a two-DoF planar CDP for the purpose of this analysis. In fact, the smaller the geometry of the end effector compared to the base, the closer the end effector is to a single-point behaviour.

Having justified the use of a two-DoF model, let us move to the objective of this sub-section, which is to determine the cable tensions $\mathbf{t}$ in the master CDPM, the cable tensions $\mathbf{t}'$ in the slave CDPM, and the force $\mathbf{f}$ applied at point P on the master's end-effector, given the position of P and the force $\mathbf{f}'$ applied at point P' on the slave CDPM. Drawing the two-dimensional version of Fig. 1.15 to get free-body diagrams of the master and slave end-effectors would lead to the following equilibrium equations

$$\mathbf{W}\mathbf{t} = \mathbf{f}, \tag{1.51}$$

$$\mathbf{W}'\mathbf{t}' = \mathbf{f}', \tag{1.52}$$

where $\mathbf{W}$ is the Jacobian matrix of the master CDPM, and $\mathbf{W}'$ is that of the slave CDPM.

It should be noted that in the case of a cable-driven pantograph, we have $\mathbf{W} = \mathbf{W}'$. The pose-dependent wrench matrix $\mathbf{W}$ is mathematically derived for a general planar three-DoF CDPM in Appendix A.1. But since in our case we can neglect one DoF, $\mathbf{W}$ can be simply expressed as follows

$$\mathbf{W} = \begin{bmatrix} \frac{\mathbf{c}_1}{c_1} & \frac{\mathbf{c}_2}{c_2} & \frac{\mathbf{c}_3}{c_3} \end{bmatrix}, \tag{1.53}$$

where the length of the i^{th} cable is

$$c_i = ||\mathbf{c}_i||_2 = \sqrt{(\mathbf{a}_i - \mathbf{p} - \mathbf{b}_i)^T(\mathbf{a}_i - \mathbf{p} - \mathbf{b}_i)}. \tag{1.54}$$

Then, free-body diagrams of each of the three pulleys yield the equilibrium equations

$$\frac{d}{2}\mathbf{t} + \frac{d}{2}\kappa_s\mathbf{t}' = \boldsymbol{\tau}, \tag{1.55}$$

where $\boldsymbol{\tau} \equiv [\tau_1\, \tau_2\, \tau_3]^T$. Equations (1.51–1.55) form a set of seven equations into eight unknowns, namely, $\mathbf{f}$, $\mathbf{t}$ and $\mathbf{t}'$. Hence, the two-degree-of-freedom cable-driven pantograph is statically indeterminate, as is its one-degree-of-freedom counterpart. Solving for all the unknowns requires an additional deformation equation, but if one is only interested in the force $\mathbf{f}$, the static equilibrium equations are sufficient.

To solve for $\mathbf{f}$ without resorting to an additional deformation equation, consider the premultiplication of Eq. (1.55) with $\mathbf{W}$, which yields

$$\mathbf{W}\mathbf{t} + \kappa_s\mathbf{W}\mathbf{t}' = \frac{2}{d}\mathbf{W}\boldsymbol{\tau}. \tag{1.56}$$

Since $\mathbf{W} = \mathbf{W}'$, we can substitute Eqs. (1.51–1.52) into Eq. (1.56), which gives

$$\mathbf{f} + \kappa_s\mathbf{f}' = \frac{2}{d}\mathbf{W}\boldsymbol{\tau}, \tag{1.57}$$

$$\mathbf{f} = \frac{2}{d}\mathbf{W}\boldsymbol{\tau} - \kappa_s\mathbf{f}'. \tag{1.58}$$

From Eq. (1.58), it is interesting to note that if $\mathbf{f}' = \mathbf{0}_2$, the resulting force at the master end-effector is exactly as that for a single CDPM, i.e., where there is no slave sub-system.

Solving now for the tensions $\mathbf{t}$ and $\mathbf{t}'$ requires an additional deformation equation, which, similarly to the one-DoF case, we derive at the price of the following assumptions:

- All cables, in both master and slave CDPMs, are made of the same elastic material with Young's modulus E, and have the same cross-sectional area A.
- A cable slips without friction on its drum, so that the complete length of each cable undergoes deformation under a corresponding tension.

- l is the total length of each cable of the master CDPM, as it comprises the winded and unwinded lengths of a cable. Similarly, $\kappa_s l$ is the total length of each cable of the slave CDPM.
- Any deformation of the cable is sufficiently small to have no effect on the overall posture of the mechanism, i.e., the geometry and Jacobian matrices are unaffected by cable deformations.

The cable elasticity induces small variations $\delta\mathbf{c}$ in the unwinded lengths of the three master-CDPM cables, and the analogous variations $\delta\mathbf{c}'$ in the lengths of the slave-CDPM cables. In turn, the unwinded-cable-length variations produce small displacements $\delta\mathbf{p}$ and $\delta\mathbf{p}'$ of points P and P' on the master and slave end effectors, respectively. More precisely, the relationships between these variations are

$$\mathbf{W}^T\delta\mathbf{p} = \delta\mathbf{c}, \tag{1.59}$$

$$(\mathbf{W}')^T\,\delta\mathbf{p}' = \delta\mathbf{c}'. \tag{1.60}$$

Notice that each of Eqs. (1.59–1.60) forms an overdetermined system of linear equations, granted that $\mathbf{W} = \mathbf{W}'$ has full rank. A necessary and sufficient condition for each system to admit exactly one solution $\delta\mathbf{p}$ (or $\delta\mathbf{p}'$) is that the vector $\delta\mathbf{c}$ (or $\delta\mathbf{c}'$) lies in the range of $\mathbf{W}^T$. Equivalently, the vector $\delta\mathbf{c}$ (or $\delta\mathbf{c}'$) must be orthogonal to the left nullspace of $\mathbf{W}^T$. Mathematically, this may be expressed as

$$\mathbf{v}_3^T\delta\mathbf{c} = 0, \tag{1.61}$$

$$\mathbf{v}_3^T\delta\mathbf{c}' = 0, \tag{1.62}$$

where $\mathbf{v}_3 \equiv \mathbf{v}_1 \times \mathbf{v}_2$, and $\mathbf{W}^T \equiv [\mathbf{v}_1\,\mathbf{v}_2]$. The mechanical interpretation of Eqs. (1.61–1.62) is that the cable-length variations must be compatible with the mechanism constraints, i.e., they must generate common displacements of points P and P'.

In the case of the master CDPM, the cable-length variations are decomposed as

$$\delta\mathbf{c} = \delta\mathbf{c}_\phi + \delta\mathbf{c}_e, \tag{1.63}$$

where $\delta\mathbf{c}_\phi$ are the variations due to small pulley rotations, and $\delta\mathbf{c}_e$ are the variations due to cable elongations. Likewise, in the case of the slave CDPM, we have

$$\delta\mathbf{c}' = \delta\mathbf{c}'_\phi + \delta\mathbf{c}'_e, \tag{1.64}$$

and $\delta\mathbf{c}'_\phi$ are the variations due to pulley rotations, while $\delta\mathbf{c}'_e$ are the variations due to cable elongations.

From the assumptions above, the cable elongations $\delta\mathbf{c}_e$ are governed by Hooke's law, which gives,

$$\delta\mathbf{c}_e = \frac{l}{EA}\mathbf{t}, \tag{1.65}$$

$$\delta\mathbf{c}'_e = \frac{\kappa_s l}{EA}\mathbf{t}'. \tag{1.66}$$

Furthermore, two cables connected to the same pulley are coupled, and the relationship between their length variations due to pulley rotations are expressed mathematically as

$$\delta\mathbf{c}'_\phi = \kappa_s \delta\mathbf{c}_\phi. \tag{1.67}$$

Upon substituting Eqs. (1.63–1.67) into Eqs. (1.61–1.62), we obtain

$$\mathbf{v}_3^T \delta\mathbf{c}_\phi + \mathbf{v}_3^T \frac{l}{EA}\mathbf{t} = 0, \tag{1.68}$$

$$\mathbf{v}_3^T \kappa_s \delta\mathbf{c}_\phi + \mathbf{v}_3^T \frac{\kappa_s l}{EA}\mathbf{t}' = 0. \tag{1.69}$$

Let us eliminate $\mathbf{v}_3^T \delta\mathbf{c}_\phi$ by substitution of the last two equations into one another, which, after some simplifications, yields the deformation equation sought:

$$\mathbf{v}_3^T(\mathbf{t} - \mathbf{t}') = 0. \tag{1.70}$$

In summary, the cable tensions can be computed by solving the following linear system of six equations with six unknowns:

$$\begin{bmatrix} \mathbf{v}_3^T & -\mathbf{v}_3^T \\ \mathbf{1}_{3\times 3} & \kappa_s \mathbf{1}_{3\times 3} \\ \mathbf{0}_{2\times 3} & \mathbf{W} \end{bmatrix} \begin{bmatrix} \mathbf{t} \\ \mathbf{t}' \end{bmatrix} = \begin{bmatrix} 0 \\ \frac{2}{d}\boldsymbol{\tau} \\ \mathbf{f}' \end{bmatrix}. \tag{1.71}$$

The solution of Eq. (1.71) can be obtained with the following expression:

$$\begin{bmatrix} \mathbf{t} \\ \mathbf{t}' \end{bmatrix} = \begin{bmatrix} \mathbf{A} & \mathbf{B} \\ \mathbf{C} & \mathbf{D} \end{bmatrix}^{-1} \begin{bmatrix} \boldsymbol{\alpha} \\ \boldsymbol{\beta} \end{bmatrix}, \tag{1.72}$$

where $\mathbf{A} = \mathbf{1}_{3\times 3}$, $\mathbf{B} = \kappa_s \mathbf{1}_{3\times 3}$, $\boldsymbol{\alpha} = \frac{2}{d}\boldsymbol{\tau}$, $\mathbf{C} = \begin{bmatrix} -\mathbf{v}_3^T \\ \mathbf{0}_{2\times 3} \end{bmatrix}$, $\mathbf{D} = \begin{bmatrix} \mathbf{v}_3^T \\ \mathbf{W} \end{bmatrix}$, and $\boldsymbol{\beta} = \begin{bmatrix} 0 \\ \mathbf{f}' \end{bmatrix}$.

The matrix inverse in Eq. (1.72) can be computed using the block matrix inversion method, i.e., when a matrix is partitioned into four blocks, it can be inverted blockwise as follows:

$$\begin{bmatrix} \mathbf{A} & \mathbf{B} \\ \mathbf{C} & \mathbf{D} \end{bmatrix}^{-1} = \begin{bmatrix} \mathbf{A}^{-1} + \mathbf{A}^{-1}\mathbf{B}(\mathbf{D} - \mathbf{C}\mathbf{A}^{-1}\mathbf{B})^{-1}\mathbf{C}\mathbf{A}^{-1} & -\mathbf{A}^{-1}\mathbf{B}(\mathbf{D} - \mathbf{C}\mathbf{A}^{-1}\mathbf{B})^{-1} \\ -(\mathbf{D} - \mathbf{C}\mathbf{A}^{-1}\mathbf{B})^{-1}\mathbf{C}\mathbf{A}^{-1} & (\mathbf{D} - \mathbf{C}\mathbf{A}^{-1}\mathbf{B})^{-1} \end{bmatrix}, \tag{1.73}$$

where $\mathbf{A}$ and $\mathbf{D}$ must be square and $\mathbf{A}$ and $(\mathbf{D}-\mathbf{C}\mathbf{A}^{-1}\mathbf{B})$ must be nonsingular, in order to be inverted.

Defining the matrix $\mathbf{E} \equiv (\mathbf{D}-\mathbf{C}\mathbf{A}^{-1}\mathbf{B})$, which in our case, can be expressed as:

$$\mathbf{E} = \begin{bmatrix} (1+\kappa_s)\mathbf{v}_3^T \\ \mathbf{W} \end{bmatrix}, \tag{1.74}$$

one can verify that its inverse is:

$$\mathbf{E}^{-1} = \begin{bmatrix} \frac{1}{(1+\kappa_s)||\mathbf{v}_3||_2^2}\mathbf{v}_3 & \mathbf{W}^T(\mathbf{W}\mathbf{W}^T)^{-1} \end{bmatrix}. \tag{1.75}$$

By substituting Eq. (1.75) into Eq. (1.73), we can then easily show that the solution for $\mathbf{t}$ and $\mathbf{t}'$ are

$$\mathbf{t} = \frac{2}{d}\boldsymbol{\tau} - \frac{\kappa_s}{(1+\kappa_s)}\frac{\mathbf{v}_3\mathbf{v}_3^T}{||\mathbf{v}_3||_2^2}\frac{2}{d}\boldsymbol{\tau} - \kappa_s\mathbf{W}^T(\mathbf{W}\mathbf{W}^T)^{-1}\mathbf{f}', \tag{1.76}$$

and

$$\mathbf{t}' = \frac{1}{(1+\kappa_s)}\frac{\mathbf{v}_3\mathbf{v}_3^T}{||\mathbf{v}_3||_2^2}\frac{2}{d}\boldsymbol{\tau} + \mathbf{W}^T(\mathbf{W}\mathbf{W}^T)^{-1}\mathbf{f}'. \tag{1.77}$$

For the purpose of this thesis, the kinetostatic analysis presented here is limited to the case of a three-cable two-DoF CDP. Nevertheless, there is no apparent reason why the principle would not be applicable to CDPs with additional degrees of freedom. The associated mathematical developments would be more involved, especially for CDPs presenting rotations at their end effectors.

1.4 Validation of the Cable-Driven Pantograph Concept by Experiment

In order to experimentally verify some of the theoretical results obtained in the previous section, we decided to design the first planar CDP prototype. This mechanism aims to be an ideal benchmark to determine the practicability of the described concept.

A simple instance of the generic concept presented in Fig. 1.8 is that of the three-cable two-DoF cable-driven pantograph, which is shown in Fig. 1.18 and with which displacement simulations have been performed in Sub-section 1.3.3. In fact, the capabilities of this device are not different from those of the original pantograph [54], which reproduced the displacements of a point in the plane. Nevertheless, we regard this simple device as a benchmark for the general case, which allows rigid-body displacements.

The computer-aided design (CAD) model of the cable-driven pantograph shown in Fig. 1.18 reports the chosen geometry for the first prototype. The base-fixed eyelets are chosen to be

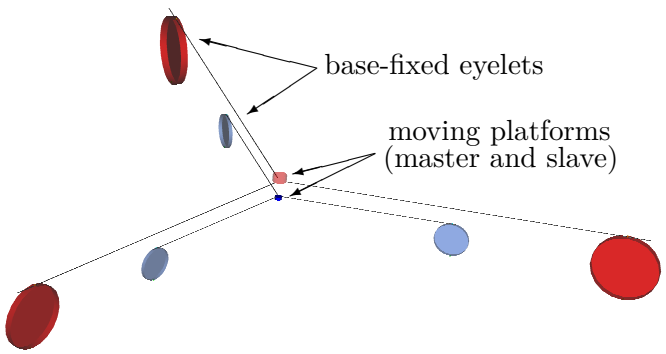

Figure 1.18 – Geometry of the devised three-cable two-DoF CDP.

located at the vertices of an equilateral triangle. The same scaled geometry describes the positions of the attachment points on the moving platforms. Moreover, the geometry of the slave is obtained by scaling that of the master by a factor of one half, i.e., $\kappa_s = 1/2$. Then, the geometry of the first prototype is described as two three-cable two-DoF planar CDPMs, which are connected together by their corresponding cables in order to obtain a three-cable two-DoF cable-driven pantograph.

1.4.1 Prototype of a Three-Cable Two-DoF Cable-Driven Pantograph

Following the geometry previously described with Figs. 1.16 and 1.18, a prototype of the three-cable two-DoF planar cable-driven pantograph having a scaling factor of $\kappa_s = 1/2$ was built, which is shown in Figs. 1.19 and 1.21. In these figures, the master moving platform appears on the left-hand side, while the slave moving platform, controlled by the master end-effector, is on the right-hand side. The distance between two fixed eyelets on the master is set to $a = 0.38$ m, whereas it is $a' = 0.19$ m on the slave. Each pulley assembly is identical and contains two drums, on which cables are wound, and one spring-loaded assembly containing a proportional spring in torsion with a spring constant k_{sp} (in this first prototype, proportional-torque springs have been preferred to constant-torque springs for cost reasons). The exploded view of the CAD model of the spring-loaded winding-pulley assembly is illustrated in Fig. 1.20.

With Fig. 1.19, the working principle of all cable-driven pantographs are easily understood. In fact, for this particular CDP, on the master side, three cables, respectively attached at points B_i, $i = 1,2,3$, constrain the point displacements of the master end-effector inside its workspace $\mathcal{A}$. Its three cables pass through their respective base-fixed eyelets (points A_i) at each vertex of $\mathcal{A}$. Then, each cable passes through a set of pulleys, which are mounted on ball bearings to reduce friction, in order to reach their respective spring-loaded winding-pulley assembly. The positions of these idler pulleys have been determined in order to minimize their numbers and the cable angles—directly related to the level of friction—when going in and out of the base-fixed eyelets and of the spring-loaded winding-pulley assemblies. An alu-

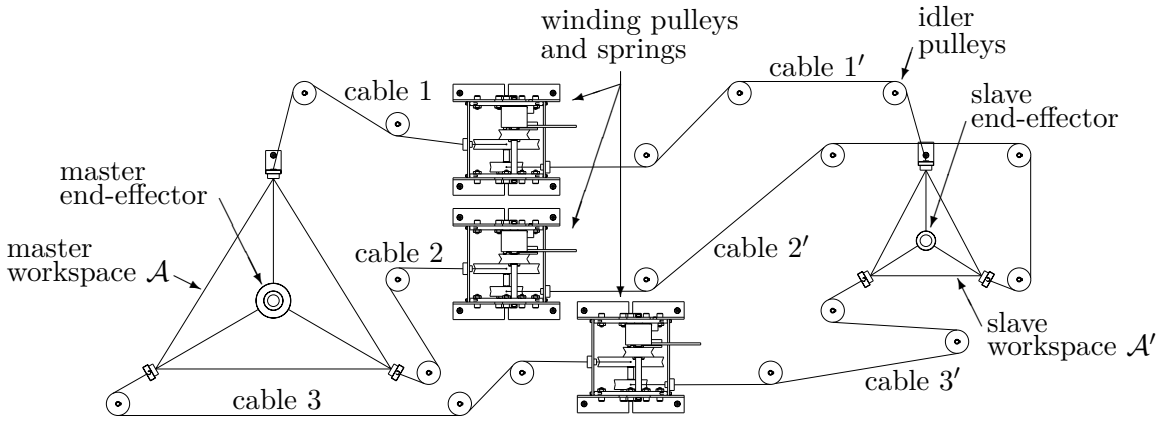

Figure 1.19 – CAD model of the three-cable two-DoF cable-driven pantograph.

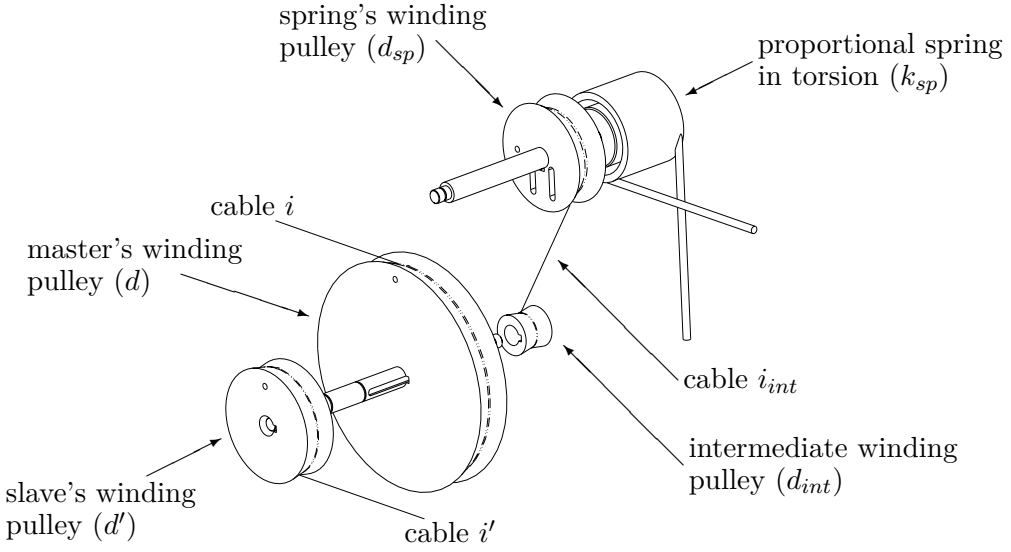

Figure 1.20 – Exploded view of the CAD model of a spring-loaded winding-pulley assembly.

minium bread board containing a pattern of pre-drilled holes with center-to-center distances of 0.0254 m (1 in) (see Fig. 1.21) was used for this purpose. Once inside the spring-loaded winding-pulley assembly, each cable is wound around a winding pulley of diameter d (here fixed to 0.1016 m (4 in)). On the other side, i.e., on the slave side, cable i' is wound on a drum of diameter $d' = \kappa_s d$ (0.0508 m (2 in)), which is rigidly attached to its counterpart drum. Then, each of these cables passes through a set of idler pulleys in order to reach the slave base-fixed eyelets (points A'_i), and attaches finally to the slave end-effector at points B'_i. In this way, cables i' constrain the planar two-DoF displacements of the reference point P' of the slave end-effector over its workspace $\mathcal{A}'$.

Moreover, in order to ensure a minimum tension $t_{\min}$ in the cables, each set of master-slave winding drums has a spring-loaded assembly attached in parallel and designed to generate

the minimum required torque when the cable length is $c_i = 0$ m, i.e., when the point B_i coincides with point A_i. Then, a third winding pulley that is rigidly attached to the two other master-slave drums is fixed on the same axis. This intermediate pulley of diameter d_{int} is linked by a cable to another pulley of diameter d_{sp} on which a proportional-torque spring with a spring constant k_{sp} is mounted (see Fig. 1.20). This additional cable linkage is set to provide the required angular displacement ratio k_r (and necessarily a torque ratio) between the axis on which the cables i and i' are attached and the one on which the torsional spring is mounted in order to stay within the working angular range $\Delta\phi_{sp}$ of the chosen spring when covering a distance a with a cable i, i.e., $\Delta c_{\phi_i} = a$ (or by similitude, a distance a' with a cable i', i.e., $\Delta c'_{\phi'_i} = a' = \kappa_s a$). This constant ratio k_r can be expressed as:

$$k_r = \frac{d_{sp}}{d_{int}} = \frac{2}{d}\frac{a}{\Delta\phi_{sp}} = \frac{2}{d'}\frac{a'}{\Delta\phi_{sp}}. \tag{1.78}$$

Then, in order to determine k_r, we had to find $\Delta\phi_{sp}$ by selecting a proper proportional-torque spring for the application. We fixed our choice to a spring with a torque constant of $k_{sp} = 1.027617$ N·m/rad (9.095176 lbs·in/rad) and with an angular range $\Delta\phi_{sp}$ of 270 ° ($\phi_{sp} \in [0\,^\circ, 270\,^\circ]$). In fact, we selected the spring presenting the highest torque-constant value for a good compromise between cost and dimension for our design. We also established the minimum cable tension $t_{\min}$ to 5 N in order to support the weight of the end effector of the master at all times ($t'_{\min}$ to 2.5 N since the end effector of the slave part is assumed to be κ_s times of the weight of the master one). Moreover, in the event where we would need to modify $t_{\min}$ in order to increase cable tensions, we decided to restrict the maximum spring angular displacements to 240 °. In this way,

$$\Delta\phi_{sp} = \frac{4\pi}{3} - \phi_{sp,\min}, \tag{1.79}$$

where $\phi_{sp,\min}$ is the angular position of the torsion spring required to ensure $t_{\min}$ in cable i and $t'_{\min}$ in cable i'. Upon assuming the worst-case scenario, i.e., that the torque produced by the torsion spring must balance the sum of the torques generated by the cables i (master side) and i' (slave side), when each single cable has to generate the highest $\tau_{\min}$ ($\tau_{\min} = t_{\min} d/2 = 0.2540$ N·m compared with $\tau_{\min} = t'_{\min} d'/2 = 0.0635$ N·m), we can derive the following expression for $\phi_{sp,\min}$:

$$\phi_{sp,\min} = \frac{k_r}{k_{sp}}\left(t_{\min}\frac{d}{2} + t'_{\min}\frac{d'}{2}\right) = \frac{k_r}{k_{sp}}\frac{d}{2}(t_{\min} + \kappa_s t'_{\min}), \tag{1.80}$$

where $t_{\min} = 5$ N and $t'_{\min} = 10$ N instead of 2.5 N. Then, using Eqs. (1.78) to (1.80), we obtain a quadratic expression for k_r and the two solutions are $k_{r,1} = 2.5581$ and $k_{r,2} = 5.9153$. We selected the solution $k_{r,1} = 2.5581$ in order to minimize the difference between d_{sp} and d_{int}.

For this first CDP prototype, we chose to use stainless steel cables with a nominal diameter of 0.0006096 m (0.024 in) (see item $2024SN$ manufactured by Carl Stahl® Sava Industries [199]).

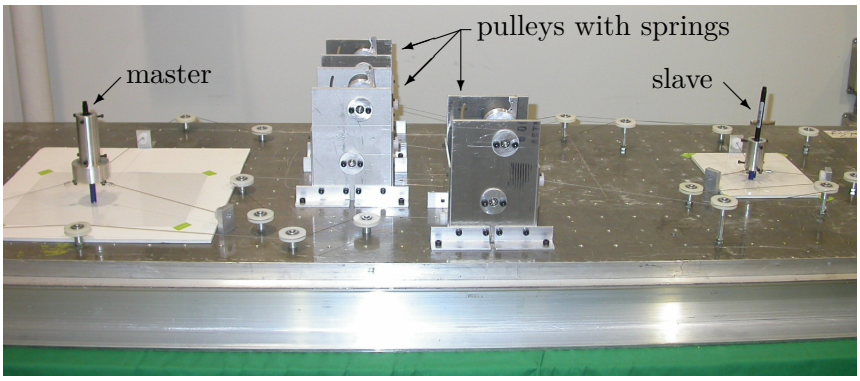

Figure 1.21 – Embodiment of the devised three-cable two-DoF CDP.

Thence, we set d_{int} to 0.01651 m (0.65 in), which is slightly higher than the manufacturer's recommendation regarding the minimum pulley diameters for the chosen cable. This leads us to a diameter d_{sp} of 0.0422334 m (1.6627337 in), which we round to 0.041275 m (1.625 in), in order to facilitate manufacturing. Finally, this small adjustment brings us to a new k_r value of 2.5. With this new k_r value and Eq. (1.80), we determine that $\phi_{sp,\min} = 1.235869$ rad (70.81 $^\circ$). With Eq. (1.78), the actual usable range $\Delta\phi_{sp}$ becomes 2.992126 rad (171.44 $^\circ$), so that the spring maximal angular position is now shifted to $\phi_{sp,\max} = 4.227995$ rad (242.25 $^\circ$). This gives us a range of 27.75 $^\circ$ to shift up $t_{\min}$ and $t'_{\min}$, if necessary, before to reach the mechanical limit of the chosen spring.

Therefore, by modifying Eq. (1.80), $t_{\max}$ and $t'_{\max}$ can easily be expressed as follows:

$$t_{\max} + \kappa_s t'_{\max} = \frac{k_{sp}}{k_r}\frac{2}{d}\phi_{sp,\max}, \tag{1.81}$$

and by solving this equation, again with the worst-case scenario, we obtain $t_{\max} = 34.21$ N when $t'_{\max} = 0$ N, and $t'_{\max} = 68.42$ N when $t_{\max} = 0$ N. Moreover, the tension within the cable linking the proportional-torque spring pulley to the intermediate pulley has to be assessed when $\phi_{sp,\max}$ is reached. To do so, the maximum cable tension $t_{int,\max}$ can be found as

$$t_{int,\max} = \frac{2k_{sp}}{d_{sp}}\phi_{sp,\max}, \tag{1.82}$$

and a maximum cable tension of $t_{int,\max} = 210.53$ N is obtained ($t_{int,\max} = 234.65$ N if $\phi_{sp,\max} = 270^\circ$). It is noted that these values are all below the minimum breaking force of the selected cable, which is approximately 312 N. Finally, the first prototype has been assembled and Fig. 1.21 shows a photograph taken of this three-cable two-DoF CDP.

From the previous information and the kinetostatic model provided in Sub-section 1.3.5 for a three-cable two-DoF planar CDP, it is now possible to determine the theoretical behaviour of the devised CDP as a function of the master's end-effector positions over the workspace $\mathcal{A}$. Because proportional-torque springs cannot produce a neutral static equilibrium of the end effector over all the CDP's workspace, it has been decided to evaluate the force magnitude

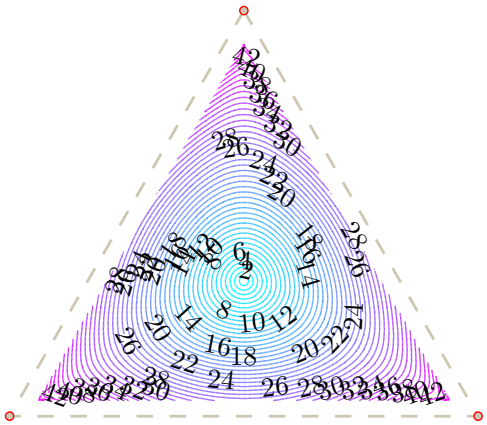

Figure 1.22 – Theoretical $||\mathbf{f}_r||_2$ (N) computed over $\mathcal{A}$ for the devised prototype.

that a user would have to provide in order to move the master end-effector, which is linked to the slave end-effector, over $\mathcal{A}$. For this purpose, the vector $\mathbf{f}_r$ of the resulting force can be written as follows:

$$\mathbf{f}_r = \begin{bmatrix} f_x \\ f_y \end{bmatrix}, \tag{1.83}$$

where f_x and f_y are obtained from Eq. (1.58), when

$$\tau_i(c_i) = \frac{k_{sp}}{k_r}\left(\frac{2}{d}\frac{c_i}{k_r} + \phi_{sp,\min}\right), \tag{1.84}$$

Then, the magnitude of the resulting force can be expressed as

$$||\mathbf{f}_r||_2 = \sqrt{\mathbf{f}_r^T \mathbf{f}_r}. \tag{1.85}$$

Also, for this numerical computation, it should be noted that we fixed $f'_x = 0$ N and $f'_y = 0$ N, i.e., we assumed that no external force is applied on the slave end-effector.

Figures 1.22 and 1.23 illustrate the computed square norm of the expected resulting force that should be applied by a user on the master end-effector when moving it over its workspace, and similarly, moving its slave counterpart at the same time. Figure 1.22 shows the isocontour lines by increments of 1 N and Fig. 1.23 shows a tridimensional view of the evolution of the force magnitude. In both figures, it is easily seen that the only force-neutral position is at the geometric centre of the equilateral triangle. The root mean square (RMS) value of $||\mathbf{f}_r||_2$ over $\mathcal{A}$ is 24.7678 N, which has been computed by numerical integration (function `quad2d` from MATLAB®) using the following relation:

$$||\mathbf{f}_r||_{2,\text{rms}} = \sqrt{\frac{1}{A}\int_{\mathcal{A}} ||\mathbf{f}_r||_2^2 dA}. \tag{1.86}$$

In the next sub-section, the constructed three-cable two-DoF cable-driven pantograph is tested in order to validate this predicted behaviour and the proper functioning of this class of mechanisms.

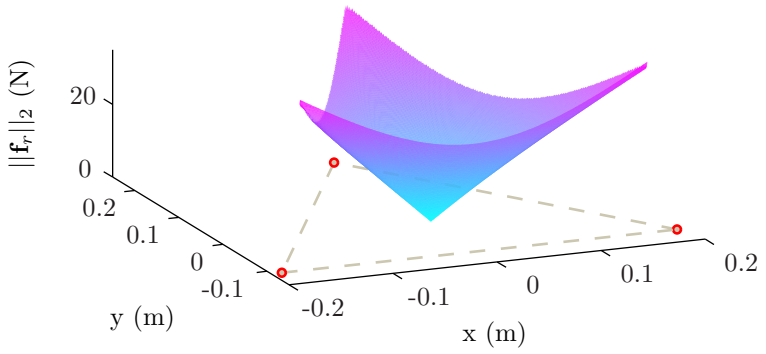

Figure 1.23 – Representation in 3D of theoretical $||\mathbf{f}_r||_2$ computed over $\mathcal{A}$.

1.4.2 Verification of the prototype performances

The first prototype of a planar cable-driven pantograph was built and tested. This system, which relies on two cable-driven parallel mechanisms connected together by their corresponding cables, is a purely mechanical telemanipulator that allows the reproduction of two-DoF point displacements in the proportion of a scaling factor κ_s between its two parts, i.e., its master and its slave sub-systems. The tension in the cables is ensured by the use of proportional-torque springs, which is a passive method of accumulating energy without using electrical components as in most conventional devices. This system design is based on a relatively simple and low-cost architecture, and presents a simple and intuitive control, since the master displacements are exactly reproduced by the slave.

In this sub-section, two experimental tests have been performed on the first prototype of a three-cable two-DoF cable-driven pantograph. The first test is intended to validate the kinematic behaviour of our prototype, i.e., to assess if the chosen scaling factor $\kappa_s = 1/2$ between the master and the slave geometries is accurately reproduced within the CDP displacements. The second one is rather intended to validate the kinetostatic behaviour of the prototype by measuring the exact external forces that must be applied by the user on the master's end-effector in order to maintain a static equilibrium over its workspace $\mathcal{A}$.

Preliminary Validation of the Kinematic Behaviour

In order to perform this first experimental test, we attached a pen on the effector of the master and the slave mechanisms and wrote the word "Laval" by controlling the master (see Fig. 1.21). The same word was traced simultaneously by the slave, but assumed to be scaled by the factor $\kappa_s = 1/2$. A photograph of these two "handwritten" words is displayed in Fig. 1.24 in order to observe the degree of similarity that can be obtained.

Then, in order to assess the resulting similitude ratio between the root word and the reproduced one, we first took a close and perpendicular photograph of the two superimposed words with a high-definition camera, which is shown in Fig. 1.24. We then cropped with an image

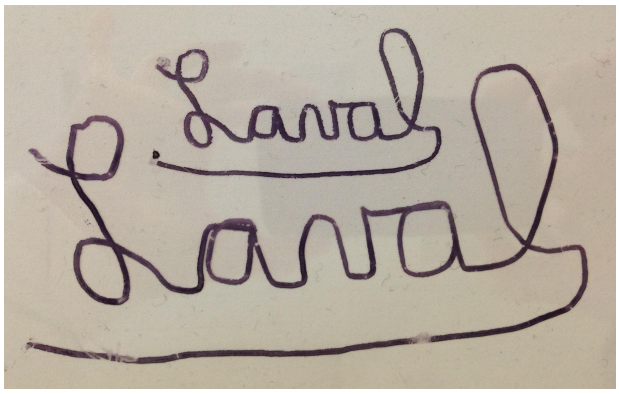

Figure 1.24 – Handwritten words simultaneously traced at the master (large characters) and the slave (small characters).

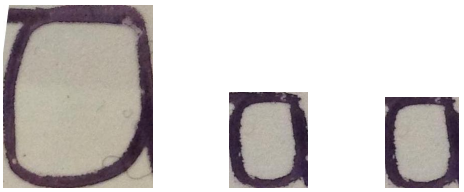

(a) (b) (c)

Figure 1.25 – Comparison of the handwritten words ratio: (a) second letter "a" (master), (b) second letter "a" (slave), and (c) second modified letter "a" (slave).

editing software the second letter "a" belonging to each written word (see Figs. 1.25a and 1.25b). In order to perform a proper comparison, we rotated these two images to make the upper segment of both letters as horizontal as possible (from Fig. 1.24, by 7 ° and by 3.5 ° for the large and the small "a", respectively, both with a right rotation). Then, after cropping both rotated images in order to determine their smallest envelops, we used the images resolution (number of pixels) as a comparison tool. We initially found an approximate ratio of $\kappa_s^{w,h} \approx 0.53$ in both directions, i.e, the width and the height of the image, instead of our prescribed CDP ratio of $\kappa_s = 1/2$.

During this experiment, however, the tips of the pens used to write these two words were of the same size, which is against the first rule established in Sub-section 1.3.3. In fact, in order to complete a meaningful comparison, the tip of the pen attached to the slave end-effector should have been half of the size of that used at the master end-effector (following the prescribed ratio $\kappa_s = 1/2$). Then, a number of pixels equivalent to a quarter of the full thickness of the pen trace has been removed from the final image of the small letter "a" (see Fig. 1.25c). In this way, the resulting width and height ratios are now $\kappa_s^w \approx 0.49$ and $\kappa_s^h \approx 0.50$, respectively. Table 1.1 contains the resolution of each image and its corresponding resulting ratio. These results show that our prototype of a three-cable two-DoF planar cable-driven pantograph can transmit displacements from the master to the slave following the prescribed scaling factor of $\kappa_s = 1/2$ with reasonable accuracy.

Table 1.1 – Image specifications (Fig. 1.25) and resulting similitude ratios.

	Resolution (W x H)	Resulting ratio	
		κ_s^w	κ_s^h
Large "a" (Fig. 1.25a)	297 x 364 pixels	—	—
Small "a" (Fig. 1.25b)	156 x 191 pixels	≈ 0.53	≈ 0.53
Small modified "a" (Fig. 1.25c)	146 x 182 pixels	≈ 0.49	≈ 0.50

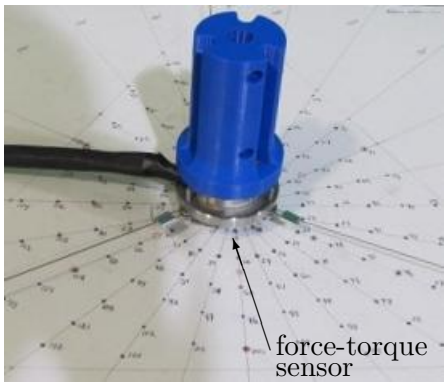

(a) The master end-effector with the force-torque sensor

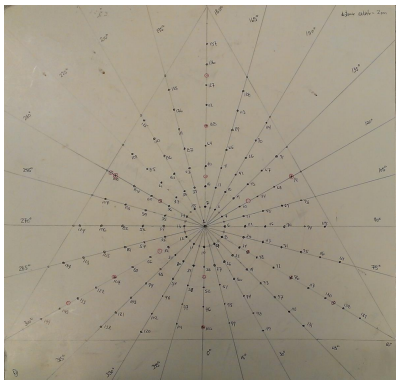

(b) The chosen position measurements benchmark

Figure 1.26 – The experimental setup.

Preliminary Validation of the Kinetostatic Behaviour

When using proportional-torque springs, the second assumption of Sub-section 1.3.4 according to which the springs should maintain a perfect neutral equilibrium over the workspace is far from being true. As a result, the balancing force required to maintain the master in a given posture is neither null nor negligible, except at the centroid of its triangular workspace $\mathcal{A}$, as it was mentioned in the previous section (see Figs. 1.22 and 1.23).

In order to verify the real level of neutral equilibrium reached over the workspace of the devised three-cable two-DoF planar CDP, an experiment was performed to measure the forces applied on the end effector of the master while it is moved over $\mathcal{A}$. The end effector was manually held in place for approximately five seconds at each of a sequence of 151 positions, scattered over the workspace according to the pattern shown in Fig. 1.26b. More specifically, these points are equally distributed by intervals of two centimetres along line segments starting from the centroid of $\mathcal{A}$ and ending at its edges and oriented by increments of fifteen degrees in order to span the entire working area. A force-torque sensor from ATI Industrial Automation [200] was used to record the balancing forces applied on the plane of motion (see Fig. 1.26a). Then, the distribution of the balancing-force magnitude over the workspace is traced in Figs. 1.27 and 1.28. The experimental RMS value of $||\mathbf{f}_r||_2$ over $\mathcal{A}$ was ≈ 19.7 N, which was determined

by computing the volume under the surface formed by our set of measurements $||\mathbf{f}_r||_2$ using the following relation:

$$||\mathbf{f}_r||_{2,\text{rms}} = \sqrt{\frac{1}{A}\sum_{i=1}^{p} V_{\text{mesh},i}} \equiv \sqrt{\frac{1}{A}\int_{\mathcal{A}} ||\mathbf{f}_r||_2^2 dA}, \tag{1.87}$$

where $V_{\text{mesh},i}$ is the volume of the i^{th} irregular triangular prism associated to the mesh grid that best fits our set of experimental measures and p is the number of discrete triangles required to form this mesh grid ($p = 285$). The function `delaunay` from the MATLAB® package [201] is well suited to accomplish this task since it creates a bidimensional triangulation for a given set of points. It should be noted that each irregular triangular prism is defined in three dimensions by the planar Cartesian position of three points $\{\mathbf{v}_{i,1},\mathbf{v}_{i,2},\mathbf{v}_{i,3}\}$ belonging to $\mathcal{A}$ and the square of the norm of their associated measured force, i.e., $\{||\mathbf{f}_{r,i,1}||_2^2,||\mathbf{f}_{r,i,2}||_2^2,||\mathbf{f}_{r,i,3}||_2^2\}$. The volume $V_{\text{mesh},i}$ of the i^{th} irregular triangular prism can be then computed using the following equation:

$$V_{\text{mesh},i} = \frac{1}{3}(||\mathbf{f}_{r,i,1}||_2^2 + ||\mathbf{f}_{r,i,2}||_2^2 + ||\mathbf{f}_{r,i,3}||_2^2)\frac{|(\mathbf{E}(\mathbf{v}_{i,2} - \mathbf{v}_{i,1}))^T(\mathbf{v}_{i,1} - \mathbf{v}_{i,3})|}{2}, \tag{1.88}$$

where the second term on the right-hand side represents the area of the base section of the irregular triangular prism and $\mathbf{E}$ is a rotation matrix of $\pi/2$ rad defined by

$$\mathbf{E} = \begin{bmatrix} 0 & -1 \\ 1 & 0 \end{bmatrix}. \tag{1.89}$$

In Fig. 1.27, it is observed that, as expected in Sub-section 1.4.1, only one position inside the workspace, i.e., the centroid of $\mathcal{A}$, produces a neutral equilibrium of the three forces—one force per cable—applied on the end effector by its cables. Also, when comparing the expected with the measured $||\mathbf{f}_r||_{2,\text{rms}}$ values, it is noticed that the magnitude of the experimental resulting forces are lower than expected, the measured RMS value is $\approx$ 19.7 N, for a difference of $\approx$ 5.1 N when compared with the theoretical value.

It is also interesting to notice that, when only the master side of the CDP is attached to the spring-loaded pulleys, i.e., a system equivalent to a simple three-cable two-DoF CDPM, the user has to apply a similar amount of forces in order to maintain the exact same end-effector poses. Indeed, the measured $||\mathbf{f}_r||_{2,\text{rms}}$ value is $\approx$ 19.4 N, instead of $\approx$ 19.7 N when the full CDP (including the slave part) was mounted. This observation clearly shows that the presence of the slave part of the CDP does not seem to generate a significant fluctuation of the external force required by the user on the master end-effector in order to statically balance the CDP. This negligible difference observed between these two measurements is only valid, however, when no external force is applied at the slave end-effector of the full CDP. The reader should also note that this observation corroborates Eq. (1.58). Figures 1.29 and 1.30 present the distribution of the balancing-force magnitude over the workspace $\mathcal{A}$ when the master side only is attached to the CDP.

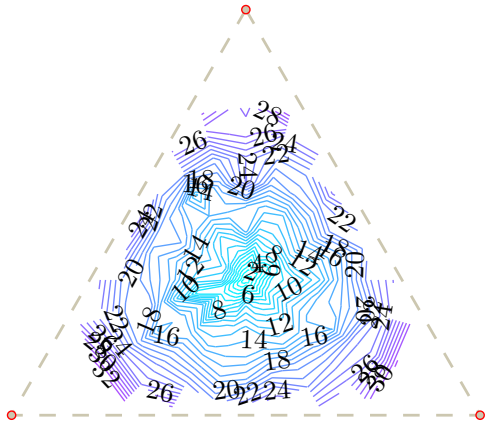

Figure 1.27 – Experimental $||\mathbf{f}_r||_2$ (N) measured over $\mathcal{A}$ resulting from the devised prototype.

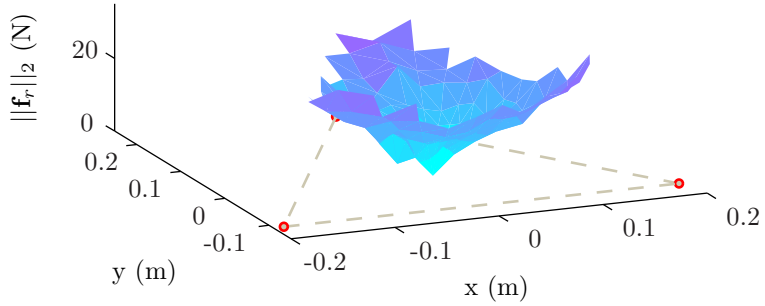

Figure 1.28 – Representation in 3D of experimental $||\mathbf{f}_r||_2$ measured over $\mathcal{A}$.

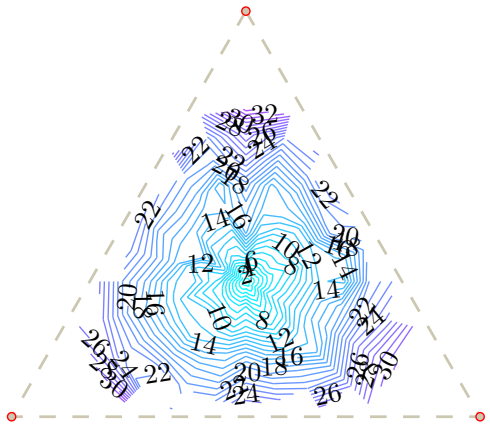

Figure 1.29 – Experimental $||\mathbf{f}_r||_2$ (N) measured over $\mathcal{A}$ resulting from the devised prototype (master only).

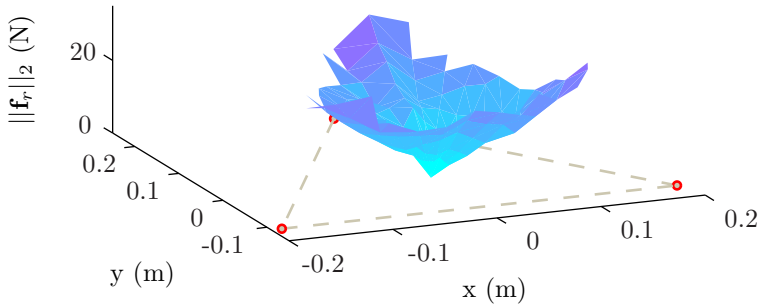

Figure 1.30 – Representation in 3D of experimental $||\mathbf{f}_r||_2$ measured over $\mathcal{A}$ (master only).

The differences between theoretical mathematical models and experimental measurements can be first explained by the possible errors related to the angular position of $\phi_{sp,\min}$ when assembling the prototype, which possibly modifies the forces distribution on the master-slave end effectors over their workspace. If the exact value of $\phi_{sp,\min}$ is set to be lower than the computed value, the tension profile in the cables will shift down compared to the theory. Another possible reason is the presence of friction in the system, which can reduce the resulting forces felt by the force-torque sensor. From the use of the prototype, a relatively high level of friction seemed to occur in the system, mainly between the cables and the fixed eyelets and within the idler pulleys. Each cable has a different cable routing with a different number of idler pulleys and different in-out angles, all of which affect the friction applied on their corresponding cable of the CDP. Also, with friction, it is possible that the slave sub-system provides a lower or a higher level of torque than expected on each winding pulley when one moves the master end-effector, which in turn alters the tension in the master cables. In addition, the experimental measurement process itself may contain several uncertainties such as an increasing bias error from the force-torque sensor over the time, the possible inaccuracy of the measured values, small unintentional displacements at the master end-effector while recording the data, etc.

Finally, this prototype does not present the high level of safety initially desired because the end effector is not in equilibrium over the entire workspace, but rather at a single position, the centroid of the workspace. Therefore, if one releases the master end-effector, it will automatically return to its equilibrium position. Based on this result, at this point, the equations defined in Sub-section 1.3.4 cannot be directly applied because of the friction level in the system and of the imperfect static equilibrium over the workspace. Despite the relatively high forces required to control the prototype, however, it can still be used to reproduce two-dimensional point displacements, as it was shown in Sub-section 1.4.2. It is also noted that the maximum force that can be applied by the slave end-effector on its environment is limited by the resulting forces that its cables can apply on it in a particular direction. In fact, the use of stiffer springs would lead to a higher capacity of the slave end-effector to apply forces on its environment. Moreover, for a specific application, if the necessary resulting force $\mathbf{f}'_r$ that must

be applied on the slave's environment requires a cable tension higher than $t'_{\max}$, tensions in other system's cables may reach a value lower than $t_{\min}$ or $t'_{\min}$, which can lead to a loss of the mechanism geometry. In order to complete the validation of the kinetostatic model presented in Sub-section 1.3.5, additional measuring instruments such as load cells would be necessary to determine the experimental tension profile in each cable of the devised CDP while applying external forces at both end effectors.

1.5 Summary

In this chapter, we proposed a new family of pantographs: the *cable-driven pantographs*. This type of mechanisms, for which the force transmission between the master and the slave components relies on cables, allows the reproduction of point or rigid-body displacements. The general concept simply consists in connecting together two homothetic cable-driven parallel mechanisms. One of them acts as the master, the other as the slave, which allows the reproduction of trajectories imposed from the master end-effector to the slave end-effector following a prescribed scaling factor κ_s. Since CDPs are formed by the combination of conventional pantographs and CDPMs, Sections 1.1 and 1.2 were dedicated to the description of these two distinct classes of mechanisms.

In Section 1.3, the working principle of CDPs was described by their two main characteristics: (i) they are purely mechanical and (ii) they are formed with cable-driven parallel mechanisms. Then, the fundamental component used to develop this class of mechanisms was shown, in Sub-section 1.3.1, as a one-DoF linear CDP in which the displacement ratio between the master and slave end-effectors is defined by $\kappa_s = d'/d$, the winding-drum diameter of the slave divided by the winding-drum diameter of the master. As the conceptual design could not maintain the cables in tension, springs were added to the design. We extended this elementary CDP to a n-DoF CDP in Sub-section 1.3.2. Moreover, the input-output displacement and load relationships of CDPs were established in Sub-sections 1.3.3 and 1.3.4, respectively. In summary, the relationships describing the theoretical behaviour of CDPs are simply $\mathbf{p}' = \kappa_s \mathbf{p}$, $\dot{\mathbf{p}}' = \kappa_s \dot{\mathbf{p}}$, $\ddot{\mathbf{p}}' = \kappa_s \ddot{\mathbf{p}}$, $\mathbf{Q}' = \mathbf{Q}$, $\dot{\mathbf{Q}}' = \dot{\mathbf{Q}}$, $\ddot{\mathbf{Q}}' = \ddot{\mathbf{Q}}$, $\mathbf{f}' = -(1/\kappa_s)\mathbf{f}$ and $\mathbf{n}' = -\mathbf{n}$. Then in Sub-section 1.3.5, kinetostatic models have been established for a two-cable one-DoF linear CDP and for a three-cable two-DoF planar CDP. Due to the fact that CDPs are statically indeterminate by nature, it has been demonstrated that compatibility equations are necessary in order to solve the corresponding system of equations. These theoretical models allow us to approximate the behaviour of a CDP with regards to its cable tensions and the external forces applied at its master-slave end-effectors.

The balance of this chapter was focused on the preliminary validation of the CDP concept in Section 1.4. In Sub-section 1.4.1, we described the chosen geometry of the first CDP prototype as a three-cable two-Dof cable-driven pantograph and its master workspace was

selected to be an equilateral triangle with an edge length of $a = 0.38$ m and, by homothecy, with a scaling factor $\kappa_s = 1/2$, its slave workspace was set to be an equilateral triangle with an edge length of $a' = 0.19$ m. Then, as a first step towards the development of this family of pantographs, we built a two-Dof prototype. In order to solve the problem of maintaining a sufficient level of tension in the cables, proportional-torque springs were installed in parallel to the cable winding pulleys. This solution ensured a minimum tension of 5 N in cables of the master and, by similitude, a minimum tension of 2.5 N in cables of the slave part. Moreover, knowing that the use of proportional-torque springs does not allow a perfect static equilibrium over the workspace, the mapping of the theoretical resulting forces that a user will have to apply to hold the master end-effector, and necessarily the linked slave end-effector, at a given position was determined with the relations established in Sub-section 1.3.5. In Sub-section 1.4.2, we presented the first experimental results. Firstly, the prototype was shown to allow the reproduction of a handwritten word. This drawing demonstrated the capability of the devised cable-driven pantograph to suitably generate an image following the prescribed scaling ratio of $\kappa_s = 1/2$. These results confirmed that selecting the proper diameter of the master-slave winding drums and the proper base and end-effector geometries (positions of points $\{A_i, A'_i\}$ and $\{B_i, B'_i\}$, respectively) with respect to a prescribed constant ratio κ_s leads to a constant proportion in all directions between the root image and the resulting image. The prototype of the three-cable two-Dof CDP was secondly assessed in order to measure the user-applied input forces when one desires to move and hold the master end-effector over the CDP workspace. This analysis showed that relatively high forces are required from the user in order to move the end effector out of its reference position, i.e., the centroid of the workspace where the neutral equilibrium is reached. In fact, it was showed that the measured input forces required by the user to move the end effector were lower than the expected values, due to potential assembly and measurement errors and the presence of friction within the mechanism. This result was observed when both the full CDP and the master-only CDP were under evaluation. Then, in summary, this first prototype was used to demonstrate the practicability of the cable-driven pantographs concept. Improvements should be made, however, in order to decrease the level of forces required by the user to move its end effector over the whole workspace. The next chapter proposes a method to achieve this important safety requirement, which is possible based on the observation that, when no external forces are applied on the slave end-effector, the force that a user must provide at the master end-effector is independent from the presence of a slave CDPM.

Chapter 2

Static Equilibrium of Cable-Driven Pantographs

"To every action there is always
opposed an equal reaction."
- Isaac Newton

In Chapter 1, it has been discussed that for cable-driven pantographs (CDPs), as well as for general cable-driven parallel mechanisms (CDPMs), the unilaterality of force transmission requires a minimum level of tension in the cables in order to preserve their geometry. As a result, in most of the cases, driving electrical motors are needed to produce continuous torques to maintain the cables taut at all times. An alternative solution, for a purely-mechanical approach, is to add springs in parallel with the winding pulleys in order to generate these torques. However, as it has been previously demonstrated, the use of conventional springs only, even though it provides the required minimum torques, generates additional forces that must be balanced by an undesirable input-force from the user's hand at the CDP end-effector.

In this chapter, we propose to use passive nonlinear springs to generate these minimum torques, while altering as little as possible the CDP neutral equilibrium over its workspace. In this way, the user only needs to produce the additional forces, i.e., those forces needed to generate accelerations, compensate internal friction and balance external forces applied to the end effector. The design of the required nonlinear springs couples a four-bar linkage with commercially available springs.

In the last decades, mechanical static balancing of mechanisms has received sustained interest from researchers, since it allows to significantly decrease the size of the actuators for equivalent displacements of the end effector. Indeed, the actuators do not have to produce the required input energy to counterbalance the usual variations of the potential energy of the system between each pose of the end effector. This role is generally rather fulfilled by springs,

counterweights, pneumatic or hydraulic cylinders, and even by electromagnetic devices.

Springs are widely used since, unlike counterweights, they do not increase significantly the mechanism's inertia. For this reason, many researchers have chosen springs in order to statically balance their mechanism. As examples, let us cite the work of Nathan [202, 203], which has designed constant force generator mechanisms using springs for an adjustable seat application, and the work of Arakelian *et al.* [204] and Lin *et al.* [205], who have worked on the balancing of a leg orthosis and a mobile arm support, respectively. Other authors such as Herder [206], Tuijthof and Herder [207], Streit and Shin [208], Shin and Streit [209], Laliberté *et al.* [210], Deepak *et al.* [211], which have worked on the static balancing of different planar mechanisms, have also used springs as fundamental components of their analyses. Other researches have focused on the exact balancing of spatial mechanisms [212, 213, 214, 206, 215, 216, 217] as well as on their partial gravity compensation [218] in adding either compression, extension, and torsion springs.

Even if, in general, counterweights add inertia to the original system, they have been extensively used as a means of statically balancing mechanisms. From the literature, we can cite, as examples, the work of Russo *et al.* [219] and Baradat *et al.* [220], who both combined counterweights with pantograph linkage in order to reach their goal. Also, more recently, Lacasse *et al.* [221] proposed the design of a statically balanced serial robot by using remote counterweights connected to the robot via a low-pressure hydraulic transmission. More generally, other research groups have also used counterweights to statically balance planar and spatial mechanisms [222, 223, 224, 225].

If springs or counterweights are insufficient or unpractical for a specific application, the use of pneumatic or hydraulic cylinders may be considered. Indeed, some researchers have chosen to rather include these technologies into their design, such as Idan *et al.* [226] and Windenberg [227], who directly connected these additional components to the moving platform of their mechanism for partial static gravity balancing. Similarly, Segawa *et al.* [228] proposed the use of permanent magnets attached on the base and to the moving platform of a given mechanism in order to statically equilibrate its weight.

On the other hand, we know, from Chapter 1 (see Section 1.2), that cable-driven parallel mechanisms have been the topic of many publications since they are interesting candidates for several robotic applications, because of advantages they hold over conventional robots. However, even if the static balancing of mechanisms and CDPMs have been widely studied separately, to our best knowledge, no attention has been given to the static balancing of CDPMs, and by extension, to the static balancing of CDPs.

The proper application of static-balancing principles to CDPMs, in general, could lead to better safety and lower power consumption. Indeed, even with partial static balancing, a sudden shortage in electrical power would be less dangerous, as the resulting variation in

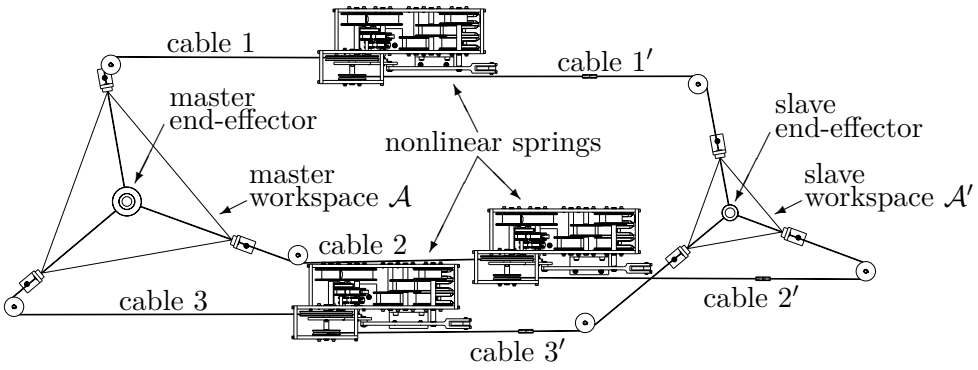

Figure 2.1 – Computer-aided design (CAD) model of the three-cable two-DoF planar CDP devised benchmark.

potential energy would be reduced. Moreover, the maximum continuous torques required from the motors would be smaller, thus reducing their size and weight, and more importantly, their inherent risk for user safety. Currently, in most of the CDPMs, the driving electrical motors are used to generate the prescribed accelerations and to balance out the external forces applied at the end effector while maintaining a minimum level of tension in each cable. In this case, continuous torques must be produced by the actuators even if no motion or applied wrench are required. These constant torques may be considered as an unnecessary expenditure of electrical energy. Hence, a conservative purely-mechanical sub-system that could passively generate the required cable tensions would significantly reduce the wasted energy and increase the safety level of the global system.

As previously revealed, we present here a method of designing a nonlinear spring to maintain a given minimum tension in the cables of a CDP (which method can be directly applied to more simple CDPMs), while approaching neutral static equilibrium over its master workspace, and inherently over its slave workspace (see Fig. 2.1 for an overview of the final CDP devised benchmark), a method akin to those proposed by Herder [206]. Thence, the desired nonlinear springs are approximated by combining commercial springs with four-bar linkages. More specifically, in this chapter, Section 2.1 introduces the definitions of an exact static equilibrium (ESE) in Sub-section 2.1.1 and an approximate static equilibrium (ASE) in Sub-section 2.1.2. Then, Section 2.2 demonstrates the methodology used to choose the optimal tension profile in the cables and the nonlinear springs best suited for the three-cable two-DoF planar CDP previously presented in Sub-section 1.4.1 of Chapter 1. More precisely, Sub-section 2.2.1 recalls the geometry of the chosen CDP, Sub-section 2.2.2 presents the optimization process followed to determine the cable tension profile that best balances this mechanism, Sub-section 2.2.3 reports on the optimization of the design parameters of the chosen nonlinear springs, namely, the dimensions of the four-bar linkage, the properties of the springs, and the assembly specifications of the sub-system, and finally, Sub-section 2.2.4 contains the experimental verification of the theoretical results, where the external forces generated at the master end-effector are

measured and compared with those predicted by the kinetostatic model. A summary of this chapter is then proposed in Section 2.3.

2.1 Exact Versus Approximate Static Equilibrium

In general, an object is said to be in exact static equilibrium (ESE) when the sum of all forces and torques—or the sum of all wrenches—exerted on it is null. In particular, a mechanism, such as a n-DoF CDPM or a n-DoF CDP, is normally considered to be statically balanced when the combination of all internal wrenches $\mathbf{w}$, i.e., those wrenches generated by the cables and the gravity effect, exerted on each end effector is equal to $\mathbf{0}_n \in \mathbb{R}^n$. Moreover, this result must be true for every end-effector pose over the workspace. In fact, it means that the system is at its lowest level of potential energy for all possible poses of its end effector, i.e., its potential energy U is constant over the entire workspace.

On the other hand, an approximate static equilibrium (ASE) occurs when one cannot reach a state of perfect equilibrium, i.e., the ESE, but rather only approximates it for every end-effector pose over the entire workspace. As a result, for some particular combinations of the end-effector positions and orientations, a resulting wrench $\mathbf{w} \neq \mathbf{0}_n$ is generated and the moving parts of the n-DoF CDPM, or the n-DoF CDP, automatically move by themselves to the closest stable equilibrium pose. If one wants the system to hold a given unstable pose, an external wrench $\mathbf{w}_e = -\mathbf{w}$ needs to be applied by the environment, e.g., by the user directly or by additional actuators, on the mechanism end-effector. In summary, this type of mechanism presents different levels of potential energy over its workspace (U is not constant) and reaching an ASE amounts to minimizing $|\Delta U|$, or similarly the magnitude of $\mathbf{w}$, over the workspace. If no additional wrench $\mathbf{w}_e$ is applied to cancel the gradient ∇U, then the system will always drift towards a minimum of U.

2.1.1 Exact Static Equilibrium of Cable-Driven Pantographs

For a m-cable n-DoF cable-driven pantograph (either for the master or the slave part), or by similarity, for a simple m-cable n-DoF cable-driven parallel mechanism, the exact static equilibrium relation can be written as:

$$\mathbf{w} = \mathbf{W}\mathbf{t} + \mathbf{w}_g = \mathbf{0}_n, \ \mathbf{t} > \mathbf{0}_m, \tag{2.1}$$

where $\mathbf{W}$ is the pose-dependent wrench matrix of dimensions $n \times m$, the vector $\mathbf{t}$ contains the strictly-positive tensions of the m cables of the CDPM, which can be written as

$$\mathbf{t} = \begin{bmatrix} t_1 & t_2 & \cdots & t_m \end{bmatrix}^T, \tag{2.2}$$

the vector $\mathbf{w}_g$ represents the wrench generated by the gravity effect applied on the mechanism end-effector, and $\mathbf{0}_n$ and $\mathbf{0}_m$ are zero vectors in $\mathbb{R}^n$ and $\mathbb{R}^m$, respectively.

When applying Eq. (2.1) to a generic m-cable n-DoF CDPM, determining the matrix $\mathbf{W}$ is not as simple as in the case of the three-cable two-DoF planar CDP presented in Subsection 1.4.2. This is mainly due to the capability of the mechanism to perform rotations. Then, in order to determine the internal components of $\mathbf{W}$ for any CDPMs, we can use the principle of virtual work, which allows us to shift from the mechanism's velocity relations to its static relations and *vice versa*. The mathematical derivation of this matrix $\mathbf{W}$ is presented in Appendix A.1 for the three-DoF planar case (two translations and one rotation) and in Appendix A.2 for the spatial case (six DoFs).

Although reaching an ESE by solving Eq. (2.1) would be the best case scenario for any purely-mechanical CDPM and CDP designs in general, achieving perfect static balancing of such a mechanism over its entire workspace, as defined in this sub-section, is an extremely challenging task in practice. Nevertheless, one may seek and find a method that brings the CDPM or CDP close to static equilibrium. We leave to the next sub-section the definition of *closeness to static equilibrium*.

2.1.2 Approximate Static Equilibrium of Cable-Driven Pantographs

When designing a purely mechanical CDP, achieving global ESE is a very challenging problem. The vector sum of the cable tensions must be null for every single end-effector pose of the workspace. In general, this requires that all cable tensions be coupled to all cable lengths through a complex relationship. Achieving this relationship through a passive mechanical system is thus impractical. Hence, instead of targeting an ESE, we rather target an approximate static equilibrium (ASE). The goal is to approach perfect neutral equilibrium, or, in other words, to reach as close as possible to static equilibrium.

From Eq. (2.1), *closeness to equilibrium* can be expressed as follows:

$$\mathbf{w} = \mathbf{W}\mathbf{t} + \mathbf{w}_g \approx \mathbf{0}_n, \ \mathbf{t} > \mathbf{0}_m. \tag{2.3}$$

This approximate equality illustrates that the wrenches applied by the cables cannot, in general, perfectly compensate for the wrench applied by the gravity on the end effector. The cable tensions are then chosen to tend, as much as possible, towards the ESE. Obviously, in order to claim that one has achieved the ASE for a given system, Eq. (2.3) must be verified for every pose of the CDP end-effector workspace (for both the master and slave CDPMs).

In order to design a system that reaches a high level of static equilibrium, different approaches can be used. The first one is naturally to create a method allowing the determination of the best architecture (points A_i and B_i) and the best tension profiles t_i in the cables, simultaneously, for a prescribed n-DoF CDPM workspace. Several objective functions can be chosen and then optimized while evaluating the infinite range of the different parameters combinations. Although this option seems promising, it can easily lead to a system of equations with a high level of complexity and interrelation.

Then, with the aim of keeping the problem complexity reasonably low, it is possible to use the square of the variance of the potential energy U as an objective function. This amounts to minimizing the fluctuations of U over the mechanism workspace [229]. This problem is symbolically expressed as

$$f \equiv \int_V (U - \overline{U})^2 dV \;\longrightarrow\; \min_{A_i,\ B_i,\ i=1,\ldots,m}, \tag{2.4}$$

where f is the objective function, V represents the volume of the n-DoF workspace, U represents the potential energy for a given end-effector pose and $\overline{U}$ is the mean value of the potential energy over the entire workspace. In summary, here, the position of the CDPM eyelets A_i and its end-effector attachment points B_i are chosen to minimize the objective function f while the profile tensions t_i in the cables are known as a function of the cable lengths. It is noted that this is equivalent to minimizing the external required input wrenches $\mathbf{w}_e$ when moving the end effector out of a neutral equilibrium pose.

Another approach, when one knows the geometry of the CDPM, i.e., the positions of points A_i and B_i, is to use the norm of the resultant wrench $\mathbf{w}$ from the cable tensions and the effect of gravity acting on the moving platform as the objective function. Then, the *closeness to equilibrium* may be expressed as

$$f \equiv \int_V ||\mathbf{W}\mathbf{t} + \mathbf{w}_g|| dV \;\longrightarrow\; \min_{t_i>0,\ i=1,\ldots,m}, \tag{2.5}$$

where t_i must be positive in order to preserve the mechanism geometry. Here, the relationship between the tension t_i of the i^{th} cable and its length c_i is to be chosen in order to minimize the objective function f. It is noted that, for CDPMs generating both rotations and translations of their moving platforms, the norm has to include weights that take into account the dimensionally non-homogeneous nature of their associated wrenches. In this work, the second method has been preferred to the others, taking into account that the geometry of the CDP or CDPM has been initially optimized using other optimization criteria in order to simplify the problem.

2.2 Approximate Static Equilibrium of a Three-Cable Two-DoF Planar Cable-Driven Pantograph

In order to achieve ASE and apply it to a CDP, we decided to first develop and evaluate the proposed technique for a simple case, namely, a three-cable two-DoF planar CDP with an equilateral triangle as workspace for each of its sub-systems—the master and the slave CDPMs. Here, we seek static balancing when no external wrench $\mathbf{w}_e$ is applied on both end effectors. Moreover, the gravity effect is assumed to be negligible since the gravity field is chosen to act perpendicularly to the CDP's planar workspace and the minimum tensions $t_{\min}$ and $t'_{\min}$ will be chosen in order to compensate for the weight of the moving parts. Also, since

the workspaces of the chosen master and slave CDPMs are symmetric, we have assumed the tension profiles to be identical for each cable.

As we know, designing a passive mechanical device that would achieve perfect static equilibrium of the end effector over the planar CDP workspace while maintaining sufficient cable tensions is a challenging task. Although such a mechanical apparatus may exist, we conjecture that it will be prohibitively complex. Previous work has demonstrated however, that, when the base eyelets are fixed, it is possible to approximate the static equilibrium of a planar CDPM while maintaining a minimum level of cable tensions by adding a reasonable number of parts [230]. Then, based on these results and the design presented in Section 1.4 of Chapter 1, a complete method is proposed for optimizing the design parameters of a four-bar mechanism combined with commercial springs, to approximate the neutral equilibrium of the three-cable two-DoF planar CDP.

2.2.1 Description of the Geometry

The geometry of the mechanism used throughout this section is similar to the geometry previously shown in Section 1.4, i.e., a three-cable two-DoF planar CDP. The mechanism description is given in Sub-section 1.3.5 and a kinematic modelling of its master part is presented with Fig. 1.16. It is noted that a similar geometry is used for its slave part, following the chosen scaling factor $\kappa_s = 1/2$. It is recalled that the end effector is considered to be a rigid body instead of a point in order to better represent our experimental testbed (see Fig. 2.1). It is also considered to only have two DoFs instead of three based on its particular equilateral triangle geometry, a hypothesis that was validated in Sub-section 1.3.5. Although the planar case is studied here, the whole work could be extrapolated quite naturally to the more general spatial case, at least for a CDP presenting a constant end-effector orientation, at the cost of more demanding mathematical formulations.

2.2.2 Determining the Minimum Cable Tensions

In order to approximate the static equilibrium of the three-cable two-DoF planar CDP over $\mathcal{A}$ while maintaining a minimum positive tension $t_{\min}$ in all cables of the master CDPM and $t'_{\min}$ in all cables of the slave, the following technique is proposed. But first, since it has been demonstrated in Chapter 1, when no external forces $\mathbf{w}_e$ are applied at the slave end-effector, that the force required at the master end-effector to hold a given pose is independent of the presence of the slave CDPM, it is assumed here, that reaching the ASE on the master CDPM only will automatically guarantee the ASE at the slave CDPM; the slave CDPM mimics the behaviour of the master CDPM at all times, when no external perturbation occurs. Based on this assumption, the following mathematical derivation will be focusing on the master part of the CDP only.

Consequently, in order to reach an ASE of the three-cable two-DoF master CDPM, and inherently of the slave CDPM, the equation below must be verified for any pose of the master end-effector:

$$\mathbf{w} = \mathbf{W}\mathbf{t} \approx \mathbf{0}_2, \ \mathbf{t} \geq \mathbf{t}_{\min} > \mathbf{0}_3, \tag{2.6}$$

where $\mathbf{t}$ is the vector of the cable tensions, $\mathbf{0}_2$ and $\mathbf{0}_3$ are the zero vectors in $\mathbb{R}^2$ and $\mathbb{R}^3$, respectively, and $\mathbf{W}$ is the pose dependent wrench matrix (its mathematical derivation can be found in Appendix A.1, by removing the degree of freedom in rotation) defined as

$$\mathbf{W} = \begin{bmatrix} \frac{\mathbf{c}_1}{c_1} & \frac{\mathbf{c}_2}{c_2} & \frac{\mathbf{c}_3}{c_3} \end{bmatrix}. \tag{2.7}$$

It should be noted that Eq. (2.6) is the direct application of Eq. (2.3) to a three-cable two-DoF planar mechanism. Here, because the end-effector motions are assumed to lie in a horizontal plane perpendicular to the gravity field, the gravity wrench $\mathbf{w}_g$ has no effect on the static balancing.

In order to represent an arbitrary tension profile, we use a polynomial of degree $\eta - 1$ of the Bernstein form, i.e., a linear combination of Bernstein bases [231]. The components t_i of the tension vector $\mathbf{t}$ can thus be expressed as

$$t_i = t(c_i) = \sum_{\nu=0}^{\eta-1} \beta_\nu b_{\nu,\eta-1}(c_i^\dagger) = f_i(c_i), \tag{2.8}$$

where β_ν are the Bernstein coefficients, and $b_{\nu,\eta-1}(c_i^\dagger)$ are the η Bernstein bases. These bases are functions of the normalized length $c_i^\dagger \equiv (c_i - c_{\min})/(c_{\max} - c_{\min})$ of the i^{th} cable, and are defined as

$$b_{\nu,\eta-1}(c_i^\dagger) = \begin{pmatrix} \eta - 1 \\ \nu \end{pmatrix} (c_i^\dagger)^\nu (1 - c_i^\dagger)^{\eta-\nu-1}, \tag{2.9}$$

where $\begin{pmatrix} \eta - 1 \\ \nu \end{pmatrix}$ is a binomial coefficient. In our case, this binomial coefficient can be expressed as

$$\begin{pmatrix} \eta - 1 \\ \nu \end{pmatrix} = \frac{(\eta - 1)!}{(\eta - \nu - 1)!\nu!}. \tag{2.10}$$

This differentiates the method from that presented in our previous work [232], where standard polynomials had been used instead of Bernstein polynomials. Bernstein bases allow us to minimize the variation of the potential energy of a planar CDPM over its workspace without stumbling on numerical sensitivity problems, since these bases are numerically more robust [233, 234].

Then, for the sake of conciseness, we may rewrite Eq. (2.8) as

$$t(c_i) = \boldsymbol{\gamma}_i^T \mathbf{s}, \ i = 1,2,3, \tag{2.11}$$

where $\boldsymbol{\gamma}_i \equiv [\ b_{0,\eta-1}(c_i^\dagger) \quad b_{1,\eta-1}(c_i^\dagger) \quad \cdots \quad b_{\eta-1,\eta-1}(c_i^\dagger)\ ]^T$ and $\mathbf{s} \equiv [\ \beta_0 \quad \beta_1 \quad \cdots \quad \beta_{\eta-1}\ ]^T$.

Reaching Eq. (2.6), i.e., approximating the neutral equilibrium over the workspace $\mathcal{A}$, is equivalent to minimizing the Euclidean-norm of the resulting force $\mathbf{f}_r \equiv \mathbf{W}\mathbf{t}$ applied on the moving end-effector over $\mathcal{A}$. Moreover, since $||\mathbf{f}_r||_2$ is a positive convex function[1], minimizing the square of this function is equivalent to minimizing the function itself [235]. Hence, we set out to minimize the following expression:

$$||\mathbf{f}_r||_2^2 = \mathbf{f}_r^T\mathbf{f}_r = \left(\sum_{i=1}^{3}\boldsymbol{\gamma}_i^T\mathbf{s}\frac{\mathbf{c}_i}{c_i}\right)^T\left(\sum_{i=1}^{3}\boldsymbol{\gamma}_i^T\mathbf{s}\frac{\mathbf{c}_i}{c_i}\right), \tag{2.12}$$

$$= \mathbf{s}^T\mathbf{C}^T\mathbf{C}\mathbf{s}, \tag{2.13}$$

where

$$\mathbf{C} \equiv \sum_{i=1}^{3}\frac{\mathbf{c}_i}{c_i}\boldsymbol{\gamma}_i^T. \tag{2.14}$$

Since $\mathbf{C}$ is a function of $\mathbf{p}$, i.e., the length and the direction of each cable depends on the position of point P in the workspace $\mathcal{A}$, we may formulate our objective function as

$$f(\mathbf{s}) \equiv \frac{1}{2A}\int_{\mathcal{A}}\mathbf{s}^T\mathbf{C}(\mathbf{p})^T\mathbf{C}(\mathbf{p})\mathbf{s}dA, \tag{2.15}$$

where dA is an infinitely small element of area of the workspace $\mathcal{A}$. This objective function is equivalent to

$$f(\mathbf{s}) \equiv \frac{1}{2}\mathbf{s}^T\mathbf{P}\mathbf{s}, \tag{2.16}$$

where

$$\mathbf{P} \equiv \frac{1}{A}\int_{\mathcal{A}}\mathbf{C}(\mathbf{p})^T\mathbf{C}(\mathbf{p})dA. \tag{2.17}$$

We note that $f(\mathbf{s})$ must be minimized over $\mathbf{s}$, the set of Bernstein coefficients, and that matrix $\mathbf{P}$ can be computed prior to the minimization, as it is independent from $\mathbf{s}$, using the function `quad2d` from MATLAB® software. In our case, the workspace is an equilateral triangle, and, in order to reduce the computing time, Eq. (2.17) can be written as

$$\mathbf{P} \equiv \frac{6}{A}\int_0^{\frac{1}{2}}\int_{-\frac{\sqrt{3}}{6}}^{-\frac{\sqrt{3}x}{3}}\mathbf{C}(\mathbf{p})^T\mathbf{C}(\mathbf{p})dydx. \tag{2.18}$$

Furthermore, since a minimum level of tension in the cables must be kept to maintain the mechanism geometry even if no external wrench is applied on the moving platform, we must submit $f(\mathbf{s})$ to additional constraints. These constraints must be defined in order to ensure cable tensions $t(c_i) \geq t_{\min}$, where $t_{\min}$ is the minimum allowed tension. This minimum is chosen to prevent cable sag while moving the end effector and to overcome the gravity field acting on the end effector, which is perpendicular to the workspace plane. Moreover, since

[1] A convex function is a continuous function whose value at the midpoint of every interval in its domain does not exceed the arithmetic mean of its values at the ends of the interval.

$\mathcal{A}$ is an equilateral triangle, each cable has the same range of lengths $c_i \in [c_{\min}, c_{\max}]$, where $c_{\max} - c_{\min} \equiv a$. Hence, we should verify that the constraint $t(c_i) \geq t_{\min}$ is satisfied for any $c_i \in [0, a]$. In practice, however, we evenly discretize the cable length interval $[0, a]$ into q constraints, each corresponding to a fixed length c_i. The resulting constraints are

$$\mathbf{G}\mathbf{s} \geq \mathbf{1}_q t_{\min}, \tag{2.19}$$

where $\mathbf{1}_q \equiv [\ 1 \quad 1 \quad \cdots \quad 1\ ]^T \in \mathbb{R}^q$, $\mathbf{G} \equiv [\ \boldsymbol{\gamma}_1 \quad \cdots \quad \boldsymbol{\gamma}_q\ ]^T \in \mathbb{R}^{q\times(\eta-1)}$, and

$$\boldsymbol{\gamma}_i \equiv [\ b_{0,\eta-1}(c_i^\dagger) \quad b_{1,\eta-1}(c_i^\dagger) \quad \cdots \quad b_{\eta-1,\eta-1}(c_i^\dagger)\ ]^T. \tag{2.20}$$

By choosing $q >> \eta$, we obtain many more constraints than the degree $\eta-1$ of the polynomial, and the constraint $t(c) \geq t_{\min}$, $c \in [0, a]$, is fulfilled, for all practical purposes.

In summary, we have defined a convex quadratic objective function, which allows to approach the neutral equilibrium over the three-cable two-DoF planar CDPM workspace, and an affine convex function[2], which constrains the resulting cable tensions above a prescribed threshold:

$$\begin{array}{ll} \text{minimize} & \frac{1}{2}\mathbf{s}^T\mathbf{P}\mathbf{s}, \\ \text{subject to} & -\mathbf{G}\mathbf{s} \leq -\mathbf{1}_q t_{\min}, \\ \text{over} & \mathbf{s}. \end{array} \tag{2.21}$$

Thus, the problem defined in Eqs. (2.16) and (2.19) forms a quadratic problem (QP) with inequality constraints and it can be directly computed using scientific software such as MATLAB®. In this case, the `quadprog` function from the standard optimization toolbox is dedicated to solving convex quadratic programs. Notice that $\mathbf{P}$ must be symmetric positive semidefinite[3] for the QP to converge towards a global optimum, i.e., for the problem to be convex [236].

Moreover, since it is usually more important to reach static equilibrium at the origin of $\mathcal{A}$ and its surroundings than at its boundaries, a weighting function is used. This function can be geometrically described as a cone over $\mathcal{A}$, centred at the origin O, and with an unit height. This weighting function is applied to $\mathbf{P}$ in order to obtain $\mathbf{P}_w$, which is defined as

$$\mathbf{P}_w \equiv \frac{1}{A}\int_{\mathcal{A}} \mathbf{C}(\mathbf{p})^T\mathbf{C}(\mathbf{p})w(\mathbf{p})dA, \tag{2.22}$$

or in our case

$$\mathbf{P}_w \equiv \frac{6}{A}\int_0^{\frac{1}{2}} \int_{-\frac{\sqrt{3}}{6}}^{-\frac{\sqrt{3}x}{3}} \mathbf{C}(\mathbf{p})^T\mathbf{C}(\mathbf{p})w(\mathbf{p})dydx, \tag{2.23}$$

[2] A one-dimension affine function is a function composed of a linear function and a constant and its graph is a straight line. The general equation for an affine function in one dimension is: $y = f(x) = ux + v$, where u and v are constants.

[3] A $n \times n$ matrix $\mathbf{M}$ is called positive semidefinite (or sometimes nonnegative-definite) if $\mathbf{x}^T\mathbf{M}\mathbf{x} \geq 0$ for all $\mathbf{x} \in \mathbb{R}^n$.

and where the weighting function $w(\mathbf{p})$ is set to

$$w(\mathbf{p}) = \left(1 - \frac{\sqrt{3}||\mathbf{p}||_2}{a}\right). \tag{2.24}$$

Finally, the QP is defined as follows to determine the optimal solution $\mathbf{s}^\star$ in order to ensure the minimization of the resulting forces applied by the user to maintain static equilibrium of the planar CDPM:

$$\begin{array}{ll} \text{minimize} & \frac{1}{2}\mathbf{s}^T\mathbf{P}_w\mathbf{s}, \\ \text{subject to} & -\mathbf{G}\mathbf{s} \leq -\mathbf{1}_q t_{\min}, \\ \text{over} & \mathbf{s}. \end{array} \tag{2.25}$$

Then, let us minimize the objective function for $\eta - 1 = 0, \ldots, 9$. Computations show that $\mathbf{P}$ and $\mathbf{P}_w$ are symmetric positive-definite for all these values of η. The distance a (see Fig. 1.16) is set to 0.38 m, the tension threshold is set to $t_{\min} = 5$ N, which is assumed to be enough to prevent any sag in the cables and to overcome the gravity field acting on the end effector, and $q = 40(\eta - 1)$, which is largely sufficient to ensure $t(c) \geq t_{\min}$ over $c \in [0, a]$.

This QP yields the results shown in Figs. 2.2 and 2.3. These figures contain the ten optimized polynomial functions, each of which corresponds to the optimal tension profile for a specific value of η. Their related objective function values are also given, as well as their values of the RMS of $||\mathbf{f}_r||_2$ over $\mathcal{A}$, which is defined as

$$||\mathbf{f}_r||_{2,\text{rms}} = \sqrt{\mathbf{s}^T\mathbf{P}\mathbf{s}}. \tag{2.26}$$

As expected, we note that the value of $f(\mathbf{s}^\star)$ decreases as η increases, and the constraints are properly satisfied, since all of the tension profiles lie above $t_{\min} = 5$ N.

On Figs. 2.4 and 2.5, we can observe the isocontours of the magnitude of the resultant of the three cable tensions over $\mathcal{A}$ for $\eta - 1 = 0, \ldots, 5$ and $\eta - 1 = 6, \ldots, 9$, respectively. As expected, we note that a higher degree of the polynomial results in a better approximation of the neutral equilibrium over the workspace. Moreover, the effect of the weighting function of Eq. (2.24) is easily noted from the results, since the region reaching neutral equilibrium around the origin O becomes larger as the degree of the polynomial increases. Also, it is noticed that between $\eta - 1 = 4$ and $\eta - 1 = 9$, only marginal gains are made.

Finally, from Fig. 2.2, it is interesting to note that for $\eta - 1 = 1$, i.e., when a proportional-force spring or a proportional-torque spring is selected, this optimization demonstrates that, in order to reach an ASE over $\mathcal{A}$, the highest tension in the cable must be achieved when $c_i = 0$, which is considered to be difficult to reproduce in practice. Indeed, this is the behaviour opposite to that of our initial prototype (see Sub-section 1.4.1 of Chapter 1) since the tension in a cable normally increases when the cable is unwound from its winding pulley.

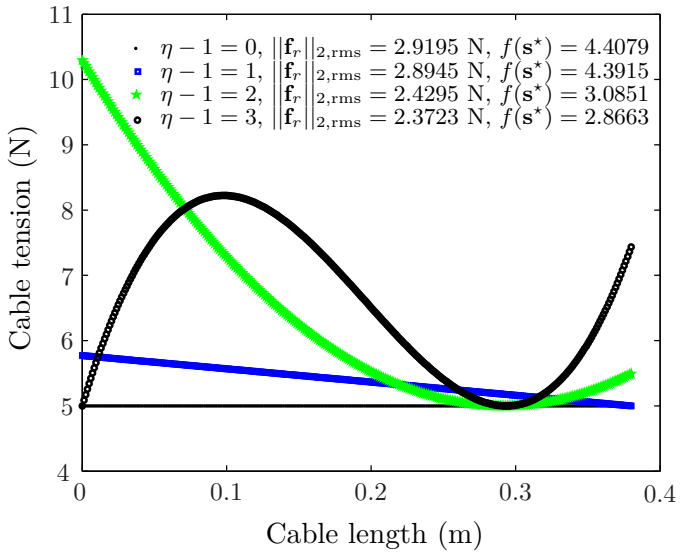

Figure 2.2 – Tension in the cables as a function of the degree $\eta - 1 = 0, \ldots, 3$ of the polynomial function.

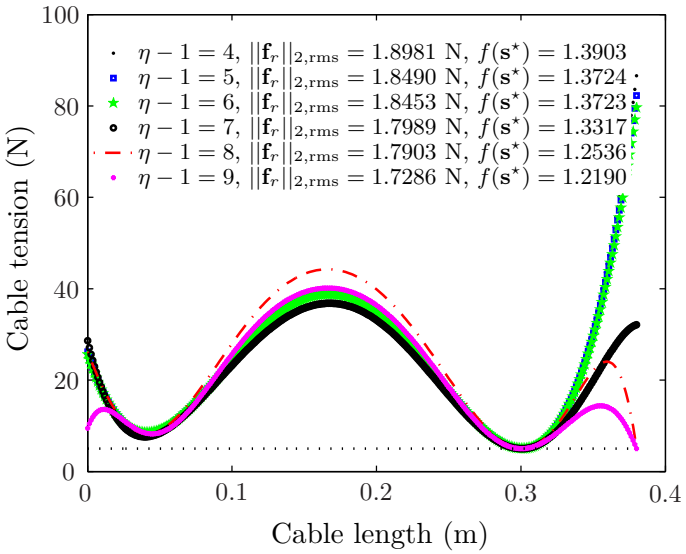

Figure 2.3 – Tension in the cables as a function of the degree $\eta - 1 = 4, \ldots, 9$ of the polynomial function.

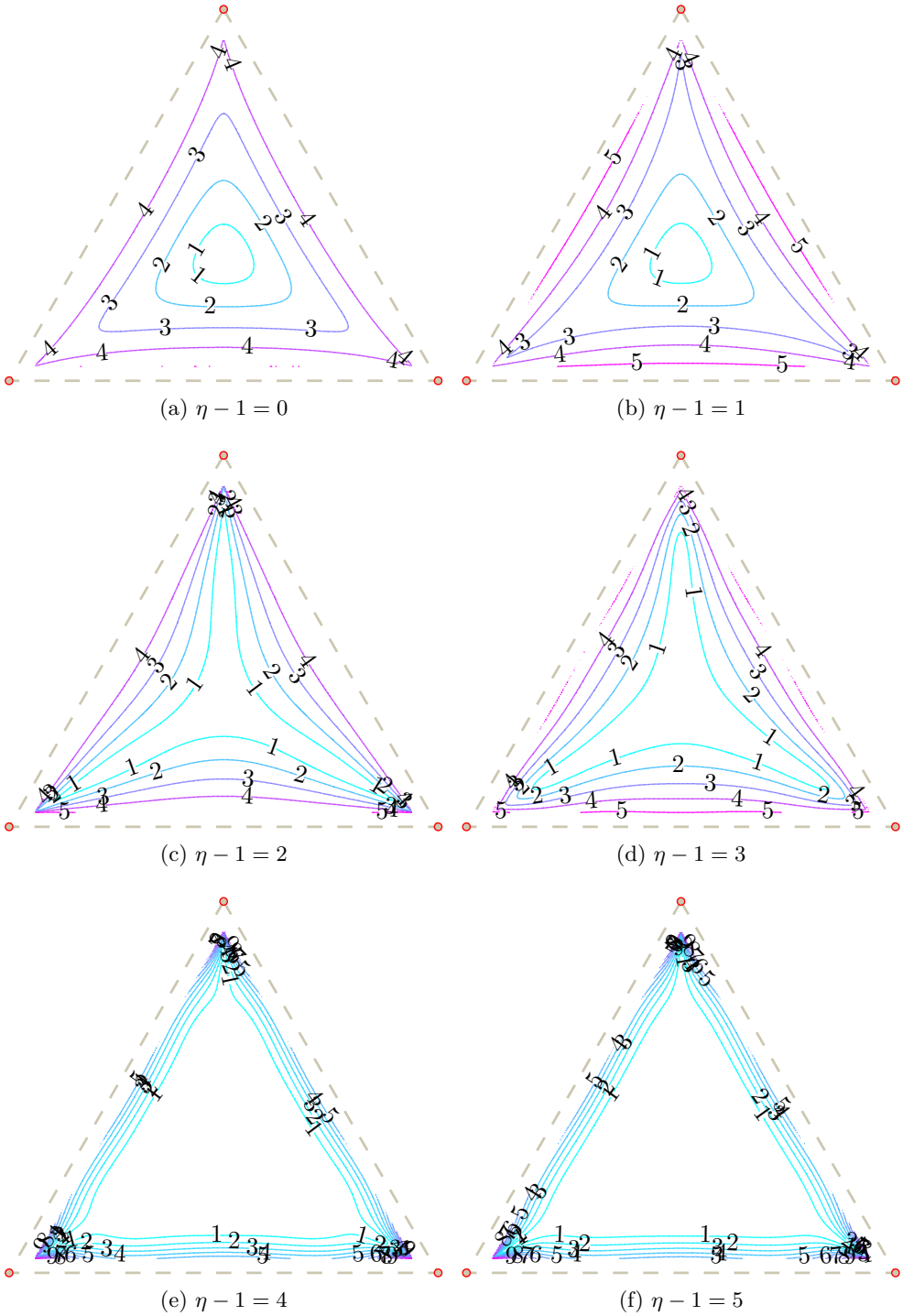

(a) $\eta - 1 = 0$ (b) $\eta - 1 = 1$

(c) $\eta - 1 = 2$ (d) $\eta - 1 = 3$

(e) $\eta - 1 = 4$ (f) $\eta - 1 = 5$

Figure 2.4 – Theoretical $||\mathbf{f}_r||_2$ (N) over $\mathcal{A}$ from optimized polynomials of degree $\eta - 1 = 0, \ldots, 5$.

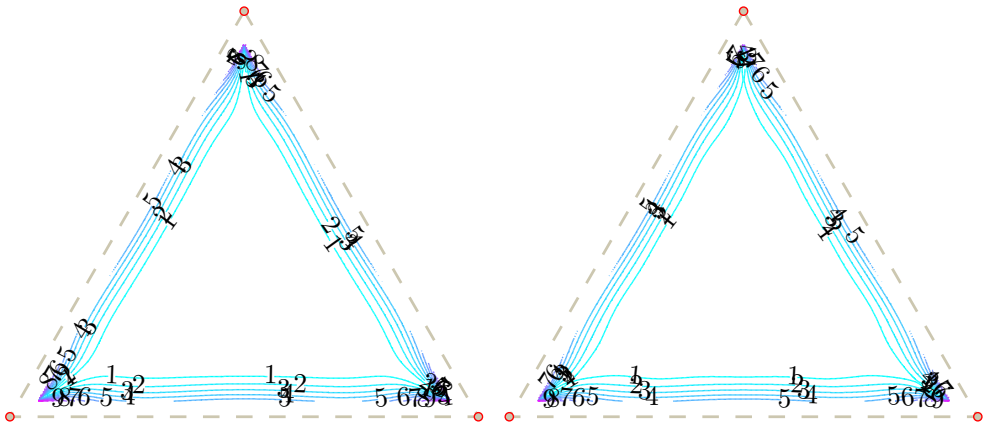

(a) $\eta - 1 = 6$ (b) $\eta - 1 = 7$

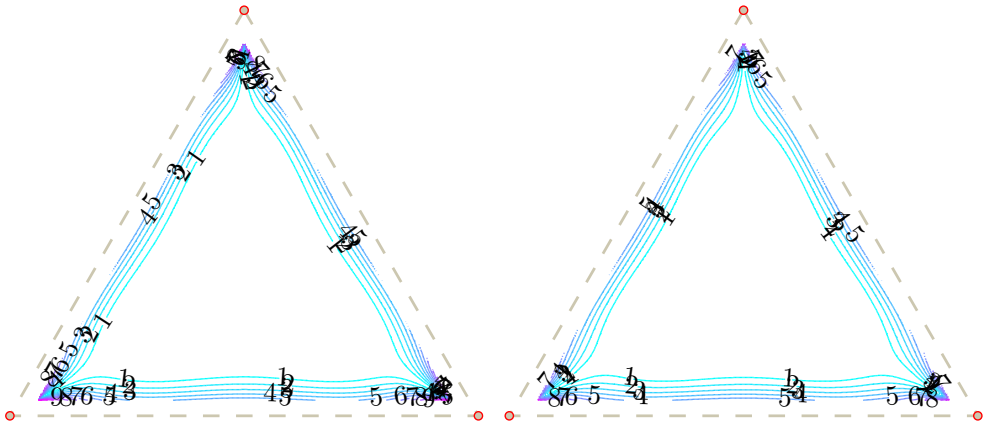

(c) $\eta - 1 = 8$ (d) $\eta - 1 = 9$

Figure 2.5 – Theoretical $||\mathbf{f}_r||_2$ (N) over $\mathcal{A}$ from optimized polynomials of degree $\eta - 1 = 6, \ldots, 9$.

2.2.3 Design of the Spring-Loaded Reels

In order to design a conservative purely-mechanical sub-system for reproducing the nonlinear tension profiles in the cables of a three-cable two-DoF planar CDPM, we decided to combine a four-bar mechanism and commercially-available constant-torque springs (Neg'ator® Spring Motors marketed by SDP/SI [197]). Notice that the synthesis of four-bar linkages has been studied extensively over last decades (see, e.g., the work of Freudenstein [237, 238], Chen [239], Khare and Dave [240], Gosselin and Angeles [241, 242], Dudita *et al.* [243], and more recently Todorov [244]). Moreover, similar designs, i.e., a combination of a four-bar linkage and springs, have been previously used by Harmening [245] and Simionescu *et al.* [246] to statically balance a mass. Cams could also be used for the same purpose (see Refs. [247, 248, 249]), but because their manufacture is more difficult, and they generally involve more friction, we preferred the first option.

Then, let us start from Figs. 2.2 and 2.3, from which we note that only the curves correspond-

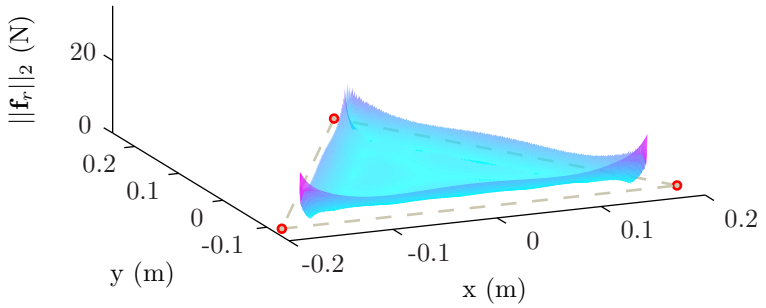

Figure 2.6 – Representation in 3D of theoretical $||\mathbf{f}_r||_2$ computed over $\mathcal{A}$ for $\eta - 1 = 7$.

ing to $\eta - 1 = 0$, 1, 2, 3, and 7 seem to provide behaviours reproducible by planar four-bar linkages. Indeed, the polynomial curves of degree 4, 5, and 6 present a significant increase of the tension level for $c \in [0.3, 0.38]$. Then, the curves of degree 8 and 9 contain nonperiodic peak values over $c \in [0, a]$, which are difficult to reproduce based on the behaviour of a four-bar mechanism.

Moreover, it is interesting to note that the result associated with $\eta - 1 = 0$ is equivalent to using only a constant force spring attached to each cable of the planar CDPM while $\eta - 1 = 1$ is theoretically reproducible with a linear spring attached to the cables or a torsion spring attached at the cable reel. However, even if the tension profile obtained from polynomials of degree 0, 1, 2, and 3 seems to be easier to mechanically reproduce, they result in less faithfull approximations of the static equilibrium of the planar CDPM over $\mathcal{A}$ (see Fig. 2.4). We consequently choose to reproduce the tension profile corresponding to $\eta - 1 = 7$, which corresponds to the following Bernstein coefficients:

$$\mathbf{s}^\star = [\ 28.607 \quad -42.073 \quad 73.566 \quad 4.899 \quad 141.417 \quad -101.426 \quad 26.139 \quad 32.128\ ]^T. \tag{2.27}$$

For the sake of future comparison, Fig. 2.6 shows the tridimensional view of the evolution of the force magnitude $||\mathbf{f}_r||_2$ computed over $\mathcal{A}$ corresponding to $\eta - 1 = 7$ (its corresponding isocontour graph was shown in Fig. 2.5b).

Thus, we are after the crank-rocker[4] four-bar mechanism that allows the best approximation of the optimum degree-seven polynomial. Figure 2.7 presents the set of parameters over which we are to optimize. Scalars l_i, $i = 1, \ldots, 4$, represent the lengths of the rigid links of the mechanism, while ϕ and ψ are its input and output angles, respectively. The variable ψ_i is the initial output angle, whereas ϕ_i and ϕ_f are the initial and the final angular positions of the input link, respectively. Here, the input is taken to be connected to both the spool of the corresponding cable and a constant-torque spring, whereas the output is only connected to a constant-torque spring. Then, variable τ_2 represents the torque value of the constant-torque spring attached to the input link and link 2, while τ_4 is the one corresponding to the output

[4]Note: A crank can rotate a full 360 degrees and a rocker can rotate through a limited range of angles which does not include 0 ° or 180 ° .

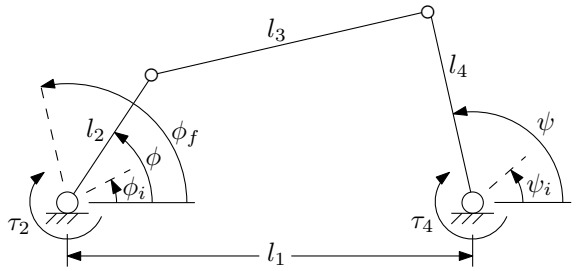

Figure 2.7 – Design parameters of the four-bar mechanism with constant-torque springs.

link and link 4. Notice that the spring corresponding to τ_2 is assumed to produce the mean value of the nonlinear quasi-periodic tension profile, while the one corresponding to τ_4 will generate the required tension variations based on a specific four-bar linkage behaviour.

Determination of the Prescribed Four-Bar Linkage Behaviour

We first determine the desired relationship between the input and output angles, ϕ and ψ, irrespective of the kinematic constraints imposed by the four-bar linkage. Hence, we seek to exactly reproduce the tension profile corresponding to the polynomial of degree seven using some ideal mechanism, which we treat as a black box.

Applying the virtual work principle on the four-bar linkage kinematic model, we obtain the following relationship:

$$t(c)\delta c - \tau_2 \delta\phi = \tau_4 \delta\psi, \tag{2.28}$$

where $t(c)$ is the nonlinear tension function in the cable and where δc, $\delta\phi$, and $\delta\psi$ are an infinitesimal elongation of the cable and rotations of the input and output links, respectively. Then, we can rearrange Eq. (2.28) to obtain the separable ordinary differential equation (ODE):

$$\frac{d\psi}{dc} = \frac{t(c) - \tau_2/c_\phi}{\tau_4}, \tag{2.29}$$

where the relationship $c_\phi d\phi = dc$ was used to eliminate the input angle. The variable c_ϕ is defined as $c_\phi = r/r_\phi$, where r is the pulley radius on which the cable is wound, which is set to 0.0508 m (2 in), and r_ϕ is the gear ratio of a spur-gear transmission between the input link of the four-bar linkage and the pulley. However, since c_ϕ is a function of the range of the cable lengths $\Delta c \equiv c_{\max} - c_{\min}$ and the range of the input angle $\Delta\phi \equiv \phi_f - \phi_i$, it can be also written as

$$c_\phi = \frac{\Delta c}{\Delta\phi} = \frac{c_{\max} - c_{\min}}{\phi_f - \phi_i}, \tag{2.30}$$

where Δc is set to 0.38 m, which is the length of an edge of the boundary of $\mathcal{A}$ and, in fact, the length of cable necessary to cover it. Hence, the only unknowns are ϕ_i and ϕ_f.

Finally, upon solving Eq. (2.29) for ψ, we obtain the desired function $\psi_d(\phi)$ to generate a specific tension profile $t(c)$ in the cables

$$\psi_d(\phi) = \frac{1}{\tau_4}\int_0^{\Delta c}(t(c) - \tau_2/c_\phi)dc + \psi_i, \tag{2.31}$$

and the only remaining unknowns are ϕ_i, ϕ_f, ψ_i, τ_2, and τ_4.

Optimization of the Four-Bar Linkage Parameters

Based on the work of Freudenstein [238], we may write the constraint equation of the planar four-bar linkage as

$$-k_1\cos\phi + k_2\cos\psi + k_3 = \cos(\psi - \phi), \tag{2.32}$$

where $k_1 = l_1/l_4$, $k_2 = l_1/l_2$, and $k_3 = (l_1^2 + l_2^2 - l_3^2 + l_4^2)/(2l_2l_4)$. For the sake of conciseness, we rewrite Eq. (2.32) as

$$\boldsymbol{\lambda}^T\mathbf{k} = \mu, \tag{2.33}$$

where $\boldsymbol{\lambda} = [\ -\cos\phi \quad \cos\psi \quad 1\ ]^T$, $\mathbf{k} = [\ k_1 \quad k_2 \quad k_3\ ]^T$, and $\mu = \cos(\psi - \phi)$.

We compute the Freudenstein parameters $\mathbf{k}$ that minimize the squared residual (noted R^2) of Eq. (2.33) when substituting in the desired input-output relationship $\psi_d(\phi)$. Since this squared residual is to be minimized over the entire range of ϕ, the objective function may be expressed as

$$\begin{aligned} R^2 &= \int_{\phi_i}^{\phi_f}\left(\boldsymbol{\lambda}^T\mathbf{k} - \mu\right)^2 d\phi \\ &= \mathbf{k}^T\left(\int_{\phi_i}^{\phi_f}\boldsymbol{\lambda}\boldsymbol{\lambda}^T d\phi\right)\mathbf{k} - 2\left(\int_{\phi_i}^{\phi_f}\mu\boldsymbol{\lambda}^T d\phi\right)\mathbf{k} \\ &\quad + \int_{\phi_i}^{\phi_f}\mu^2 d\phi. \end{aligned} \tag{2.34}$$

Notice that Eq. (2.34) is a quadratic function of $\mathbf{k} \in \mathbb{R}^3$, which is easily minimized by solving a linear system of three equations in three unknowns.

However, in order to obtain a crank-rocker mechanism, the optimized geometry of the four-bar linkage must always allow a real solution for ψ over the complete range of ϕ. Moreover, for practical reasons, we set $l_1 = 0.15$ m, constrain l_2 and l_4 within [0.015,0.15] m while l_3 must allow the four-bar linkage to be assembled. Hence, mathematical constraints should be defined to guarantee this result.

Based on the work of Gosselin and Angeles [241, 242], the two following conditions are formulated, which are necessary and sufficient for the mechanism to be of the crank-rocker type:

$$(k_1 + k_3)^2 \leq (k_2 + 1)^2, \tag{2.35}$$

$$(k_1 - k_3)^2 \leq (k_2 - 1)^2. \tag{2.36}$$

These quadratic inequalities are equivalent to four affine conditions, which can be expressed as $\mathbf{Ck} \leq \mathbf{d}$, where

$$\mathbf{C} = \begin{bmatrix} 1 & -1 & 1 \\ 1 & -1 & -1 \\ -1 & -1 & 1 \\ -1 & -1 & -1 \end{bmatrix}, \quad \text{and} \quad \mathbf{d} = \begin{bmatrix} 1 \\ -1 \\ -1 \\ 1 \end{bmatrix}. \tag{2.37}$$

In turn, the bounds on the link lengths can be written as $1 \leq k_1, k_2 \leq 10$.

Thence, the optimization problem is expressed as

$$\begin{array}{ll} \text{minimize} & \frac{1}{2}\mathbf{k}^T\mathbf{H}\mathbf{k} + \mathbf{f}^T\mathbf{k}, \\ \text{subject to} & \mathbf{Ck} \leq \mathbf{d}, \\ & \mathbf{l}_\text{l} \leq \mathbf{k} \leq \mathbf{l}_\text{u}, \\ \text{over} & \mathbf{k}, \end{array} \tag{2.38}$$

where

$$\mathbf{H} = 2\int_{\phi_i}^{\phi_f} \boldsymbol{\lambda}\boldsymbol{\lambda}^T d\phi, \quad \text{and} \quad \mathbf{f} = -2\int_{\phi_i}^{\phi_f} \mu\boldsymbol{\lambda} d\phi, \tag{2.39}$$

while $\mathbf{l}_\text{l} = [\ 1 \quad 1 \quad -\infty\ ]^T$ and $\mathbf{l}_\text{u} = [\ 10 \quad 10 \quad \infty\ ]^T$ are the vectors containing the lower and upper bounds for $\mathbf{k}$, respectively.

Similarly to the problem of Eq. (2.25), the optimization problem defined in Eq. (2.38) forms a QP with bound constraints. We note that the last term of Eq. (2.34) has been removed from the QP since it has no effect on its solution. Moreover, the matrix $\mathbf{H}$ is easily shown to be symmetric positive semidefinite, since $\mathbf{k}^T\boldsymbol{\lambda}\boldsymbol{\lambda}^T\mathbf{k} \equiv (\mathbf{k}^T\boldsymbol{\lambda})^2 \geq 0$ and the sum of positive values always provides a positive result. Therefore, this optimization problem leads to a convex QP [236].

Determination of the Optimum Nonlinear Spring Parameters

Previously, we have found the desired four-bar linkage behaviour $\psi_d(\phi)$ corresponding to an arbitrary tension profile $t(c)$ and then a reliable method to compute Freudenstein parameters $\{k_1, k_2, k_3\}$. We now set out to determine the best values of the spring properties $\{\tau_2, \tau_4\}$ and the assembly specifications $\{\phi_i, \phi_f, \psi_i\}$ to reproduce the chosen seven-degree polynomial.

In order to find a suitable nonlinear spring, an optimization problem must be properly defined. The objective function is chosen to be the RMS error between the prescribed tension profile $t_7(\phi)$ (from the polynomial of degree seven) and the resulting tension profile produced by the nonlinear spring over the entire range of ϕ. Clearly, this objective function should be minimized.

Let us first compute the resulting cable tensions generated with the spring-loaded four-bar linkage for fixed values of $\{\phi_i, \phi_f, \psi_i, \tau_2, \tau_4\}$. The derivative of ψ with respect to ϕ is obtained

from Eq. (2.32), which gives

$$\frac{d\psi}{d\phi} = \frac{\sin(\psi-\phi) - k_1 \sin\phi}{\sin(\psi-\phi) - k_2 \sin\psi}. \tag{2.40}$$

Using the Weierstrass substitution formulas[5] for ψ, Eqs. (2.32) and (2.40) may be respectively written as

$$uz^2 + vz + w = 0, \tag{2.41}$$

where

$$u = -k_1 \cos\phi - k_2 + k_3 + \cos\phi, \tag{2.42}$$

$$v = -2\sin\phi, \tag{2.43}$$

$$w = -k_1 \cos\phi + k_2 + k_3 - \cos\phi, \tag{2.44}$$

and

$$\frac{d\psi}{d\phi} = -\frac{(k_1-1)\sin\phi z^2 - 2\cos\phi z + (k_1+1)\sin\phi}{\sin\phi z^2 + 2(\cos\phi - k_2)z - \sin\phi}. \tag{2.45}$$

Then, solving the quadratic function of Eq. (2.41) for z gives

$$z_{1,2} = \frac{\sin\phi \pm \sqrt{\Delta}}{u}, \tag{2.46}$$

where

$$\Delta = -(k_3 - k_1\cos\phi)^2 + (k_2 - \cos\phi)^2 + \sin^2\phi. \tag{2.47}$$

Finally, upon substituting Eq. (2.46) into Eq. (2.45), and the resulting equation into Eq. (2.28), but expressed as a function of only $\delta\phi$ and $\delta\psi$ by using the fact that $c_\phi d\phi = dc$, we obtain the following relation for the cable tension profile $t(\phi)$ generated by the nonlinear spring:

$$t(\phi)_{1,2} = \frac{1}{c_\phi}\left[\tau_4 \frac{d\psi_{1,2}}{d\phi} + \tau_2\right], \tag{2.48}$$

or

$$t(\phi)_{1,2} = \frac{-1}{c_\phi}\left[\tau_4 \frac{\sin\phi \mathbf{k}^T\mathbf{e} \pm \sqrt{\Delta} g}{\sin\phi\Delta \pm \frac{1}{2}\sqrt{\Delta} h} - \tau_2\right], \tag{2.49}$$

where $\mathbf{e} \equiv [\ e_1 \quad e_2 \quad e_3\ ]^T$, and

$$e_1 = 1 - k_2 u - k_3 \cos\phi \tag{2.50}$$

$$e_2 = \cos\phi - k_3, \tag{2.51}$$

$$e_3 = k_3 - k_3^{-1}, \tag{2.52}$$

$$g = k_1 - 1 + \cos\phi(k_2 - k_3), \tag{2.53}$$

$$h = u^2 + \Delta + \sin^2\phi. \tag{2.54}$$

[5]The Weierstrass substitution is the trigonometric substitution $z = \tan(\frac{\psi}{2})$ which transforms an integral of the form $\int f(\cos\psi, \sin\psi)d\psi$ into one of the form $\int f(\frac{1-z^2}{1+z^2}, \frac{2z}{1+z^2})\frac{2dz}{1+z^2}$.

Notice that Eq. (2.46) yields two possible output angles for a chosen input angle. Hence, the four-bar linkage may be assembled in two different ways, but only one of them will suitably approximate the desired function $\psi_d(\phi)$ (see Eq. (2.31)).

Having found the effective tension profile of a generic four-bar linkage, we define the objective of our synthesis algorithm. A suitable measure of the deviation of the effective tension profile from the prescribed tension profile is its RMS error over the travel of the linkage. Symbolically, this gives

$$\begin{aligned} f(\mathbf{x}) \equiv & \Delta t_{\text{rms}} \\ \equiv & \sqrt{\frac{\min(\int_{\phi_i}^{\phi_f} \Delta t(\phi)_1^2 d\phi, \int_{\phi_i}^{\phi_f} \Delta t(\phi)_2^2 d\phi)}{\phi_f - \phi_i}}, \end{aligned} \tag{2.55}$$

where $\mathbf{x} \equiv \begin{bmatrix} \phi_i & \phi_f & \psi_i & \tau_2 & \tau_4 \end{bmatrix}^T$, $\Delta t(\phi)_1 = t(\phi)_1 - t_7(\phi)$, and $\Delta t(\phi)_2 = t(\phi)_2 - t_7(\phi)$. Equation (2.55) means that the tension profiles of both assembly modes are compared with the prescribed cable tension profile $t_7(\phi)$, and the best approximation is kept to compute $f(\mathbf{x})$. It is important to notice that the geometric parameters $\mathbf{k}$ of the four-bar linkage are not included into $\mathbf{x}$ because they are directly computed from ϕ_i, ϕ_f, ψ_i, τ_2 and τ_4 by solving the QP defined in Eq. (2.38).

Since our objective function $f(\mathbf{x})$ is not convex, minimizing it using descent methods (further details will be given in Chapter 4 regarding different optimization methods available) will lead to local solutions, which strongly depend on the initial guess $\mathbf{x}_0$. Hence, in order to improve the likelihood of converging towards a practical solution, we define additional constraints. Based on the observations of the tension profile from the seven-degree polynomial, we conclude that we should have $\phi_f - \phi_i \geq 3\pi$. Furthermore, the solution should be included into $\phi_i \in [0,2\pi]$, $\phi_f \in [0,6\pi]$, $\psi_i \in [0, \pi]$, $\tau_2 \in [0.01, \infty]$, and $\tau_4 \in [0.01, \infty]$. Note that the lower bound for τ_2 and τ_4 is set to 0.01 N·m instead of 0 N·m in order to avoid mathematical singularities from Eq. (2.31). Finally, twenty randomly-selected initial guesses belonging to the feasible set of parameters $\mathbf{x}$ have been used in order to obtain a suitable final solution $\mathbf{x}^\star$.

The function `fmincon`, with the interior-point algorithm, from the MATLAB® optimization toolbox is applied to solve the problem, which is expressed as

$$\begin{array}{ll} \text{minimize} & f(\mathbf{x}), \\ \text{subject to} & \mathbf{c}^T\mathbf{x} \leq d, \\ & \mathbf{l}_\text{l} \leq \mathbf{x} \leq \mathbf{l}_\text{u}, \\ \text{over} & \mathbf{x}, \end{array} \tag{2.56}$$

where

$$\mathbf{c} \equiv \begin{bmatrix} 1 & -1 & 0 & 0 & 0 \end{bmatrix}^T, \tag{2.57}$$

$$d = -3\pi, \tag{2.58}$$

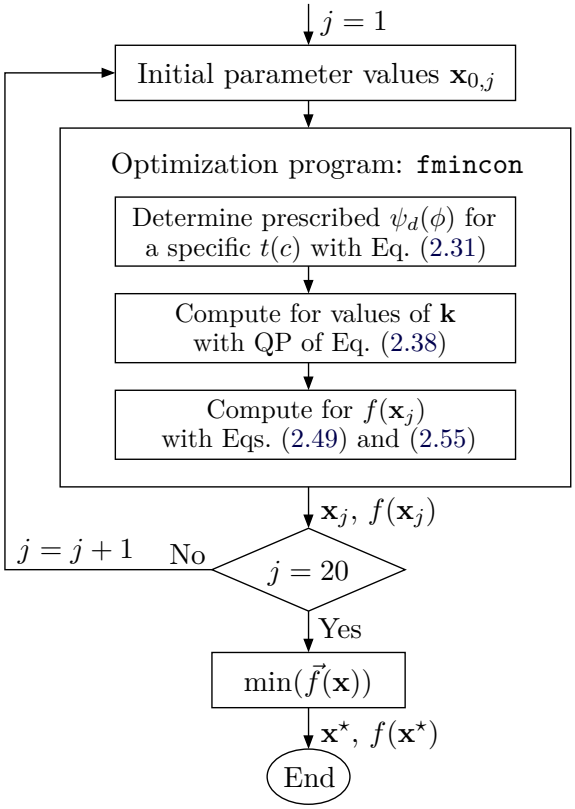

Figure 2.8 – Flowchart of the optimization method.

$$\mathbf{l}_\mathrm{l} = [\ 0 \quad 0 \quad 0 \quad 0.01 \quad 0.01\ ]^T, \tag{2.59}$$

$$\mathbf{l}_\mathrm{u} = [\ 2\pi \quad 6\pi \quad \pi \quad \infty \quad \infty\ ]^T. \tag{2.60}$$

In summary, Fig. 2.8 shows the different steps of the algorithm devised to determine an appropriate set of geometric parameters for the four-bar mechanism, the initial assembly values, as well as the required constant-torque springs values attached to each driving shaft of the linkage (input and output). First, an initial guess is sent to the optimization function `fmincon`. Then, Eq. (2.31) is used to compute the prescribed function $\psi_d(\phi)$, which enables reproducing the exact cable tension profile from the optimized polynomial of degree seven. The geometric parameters of the four-bar linkage are then determined by solving the quadratic program of Eq. (2.38), and $f(\mathbf{x})$ is computed by solving Eqs. (2.49) and (2.55). Finally, these steps are performed in loop until we have evaluated twenty different initial guesses $\mathbf{x}_0$. The minimum of the twenty final results $f(\mathbf{x}_j)$, where $j = 1, \ldots, 20$, is chosen as the final (locally) optimum solution $\mathbf{x}^\star$. Tables 2.1 and 2.2 contain the twenty initial guesses $\mathbf{x}_{0,j}$ and the twenty final results, respectively, that we used to determine the final solution $\mathbf{x}^\star$ to the problem defined in Eq. (2.56).

At the end, an appropriate set of parameters defining the spring-loaded four-bar mechanism is obtained, which minimizes the RMS error between the prescribed and effective cable-tension

Table 2.1 – The twenty initial guesses $\mathbf{x}_{0,j}$ for the problem defined in Eq. (2.56).

	ϕ_i (rad)	ϕ_f (rad)	ψ_i (rad)	τ_2 (N·m)	τ_4 (N·m)
$\mathbf{x}_{0,1}$	0.5	6.5	0.0	1.0	2.5
$\mathbf{x}_{0,2}$	0.5	9.5	1.0	1.0	2.5
$\mathbf{x}_{0,3}$	1.0	10.0	1.0	1.0	2.5
$\mathbf{x}_{0,4}$	1.5	11.0	0.5	1.0	2.5
$\mathbf{x}_{0,5}$	2.0	11.5	1.0	1.0	2.5
$\mathbf{x}_{0,6}$	2.5	12.0	1.0	1.0	2.5
$\mathbf{x}_{0,7}$	3.0	12.5	1.0	1.0	2.5
$\mathbf{x}_{0,8}$	3.5	13.0	1.0	0.8	2.5
$\mathbf{x}_{0,9}$	4.0	13.5	1.0	0.8	2.5
$\mathbf{x}_{0,10}$	4.0	13.5	1.0	1.0	2.1
$\mathbf{x}_{0,11}$	4.5	14.0	1.0	0.9	2.4
$\mathbf{x}_{0,12}$	5.0	14.5	1.0	0.9	2.4
$\mathbf{x}_{0,13}$	5.5	15.0	1.0	0.9	2.4
$\mathbf{x}_{0,14}$	6.0	15.5	1.0	0.9	2.4
$\mathbf{x}_{0,15}$	4.0	13.5	1.0	0.9	2.4
$\mathbf{x}_{0,16}$	4.0	13.5	1.1	0.9	2.4
$\mathbf{x}_{0,17}$	4.0	13.5	1.1	0.9105	2.4360
$\mathbf{x}_{0,18}$	4.0	13.5	1.2	0.9105	2.4360
$\mathbf{x}_{0,19}$	4.05	13.5	1.19	0.9105	2.4360
$\mathbf{x}_{0,20}$	4.05	13.5	1.18	0.9105	2.4360

Table 2.2 – The twenty final results $\mathbf{x}_j$ and $f(\mathbf{x}_j)$ for the problem defined in Eq. (2.56).

	ϕ_i (rad)	ϕ_f (rad)	ψ_i (rad)	τ_2 (N·m)	τ_4 (N·m)	$f(\mathbf{x}_j)$
$\mathbf{x}_1$	0.0088	9.4437	1.2244	1.1634	0.0156	12.2935
$\mathbf{x}_2$	1.2625	10.8717	0.8826	0.8550	0.0612	9.7751
$\mathbf{x}_3$	1.0498	10.5281	0.0006	0.6374	0.0166	11.0456
$\mathbf{x}_4$	1.5103	11.0348	0.3513	0.4395	0.6908	10.8828
$\mathbf{x}_5$	1.2063	11.1002	0.8048	0.8071	0.0121	9.8863
$\mathbf{x}_6$	1.3334	10.8426	0.5322	0.7139	0.0952	9.8134
$\mathbf{x}_7$	3.7693	13.5859	0.2388	0.8045	0.0196	10.1465
$\mathbf{x}_8$	0.0007	9.8888	0.7600	0.5748	0.0103	11.5876
$\mathbf{x}_9$	3.8397	13.3656	0.9811	0.9377	2.0735	3.9044
$\mathbf{x}_{10}$	3.9742	13.3990	0.9970	0.8784	2.3737	4.5723
$\mathbf{x}_{11}$	4.4858	14.0104	1.0073	0.9053	2.4094	6.7773
$\mathbf{x}_{12}$	4.9941	14.4189	1.0020	0.8978	2.4167	17.1041
$\mathbf{x}_{13}$	0.0818	9.8738	1.2791	1.2677	0.0996	14.9014
$\mathbf{x}_{14}$	5.2273	14.9431	1.7930	0.8748	0.2233	7.9539
$\mathbf{x}_{15}$	4.0786	13.6029	0.9997	0.9011	2.6243	2.6725
$\mathbf{x}_{16}$	4.0074	13.5323	1.0973	0.8956	2.3973	2.7282
$\mathbf{x}_{17}$	4.0995	13.6236	1.1831	0.9025	2.3799	2.6001
$\mathbf{x}_{18}$	3.9916	13.5110	1.2001	0.9161	2.4405	2.6066
$\mathbf{x}_{19}^{\star}$	4.0634	13.4950	1.1871	0.9105	2.4077	2.4683
$\mathbf{x}_{20}$	3.9114	13.4484	1.2198	0.8959	2.4719	2.9920

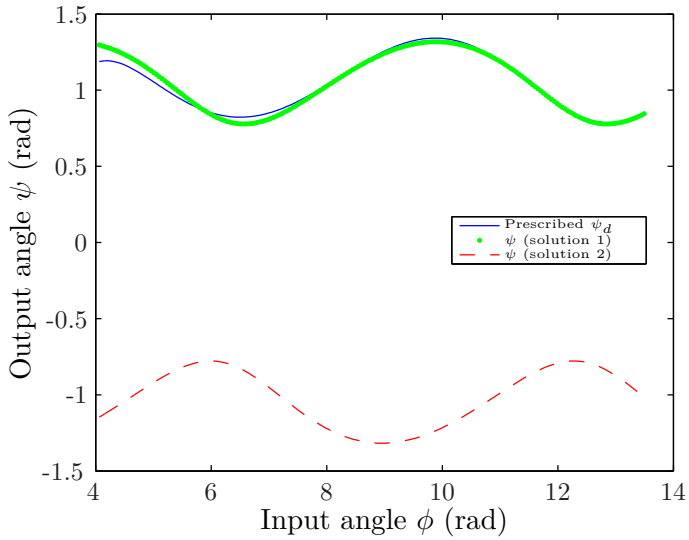

Figure 2.9 – Comparison of the effective behaviour of ψ generated by the four-bar mechanism with the prescribed behaviour ψ_d.

profiles. The optimum values, best solution $\mathbf{x}^\star$ (obtained at $j = 19$) from our proposed technique, are $\phi_i = 4.0634$ rad, $\phi_f = 13.4950$ rad, $\psi_i = 1.1871$ rad, $\tau_2 = 0.9105$ N·m, and $\tau_4 = 2.4077$ N·m. These values lead to a RMS error of 2.4684 N over the range $[\phi_i, \phi_f]$. The normalized lengths of the four-bar links are $l_1 = 1.0$ m, $l_2 = 0.1$ m, $l_3 = 1.3898$ m, and $l_4 = 0.6018$ m, and the ratio r_ϕ is approximately 1.26. It should be noted that these link lengths come from the corresponding optimized Freudenstein parameters (see Eqs. (2.38) and then (2.32)), which are $\mathbf{k}^\star = \begin{bmatrix} 1.6617 & 10 & -4.6474 \end{bmatrix}^T$, and r_ϕ from a c_ϕ value of 0.0403. Figures 2.9 and 2.10 present the optimized four-bar behaviour corresponding to the two solutions ($\psi(\phi)_1$ and $\psi(\phi)_2$) in comparison with the prescribed behaviour ψ_d and the optimized effective tension profiles ($t(\phi)_1$ and $t(\phi)_2$) in comparison with the prescribed tension profile $t_7(\phi)$, respectively. We note that solution 1 is the true final solution, since it best approximates both the prescribed four-bar behaviour and the prescribed cable tension profile.

Figures 2.11 and 2.12 show the corresponding contours of the Euclidean-norm of the external forces that must be applied at the end effector of the three-cable two-DoF planar CDPM in order to perfectly reach the neutral equilibrium over the entire workspace $\mathcal{A}$. Comparing this result with the one shown in Fig. 2.5b, we note that the static equilibrium is not as good as with the optimized polynomial, since the spring-loaded four-bar mechanism only approximates the prescribed behaviour. Nevertheless, we observe that a vast area at the centre of the workspace is reasonably well balanced in a purely mechanical manner with the proposed nonlinear spring. In fact, the value of $||\mathbf{f}_r||_{2,\text{rms}}$ over $\mathcal{A}$ is 4.1180 N for the result shown with Fig. 2.11 instead of 1.7989 N for the result shown with Fig. 2.5b. The effective $||\mathbf{f}_r||_{2,\text{rms}}$, which was computed by numerical integration over the workspace $\mathcal{A}$ using the

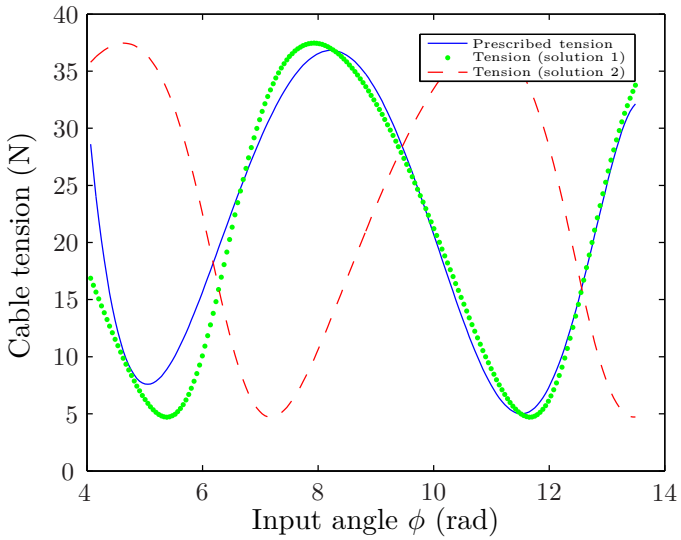

Figure 2.10 – Comparison of the effective tension profiles generated by the nonlinear spring with the prescribed tension profile.

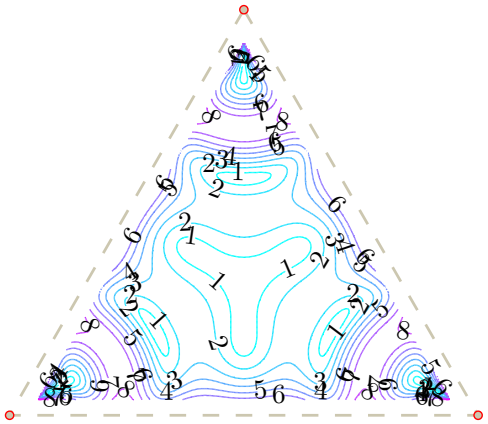

Figure 2.11 – Effective $||\mathbf{f}_r||_2$ (N) over $\mathcal{A}$ obtained with the nonlinear spring (solution 1).

following relation:

$$||\mathbf{f}_r||_{2,\text{rms}} = \sqrt{\frac{1}{A}\int_{\mathcal{A}} ||\mathbf{f}_r||_2^2 dA}, \tag{2.61}$$

is significantly higher than the theoretical one, but over the important region of $\mathcal{A}$, i.e., close to the origin, we obtain a useful approximation of the neutral equilibrium.

Finally, for comparison purposes, we show with Figs. 2.13 and 2.14 the mapping of the norm of the effective resultant forces over $\mathcal{A}$ when solution 2 is selected rather than solution 1. This solution does not allow to reach a suitable ASE over $\mathcal{A}$ as it can be confirmed by looking at Figs. 2.9 and 2.10. Indeed, the corresponding value of $||\mathbf{f}_r||_{2,\text{rms}}$ is 35.8773 N for this solution instead of 4.1180 N with solution 1 and, as seen with Fig. 2.14, a neutral equilibrium seems to be reached at only four specific regions over $\mathcal{A}$.

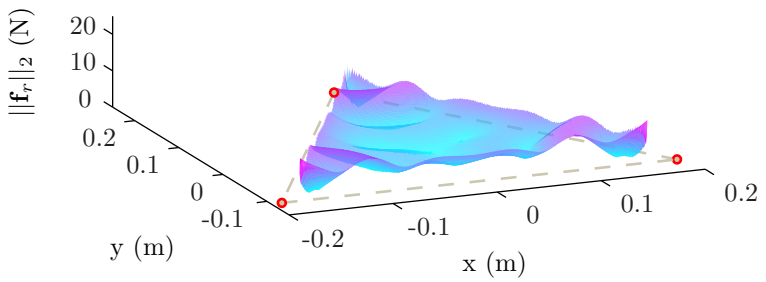

Figure 2.12 – Representation in 3D of effective $||\mathbf{f}_r||_2$ (N) over $\mathcal{A}$ (solution 1).

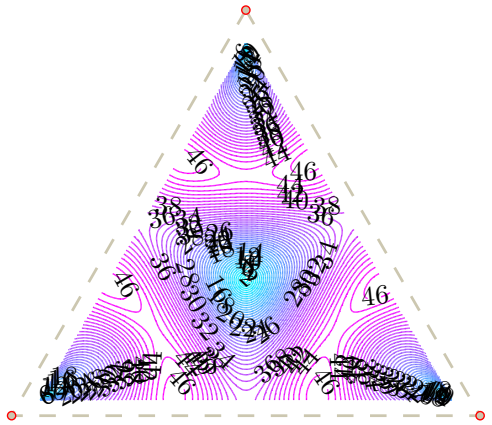

Figure 2.13 – Effective $||\mathbf{f}_r||_2$ (N) over $\mathcal{A}$ obtained with the nonlinear spring (solution 2).

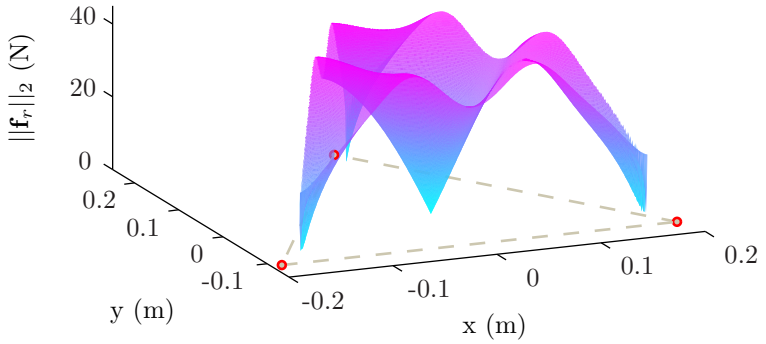

Figure 2.14 – Representation in 3D of effective $||\mathbf{f}_r||_2$ (N) over $\mathcal{A}$ (solution 2).

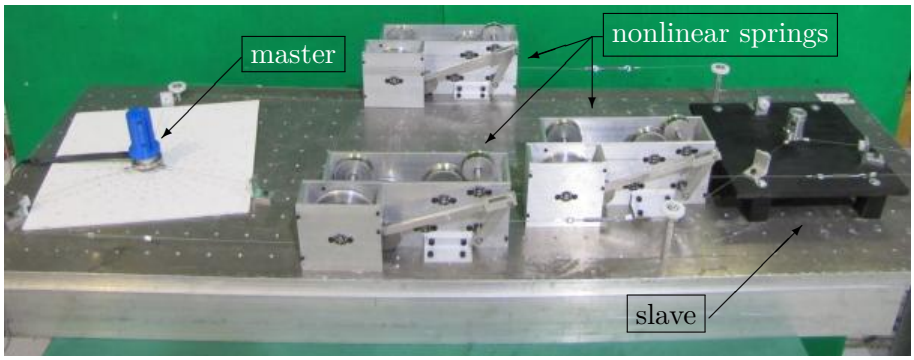

Figure 2.15 – Embodiment of the devised three-cable two-DoF cable-driven pantograph.

2.2.4 Implementation of the Optimized Nonlinear Springs in a Three-Cable Two-DoF Planar Cable-Driven Pantograph

A prototype of the three-cable two-DoF planar CDP has been built including the optimum nonlinear springs obtained in Sub-section 2.2.3. A top view of the CAD model of this testbed was previously shown in Fig. 2.1. This figure shows the main components of the planar CDP. The master end-effector, which is moved by the user's hand over the workspace $\mathcal{A}$, is constrained by three cables. The opposite end of each cable is attached to a nonlinear spring in order to maintain the minimum cable tensions while producing the quasi-neutral equilibrium over $\mathcal{A}$. From these same nonlinear springs, another set of three cables is then routed to the slave end-effector, which mimics the motion of the master, following a scaling factor κ_s, over the workspace $\mathcal{A}'$.

Prototype of a Three-Cable Two-DoF Planar Cable-Driven Pantograph

The prototype built for the implementation of the optimized nonlinear springs is identical to the one designed and presented in Chapter 1 except for two main differences. The first difference is the replacement of the proportional-torque spring assemblies by nonlinear spring assemblies and the second is that an effort has been made to decrease the number of idler pulleys guiding the set of cables from the master end-effector to the slave end-effector (from seventeen to six pulleys (see Figs. 1.19 and 2.1)). This last modification helps to decrease friction in our device. The resulting prototype is illustrated in Fig. 2.15.

The mechanical design of the nonlinear springs is based on the best solution $\mathbf{x}^\star$ obtained in the previous sub-section. Hence, a constant-torque spring of 0.9105 N·m must be fixed on the input shaft of the four-bar linkage as well as one of 2.4077 N·m on the output. However, since these values do not correspond to commercial standards on the market, we decided to approach them by using two assemblies of standard constant-torque springs. In this manner, three springs of respectively 0.0384 N·m (0.34 lb·in), 0.0744 N·m (0.65 lb·in), and 0.7977 N·m (7.06 lb · in) are attached to the input shaft (for a total of 0.9105 N·m (exact desired value

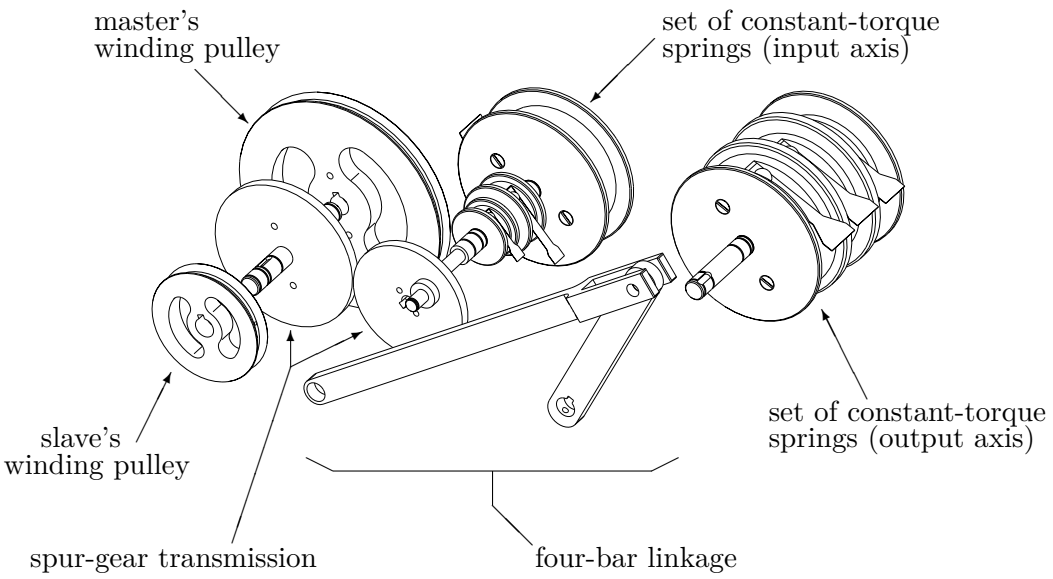

Figure 2.16 – An exploded view of a CAD representation of the main components of the nonlinear spring assembly.

τ_2)), while three others of 0.6214 N·m (5.50 lb · in), 0.7977 N·m (7.06 lb · in), and 1.0169 N·m (9.00 lb · in) are attached to the output shaft (for a total of 2.4360 N·m ($\approx$ 1.2% over the desired value τ_4)). The totality of the shafts necessary to support the springs, the pulleys, and the input-output shafts are mounted on standard ball bearings in order to minimize the effect of friction. Furthermore, a spur-gear transmission is designed as an assembly of a standard 68-teeth and a 54-teeth spur gears. The ratio c_ϕ obtained is 1.2593 instead of the optimal value of 1.26.

Figure 2.16 presents in details the internal architecture of the nonlinear spring assemblies by showing an exploded view of a CAD representation of their main components. Each of these assemblies contains, on the left-side shaft, a master's winding pulley on which a cable constraining the master end-effector is attached, its counterpart for the slave and the driving gear of the spur-gear transmission. On the center shaft (input axis of the four-bar linkage), we have the driven gear of the spur-gear transmission and the first set of constant-torque springs (τ_2). It should be noted that this driven gear shows also an eccentric axis, for which the centre-to-centre distance between the eccentric axis and its main axis represents the link l_2 of the four-bar linkage (see Fig. 2.7). Then, links l_3 and l_4 of the four-bar mechanism are respectively fixed to the eccentric axis on the driven gear and the right-side shaft (output axis of the four-bar linkage). The link l_1 is formed by the steel-design frame regrouping the nonlinear-spring assembly (see Fig. 2.15). Finally, the output shaft contains the set of constant-torque springs to generate the required torque τ_4.

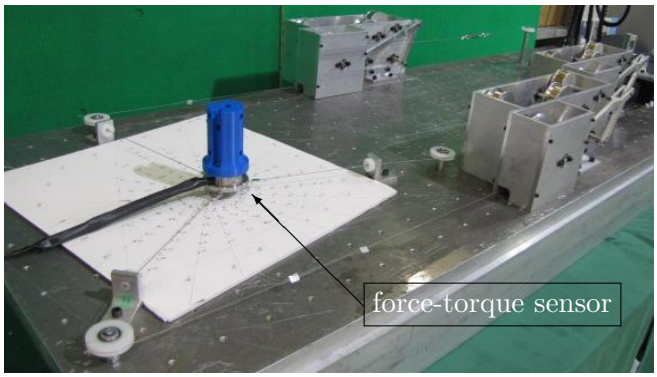

Figure 2.17 – The experimental benchmark of the three-cable two-DoF planar CDP with the nonlinear springs.

Results and Discussions

In order to verify the real level of neutral equilibrium reached over the workspace of the three-cable two-DOF planar CDP, an experiment, similar to the one completed in Chapter 1, was performed to measure the forces applied on the end effector while moving it over $\mathcal{A}$. A force-torque sensor from ATI Industrial Automation [200] was used to statically record the balancing forces applied on the plane of motion. As for the experiment performed in Chapter 1, 151 different positions were tested in order to cover $\mathcal{A}$ (see Fig. 1.26b for the points distribution) and the force applied at each of these positions was recorded. Figure 2.17 shows a picture of the experimental testbed and the measurements are shown in Figs. 2.18 and 2.19. The RMS value of $||\mathbf{f}_r||_2$ over $\mathcal{A}$ is ≈ 10.0 N instead of the expected 4.1180 N. This value was also determined by computing the volume under the surface formed by our set of measurements $||\mathbf{f}_r||_2$ using the following relation:

$$||\mathbf{f}_r||_{2,\text{rms}} = \sqrt{\frac{1}{A}\sum_{i=1}^{p} V_{\text{mesh},i}} \equiv \sqrt{\frac{1}{A}\int_{\mathcal{A}} ||\mathbf{f}_r||_2^2 dA}, \tag{2.62}$$

where $V_{\text{mesh},i}$ is the volume of the i^{th} irregular triangular prism associated to the mesh grid that best fits our set of experimental measures and p is the number of discrete triangles required to form this mesh grid ($p = 285$). It should be noted that each irregular triangular prism is defined by the Cartesian position of three points belonging to $\mathcal{A}$ and the square of the norm of their associated measured force, i.e., $||\mathbf{f}_r||_2^2$.

In order to explain the difference between the expected and experimental level of static equilibrium reached over $\mathcal{A}$, we enumerate the sources of errors that act inside the testbed. First of all, using constant-torque springs leads to uncertainties on the exact torque values applied to links 2 and 4 (see Fig. 2.7). Indeed, we based our choice of commercial constant-torque springs on their nominal values. However, this kind of springs holds a possible error range of $\pm 10\%$. Also, as mentioned above, our nominal value for τ_4 is 1.2% over the optimum value and our spur-gear ratio c_ϕ is 1.2593 instead of 1.26. Moreover, a small error on the initial

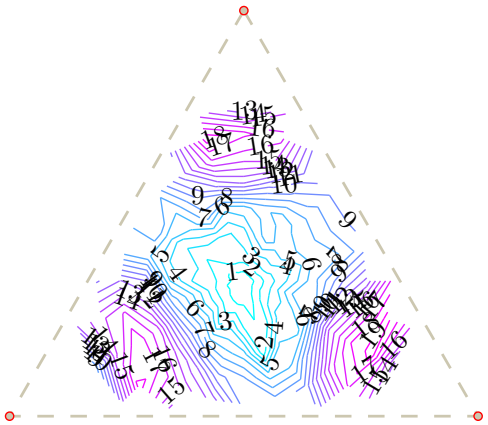

Figure 2.18 – Experimental $||\mathbf{f}_r||_2$ (N) measured over $\mathcal{A}$ resulting from the devised nonlinear springs.

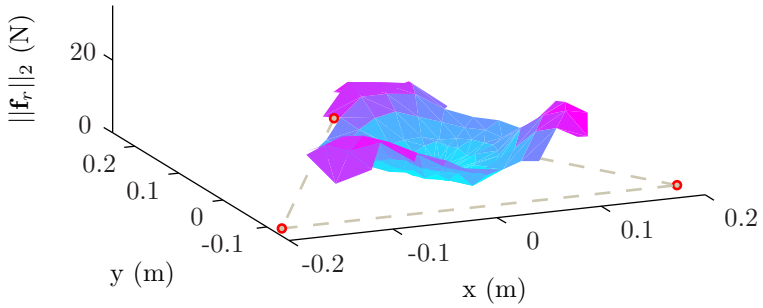

Figure 2.19 – Representation in 3D of experimental $||\mathbf{f}_r||_2$ (N) measured over $\mathcal{A}$.

input and output angles (ϕ_i and ψ_i, respectively) may easily lead to inaccurate forces applied by each cable on the planar CDPM end-effector. These errors are thought to be those that are mainly responsible for the results difference, over manufacturing, assembly and measurement errors.

Despite these important errors, the results presented in Figs. 2.18 and 2.19 show that our experimental prototype helps in balancing the planar CDP end-effector around the center of its workspace $\mathcal{A}$, i.e., the most useful region. Moreover, similarly to Chapter 1, we assessed the magnitude of the input force required in order to hold the master end-effector at different positions over $\mathcal{A}$ when no slave CDPM is attached to the nonlinear springs. Figures 2.20 and 2.21 show the corresponding graphs, i.e., respectively using isocontours and a tridimensional view to represent the distribution of $||\mathbf{f}_r||_2$ over $\mathcal{A}$. As a result, the RMS value of $||\mathbf{f}_r||_2$ over $\mathcal{A}$ is $\approx$ 10.1 N, which is equivalent to the corresponding value for the full CDP. This result proves again that, when no external force is applied on the slave end-effector of the CDP, its presence does not alter the force that a user must apply on the master end-effector in order to balance out the mechanism.

Finally, as future work, it would be now interesting to modify the previous method in order

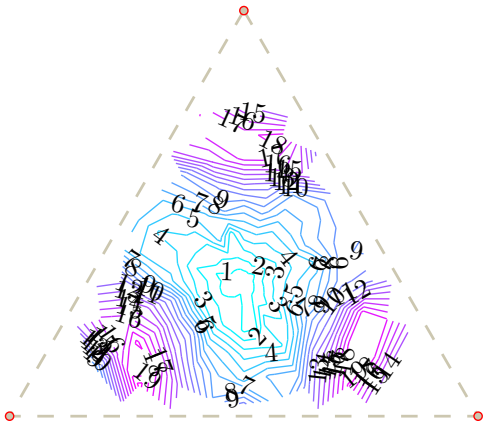

Figure 2.20 – Experimental $||\mathbf{f}_r||_2$ (N) measured over $\mathcal{A}$ resulting from the devised nonlinear springs (master only).

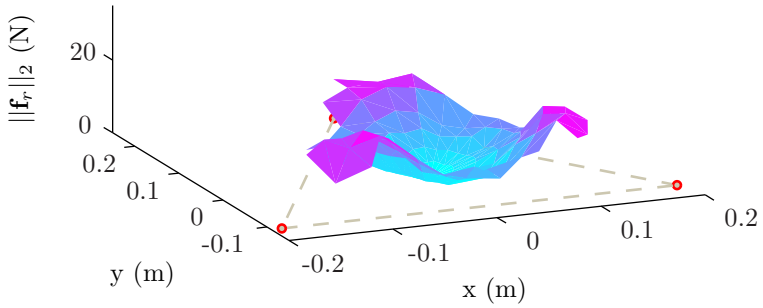

Figure 2.21 – Representation in 3D of experimental $||\mathbf{f}_r||_2$ (N) measured over $\mathcal{A}$ (master only).

to approximate the static balancing of spatial CDPs. Although this work could probably be extrapolated from the planar to the spatial case without encountering major theoretical hurdles, at least for a constant-orientation spatial CDP, it is not clear whether this method would approximate sufficiently well static equilibrium in mechanisms with less symmetry and more degrees of freedom. In fact, based on the experimental results, it is found to be relatively difficult to reach a sufficient level of ASE for fixed-eyelet CDPs with a purely-mechanical nonlinear-spring design based on a four-bar linkage and commercially-available constant-torque springs, even for the simple planar case. Consequently, further work would be necessary to clarify this matter.

2.3 Summary

In summary, this chapter reports on a novel method to approximate the static balancing of a planar CDP, or similarly a planar CDPM, based on the design of nonlinear springs. Instead of suitably controlling conventional electrical motors in order to produce the minimum cable tensions required to maintain the geometry of the mechanism while generating neutral equilibrium over its workspace, purely-mechanical nonlinear springs containing four-bar linkages

and constant-torque springs are designed. The main advantage of this method is to increase the level of security of CDPs or CDPMs, by ensuring a level of static equilibrium over the workspace while removing any dependencies to electrical components. In this way, such a mechanism can be used anywhere, even where sources of electricity are unavailable or prohibited. In addition, however, if used in parallel with electrical motors, these passive nonlinear springs can reduce to a minimum the continuous expenditure of electrical energy from motors even when no acceleration or force is applied on the end effector.

This chapter was divided in two main sections. The first, Section 2.1, defined for the reader the meaning of an exact static equilibrium and an approximate static equilibrium. From there, the second section, Section 2.2, described the methodology proposed to design purely-mechanical nonlinear springs that approximate the static balancing of a three-cable two-DoF planar cable-driven pantograph. This method was then presented in four parts. First, in Sub-section 2.2.1, we presented the chosen geometry of the planar CDP as a three-cable two-DoF master-slave architecture for which the master and the slave workspaces have an equilateral-triangle shape, following a given scaling factor of $\kappa_s = 1/2$, a geometry similar to the one previously used in Section 1.4. In Sub-section 2.2.2, we have determined the best nonlinear tension profile in the cables in order to approximate a neutral equilibrium over the workspace of the master CDPM only, based on a principle previously established in Chapter 1. The objective was to minimize over the workspace the Euclidean-norm of the resultant of all forces applied on the end effector while ensuring a minimum tension in the cables. As expected, the results show that a higher degree of the polynomial yields a better approximation of the neutral equilibrium.

The object of the third main sub-section, Sub-section 2.2.3, was the detailed optimum design of the nonlinear spring to reproduce the desired cable tension profile. Because the spring was to consist of a four-bar linkage, the optimum seven-degree polynomial was chosen as the tension profile to reproduce. This choice was explained by the quasi-periodicity of this resulting function, its relatively low peaks of tension as well as the closeness to neutral equilibrium reached over the workspace. Then, the desired four-bar linkage input-output relationship was determined. Based on the work of Freudenstein, a quadratic program was then defined in order to obtain the four-bar linkage that best corresponds to the desired behaviour. Finally, an algorithm was proposed to optimize the values of the properties of the springs and the assembly. The objective function was defined as the verification of the root mean square deviation of the resulting tension from the prescribed tension. The global problem being non-convex, different randomly-chosen initial solutions have been used in order to find a suitable final solution to our problem.

The balance of this chapter, Sub-section 2.2.4, focused on the implementation of the optimized nonlinear springs within a three-cable two-DoF planar CDP. A prototype of the resulting nonlinear spring was built and tested, as well as the three-cable two-DoF planar CDP acting as

the experimental test bench, which was the same prototype used in Chapter 1. An experiment was performed in order to verify the closeness to the neutral equilibrium reached over the workspace. The results have shown a RMS value of the force that the user should apply on the end effector of ≈ 10.0 N over the entire workspace instead of the expected value of 4.1180 N. This difference has been mainly explained by inaccurate constant-torque values provided by the chosen commercial springs, by a non-optimal spur-gear ratio and inaccurate initial input and output angles on the manufactured nonlinear springs.

In fact, because of these factors, which are difficult to control to desired precision, one should be careful when endeavouring to build such a complex passive spring. Here, since we added nonlinear springs within the system, we approached the static equilibrium better on certain regions of the workspace than on others. Nevertheless, we should mention that the mechanism "feels" close to neutral equilibrium when manipulated over the central part of its workspace. Indeed, in this area, the end effector can be moved about only with a small press of the finger. It is also interesting to note that compared to the experimental results shown in Chapter 1, i.e., a measured RMS value of ≈ 19.7 N over $\mathcal{A}$, the results including the nonlinear spring-loaded reels allowed us to decrease the required input forces at the master end-effector to move it across its workspace by $\approx 50\%$.

Moreover, as previously discussed in Chapter 1, the current experimental measurements demonstrate again that the addition of the slave part to the master-slave system does not have a significant effect on the forces felt at the master's end-effector when no external forces are applied to its end effector. Also, the proposed technique for the approximate static balancing of a planar CDP could be transposed to the spatial case, at least for a constant-orientation spatial CDP. However, since the experimental results presented in this chapter do not allow to reach a suitable level of ASE, even for the simple planar two-DoF case, additional work would need to be performed in order to determine if the combination of four-bar linkages with constant-torque springs is an efficient means of approximating neutral equilibrium over the n-DoF workspace of a spatial CDP.

Before we investigate this open problem, it is necessary to ensure that we have the relevant tools in order to determine the best geometry of a m-cable n-DoF spatial CDP for a given application. The following chapter aims at providing such a tool, by which the effect on the workspace of self-collisions within a CDPM can be visualized.

Chapter 3

Mechanical Interferences in Cable-Driven Pantographs

"Do not worry about your difficulties in mathematics.
I can assure you that mine are still greater."
- Albert Einstein

In previous chapters, it was seen that the architecture of a cable-driven pantograph (CDP) is chosen to be the assembly of two homothetic cable-driven parallel mechanisms (CDPMs). Thence, when one aims to select the geometry of a CDP for a particular application, it is possible to simplify the problem by focusing only on the performance evaluation of either one of the two sides of the master-slave device.

In this chapter, we use this fact in order to facilitate the study of one major drawback associated with the selection of the geometry of a spatial CDP: the high probability of mechanical interferences between the moving parts of both sub-mechanisms. This phenomenon is described here under the assumption that a cable is a line segment in space. When a mechanical contact occurs between two cables or between a cable and an edge of the end effector, these entities necessarily lie in the same plane, and then the three-dimensional problem becomes two-dimensional. This fact is used to simplify the equations, and leads to exhaustive descriptions of the associated interference loci in the constant-orientation workspace of a CDPM. It will be seen that these results provide a fast method to graphically represent all interference regions in the manipulator workspace, given its geometry and the orientation of its end effector. Although this tool was initially meant to facilitate the development of cable-driven pantographs, it is directly applicable to the design of any CDPM.

As enumerated in Chapter 1, CDPMs hold several advantages over conventional parallel mechanisms such as higher accelerations, modularity, and potentially larger workspaces. However, we cannot disregard the drawbacks related to the use of this kind of mechanisms. Among

those, there are the vibrations, which can be observed at the end effector if the stiffness of the mechanism is insufficient [81]. Another drawback, possibly the most important one, is the unilaterality of the force transmission in cables, which can only pull and not push. This requires a minimum of $n+1$ cables to suitably constrain n-DoF [82, 148]. Finally, interferences between two cables or between a cable and another object in the workspace are possible. This limitation is often as constraining as any other, but has received relatively little attention in the literature.

For example, a group of researchers worked on the extension of the workspace of a CDPM by permitting collisions between wires in tension [250]. Another group worked on permitting collisions between two cables by releasing the tension in one of them [103, 251, 252]. Since their articles are concerned with the management of cable collisions, they are complementary to this work, which is concerned with their detection.

A few other researchers worked on the development of methods to detect and avoid interferences in CDPMs. Among them, we may cite Lafourcade and Verhoeven [106, 107], who noted that reducing the number of attachment points on the end effector and on the base, i.e., regrouping attachment points together, tends to decrease the risk of interference. Others proposed a hybrid method—symbolical and numerical—to verify the occurrence of interferences between cables during specific trajectories of the end effector [79, 101, 118]. These techniques, in general, are based on the computation of distance between line segments [253]. This way of detecting interferences is suitable when the manipulator working trajectories are planned in advance. It soon becomes computationally intensive, however, when there are many possible trajectories. Another drawback is the risk of not detecting all the mechanical contacts between entities depending on the level of refinement in the discretization of the trajectories. In summary, this is a local method and not a global one, since it does not allow to determine the set of interference loci inside the prescribed workspace, but only those belonging to specific trajectories.

To circumvent these problems, some symbolical and numerical approaches are proposed in the literature to detect collision regions within the CDPM workspace. Andrade-Cetto *et al.* [254] designed a wire-based active tracker and resorted to the separating axis theorem[1] to prevent wire interferences within their device. Although this technique prevents interferences, it only indicates a risk of interference, and, therefore, it unnecessarily constrains the CDPM workspace. Another method was proposed by Merlet [187], who symbolically expressed the regions of interference between cables, and between a cable and a polyhedral end effector. He used this work inside numerical algorithms to compute the constant-orientation interference regions. More recently, a group of researchers worked on a numerical method to determine the interference-free wrench-closure workspace while taking into account cable-mass effects, i.e.,

[1]The separating axis theorem (SAT) says that two convex objects do not overlap if there exists a line (called axis) onto which the two objects' projections do not overlap.

the sag of the cables [255]. Also, another group has worked on a symbolical and numerical method to determine the interference loci (cable-cable, cable-edge of the end effector and cable-surface of the end effector) within a CDPM workspace with a given constant-orientation end-effector [256].

Other work was devoted to the detection of collisions inside the workspace of a conventional parallel robot. Pott *et al.* [257] used methods similar to those of references [79, 101, 103, 118] to detect rigid-link interferences inside intervals, and thence, analyzed the workspaces of parallel kinematic machines. Ketchel *et al.* [258] proposed a formulation to detect self-collisions in spatial closed chains between right circular cylindrical objects performing specific trajectories. Finally, Merlet *et al.* [259] proposed algorithms based on interval analysis to detect leg-interferences over a given workspace or trajectory. In this reference, the authors compared three different mathematical descriptions of interferences and evaluated their equivalence in terms of numerical efficiency.

Although the methods devised for rigid-link mechanisms may be a source of inspiration for interference detection in CDPs or CDPMs, they cannot be applied directly. In this chapter, the proposed approach is similar to that taken in Refs. [187, 256], while pushing further the symbolical analysis. It was originally published in [188], after [187] and before [256]. This approach results in a streamlined method to exhaustively compute the interference regions between two cables and between a cable and an edge of the end effector inside the constant-orientation workspace of any given CDPM, or by similitude, any cable-driven pantograph. Moreover, the resulting concise symbolical expressions of the interference regions allow one to draw general conclusions, which should prove useful at the design stage.

This chapter is organized as follows. Section 3.1 defines the phenomenon of a mechanical interference, which motivates this work. Section 3.2 examines mechanical interferences for planar CDPMs, Section 3.3 describes the methodology proposed to determine interference regions for constant-orientation spatial CDPMs and, finally, Section 3.4 summarizes and highlights the main results presented in this chapter.

3.1 Definition of a Mechanical Interference

A general definition of the word *interference*, from the Oxford English Dictionary [3], is: *the action or fact of interfering or intermeddling (with a person, etc., or in some action)*. This word has many different uses such as in electronics for the distorted portion of a received signal, in physics for the variation of wave amplitude that occurs when different waves come together, and also in sports for an illegal obstruction or hindrance of an opposing player.

In this work, an interference will be defined as the physical collision between two entities, which partially or fully blocks the movement of one or both objects. This will be called a

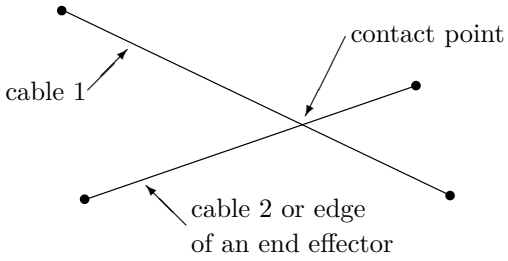

Figure 3.1 – Physical collision between two cables or between a cable and an edge of the end effector.

mechanical interference. When applied to CDPMs, this phenomenon relates to the physical contact between a pair of cables or between a cable and an object in the CDPM workspace. This object is either the CDPM end-effector itself or its payload.

The analysis presented in this chapter concerns the determination of the interference regions in cases of cable-cable and cable-edge contacts (edges of the end-effector geometry). The same method can easily be adapted to the detection of mechanical interferences between a cable and an additional object in the workspace when knowing its wire-frame model but this task is kept for future investigations. Figure 3.1 illustrates the phenomenon of a mechanical interference for the purpose of the current work. Before addressing mechanical interferences for a generic CDPM, let us first explore this phenomenon for planar CDPMs.

3.2 Mechanical Interferences in Planar Cable-Driven Parallel Mechanisms

A planar CDPM is a branch of the CDPM family which is constrained to move over a plane $\mathcal{P}$ of the Cartesian space, and its reels also belong to $\mathcal{P}$. The end effector of these mechanisms may have two degrees of freedom (translational CDPM moving over $\mathcal{P}$) or three degrees of freedom (translational CDPM moving over $\mathcal{P}$ with an orthogonal rotational axis). It is noted that a CDPM having only one degree of freedom is either called a linear CDPM or a purely rotational CDPM. If a CDPM has more than three DoFs, the motion of the mechanism is no longer constrained by a plane or its reels must be distributed in a tridimensional space and its workspace $\mathcal{W}$ is rather defined as a part of (four or five DoFs) or the full Cartesian space (six DoFs).

Based on the previous definition, Fig. 3.2 presents the two possible types of planar CDPMs. Figure 3.2a represents the two-DoF planar CDPM $\{x, y\}$ and Fig. 3.2b is the three-DoF planar CDPM $\{x, y, \phi\}$. Their end-effector and base geometries are arbitrarily chosen to be a square and a rectangle, respectively. Moreover, as it can be observed in Fig. 3.2, both mechanisms are fully constrained by four cables. Their workspaces $\mathcal{W}$ are defined as the convex hulls of the four base anchor points, so as to avoid collisions between the end effector and the reels

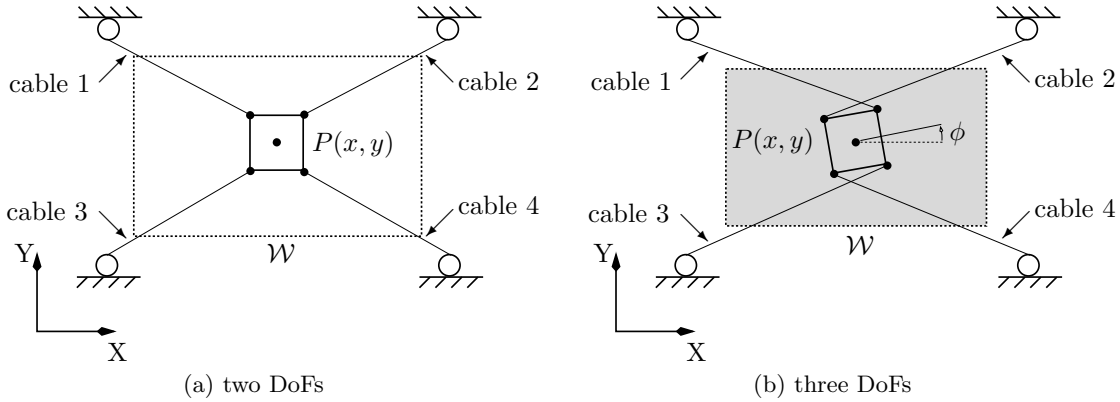

(a) two DoFs (b) three DoFs

Figure 3.2 – Arbitrary planar CDPM geometries.

on the base.

Mechanical interferences for planar CDPMs do not necessarily need extensive analysis and computations to be determined and completely avoided. Moreover, some basic rules can be followed in order to choose a geometry with no or only a limited number of interference regions within its planar workspace. Even if these rules or conditions might seem obvious to some readers, we endeavour to define them rigorously, for the sake of completeness. Also, it should be noted that, in practice, crossed cables in planar CDPMs are normally accepted by roboticists, since it is possible to have them in contact with no significant effect on the mechanism's behaviour, provided that their diameters be relatively small. In practice, however, this kind of cable arrangement may lead to more friction within the CDPM and potentially undesired wrenches applied to its end effector.

In general, the idea behind the avoidance of mechanical interferences between two entities is to keep them apart from each other for every posture of the planar CDPM. However, to the opposite of the previous statement, Lafourcade [106] and Verhoeven [107] remarked that we can also avoid interferences if cables share a common attachment point. Indeed, two straight segments that are not collinear and overlapping cannot intersect at more than one point. This rule is only true under the assumption that the tension is sufficient to keep the cables taut, i.e., to avoid cable sag in order to be considered as straight segments.

A four-cable two-DoF planar CDPM is depicted on Fig. 3.2a. From this sketch, it is obvious that no mechanical interferences can occur between the cables when translating the end effector over the workspace $\mathcal{W}$. Moreover, with this architecture, no collisions are expected between a cable and an edge of the end effector. Consequently, we can say that $\mathcal{W}$ is free of mechanical interferences. It is important to note that the same statement holds for every CDPM for which the end effector is a point, because all cables attach to the same point.

In order to generate physical collisions inside $\mathcal{W}$, we would have to add a new cable and to

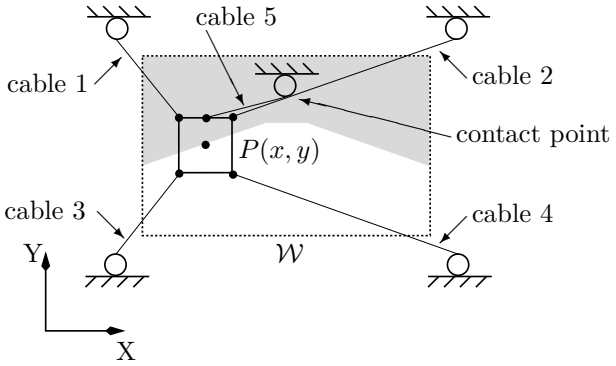

Figure 3.3 – Arbitrary two-DoF planar CDPM with a mechanical interference.

position its corresponding reel inside the workspace. Hence, in a specific region of $\mathcal{W}$, cable-cable or cable-edge contacts would be observed. Figure 3.3 shows the case where a mechanical interference occurs between cables 2–5. In this figure, the initial workspace $\mathcal{W}$ is separated into two distinct regions: a white region and a light gray region. The white region is free of interferences and the light gray region represents end-effector poses for which the planar CDPM is now unable to reach without causing a mechanical interference between two cables or between a cable and an edge of the end effector. Collisions between the moving parts and the fifth reel could also occur.

The boundaries of the light gray region in Fig. 3.3 are the information we must determine in order to limit the movement of the end effector to its interference-free workspace, the white region. The method to determine these limits can be based on pure geometry and observation. For instance, in the specific pose of Fig. 3.3, cable 2 starts being in contact with cable 5 when it is parallel to the segment connecting reels 2 and 5. Hence, if we move the reference point P of the end effector in order to keep cable 2 in this angle, we draw the left limit line segment of the mechanical interference region of $\mathcal{W}$. The right limit line is easily obtained by moving the end effector in order to reach the position where cables 1 and 5 begin to intersect each other. The horizontal upper limit is only defined by the line formed when the upper end-effector edge, which contains attachment points of cables 1, 5 and 2, is in contact with the reel of cable 5.

Now, by looking at Fig. 3.2b, a four-cable three-DoF planar CDPM, it is clear that mechanical interferences occur for every pose $\{x, y, \phi\}$ of the end effector between cables 1–2 and cables 3–4. Hence, we can say that $\mathcal{W}$ represents the interference region of this mechanism as it is displayed in light gray. We also observe that a mechanical interference between two cables only vanishes when an interference between a cable and an edge starts. From this fact, there are only two ways to eliminate these mechanical interferences while keeping the exact same end-effector orientation and geometry. One could either modify the attachment points on the end effector to have one common attachment point for cables 1–2 and one common attachment

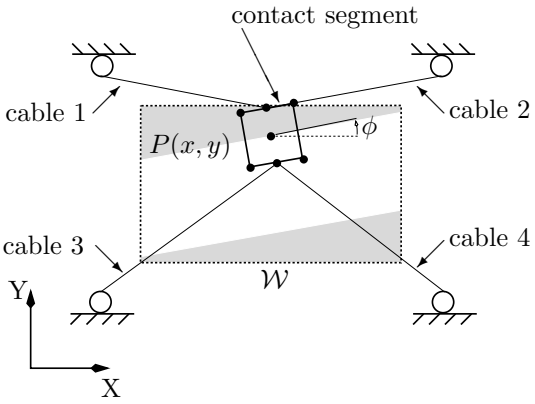

Figure 3.4 – Arbitrary three-DoF planar CDPM with only two end-effector attachment points.

point for cables 3–4; or one could move the two upper reels (cables 1 and 2) together at the same point and similarly for the two bottom reels (cables 3 and 4). However, the Cartesian workspace in translation $\{x, y\}$ and in rotation $\{\phi\}$ would then be significantly reduced.

Figure 3.4 illustrates the first option, i.e., moving together in pairs the upper and bottom attachment points on the end effector. In this modified planar CDPM, it is easily noticed that no interference between two cables can occur. However, for the given orientation, mechanical interferences between a cable and an edge of the end effector are expected. Indeed, by observation, we can define the upper limit of the interference-free workspace simply by drawing the line supporting the reference point P when cable 2 is collinear with the upper edge of the end effector (the upper limit line is then parallel to cable 2). Similarly, the lower limit line is defined by the line parallel to cable 3 when it is collinear with the bottom edge of the end effector. We also note that an orientation of $\phi = 0^\circ$, the reference orientation, leads to an interference-free workspace identical to the one presented in Fig. 3.2a. In fact, a larger value of ϕ yields a smaller interference-free workspace.

Figure 3.5 illustrates the second option, which consists in moving together the upper reels and bottom reels. As expected, this modification leads to a workspace $\mathcal{W}$ free of interferences but with a very small area, because of the distribution of the reels on the base. The previous workspace $\mathcal{W}$ is displayed in light color for comparison purposes. For the orientation shown, the workspace $\mathcal{W}$ is now limited by the inability of cable 4 to pull the end effector further to the left [148, 149] instead of being limited by mechanical interferences. The same limitation can be observed on the right side with cable 1. This figure illustrates how, when designing a planar CDPM, we have to find the best compromise between translational workspace, rotational workspace and mechanical interferences, depending on the specific requirements of the targeted application.

These two examples allow us to enumerate a few basic rules that can be applied in order to minimize the occurrence of mechanical interferences when designing a planar CDPM:

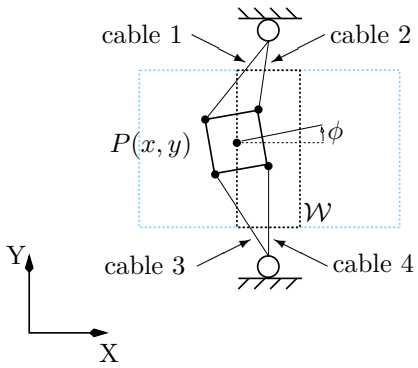

Figure 3.5 – Arbitrary three-DoF planar CDPM with only two base attachment points.

1. Minimize the number of cables used to constrain the end effector, keeping in mind that a minimum of $n + 1$ cables is required to fully constrain a n-DoF CDPM [82, 148];

2. Minimize the number of attachment points (on the end effector and on the base). An anchor point can be shared by two or more cables in order to eliminate the possibility of mechanical interferences between them [106, 107];

3. Prioritize base anchors position and end-effector attachment points to be distributed on the surface of a convex shape. The likelihood of mechanical interference is decreased when the base anchor points and attachment points on the end effector both have convex geometries (see the examples of Figs. 3.2a and 3.3).

In summary, following these rules does not guarantee an interference-free workspace for a given planar CDPM. However, these rules represent general guidelines to be taken into account when designing new geometries. If mechanical interferences between two cables or a cable and an edge of the end effector are expected, we saw that it is possible to easily determine the boundaries of the interference-free workspace by observing the geometry of the planar CDPM.

Unlike mechanical interferences for planar CDPMs, those occurring in spatial CDPMs require some mathematical skills. The next section presents how we are able to simplify the mathematical description of this phenomenon and obtain exact interference regions inside a generic constant-orientation spatial CDPMs.

3.3 Mechanical Interferences in Spatial Cable-Driven Parallel Mechanisms

Even if the rules enumerated in the previous section can be applied when choosing the geometry of a spatial CDPM, they are not sufficient to ensure that its workspace is free of

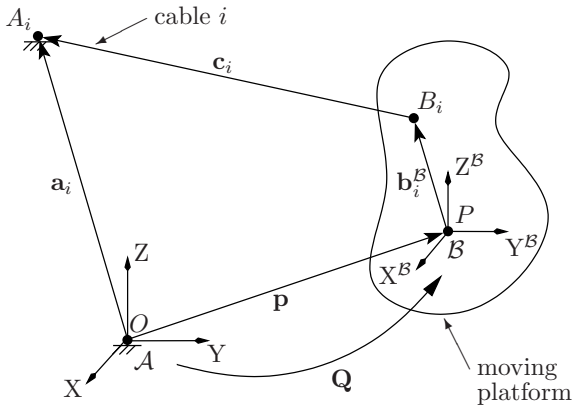

Figure 3.6 – Kinematic modelling.

mechanical interferences. This section proposes a method for the exact determination of the interference-free constant-orientation workspace of a generic CDPM.

3.3.1 Kinematic Model of a Cable-Driven Parallel Mechanism

Let us first describe the main assumptions forming the basis for the following analysis. The main hypothesis is that the cables are straight-line segments in space. Hence, sag is neglected, which is a valid assumption, provided that the cable tensions are sufficiently high [196]. Moreover, we assume the cable diameter to be negligibly small when compared to its length.

Thus, in general, a CDPM can be schematized as in Fig. 3.6. The associated variables are defined as follows:

- Vector $\mathbf{a}_i$ represents the position of the actuated reel A_i in the fixed frame $\mathcal{A}$;
- Vector $\mathbf{b}_i^{\mathcal{B}}$, expressed in frame $\mathcal{B}$, represents the position of the attachment point B_i of cable i on the moving platform;
- Vector $\mathbf{p}$, which is expressed in $\mathcal{A}$, represents the position of the operation point P on the moving platform, with respect to point O;
- Vector $\mathbf{c}_i$ points from B_i to A_i, its magnitude being the length of the i^{th} cable.

Let $\mathbf{Q}$ be the matrix that rotates frame $\mathcal{A}$ onto frame $\mathcal{B}$ (see Eq. (A.17) of Appendix A.2 for the mathematical definition of $\mathbf{Q}$). Hence, we express vector $\mathbf{b}_i^{\mathcal{B}}$ in the inertial frame as

$$\mathbf{b}_i = \mathbf{Q}\mathbf{b}_i^{\mathcal{B}}. \tag{3.1}$$

From Fig. 3.6 and Eq. (3.1), we have

$$\mathbf{c}_i = \mathbf{a}_i - \mathbf{b}_i - \mathbf{p}. \tag{3.2}$$

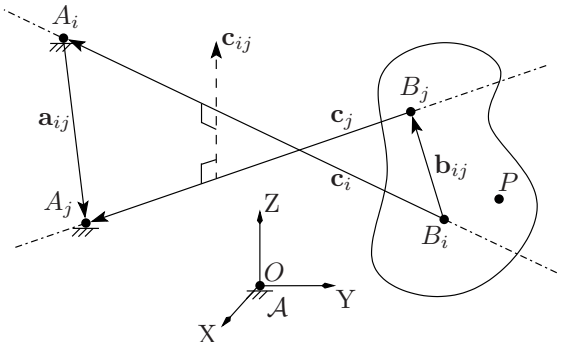

Figure 3.7 – The moving platform and a pair of cables that are attached to it.

3.3.2 Interference Regions

From the kinematic modelling of the CDPM, we describe the conditions under which an interference between two cables occurs. Since a six-DoF workspace cannot be represented directly, we decided to constrain three of those DoFs. In this work, we focus on the case where the orientation is constant, i.e., $\mathbf{Q}$ is fixed. This leaves us with the slice of the six-DoF workspace over which the end effector is translated at a given orientation. Hence, the goal of the following analysis is to determine the loci of interference between any two cables within the constant-orientation workspace. The interference between a cable and an end-effector edge will be discussed later in this sub-section. If one is interested in several orientations of the moving platform, i.e., in the case where $\mathbf{Q}$ is not fixed, then it is always possible to apply the following results to a sequence of distinct end-effector attitudes.

Figure 3.7 shows the cables i and j, which could potentially interfere. We also define $\mathbf{a}_{ij} \equiv \mathbf{a}_j - \mathbf{a}_i$, which points from A_i to A_j, while $\mathbf{b}_{ij} \equiv \mathbf{b}_j - \mathbf{b}_i$ points from B_i to B_j. Moreover, $\mathbf{c}_{ij} \equiv \mathbf{c}_i \times \mathbf{c}_j$ is perpendicular to cables i and j.

Interference Conditions

From Fig. 3.7, we observe that an interference between cables i and j can only occur if $\mathbf{c}_i$ and $\mathbf{c}_j$ are coplanar, or, similarly, if points A_i, B_i, A_j and B_j are coplanar. This necessary condition can be expressed either as

$$\mathbf{c}_{ij}^T \mathbf{b}_{ij} = 0, \tag{3.3}$$

or, equivalently, as

$$\mathbf{c}_{ij}^T \mathbf{a}_{ij} = 0. \tag{3.4}$$

Hence, the interference locus must lie on a plane of the constant-orientation workspace of the CDPM. Let us call this plane $\mathcal{P}_{ij}$, and provide an alternative expression, which will be useful

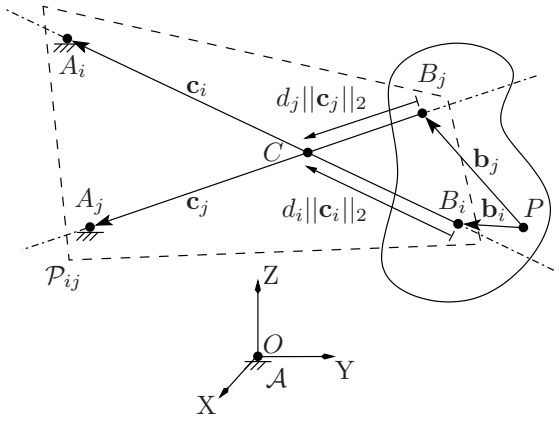

Figure 3.8 – Interference between cables i and j.

at the computer implementation stage in Sub-section 3.3.3, as follows

$$\mathcal{P}_{ij} = \{\mathbf{p} \in \mathbb{R}^3 | \mathbf{n}_{ij}^T(\mathbf{p} - (\mathbf{a}_i - \mathbf{b}_i)) = 0\}, \tag{3.5}$$

where $\mathbf{n}_{ij} \equiv \mathbf{a}_{ij} \times \mathbf{b}_{ij}$. This formulation is equivalent to Eqs. (3.3) and (3.4), since it merely states that vectors $\mathbf{a}_{ij}$, $\mathbf{b}_{ij}$, and $-\mathbf{c}_i$, should lie in the same plane.

This condition is not sufficient, however, since the lines supporting $\mathbf{c}_i$ and $\mathbf{c}_j$ can be coplanar while intersecting outside segments $\overline{A_iB_i}$ and $\overline{A_jB_j}$. They may even intersect at infinity, when $\mathbf{c}_i \parallel \mathbf{c}_j$. Since the contact point must belong to the two segments $\overline{A_iB_i}$ and $\overline{A_jB_j}$ simultaneously for an interference to occur, an additional necessary condition must be satisfied.

Figure 3.8 shows cables i and j when an interference is occurring at the contact point C. We observe that these cables follow the necessary condition from Eqs. (3.3) or (3.4), i.e., they lie in the common plane $\mathcal{P}_{ij}$. Assuming that Eqs. (3.3) and (3.4) hold, the position $\mathbf{c}$ of the contact point C between cables i and j can be written as

$$\mathbf{c} = \mathbf{p} + \mathbf{b}_i + d_i\mathbf{c}_i = \mathbf{p} + \mathbf{b}_j + d_j\mathbf{c}_j, \tag{3.6}$$

where the variables d_i and d_j are dimensionless parameters such that $\overrightarrow{B_iC} = d_i\mathbf{c}_i$ and $\overrightarrow{B_jC} = d_j\mathbf{c}_j$.

Since point C must lie on the two segments at the same time for an interference to occur, the following conditions are needed:

$$0 \leq d_i \leq 1 \quad \text{and} \quad 0 \leq d_j \leq 1. \tag{3.7}$$

Thus, from Fig. 3.8, Eqs. (3.3) and (3.7) are necessary and sufficient conditions for the occurrence of a mechanical interference between cables i and j.

Computing Closed-Form Expressions of d_i and d_j

With the aim of drawing general conclusions regarding the interference regions of a CDPM, we compute closed-form expressions of d_i and d_j. To this end, we write $\mathbf{b}_j - \mathbf{b}_i$ as

$$\mathbf{b}_{ij} = d_i\mathbf{c}_i - d_j\mathbf{c}_j. \tag{3.8}$$

We rewrite this linear system of equations in matrix form:

$$\mathbf{C}_{ij}\mathbf{d}_{ij} = \begin{bmatrix} \mathbf{c}_i & -\mathbf{c}_j \end{bmatrix} \begin{bmatrix} d_i \\ d_j \end{bmatrix} = \mathbf{b}_{ij}. \tag{3.9}$$

In order to find the position along the cables where a contact occurs, we have to solve Eq. (3.9) for $\mathbf{d}_{ij}$. This linear system of three equations in two unknowns admits a solution if and only if vectors $\mathbf{c}_i$, $\mathbf{c}_j$ and $\mathbf{b}_{ij}$ are linearly dependent, i.e., coplanar. This requirement is fulfilled if and only if Eq. (3.3) is satisfied. Moreover, we only have one solution whenever $\mathbf{c}_i \nparallel \mathbf{c}_j$, which is the general, non-degenerate case. Otherwise, the mechanical interference occurs at infinity, and there is no interference.

In order to solve Eq. (3.9) for $\mathbf{d}_{ij}$, we compute the left Moore-Penrose pseudoinverse of matrix $\mathbf{C}_{ij}$ [260, 261, 262],

$$\mathbf{C}_{ij}^{\dagger} = (\mathbf{C}_{ij}^T\mathbf{C}_{ij})^{-1}\mathbf{C}_{ij}^T, \tag{3.10}$$

$$\mathbf{C}_{ij}^{\dagger} = \frac{\begin{bmatrix} (\mathbf{c}_j^T\mathbf{c}_j)\mathbf{c}_i^T - (\mathbf{c}_i^T\mathbf{c}_j)\mathbf{c}_j^T \\ (\mathbf{c}_i^T\mathbf{c}_j)\mathbf{c}_i^T - (\mathbf{c}_i^T\mathbf{c}_i)\mathbf{c}_j^T \end{bmatrix}}{(\mathbf{c}_i^T\mathbf{c}_i)(\mathbf{c}_j^T\mathbf{c}_j) - (\mathbf{c}_i^T\mathbf{c}_j)^2}. \tag{3.11}$$

Finally, by using scalar and cross-product properties, the symbolic expression of $\mathbf{d}_{ij}$ is

$$\mathbf{d}_{ij} = \begin{bmatrix} d_i \\ d_j \end{bmatrix} = \frac{\begin{bmatrix} (\mathbf{c}_j \times (\mathbf{c}_i \times \mathbf{c}_j))^T \\ (\mathbf{c}_i \times (\mathbf{c}_i \times \mathbf{c}_j))^T \end{bmatrix}}{||\mathbf{c}_i||_2^2||\mathbf{c}_j||_2^2 - (\mathbf{c}_i^T\mathbf{c}_j)^2}\mathbf{b}_{ij}. \tag{3.12}$$

Boundaries of the Interference Loci

In order to define the interference loci corresponding to the pair of cables (i, j), we first compute the set of positions that bound these loci. Thus, to simplify the problem, it is practical to verify only the extreme cases: $d_i = 0$, $d_i = 1$, $d_j = 0$ and $d_j = 1$ (see conditions 3.7). Clearly, these four limiting conditions bound the loci where an interference between cables i and j occurs on plane $\mathcal{P}_{ij}$.

First, we find the equation of the boundary corresponding to $d_i = 0$ on the plane $\mathcal{P}_{ij}$. Accordingly, we have to solve Eq. (3.12) for $\mathbf{p}$ as follows

$$d_i = [\mathbf{C}_j(\mathbf{C}_i\mathbf{c}_j)]^T\mathbf{b}_{ij} = 0, \tag{3.13}$$

where $\mathbf{C}_i$ and $\mathbf{C}_j$ are the cross-product matrices[2] of $\mathbf{c}_i$ and $\mathbf{c}_j$, respectively. This expression can be rewritten as

$$d_i = (\mathbf{C}_i\mathbf{c}_j)^T(\mathbf{C}_j^T\mathbf{b}_{ij}) = 0, \tag{3.14}$$

and then,

$$d_i = \mathbf{c}_{ij}^T(\mathbf{B}_{ij}\mathbf{c}_j) = 0, \tag{3.15}$$

where $\mathbf{B}_{ij}$ is the cross-product matrix of $\mathbf{b}_{ij}$.

For a mechanical interference to occur, $\mathbf{c}_i$, $\mathbf{c}_j$ and $\mathbf{b}_{ij}$ must be coplanar (see Eq. (3.3)). Furthermore, we rule out the degenerate case where $\mathbf{c}_i$ and $\mathbf{c}_j$ are parallel, i.e., $\mathbf{c}_{ij} = \mathbf{0}_3$, from which we conclude that Eq. (3.15) is satisfied if and only if $\mathbf{B}_{ij}\mathbf{c}_j = \mathbf{0}_3$, that is,

$$\mathbf{B}_{ij}(\mathbf{a}_j - \mathbf{b}_j - \mathbf{p}) = \mathbf{0}_3. \tag{3.16}$$

In this equation, the rank of $\mathbf{B}_{ij}$ is two (only two rows or columns are linearly independent), its nullspace being the line spanned by $\mathbf{b}_{ij}$. Consequently, in order to fulfill the condition stated by Eq. (3.16), the associated boundary in the CDPM workspace is the line parallel to $\mathbf{b}_{ij}$ and passing through point $\mathbf{a}_j - \mathbf{b}_j$.

The same process can be applied to the limiting case $d_j = 0$, which gives:

$$d_j = [\mathbf{C}_i(\mathbf{C}_i\mathbf{c}_j)]^T\mathbf{b}_{ij} = 0, \tag{3.17}$$

$$d_j = (\mathbf{C}_i\mathbf{c}_j)^T(\mathbf{C}_i^T\mathbf{b}_{ij}) = 0, \tag{3.18}$$

$$d_j = \mathbf{c}_{ij}^T(\mathbf{B}_{ij}\mathbf{c}_i) = 0, \tag{3.19}$$

and then,

$$\mathbf{B}_{ij}(\mathbf{a}_i - \mathbf{b}_i - \mathbf{p}) = \mathbf{0}_3, \tag{3.20}$$

i.e., the line parallel to $\mathbf{b}_{ij}$ and passing through $\mathbf{a}_i - \mathbf{b}_i$.

For the two cases $d_i = 1$ and $d_j = 1$, the problem remains the same, with computations that are slightly more involved. Upon substituting $d_i = 1$ into Eq. (3.12), we obtain

$$[\mathbf{C}_j(\mathbf{C}_i\mathbf{c}_j)]^T\mathbf{b}_{ij} = ||\mathbf{c}_i||_2^2||\mathbf{c}_j||_2^2 - (\mathbf{c}_i^T\mathbf{c}_j)^2. \tag{3.21}$$

From this expression, we obtain

$$\mathbf{c}_{ij}^T(\mathbf{B}_{ij}\mathbf{c}_j) = \mathbf{c}_{ij}^T\mathbf{c}_{ij}. \tag{3.22}$$

Then, since, from Fig. 3.7, $\mathbf{b}_{ij} = \mathbf{c}_i + \mathbf{a}_{ij} - \mathbf{c}_j$, the last equation becomes

$$\mathbf{c}_{ij}^T(\mathbf{C}_i\mathbf{c}_j + \mathbf{A}_{ij}\mathbf{c}_j - \mathbf{C}_j\mathbf{c}_j) = \mathbf{c}_{ij}^T\mathbf{c}_{ij}, \tag{3.23}$$

[2]The cross-product matrix $\mathbf{X}$ of $\mathbf{x} \in \mathbb{R}^3$ is defined as $\mathbf{X} \equiv \partial(\mathbf{x} \times \mathbf{y})/\partial\mathbf{y},\ \mathbf{y} \in \mathbb{R}^3$.

and,

$$\mathbf{c}_{ij}^T(\mathbf{A}_{ij}\mathbf{c}_j) = 0, \tag{3.24}$$

or simply

$$\mathbf{A}_{ij}(\mathbf{a}_j - \mathbf{b}_j - \mathbf{p}) = \mathbf{0}_3, \tag{3.25}$$

where $\mathbf{A}_{ij}$ is the cross-product matrix of $\mathbf{a}_{ij}$. Thus, the boundary corresponding to $d_i = 1$ is the line parallel to $\mathbf{a}_{ij}$, and passing through the point $\mathbf{a}_j - \mathbf{b}_j$.

A similar method is used for the case $d_j = 1$,

$$[\mathbf{C}_i(\mathbf{C}_i\mathbf{c}_j)]^T\mathbf{b}_{ij} = ||\mathbf{c}_i||_2^2||\mathbf{c}_j||_2^2 - (\mathbf{c}_i^T\mathbf{c}_j)^2, \tag{3.26}$$

$$\mathbf{c}_{ij}^T(\mathbf{B}_{ij}\mathbf{c}_i) = \mathbf{c}_{ij}^T\mathbf{c}_{ij}, \tag{3.27}$$

$$\mathbf{c}_{ij}^T(\mathbf{C}_i\mathbf{c}_i + \mathbf{A}_{ij}\mathbf{c}_i - \mathbf{C}_j\mathbf{c}_i) = \mathbf{c}_{ij}^T\mathbf{c}_{ij}, \tag{3.28}$$

and,

$$\mathbf{c}_{ij}^T(\mathbf{A}_{ij}\mathbf{c}_i) = 0, \tag{3.29}$$

which yields $\mathbf{A}_{ij}(\mathbf{a}_i - \mathbf{b}_i - \mathbf{p}) = \mathbf{0}_3$, the line passing through the point $\mathbf{a}_i - \mathbf{b}_i$.

In summary, the four lines bounding the interference loci on the plane $\mathcal{P}_{ij}$ are shown in Fig. 3.9. On this figure, it is important to note that vectors $\mathbf{a}_{ij}$ and $\mathbf{b}_{ij}$ do not appear exactly as those presented in Fig. 3.8 to facilitate the graphical representation. We observe that the resulting lines are parallel by pairs, which gives four different intersection points noted D_{ii}, D_{jj}, D_{ij}^+ and D_{ij}^-. D_{ii} represents the intersection point of the lines $d_i = 0$ and $d_i = 1$, D_{jj} is the intersection point of lines $d_j = 0$ and $d_j = 1$, D_{ij}^+ is the common point for lines $d_i = 0$ and $d_j = 1$ (following positive directions of $\mathbf{a}_{ij}$ and $\mathbf{b}_{ij}$ from D_{ii} and D_{jj}, respectively) and finally D_{ij}^- is the intersection point of lines $d_i = 1$ and $d_j = 0$ (following negative directions of $\mathbf{a}_{ij}$ and $\mathbf{b}_{ij}$ from D_{ii} and D_{jj}, respectively).

Since we know the equations of these four lines, we can easily compute their intersection points. In fact, we already know that the lines corresponding to $d_i = 0$ and $d_i = 1$ both pass through point $\mathbf{a}_j - \mathbf{b}_j$, which is thus the position of D_{ii}. The same reasoning applies to the intersection point of $d_j = 0$ and $d_j = 1$, and the position of D_{jj} is $\mathbf{a}_i - \mathbf{b}_i$. From Fig. 3.9, we observe that the intersection points D_{ij}^+ and D_{ij}^- can be found by following the directions of vectors $\mathbf{a}_{ij}$ and $\mathbf{b}_{ij}$ from points D_{ii} and D_{jj}, respectively. In fact, we can formulate the relations defining the intersection point D_{ij}^+ as

$$\mathbf{a}_i - \mathbf{b}_i + \alpha\mathbf{a}_{ij} = \mathbf{a}_j - \mathbf{b}_j + \beta\mathbf{b}_{ij}, \tag{3.30}$$

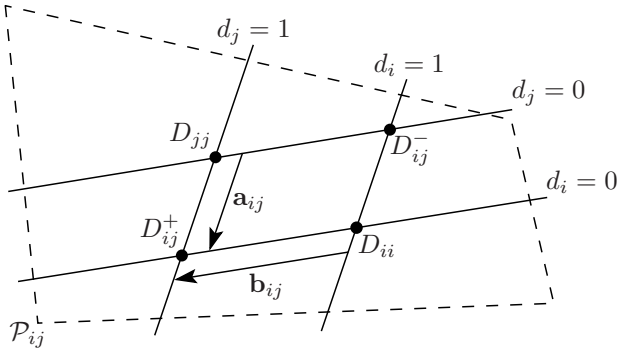

Figure 3.9 – Conditions for interference between cables.

and similarly for D_{ij}^-

$$\mathbf{a}_i - \mathbf{b}_i - \beta \mathbf{b}_{ij} = \mathbf{a}_j - \mathbf{b}_j - \alpha \mathbf{a}_{ij}, \tag{3.31}$$

where α and β are dimensionless coefficients. Upon resolving these two equations for α and β, we obtain $\alpha = \beta = 1$. As a result, the position of D_{ij}^+ is $\mathbf{a}_j - \mathbf{b}_i$, and that of D_{ij}^- is $\mathbf{a}_i - \mathbf{b}_j$.

Determination of the Interference Regions

In this sub-section, we determine the mechanical interference regions, i.e., which regions of $\mathcal{P}_{ij}$ correspond to $0 \leq d_i \leq 1$ and $0 \leq d_j \leq 1$. To this end, we analyze the infinitesimal variations of d_i and d_j on each of the four boundaries and determine the side of the boundary that corresponds to an interference. Since d_i and d_j are known functions of $\mathbf{p}$, it is possible to compute their gradient vectors with respect to $\mathbf{p}$ at different points.

Upon differentiating Eq. (3.8), we obtain

$$\mathbf{c}_i \left(\frac{\partial d_i}{\partial \mathbf{p}}\right)^T + d_i \left(\frac{\partial \mathbf{c}_i}{\partial \mathbf{p}}\right) - \mathbf{c}_j \left(\frac{\partial d_j}{\partial \mathbf{p}}\right)^T - d_j \left(\frac{\partial \mathbf{c}_j}{\partial \mathbf{p}}\right) = \frac{\partial \mathbf{b}_{ij}}{\partial \mathbf{p}}, \tag{3.32}$$

which we substitute into Eq. (3.2), to obtain the following expression

$$\mathbf{c}_i \left(\frac{\partial d_i}{\partial \mathbf{p}}\right)^T - \mathbf{c}_j \left(\frac{\partial d_j}{\partial \mathbf{p}}\right)^T + (d_j - d_i)\mathbf{1}_{3\times 3} = \mathbf{0}_{3\times 3}. \tag{3.33}$$

From Fig. 3.9, if we simultaneously consider variables d_i and d_j, we notice that the value of d_i is both 0 and 1 at point D_{ii}, and that the value of d_j is 0 and 1 at point D_{jj}. This curious behaviour is due to discontinuities of d_i and d_j at these points. In fact, this situation occurs when $\mathbf{c}_i \parallel \mathbf{c}_j$, that is, when matrix $\mathbf{C}_{ij}$ in Eq. (3.9) becomes rank-deficient. In this particular case, we know that

$$\mathbf{c}_{ij} = \mathbf{0}_3, \tag{3.34}$$

and, in substituting Eq. (3.2), we obtain

$$(\mathbf{a}_i - \mathbf{b}_i - \mathbf{p}) \times (\mathbf{a}_j - \mathbf{b}_j - \mathbf{p}) = \mathbf{0}_3, \tag{3.35}$$

which can be rearranged as

$$(\mathbf{a}_i - \mathbf{b}_i) \times (\mathbf{a}_j - \mathbf{b}_j) + \mathbf{p} \times (\mathbf{a}_i - \mathbf{b}_i) - \mathbf{p} \times (\mathbf{a}_j - \mathbf{b}_j) = \mathbf{0}_3. \tag{3.36}$$

This expression simplifies to

$$(\mathbf{A}_{ij} - \mathbf{B}_{ij})\,\mathbf{p} = (\mathbf{a}_j - \mathbf{b}_j) \times (\mathbf{a}_i - \mathbf{b}_i). \tag{3.37}$$

The solution to this equation is the line $\mathcal{L}$ parallel to $\mathbf{a}_{ij} - \mathbf{b}_{ij}$, since this vector spans the nullspace of $\mathbf{A}_{ij} - \mathbf{B}_{ij}$. In substituting $\mathbf{p} = \mathbf{a}_j - \mathbf{b}_j$ and similarly $\mathbf{p} = \mathbf{a}_i - \mathbf{b}_i$ into Eq. (3.37), we see that the equality is preserved in both cases (as for example, if $\mathbf{p} = \mathbf{a}_j - \mathbf{b}_j$, $(\mathbf{A}_{ij} - \mathbf{B}_{ij})\mathbf{p}$ becomes $(\mathbf{a}_{ij} - \mathbf{b}_{ij}) \times (\mathbf{a}_j - \mathbf{b}_j)$ and then $(\mathbf{a}_j - \mathbf{b}_j) \times (\mathbf{a}_i - \mathbf{b}_i)$). Hence, $\mathcal{L}$ passes through points D_{ii} and D_{jj}. Because of this discontinuity, it is impossible to evaluate the gradients of d_i and d_j at these points.

Nevertheless, we can compute $\boldsymbol{\nabla} d_i$ at points D_{ij}^+ on the line $d_i = 0$, and D_{ij}^- on the line $d_i = 1$. Similarly, we evaluate $\boldsymbol{\nabla} d_j$ at the same points, but on the lines $d_j = 1$ and $d_j = 0$, respectively. Since at D_{ij}^+, $\mathbf{p} = \mathbf{a}_j - \mathbf{b}_i$, $d_i = 0$, $d_j = 1$, $\mathbf{c}_i \equiv -\mathbf{a}_{ij}$ and $\mathbf{c}_j \equiv -\mathbf{b}_{ij}$ (by substituting $\mathbf{p}$ in Eq. (3.2)), Eq. (3.33) simplifies to

$$\mathbf{a}_{ij} \left(\frac{\partial d_i}{\partial \mathbf{p}}\right)^T - \mathbf{b}_{ij} \left(\frac{\partial d_j}{\partial \mathbf{p}}\right)^T = \mathbf{1}_{3\times 3}. \tag{3.38}$$

We determine the direction of $\boldsymbol{\nabla} d_i$ by premultiplying vector $\mathbf{a}_{ij}$ with both sides of this equation, namely,

$$\mathbf{a}_{ij} \left(\frac{\partial d_i}{\partial \mathbf{p}}\right)^T \mathbf{a}_{ij} - \mathbf{b}_{ij} \left(\frac{\partial d_j}{\partial \mathbf{p}}\right)^T \mathbf{a}_{ij} = \mathbf{a}_{ij}, \tag{3.39}$$

or,

$$\left[\left(\frac{\partial d_i}{\partial \mathbf{p}}\right)^T \mathbf{a}_{ij}\right] \mathbf{a}_{ij} - \left[\left(\frac{\partial d_j}{\partial \mathbf{p}}\right)^T \mathbf{a}_{ij}\right] \mathbf{b}_{ij} = \mathbf{a}_{ij}. \tag{3.40}$$

Since, in general, $\mathbf{a}_{ij} \nparallel \mathbf{b}_{ij}$, the only solution to this linear system of equations is

$$\left(\frac{\partial d_i}{\partial \mathbf{p}}\right)^T \mathbf{a}_{ij} = 1, \quad \text{and} \quad \left(\frac{\partial d_j}{\partial \mathbf{p}}\right)^T \mathbf{a}_{ij} = 0. \tag{3.41}$$

Moreover, since $\boldsymbol{\nabla} d_i$ is perpendicular to the line $d_i = 0$, and its projection onto $\mathbf{a}_{ij}$ is positive, we know that d_i increases in this direction. Since, at D_{ij}^+, $d_i = 0$, we know the direction of increasing d_i, we know that the corresponding region of $\mathcal{P}_{ij}$ is one of possible interference, because $d_i \in [0,1]$. Similarly, we multiply both sides of Eq. (3.38) with $\mathbf{b}_{ij}$, and we find $(\partial d_j/\partial \mathbf{p})^T \mathbf{b}_{ij} = -1$, i.e., d_j increases in the direction opposite to $\mathbf{b}_{ij}$. Finally, this procedure is applied at point D_{ij}^- for which $\mathbf{c}_i \equiv \mathbf{b}_{ij}$, $\mathbf{c}_j \equiv \mathbf{a}_{ij}$, $d_i = 1$ and $d_j = 0$. We then obtain

$$\left(\frac{\partial d_i}{\partial \mathbf{p}}\right)^T \mathbf{b}_{ij} = 1, \quad \text{and} \quad \left(\frac{\partial d_j}{\partial \mathbf{p}}\right)^T \mathbf{a}_{ij} = -1. \tag{3.42}$$

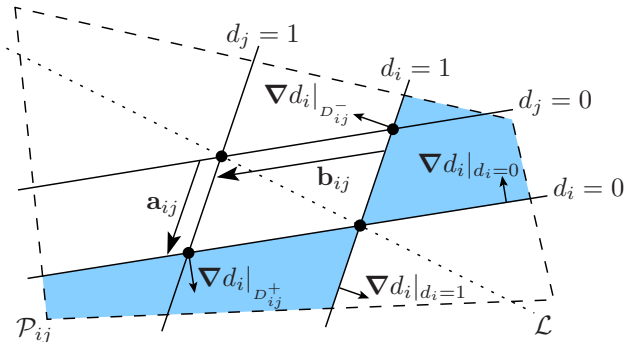

Figure 3.10 – Regions of $\mathcal{P}_{ij}$ for which $d_i \in [0,1]$.

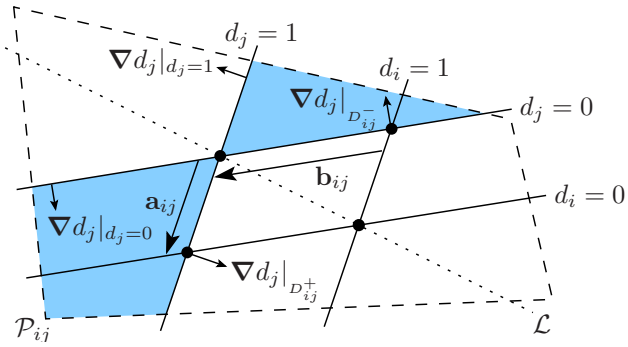

Figure 3.11 – Regions of $\mathcal{P}_{ij}$ for which $d_j \in [0,1]$.

These results are presented in Figs. 3.10 and 3.11 and they show the two potential interference regions for each function, d_i and d_j. Notice that the points D_{ii} and D_{jj} lie on line $\mathcal{L}$, which is the discontinuity locus of both functions d_i and d_j. Finally, to complete our analysis, since a mechanical interference between cables i and j only occurs when $d_i \in [0,1]$ and $d_j \in [0,1]$ simultaneously, the interference regions are the intersection of those represented in Figs. 3.10 and 3.11. This final result is shown in Fig. 3.12.

From Fig. 3.12, we see that the interference region associated with cables i and j is formed of two disjoint sub-regions. Both of these sub-regions lie in plane $\mathcal{P}_{ij}$ containing $\mathbf{a}_{ij}$ and $\mathbf{b}_{ij}$, and may be described as a sector of $\mathcal{P}_{ij}$. It is fully determined by its apex, which is either $\mathbf{a}_j - \mathbf{b}_i$ or $\mathbf{a}_i - \mathbf{b}_j$, and its two bounding half-lines, whose positive directions are given by $\mathbf{a}_{ij}$ and $\mathbf{b}_{ij}$, and $-\mathbf{a}_{ij}$ and $-\mathbf{b}_{ij}$, respectively. Hence, only the vectors $\mathbf{a}_i$, $\mathbf{a}_j$, $\mathbf{b}_i$ and $\mathbf{b}_j$ are needed to compute the interference region of cables i and j.

Formally, we can define the set $\mathcal{C}_{ij}$ of the interference locus corresponding to cables i and j as

$$\mathcal{C}_{ij} \equiv \mathcal{C}_{ij}^+ \bigcup \mathcal{C}_{ij}^-, \tag{3.43}$$

where $i = 1, \ldots, m$, $j = i+1, \ldots, m$, and where

$$\mathcal{C}_{ij}^+ = \{\mathbf{p} \in \mathbb{R}^3 | \mathbf{p} = \mathbf{a}_j - \mathbf{b}_i + \alpha \mathbf{a}_{ij} + \beta \mathbf{b}_{ij}, \alpha, \beta \geq 0\}, \tag{3.44}$$

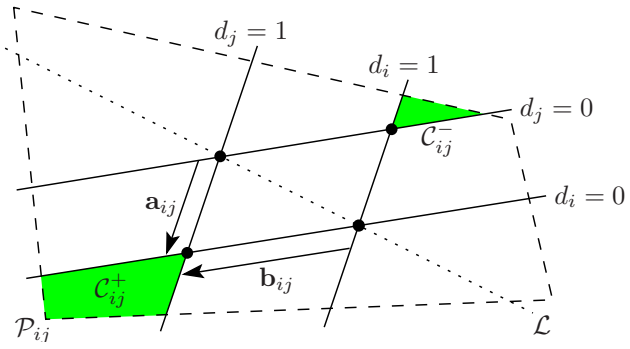

Figure 3.12 – Regions $\mathcal{C}_{ij}^+$ and $\mathcal{C}_{ij}^-$ which include interferences between cables i and j.

and

$$\mathcal{C}_{ij}^- = \{\mathbf{p} \in \mathbb{R}^3 | \mathbf{p} = \mathbf{a}_i - \mathbf{b}_j + \alpha \mathbf{a}_{ij} + \beta \mathbf{b}_{ij}, \alpha, \beta \leq 0\}. \tag{3.45}$$

In the special case where $\mathbf{a}_{ij} \parallel \mathbf{b}_{ij}$ and $\mathbf{a}_{ij}^T \mathbf{b}_{ij} > 0$, the cables are not crossed (for example, see the case in Fig. 3.2a), and, from Fig. 3.12, the region becomes the line through points D_{ij}^+ and D_{ij}^- minus the segment $\overline{D_{ij}^+ D_{ij}^-}$. Finally, when $\mathbf{a}_{ij} \parallel \mathbf{b}_{ij}$ and $\mathbf{a}_{ij}^T \mathbf{b}_{ij} < 0$, the interference regions fill the entire plane $\mathcal{P}_{ij}$ (for example, see the case in Fig. 3.2a when $\phi = 0^\circ$). This situation should generally be avoided when designing a spatial CDPM.

Finally, in order to obtain a more concise formulation of Eqs. (3.44) and (3.45), we can regroup these two equations in a single one, based on the fact that $\mathbf{a}_{ij} = -\mathbf{a}_{ji}$ and $\mathbf{b}_{ij} = -\mathbf{b}_{ji}$. This statement directly leads to $\mathcal{C}_{ij}^+ = \mathcal{C}_{ji}^-$ and $\mathcal{C}_{ij}^- = \mathcal{C}_{ji}^+$ and allows us to define the ordered pairs of cables (i,j) and their respective region of interferences such as $\mathcal{C}_{ij} \equiv \mathcal{C}_{ij}^+$ and $\mathcal{C}_{ji} \equiv \mathcal{C}_{ij}^-$. Then, Eqs. (3.44) and (3.45) can be reformulated as

$$\mathcal{C}_{ij} = \{\mathbf{p} \in \mathbb{R}^3 | \mathbf{p} = \mathbf{a}_j - \mathbf{b}_i + \mathbf{\Gamma}_{ij} \boldsymbol{\gamma}, \boldsymbol{\gamma} \geq \mathbf{0}_2\}, \tag{3.46}$$

where $i = 1, \ldots, m$, $j = 1, \ldots, m$ $(j \neq i)$, and where

$$\mathbf{\Gamma}_{ij} = \begin{bmatrix} \mathbf{a}_{ij} & \mathbf{b}_{ij} \end{bmatrix} \quad \text{and} \quad \boldsymbol{\gamma} = \begin{bmatrix} \alpha & \beta \end{bmatrix}^T. \tag{3.47}$$

Interference Between a Cable and an End-Effector Edge

Alike interferences between two cables, interferences between a cable and the moving platform of a CDPM may considerably reduce its workspace. Therefore, it is important to mathematically define this other kind of interferences, with the aim of designing an architecture that avoids them.

An interference between a cable and an edge of the end effector can be modelled in a way similar to one between two cables. However, the difference is that an edge is fixed to the end effector and its length is constant while the cable length and direction change with the pose of the moving platform in the workspace. This has a slight effect on the mathematical representation of the phenomenon.

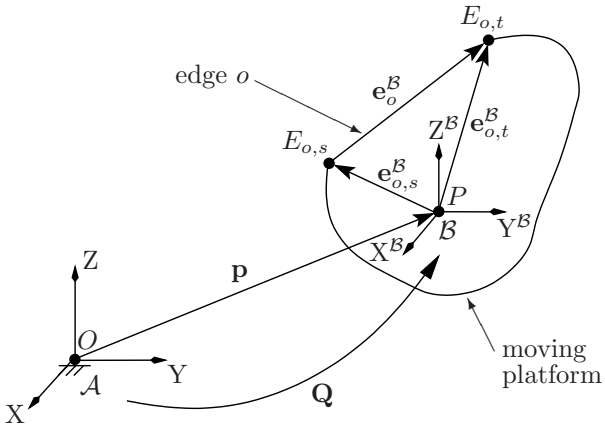

Figure 3.13 – Kinematic modelling of an end-effector edge.

In general, an end-effector edge can be represented as in Fig. 3.13, in which it is modelled as a line segment. Curved edges may be approximated with chains of line segments, whereas curved surfaces can be represented with wire-frame models. In such a model, the o^{th} edge is defined by its two end points, $E_{o,s}$ and $E_{o,t}$. Vector $\mathbf{e}_{o,s}^{\mathcal{B}}$ points from the operation point P to the vertex $E_{o,s}$, vector $\mathbf{e}_{o,t}^{\mathcal{B}}$ points from P to point $E_{o,t}$, and vector $\mathbf{e}_o^{\mathcal{B}}$ points from $E_{o,s}$ to $E_{o,t}$, its magnitude being the length of the o^{th} edge. We notice that all these vectors are expressed in frame $\mathcal{B}$, which is attached to the moving platform.

Thus, we can write $\mathbf{e}_o^{\mathcal{B}}$ in the fixed frame $\mathcal{A}$ as

$$\mathbf{e}_o = \mathbf{Q}\mathbf{e}_o^{\mathcal{B}} = \mathbf{Q}(\mathbf{e}_{o,t}^{\mathcal{B}} - \mathbf{e}_{o,s}^{\mathcal{B}}). \tag{3.48}$$

From Fig. 3.14, a necessary condition for the occurrence of a mechanical interference between a cable and an edge of the end effector is that they lie in the same plane, which can be expressed as

$$\mathbf{v}_{io}^T \mathbf{r}_{io,s} = 0, \tag{3.49}$$

or, equivalently, as

$$\mathbf{v}_{io}^T \mathbf{r}_{io,t} = 0, \tag{3.50}$$

where $\mathbf{v}_{io} = \mathbf{c}_i \times \mathbf{e}_o$, $\mathbf{r}_{io,s}$ points from B_i to $E_{o,s}$, and $\mathbf{r}_{io,t}$ points from B_i to $E_{o,t}$. When Eqs. (3.49) and (3.50) are satisfied, we denote $\mathcal{P}_{io}$ the associated plane in the CDPM workspace.

As in the case of an interference between two cables, the plane $\mathcal{P}_{io}$ is defined by Eq. (3.5), except that $\mathbf{n}_{ij}$ is replaced by $\mathbf{n}_{io} \equiv \mathbf{r}_{io,s} \times \mathbf{r}_{io,t}$. Still, this condition is necessary but not sufficient for a mechanical interference to occur: the intersection point between the lines supporting $\mathbf{c}_i$ and $\mathbf{e}_o$ should lie on the line segments $\overline{A_i B_i}$ and $\overline{E_{o,s}E_{o,t}}$.

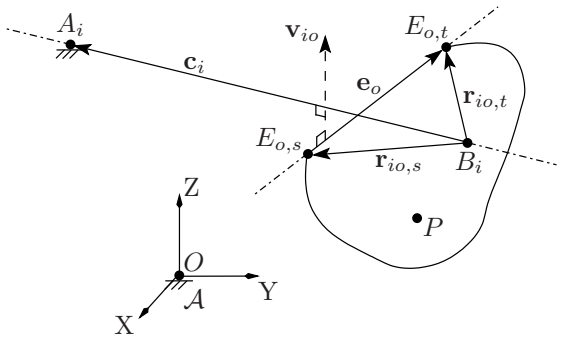

Figure 3.14 – A combination of a cable and an edge.

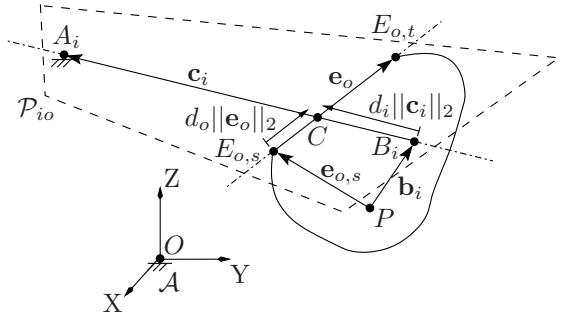

Figure 3.15 – Interference between a cable and an edge.

From Fig. 3.15, the position vector $\mathbf{c}$ of the contact point C between the two entities is given by

$$\mathbf{c} = \mathbf{p} + \mathbf{b}_i + d_i\mathbf{c}_i = \mathbf{p} + \mathbf{e}_{o,s} + d_o\mathbf{e}_o, \tag{3.51}$$

where d_i and d_o are dimensionless parameters, which are now chosen such that $\overrightarrow{B_iC} = d_i\mathbf{c}_i$ and $\overrightarrow{E_{o,s}C} = d_o\mathbf{e}_o$. This leads to the following rearranged equation

$$d_i\mathbf{c}_i - d_o\mathbf{e}_o = \mathbf{r}_{io,s}, \tag{3.52}$$

and to the additional conditions:

$$0 \leq d_i \leq 1 \quad \text{and} \quad 0 \leq d_o \leq 1, \tag{3.53}$$

which, along with Eq. (3.49), form a necessary and sufficient set of conditions for an interference to occur.

However, since the edge $\mathbf{e}_o$ and the point B_i are both fixed to the end effector, the distance between these two entities remains constant, and is generally different from zero. Hence, it is impossible to reach the condition $d_i = 0$. An exception occurs when B_i belongs to the line supporting $\mathbf{e}_o$, but in this case, there is generally no collision from a practical viewpoint [106, 107], and we do not take this particular situation into account. However, when $\mathbf{e}_o$ is collinear

with $\mathbf{c}_i$, an interference may occur in practice, which is taken into account in the following analysis.

As a result, we discard the case where $d_i = 0$. The necessary and sufficient conditions for the occurrence of an interference between cable i and edge o are given by Eq. (3.49) and by

$$0 < d_i \leq 1 \quad \text{and} \quad 0 \leq d_o \leq 1, \tag{3.54}$$

where we have replaced the first inequality with a strict inequality.

Upon assuming that Eq. (3.49) is fulfilled, we compute d_i and d_o, the least-squares solution to Eq. (3.52), namely,

$$\mathbf{d}_{io} = \begin{bmatrix} d_i \\ d_o \end{bmatrix} = \frac{\begin{bmatrix} (\mathbf{e}_o \times (\mathbf{c}_i \times \mathbf{e}_o))^T \\ (\mathbf{c}_i \times (\mathbf{c}_i \times \mathbf{e}_o))^T \end{bmatrix}}{||\mathbf{c}_i||_2^2||\mathbf{e}_o||_2^2 - (\mathbf{c}_i^T\mathbf{e}_o)^2}\mathbf{r}_{io,s}. \tag{3.55}$$

Similarly to the case of an interference between two cables, we are first interested by the boundaries of the interference regions. As mentioned above, the condition $d_i = 0$ cannot be reached in general. However, one may approach arbitrarily close to $d_i = 0$ by increasing the length of the cable i towards infinity. Therefore, we may say that the boundary corresponding to $d_i = 0$ lies at infinity. It can never be reached, which justifies the limitation of the following analysis to the three remaining boundaries: $d_i = 1$, $d_o = 0$ and $d_o = 1$.

Upon substituting $\mathbf{r}_{io,s} = \mathbf{c}_i + \overrightarrow{A_iE_{o,t}} - \mathbf{e}_o$ in Eq. (3.55) and setting $d_i = 1$, we obtain

$$\mathbf{v}_{io}^T(\mathbf{e}_o \times \overrightarrow{A_iE_{o,t}}) = 0, \tag{3.56}$$

where $\overrightarrow{A_iE_{o,t}} \equiv \mathbf{p} + \mathbf{e}_{o,t} - \mathbf{a}_i$. Furthermore, we rule out the degenerate case where $\mathbf{c}_i$ and $\mathbf{e}_o$ are parallel, i.e., $\mathbf{v}_{io} = \mathbf{0}_3$. Then, we finally obtain

$$\mathbf{E}_o(\mathbf{a}_i - \mathbf{e}_{o,t} - \mathbf{p}) = \mathbf{0}_3, \tag{3.57}$$

where $\mathbf{E}_o$ is the cross-product matrix of $\mathbf{e}_o$. Apparently, $d_i = 1$ corresponds to the line parallel to $\mathbf{e}_o$ and passing through the point $\mathbf{a}_i - \mathbf{e}_{o,t}$. A similar process is used for the case $d_o = 0$ and we obtain

$$\mathbf{v}_{io}^T(\mathbf{R}_{io,s}\mathbf{c}_i) = 0, \tag{3.58}$$

and then

$$\mathbf{R}_{io,s}(\mathbf{a}_i - \mathbf{b}_i - \mathbf{p}) = \mathbf{0}_3. \tag{3.59}$$

For the case $d_o = 1$, by using the fact that $\mathbf{r}_{io,s} = \mathbf{r}_{io,t} - \mathbf{e}_o$, we find

$$\mathbf{v}_{io}^T(\mathbf{R}_{io,t}\mathbf{c}_i) = 0, \tag{3.60}$$

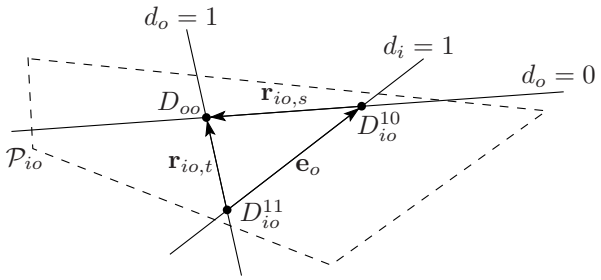

Figure 3.16 – Conditions for an interference between a cable and an edge.

and this result leads to

$$\mathbf{R}_{io,t}(\mathbf{a}_i - \mathbf{b}_i - \mathbf{p}) = \mathbf{0}_3. \tag{3.61}$$

It is noted that $\mathbf{R}_{io,s}$ and $\mathbf{R}_{io,t}$ are the cross-product matrices of $\mathbf{r}_{io,s}$ and $\mathbf{r}_{io,t}$, respectively. Hence, $d_o = 0$ is a line parallel to $\mathbf{r}_{io,s}$ and passing through the point $\mathbf{a}_i - \mathbf{b}_i$, while $d_o = 1$ is a line parallel to $\mathbf{r}_{io,t}$ and passing through the point $\mathbf{a}_i - \mathbf{b}_i$ as well.

Figure 3.16 represents the three lines bounding the interference regions in the plane $\mathcal{P}_{io}$. There are three distinct intersection points, which are noted D_{oo} (intersection point between lines $d_o = 0$ and $d_o = 1$), D_{io}^{10} (intersection point between lines $d_i = 1$ and $d_o = 0$) and D_{io}^{11} (intersection point between lines $d_i = 1$ and $d_o = 1$). One may readily verify, through substitutions in Eqs. (3.57,3.59,3.61), that the coordinates of D_{oo}, D_{io}^{10} and D_{io}^{11} are $\mathbf{a}_i - \mathbf{b}_i$, $\mathbf{a}_i - \mathbf{e}_{o,s} = \mathbf{a}_i - \mathbf{b}_i - \mathbf{r}_{io,s}$ and $\mathbf{a}_i - \mathbf{e}_{o,t} = \mathbf{a}_i - \mathbf{b}_i - \mathbf{r}_{io,t}$, respectively. Indeed, each of these three position vectors is a solution to exactly two of the three boundary equations, those of the two lines intersecting at this point.

As in the case of interferences between two cables, we have to determine the regions of the plane $\mathcal{P}_{io}$ shown in Fig. 3.16 containing interferences between the cable i and the edge o. Following the same strategy, we evaluate the gradient vectors $\boldsymbol{\nabla} d_i$ and $\boldsymbol{\nabla} d_o$ related to $\mathbf{p}$ to determine which sides of the three boundary lines ($d_i = 1$, $d_o = 0$ and $d_o = 1$) form the interference regions.

The following equation is obtained from the differentiation of Eq. (3.52) with respect to $\mathbf{p}$

$$\mathbf{c}_i \left(\frac{\partial d_i}{\partial \mathbf{p}}\right)^T + d_i \left(\frac{\partial \mathbf{c}_i}{\partial \mathbf{p}}\right) - \mathbf{e}_o \left(\frac{\partial d_o}{\partial \mathbf{p}}\right)^T - d_o \left(\frac{\partial \mathbf{e}_o}{\partial \mathbf{p}}\right) = \frac{\partial \mathbf{r}_{io,s}}{\partial \mathbf{p}}, \tag{3.62}$$

which we substitute into Eq. (3.2), to obtain the following expression

$$\mathbf{c}_i \left(\frac{\partial d_i}{\partial \mathbf{p}}\right)^T - \mathbf{e}_o \left(\frac{\partial d_o}{\partial \mathbf{p}}\right)^T - d_i \mathbf{1}_{3\times 3} = \mathbf{0}_{3\times 3}. \tag{3.63}$$

We begin our analysis on point D_{io}^{10}, for which $d_i = 1$, $d_o = 0$ and $\mathbf{c}_i = \mathbf{r}_{io,s}$ and Eq. (3.63) simplifies to

$$\mathbf{r}_{io,s} \left(\frac{\partial d_i}{\partial \mathbf{p}}\right)^T - \mathbf{e}_o \left(\frac{\partial d_o}{\partial \mathbf{p}}\right)^T = \mathbf{1}_{3\times 3}. \tag{3.64}$$

As for an interference between two cables, we first verify the signs of the projections of $\boldsymbol{\nabla} d_i$ on $\mathbf{r}_{io,s}$ and we obtain

$$\mathbf{r}_{io,s}\left(\frac{\partial d_i}{\partial \mathbf{p}}\right)^T \mathbf{r}_{io,s} - \mathbf{e}_o\left(\frac{\partial d_o}{\partial \mathbf{p}}\right)^T \mathbf{r}_{io,s} = \mathbf{r}_{io,s}, \tag{3.65}$$

or,

$$\left[\left(\frac{\partial d_i}{\partial \mathbf{p}}\right)^T \mathbf{r}_{io,s}\right]\mathbf{r}_{io,s} - \left[\left(\frac{\partial d_o}{\partial \mathbf{p}}\right)^T \mathbf{r}_{io,s}\right]\mathbf{e}_o = \mathbf{r}_{io,s}. \tag{3.66}$$

Since, in general, $\mathbf{e}_o \nparallel \mathbf{r}_{io,s}$, the only solution to this linear system of equations is

$$\left(\frac{\partial d_i}{\partial \mathbf{p}}\right)^T \mathbf{r}_{io,s} = 1, \quad \text{and} \quad \left(\frac{\partial d_o}{\partial \mathbf{p}}\right)^T \mathbf{r}_{io,s} = 0. \tag{3.67}$$

Hence, we know the direction towards which d_i increases, i.e., perpendicular to the line $d_i = 1$ and towards the positive direction of $\mathbf{r}_{io,s}$.

Similarly, we verify the signs of the projections of $\boldsymbol{\nabla} d_o$ on $\mathbf{e}_o$ by multiplying both sides of Eq. (3.64) with $\mathbf{e}_o$, and we find $(\partial d_o/\partial \mathbf{p})^T \mathbf{e}_o = -1$, i.e., d_o increases in the direction opposite to $\mathbf{e}_o$. It is interesting to notice that the case where $\mathbf{e}_o \parallel \mathbf{r}_{io,s}$ only occurs when B_i belongs to the line supporting $\mathbf{e}_o$. However, this situation is not considered as a mechanical interference in practice.

Finally, the same method is used at D_{io}^{11} with projections on $\mathbf{r}_{io,t}$ and $\mathbf{e}_o$, respectively. Knowing that $\mathbf{c}_i \equiv \mathbf{r}_{io,t}$, $d_i = 1$ and $d_o = 1$, we now obtain

$$\left(\frac{\partial d_i}{\partial \mathbf{p}}\right)^T \mathbf{r}_{io,t} = 1, \quad \text{and} \quad \left(\frac{\partial d_o}{\partial \mathbf{p}}\right)^T \mathbf{e}_o = -1. \tag{3.68}$$

These results mean that, at D_{io}^{11}, $\boldsymbol{\nabla} d_i$ is positive following the direction of $\mathbf{r}_{io,t}$ and $\boldsymbol{\nabla} d_o$ is positive following the direction opposite to $\mathbf{e}_o$.

The results are illustrated with Figs. 3.17 and 3.18, which present the positive-slope directions of the dimensionless coefficients d_i and d_o over $\mathcal{P}_{io}$. The regions following from the conditions of Eq. (3.54) are shown in shading on the same graphs. Also on these graphs is the line $\mathcal{L}$ for which d_i and d_o are discontinuous. In fact, this happens whenever $\mathbf{c}_i \parallel \mathbf{e}_o$, or, equivalently, when

$$\mathbf{v}_{io} = \mathbf{0}_3. \tag{3.69}$$

This equation can be rewritten as

$$\mathbf{E}_o(\mathbf{a}_i - \mathbf{b}_i - \mathbf{p}) = \mathbf{0}_3. \tag{3.70}$$

Clearly, the solution for $\mathbf{p}$ of Eq. (3.70) is line $\mathcal{L}$, which is parallel to $\mathbf{e}_o$ and passes through the point D_{oo} of coordinates $\mathbf{a}_i - \mathbf{b}_i$. Furthermore, it is interesting to note that the length of the cable i is null when the end effector reaches this specific point, that is, $A_i = B_i$.

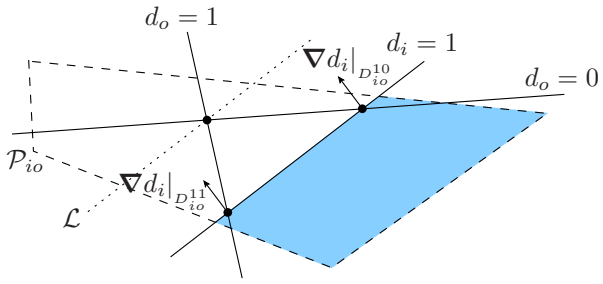

Figure 3.17 – Regions of $\mathcal{P}_{io}$ for which $d_i \in]0,1]$.

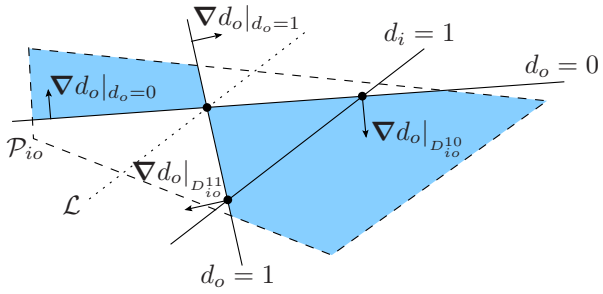

Figure 3.18 – Regions of $\mathcal{P}_{io}$ for which $d_o \in [0,1]$.

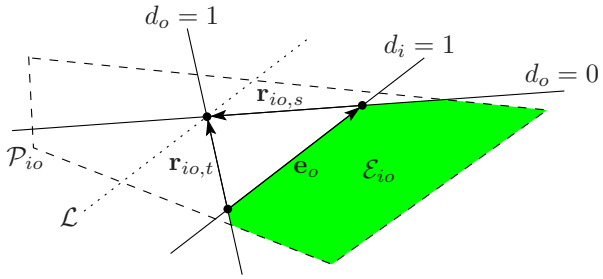

Figure 3.19 – Region $\mathcal{E}_{io}$ which includes interferences between cable i and edge o.

Moreover, when $\mathbf{c}_i \parallel \mathbf{e}_o$ and $\mathbf{p} \neq \mathbf{a}_i - \mathbf{b}_i$, the mechanical interference region is a line segment in $\mathcal{P}_{io}$ if and only if $\mathbf{e}_o$ lies partially or totally on $\mathbf{c}_i$. Otherwise, if $\mathbf{c}_i \parallel \mathbf{e}_o$ and the two entities are not overlapping each other, there is no mechanical interference.

Finally, Fig. 3.19 represents the intersection of the potential interference regions associated with functions d_i and d_o, respectively. We note that D_{io}^{10} $(\mathbf{a}_i - \mathbf{e}_{o,s})$, D_{io}^{11} $(\mathbf{a}_i - \mathbf{e}_{o,t})$, $\mathbf{r}_{io,s} \equiv \mathbf{e}_{o,s} - \mathbf{b}_i$, and $\mathbf{r}_{io,t} \equiv \mathbf{e}_{o,t} - \mathbf{b}_i$ completely define the interference region on $\mathcal{P}_{io}$. Thus, we can define the set $\mathcal{E}_{io}$ of the interference locus on plane $\mathcal{P}_{io}$ as

$$\begin{aligned}\mathcal{E}_{io} = \{\mathbf{p} \in \mathbb{R}^3 | \mathbf{p} = \mathbf{a}_i - \mathbf{b}_i + \epsilon_s(\mathbf{e}_{o,s} - \mathbf{b}_i) + \epsilon_t(\mathbf{e}_{o,t} - \mathbf{b}_i),\ \epsilon_s, \epsilon_t \leq 0,\\ \epsilon_s + \epsilon_t \leq -1\},\end{aligned} \tag{3.71}$$

where $i = 1, \ldots, m$, $o = 1, \ldots, f$, and ϵ_s and ϵ_t are dimensionless coefficients.

Moreover, similarly to Eq. (3.46), we can rewrite the previous equation in a more compact

manner such as

$$\mathcal{E}_{io} = \{\mathbf{p} \in \mathbb{R}^3 | \mathbf{p} = \mathbf{a}_i - \mathbf{b}_i + \mathbf{\Lambda}_{io}\boldsymbol{\lambda}, \boldsymbol{\lambda} \leq \mathbf{0}_2, \lambda_1 + \lambda_2 \leq -1\}, \tag{3.72}$$

where

$$\mathbf{\Lambda}_{io} = \begin{bmatrix} (\mathbf{e}_{o,s} - \mathbf{b}_i) & (\mathbf{e}_{o,t} - \mathbf{b}_i) \end{bmatrix} \quad \text{and} \quad \boldsymbol{\lambda} = \begin{bmatrix} \lambda_1 & \lambda_2 \end{bmatrix}^T = \begin{bmatrix} \epsilon_s & \epsilon_t \end{bmatrix}^T. \tag{3.73}$$

3.3.3 Proposed Algorithm for Interference Detection

In this sub-section, we summarize the theory of Sub-section 3.3.2 in two algorithms for the computation of the interference regions of a m-cable constant-orientation CDPM whose end effector has f edges. First, the algorithm related to the detection of the interference region between two cables is presented. The input data are vectors $\mathbf{a}_i$, $\mathbf{b}_i$, $i = 1, \ldots, m$, and a box $\mathcal{W}$ representing the considered workspace.

Compute all cable-cable interference regions $\mathcal{C}_{ij}$:

for $i = 1, \ldots, m$
for $j = i + 1, \ldots, m$

1. Compute the equation of plane $\mathcal{P}_{ij}$ (Eq. (3.5)):

$$\begin{aligned} \mathbf{a}_{ij} &= \mathbf{a}_j - \mathbf{a}_i, \\ \mathbf{b}_{ij} &= \mathbf{b}_j - \mathbf{b}_i, \\ \mathbf{n}_{ij} &= \mathbf{a}_{ij} \times \mathbf{b}_{ij}. \end{aligned}$$

2. Compute the coordinates of D_{ij}^+ and D_{ij}^-:

$$\begin{aligned} \mathbf{d}_{ij}^+ &= \mathbf{a}_j - \mathbf{b}_i, \\ \mathbf{d}_{ij}^- &= \mathbf{a}_i - \mathbf{b}_j. \end{aligned}$$

3. Compute the four intersection points of the boundaries of $\mathcal{C}_{ij}^+$ (Eq. (3.44)) and $\mathcal{C}_{ij}^-$ (Eq. (3.45)), with the faces of box $\mathcal{W}$.

   if the two points associated to $\mathcal{C}_{ij}^+$ are identical then

   a) $\mathcal{C}_{ij}^+$ and $\mathcal{C}_{ij}^-$ degenerate into two rays, and $\mathcal{C}_{ij}^+ \bigcap \mathcal{W}$ and $\mathcal{C}_{ij}^- \bigcap \mathcal{W}$ are two line segments.

   else

a) Compute all the intersection points between plane $\mathcal{P}_{ij}$ and the edges of box $\mathcal{W}$.

b) Keep only the intersection points belonging to $\mathcal{C}_{ij}^{+}$[3].

c) The remaining points and D_{ij}^{+} computed in step 2 are the vertices of the polygon $\mathcal{C}_{ij}^{+} \bigcap \mathcal{W}$.

d) Repeat steps (b) and (c) for $\mathcal{C}_{ij}^{-}$.

end

end
end

The set of all interferences between two cables of the CDPM in the considered workspace is

$$\mathcal{C} \bigcap \mathcal{W} = \bigcup_{\substack{i=1 \\ j=i+1}}^{m} \left(\mathcal{C}_{ij} \bigcap \mathcal{W} \right).$$

The algorithm used to determine the interference regions between cables and edges of the end effector of a constant-orientation CDPM is outlined below. The required data are $\mathbf{a}_i$, $\mathbf{b}_i$, $i = 1, \ldots, m$, $\mathbf{e}_{o,s}$, $\mathbf{e}_{o,t}$, $o = 1, \ldots, f$, and $\mathcal{W}$, the prescribed workspace.

Compute all cable-edge interference regions $\mathcal{E}_{io}$:

for $i = 1, \ldots, m$
for $o = 1, \ldots, f$

1. Compute the equation of plane $\mathcal{P}_{io}$ (Eq. (3.5)):

$$\mathbf{r}_{io,s} = \mathbf{e}_{o,s} - \mathbf{b}_i,$$
$$\mathbf{r}_{io,t} = \mathbf{e}_{o,t} - \mathbf{b}_i,$$
$$\mathbf{n}_{io} = \mathbf{r}_{io,s} \times \mathbf{r}_{io,t}.$$

2. Compute the coordinates of D_{io}^{10}, D_{io}^{11} and D_{oo}:

$$\mathbf{d}_{io}^{10} = \mathbf{a}_i - \mathbf{e}_{o,s},$$
$$\mathbf{d}_{io}^{11} = \mathbf{a}_i - \mathbf{e}_{o,t},$$
$$\mathbf{d}_{oo} = \mathbf{a}_i - \mathbf{b}_i.$$

[3]The *inpolygon* function may be used for this purpose in MATLAB®

3. Compute the two intersection points of the boundaries $\mathcal{E}_{io}$ (Eq. (3.72)) with the faces of box $\mathcal{W}$.

   if point B_i lies on the edge $\mathbf{e}_o$ then

   a) $\mathcal{E}_{io}$ degenerates into a ray, and the interference region is a line segment in $\mathcal{W}$.

   else

   a) Compute all the intersection points between plane $\mathcal{P}_{io}$ and the edges of box $\mathcal{W}$.

   b) Keep only the intersection points belonging to $\mathcal{E}_{io}$[4].

   c) The remaining points and D_{io}^{10} and D_{io}^{11} computed in step 2 are the vertices of the polygon $\mathcal{E}_{io} \bigcap \mathcal{W}$.

   end

end
end

The set of all interferences between a cable and an end-effector edge of the CDPM in the considered workspace is

$$\mathcal{E} \bigcap \mathcal{W} = \bigcup_{i=1}^{m} \left(\bigcup_{o=1}^{f} \left(\mathcal{E}_{io} \bigcap \mathcal{W} \right) \right).$$

The two previous algorithms are easily implemented in scientific software such as MATLAB®. It is possible to obtain, in a very short computation time, the set of interference loci $\mathcal{I} \bigcap \mathcal{W} \equiv (\mathcal{C} \bigcap \mathcal{W}) \bigcup (\mathcal{E} \bigcap \mathcal{W})$ over the prescribed constant-orientation workspace of a given CDPM.

3.3.4 Validation of the Methodology

This sub-section shows two results obtained from the use of the algorithms described in Subsection 3.3.3. First, it presents an example of application for a six-degree-of-freedom CDPM having six cables and six end-effector edges. Then it compares experimental and theoretical data associated to a mechanical interference between two given cables of an eight-cable 31-edge six-DoF CDPM.

[4]The *inpolygon* function may be used for this purpose in MATLAB®

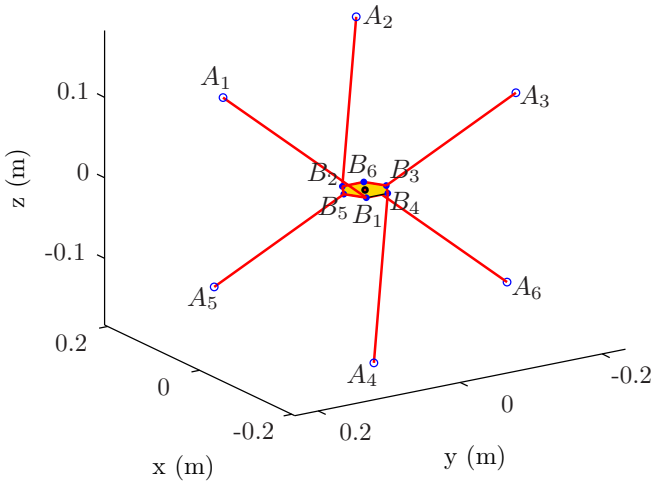

Figure 3.20 – Architecture of a generic six-cable six-edge six-DoF CDPM.

Table 3.1 – Geometric parameters $\mathbf{a}_i$ and $\mathbf{b}_i^{\mathcal{B}}$ of the architecture presented in Fig. 3.20.

	$\mathbf{a}_1$	$\mathbf{a}_2$	$\mathbf{a}_3$	$\mathbf{a}_4$	$\mathbf{a}_5$	$\mathbf{a}_6$
x (m)	0.0000	0.1732	−0.1732	−0.1732	0.1732	0.0000
y (m)	0.2000	−0.1000	−0.1000	0.1000	0.1000	−0.2000
z (m)	0.1500	0.1500	0.1500	−0.1500	−0.1500	−0.1500
	$\mathbf{b}_1^{\mathcal{B}}$	$\mathbf{b}_2^{\mathcal{B}}$	$\mathbf{b}_3^{\mathcal{B}}$	$\mathbf{b}_4^{\mathcal{B}}$	$\mathbf{b}_5^{\mathcal{B}}$	$\mathbf{b}_6^{\mathcal{B}}$
$x^{\mathcal{B}}$ (m)	−0.0260	0.0260	0.0000	−0.0260	0.0000	0.0260
$y^{\mathcal{B}}$ (m)	0.0150	0.0150	−0.0300	−0.0150	0.0300	−0.0150
$z^{\mathcal{B}}$ (m)	0.0000	0.0000	0.0000	0.0000	0.0000	0.0000

Numerical Results: a Six-Cable Six-Edge Six-DoF Cable-Driven Parallel Mechanism

The first case-study is that of a six-cable, six-edge, six-degree-of-freedom CDPM whose geometry is shown on Fig. 3.20. Table 3.1 shows the geometric parameters $\mathbf{a}_i$ and $\mathbf{b}_i^{\mathcal{B}}$ of this architecture, i.e., the position of the cable attachment points on the base and on the end effector, respectively. This architecture is taken from ref. [187], where its interference regions were traced as line segments over a slice of its constant-orientation workspace. It should be also noted here that this spatial CDPM is not fully constrained by its cables since $m \ngeq n+1$. However, it may serve as a simple example for the application of the algorithms described in Sub-section 3.3.3.

Here, we trace these mechanical interference surfaces directly in the constant-orientation workspace by the computing algorithms presented above. Indeed, Fig. 3.21 shows the interference loci for all possible combinations of cables and of a cable with an edge of the end effector over the prescribed workspace, i.e., the set $\mathcal{I} \bigcap \mathcal{W}$. Notice that the shape of the end

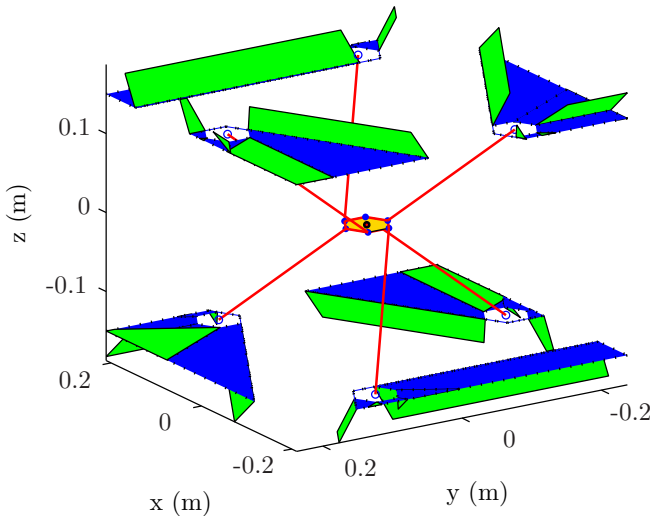

Figure 3.21 – Cable-cable and cable-edge interference regions for a generic CDPM with reference orientation $\{\theta_z = 0\,^\circ\,,\, \theta_{y^{\mathrm{I}}} = 0\,^\circ\,,\, \theta_{x^{\mathrm{II}}} = 0\,^\circ\,\}$.

effector is a regular hexagon with zero thickness. The chosen orientation corresponds to the reference one, i.e, $\{\theta_z = 0\,^\circ\,,\, \theta_{y^{\mathrm{I}}} = 0\,^\circ\,,\, \theta_{x^{\mathrm{II}}} = 0\,^\circ\,\}$ in a ZYX Euler angles convention. The result contains the interference regions between cables (the green regions, which appear in light gray in black and white) and between a cable and an edge (the blue regions, which appear in dark gray in black and white). Interestingly, the geometry of the moving platform of the CDPM appears in the results of the detection of cable-edge interferences. This is only natural, since vectors $\mathbf{e}_o$, $\mathbf{r}_{io,s}$ and $\mathbf{r}_{io,t}$ directly come from the geometry of the end effector.

It is worth noting that the computation time is less than 0.4 s for each algorithm: ≈ 0.38 s for all cable-cable interferences and ≈ 0.19 s for all cable-edge ones. These algorithms were implemented in MATLAB® 7.6.0 on a PC equipped with an Intel® Core™ 2 CPU 6400 running at 2.13 GHz. In fact, the symbolic representations of the interference regions reported in this paper are so simple that, the quasi-total of the computation time is dedicated to the intersection points between each interference plane and the edges of the prescribed workspace $\mathcal{W}$ (see step 3 in Sub-section 3.3.3).

Additional results are presented in Fig. 3.22, which displays the evolution of the mechanical interference regions in the workspace of this six-cable six-edge six-DoF CDPM for nine different attitudes of its end effector. We observe a strong inter-relation between end-effector orientation and the resulting interference regions. These results prove useful when one is comparing different CDPM architectures for a prescribed range of orientations and for a specific application. It allows the quick determination and visualization of all possible mechanical interferences.

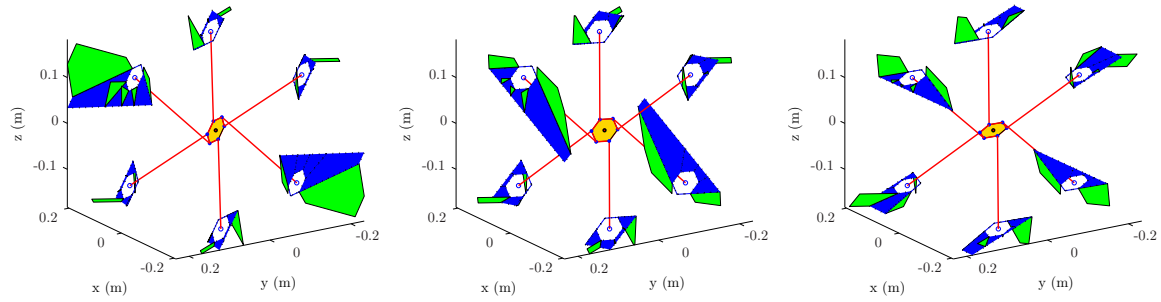

(a) $\{-45^\circ, -45^\circ, -45^\circ\}$ (b) $\{-45^\circ, -45^\circ, -15^\circ\}$ (c) $\{-45^\circ, -15^\circ, -15^\circ\}$

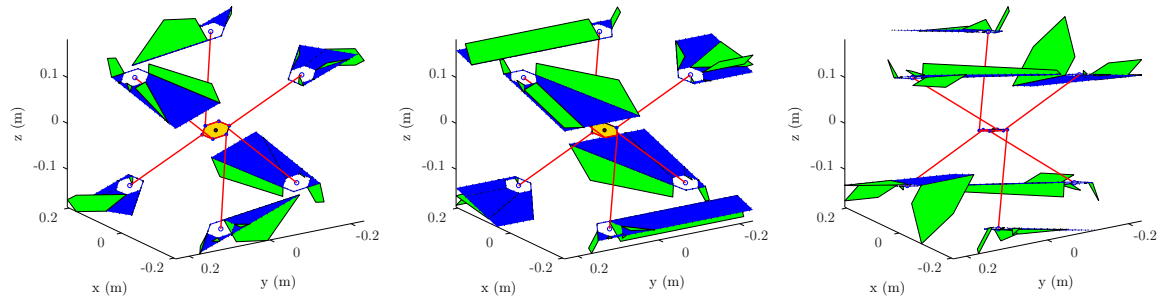

(d) $\{-15^\circ, -15^\circ, -15^\circ\}$ (e) $\{0^\circ, -15^\circ, 0^\circ\}$ (f) $\{15^\circ, 15^\circ, 15^\circ\}$

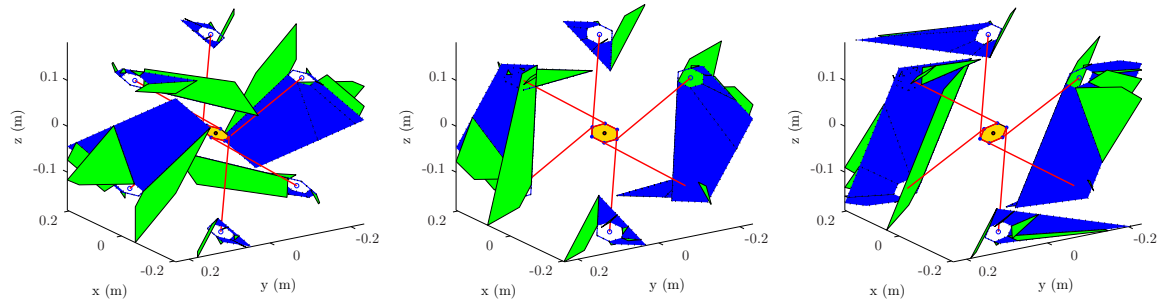

(g) $\{15^\circ, 15^\circ, 45^\circ\}$ (h) $\{15^\circ, 45^\circ, 45^\circ\}$ (i) $\{45^\circ, 45^\circ, 45^\circ\}$

Figure 3.22 – Mechanical interference regions for nine chosen attitudes $\{\theta_z,\ \theta_{y^{\mathrm{I}}},\ \theta_{x^{\mathrm{II}}}\}$ of the end effector.

Experimental Verification: an Eight-Cable 31-Edge Six-DoF Cable-Driven Parallel Mechanism

With the aim of comparing the theoretical results against experimental ones, a second example is included. For this test, we measured the end-effector pose of a prototype CDPM called NELI (network-enabled locomotion interface), which has been built at the Laval University Robotics Laboratory (see Refs. [99, 101, 102, 103, 104] and Fig. 3.23). Since this system was originally designed to avoid mechanical interferences within its workspace, we had to alter its geometry in order to produce a collision between cables 2 and 6 (the position of the attachment point A_6 along the Z axis has been moved from 0.733 to 1.155 metres), shown on Fig. 3.24. The geometric parameters $\mathbf{a}_i$ and $\mathbf{b}_i^{\mathcal{B}}$ of this modified architecture are given in Tab. 3.2. Notice that a similar method, i.e., alteration of the initial geometry, has been used

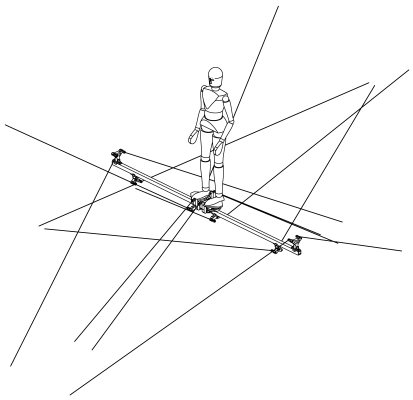

(a) Conceptual design of NELI

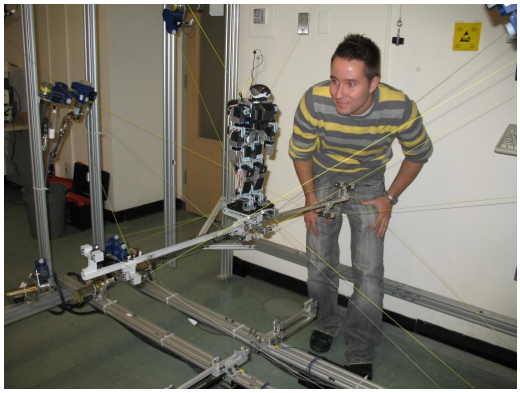

(b) Prototype built at the Laval University Robotics Laboratory

Figure 3.23 – Mechanical architecture of an eight-cable 31-edge six-DoF CDPM (NELI project).

Table 3.2 – Geometric parameters $\mathbf{a}_i$ and $\mathbf{b}_i^{\mathcal{B}}$ of the modified CDPM NELI.

	$\mathbf{a}_1$	$\mathbf{a}_2$	$\mathbf{a}_3$	$\mathbf{a}_4$	$\mathbf{a}_5$	$\mathbf{a}_6$	$\mathbf{a}_7$	$\mathbf{a}_8$
x (m)	−0.823	0.804	0.742	−0.740	−0.956	0.964	1.005	−1.004
y (m)	−0.387	−0.390	−0.031	−0.038	−0.026	−0.023	−0.184	−0.177
z (m)	1.020	1.016	0.124	0.127	0.733	1.155	0.055	0.058
	$\mathbf{b}_1^{\mathcal{B}}$	$\mathbf{b}_2^{\mathcal{B}}$	$\mathbf{b}_3^{\mathcal{B}}$	$\mathbf{b}_4^{\mathcal{B}}$	$\mathbf{b}_5^{\mathcal{B}}$	$\mathbf{b}_6^{\mathcal{B}}$	$\mathbf{b}_7^{\mathcal{B}}$	$\mathbf{b}_8^{\mathcal{B}}$
$x^{\mathcal{B}}$ (m)	−0.031	0.031	0.067	−0.067	−0.017	0.017	0.024	−0.024
$y^{\mathcal{B}}$ (m)	−0.050	−0.050	0.013	0.013	−0.399	−0.399	−0.513	−0.513
$z^{\mathcal{B}}$ (m)	−0.024	−0.024	0.046	0.046	−0.042	−0.042	0.056	0.056

in [103] to analyze the same interference along a specific end-effector trajectory. On Fig. 3.24, one should note that the position of the mechanical interference between cable 2 and cable 6 is highlighted by white circles while the CDPM's end-effector is moving on the interference plane $\mathcal{P}_{26}$ inside its workspace with a constant orientation.

In the actual case-study, the end effector of the CDPM was translated, by hand, twelve times along a rectangular trajectory over which the two cables remained in contact, its orientation being constrained by the servo-actuated cables. Because the errors on the positions of the fixed spools limit the accuracy of the estimates of the end-effector pose, an additional displacement sensor was used. The orientation measurements of this sensor were used to compensate for the errors on the end-effector attitude estimates computed from the encoder signals. The displacement sensor in question is a Flock of Birds™, manufactured by Ascension Technology Corp. [263]. We have compensated the end-effector attitude estimates by a mean orientation of $\{\theta_z = 0.96\,^\circ\,,\ \theta_{y^{\mathrm{I}}} = -5.75\,^\circ\,,\ \theta_{x^{\mathrm{II}}} = 4.61\,^\circ\,\}$.

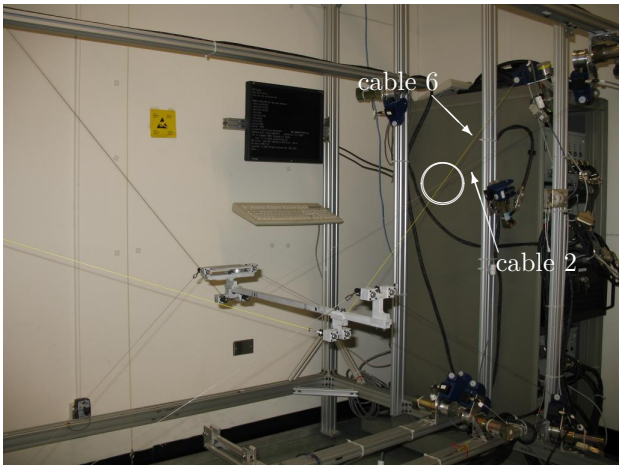

(a)

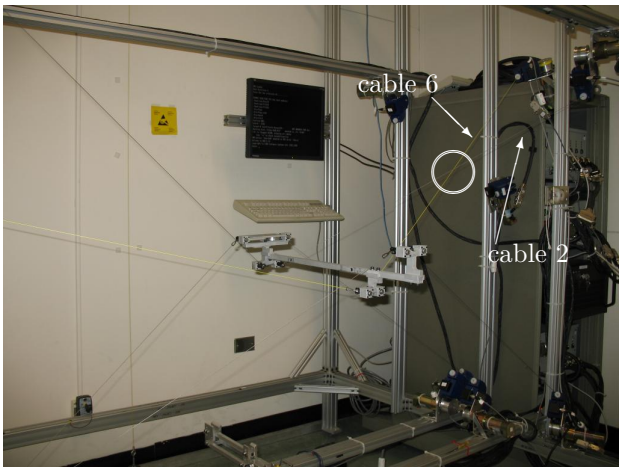

(b)

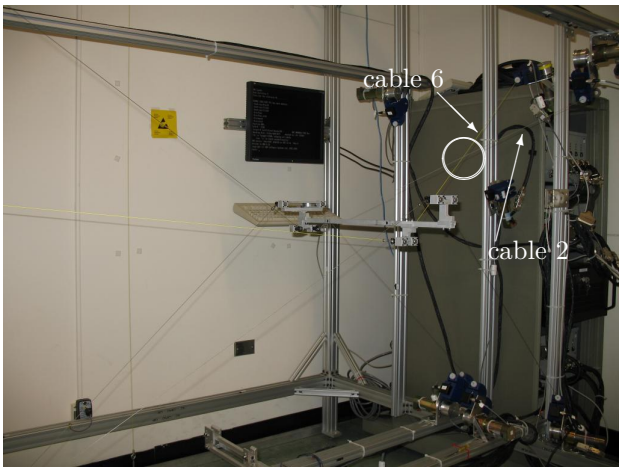

(c)

Figure 3.24 – Photographs of the experimental setup (mechanical interferences between cable 2 and cable 6).

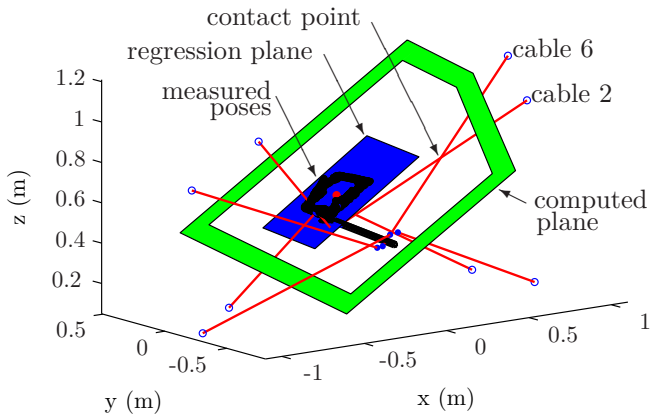

Figure 3.25 – Comparison of experimental measures and theoretical results.

As the end effector was moved over the chosen interference region, 3 891 sets of actuated-joint encoder measurements were acquired. The forward kinematics problem was solved for all these sets of joint positions, which yielded the same number of end-effector poses. The end-effector orientation being kept approximately constant, the 3 891 positions of point P are traced on Fig. 3.25. Apparently, the cloud of points takes the shape of a plane. We computed the plane that fits best the cloud of points in the least-squares sense. This plane has to pass through the centroid of the cloud of points, which was computed to be $\mathbf{p}_c = \begin{bmatrix} -0.076 & -0.023 & 0.597 \end{bmatrix}^T$ m. The normal of this measured plane is $\hat{\mathbf{n}} = \begin{bmatrix} 0.510 & 0.067 & -0.857 \end{bmatrix}^T$. This experimentally determined plane is shown in blue (dark gray in black and white) on Fig. 3.25.

On the other hand, the application of the algorithm to the same pair of interfering cables yielded the plane $\mathcal{P}_{26}$ with normal vector $\mathbf{n}_{26} = \begin{bmatrix} 0.489 & 0.113 & -0.865 \end{bmatrix}^T$, and passing through point $\mathbf{a}_2 - \mathbf{b}_2 = \begin{bmatrix} 0.769 & -0.343 & 1.041 \end{bmatrix}^T$. This plane is shown in green (light gray in black and white) on Fig. 3.25, and notice that it is partially shown to facilitate the graphical representation of the other parts illustrated in this figure.

The distance between the theoretical plane and the centroid of the measured cloud of points is 7 mm. This corroborates the proposed model of cable interferences, since a 7 mm error is small when compared to the size of the CDPM ($2.0 \times 1.2 \times 1.0$ m^3). The relative angle between the normal vectors of the two planes is 3 $^\circ$. These errors are relatively small, when considering all possible sources of errors in this simple experiment, such as the errors of the positions of the attachment points of the cables on the frame and end effector, and manipulation errors when translating the end effector while maintaining a contact between cables 2 and 6. Hence, these results are thought to validate the model and its ensuing analysis.

Finally, it is interesting to also calculate the full set of interference regions of this particular CDPM, i.e., an eight-cable six-degree-of-freedom CDPM with an end effector composed of

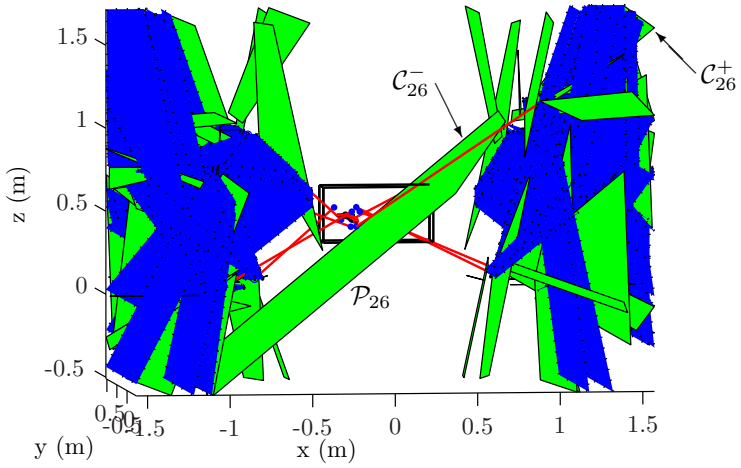

Figure 3.26 – All mechanical interference regions (cable-cable and cable-edge) for the CDPM NELI with the reference end-effector orientation $\{\theta_z = 0^\circ, \theta_{y^{\mathrm{I}}} = 0^\circ, \theta_{x^{\mathrm{II}}} = 0^\circ\}$.

31 edges. In MATLAB®, and on the same PC equipped with an Intel® Core™ 2 CPU 6400 running at 2.13 GHz, the required computation time is ≈ 0.42 s for all cable-cable interferences, and ≈ 0.76 s for all cable-edge interferences. The reference end-effector orientation $\{\theta_z = 0^\circ, \theta_{y^{\mathrm{I}}} = 0^\circ, \theta_{x^{\mathrm{II}}} = 0^\circ\}$ was used to perform this numerical experiment. This result is shown in Fig. 3.26. It is easily observed that this CDPM was originally designed to minimize the occurrence of mechanical interferences because interference regions all lie outside of the prescribed translational workspace (black wire-frame box in the middle of the figure). However, since we analyzed an altered version of this CDPM, plane $\mathcal{P}_{26}$, which supports the two interference regions ($\mathcal{C}_{26}^{-}$ and $\mathcal{C}_{26}^{+}$) corresponding to a mechanical interference between cables 2 and 6, crosses the prescribed workspace. Finally, even if the graphical representation of the full set of mechanical interference regions for this CDPM appears intricate, the designer is mostly interested in the interference-free workspace, which is easily visualized.

3.4 Summary

In this chapter, the study of mechanical interferences in cable-driven pantographs has been simplified to the study of this phenomenon in cable-driven parallel mechanisms, based on the fact that a CDP is constituted of two CDPMs. First, we defined in Section 3.1 the meaning of a *mechanical interference*, i.e., a physical collision between two entities which partially or fully blocks the movement of one or both objects. In this current work, object calls for a cable or an edge of the end-effector geometry of the studied CDPM.

Then, mechanical interferences for planar CDPMs were covered in Section 3.2. Even though, in practice, crossed cables in planar CDPMs are generally accepted by roboticists, it is important to understand the geometrical conditions for their occurrence. To this end, two examples of four-cable planar CDPMs were used in order to determine basic rules for the design of a

planar CDPM while keeping the interference regions to a minimum. These are, first, to minimize the number of cables used to constrain the end effector; Second, to minimize the number of attachment points; And third, to place the attachment points on the surface of convex shapes on the base and on the end effector.

Even if these rules can be applied to spatial CDPMs as well, it is more difficult to predict or visualize mechanical interference loci when designing a tridimensional CDPM. Hence, in Section 3.3, we pushed further the analysis of interferences between two cables and between a cable and an end-effector edge of a CDPM following the direction pointed in [187]. The work presented in this section provides an exhaustive symbolical analysis of this phenomenon, based on the assumption that a cable is a straight line segment in space. The results lead to an exact description of the interference regions inside a constant-orientation workspace of any given CDPM.

We first described, in Sub-section 3.3.1, the kinematic modelling of an arbitrary spatial CDPM. In Sub-section 3.3.2, we defined the conditions for the occurrence of a mechanical interference between two cables, i.e., the two cables must lie in the same plane $\mathcal{P}_{ij}$ and the contact point must simultaneously belong to the line segment of each cable. This analysis led to the separation of each interference plane into nine regions, of which only two fulfill all the conditions for an interference to occur between two given cables. These two regions can be quickly computed from the simple symbolical expressions found, given the geometry of a CDPM.

A similar approach was used to compute the interference regions between a cable and an end-effector edge inside the constant-orientation workspace. In this case, we obtain only one interference region in each interference plane $\mathcal{P}_{io}$.

Furthermore, two algorithms were proposed in Sub-section 3.3.3, which summarize the analysis and compute the interference regions with scientific software such as MATLAB®. The application of these algorithms was illustrated by two examples in Sub-section 3.3.4. The first one yields the set $\mathcal{I}$ of interference regions for the constant-orientation workspace of a generic six-cable six-edge six-DoF CDPM. The computation time associated with this result was less than 0.4 s on a regular PC, which is faster than the running times reported in ref. [187]. The second experiment compared theoretical results with experimental data measured from a prototype of an eight-cable 31-edge six-DoF CDPM built at the Laval University Robotics Laboratory. Since the results obtained with the two methods are very close, their comparison corroborates the proposed model of cable interferences.

The application of the proposed method in this chapter does not require a trajectory of the end effector to detect interferences: it only requires the geometry of the mechanism, the orientation of the end effector and the prescribed workspace. The resulting mathematical description of the interference regions can be used for the design of CDPMs. Moreover,

this work may be used to plan trajectories that avoid interference regions inside the CDPM workspace. Two different approaches to this objective can be considered. One is to keep a constant orientation of the end effector and, in order to move from point A to B, define an alternative trajectory avoiding interference regions. The second is to follow a straight line from point A to point B while modifying the end-effector attitude in order to free the chosen path by adjusting the mechanical interference regions along the end-effector trajectory.

It is possible to extend this work to the determination of the mechanical interference regions over ranges of end-effector orientations at the cost of an increased complexity. However, most of the tools available for the design of CDPMs assume a constant orientation of the end effector, e.g., the wrench-closure workspace (WCW) [148]. In the same line of thought, the next chapter will propose an optimization algorithm that takes advantage of the proposed constant-orientation analysis in order to synthesize spatial CDPMs, and by extension, spatial CDPs.

Chapter 4

Synthesis of Spatial Cable-Driven Pantographs

"The process of preparing programs for a digital computer is especially attractive, not only because it can be economically and scientifically rewarding, but also because it can be an aesthetic experience much like composing poetry or music."
- Donald Ervin Knuth

This chapter proposes a new algorithm to optimize the geometric parameters—dimensional synthesis—of spatial cable-driven parallel mechanisms (CDPMs) or, more specifically for the context of this thesis, simultaneously both sides of spatial cable-driven pantographs (CDPs). The main objective is to maximize the reachable workspace of the mechanism, which must be sufficient to fulfill its prescribed requirements, following three different criteria. The first criterion is based on the maximization of the wrench-closure workspace (WCW), which is known as the region where it is possible to fully constrain a set of mechanism's end-effector poses with its cables. The second criterion is to maximize the reachable workspace where no mechanical interferences can occur between any pair of cables. Then, the third one is defined by the maximization of the region where no mechanical interferences can occur between any cable and edge of the mechanism's end-effector. The proposed method is thus to find a mechanism geometry that allows the best compromise between these three criteria for a specific application, i.e., for a prescribed workspace in translation and in rotation.

First, an overview of well-known techniques available in the literature to solve different types of optimization problems is presented in Section 4.1. More specifically, Sub-section 4.1.1 enumerates general optimization techniques while Sub-section 4.1.2 discusses work where optimization techniques are applied to the synthesis of CDPMs. Then, as the main objective of this chapter, a new optimization method for the dimensional synthesis of CDPs,

and inherently CDPMs, is proposed in Section 4.2. First, the definition of the translational workspace required to apply this novel technique is given in Sub-section 4.2.1. The theory underneath each criterion of the proposed algorithm, i.e., the constant-orientation wrench-closure workspace (COWCW), the constant-orientation cable-cable interference (COCCI) and the constant-orientation cable-edge interference (COCEI), is described in Sub-sections 4.2.2, 4.2.3 and 4.2.4, respectively. The complete optimization problem is shown in Sub-section 4.2.5. In Section 4.3, for the sake of numerical validation, this technique is applied to the synthesis of two different mechanisms. It is first tested on an arbitrary seven-cable nine-edge six-DoF CDPM in Sub-section 4.3.1. Afterwards, in Sub-section 4.3.2, it is applied to the optimization of the geometric parameters of an eight-cable seventeen-edge six-DoF spatial CDP intended for a medical application. Finally, the main outcomes of this chapter are summarized in Section 4.4.

4.1 Overview of Optimization Techniques

Nowadays, when designing a system, engineers can count on the help of different computer-assisted tools available on the market in order to facilitate or refine their creations. One can easily think of mechanical design software such as Pro/ENGINEER and SolidWorks® or dynamics, symbolical and numerical analysis software programs such as Adams, Maple™ and MATLAB®, respectively. These tools, which contain embedded geometry and mathematics toolboxes, such as general optimization tools, are very helpful to accelerate the process involved in the design or the performance analyses of a wide range of systems.

But when one desires to determine the architecture of the system that best fits its specific application's requirements, particular evaluation and comparison techniques must be still defined by designers in order to make a judicious and final choice. In the same way, and similarly to what was performed in Chapter 2, i.e., for the design of the nonlinear spring-loaded reels, a rigorous selection of optimization methods combined with the elaboration of appropriate criteria is necessary when it comes to the synthesis of cable-driven pantographs or the synthesis of single cable-driven parallel mechanisms.

4.1.1 General Optimization Techniques

In the literature, the word *optimization*, as a scientific discipline, can be traced as early as to the development of the first digital computer in the $40s$ [264], named ENIAC for electronic numerical integrator and computer (see Fig. 4.1 for an archive photograph). This machine was developed primarily for the purpose of calculating optimized artillery firing tables for the armed forces [265]. Since this major step in the world of automated computation, optimization techniques have been extensively studied worldwide by research groups due to their attractive potential outcomes, i.e., the determination of the best solution—global optimum—or one of

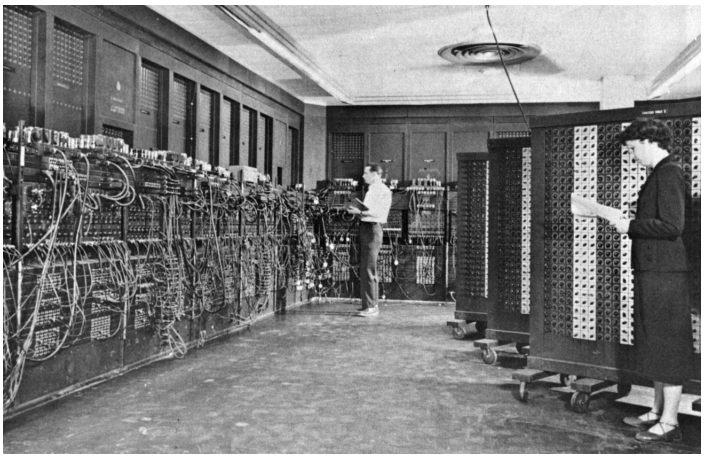

Figure 4.1 – The world's first digital computer: ENIAC.

the best solutions—local optimum—to a given problem. From linear to nonlinear problems, from unconstrained to constrained problems, in general, there is an optimization method that now exists to help solving it. Basically, we can divide the optimization discipline in two sub-groups: the *local* and the *global* optimization tools.

The *local* optimization tools are well suited for relatively simple problems, but not limited to them. As examples, we may cite convex problems [266] such as unconstrained linear functions, linear functions with linear constraints, and convex quadratic functions with linear constraints. Indeed, finding the global optimum with a local optimization tool is always guaranteed with convex problems, i.e., problems that are defined by a convex objective function, convex inequality constraints and affine equality constraints. This is because they have either only one possible solution or no solution at all. As it is illustrated in Fig. 4.2a for a simple one-dimensional function $f_\alpha(x)$, the problem of minimizing an unconstrained convex n-dimensional objective function $f_\alpha(\mathbf{x})$, $\mathbf{x} \in \mathbb{R}^n$, is generally solved without difficulty. The global minimum $\mathbf{x}^\star$ can easily be computed by conventional numerical derivative methods, from any initial solution $\mathbf{x}_0$ within the range $\Delta\mathbf{x} \equiv [\mathbf{x}_1, \mathbf{x}_2]$. When the same optimization problem is now constrained with a nonlinear convex function $f_\beta(\mathbf{x})$, such that $f_\beta(\mathbf{x}) \leq 0$, Fig. 4.2c shows that the optimum is also easily reached and that there is only one possible solution. On the other hand, if local optimization techniques are applied to an unconstrained non-convex problem as shown in Fig. 4.2b, depending on the initial guess $\mathbf{x}_0$, $\mathbf{x}_0 \in [\mathbf{x}_1, \mathbf{x}_2]$, the final solution is to be a local minimum and there is no way to verify that it is the global minimum. Finally, in the case where a local minimization is applied to a constrained non-convex problem as shown in Fig. 4.2d, again the resulting minimum is local, but there is no guarantee as to its globality.

From the literature, we can logically sub-divide the local optimization approaches in two distinct groups: those intended for *unconstrained* problems and those for *constrained* problems.

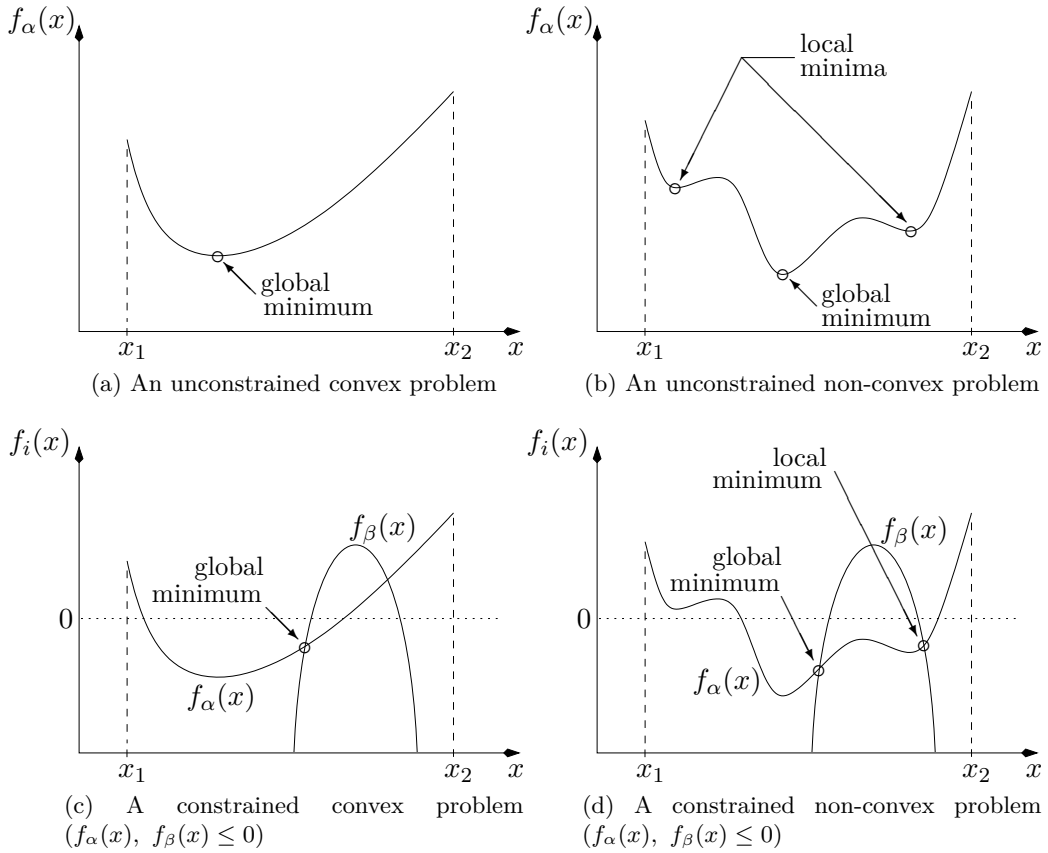

(a) An unconstrained convex problem

(b) An unconstrained non-convex problem

(c) A constrained convex problem ($f_\alpha(x),\ f_\beta(x) \leq 0$)

(d) A constrained non-convex problem ($f_\alpha(x),\ f_\beta(x) \leq 0$)

Figure 4.2 – Simple illustration of four different types of minimization problems, with arbitrary one-dimensional functions $f_i(x)$, $i = \alpha$ and β, $x \in [x_1, x_2]$, and their associated minima.

For the unconstrained problems, among all of the local optimization techniques, *Newton's method* is considered one of the most powerful algorithms for solving them [267]. It relies on the approximation of the solution by computing the second-order Taylor expansion in order to find the stationary point of a function $f(\mathbf{x})$, i.e., $\partial f(\mathbf{x})/\partial \mathbf{x} = \mathbf{0}_n$, where $\mathbf{x} \in \mathbb{R}^n$. An initial solution $\mathbf{x}_0$ is required to initialize this iterative method. Also, one should note that the Newton's method can be used to solve unconstrained linear problems and, in this particular case, the approximation of the solution is computed by using the first-order Taylor expansion only. A second algorithm is the *Gradient method* [264], also known as *Steepest-Descent method*. This technique is considered as a basic method for unconstrained optimizations and it is governed by the direction of the negative of the first-order derivative of the function $f(\mathbf{x})$. This approach is suitable for functions with undefined second-order derivative, i.e., to which Newton's method is inapplicable. If one uses the Gradient method instead of Newton's method for a nonlinear problem for which the second derivative $\partial^2 f(\mathbf{x})/\partial \mathbf{x}^2$ exists, an optimum will still be reached, but often at a slower pace.

Regarding local optimization algorithms for *constrained* problems, the *simplex methods* family

is one of the first technique that takes into account linear inequalities [268, 269]. In fact, this method relies on the finding of a series of basic solutions toward an optimal basic solution and is one of the most efficient algorithms to solve linear programming problems [264]. Geometrically, the method consists in following the boundary of the set of feasible solutions, a polyhedron where each vertex is a potential solutions. The optimum is reached when both the feasibilities of the primal and the dual problems[1] are verified. A second family of algorithms for constrained problems is that of *interior-point methods* [270]. These methods are normally applied to linear and convex nonlinear problems but some varieties are suitable to solve non-convex nonlinear problems as well [271]. Basically, the interior-point methods seek to approach the optimal solution through a sequence of points, as do the simplex methods. The difference, however, is that instead of following the edges of the set of feasible solutions, this technique reaches an optimal solution by traversing the interior of the feasible set. In general, this decreases the computation time required to reach an optimum. Another family of algorithms is that of *sequential quadratic programming (SQP) methods* [272]. As stated in [264], this approach can be viewed as a generalization for constrained optimization of Newton's methods for unconstrained optimization in that it finds a step away from the current point by minimizing a quadratic model of the problem. The basic idea of SQP methods is to model the nonlinear optimization problem at a given point as a quadratic programming sub-problem, and then to use the solution to this sub-problem as a better estimate of the optimum. This process is iterated to create a sequence of approximations that, it is hoped, converges to the global optimum of the original problem [273]. The SQP is often reported as the most successful method for solving nonlinearly constrained optimization problems.

On the other hand, *global* optimization techniques can also be separated in two different subdivisions: those leading to a *guaranteed* optimum, also known as *exact* techniques, and those leading to a *non-guaranteed* optimum, known as *heuristic* techniques. In general, the use of global optimization tools is restricted to cases where the use of local optimization tools is not sufficient to result with the global minimum. This is the case with non-convex optimization problems (unconstrained or constrained) as illustrated with Figs. 4.2b and 4.2d. Finding the global optimum with non-convex problems is not an easy task, since the result highly depends on the choice of the initial guess $\mathbf{x}_0$. When a minimization problem is defined by a non-convex n-dimensional function $f(\mathbf{x})$, $\mathbf{x} \in \mathbb{R}^n$, the global optimum $\mathbf{x}^\star$ is not guaranteed with conventional local optimization tools. In most cases, a local optimum different from the global optimum for the given range $\Delta\mathbf{x} \equiv [\mathbf{x}_1, \mathbf{x}_2]$ is to be obtained. Moreover, optimization algorithms that aim at approaching the global optimum are, in general, computationally

[1] In summary, the primal of a linear problem can be seen as the original problem and the dual problem its alternative, i.e., two different viewpoints to approach a given problem. For instance, if the primal problem is the minimization of an objective function $\mathbf{c}^T\mathbf{x}$, where $\mathbf{x}$ is a vector of n variables and $\mathbf{c} \in \mathbb{R}^n$, subject to m inequality constraints $\mathbf{A}\mathbf{x} \leq \mathbf{0}_m$, where $\mathbf{A} \in \mathbb{R}^{m \times n}$, its corresponding dual problem is the maximization of a null function, i.e., 0, subject to n equality constraints $\mathbf{A}^T\mathbf{y} + \mathbf{c} = \mathbf{0}_n$, where $\mathbf{y} \in \mathbb{R}^m$, and m inequality constraints $\mathbf{y} \geq \mathbf{0}_m$. In fact, the optimal solution $\mathbf{x} = \mathbf{0}_n$ is reached when the primal problem is infeasible, or alternatively, when the dual problem is feasible (see Farka's lemma [235]).

time consuming and additional attention must be directed to rigorously choose the evaluation criteria.

From the literature, available global optimization tools with *guaranteed* convergence to the global optimum are efficiently applicable, in general, to a specific group of optimization problems only, or when problems with a limited number of dimensions are involved. The *Cutting Plane methods* are among them as they provide tools for the solution of convex, concave and structured non-convex global optimization problems [274, 275]. Basically, when solving global optimization problems, cuts are used as a device to discard portions of the feasible set of solutions where it is known that no optimal solution can be found. Each cut is defined as an additional inequality constraint to the initial problem and iteration after iteration, the feasible set is refined until the global or the exact solution is obtained. Another technique that guarantees optimality of the solution is the family of *Branch and Bound methods* [276]. These global optimization techniques are suitable to find exact solutions of non-convex problems. In these methods, the feasible set of the original problem is decomposed into subsets of smaller sizes. Each subset is further partitioned until each smaller problem is either solved or proved not to yield an optimal solution of the original problem. This proof can be obtained by determining lower or upper bounds on the objective value over the subset. If the upper bound in a given subset is lower than the lower bound in another subset, then the global minimum is necessarily outside that subset. Thus, this subset can be excluded from the search. In [264], it is reported that very successful techniques designed to solve a wide variety of optimization problems, while providing a guarantee of optimality, are based on the combination of the two techniques above. These methods are known as the *Branch and Cut methods*. In addition, another variety of global optimization tools is the *Homotopy methods* [277]. These strategies have the objective of visiting all stationary points of the objective function. This search effort then leads to the list of all optima (global and local). These methods are applicable to smooth[2] global optimization problems but they can be computationally intensive. Other methods can also be found in the literature such as the *Bayesian Search algorithms* [278].

When *guaranteed*-optimum global optimization tools are not suitable for a given problem, e.g., when it contains a large number of variables and constraints or the computational time available is limited, one may want to choose a global optimization tool among the numerous *unguaranteed*-optimum global optimization techniques. Here, we cite just a few that are well known in literature. One of the well-known methods is the *Simulated Annealing techniques* [279]. Theses techniques are based on the physical analogy of cooling crystal structures that spontaneously arrive at a stable configuration characterized by—globally or locally—minimal potential energy. During the optimization process, solutions with poor objective function values, or temperature, can be allowed in order to avoid being trapped by

[2] A smooth optimization problem, in general, contains an objective function and constraint functions that have derivatives of second order, i.e., it is possible to compute their gradient and their Hessian for the full range of the problem variables.

local solutions that are close to the initial guesses. Other strategies are based on evolution theory, such as *Genetic Algorithms* [280]. Evolutionary optimization approaches heuristically mimic biological evolution models. The basic idea is to evolve a population of candidate solutions to the given problem, using operators inspired by natural genetic variations and natural selection such as reproduction, crossover and mutation between genes (variables) of evaluated candidates (solutions). Other evolutionary methods are reported in the literature such as *Scatter Search methods* and *Ant Colony Optimization methods* [264]. An additional variety of global optimization approaches is the *Multi-Start methods* [281]. As their name indicates, the main idea here is to start the optimization process from various initial solutions covering the domain as much as possible, which generally increases the probability of reaching a global optimum. There are three key elements in Multi-Start methods. The first is the *Memory*, which is used to empirically identify the factors that lead to good solutions. The second is the *Randomization*, which is the method of selection of the multi-start initial solutions, and generally varies between fully randomized guesses and completely systematic algorithms. The third element is the *Degree of Rebuild*, which indicates the elements that remain fixed from one iteration to the next. It is clear that heuristic approaches for global optimization can be used to solve or approximate the solution to any global optimization problem. While they can also rapidly become time-consuming when applied to problems containing high numbers of variables and constraints, they remain relevant when the use of exact methods is, in practice, impossible.

In this brief overview, as the reader can easily imagine, the author described only a few of all the techniques available to solve *local* and *global* optimization problems. For a more exhaustive list, the reader is referred to the books of Pardalos and Resende [264], Boyd and Vendenberghe [235], Dattorro [282] and Bertsekas [283] for convex optimization techniques and to the books of Horst *et al.* [284] and Pardalos and Romeijn [278] for non-convex optimization methods.

In the continuity of this section, the following part now focuses on the optimization techniques applied to the synthesis of CDPMs. A short overview of the literature on that specific topic is presented.

4.1.2 Optimization Techniques for the Synthesis of Cable-Driven Parallel Mechanisms

The dimensional synthesis of CDPMs only represents a tiny portion of the wide range of possible applications of the optimization techniques described above, since this relatively recent subject of interest did not receive much attention so far. Basically, it can be summarized as that of finding the best positions in the Cartesian space of the attachment points A_i and B_i of all cables of a CDPM (see Fig. 4.3 for an example with seven cables), which is to be used inside a prescribed workspace $\mathcal{W}_p$ corresponding to the intended application. The main

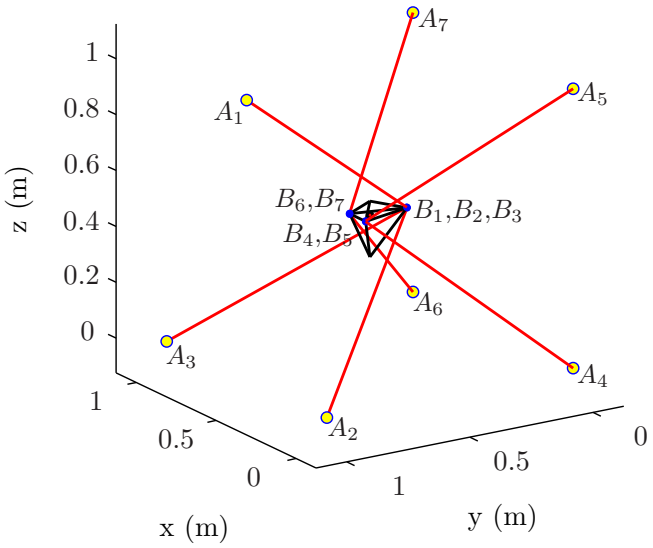

Figure 4.3 – Position of attachment points A_i and B_i, $i = 1, \ldots, 7$, of a generic seven-cable spatial CDPM.

difficulty of this problem lies in the strong nonlinearity of the equations related to CDPMs in regards to the decision variables, i.e., the coordinates of points A_i and B_i.

Even though designer intuition can lead to high-performance CDPMs (see [190] for an example of an ultra-high speed CDPM reported in the mid 90s), the use of a more systematic method to synthesize such a mechanism can reveal optimal solutions that would have been difficult to envision otherwise. Among all of the research scientists who work on CDPMs, only a few have published results on their synthesis. Here, a summary of the literature on that matter is presented, mostly based on what has been previously reported in [285, 77].

It seems that one of the first reported work on the synthesis of CDPMs comes from Tadokoro *et al.* [286]. The authors proposed to perform the CDPMs synthesis through the enumeration of a heuristically chosen set of geometries. These geometries are then filtered by considering in sequence the size of their workspaces and a set of criteria, which includes a verification of cable interferences by numerically computing the shortest distance between each pair of cables. Another publication on that matter is the work of Hay and Snyman [168]. In this paper, the dexterous workspace of a planar CDPM is defined as the intersection of all constant-orientation workspaces for a given set of rotations, while cable tensions are constrained to lie within a given range, and cable lengths are greater than a given minimum. Their main goal is to maximize the area of the dexterous workspace by finding the locations of fixed points of the manipulator along the fixed rectangular frame of the base, while the attachment points on the end effector have already been assumed. In [99, 100, 101], a numerical optimization, which combines a sequential algorithm and a genetic algorithm, was used to synthesize an eight-cable 31-edge six-DoF CDPM while ensuring wrench capabilities and avoiding mechan-

ical interferences. These mechanical interferences (cable-cable and cable-edge) were analyzed following a few given trajectories of the end-effector position and orientation. In this work, both the attachment points on the base and on the CDPM end-effector are optimized, while preserving rules of symmetry in the mechanism geometry in order to decrease the number of variables of the synthesis problem. Another group of researchers, Abdelaziz *et al.* [124, 287], has worked on the synthesis of a planar CDPM for a given wrench-feasible workspace (WFW) while minimizing the manipulator overall size. This group used zonotopes[3] to represent the wrench space of their CDPM and applied the hyperplane shifting method in order to ensure that the CDPM can generate the prescribed set of wrenches, as proposed in [146]. More recently, the dimensional synthesis of planar CDPMs was mathematically formulated using a global optimization method, i.e., the convex relaxations [173, 288]. The optimization objective was to maximize the intersection region of the constant-orientation wrench-closure workspace (COWCW) of an arbitrary planar CDPM for a given set of end-effector rotations. Afterwards, this concept was generalized by the same researchers and applied to the dimensional synthesis of spatial CDPMs in [285, 289]. In the work of Gagliardini *et al.* [290, 291], the optimal design of a CDPM devised for the maintenance of large industrial structures was proposed. This group chose the volume occupied by the CDPM as the objective function to be minimized while ensuring the wrench feasibility of the manipulator poses with respect to a given set of wrenches, avoiding interferences between cables and between the cables and an external structure, and following a prescribed accuracy, all of this for a given trajectory of the moving platform. Their synthesis aimed to determine the optimal position of the attachment points A_i on the base only, the attachment points B_i on the end-effector geometry being assumed to be fixed. The mechanical interferences are detected by numerically computing the minimal distance between two entities by means of Lumelsky's approach [253]. Finally, Gouttefarde *et al.* have recently published a paper on the geometry selection of a six-DoF cable-suspended parallel robot that is redundantly actuated and intended for heavy-load manipulation [292]. Their geometry selection process is divided in two phases: Generating and testing a large discrete number of possible CDPM geometries and then refining their best result using a gradient-based optimization. In this work, they introduced a new performance index defined as the maximum acceptable horizontal distance between the centroid of the end effector and the center of mass of the end effector and its payload, which is relevant when dealing with crane-type CDPMs where the payload can vary. Their dimensional synthesis method allows to optimize both the attachment points of the CDPM's cables on its base and on its end effector and includes a numerical collision-detection method similar to that previously proposed by Gagliardini *et al.*

Based on the literature, and to our best knowledge, among the few researchers who have tack-

[3] A zonotope is a set of points in n-dimensional space constructed from vectors $\mathbf{v}_i$ by taking the sum of $a_i\mathbf{v}_i$, where each a_i is a scalar between 0 and 1. Different choices of scalars give different points, and the zonotope is the set of all such points.

led the dimensional synthesis of CDPMs, none has combined into a single synthesis algorithm an exact geometric interference index (as presented in Section 3.3 of this thesis), which is not based on given trajectories, with a wrench workspace index, such as the wrench-closure workspace. This type of particular synthesis method is devised in this chapter, and its precise formulation is the topic of the next section.

4.2 Proposed Synthesis Method

Similar to what was performed in Chapter 3, instead of working directly on the synthesis of cable-driven pantographs, the following synthesis technique rather focuses on the optimal design of a single generic cable-driven parallel mechanism, which forms the basis of our CDP concept. Consequently, this section presents the proposed technique for the dimensional synthesis of spatial CDPMs or, similarly, for the dimensional synthesis of simultaneously both parts—the master and the slave—of spatial CDPs.

Here, the prescribed workspace in translation $\mathcal{W}_{p,t}$ of the CDPM is mapped to an ellipsoid $\mathcal{W}_e$ and the prescribed workspace in rotation $\mathcal{W}_{p,r}$ of the CDPM is discretized into q constant orientations $\mathbf{Q}_k$, $k = 1, \ldots, q$. This optimization problem is based on three different criteria. The first criterion requires that $\mathcal{W}_e$ be fully included inside the COWCW of the CDPM, for all $\mathbf{Q}_k$. The second criterion requires that $\mathcal{W}_e$ be free of mechanical interferences between any pair of cables attached to the CDPM end-effector, for all $\mathbf{Q}_k$. The third criterion requires that $\mathcal{W}_e$ be free of mechanical interferences between any combination of a cable and an edge of the CDPM's end-effector, for all $\mathbf{Q}_k$. The global objective of the optimization problem is then to maximize $\mathcal{W}_e$ in order that $\mathcal{W}_e \supset \mathcal{W}_{p,t}$, for $\mathbf{a}_i$ and $\mathbf{b}_i^{\mathcal{B}}$, $i = 1, \ldots, m$, which are the attachment points on the base and on the end effector (represented in a mobile reference frame $\mathcal{B}$ attached to the end effector), respectively, of the m cables of the CDPM.

4.2.1 Translational Workspace: An Ellipsoid

When designing a generic spatial m-cable f-edge n-DoF CDPM, in general, one must define the prescribed workspace $\mathcal{W}_p$ of the CDPM in translation and in rotation, $\mathcal{W}_{p,t}$ and $\mathcal{W}_{p,r}$, respectively, for the envisioned application. Since it is difficult to graphically represent a workspace in more than three dimensions, it is proposed to optimize the geometry of a CDPM (the position of points $\mathbf{a}_i$ and $\mathbf{b}_i^{\mathcal{B}}$ of the m cables of the CDPM) by maximizing its workspace in translation $\mathcal{W}_t$ in order to cover $\mathcal{W}_{p,t}$ for q constant orientations $\mathbf{Q}_k$, $k = 1, \ldots, q$, which cover $\mathcal{W}_{p,r}$. It should be noted that, for a spatial CDPM, $\mathbf{Q}_k$ is a 3×3 orthogonal matrix, which may be decomposed into three successive rotations $\{\theta_{x,k},\ \theta_{y^{\mathrm{I}},k},\ \theta_{z^{\mathrm{II}},k}\}$. These angles are the three components of the vector $\boldsymbol{\theta}_k \in \mathbb{R}^3$ representing the rotation of the CDPM end-effector, which here follows the Euler angles convention XYZ.

In this work, we decided to rely on the parametric equation of an ellipsoid in order to represent

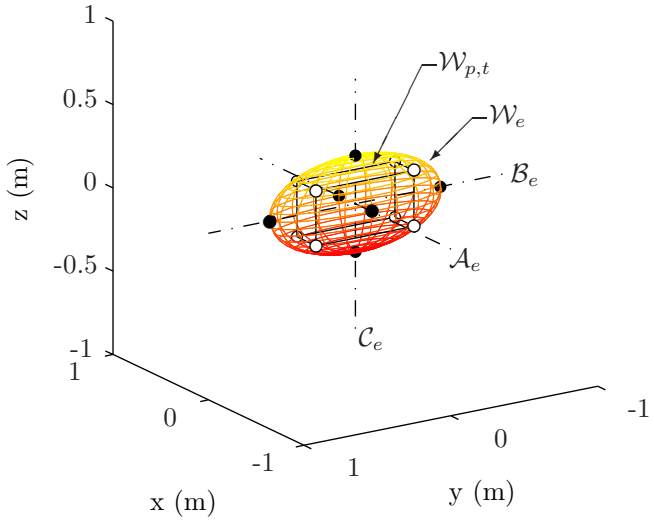

Figure 4.4 – Example of a prescribed workspace in translation $\mathcal{W}_{p,t}$ and its corresponding ellipsoid $\mathcal{W}_e$ ($\kappa = 1$).

$\mathcal{W}_{p,t}$, and, by extension, the resulting CDPM workspace in translation $\mathcal{W}_t$. In reality, this ellipsoid is to supersede the prescribed workspace, since $\mathcal{W}_{p,t}$ is often a box with $p = 8$ vertices, i.e., p points $\mathbf{p}_w = [\ x_w \quad y_w \quad z_w\ ]^T$, $w = 1, \ldots, p$. We constrain these points to lie on the surface of the ellipsoid (see Fig. 4.4, where white circles represent the eight points $\mathbf{p}_w$ lying on the surface of $\mathcal{W}_e$ and black circles represent the six intersection points between the ellipsoid's surface and its three main axes $\{\mathcal{A}_e,\ \mathcal{B}_e,\ \mathcal{C}_e\}$). Even though an ellipsoid over-estimates $\mathcal{W}_{p,t}$, this choice was made in order to minimize the number of constraints required to define the workspace in translation. With only one parametric equation, it is possible to completely define an ellipsoid, which is not true if one desires to define the six surfaces of a box.

The general equation of the surface of an ellipsoid is

$$\frac{(x - x_0)^2}{a_e^2} + \frac{(y - y_0)^2}{b_e^2} + \frac{(z - z_0)^2}{c_e^2} = 1, \tag{4.1}$$

where $\{a_e,\ b_e,\ c_e\}$ are the semi-axis parametric constants of the ellipsoid, $\{x,\ y,\ z\}$ are the coordinates of a point lying on the surface of the ellipsoid and $\{x_0,\ y_0,\ z_0\}$ are the coordinates of the reference point of the ellipsoid, i.e., its centroid.

In order to represent an ellipsoid in Cartesian space, one can express Eq. (4.1) as

$$\frac{(x - x_0)^2}{a_e^2} + \frac{(y - y_0)^2}{b_e^2} + \frac{(z - z_0)^2}{c_e^2} = \kappa^2, \tag{4.2}$$

where κ is a scaling factor, $\kappa \in [0, \infty]$. Notice that this representation only applies to ellipsoids with their principal axes aligned with the coordinate axes. This equation can also be rearranged as follows

$$\mathbf{p}^T \mathbf{\Pi} \mathbf{p} + 2\mathbf{f}^T \mathbf{p} + g = 0, \tag{4.3}$$

where

$$\mathbf{\Pi} \equiv \begin{bmatrix} 1/a_e^2 & 0 & 0 \\ 0 & 1/b_e^2 & 0 \\ 0 & 0 & 1/c_e^2 \end{bmatrix}, \tag{4.4}$$

$$\mathbf{p} \equiv \begin{bmatrix} x & y & z \end{bmatrix}^T, \tag{4.5}$$

$$\mathbf{f} \equiv -\mathbf{\Pi}\mathbf{p}_0, \tag{4.6}$$

$$g \equiv \mathbf{p}_0^T\mathbf{\Pi}\mathbf{p}_0 - \kappa^2, \tag{4.7}$$

and,

$$\mathbf{p}_0 \equiv \begin{bmatrix} x_0 & y_0 & z_0 \end{bmatrix}^T. \tag{4.8}$$

Finally, the set $\mathcal{W}_e$ of points $\mathbf{p}$ contained within an ellipsoid, for a given κ, is defined as

$$\mathcal{W}_e = \{\mathbf{p} \in \mathbb{R}^3 | \mathbf{p}^T\mathbf{\Pi}\mathbf{p} + 2\mathbf{f}^T\mathbf{p} + g \leq 0\}. \tag{4.9}$$

In order to determine the smallest ellipsoid $\mathcal{W}_e$ that contains $\mathcal{W}_{p,t}$, i.e., $\min(\mathcal{W}_e) \supset \mathcal{W}_{p,t}$, we find the value of each semi-axis parametric constant $\{a_e,\ b_e,\ c_e\}$ that defines the prescribed ellipsoid by computing the following nonlinear problem with linear equalities:

$$\begin{aligned} &\text{minimize} && \mathcal{W}_e = \frac{4\pi}{3}(v_1 v_2 v_3)^{-1/2}, \\ &\text{subject to} && \mathbf{\Upsilon}\boldsymbol{\upsilon} = \mathbf{1}_p, \\ &\text{for} && \boldsymbol{\upsilon} \equiv \begin{bmatrix} v_1 & v_2 & v_3 \end{bmatrix}^T = \begin{bmatrix} 1/a_e^2 & 1/b_e^2 & 1/c_e^2 \end{bmatrix}^T, \end{aligned} \tag{4.10}$$

where

$$\mathbf{\Upsilon} \equiv \begin{bmatrix} (x_1 - x_0)^2 & \cdots & (x_w - x_0)^2 & \cdots & (x_p - x_0)^2 \\ (y_1 - y_0)^2 & \cdots & (y_w - y_0)^2 & \cdots & (y_p - y_0)^2 \\ (z_1 - z_0)^2 & \cdots & (z_w - z_0)^2 & \cdots & (z_p - z_0)^2 \end{bmatrix}^T. \tag{4.11}$$

This problem aims at minimizing the volume of the target ellipsoid that matches the set of p points $\mathbf{p}_w$ (in general, $p = 8$) defined from $\mathcal{W}_{p,t}$. The solution provides the value of parametric constants $\{a_e,\ b_e,\ c_e\}$ that allow vertices of $\mathcal{W}_{p,t}$ to lie on the ellipsoid surface when $\kappa = 1$.

Once the parametric constants of $\mathcal{W}_e$ are determined, in general, for a given CDPM, i.e., for constant $\mathbf{a}_i$ and $\mathbf{b}_i^{\mathcal{B}}$, if $\kappa \geq 1$, we can assume that the resulting n-DoF CDPM workspace $\mathcal{W}$ includes the prescribed n-DoF workspace $\mathcal{W}_p$, at least for every evaluated CDPM attitude $\mathbf{Q}_k$. Also, it is interesting to note that if $\mathcal{W}_{p,t}$ can be represented by a cube, the resulting workspace $\mathcal{W}_e$ is a sphere, i.e., $a_e = b_e = c_e$.

The main optimization problem, as previously said, is based on three embedded optimization sub-problems. Each of these problems is described in the following sub-sections.

4.2.2 First Criterion: Constant-Orientation Wrench-Closure Workspace

Our first criterion for the synthesis of spatial m-cable f-edge n-DoF CDPMs is the size of its constant-orientation wrench-closure workspace (COWCW). This property is important, as it allows to verify whether a given CDPM can hold all positions of $\mathcal{W}_{p,t}$ for a particular attitude $\mathbf{Q}_k$ of its end effector. The merit of using the COWCW over the other similar criteria is its simplicity of implementation within an optimization programming, since it involves a relatively low number of constraints[4]. Then, if a CDPM can hold every positions of its $\mathcal{W}_{p,t}$ for every end-effector's orientations of its $\mathcal{W}_{p,r}$, we may call this workspace its wrench-closure workspace (WCW).

Thus, from [148], an end-effector's pose of a m-cable n-DoF CDPM ($m \geq n+1$) belongs to the COWCW if and only if

$$\text{rank}(\mathbf{W}) = n, \tag{4.12}$$

and

$$\exists \mathbf{t} \in \ker(\mathbf{W}) | \mathbf{t} > \mathbf{0}_m, \tag{4.13}$$

where $\mathbf{W}$ is the pose-dependent matrix—or the Jacobian matrix—of the CDPM and $\mathbf{t}$ is the vector containing the magnitude of the tension in its m cables.

For a more practical definition, we can express Eq. (4.13) as the condition for the CDPM to be in static equilibrium:

$$\exists \mathbf{t} \geq \mathbf{0}_m | \mathbf{W}\mathbf{t} = \mathbf{0}_n, \mathbf{1}_m^T \mathbf{t} = 1. \tag{4.14}$$

This linear problem[5], which is convex, means that, for a given $\mathbf{t} \geq \mathbf{0}_m$, there must be always a cable that can pull in the opposite direction of the resulting force and wrench generated by the $m-1$ other cables of the CDPM. In such case, the end-effector's pose is fully constrained and it is inside the COWCW. Moreover, in order to avoid the trivial solution $\mathbf{t} = \mathbf{0}_m$, the linear constraint $\mathbf{1}_m^T \mathbf{t} = 1$ is added, so that the sum of the m cable tensions must always be 1. Consequently, we restrict the solution of the i^{th} cable tension to be anywhere between 0 and 1, i.e., $t_i \in [0,1]$, but the solution $\mathbf{t} = \mathbf{0}_m$ does not satisfy the set of constraints.

In this work, and as explained above, we choose to evaluate the COWCW of a CDPM q times, i.e., for each chosen end-effector attitude $\mathbf{Q}_k$ that spans $\mathcal{W}_{p,r}$. This choice is directly related to the matrix $\mathbf{W}$, since it is a function of $\mathbf{Q}_k$. In fact, for the need of our optimization problem, instead of using the matrix $\mathbf{W}$ as defined in Eq. (A.32) of Appendix A.2, we rather use its simplified version, i.e., $\mathbf{W}_k^{\diamond} = -\mathbf{J}_k^T$ (noted here with the index k because $\mathbf{W}$ must be

[4] It should be noted that another suitable measure could have been its constant-orientation wrench-feasible workspace (COWFW), if the intended application of the mechanism is known and a set of prescribed wrenches can be defined. In this case, however, additional constraints would be necessary to the current synthesis problem. In this research, for the sake of simplicity, the COWCW is preferred over the COWFW.

[5] For the sake of completeness, the dual of the problem of Eq. (4.14) is derived in Appendix B.1, since this alternative has been previously explored in preliminary attempts to design the synthesis problem.

computed for each $\mathbf{Q}_k$). Consequently, we define the i^{th} column of this new matrix as follows

$$\mathbf{w}_{k,i}^{\diamond} = \begin{bmatrix} \mathbf{a}_i - \mathbf{p} - \mathbf{Q}_k \mathbf{b}_i^{\mathcal{B}} \\ \mathbf{Q}_k \mathbf{b}_i^{\mathcal{B}} \times (\mathbf{a}_i - \mathbf{p} - \mathbf{Q}_k \mathbf{b}_i^{\mathcal{B}}) \end{bmatrix}, \; i = 1, \ldots, m, \tag{4.15}$$

and then

$$\mathbf{W}_k^{\diamond} = \begin{bmatrix} \mathbf{w}_{k,1}^{\diamond} & \cdots & \mathbf{w}_{k,i}^{\diamond} & \cdots & \mathbf{w}_{k,m}^{\diamond} \end{bmatrix} = \begin{bmatrix} \mathbf{A} - \mathbf{p}\mathbf{1}_m^T - \mathbf{Q}_k \mathbf{B} \\ \mathbf{E}_k + \mathbf{P}\mathbf{Q}_k \mathbf{B} \end{bmatrix}, \tag{4.16}$$

where

$$\mathbf{A} \equiv \begin{bmatrix} \mathbf{a}_1 & \cdots & \mathbf{a}_i & \cdots & \mathbf{a}_m \end{bmatrix}, \tag{4.17}$$

$$\mathbf{B} \equiv \begin{bmatrix} \mathbf{b}_1^{\mathcal{B}} & \cdots & \mathbf{b}_i^{\mathcal{B}} & \cdots & \mathbf{b}_m^{\mathcal{B}} \end{bmatrix}, \tag{4.18}$$

$$\mathbf{P} \equiv \text{cpm}(\mathbf{p}), \tag{4.19}$$

$$\mathbf{E}_k \equiv \begin{bmatrix} (\mathbf{Q}_k \mathbf{b}_1^{\mathcal{B}}) \times \mathbf{a}_1 & \cdots & (\mathbf{Q}_k \mathbf{b}_i^{\mathcal{B}}) \times \mathbf{a}_i & \cdots & (\mathbf{Q}_k \mathbf{b}_m^{\mathcal{B}}) \times \mathbf{a}_m \end{bmatrix}. \tag{4.20}$$

This simplification is possible since the exact values of the cable tensions are not required to determine whether the wrench-closure condition is satisfied. Indeed, matrices $\mathbf{W}_k^{\diamond}$ and $\mathbf{W}_k$ are related by a post-multiplication with a positive-definite diagonal matrix. Hence their nullspaces have the same number of dimensions, and the components of the vectors share the same signs. For the purpose of our synthesis problem, this simple trick leads to the exact same result and allows to decrease the computation time corresponding to this part of the algorithm. It should be noted that this mathematical shortcut would not have been directly applicable if the constant-orientation wrench-feasible workspace (COWFW) method was used instead of the COWCW, because cable tensions must belong to a prescribed range $t_i \in [t_{\min}, t_{\max}]$ with COWFW and consequently the computation of the Jacobian $\mathbf{W}_k$ would have been, in general, mandatory to determine the exact cable tensions.

Furthermore, as explained in Sub-section 4.2.1, we approximated the prescribed workspace $\mathcal{W}_{p,t}$ of the CDPM with an ellipsoid $\mathcal{W}_e$ with $\kappa = 1$. So we need to determine the ellipsoid that is fully included within its COWCW for the q given $\mathbf{Q}_k$. One possible way consists in selecting a set of nb points $\mathbf{p}_{\epsilon,0}$, $\epsilon = 1, \ldots, nb$, that belong to the surface of $\mathcal{W}_e$ when $\kappa = 1$ and assess their corresponding points $\mathbf{p}_\epsilon$ for $\kappa \in [0, \infty]$ (note that, here, $\mathbf{p}_\epsilon \equiv \mathbf{p}$ in Eq. (4.16)). The relation for $\mathbf{p}_\epsilon$ is expressed as follows

$$\mathbf{p}_\epsilon = \mathbf{p}_0 + \kappa(\mathbf{p}_{\epsilon,0} - \mathbf{p}_0). \tag{4.21}$$

The idea is thus to modify points $\mathbf{a}_i$ and $\mathbf{b}_i^{\mathcal{B}}$ to maximize κ while ensuring that the nb points $\mathbf{p}_\epsilon$ are inside the CDPM COWCW for every $\mathbf{Q}_k$.

For practical reasons, we choose to set $nb = 14$. These points are separated in two groups: the first group of six points $\mathbf{p}_{\epsilon,0}$ represents the intersection points between the three principal axes of the ellipsoid and its surface (see the black circles in Fig. 4.4), and the second group,

which contains the remaining eight points $\mathbf{p}_{\epsilon,0}$, are the eight vertices of the box representing $\mathcal{W}_{p,t}$, i.e., the points $\mathbf{p}_w$ defined in Sub-section 4.2.1 (see the white circles in Fig. 4.4). Using this set of strategic points, and knowing that they lie in the CDPM COWCW for all $\mathbf{Q}_k$, we can, in general, assume $\mathcal{W}_e$ to be included in the WCW of the mechanism, taking as a fact that we span $\mathcal{W}_{p,r}$ with a representative set of q attitudes $\mathbf{Q}_k$. Moreover, if it is found that $\mathcal{W}_e$ is not fully included in the WCW even when all points $\mathbf{p}_\epsilon$ are included, it is probable that $\mathcal{W}_{p,t}$ should be completely contained in the CDPM's WCW, taking into account that $\mathcal{W}_{p,t}$ is over-estimated in the proposed scheme and the inclusion of all $\mathbf{p}_\epsilon$.

Finally, the optimization problem related to this first criterion can be formulated as follows:

$$
\begin{aligned}
\kappa_{\mathrm{COWCW},k} = \text{maximize} \quad & \kappa, \\
\text{subject to} \quad & \mathbf{W}^{\diamond}_{k,\epsilon}\mathbf{t}_{k,\epsilon} = \mathbf{0}_n, && \text{(4.22a)} \\
& -\mathbf{t}_{k,\epsilon} \leq \mathbf{0}_m, && \text{(4.22b)} \\
& \mathbf{1}_m^T\mathbf{t}_{k,\epsilon} = 1, && \text{(4.22c)} \\
& \mathbf{p}_\epsilon = \mathbf{p}_0 + \kappa(\mathbf{p}_{\epsilon,0} - \mathbf{p}_0), && \text{(4.22d)} \\
\text{for} \quad & \kappa,\ \mathbf{a}_i,\ \mathbf{b}_i^{\mathcal{B}},\ \mathbf{p}_\epsilon \text{ and } \mathbf{t}_{k,\epsilon}.
\end{aligned}
$$

In summary, this problem requires to maximize the volume of an ellipsoid by maximizing its scaling factor κ and modifying accordingly the CDPM geometry while satisfying the wrench-closure constraints of the nb evaluated points $\mathbf{p}_\epsilon$. Moreover, if we cover $\mathcal{W}_{p,r}$ with a representative set of q CDPM's end-effector attitudes $\mathbf{Q}_k$, we assume that the resulting CDPM workspace $\mathcal{W}$ is equivalent or a subset of the CDPM's WCW.

4.2.3 Second Criterion: Constant-Orientation Cable-Cable Interference

The second criterion considered in the synthesis of spatial m-cable f-edge n-DoF CDPMs is the possibility of interference between two cables, more specifically, the constant-orientation cable-cable interference (COCCI). The potential occurrence of mechanical interferences between the cables constraining the end-effector pose of a CDPM is often under-estimated when designing it. As demonstrated in Chapter 3, the interference regions are highly dependent on the CDPM end-effector attitude and can significantly limit its reachable workspace. Here, we include this verification into our dimensional synthesis problem.

Let us recall that the interference region between the i^{th} and j^{th} cables of a CDPM, for a given end-effector attitude $\mathbf{Q}_k$, is defined as the union of two two-dimensional polytopes, i.e., a first polygon associated to the ordered pair of cables (i, j), named $\mathcal{C}_{i,j,k}$, and a second for the opposite pair (j, i), named $\mathcal{C}_{j,i,k}$, which can be both mathematically expressed by the single relation

$$
\mathcal{C}_{i,j,k} = \{\mathbf{p} \in \mathbb{R}^3, \boldsymbol{\gamma} \in \mathbb{R}^2_+ | \mathbf{p} = \mathbf{s}_{i,j,k} + \mathbf{S}_{i,j,k}\boldsymbol{\gamma}\}, \tag{4.23}
$$

where

$$\mathbf{S}_{i,j,k} \equiv \left[\begin{array}{cc} \mathbf{a}_j - \mathbf{a}_i & \mathbf{Q}_k(\mathbf{b}_j^{\mathcal{B}} - \mathbf{b}_i^{\mathcal{B}}) \end{array} \right], \tag{4.24}$$

$$\mathbf{s}_{i,j,k} \equiv \mathbf{a}_j - \mathbf{Q}_k \mathbf{b}_i^{\mathcal{B}}, \tag{4.25}$$

and where $\mathbb{R}_+^2$ represents the set of all non-negative real numbers, $i = 1, \ldots, m$, and $j = 1, \ldots, m$ $(j \neq i)$.

Then from Eqs. (4.9) and (4.23), we want to find a set of constraints which, when satisfied, guarantees that the intersection between the polygon $\mathcal{C}_{i,j,k}$ and the ellipsoid $\mathcal{W}_e$ is an empty set.

First, we can start by writing the constraints that generate a non-empty set for the intersection between $\mathcal{C}_{i,j,k}$ and $\mathcal{W}_e$—the primal problem—which is an easier problem to formulate. Indeed, by substituting the relation of $\mathbf{p}$ defined with Eq. (4.23) into Eq. (4.9), we obtain the following constraints:

$$\begin{array}{ll} \text{satisfy} & \boldsymbol{\gamma}^T \mathbf{H}_{i,j,k} \boldsymbol{\gamma} + 2\mathbf{h}_{i,j,k}^T \boldsymbol{\gamma} + h_{i,j,k} \leq 0, \\ \text{for} & \boldsymbol{\gamma} \geq \mathbf{0}_2, \end{array} \tag{4.26}$$

where

$$\mathbf{H}_{i,j,k} \equiv \mathbf{S}_{i,j,k}^T \boldsymbol{\Pi} \mathbf{S}_{i,j,k}, \tag{4.27}$$

$$\mathbf{h}_{i,j,k} \equiv \mathbf{S}_{i,j,k}^T \boldsymbol{\Pi} \mathbf{s}_{i,j,k} + \mathbf{S}_{i,j,k}^T \mathbf{f}, \tag{4.28}$$

$$h_{i,j,k} \equiv \mathbf{s}_{i,j,k}^T \boldsymbol{\Pi} \mathbf{s}_{i,j,k} + 2\mathbf{s}_{i,j,k}^T \mathbf{f} + g. \tag{4.29}$$

If we write the previous set of satisfactory constraints as a minimization problem, we obtain

$$\begin{array}{lll} p_{\mathcal{C}}^\star = \underset{\boldsymbol{\gamma}}{\text{minimize}} & f(\boldsymbol{\gamma}) = \boldsymbol{\gamma}^T \mathbf{H}_{i,j,k} \boldsymbol{\gamma} + 2\mathbf{h}_{i,j,k}^T \boldsymbol{\gamma}, \\ \text{subject to} & -\boldsymbol{\gamma} \leq \mathbf{0}_2. \end{array} \tag{4.30}$$

When this problem has a solution, it means that $\mathcal{C}_{i,j,k}$ intersects $\mathcal{W}_e$, if and only if $p_{\mathcal{C}}^\star \leq -h_{i,j,k}$.

On the other hand, the dual problem of Eq. (4.30) can be formulated as follows (see Appendix B.2 for its mathematical derivation):

$$\begin{array}{lll} d_{\mathcal{C}}^\star = \underset{\boldsymbol{\lambda}}{\text{maximize}} & g(\boldsymbol{\lambda}) = -\dfrac{1}{4}\boldsymbol{\lambda}^T \mathbf{H}_{i,j,k}^{-1} \boldsymbol{\lambda} + \mathbf{h}_{i,j,k}^T \mathbf{H}_{i,j,k}^{-1} \boldsymbol{\lambda} - \mathbf{h}_{i,j,k}^T \mathbf{H}_{i,j,k}^{-1} \mathbf{h}_{i,j,k}, \\ \text{subject to} & \boldsymbol{\lambda} \geq \mathbf{0}_2. \end{array} \tag{4.31}$$

When this problem is found feasible, this means that $\mathcal{C}_{i,j,k}$ does not intersect $\mathcal{W}_e$, if and only if $d_{\mathcal{C}}^\star > -h_{i,j,k}$. With the assumption that the ellipsoid $\mathcal{W}_e$ is not degenerate and the fact that our original problem is convex, Slater's condition holds [235], and we know that we have strong duality between both problems—the primal and the dual—so that we may write that $d_{\mathcal{C}}^\star \equiv p_{\mathcal{C}}^\star$.

Thence, if we can demonstrate that $d_{\mathcal{C}}^{\star} > -h_{i,j,k}$, we will have demonstrated that $\mathcal{C}_{i,j,k} \bigcap \mathcal{W}_e = \varnothing$. To demonstrate $d_{\mathcal{C}}^{\star} > -h_{i,j,k}$, we merely have to resolve the following problem of constraint satisfaction, where $\boldsymbol{\lambda}$ has been replaced by $\boldsymbol{\mu} + 2\mathbf{h}_{i,j,k}$ in order to simplify the notation presented in Eq. (4.31):

$$\begin{aligned} &\text{satisfy} \quad \boldsymbol{\mu}^T \mathbf{H}_{i,j,k}^{-1} \boldsymbol{\mu} - 4h_{i,j,k} < 0, \\ &\text{for} \qquad\qquad \boldsymbol{\mu} + 2\mathbf{h}_{i,j,k} \geq \mathbf{0}_2. \end{aligned} \tag{4.32}$$

When the problem of Eq. (4.32) has a solution, there is no intersection between $\mathcal{C}_{i,j,k}$ and $\mathcal{W}_e$. Otherwise, such an intersection exists and the evaluated pair of cables (i,j) is in interference for that specific end-effector pose in $\mathcal{W}_e$.

Finally, the optimization problem related to this second criterion can be formulated as follows:

$$\begin{aligned} \kappa_{\text{COCCI},i,j,k} = \text{maximize} \quad & \kappa, \\ \text{subject to} \quad & \boldsymbol{\mu}_{i,j,k}^T \text{adj}(\mathbf{H}_{i,j,k}) \boldsymbol{\mu}_{i,j,k} - 4h_{i,j,k} \det(\mathbf{H}_{i,j,k}) \leq 0, && \text{(4.33a)} \\ & -\boldsymbol{\mu}_{i,j,k} - 2\mathbf{h}_{i,j,k} \leq \mathbf{0}_2, && \text{(4.33b)} \\ \text{for} \quad & \kappa,\ \mathbf{a}_i,\ \mathbf{b}_i^{\mathcal{B}} \text{ and } \boldsymbol{\mu}_{i,j,k}. \end{aligned}$$

It is noted here that $\text{adj}(\mathbf{H}_{i,j,k})$ and $\det(\mathbf{H}_{i,j,k})$ represent the adjoint and the determinant of the matrix $\mathbf{H}_{i,j,k}$, respectively. This modified mathematical expression is used in order to avoid the repetitive computation of the inverse of a matrix within our optimization algorithm, which normally increases the computation time. Also, we set the first constraint of this optimization problem, i.e., Eq. (4.33a), as a non-strictly negative constraint, which allows the surface of our solution ellipsoid to correspond directly to a locus where a cable-cable interference first appears.

In summary, for each end-effector's attitude $\mathbf{Q}_k$, these constraints must be satisfied for every ordered pair of cables i and j. In this optimization problem κ is maximized by modifying the CDPM geometry while avoiding any intersection between the cable-cable interference loci $\mathcal{C}_{i,j,k}$ and the prescribed ellipsoid $\mathcal{W}_e$. Moreover, as we cover $\mathcal{W}_{p,r}$ with a representative set of q CDPM's end-effector attitudes $\mathbf{Q}_k$, we assume that the workspace $\mathcal{W}$ of the solution CDPM is free of any cable-cable interference.

4.2.4 Third Criterion: Constant-Orientation Cable-Edge Interference

The third criterion for the synthesis of spatial m-cable f-edge n-DoF CDPMs is the constant-orientation cable-edge interference (COCEI). In addition to Sub-section 4.2.3, the occurrence of mechanical interferences between the CDPM cables and edges of its end effector can also limit its reachable workspace. We then choose to include this verification within the current dimensional synthesis problem.

We recall that the interference region between the i^{th} cable and the o^{th} end-effector's edge of a CDPM, for a given end-effector attitude $\mathbf{Q}_k$, is defined by a two-dimensional polytope, named $\mathcal{E}_{i,o,k}$, which can be mathematically expressed as follows

$$\mathcal{E}_{i,o,k} = \{\mathbf{p} \in \mathbb{R}^3, \boldsymbol{\alpha} \in \mathbb{R}^2_- | \mathbf{p} = \mathbf{r}_{i,o,k} + \mathbf{R}_{i,o,k}\boldsymbol{\alpha}, \alpha_1 + \alpha_2 \leq -1\}, \tag{4.34}$$

where

$$\mathbf{R}_{i,o,k} \equiv \begin{bmatrix} \mathbf{Q}_k(\mathbf{e}^{\mathcal{B}}_{o,s} - \mathbf{b}^{\mathcal{B}}_i) & \mathbf{Q}_k(\mathbf{e}^{\mathcal{B}}_{o,t} - \mathbf{b}^{\mathcal{B}}_i) \end{bmatrix}, \tag{4.35}$$

$$\mathbf{r}_{i,k} \equiv \mathbf{a}_i - \mathbf{Q}_k\mathbf{b}^{\mathcal{B}}_i, \tag{4.36}$$

and where $\mathbb{R}^2_-$ represents the set of all non-positive real numbers, $\mathbf{e}^{\mathcal{B}}_{o,s}$ and $\mathbf{e}^{\mathcal{B}}_{o,t}$ represent the starting and ending points, respectively, of the o^{th} edge of the end-effector geometry (expressed in the mobile reference frame attached to the CDPM's end-effector), $i = 1, \ldots, m$, and $o = 1, \ldots, f$. It should be noted that the set of edges is intended to represent only the wire-frame model of the CDPM end-effector and its payload. Consequently, interferences with an arbitrary object added inside the CDPM's workspace cannot be directly evaluated using the proposed technique, since its pose relative to the CDPM end-effector varies across the workspace, a case that was not taken into account in Chapter 3.

Similarly to what was done in Sub-section 4.2.3, we want to find from Eqs. (4.9) and (4.34) a set of constraints which, when satisfied, guarantee that the intersection between the polygon $\mathcal{E}_{i,o,k}$ and the ellipsoid $\mathcal{W}_e$ is the empty set.

First, we start by defining the constraints that generate a non-empty set for the intersection between $\mathcal{E}_{i,o,k}$ and $\mathcal{W}_e$—the primal problem. By substituting the relation of $\mathbf{p}$ defined with Eq. (4.34) into Eq. (4.9), we obtain the following constraints:

$$\begin{aligned} &\text{satisfy} \quad \boldsymbol{\alpha}^T\mathbf{N}_{i,o,k}\boldsymbol{\alpha} + 2\mathbf{n}^T_{i,o,k}\boldsymbol{\alpha} + n_{i,k} \leq 0, \\ &\text{for} \qquad\qquad\qquad\qquad \mathbf{C}\boldsymbol{\alpha} + \mathbf{c} \leq \mathbf{0}_3, \end{aligned} \tag{4.37}$$

where

$$\mathbf{N}_{i,o,k} \equiv \mathbf{R}^T_{i,o,k}\boldsymbol{\Pi}\mathbf{R}_{i,o,k}, \tag{4.38}$$

$$\mathbf{n}_{i,o,k} \equiv \mathbf{R}^T_{i,o,k}\boldsymbol{\Pi}\mathbf{r}_{i,k} + \mathbf{R}^T_{i,o,k}\mathbf{f}, \tag{4.39}$$

$$n_{i,k} \equiv \mathbf{r}^T_{i,k}\boldsymbol{\Pi}\mathbf{r}_{i,k} + 2\mathbf{r}^T_{i,k}\mathbf{f} + g, \tag{4.40}$$

$$\mathbf{C} \equiv \begin{bmatrix} 1 & 1 & 0 \\ 1 & 0 & 1 \end{bmatrix}^T, \tag{4.41}$$

$$\mathbf{c} \equiv \begin{bmatrix} 1 & 0 & 0 \end{bmatrix}^T. \tag{4.42}$$

If we write the constraints above as a minimization problem, we obtain

$$\begin{aligned} p^\star_{\mathcal{E}} = \underset{\boldsymbol{\alpha}}{\text{minimize}} \qquad & f(\boldsymbol{\alpha}) = \boldsymbol{\alpha}^T\mathbf{N}_{i,o,k}\boldsymbol{\alpha} + 2\mathbf{n}^T_{i,o,k}\boldsymbol{\alpha}, \\ \text{subject to} \quad & \mathbf{C}\boldsymbol{\alpha} + \mathbf{c} \leq \mathbf{0}_3. \end{aligned} \tag{4.43}$$

When this problem has a solution, it means that $\mathcal{E}_{i,o,k}$ intersects $\mathcal{W}_e$, if and only if $p^\star_{\mathcal{E}} \leq -n_{i,k}$.

Moreover, the dual problem of Eq. (4.43) can be formulated as follows (see Appendix B.3 for its mathematical derivation):

$$\begin{aligned} d^\star_{\mathcal{E}} = \underset{\boldsymbol{\phi}}{\text{maximize}} \quad & g(\boldsymbol{\phi}) = -\frac{1}{4}\boldsymbol{\phi}^T \mathbf{C}\mathbf{N}^{-1}_{i,o,k}\mathbf{C}^T\boldsymbol{\phi} + (\mathbf{c}^T - \mathbf{n}^T_{i,o,k}\mathbf{N}^{-1}_{i,o,k}\mathbf{C}^T)\boldsymbol{\phi} \\ & \qquad - \mathbf{n}^T_{i,o,k}\mathbf{N}^{-1}_{i,o,k}\mathbf{n}_{i,o,k}, \\ \text{subject to} \quad & \boldsymbol{\phi} \geq \mathbf{0}_3. \end{aligned} \tag{4.44}$$

When this problem is found feasible, we know that $\mathcal{E}_{i,o,k}$ does not intersect $\mathcal{W}_e$, if and only if $d^\star_{\mathcal{E}} > -n_{i,k}$. Again, with the assumption that the ellipsoid $\mathcal{W}_e$ is not degenerate and given the fact that our original problem is convex, Slater's condition holds and we therefore have strong duality between the primal and dual problems, i.e., $d^\star_{\mathcal{E}} \equiv p^\star_{\mathcal{E}}$.

Therefrom, if we can demonstrate that $d^\star_{\mathcal{E}} > -n_{i,k}$, we will have demonstrated that $\mathcal{E}_{i,o,k} \bigcap \mathcal{W}_e = \varnothing$. To demonstrate $d^\star_{\mathcal{E}} > -n_{i,k}$, we simply need to resolve the following constraint satisfaction problem, where $\boldsymbol{\phi}$ has been replaced with $\mathbf{D}^{-1}(\boldsymbol{\eta} - 2\mathbf{z}_{i,o,k})$ in order to simplify the notation of Eq. (4.44):

$$\begin{aligned} & \text{satisfy} \quad \boldsymbol{\eta}^T\mathbf{Z}_{i,o,k}\boldsymbol{\eta} - 4(\mathbf{c}^T\boldsymbol{\eta} + n_{i,k}) < 0, \\ & \text{for} \qquad\qquad \mathbf{D}^{-1}(\boldsymbol{\eta} - 2\mathbf{z}_{i,o,k}) \geq \mathbf{0}_3, \end{aligned} \tag{4.45}$$

where

$$\mathbf{D} \equiv \begin{bmatrix} \mathbf{c}^T \\ \mathbf{C}^T \end{bmatrix}, \; \mathbf{Z}_{i,o,k} \equiv \begin{bmatrix} 0 & \mathbf{0}_2^T \\ \mathbf{0}_2 & \mathbf{N}^{-1}_{i,o,k} \end{bmatrix}, \text{ and } \mathbf{z}_{i,o,k} \equiv \begin{bmatrix} 0 \\ \mathbf{n}_{i,o,k} \end{bmatrix}. \tag{4.46}$$

When the problem of Eq. (4.45) has a solution, there is no intersection between $\mathcal{E}_{i,o,k}$ and $\mathcal{W}_e$. Otherwise, such an intersection exists and the evaluated pair composed of a cable i and an edge o is in interference for that specific end-effector pose in $\mathcal{W}_e$.

Finally, the optimization problem related to this third criterion can be formulated as follows:

$$\begin{aligned} \kappa_{\text{COCEI},i,o,k} = \text{maximize} \quad & \kappa, \\ \text{subject to} \quad & \boldsymbol{\eta}^T_{i,o,k}\mathbf{Z}^a_{i,o,k}\boldsymbol{\eta}_{i,o,k} - 4\det(\mathbf{N}_{i,o,k})(\mathbf{c}^T\boldsymbol{\eta}_{i,o,k} + n_{i,k}) \leq 0, & \text{(4.47a)} \\ & -\mathbf{D}^{-1}(\boldsymbol{\eta}_{i,o,k} - 2\mathbf{z}_{i,o,k}) \leq \mathbf{0}_3, & \text{(4.47b)} \\ \text{for} \quad & \kappa, \; \mathbf{a}_i, \; \mathbf{b}_i^{\mathcal{B}} \text{ and } \boldsymbol{\eta}_{i,o,k}, \end{aligned}$$

and where

$$\mathbf{Z}^a_{i,o,k} \equiv \begin{bmatrix} 0 & \mathbf{0}_2^T \\ \mathbf{0}_2 & \text{adj}(\mathbf{N}_{i,o,k}) \end{bmatrix}. \tag{4.48}$$

It is noted here that $\text{adj}(\mathbf{N}_{i,o,k})$ and $\det(\mathbf{N}_{i,o,k})$ represent the adjoint and the determinant of the matrix $\mathbf{N}_{i,o,k}$, respectively. As we did for the previous criterion, we set the first constraint

of this optimization problem, i.e., Eq. (4.47a), as a non-strict inequality, which allows the solution ellipsoid to share one point with a locus where an cable-edge interference first occurs.

In summary, for each CDPM's end-effector attitude $\mathbf{Q}_k$, these constraints must be satisfied for every combination of a cable i and an edge o. This optimization problem allows to maximize κ while modifying the CDPM geometry, as long as the evaluated points $\mathbf{p} \in \mathbb{R}^3$ imply that the cable-edge interference constraints are fully satisfied. Moreover, we discretize $\mathcal{W}_{p,r}$ with a representative set of q CDPM end-effector attitudes $\mathbf{Q}_k$, and assume from there that the workspace $\mathcal{W}$ of the solution CDPM is free of any cable-edge interference.

4.2.5 Synthesis Problem

The complete dimensional synthesis problem can be formulated as follows, when one desires to test for a given set of CDPM end-effector orientations $\mathbf{Q}_k$, $k = 1, \ldots, q$, that the CDPM has m cables, and that its end effector, with possibly its attached payload, is represented by a total of f edges:

$$\begin{aligned}
&\text{maximize} \quad \kappa, \\
&\text{subject to} \quad \text{Eqs. } (4.22a, 4.22b, 4.22c, 4.22d),\ k = 1, \ldots, q,\ \epsilon = 1, \ldots, nb, \\
&\qquad\qquad \text{Eqs. } (4.33a, 4.33b),\ i = 1, \ldots, m,\ j = 1, \ldots, m,\ i \neq j,\ k = 1, \ldots, q, \\
&\qquad\qquad \text{Eqs. } (4.47a, 4.47b),\ i = 1, \ldots, m,\ o = 1, \ldots, f,\ k = 1, \ldots, q, \\
&\text{for} \qquad \kappa,\ \mathbf{a}_i,\ \mathbf{b}_i^{\mathcal{B}},\ \mathbf{p}_\epsilon,\ \mathbf{t}_{k,\epsilon},\ \boldsymbol{\mu}_{i,j,k} \text{ and } \boldsymbol{\eta}_{i,o,k}.
\end{aligned} \tag{4.49}$$

In this problem, we recall that Eqs. (4.22a,4.22b,4.22c,4.22d) represent the constraints to be satisfied in order to guarantee that at least nb points on the surface of the ellipsoid $\mathcal{W}_e$ are inside the CDPM COWCW. Notice that there is one scaling factor κ for all orientations $\mathbf{Q}_k$. Equations (4.33a,4.33b) represent the constraints to be satisfied in order to guarantee that none of the interference regions associated with ordered pairs of cables (i, j) intersects the interior of ellipsoid $\mathcal{W}_e$ for each attitude $\mathbf{Q}_k$. Since each pair of cables is ordered, the interference region corresponding to the pair (j, i) is different from the one corresponding to the pair (i, j). Equations (4.47a,4.47b) represent the constraints to be satisfied in order to guarantee that none of the interference regions associated with cable-edge pairs intersects with the interior of ellipsoid $\mathcal{W}_e$ for each attitude $\mathbf{Q}_k$.

It is also important to note that κ represents the objective function of this optimization problem, which needs to be maximized. The vectors $\mathbf{a}_i$ and $\mathbf{b}_i^{\mathcal{B}}$, which define the geometry of the CDPM, are to be modified in order to allow this maximization. Finally, variables $\mathbf{p}_\epsilon$, $\mathbf{t}_{k,\epsilon}$, $\boldsymbol{\mu}_{i,j,k}$ and $\boldsymbol{\eta}_{i,o,k}$ are internal variables which must be optimized in order to verify that the entire set of constraints is fully satisfied. This optimization problem, devised for the synthesis of CDPMs, and inherently CDPs, is numerically implemented in the following section as a proof of it relevance and practicability.

4.3 Numerical Applications

In order to program the synthesis problem described in the previous section, we use the *Optimization Toolbox* available with the MATLAB® package. Since our problem contains inequality and equality nonlinear constraints, the minimization tool `fmincon` is found suitable for our purpose. In such a way, the maximization problem of Eq. (4.49) can easily be reformulated as a minimization problem as follows:

$$\begin{aligned} f(\mathbf{v}) = \text{minimize} \quad & -\kappa, \\ \text{subject to} \quad & \mathbf{c}_{\text{ineq}}(\mathbf{v}) \leq \mathbf{0}_{(3(m^2-m)q+4mfq)\times 1}, \\ & \mathbf{c}_{\text{eq}}(\mathbf{v}) = \mathbf{0}_{(nqnb)\times 1}, \\ & \mathbf{A}_{\text{eq},(3nb+qnb)\times dim}\mathbf{v} = \mathbf{b}_{\text{eq},(3nb+qnb)\times 1}, \\ & \mathbf{l}_b \leq \mathbf{v} \leq \mathbf{u}_b, \\ \text{for} \quad & \mathbf{v} \equiv \left[\begin{array}{ccccccc} \kappa & \mathbf{a}^T & \mathbf{b}^{\mathcal{B}\,T} & \mathbf{p}_{aug}^T & \mathbf{t}_{aug}^T & \boldsymbol{\mu}_{aug}^T & \boldsymbol{\eta}_{aug}^T \end{array} \right]_{dim\times 1}^T, \end{aligned} \tag{4.50}$$

where

$$\mathbf{A}_{\text{eq}} \equiv \left[\begin{array}{ccccc} -(\mathbf{p}_{aug} - \mathbf{p}_{0,aug}) & \mathbf{0}_{3nb\times 6m} & \mathbf{1}_{3nb\times 3nb} & \mathbf{0}_{3nb\times mqnb} & \mathbf{0}_{3nb\times dim_1} \\ \mathbf{0}_{qnb\times 1} & \mathbf{0}_{qnb\times 6m} & \mathbf{0}_{qnb\times 3nb} & \mathbf{U} & \mathbf{0}_{qnb\times dim_1} \end{array} \right], \tag{4.51}$$

$$\mathbf{b}_{\text{eq}} \equiv \left[\begin{array}{cc} \mathbf{p}_{0,aug}^T & \mathbf{1}_{qnb}^T \end{array} \right]^T, \tag{4.52}$$

$$\mathbf{p}_{0,aug} \equiv \left[\begin{array}{ccc} \mathbf{p}_0^T & \cdots & \mathbf{p}_0^T \end{array} \right]_{3nb}^T, \tag{4.53}$$

$$\mathbf{U} \equiv \left[\begin{array}{ccc} \mathbf{1}_m^T & \cdots & \mathbf{0}_m^T \\ \vdots & \ddots & \vdots \\ \mathbf{0}_m^T & \cdots & \mathbf{1}_m^T \end{array} \right]_{qnb\times mqnb}, \tag{4.54}$$

$$\mathbf{l}_b \equiv \left[\begin{array}{ccccccc} 0 & \underline{\mathbf{a}}_{3m}^T & \underline{\mathbf{b}}_{3m}^{\mathcal{B}\,T} & -\boldsymbol{\infty}_{3nb}^T & \mathbf{0}_{mqnb}^T & -\boldsymbol{\infty}_{2(m^2-m)q}^T & -\boldsymbol{\infty}_{3mfq}^T \end{array} \right]^T, \tag{4.55}$$

$$\mathbf{u}_b \equiv \left[\begin{array}{ccccccc} \infty & \overline{\mathbf{a}}_{3m}^T & \overline{\mathbf{b}}_{3m}^{\mathcal{B}\,T} & \boldsymbol{\infty}_{3nb}^T & \mathbf{1}_{mqnb}^T & \boldsymbol{\infty}_{2(m^2-m)q}^T & \boldsymbol{\infty}_{3mfq}^T \end{array} \right]^T, \tag{4.56}$$

$$\mathbf{a} \equiv \left[\begin{array}{ccccc} \mathbf{a}_1^T & \cdots & \mathbf{a}_i^T & \cdots & \mathbf{a}_m^T \end{array} \right]_{3m}^T, \tag{4.57}$$

$$\mathbf{b}^{\mathcal{B}} \equiv \left[\begin{array}{ccccc} \mathbf{b}_1^{\mathcal{B}\,T} & \cdots & \mathbf{b}_i^{\mathcal{B}\,T} & \cdots & \mathbf{b}_m^{\mathcal{B}\,T} \end{array} \right]_{3m}^T, \tag{4.58}$$

$$\mathbf{p}_{aug} \equiv \left[\begin{array}{ccccc} \mathbf{p}_1^T & \cdots & \mathbf{p}_\epsilon^T & \cdots & \mathbf{p}_{nb}^T \end{array} \right]_{3nb}^T, \tag{4.59}$$

$$\mathbf{t}_{aug} \equiv \left[\begin{array}{ccccc} \mathbf{t}_{1,1}^T & \cdots & \mathbf{t}_{1,q}^T & \cdots & \mathbf{t}_{nb,q}^T \end{array} \right]_{mqnb}^T, \tag{4.60}$$

$$\boldsymbol{\mu}_{aug} \equiv \left[\begin{array}{ccccccc} \boldsymbol{\mu}_{2,1,1}^T & \cdots & \boldsymbol{\mu}_{m,1,1}^T & \boldsymbol{\mu}_{1,2,1}^T & \boldsymbol{\mu}_{3,2,1}^T & \cdots & \boldsymbol{\mu}_{m-1,m,q}^T \end{array} \right]_{2(m^2-m)q}^T, \tag{4.61}$$

$$\boldsymbol{\eta}_{aug} \equiv \left[\begin{array}{ccccccc} \boldsymbol{\eta}_{1,1,1}^T & \cdots & \boldsymbol{\eta}_{1,f,1}^T & \boldsymbol{\eta}_{2,1,1}^T & \cdots & \boldsymbol{\eta}_{m,f,q}^T \end{array} \right]_{3mfq}^T, \tag{4.62}$$

$$dim \equiv 1 + 6m + 3nb + mqnb + dim_1, \tag{4.63}$$

and

$$dim_1 \equiv 2(m^2 - m)q + 3mfq. \tag{4.64}$$

For the sake of clarity, the details of the inequality and equality nonlinear constraints, $\mathbf{c}_{\text{ineq}}(\mathbf{v})$ and $\mathbf{c}_{\text{eq}}(\mathbf{v})$, respectively, are presented in Appendix C.1. Moreover, it should be noted that, a bounding box limiting the positions of the attachment points of the m cables should be defined when one desires to optimize the geometry of a CDPM for a particular application. Here these constraining values are represented by $\underline{\mathbf{a}}$, $\underline{\mathbf{b}}^{\mathcal{B}}$, $\overline{\mathbf{a}}$ and $\overline{\mathbf{b}}^{\mathcal{B}}$, which are vectors of dimensions $3m$ and contain the lower and the upper bounds for each vector $\mathbf{a}_i$ and $\mathbf{b}_i^{\mathcal{B}}$, respectively.

As for the majority of complex engineering problems, this dimensional synthesis problem is nonlinear and non-convex. Consequently, the resulting optimum is known to be strongly dependent on the initial guess solution and there is no guarantee that a global optimum will be ever reached. From this fact, we choose to follow an approach similar to the heuristic *Multi-Start methods*, which was discussed in Sub-section 4.1.1, in order to improve the likelihood to generate the best solution. A total of ms initial guesses are generated and each ι^{th} guess, $\iota = 1, \ldots, ms$, is to be optimized using the program of Eq. (4.50). Figure 4.5 illustrates the flowchart of this proposed CDPM synthesis technique.

The first step when one desires to develop a CDPM for a specific application is to define its requirements. These expected specifications, here, are the prescribed workspace $\mathcal{W}_p$ of the envisioned CDPM, which represents both the prescribed workspaces in translation and in rotation, $\mathcal{W}_{p,t}$ and $\mathcal{W}_{p,r}$, respectively, the bounding box where each attachment point $\mathbf{a}_i$ and $\mathbf{b}_i^{\mathcal{B}}$ can be placed, i.e., $\underline{\mathbf{a}}$, $\underline{\mathbf{b}}^{\mathcal{B}}$, $\overline{\mathbf{a}}$, and, $\overline{\mathbf{b}}^{\mathcal{B}}$, the reference position $\mathbf{p}_0$—normally the centroid of $\mathcal{W}_{p,t}$—of the reference point P fixed to the CDPM's end-effector, the reference orientation $\mathbf{Q}_0$—normally the centroid of $\mathcal{W}_{p,r}$—of the frame $\mathcal{B}$ attached to the end effector, the chosen number of degrees of freedom n, the total number of cables m ($m \geq n+1$) and the total number of edges f. In addition, we also need to choose the number of end-effector orientations q, the number of checkpoints nb on the ellipsoid surface, the maximum allowed number of iterations mr, and the number of initial guesses ms selected to span the domain of solutions. These selections are directly based on the constraints of the intended application for the CDPM and on the experience of the designer.

From the given prescribed workspace in translation $\mathcal{W}_{p,t}$, the second step is to determine the parametric constants of the target ellipsoid $\mathcal{W}_e$ that best represents $\mathcal{W}_{p,t}$, with $\kappa = 1$, by using Eq. (4.10). This ellipsoid serves then as a threshold to know if the resulting geometry fulfills its performance requirements, i.e., we ultimately seek for $\kappa \geq 1$.

The third step is the generation of the ι^{th} initial solution. This step is separated into two sub-steps: a randomly-selected CDPM geometry, i.e., $\mathbf{a}_{\iota,r}$ and $\mathbf{b}_{\iota,r}^{\mathcal{B}}$, and its corresponding closest-feasible solution $\mathbf{v}_{\iota,0}$. The random selection of the CDPM's initial geometry is performed

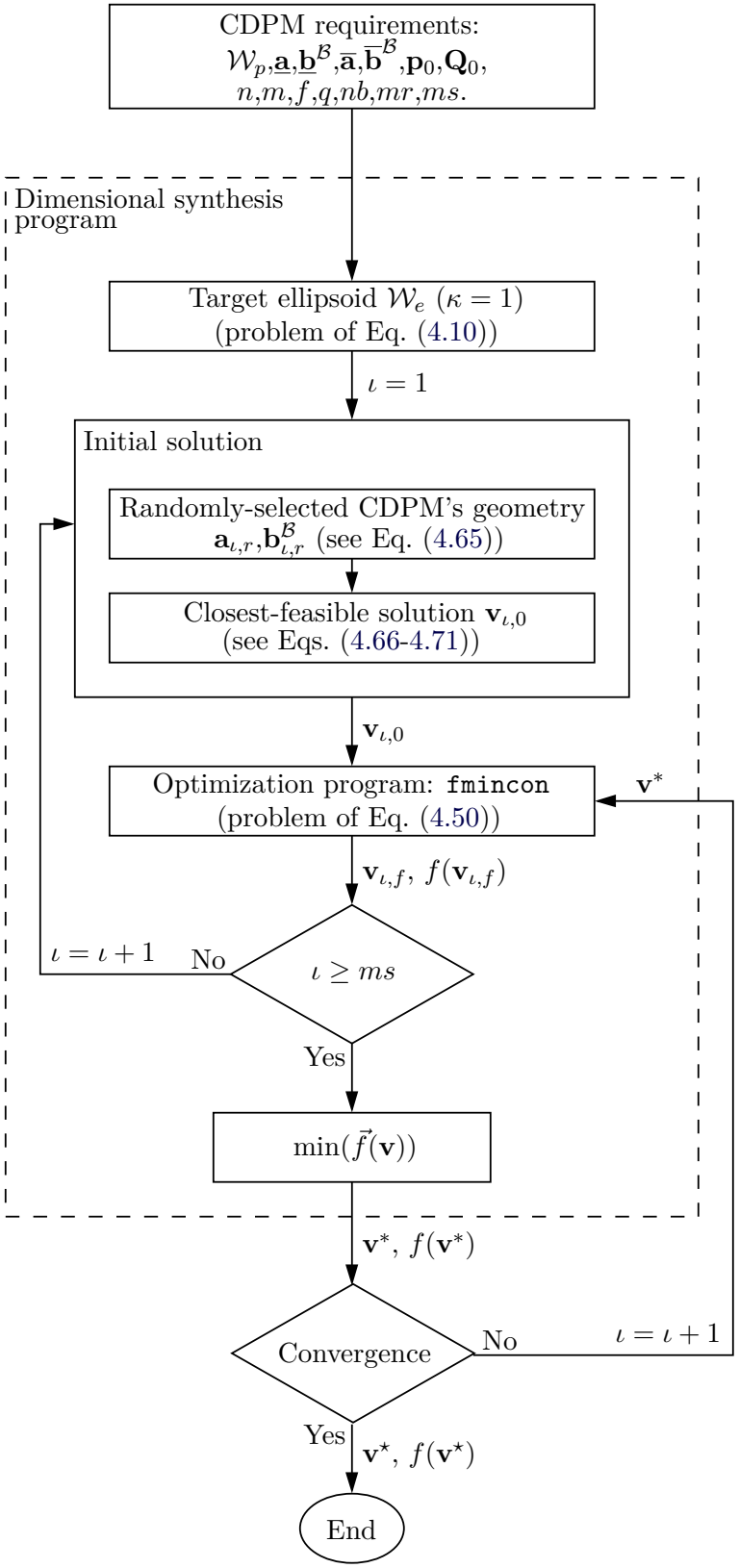

Figure 4.5 – Flowchart of the CDPM dimensional synthesis method.

using the function `random` from the *Statistics Toolbox* of the MATLAB® package. We chose a uniform distribution for this random selection in order to obtain attachment points $\mathbf{a}_{\iota,r}$ and $\mathbf{b}^{\mathcal{B}}_{\iota,r}$, that fulfill the following constraints:

$$\mathbf{a}_{\iota,r} \in \left[\underline{\mathbf{a}},\ \overline{\mathbf{a}}\right], \quad \text{and} \quad \mathbf{b}^{\mathcal{B}}_{\iota,r} \in \left[\underline{\mathbf{b}}^{\mathcal{B}},\ \overline{\mathbf{b}}^{\mathcal{B}}\right]. \tag{4.65}$$

In order to initialize the optimization algorithm from a feasible starting point, we must first ensure that the resulting random geometry represents a feasible initial geometry, i.e., that at minimum the reference position $\mathbf{p}_0$ of this given CDPM end-effector belongs to its WCW, at least for the q orientations $\mathbf{Q}_k$. This is ensured by computing its projection on the domain of feasible solutions before launching the optimization program of Eq. (4.50). To do so, we first find the closest-feasible geometry by solving the following problem:

$$\begin{aligned}
\text{minimize} \quad & f(\mathbf{x}_{\iota,0}) \equiv ||\mathbf{x}_{\iota,0} - \mathbf{x}_{\iota,r}||_2^2 = (\mathbf{x}_{\iota,0} - \mathbf{x}_{\iota,r})^T(\mathbf{x}_{\iota,0} - \mathbf{x}_{\iota,r}), \\
\text{subject to} \quad & \mathbf{W}^{\diamond}_{k,\iota,0}\mathbf{t}_{k,\iota,0} = \mathbf{0}_n, \\
& -\mathbf{t}_{k,\iota,0} \leq \mathbf{0}_m, \\
& \mathbf{1}_m^T\mathbf{t}_{k,\iota,0} = 1, \\
\text{for} \quad & \mathbf{x}_{\iota,0} \text{ and } \mathbf{t}_{k,\iota,0},
\end{aligned} \tag{4.66}$$

where $\mathbf{x}_{\iota,0} \equiv [\ \mathbf{a}_{\iota,0}^T \quad \mathbf{b}_{\iota,0}^{\mathcal{B}\,T}\ ]^T$ and $\mathbf{x}_{\iota,r} \equiv [\ \mathbf{a}_{\iota,r}^T \quad \mathbf{b}_{\iota,r}^{\mathcal{B}\,T}\ ]^T$, two vectors of dimension $6m$. This minimization problem can easily be solved with the function `fmincon` from MATLAB®. The purpose of the problem of Eq. (4.66) is to minimize the square norm of the difference between a feasible CDPM's geometry and the random-selected geometry, i.e., to find the closest feasible geometry, while satisfying the COWCW constraints for each $\mathbf{Q}_k$, $k = 1, \ldots, q$, at $\mathbf{p} = \mathbf{p}_0$.

Furthermore, since a feasible initial solution for the synthesis problem presented in Eq. (4.50) is given by $\mathbf{v}_{\iota,0}$ and not only $\mathbf{x}_{\iota,0}$, we then need to determine the corresponding values for $\kappa_{\iota,0}$, $\mathbf{p}_{aug,\iota,0}$, $\mathbf{t}_{aug,\iota,0}$, $\boldsymbol{\mu}_{aug,\iota,0}$ and $\boldsymbol{\eta}_{aug,\iota,0}$. To do this, we must solve the following series of optimization sub-programs, assuming $\kappa_{\iota,0} = 0$, and consequently, $\mathbf{p}_{aug,\iota,0} = [\ \mathbf{p}_0^T \quad \cdots \quad \mathbf{p}_0^T\ ]^T_{3nb}$ from Eq. (4.22d):

$$\begin{aligned}
\text{minimize} \quad & f(\mathbf{t}_{k,\epsilon,\iota,0}) \equiv \mathbf{f}^T\mathbf{t}_{k,\epsilon,\iota,0}, \\
\text{subject to} \quad & \mathbf{W}^{\diamond}_{k,\epsilon,\iota,0}\mathbf{t}_{k,\epsilon,\iota,0} = \mathbf{0}_n, \\
& -\mathbf{t}_{k,\epsilon,\iota,0} \leq \mathbf{0}_m, \\
& \mathbf{1}_m^T\mathbf{t}_{k,\epsilon,\iota,0} = 1, \\
\text{for} \quad & \mathbf{t}_{k,\epsilon,\iota,0},
\end{aligned} \tag{4.67}$$

which can be solved with the function `linprog` for $k = 1, \ldots, q$ and $\epsilon = 1, \ldots, nb$, in order to obtain $\mathbf{t}_{aug,\iota,0}$. It should also be noted that $\mathbf{f} \equiv \mathbf{1}_{mqnb}$ in this case. Then, in order to obtain

$\boldsymbol{\mu}_{aug,\iota,0}$:

$$\begin{array}{ll} \text{minimize} & f(\boldsymbol{\mu}_{i,j,k,\iota,0}) \equiv \boldsymbol{\mu}_{i,j,k,\iota,0}^T \text{adj}(\mathbf{H}_{i,j,k,\iota,0}) \boldsymbol{\mu}_{i,j,k,\iota,0}, \\ \text{subject to} & -\boldsymbol{\mu}_{i,j,k,\iota,0} - 2\mathbf{h}_{i,j,k,\iota,0} \leq \mathbf{0}_2, \\ \text{for} & \boldsymbol{\mu}_{i,j,k,\iota,0}, \end{array} \tag{4.68}$$

which can be solved with the function `quadprog` for $i = 1, \ldots, m$, $j = 1, \ldots, m$ $(i \neq j)$ and $k = 1, \ldots, q$. We must also verify that the constraint of Eq. (4.33a) is also satisfied:

$$\boldsymbol{\mu}_{i,j,k,\iota,0}^T \text{adj}(\mathbf{H}_{i,j,k,\iota,0}) \boldsymbol{\mu}_{i,j,k,\iota,0} - 4h_{i,j,k,\iota,0} \text{det}(\mathbf{H}_{i,j,k,\iota,0}) \leq 0. \tag{4.69}$$

Finally, in order to obtain $\boldsymbol{\eta}_{aug,\iota,0}$, we must

$$\begin{array}{ll} \text{minimize} & f(\boldsymbol{\eta}_{i,o,k,\iota,0}) \equiv \boldsymbol{\eta}_{i,o,k,\iota,0}^T \mathbf{Z}_{i,o,k,\iota,0}^a \boldsymbol{\eta}_{i,o,k,\iota,0} - 4\text{det}(\mathbf{N}_{i,o,k,\iota,0}) \mathbf{c}^T \boldsymbol{\eta}_{i,o,k,\iota,0}, \\ \text{subject to} & -\mathbf{D}^{-1}(\boldsymbol{\eta}_{i,o,k,\iota,0} - 2\mathbf{z}_{i,o,k,\iota,0}) \leq \mathbf{0}_3, \\ \text{for} & \boldsymbol{\eta}_{i,o,k,\iota,0}, \end{array} \tag{4.70}$$

which can be solved with the function `quadprog` for $i = 1, \ldots, m$, $o = 1, \ldots, f$ and $k = 1, \ldots, q$. Again, one must verify that the constraint of Eq. (4.47a) is satisfied:

$$\boldsymbol{\eta}_{i,o,k,\iota,0}^T \mathbf{Z}_{i,o,k,\iota,0}^a \boldsymbol{\eta}_{i,o,k,\iota,0} - 4\text{det}(\mathbf{N}_{i,o,k,\iota,0})(\mathbf{c}^T \boldsymbol{\eta}_{i,o,k,\iota,0} + n_{i,k,\iota,0}) \leq 0. \tag{4.71}$$

In summary, from the third step, we obtain the following feasible initial solution for our CDPM dimensional synthesis problem:

$$\mathbf{v}_{\iota,0} \equiv \left[\begin{array}{ccccccc} \kappa_{\iota,0} & \mathbf{a}_{\iota,0}^T & \mathbf{b}_{\iota,0}^{\mathcal{B}T} & \mathbf{p}_{aug,\iota,0}^T & \mathbf{t}_{aug,\iota,0}^T & \boldsymbol{\mu}_{aug,\iota,0}^T & \boldsymbol{\eta}_{aug,\iota,0}^T \end{array} \right]^T. \tag{4.72}$$

The fourth step is to find the ι^{th} solution $\mathbf{v}_{\iota,f}$, which is obtained by solving the optimization program described with Eq. (4.50) and using the feasible initial solution $\mathbf{v}_{\iota,0}$ as a starting point. As previously stated, the optimization tool `fmincon` included in the *Optimization Toolbox* of the software MATLAB® is used to solve this program. More specifically, the *interior-point* algorithm is preferred from other options since it is a *large-scale* algorithm[6], which does not need to store matrices and allows to exploit their sparsity pattern in order to improve speed and reduce memory cost. In fact, although we stated in Sub-section 4.1.1 that SQP is often reported as the most successful method for solving nonlinear constrained optimization problems, it has the demerit to be a *medium-scale* algorithm. This is seen as a strong inconvenient when one aims at solving synthesis problem with a high number of

[6]From [201], an optimization algorithm is said *large scale*, by opposition to *medium scale*, when it uses linear algebra that does not need to store, nor operate on, full matrices. This may be done internally by storing sparse matrices, and by using sparse linear algebra for computations whenever possible. Furthermore, the internal algorithms either preserve sparsity, such as a sparse Cholesky decomposition [293], or do not generate matrices, such as a conjugate gradient method [294].

variables and constraints and that involves large sparse matrices, such as the dimensional synthesis of CDPMs. Furthermore, sub-problems of the interior-point algorithm are set to be solved with the *Conjugate Gradient method* [294], which is derived from the family of the *Gradient methods* and known to be an efficient method for large unconstrained nonlinear problems. Also, in order to reduce computation time, gradients of the objective function and nonlinear constraints have been analytically formulated and provided to the CDPM synthesis program. Since our objective function, shown in Eq. (4.50), is simple:

$$f(\mathbf{v}) = -\kappa, \tag{4.73}$$

the associated gradient is easily expressed as follows:

$$\nabla f(\mathbf{v}) \equiv \partial f(\mathbf{v})/\partial \mathbf{v} = \begin{bmatrix} -1 & \mathbf{0}^T_{6m+3nb+mqnb+2(m^2-m)q+3mfq} \end{bmatrix}^T. \tag{4.74}$$

As for the gradients of the nonlinear inequality and equality constraints, which can be expressed as $\nabla \mathbf{c}_{\text{ineq}}(\mathbf{v}) \equiv \partial \mathbf{c}_{\text{ineq}}(\mathbf{v})/\partial \mathbf{v}$ and $\nabla \mathbf{c}_{\text{eq}}(\mathbf{v}) \equiv \partial \mathbf{c}_{\text{eq}}(\mathbf{v})/\partial \mathbf{v}$, their mathematical derivation is more involved and it is left in Appendix C.2. Once the optimization process is completed, the ι^{th} final solution is obtained:

$$\mathbf{v}_{\iota,f} \equiv \begin{bmatrix} \kappa_{\iota,f} & \mathbf{a}^T_{\iota,f} & \mathbf{b}^{\mathcal{B}T}_{\iota,f} & \mathbf{p}^T_{aug,\iota,f} & \mathbf{t}^T_{aug,\iota,f} & \boldsymbol{\mu}^T_{aug,\iota,f} & \boldsymbol{\eta}^T_{aug,\iota,f} \end{bmatrix}^T. \tag{4.75}$$

Finally, in order to define a suitable stopping criterion for the algorithm, we set a maximum number of iterations mr. Moreover, there are additional stopping options inherent to the use of the `fmincon` function such as the tolerance on the constraint violation (`TolCon`), the termination tolerance on the function value (`TolFun`) and the termination tolerance on the solution $\mathbf{v}$ (`TolX`). `TolCon`, `TolFun` and `TolX` were set to $1e^{-6}$, $1e^{-4}$ and $1e^{-5}$, respectively, their default values in MATLAB® being $1e^{-6}$, $1e^{-6}$ and $1e^{-10}$, respectively. It is noted that these values have been increased in order to relax the tolerance constraints of the optimization tool and consequently reduce the overall computation time required to obtain an acceptable final solution.

The third and fourth steps have to be performed until $\iota = ms$, where ms is the chosen number of initial guesses set for the multi-start method applied to this CDPM synthesis problem. When this number is reached, the solution $\mathbf{v}^*$ that best minimizes the objective function $f(\mathbf{v})$ is determined by finding the solution that generates $f(\mathbf{v}^*)$ over the ms final solutions, i.e., $f(\mathbf{v}^*) \equiv \min(f(\mathbf{v}_{\iota,f}))$, where $\iota = 1, \ldots, ms$.

Finally, the last step is to verify the level of convergence of the solution $\mathbf{v}^*$. To do so, we first verify if the number of iterations required to obtain this solution reached the maximum allowed mr. In the negative, this solution represents the optimum solution $\mathbf{v}^\star$ generated by our dimensional synthesis program for the given problem, i.e., our best CDPM's geometry for the given requirements. In the affirmative, however, this solution is fed back into the optimization program directly as a feasible initial solution $\mathbf{v}_{\iota+1,0}$ and a new final solution $\mathbf{v}^*$

is then obtained. This action is applied unless it is found that the corresponding value $f(\mathbf{v}^*)$, based on the evolution of the objective function, has barely changed over the last one-hundred iterations and that the optimization program's step size for each of these iterations is very small. In other words, the solution is considered optimal if there are sufficient iterations to indicate that the optimization process would have stopped soon after the mr^{th} iteration and that only unsignificant changes would have been done on the resulting CDPM geometry.

In all, this makes for an algorithm that requires minimal human interventions. This can be seen in Fig. 4.5, where only the first and the last two steps of the flowchart have to be manually performed by the designer. These steps are shown outside the central block (dashed lines) named *Dimensional synthesis program*. The first part is the determination of the CDPM requirements based on the intended application and the functional parameters of the synthesis programming and the second part is the determination of the necessity of an additional run into the optimization algorithm in view of the probability of improving the result $f(\mathbf{v}^*)$.

For the sake of numerical validation, the proposed technique is applied to the dimensional synthesis of two different mechanisms. It is first tested on an arbitrary seven-cable nine-edge six-DoF CDPM in Sub-section 4.3.1 and then, in Sub-section 4.3.2, to the optimization of the geometric parameters of an eight-cable seventeen-edge six-DoF CDP intended for a medical application. Since the envisioned CDPMs are spatial cable-driven mechanisms, the number of degrees of freedom is fixed to $n = 6$ in both examples. Also, as previously mentioned in Sub-section 4.2.2, the number of checkpoints on the ellipsoid surface for the evaluation of the COWCW is set to $nb = 14$. We decided to span the prescribed workspace in rotation $\mathcal{W}_{p,r}$ with nine different end-effector attitudes $\mathbf{Q}_k$, i.e., $q = 9$. In general, $\mathcal{W}_{p,r}$ can be represented as a box in the tridimensional space of rigid-body rotations. For this reason, the first eight orientations $\mathbf{Q}_k$ correspond to the eight vertices of $\mathcal{W}_{p,r}$, while the ninth orientation is considered to be the reference, $\mathbf{Q}_0$, which is generally represented by the 3×3 identity matrix $\mathbf{1}_{3\times3}$. With this set of strategic CDPM attitudes, we assess all the possible combinations of the extrema of the range of rotations as well as the reference orientation. We assume that any intermediary attitude $\mathbf{Q}$ is reachable when these nine end-effector attitudes $\mathbf{Q}_k$ are reachable, with respect to our three evaluation criteria and for every displacement in translation inside the CDPM workspace. If one wishes a more refined discretization of $\mathcal{W}_{p,r}$, it is possible to do so by adjusting the value q accordingly. However, one must be aware that the required computation time to evaluate a single iteration of the synthesis program would be consequently increased. Then, as per the multi-start method, we chose to start our synthesis algorithm from $ms = 14$ initial guesses $\mathbf{v}_{\iota,0}$, $\iota = 1, \ldots, ms$, for the first example and from $ms = 100$ for the second one.

4.3.1 An Arbitrary Seven-Cable Nine-Edge Six-DoF Cable-Driven Parallel Mechanism

As a first numerical application of the proposed synthesis program, we decided to tackle the design of a generic spatial CDPM. In fact, suppose we seek a spatial seven-cable nine-edge six-DoF CDPM whose WCW must contain a three-dimensional prescribed box $\mathcal{W}_{p,t}$ within a given range of orientations $\mathcal{W}_{p,r}$.

Here, we choose

$$\mathcal{W}_{p,t} \equiv \mathbf{p} \in \begin{bmatrix} (0.4)\mathbf{1}_3 & (0.6)\mathbf{1}_3 \end{bmatrix} \text{ (m)}, \tag{4.76}$$

and,

$$\mathcal{W}_{p,r} \equiv \boldsymbol{\theta} \in \begin{bmatrix} \frac{-\pi}{12}\mathbf{1}_3 & \frac{\pi}{12}\mathbf{1}_3 \end{bmatrix} \text{ (rad)}, \tag{4.77}$$

where $\boldsymbol{\theta} \equiv \begin{bmatrix} \theta_x & \theta_{y^{\mathrm{I}}} & \theta_{z^{\mathrm{II}}} \end{bmatrix}^T$ represents the XYZ Euler angles.

The number of cables is set to seven, which is the minimum required for a COWCW to exist. The geometry of the CDPM is constrained inside the following bounds:

$$\underline{\mathbf{a}} = \mathbf{0}_{3m} \quad \text{and} \quad \overline{\mathbf{a}} = \mathbf{1}_{3m} \text{ (m)}, \tag{4.78}$$

and,

$$\underline{\mathbf{b}}^{\mathcal{B}} = (-0.1)\mathbf{1}_{3m} \quad \text{and} \quad \overline{\mathbf{b}}^{\mathcal{B}} = (0.1)\mathbf{1}_{3m} \text{ (m)}. \tag{4.79}$$

Moreover, the number of degrees of freedom is naturally set to $n = 6$, the number of end-effector orientations $\mathbf{Q}_k$ used to span $\mathcal{W}_{p,r}$ is set by default to $q = 9$, the number of assessment points to ensure that $\mathcal{W}_e \subseteq$ COWCW is chosen to be $nb = 14$ as specified in Sub-section 4.2.2 and the number of edges defining the wire-frame model of its end effector is chosen to be $f = 9$ (see Fig. 4.3 for an illustration of a CDPM with the chosen end-effector geometry). Table 4.1 presents the coordinates of the starting and ending points of each edge.

The reference position $\mathbf{p}_0$ of point P on the CDPM end-effector is set to the centroid of $\mathcal{W}_{p,t}$, i.e., $\mathbf{p}_0 \equiv (0.5)\mathbf{1}_3$ (m). Similarly, the reference orientation $\mathbf{Q}_0$ of the frame $\mathcal{B}$ attached to the end effector is set to the centroid of $\mathcal{W}_{p,r}$, i.e., $\mathbf{Q}_0 \equiv \mathbf{1}_{3\times 3}$.

As for the adjustable parameters of the dimensional synthesis program, we set the maximum number of allowed iterations for each trial to $mr = 5\ 000$ and, as previously mentioned, the maximum number of trials to $ms = 14$, which is the total number of initial solutions chosen for the multi-start method. Obviously, ms could be set to a higher number so as to better span the domain of solutions, but in order to limit the computational time required to complete this synthesis program, we decided to limit ms to 14, which can be normally computed within

Table 4.1 – Coordinates of the starting and ending points of the set of edges that form the geometry attached to the CDPM's end-effector of the first example.

Edge	$\mathbf{e}_{o,s}^{\mathcal{B}}$			$\mathbf{e}_{o,t}^{\mathcal{B}}$		
	$x\ (m)$	$y\ (m)$	$z\ (m)$	$x\ (m)$	$y\ (m)$	$z\ (m)$
1	0.00	−0.15	0.00	0.00	0.00	0.05
2	−0.05	0.05	0.00	0.00	0.00	0.05
3	0.05	0.05	0.00	0.00	0.00	0.05
4	0.00	−0.15	0.00	−0.05	0.05	0.00
5	0.00	−0.15	0.00	0.05	0.05	0.00
6	−0.05	0.05	0.00	0.05	0.05	0.00
7	0.00	−0.15	0.00	0.00	0.00	−0.15
8	−0.05	0.05	0.00	0.00	0.00	−0.15
9	0.05	0.05	0.00	0.00	0.00	−0.15

a few days, using a standard PC equipped with an Intel® Quad-Core™ i7−2600 CPU running at 3.4 GHz. It should be noted that the first thirteen guesses follow the method described above, i.e., they are formed by improving a random selection of the initial geometries. The last initial guess, the fourteenth, is rather formed from the designer's intuition. In addition, the interior-point algorithm of MATLAB® allows for the adjustment of two optional parameters when applied to problems with a large number of variables. These optional parameters, when properly tuned, alleviate numerical problems associated with variables of completely different scales. The first option is called `InitBarrierParam` and it is fixed to 0.15 (default value: 0.1) and the second is `InitTrustRegionRadius` and it is set to $\sqrt{2\ 000}$ (default value: $\sqrt{v}$, where v is the number of variables, and in this example, $v = 3\ 424$). It is normally suggested to respectively increase and decrease these parameters in order to improve the efficiency of the algorithm in cases like ours [201].

Table 4.2 presents the summary of the fourteen potential solutions generated by our dimensional synthesis program. It can be observed, for each ι^{th} trial, the negative value of the final objective function $f(\mathbf{v}_{\iota,f})$, which is equivalent to $\kappa_{\iota,f}$, the number of iterations and the time required to solve the optimization program as well as the message indicating the reason why it stopped. The reader should note that the entire set of optimizations has been completed in less than 24 hours (23.42 hours).

For this example, the best result—the global minimum over the fourteen local minima—belongs to Trial 14, which is marked by a star in Tab. 4.2. This result reports a CDPM's geometry with a three-dimensional workspace in translation that can be illustrated by an ellipsoid $\mathcal{W}_e$ with $\kappa = 1.5192$ (see Eq. (4.2)). Our synthesis program ensures us that at least fourteen strategically distributed points lying on this ellipsoid surface are included in the

Table 4.2 – Summary of the results obtained from the dimensional synthesis of a seven-cable nine-edge six-DoF CDPM.

Trial ι	$\kappa_{\iota,f} = -f(\mathbf{v}_{\iota,f})$	Iterations	Time (s)	Stop Message
1	0.4798	966	3 875.6	Local minimum found
2	0.7679	1 249	5 089.8	Local minimum found
3	0.4657	382	1 498.5	Local minimum found
4	0.3240	1 148	4 935.6	Local minimum found
5	1.0306	2 644	8 475.1	Local minimum found
6	0.6066	456	1 686.2	Local minimum found
7	0.6063	746	3 092.0	Local minimum found
8	0.6468	3 456	8 646.8	Local minimum found
9	1.4468	929	4 059.6	Local minimum found
10	1.4430	2 056	8 568.8	Local minimum found
11	0.5408	5 000	18 137.0	Maximum iterations reached
12	1.4457	2 751	10 567.0	Local minimum found
13	1.3924	769	3 722.3	Local minimum found
14 ($\star$)	1.5192	458	1 961.1	Local minimum found

CDPM WCW, at least for nine different end-effector orientations $\mathbf{Q}_k$. We also know that, for each $\mathbf{Q}_k$, this workspace is free of any cable-cable and cable-edge interferences.

In order to demonstrate the practicability of our dimensional synthesis program, the following analysis will be mainly focused on the best solution $\mathbf{v}^\star$, from Trial 14, even if any trial could have been used for this purpose. First, consider Fig. 4.6a, which illustrates the evolution of the objective function $f(\mathbf{v}_{14})$ with its corresponding step size, namely, the length of each displacement in $\mathbf{v}$. In Fig. 4.6b, for comparison, the same results are shown but for Trial 9, which also generated an interesting final value of the objective function. It is observed here that both graphics of the objective function start from $f(\mathbf{v}_0) = 0$ and then gradually decrease until it reaches a local minimum—remember that we aim at minimizing $-\kappa$ as stated in Eq. (4.50). In general, as it can be seen in Tab. 4.2, a random initial solution requires more iterations in order to be transformed in a "good" solution, i.e., with a final $\kappa \geq 1$ (see Trials 5, 9, 10, 12 and 13 in comparison with Trial 14). From Fig. 4.6, we notice that slightly more than twice the number of iterations are required to optimize the modified random-selected initial geometry of Trial 9 in comparison to the designer-reflected initial solution of Trial 14. Also, as it can be expected, the step size value decreases as the optimization progresses in both cases, since both converge to a local optimum. It should be noted that, in general, a step size that does not decrease is the sign of an unsuccessful optimization.

In Fig. 4.7, we then show the difference between the WCWs of the initial and final CDPM

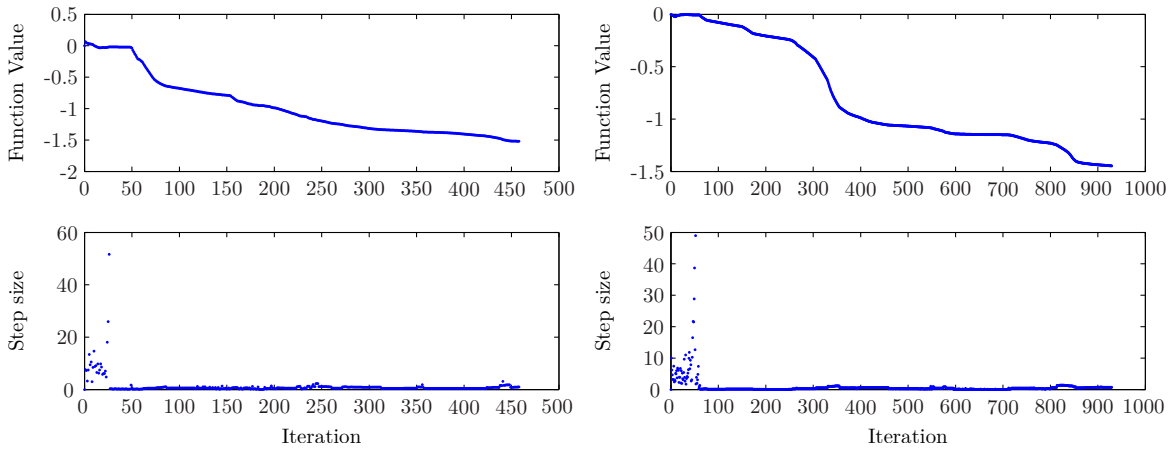

(a) Trial 14 ($\kappa_{14,f} = 1.5192$) (b) Trial 9 ($\kappa_{9,f} = 1.4468$)

Figure 4.6 – Evolution of the objective function and step size values corresponding to the optimization performed in the fourteenth and ninth trials of the first example.

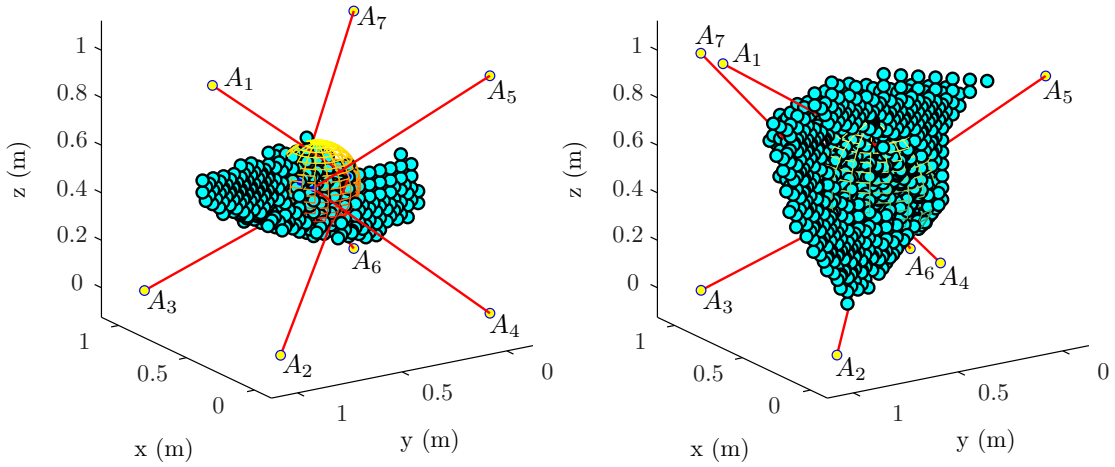

(a) Initial WCW and prescribed ellipsoid (b) Final WCW and final ellipsoid

Figure 4.7 – Comparison of the results obtained from the initial and the final CDPM's geometries (Trial 14).

geometries corresponding to Trial 14. Figure 4.7a also contains the ellipsoid representing the prescribed workspace in translation $\mathcal{W}_e$ with $\kappa = 1$ while Fig. 4.7b contains the final ellipsoid with $\kappa^\star = 1.5192$. Even if the initial CDPM geometry of Trial 14 was devised from the designer's intuition, its WCW does not fully cover the prescribed ellipsoid for all of the nine chosen end-effector orientations $\mathbf{Q}_k$. On the other hand, the final ellipsoid is covered by the WCW of the final CDPM geometry, at least at the fourteen strategically-selected points on the ellipsoid surface and for the given set of $\mathbf{Q}_k$. Figure 4.8 shows, from three different views of the final ellipsoid with its corresponding WCW, which demonstrates that $\mathcal{W}_e \subseteq$ WCW. From Figs. 4.7b and 4.8, it is clear that the final ellipsoid surface is limited by the WCW boundary.

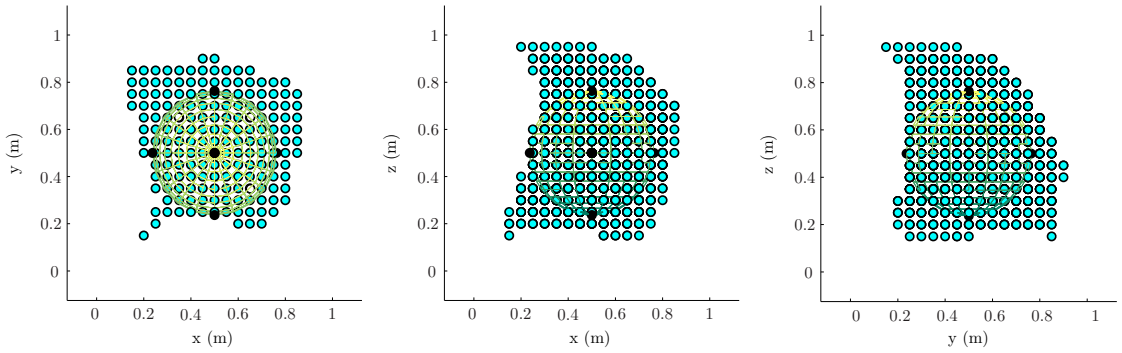

(a) An XY view (b) An XZ view (c) An YZ view

Figure 4.8 – Demonstration of the coverage of the final geometry's ellipsoid by its corresponding WCW (Trial 14).

Now that we demonstrated that the WCW of the final CDPM geometry is indeed a constraining criterion for the evolution of the resulting ellipsoid, the same analysis needs to be performed in the case of the mechanical interferences between the moving parts of the CDPM. Figures 4.9 and 4.10 show the mechanical interference regions for every cable pair and for every cable-edge pair, respectively, in the case of the initial geometry of Trial 14, and for the nine chosen attitudes $\mathbf{Q}_k$. Similarly, Figs. 4.11 and 4.12 show the mechanical interference regions for every cable pair and for every cable-edge pair, respectively, in the case of the final geometry of Trial 14, for the nine chosen attitudes $\mathbf{Q}_k$.

From these figures, however, it is hard to assess whether the dimensional synthesis program has increased the size of the interference-free workspace of the evaluated CDPM. In order to prove that it did undoubtedly, we decided to illustrate the evolution of all pairs of cables $\{i, j\}$ that constrain the expansion of the interference-free workspace, from the initial to the final CDPM geometry of Trial 14. We also did the same exercise for all cable-edge pairs.

First, Figs. 4.13 to 4.16 compare the four combinations of two cables at specific orientation that either cross or limit the prescribed ellipsoid—initial geometry—or the resulting ellipsoid—final geometry. In Fig. 4.13a, it can be observed that the plane $\mathcal{P}_{24}$, which supports the two interference regions ($\mathcal{C}_{24}^-$ and $\mathcal{C}_{24}^+$) corresponding to a mechanical interference between cables 2 and 4, slightly crosses the prescribed ellipsoid for the initial CDPM geometry of Trial 14. Once the optimization of this CDPM geometry is completed, it is apparent from Fig. 4.13b that the corresponding interference regions no longer limit the motion of the final CDPM within its workspace. In Fig. 4.14, we see that the interference region $\mathcal{C}_{36}^-$ cuts the prescribed ellipsoid with the initial geometry while $\mathcal{C}_{36}^+$ acts as a limitating region plane for the final CDPM. Then, with Figs. 4.15 and 4.16, a similar phenomenon occurs: the interference regions supported by planes $\mathcal{P}_{15}$ and $\mathcal{P}_{16}$ do not interfere with the prescribed ellipsoid but they constrain the optimized ellipsoid of the final CDPM geometry (see $\mathcal{C}_{15}^+$ and $\mathcal{C}_{16}^-$).

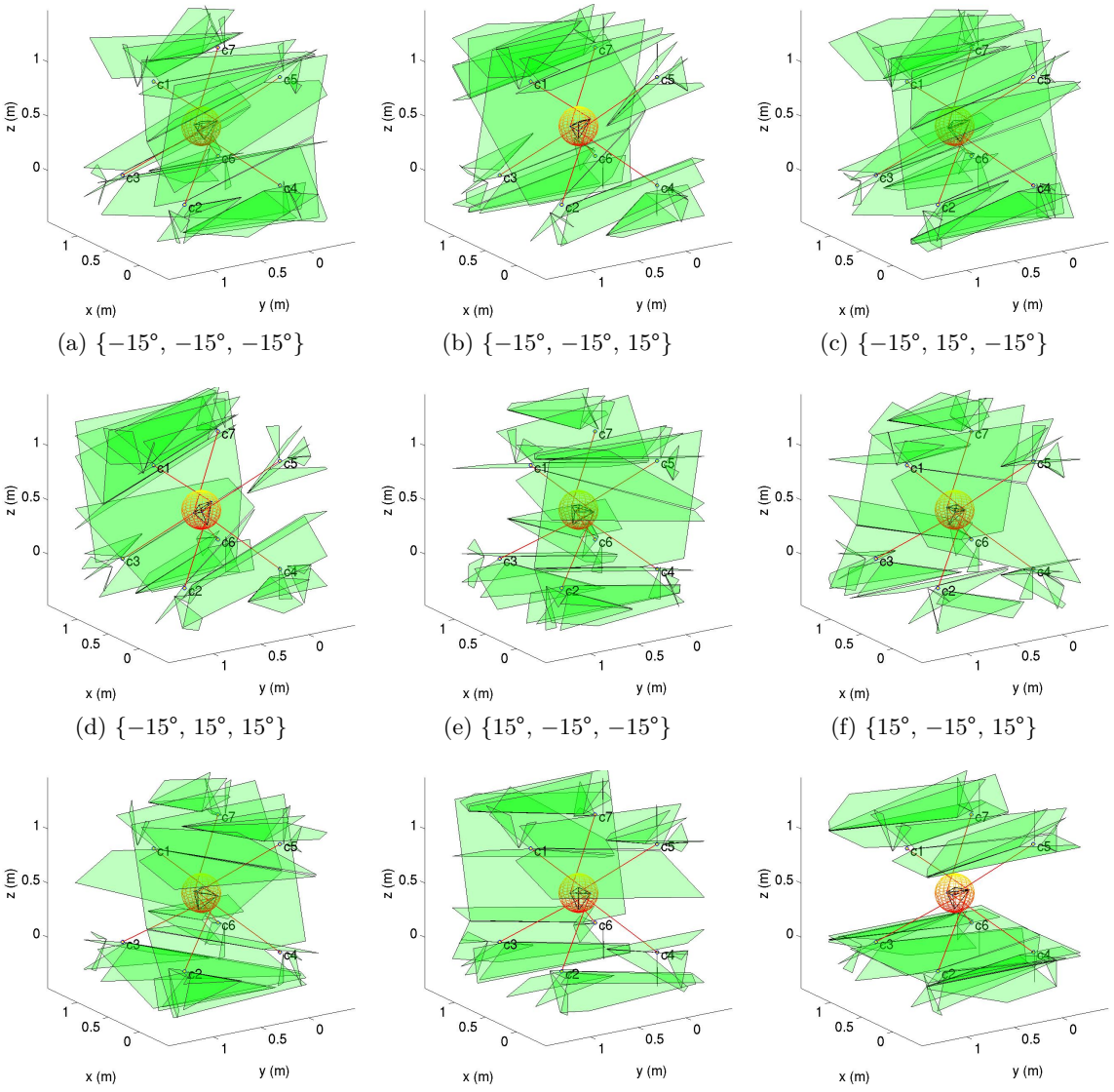

(a) $\{-15°, -15°, -15°\}$ (b) $\{-15°, -15°, 15°\}$ (c) $\{-15°, 15°, -15°\}$

(d) $\{-15°, 15°, 15°\}$ (e) $\{15°, -15°, -15°\}$ (f) $\{15°, -15°, 15°\}$

(g) $\{15°, 15°, -15°\}$ (h) $\{15°, 15°, 15°\}$ (i) $\{0°, 0°, 0°\}$

Figure 4.9 – Mechanical interference regions between two cables for the nine chosen attitudes $\{\theta_x, \theta_{y^{\mathrm{I}}}, \theta_{z^{\mathrm{II}}}\}$ of the end effector of the initial seven-cable nine-edge six-DoF CDPM.

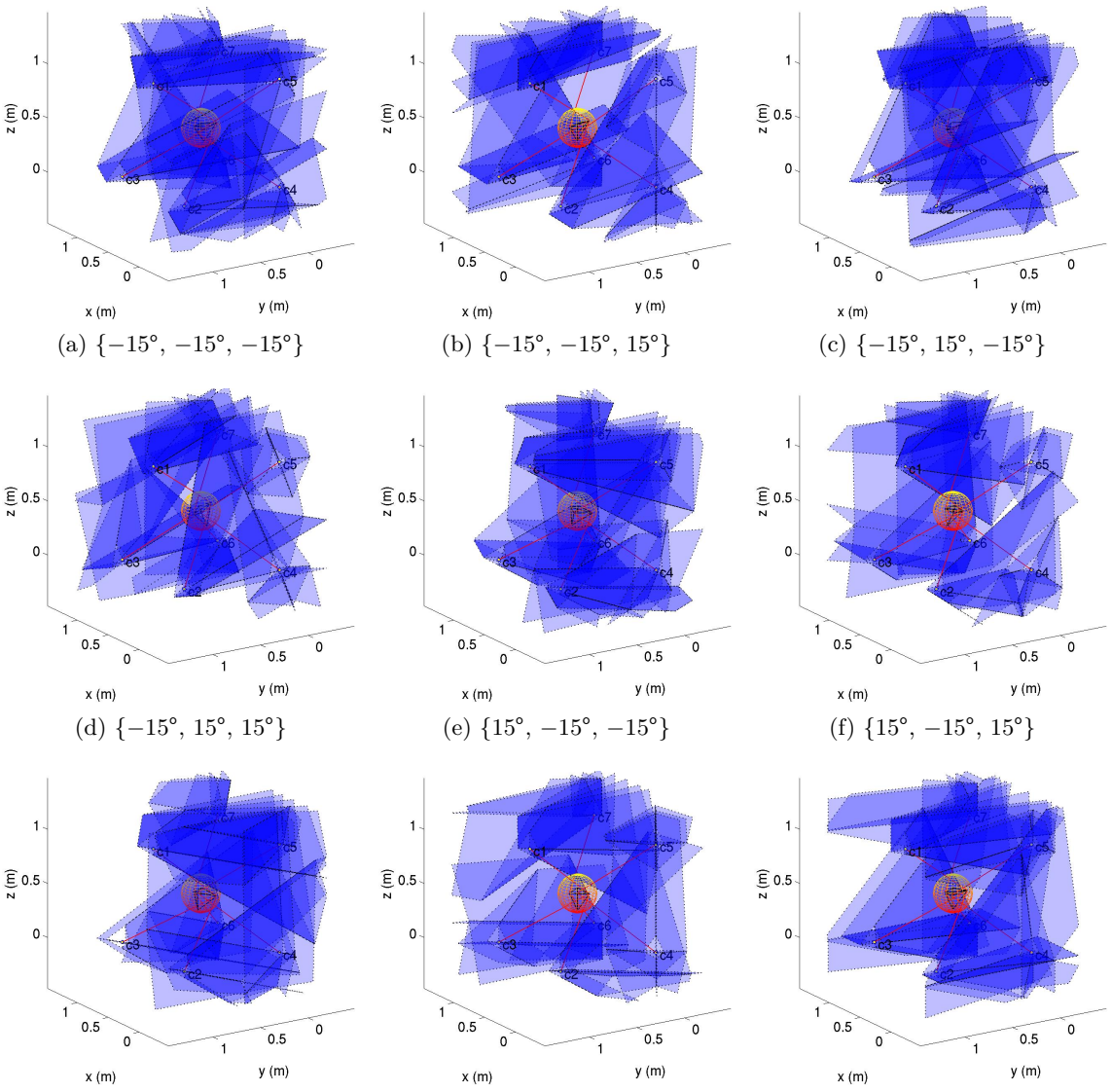

(a) $\{-15°, -15°, -15°\}$ (b) $\{-15°, -15°, 15°\}$ (c) $\{-15°, 15°, -15°\}$

(d) $\{-15°, 15°, 15°\}$ (e) $\{15°, -15°, -15°\}$ (f) $\{15°, -15°, 15°\}$

(g) $\{15°, 15°, -15°\}$ (h) $\{15°, 15°, 15°\}$ (i) $\{0°, 0°, 0°\}$

Figure 4.10 – Mechanical interference regions between a cable and an edge for the nine chosen attitudes $\{\theta_x, \theta_{y^{\mathrm{I}}}, \theta_{z^{\mathrm{II}}}\}$ of the end effector of the initial seven-cable nine-edge six-DoF CDPM.

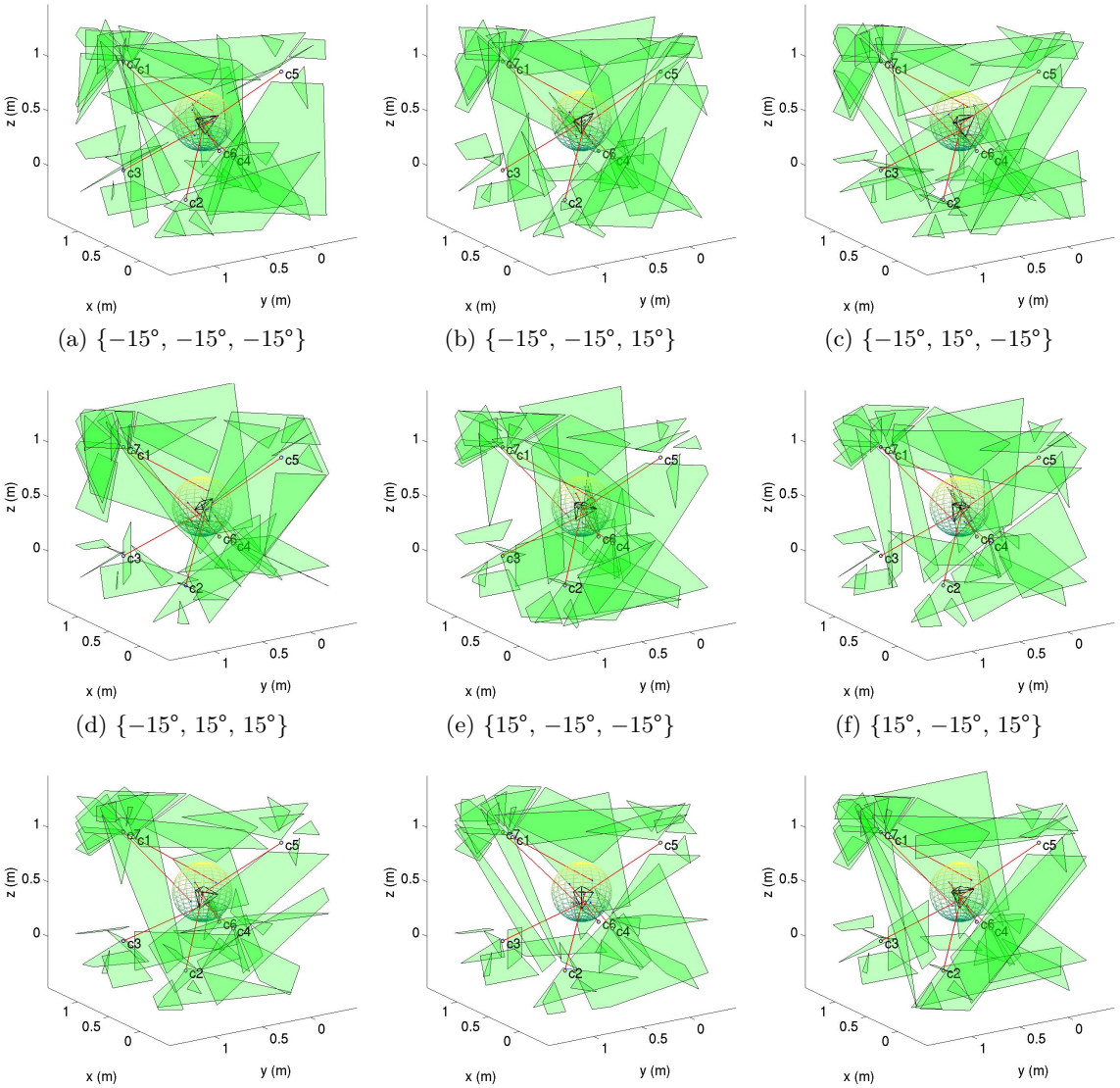

(a) $\{-15°, -15°, -15°\}$ (b) $\{-15°, -15°, 15°\}$ (c) $\{-15°, 15°, -15°\}$

(d) $\{-15°, 15°, 15°\}$ (e) $\{15°, -15°, -15°\}$ (f) $\{15°, -15°, 15°\}$

(g) $\{15°, 15°, -15°\}$ (h) $\{15°, 15°, 15°\}$ (i) $\{0°, 0°, 0°\}$

Figure 4.11 – Mechanical interference regions between two cables for the nine chosen attitudes $\{\theta_x, \theta_{y^{\mathrm{I}}}, \theta_{z^{\mathrm{II}}}\}$ of the end effector of the final seven-cable nine-edge six-DoF CDPM.

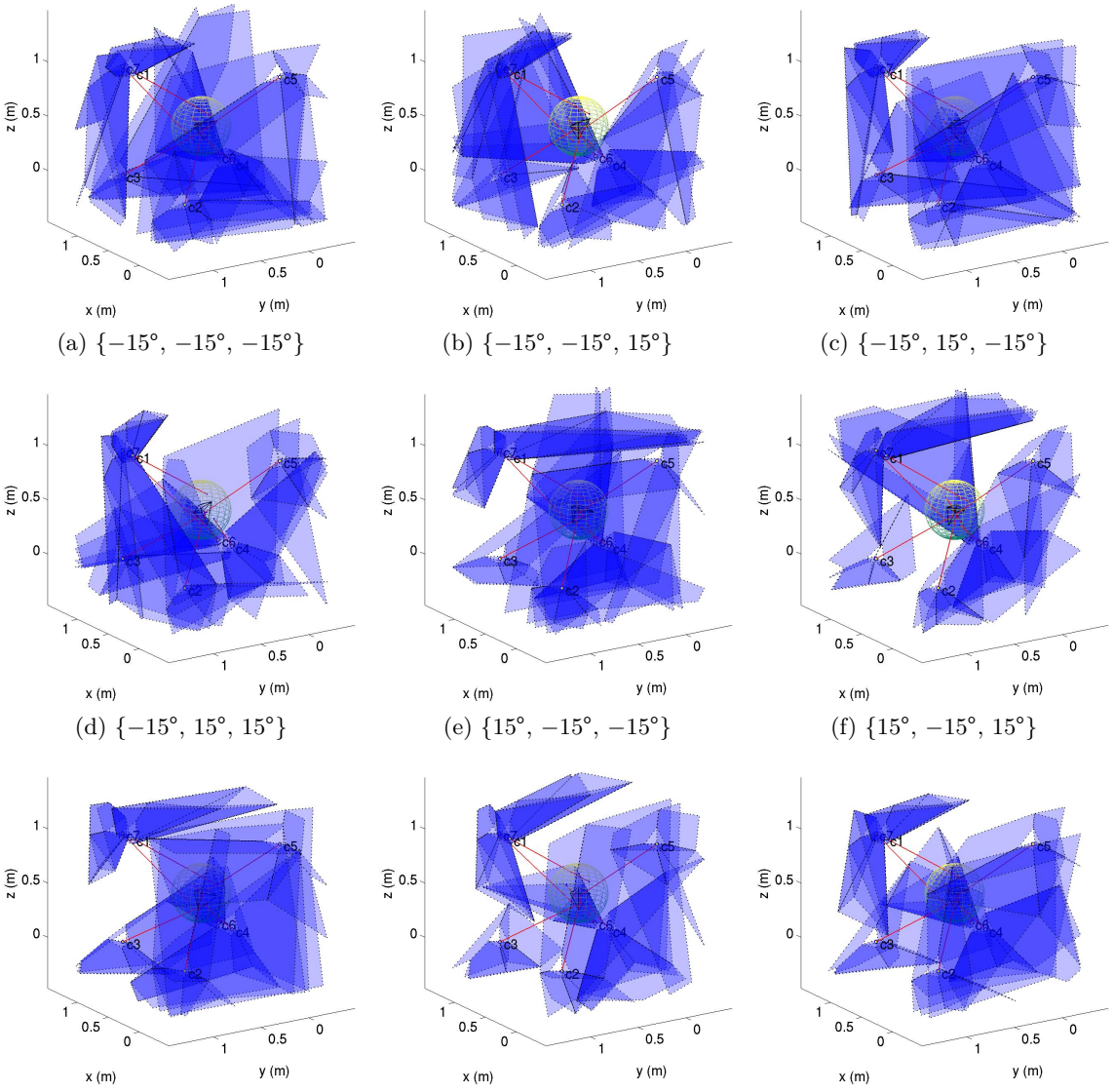

(a) $\{-15°, -15°, -15°\}$ (b) $\{-15°, -15°, 15°\}$ (c) $\{-15°, 15°, -15°\}$

(d) $\{-15°, 15°, 15°\}$ (e) $\{15°, -15°, -15°\}$ (f) $\{15°, -15°, 15°\}$

(g) $\{15°, 15°, -15°\}$ (h) $\{15°, 15°, 15°\}$ (i) $\{0°, 0°, 0°\}$

Figure 4.12 – Mechanical interference regions between a cable and an edge for the nine chosen attitudes $\{\theta_x, \theta_{y^{\mathrm{I}}}, \theta_{z^{\mathrm{II}}}\}$ of the end effector of the final seven-cable nine-edge six-DoF CDPM.

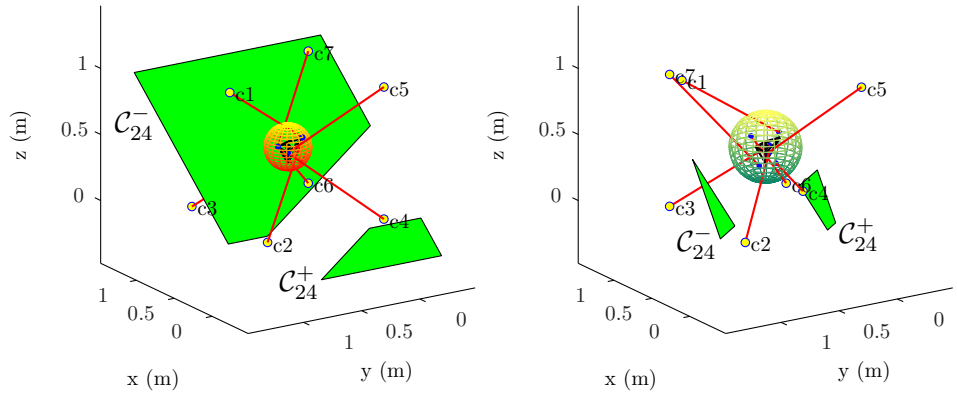

(a) Initial CDPM $\{-15°, -15°, 15°\}$ (b) Final CDPM $\{-15°, -15°, 15°\}$

Figure 4.13 – Evolution of the mechanical interference regions between cable 2 and cable 4 of the seven-cable nine-edge six-DoF CDPM.

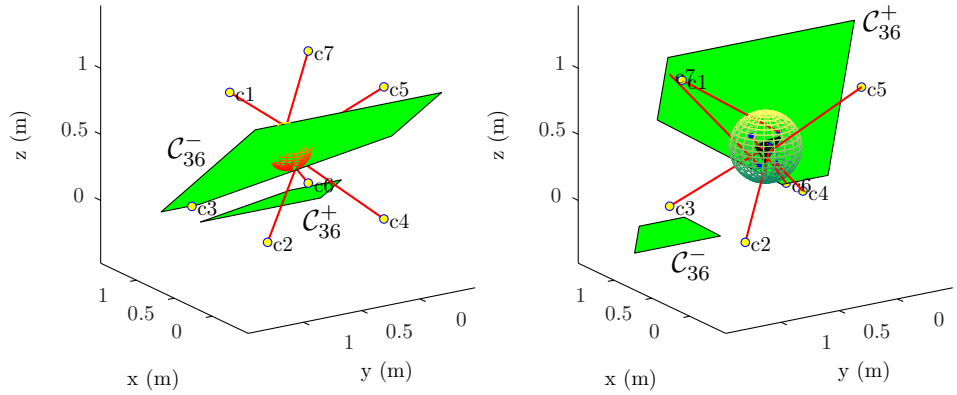

(a) Initial CDPM $\{-15°, 15°, -15°\}$ (b) Final CDPM $\{-15°, -15°, 15°\}$

Figure 4.14 – Evolution of the mechanical interference regions between cable 3 and cable 6 of the seven-cable nine-edge six-DoF CDPM.

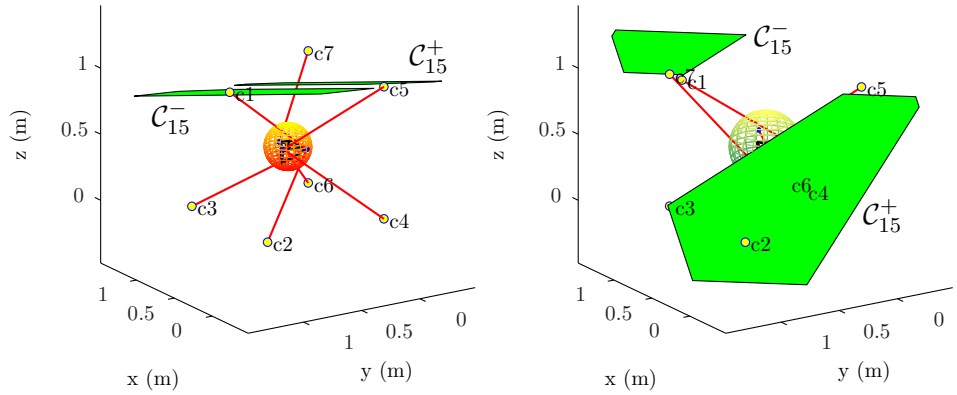

(a) Initial CDPM $\{15°, -15°, -15°\}$ (b) Final CDPM $\{15°, -15°, -15°\}$

Figure 4.15 – Evolution of the mechanical interference regions between cable 1 and cable 5 of the seven-cable nine-edge six-DoF CDPM.

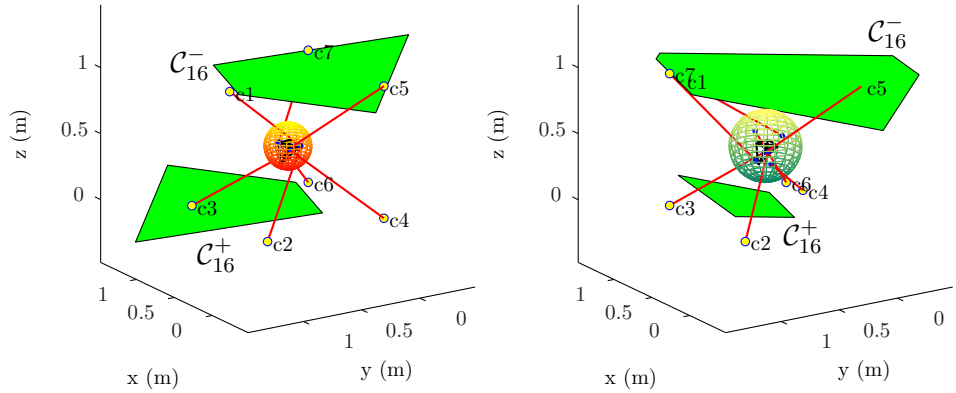

(a) Initial CDPM {15°, −15°, 15°}

(b) Final CDPM {15°, −15°, 15°}

Figure 4.16 – Evolution of the mechanical interference regions between cable 1 and cable 6 of the seven-cable nine-edge six-DoF CDPM.

Likely, the same analysis can be performed for the mechanical interference between a cable and an end-effector edge. For this purpose, Figs. 4.17 to 4.25 show the evolution of all pairs of a cable and an edge that cross or intersect the surface of the prescribed and final ellipsoids. In Figs. 4.17 to 4.23, it can be observed that the interference regions $\mathcal{E}_{11}$, $\mathcal{E}_{11}$, $\mathcal{E}_{12}$, $\mathcal{E}_{12}$, $\mathcal{E}_{13}$, $\mathcal{E}_{13}$, $\mathcal{E}_{39}$, respectively, pass through the prescribed ellipsoid for the initial CDPM geometry and are disjoint from the ellipsoid associated to the final geometry. In Fig. 4.23b, the interference region $\mathcal{E}_{39}$ is far behind the resulting ellipsoid. From Fig. 4.24, it is seen that the interference region $\mathcal{E}_{28}$, which is generated from the contact between the cable 2 and the edge 8, completely intersects the prescribed ellipsoid in Fig. 4.24a and then becomes a limitating plane for the ellipsoid corresponding to the final CDPM geometry in Fig. 4.24b. Finally, from Fig. 4.25, the region of workspace restricted by the interference of cable 4 with edge 7 lies far in front of the prescribed ellipsoid in the initial case and then becomes a limitating plane for the optimized CDPM workspace.

Based on the results and the analysis presented above, we empirically verified that the proposed dimensional synthesis program of Eq. (4.50) seeks and often finds a local minimum representing a compromise between our three criteria, and also that these three criteria are relevant for the synthesis of the geometry of a CDPM. Indeed, it was shown that the WCW and the interference regions associated to the contact between two cables and between a cable and an edge of a CDPM end-effector can all be constraining elements of its reachable workspace. It should be noted by the reader that all the combinations of two moving parts—cable or edge—that were not presented in this particular example did not generate any interference regions restricting the evaluated workspace. This is why they were not displayed in this analysis.

In addition, for the sake of completeness, the Cartesian coordinates of the attachment points of

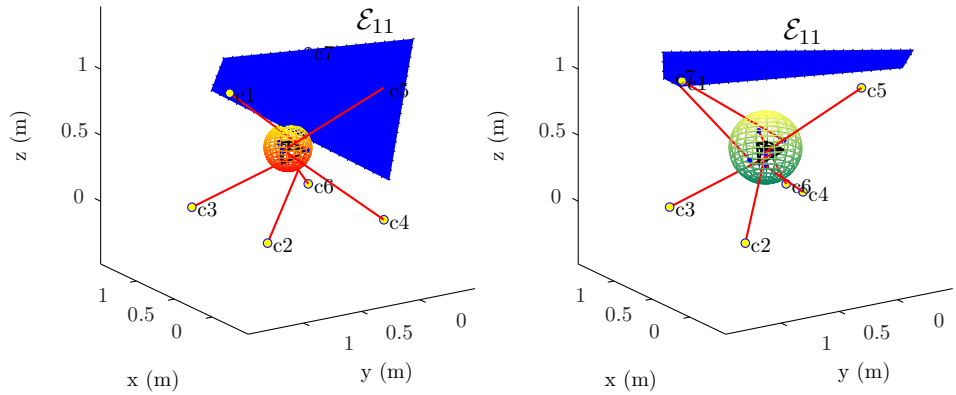

(a) Initial CDPM {15°, −15°, −15°} (b) Final CDPM {15°, −15°, −15°}

Figure 4.17 – Evolution of the mechanical interference regions between cable 1 and edge 1 of the seven-cable nine-edge six-DoF CDPM.

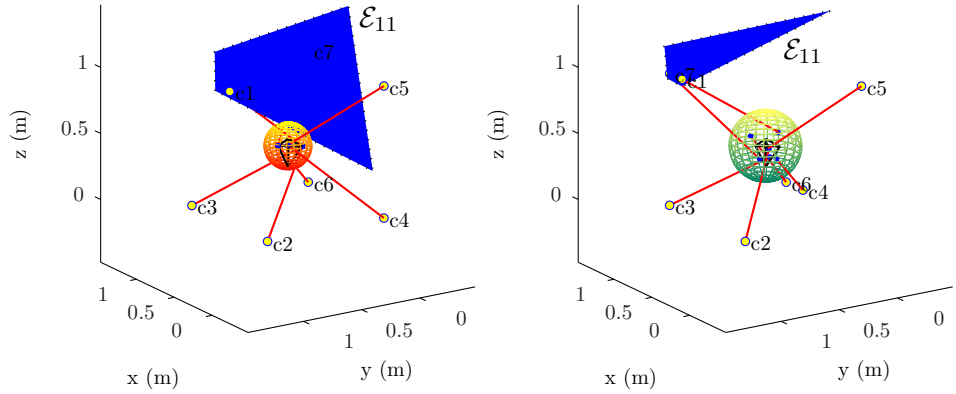

(a) Initial CDPM {15°, 15°, 15°} (b) Final CDPM {15°, 15°, 15°}

Figure 4.18 – Evolution of the mechanical interference regions between cable 1 and edge 1 of the seven-cable nine-edge six-DoF CDPM.

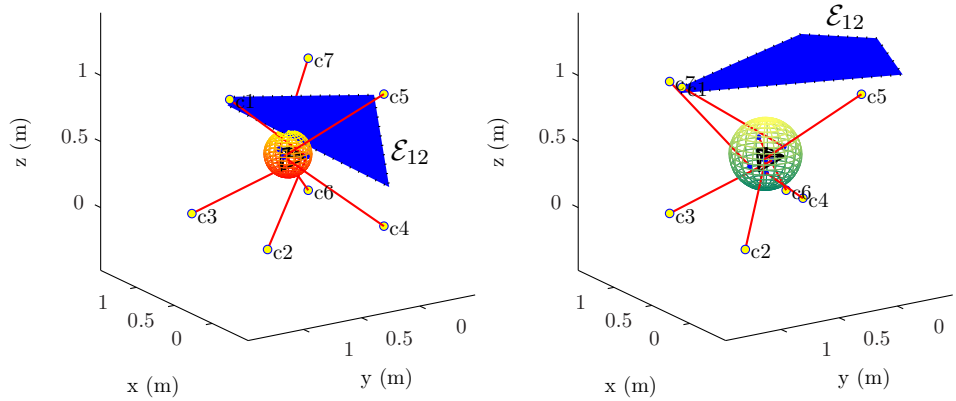

(a) Initial CDPM {15°, −15°, −15°} (b) Final CDPM {15°, −15°, −15°}

Figure 4.19 – Evolution of the mechanical interference regions between cable 1 and edge 2 of the seven-cable nine-edge six-DoF CDPM.

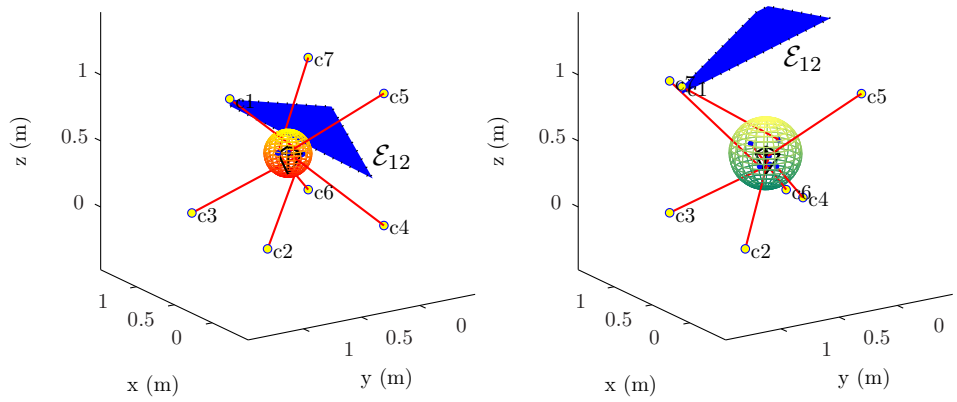

(a) Initial CDPM {15°, 15°, 15°} (b) Final CDPM {15°, 15°, 15°}

Figure 4.20 – Evolution of the mechanical interference regions between cable 1 and edge 2 of the seven-cable nine-edge six-DoF CDPM.

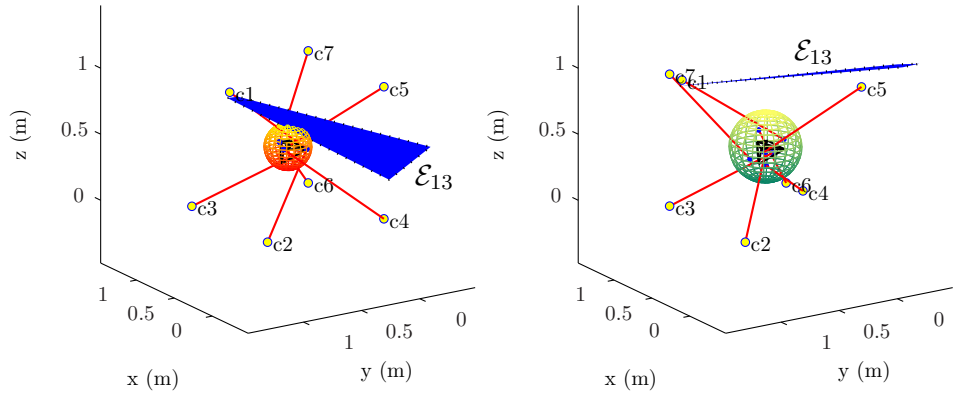

(a) Initial CDPM {15°, −15°, −15°} (b) Final CDPM {15°, −15°, −15°}

Figure 4.21 – Evolution of the mechanical interference regions between cable 1 and edge 3 of the seven-cable nine-edge six-DoF CDPM.

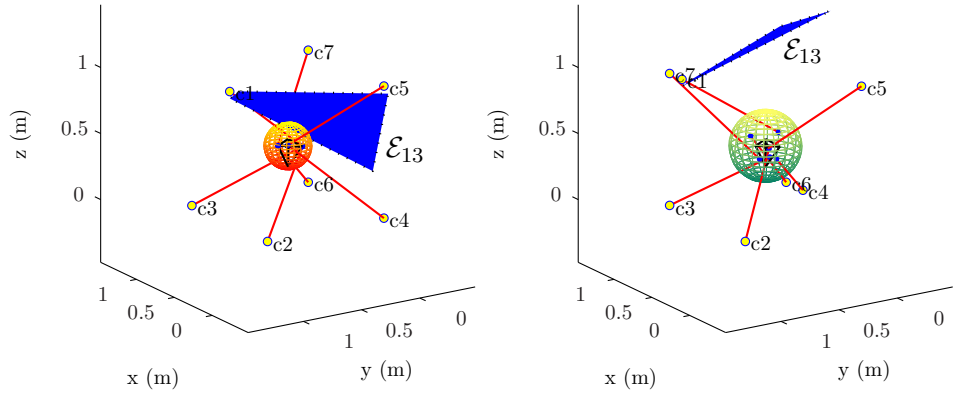

(a) Initial CDPM {15°, 15°, 15°} (b) Final CDPM {15°, 15°, 15°}

Figure 4.22 – Evolution of the mechanical interference regions between cable 1 and edge 3 of the seven-cable nine-edge six-DoF CDPM.

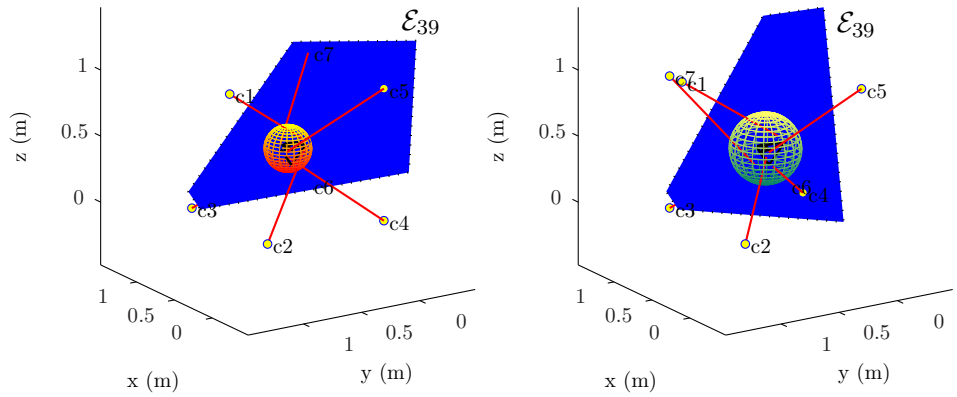

(a) Initial CDPM $\{-15°, -15°, -15°\}$ (b) Final CDPM $\{-15°, -15°, -15°\}$

Figure 4.23 – Evolution of the mechanical interference regions between cable 3 and edge 9 of the seven-cable nine-edge six-DoF CDPM.

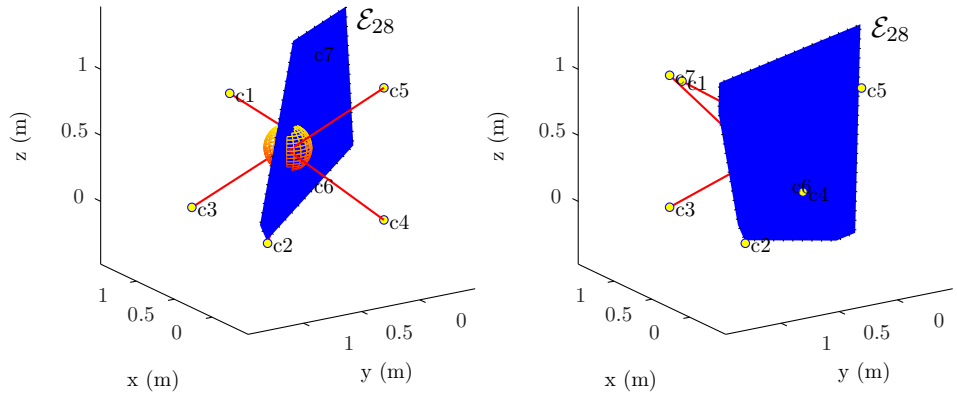

(a) Initial CDPM $\{-15°, 15°, 15°\}$ (b) Final CDPM $\{-15°, 15°, 15°\}$

Figure 4.24 – Evolution of the mechanical interference regions between cable 2 and edge 8 of the seven-cable nine-edge six-DoF CDPM.

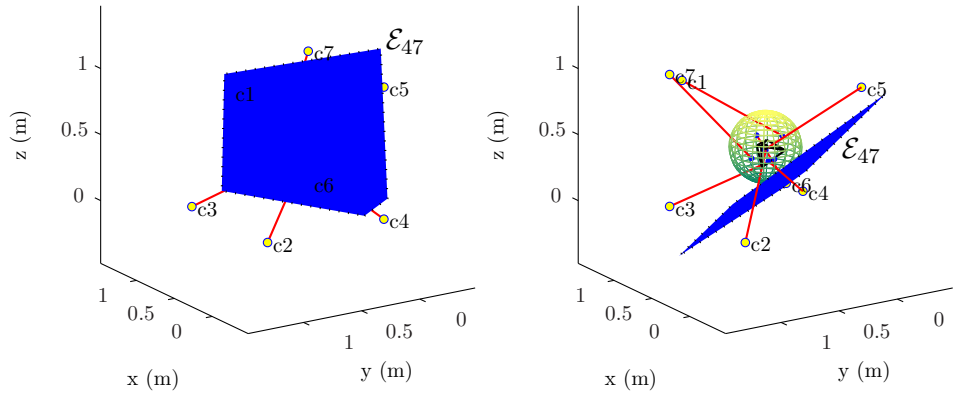

(a) Initial CDPM $\{15°, 15°, -15°\}$ (b) Final CDPM $\{15°, 15°, -15°\}$

Figure 4.25 – Evolution of the mechanical interference regions between cable 4 and edge 7 of the seven-cable nine-edge six-DoF CDPM.

the randomly-generated, closest-feasible initial and final architectures for all fourteen trials are presented in Appendix D.1. Furthermore, a graphical representation of the initial geometry, the final geometry and the final one with its WCW are included. Over the fourteen trials, six are deemed successful, since their final $\kappa \geq 1$ (Trials 5, 9, 10, 12, 13 and 14). For these optimizations, three additional graphics following three different views (XY, XZ, and YZ) are added in Appendix D.1 in order to facilitate the analysis of their final CDPM geometry.

It is indeed interesting to analyze these six local minima in order to detect any tendency in the positioning of their attachment points $\mathbf{a}_i$ and $\mathbf{b}_i^{\mathcal{B}}$, $i = 1, \ldots, m$. In general, it is noticed that, from the initial to the final positioning of points $\mathbf{a}_i$ on the base frame, the optimization program tends to expand the volume occupied by these attachment points until they approach a limit (either $\underline{\mathbf{a}}$ or $\overline{\mathbf{a}}$) for one, two or all of their Cartesian coordinates. This behaviour is easily explained by the need to increase the reachable workspace of the CDPM. Indeed, the higher the ratio between the volume of the base and the end effector, the larger the reachable workspace in translation. Regarding the positioning of the points $\mathbf{b}_i^{\mathcal{B}}$, it is generally observed that, for at least one coordinate direction, the attachment points on the end effector are on the opposite side of the axis compared to their counterpart on the base. This is also a relevant behaviour since it normally allows to increase the range of rotation of the CDPM's end-effector along the corresponding axis. From our results, no new specific pattern seems to be exactly reproduced from one trial to the other but it is clear that the optimization program tends to find the best compromise between the minimization of the volume occupied by the CDPM's end-effector to increase its workspace in translation and the maximization of the cables crossing to increase its workspace in rotation, while minimizing the mechanical interferences among its cables themselves and between these cables and the end-effector edges.

It should also be noted that, based on the different results obtained during this work, having two coincident attachment points does not seem desirable for the design of all CDPMs. This seems contradictory with common practice, where coinciding attachment points are often seen as a simple and efficient way to avoid mechanical interferences. We observed here that this geometric characteristic has rarely been generated within the final solutions since it is, in general, better to have crossed cables in order to increase the WCW of a CDPM, at least when the prescribed workspace in rotation is relatively large and no additional interferences are consequently introduced.

Finally, from the best result $\kappa^\star = 1.5192$, it is clear that the CDPM's requirements of this first example could have been slightly more demanding since the threshold to fulfill these requirements is $\kappa \geq 1$. Either the range of the CDPM end-effector orientations $\mathcal{W}_{p,r}$ or the range of the end-effector positions $\mathcal{W}_{p,t}$, or both, could have been increased. In this way, the next example proposes a more constraining and realistic application for our dimensional synthesis program.

(a) a double-donut configuration (b) a C-shaped configuration (c) a cylindrical configuration

Figure 4.26 – The three different types of available MRI devices.

4.3.2 An Eight-Cable Seventeen-Edge Six-DoF Cable-Driven Pantograph Intended for a Medical Application

The example presented in this sub-section corresponds to the envisioned application that initially led to the concept of cable-driven pantographs, which is described in the Introduction of the thesis. This application requires to manipulate needles inside an MRI scanner in order to perform image-guided punctions or simple biopsies on patients.

From the three different types of magnetic resonance imagers available, the standard cylindrical MRI system is the one that best suits this application, since it normally provides the highest image quality. This is attributed to its strong MR signal (in general, from 1.5 to 3 teslas) and its field homogeneity. The C-shaped and double-donut configurations, on the other hand, normally produce electro-magnetic fields with magnitudes below 1 tesla. These two last imaging devices offer however the best accessibility to the patient while cylindrical models present a much confined space around the patient, leaving little room for a robotic system to perform medical interventions, as it can be seen in Fig. 4.26. The closed bore of the cylindrical MRI scanner represents severely restrictive geometric constraints that must be taken into account when developing a mechanism for magnetic-resonance-guided percutaneous—through the skin—interventions such as biopsies, drainage, and insertion of energetic probes for tumour ablation.

From the literature, there are specific design criteria, in addition to geometric constraints, that must be taken into account when developing a medical robotic system to be used inside a MRI device. The FDA has published in 1997 a draft guidance on safety and compatibility recommendations between MRI scanners and other medical devices [295]. Thence, two different levels of compatibility must be followed. The first one is that the designed mechanism must be *MR-safe*. A MR-safe system is one that presents no additional risk to the patient when used in the MR environment, but that may affect the quality of the diagnostic information. The second one is that the mechanism must be *MR-compatible*. This term means that the device, when used in the MR environment, is MR-safe, and has been demonstrated to neither

significantly affect the quality of the diagnostic information nor have its operations affected by the MRI scanner.

From a more practical standpoint, these necessary qualities for a mechanism to be compatible with MRI scanners are obtained by a proper selection of materials, actuators and sensors. More specifically, materials must be non-magnetic and non-conductive, as are titanium, plastic, ceramic, fibreglass and carbon fibre [296]. Actuators installed inside the MRI device must be designed from pneumatic, hydraulic or ultrasonic technologies and sensors must be of the optical type [297]. In general, all conventional electric motors working from electromagnets are proscribed as well as conventional electrical sensors. Sometimes, such devices can be installed outside of the scanner room or at least physically isolated from the MRI electromagnetic field using Faraday cages.

As previously discussed, another design limitation is that the major parts or the entire slave mechanism must fit inside the limited available space constrained by the dimensions of the bore of the standard cylindrical MRI scanner. This workspace is even more limited by the presence of the patient, with whom no mechanical contact unwarranted by the intervention can be tolerated in order to be MR-safe [298, 299].

Over the past twenty years, several groups of researchers have worked on the design of MR-compatible systems to perform image-guided interventions on patients directly from the centre of standard cylindrical MRI scanners. One of the first published work in the field of MRI-compatible interventional robotics is that of Masumane *et al.*, who designed a six-DoF manipulator actuated with ultrasonic motors and dedicated to stereotactic[7] neurosurgical applications [301]. Early in 2000, a Canadian team has developed a MR-compatible haptic-enabled master-slave system that has eight-DoF (including tool actuation) intended to perform image-guided micro-neurosurgical tasks [27, 28]. This device is based on the well-known SCARA architecture in order to reduce the number of joints affected by the gravity and thereby improve its positional accuracy. Its main structural components are made of titanium and polyetheretherketone plastic (PEEK). Other projects have been reported for human neurological studies, e.g., the design of a spherical two-DoF haptic-interface device made entirely from polymers and suitable for use within a MR environment [302], a planar two-DoF manipulandum actuated by ultrasonic motors to perform studies on finger movements [45], a planar two-DoF master-slave haptic interface to investigate the human neural control of arm movements based on a hydrostatic transmission [194]. Two comparable haptic interface devices, one with hydrodynamic and another with pneumatic actuation, were developed to control one-DoF translational movements of a user performing functional magnetic resonance imaging (fMRI)[8] tasks [304].

[7]Stereotactic: involving, being, utilizing, or used in a surgical technique for precisely directing the tip of a delicate instrument (as a needle) or beam of radiation in three planes using coordinates provided by medical imaging in order to reach a specific locus in the body [300].

[8]Functional magnetic resonance imaging or functional MRI (fMRI) is a functional neuro-imaging procedure

Similarly to the research cited above, medical interventions such as biopsy, puncture and placement of radioactive seeds (brachytherapy) may also take advantage from the combination of imaging technologies such as MRI scanners and robotics. For example, Taillant *et al.* have developed a five-DoF pneumatically-actuated robotic architecture to perform abdominal image-guided puncture interventions within the bore of a closed MRI scanner [305]. Another group has worked on the design of a fully automated image-guided seed injector for brachytherapy interventions [306, 307]. This system has five-DoF, is pneumatically driven and optical sensors provide position feedback to ensure its MR compatibility. Another project, from Fischer *et al.*, proposes the design of a six-DoF robotic assistant to accurately target planned tissue sites. The purpose of the device is to minimize needle misplacement effects for transperineal[9] prostate interventions such as the positioning of the needle in image-guided biopsies [308, 309]. This system is actuated by MR-compatible pneumatic cylinders combined with optical encoders, while the needle is manually inserted by the physician. Moreover, Melzer *et al.* have designed a five-DoF pneumatically-driven robot attached to a 180 $^\circ$-orbiting ring that is mounted on the patient table of the scanner. This device is meant for various percutaneous interventions inside the MRI gantry [310]. Song *et al.* also used pneumatic actuators to develop a four-DoF MRI-compatible robotic system for MRI-guided transperineal prostate interventions [311]. Christoforou *et al.* and Tsekos *et al.* have developed a seven-DoF remotely controlled manipulator to perform minimally invasive diagnostic and therapeutic interventions in the abdominal and thoracic area with real-time magnetic resonance imaging guidance inside clinical cylindrical scanners [44, 49, 312]. This system is actuated by ultrasonic motors and it is connected to the MR scanner to receive the MR images and send the coordinates of the end effector for dynamic control of the imaged plane.

Chapuis *et al.* have demonstrated in 2007 that plastic or composite cables can transmit forces to the bore of a standard MRI scanner over a distance of several metres in the case of a one-DoF haptic interface [51]. Since then, some groups of researchers have investigated this avenue with a variety of designs. For example, consider the work from Abdelaziz *et al.*, where a two-DoF planar CDPM was proposed to accurately position a needle manually inserted by the physician in prostate cancer cryotherapy under MRI guidance [123, 124, 52, 287]. This MRI-compatible robotic assistant contains optical sensors to measure the cable tensions and conventional electrical motors with rotary encoders are also used since they can be placed outside the MRI room. Another group, Salimi *et al.*, has similarly worked on the design of a four-DoF cable-driven MRI-compatible robotic platform for intracardiac interventions under beating-heart conditions [313, 314]. The primary mission for this manipulator is to safely steer the cardiac catheters inside the left ventricle to reach any desired target points under MRI guidance. The four active joints are also actuated by motors through a cable transmission

using MRI technology that measures brain activity by detecting associated changes in blood flow. This technique relies on the fact that cerebral blood flow and neuronal activation are coupled. When an area of the brain is in use, blood flow to that region also increases [303].

[9] Transperineal is the region of the male body between the scrotum and the rectum.

system in order to place the conventional motors far from the MRI scanner.

On the other hand, some groups have rather worked on purely mechanical devices in order to ensure MR compatibility. For instance, Beyersdorff *et al.* demonstrated the practicability of a purely-mechanical serial device to assist the positioning of a needle. This mechanism, which was made of polyoxymethylene, was designed to perform transrectal biopsies of the prostate under MRI guidance [315]. Another group, Christoforou *et al.*, has also built a manually-actuated system [316, 299]. This device has five degrees of freedom and is designed to perform general minimally-invasive interventions under direct MRI guidance.

In this thesis, as stated in the Introduction, we follow the same direction of these previous work by seeking to develop a purely mechanical six-DoF cable-driven master-slave architecture that would be suitable to perform simple interventions such as abdominal punctures and biopsies under MRI guidance. In this sub-section, however, the focus is pointed on the geometric constraints only, the others—such as MR compatibility—being left to further investigations. Thus, this work aims at determining a suitable geometry for a CDP to perform such a task. To this end, we resort to our previously developed methods to dimensionally synthesize a CDPM—here the slave part of the CDP—that fits inside the bore of a conventional MRI scanner. The workspace $\mathcal{W}$ of the CDPM must be sufficiently large to perform simple medical spatial tasks such as image-guided biopsies while avoiding internal mechanical interferences (between cables and between cables and the end effector).

To do so, we decided to use geometric constraints similar to those established in Refs. [298, 299]. From these papers, typical gantry dimensions for cylindrical MRI devices are $60-70$ cm for the bore diameter and $1.2-2.0$ m for its length. They also provide an analysis of the free space available within the gantry of this type of imager while a patient lays inside the bore. Figure 4.27 shows their results presented in Ref. [299] when using a 60-cm bore gantry. This figure displays the radial distances between a subject of moderate body size (height of 1.65 m, weight of 71 kg, chest periphery of 92 cm and abdominal periphery of 95 cm) and the gantry wall measured on a transverse MR image at the abdominal area.

Based on Fig. 4.27, it is seen that, for a moderate body-size patient, we can in general assume an available workspace of 20 cm, 18 cm and 14 cm along the vertical axis, the oblique axes (45° and -45°) and the horizontal axis, respectively. Notice that all these axes pass through the centre of the 60-cm bore. Our current analysis is based here on a more recent model of cylindrical MRI devices manufactured by Siemens [50]: The MAGNETOM® Skyra three-tesla MRI system (see Fig. 0.10). This three-tesla MR imager presents an increased bore diameter of 70 cm and a length of 1.73 m. From these dimensions, we assume for the design of our CDP a free space over the patient's abdominal wall of 25 cm in the vertical direction, 23 cm in the oblique directions and 19 cm in both horizontal directions. Also, with a length of 1.73 m, we consider that we should be able to place attachment points over a range of at least 1.60 m.

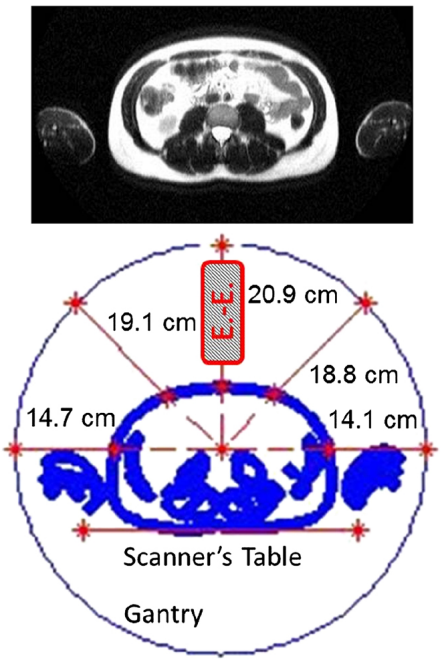

Figure 4.27 – Example of results for a free space analysis on a transverse MR image of the thoracic area of a human subject reported in published literatures.

Figures 4.28 and 4.29 respectively show transverse and longitudinal views of the considered free space with the prescribed workspace of the CDP. We used a patient body size similar to that of ref. [299] in order to determine the space available within the bore of the MRI device. It can also be seen that the prescribed workspace in translation (red boxes in the figures) is

$$\mathcal{W}_{p,t} \equiv \mathbf{p} \in \begin{bmatrix} [-0.085, 0.085] \\ [-0.30, 0.30] \\ [-0.0375, 0.0375] \end{bmatrix} \text{ (m)}. \tag{4.80}$$

Moreover, we assume that the following prescribed workspace in rotation would be sufficient for the intended application:

$$\mathcal{W}_{p,r} \equiv \boldsymbol{\theta} \in \begin{bmatrix} [\frac{-\pi}{12}, \frac{\pi}{12}] \\ [\frac{-\pi}{4}, \frac{\pi}{4}] \\ [\frac{-\pi}{18}, \frac{\pi}{18}] \end{bmatrix} \text{ (rad)}, \tag{4.81}$$

where $\boldsymbol{\theta} \equiv \begin{bmatrix} \theta_x & \theta_{y^{\mathrm{I}}} & \theta_{z^{\mathrm{II}}} \end{bmatrix}^T$ represents the XYZ Euler angles.

The number of cables is set to eight in order to increase the likelihood of the existence of a COWCW. Recall that the minimum number of cables is seven when one desires to perform a six-DoF task at the end effector. The geometry of the CDPM is constrained inside the

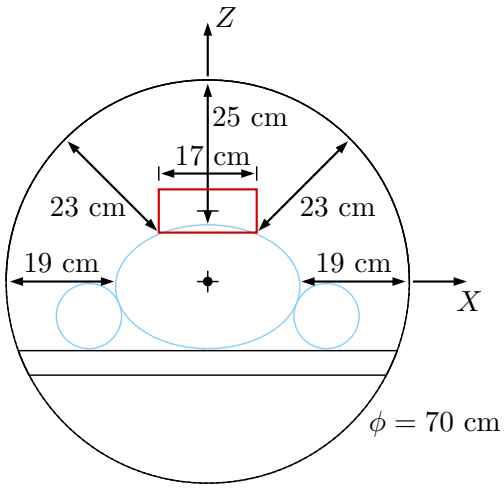

Figure 4.28 – Transverse view of the free space and workspace of the envisioned CDP.

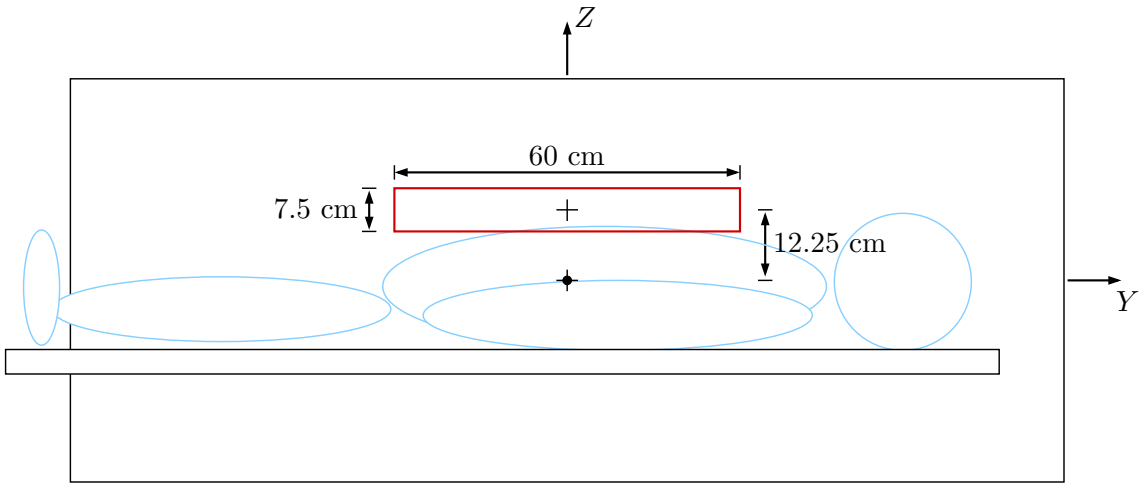

Figure 4.29 – Longitudinal view of the free space and workspace of the envisioned CDP.

following bounds:

$$\underline{\mathbf{a}}_i = \begin{bmatrix} -0.80 \\ -0.35 \\ 0.00 \end{bmatrix} \quad \text{and} \quad \overline{\mathbf{a}}_i = \begin{bmatrix} 0.80 \\ 0.35 \\ 0.35 \end{bmatrix} \text{ (m)}, \tag{4.82}$$

and,

$$\underline{\mathbf{b}}_i^{\mathcal{B}} = \begin{bmatrix} -0.04 \\ -0.04 \\ 0.00 \end{bmatrix} \quad \text{and} \quad \overline{\mathbf{b}}_i^{\mathcal{B}} = \begin{bmatrix} 0.04 \\ 0.04 \\ 0.16 \end{bmatrix} \text{ (m)}. \tag{4.83}$$

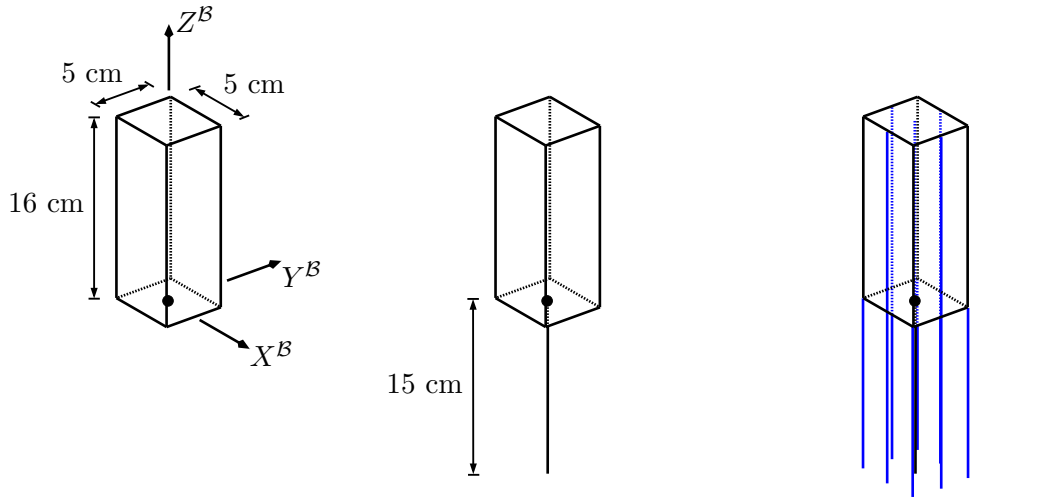

(a) volume dedicated for the slave tool

(b) slave tool with needle fully extended

(c) wire-frame model for synthesis algorithm

Figure 4.30 – Illustration of the CDP's end-effector geometry and its corresponding wire-frame model used for the synthesis optimization.

As for the previous example, the number of degrees of freedom is set to $n = 6$, the number of end-effector orientations $\mathbf{Q}_k$ used to span $\mathcal{W}_{p,r}$ is set by default to $q = 9$ and the number of assessment points to ensure that $\mathcal{W}_e \subseteq$ COWCW is chosen to be $nb = 14$ as specified in Subsection 4.2.2. The number of edges defining the wire-frame model of the end effector is here chosen to be $f = 17$ (see Fig. 4.30 for the illustration of the end-effector geometry of the CDP (4.30a and 4.30b) and its corresponding wire-frame model used for the synthesis optimization (4.30c)), which allows to suitably represent the space covered by or under the end effector where no cable must be found while moving the CDP's slave end effector. Table 4.3 contains the corresponding coordinates of the starting and ending points of each edge. It should be observed that the positioning of the attachment points on the end effector has been set to a slightly larger acceptable volume compared to the limited volume of the expected tool, i.e., $0.08 \times 0.08 \times 0.16$ m^3 and $0.05 \times 0.05 \times 0.16$ m^3, respectively. This choice allows the cables attachment points to be slightly outside the end-effector geometry. Moreover, the height of the end-effector geometry is chosen to ensure that no contact occurs between the tool and the internal wall of the MRI gantry, for the prescribed workspace.

The reference position $\mathbf{p}_0$ of point P on the CDPM end-effector is set to

$$\mathbf{p}_0 \equiv \begin{bmatrix} 0.0000 & 0.0000 & 0.1225 \end{bmatrix}^T \text{ (m)}, \tag{4.84}$$

and the reference orientation $\mathbf{Q}_0$ of the frame $\mathcal{B}$ attached to the end effector is set to the centroid of $\mathcal{W}_{p,r}$, i.e., $\mathbf{Q}_0 \equiv \mathbf{1}_{3\times3}$. As for the adjustable parameters of the optimization algorithm, we set the maximum number of allowed iterations for each trial to $mr = 10\,000$ and, as previously mentioned, the maximum number of trials to $ms = 100$, which is the total

Table 4.3 – Coordinates of the starting and ending points of the set of edges that form the geometry attached to the CDPM's end-effector of the second example.

Edge	$\mathbf{e}_{o,s}^{\mathcal{B}}$			$\mathbf{e}_{o,t}^{\mathcal{B}}$		
	$x\ (m)$	$y\ (m)$	$z\ (m)$	$x\ (m)$	$y\ (m)$	$z\ (m)$
1	−0.025	−0.025	0.160	0.025	−0.025	0.160
2	−0.025	−0.025	0.160	−0.025	0.025	0.160
3	−0.025	0.025	0.160	0.025	0.025	0.160
4	0.025	0.025	0.160	0.025	−0.025	0.160
5	−0.025	−0.025	0.160	−0.025	−0.025	−0.150
6	−0.025	0.025	0.160	−0.025	0.025	−0.150
7	0.025	0.025	0.160	0.025	0.025	−0.150
8	0.025	−0.025	0.160	0.025	−0.025	−0.150
9	−0.025	−0.025	0.000	0.025	−0.025	0.000
10	−0.025	−0.025	0.000	−0.025	0.025	0.000
11	−0.025	0.025	0.000	0.025	0.025	0.000
12	0.025	0.025	0.000	0.025	−0.025	0.000
13	0.000	0.000	0.160	0.000	0.000	−0.150
14	0.000	−0.025	0.160	0.000	−0.025	−0.150
15	−0.025	0.000	0.160	−0.025	0.000	−0.150
16	0.000	0.025	0.160	0.000	0.025	−0.150
17	0.025	0.000	0.160	0.025	0.000	−0.150

number of initial solutions chosen for the multi-start method. The first ninety-nine guesses follow the method described above, i.e., they are formed from an improved random selection of the initial geometries, and the last one, the hundredth, is formed from a human-reflected geometry based on the designer's intuitions. The two other options, i.e., `InitBarrierParam` and `InitTrustRegionRadius`, are fixed to 0.15 (default value: 0.1) and $\sqrt{4\ 000}$ (default value: $\sqrt{v}$, where v is the number of variables, and in this example, $v = 5\ 779$), respectively.

Moreover, since the goal of this example is to generate a CDP that would be installed within the bore of a cylindrical MRI, the attachment points on the base frame must fulfill additional constraints in order to fit within the geometry of the MRI gantry and stay out of the space allowed for the patient. Figure 4.31 illustrates the seven chosen linear constraints that are used here to restrict the position of points $\mathbf{a}_i$ of the CDP's geometry, where they are identified as $\varepsilon = 1, \ldots, 7$. The light blue region in this figure represents the set of acceptable positions for the attachment points $\mathbf{a}_i$ in the plane $X - Z$. The first six constraints are mathematically represented as follows:

$$a_{i,z} \leq \alpha_\varepsilon a_{i,x} + \beta_\varepsilon, \tag{4.85}$$

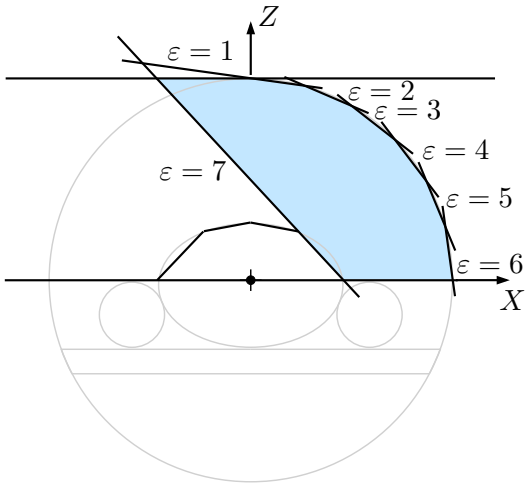

Figure 4.31 – Illustration of the additional geometric constraints on the CDP's attachment points $\mathbf{a}_i$ inside the MRI gantry.

Table 4.4 – Values corresponding to the α's and β's of the additional linear constraints for the synthesis problem.

ε	α	β
1	−0.1317	35.0000
2	−0.4142	37.5596
3	−0.7673	43.7391
4	−1.3032	57.0019
5	−2.4142	90.6770
6	−7.5958	265.8514
7	−1.1292	18.0665

where $i = 1,\ldots,4$ and $\varepsilon = 1,\ldots,6$, which restrict the CDP to be inside the cylindrical MRI. The linear constraint that forbids the points $\mathbf{a}_i$ to be positioned within the space reserved for the patient is the following:

$$-a_{i,z} \leq -\alpha_7 a_{i,x} - \beta_7, \tag{4.86}$$

where $i = 1,\ldots,4$. The values corresponding to the α's and β's are provided in Table 4.4.

As the reader may notice, the additional linear constraints defined above only restrict the first four attachment points of the base of the CDP in X and Z coordinates. In order to act on the entire set of points, we decided to force the existence of symmetry rules in the CDP's

geometry. These linear constraints are defined as follows:

$$a_{1,x} = -a_{5,x}, \qquad a_{1,y} = -a_{4,y}, \qquad a_{1,z} = a_{5,z}, \tag{4.87}$$

$$a_{2,x} = -a_{6,x}, \qquad a_{2,y} = -a_{3,y}, \qquad a_{2,z} = a_{6,z}, \tag{4.88}$$

$$a_{3,x} = -a_{7,x}, \qquad a_{5,y} = -a_{8,y}, \qquad a_{3,z} = a_{7,z}, \tag{4.89}$$

$$a_{4,x} = -a_{8,x}, \qquad a_{6,y} = -a_{7,y}, \qquad a_{4,z} = a_{8,z}. \tag{4.90}$$

These symmetry-type constraints can be observed in Fig. 4.32, which shows the initial geometry corresponding to the best result obtained from our synthesis program. Of course, these constraints limit the freedom of the optimization program to synthesize new types of CDP architectures but, on the other hand, they ensure a certain quality and higher level of practicability of the resulting geometry.

It should be noted that we defined the above linear constraints (both the inequality and equality types) since these types of constraints are known to be easily fulfilled by our optimization program, which would not have been the case with nonlinear constraints.

Finally, the synthesis problem associated to the current example is defined slightly differently from that of Eq. (4.50), namely,

$$\begin{aligned} f(\mathbf{v}) = \text{minimize} \quad & -\kappa, \\ \text{subject to} \quad & \mathbf{c}_{\text{ineq}}(\mathbf{v}) \leq \mathbf{0}_{(3(m^2-m)q+4mfq)\times 1}, \\ & \mathbf{c}_{\text{eq}}(\mathbf{v}) = \mathbf{0}_{nqnb\times 1}, \\ & \mathbf{A}_{\text{ineq},28\times dim}\mathbf{v} \leq \mathbf{b}_{\text{ineq},28\times 1}, \\ & \mathbf{A}_{\text{eq},(3nb+qnb+12)\times dim}\mathbf{v} = \mathbf{b}_{\text{eq},(3nb+qnb+12)\times 1}, \\ & \mathbf{lb} \leq \mathbf{v} \leq \mathbf{ub}, \\ \text{for} \quad & \mathbf{v} \equiv \begin{bmatrix} \kappa & \mathbf{a}^T & \mathbf{b}^{\mathcal{B}\,T} & \mathbf{p}_{aug}^T & \mathbf{t}_{aug}^T & \boldsymbol{\mu}_{aug}^T & \boldsymbol{\eta}_{aug}^T \end{bmatrix}_{dim\times 1}^T, \end{aligned} \tag{4.91}$$

where the linear inequality and equality constraints are now expressed as

$$\mathbf{A}_{\text{ineq}} \equiv \begin{bmatrix} \mathbf{0}_{28} & \mathbf{A}_{\text{ineq,sub}} & \mathbf{0}_{28\times 3m} & \mathbf{0}_{28\times(dim-1-6m)} \end{bmatrix}, \tag{4.92}$$

$$\mathbf{b}_{\text{ineq}} \equiv \begin{bmatrix} \beta_1\mathbf{1}_4^T & \beta_2\mathbf{1}_4^T & \beta_3\mathbf{1}_4^T & \beta_4\mathbf{1}_4^T & \beta_5\mathbf{1}_4^T & \beta_6\mathbf{1}_4^T & -\beta_7\mathbf{1}_4^T \end{bmatrix}^T, \tag{4.93}$$

$$\mathbf{A}_{\text{eq}} \equiv \begin{bmatrix} -(\mathbf{p}_{aug}-\mathbf{p}_{0,aug}) & \mathbf{0}_{3nb\times 6m} & \mathbf{1}_{3nb\times 3nb} & \mathbf{0}_{3nb\times mqnb} & \mathbf{0}_{3nb\times dim_1} \\ \mathbf{0}_{qnb} & \mathbf{0}_{qnb\times 6m} & \mathbf{0}_{qnb\times 3nb} & \mathbf{U} & \mathbf{0}_{qnb\times dim_1} \\ \mathbf{0}_{12} & \mathbf{A}_{\text{eq,sub}} & \mathbf{0}_{12\times 3nb} & \mathbf{0}_{12\times mqnb} & \mathbf{0}_{12\times dim_1} \end{bmatrix}, \tag{4.94}$$

$$\mathbf{b}_{\text{eq}} \equiv \begin{bmatrix} \mathbf{p}_{0,aug}^T & \mathbf{1}_{qnb}^T & \mathbf{0}_{12}^T \end{bmatrix}^T, \tag{4.95}$$

where, for the inequality constraints, we have

$$\mathbf{A}_{\text{ineq,sub}} \equiv \begin{bmatrix} \boldsymbol{\Lambda}_1 & \cdots & \boldsymbol{\Lambda}_\varepsilon & \cdots & \boldsymbol{\Lambda}_7 \end{bmatrix}^T, \tag{4.96}$$

and where

$$\mathbf{\Lambda}_{\varepsilon} \equiv \begin{bmatrix} \boldsymbol{\alpha}_{\varepsilon}^T & \mathbf{0}_3^T & \mathbf{0}_3^T & \mathbf{0}_3^T & \mathbf{0}_{12}^T \\ \mathbf{0}_3^T & \boldsymbol{\alpha}_{\varepsilon}^T & \mathbf{0}_3^T & \mathbf{0}_3^T & \mathbf{0}_{12}^T \\ \mathbf{0}_3^T & \mathbf{0}_3^T & \boldsymbol{\alpha}_{\varepsilon}^T & \mathbf{0}_3^T & \mathbf{0}_{12}^T \\ \mathbf{0}_3^T & \mathbf{0}_3^T & \mathbf{0}_3^T & \boldsymbol{\alpha}_{\varepsilon}^T & \mathbf{0}_{12}^T \end{bmatrix}^T, \quad \varepsilon = 1, \ldots, 7, \tag{4.97}$$

and

$$\boldsymbol{\alpha}_{\varepsilon} \equiv \begin{bmatrix} -\alpha_{\varepsilon} & 0 & 1 \end{bmatrix}^T, \quad \varepsilon = 1, \ldots, 6, \tag{4.98}$$

$$\boldsymbol{\alpha}_7 \equiv \begin{bmatrix} \alpha_7 & 0 & -1 \end{bmatrix}^T, \tag{4.99}$$

and for the equality constraints,

$$\mathbf{A}_{\text{eq,sub}} \equiv \begin{bmatrix} \mathbf{e}_1^T & \mathbf{0}_3^T & \mathbf{0}_3^T & \mathbf{0}_3^T & \mathbf{e}_1^T & \mathbf{0}_3^T & \mathbf{0}_3^T & \mathbf{0}_3^T & \mathbf{0}_{3m}^T \\ \mathbf{0}_3^T & \mathbf{e}_1^T & \mathbf{0}_3^T & \mathbf{0}_3^T & \mathbf{0}_3^T & \mathbf{e}_1^T & \mathbf{0}_3^T & \mathbf{0}_3^T & \mathbf{0}_{3m}^T \\ \mathbf{0}_3^T & \mathbf{0}_3^T & \mathbf{e}_1^T & \mathbf{0}_3^T & \mathbf{0}_3^T & \mathbf{0}_3^T & \mathbf{e}_1^T & \mathbf{0}_3^T & \mathbf{0}_{3m}^T \\ \mathbf{0}_3^T & \mathbf{0}_3^T & \mathbf{0}_3^T & \mathbf{e}_1^T & \mathbf{0}_3^T & \mathbf{0}_3^T & \mathbf{0}_3^T & \mathbf{e}_1^T & \mathbf{0}_{3m}^T \\ \mathbf{e}_2^T & \mathbf{0}_3^T & \mathbf{0}_3^T & \mathbf{e}_2^T & \mathbf{0}_3^T & \mathbf{0}_3^T & \mathbf{0}_3^T & \mathbf{0}_3^T & \mathbf{0}_{3m}^T \\ \mathbf{0}_3^T & \mathbf{e}_2^T & \mathbf{e}_2^T & \mathbf{0}_3^T & \mathbf{0}_3^T & \mathbf{0}_3^T & \mathbf{0}_3^T & \mathbf{0}_3^T & \mathbf{0}_{3m}^T \\ \mathbf{0}_3^T & \mathbf{0}_3^T & \mathbf{0}_3^T & \mathbf{0}_3^T & \mathbf{e}_2^T & \mathbf{0}_3^T & \mathbf{0}_3^T & \mathbf{e}_2^T & \mathbf{0}_{3m}^T \\ \mathbf{0}_3^T & \mathbf{0}_3^T & \mathbf{0}_3^T & \mathbf{0}_3^T & \mathbf{0}_3^T & \mathbf{e}_2^T & \mathbf{e}_2^T & \mathbf{0}_3^T & \mathbf{0}_{3m}^T \\ \mathbf{e}_3^T & \mathbf{0}_3^T & \mathbf{0}_3^T & \mathbf{0}_3^T & -\mathbf{e}_3^T & \mathbf{0}_3^T & \mathbf{0}_3^T & \mathbf{0}_3^T & \mathbf{0}_{3m}^T \\ \mathbf{0}_3^T & \mathbf{e}_3^T & \mathbf{0}_3^T & \mathbf{0}_3^T & \mathbf{0}_3^T & -\mathbf{e}_3^T & \mathbf{0}_3^T & \mathbf{0}_3^T & \mathbf{0}_{3m}^T \\ \mathbf{0}_3^T & \mathbf{0}_3^T & \mathbf{e}_3^T & \mathbf{0}_3^T & \mathbf{0}_3^T & \mathbf{0}_3^T & -\mathbf{e}_3^T & \mathbf{0}_3^T & \mathbf{0}_{3m}^T \\ \mathbf{0}_3^T & \mathbf{0}_3^T & \mathbf{0}_3^T & \mathbf{e}_3^T & \mathbf{0}_3^T & \mathbf{0}_3^T & \mathbf{0}_3^T & -\mathbf{e}_3^T & \mathbf{0}_{3m}^T \end{bmatrix}, \tag{4.100}$$

where

$$\mathbf{e}_1 = \begin{bmatrix} 1 & 0 & 0 \end{bmatrix}^T, \tag{4.101}$$

$$\mathbf{e}_2 = \begin{bmatrix} 0 & 1 & 0 \end{bmatrix}^T, \tag{4.102}$$

$$\mathbf{e}_3 = \begin{bmatrix} 0 & 0 & 1 \end{bmatrix}^T. \tag{4.103}$$

From the flowchart shown in Fig. 4.5, notice that these new geometrical constraints must be applied to the steps where the closest-feasible solution $\mathbf{v}_{\iota,0}$ (more specifically in Eq. (4.66)) is determined and where the solution $\mathbf{v}_{\iota,f}$ is determined by solving the general optimization program of Eq. (4.91) instead of Eq. (4.50).

Table 4.5 presents the summary of the hundred runs of our dimensional synthesis program. This table contains the negative value of the final objective function $f(\mathbf{v}_{\iota,f})$ of each trial ι, its number of iterations, its duration, and the message indicating the reason why it stopped.

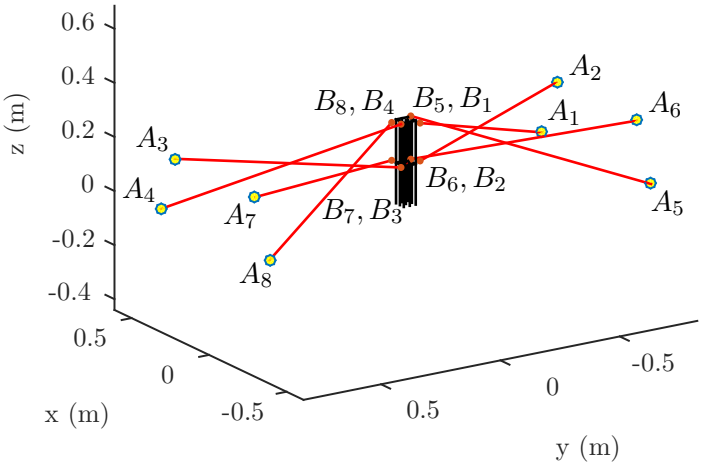

Figure 4.32 – Illustration of the initial geometry corresponding to the best result obtained with the synthesis program (Trial 100).

It is important to note that it has been decided to stop the progress of a solution when its objective function value falls below $\kappa_{\iota,f} = 0.25$ after 500 iterations in order to reduce the overall computation time, since these trials are unlikely to produce interesting results. It took 270.56 hours (approximately eleven days and seven hours) to compute the hundred trials of this example.

Trial ι	$\kappa_{\iota,f} = -f(\mathbf{v}_{\iota,f})$	Iterations	Time (s)	Stop Message
1	– – –	500	5 572.7	Rejected solution
2	– – –	500	5 528.8	Rejected solution
3	– – –	500	7 162.3	Rejected solution
4	– – –	500	8 214.9	Rejected solution
5	0.3982	1 274	13 747.1	Local minimum found
6	0.6913	10 000	86 412.2	Maximum iterations reached
7	0.8942	5 149	38 190.0	Local minimum found
8	– – –	500	7 285.7	Rejected solution
9	– – –	500	4 970.9	Rejected solution
10	0.4933	1 523	12 112.8	Local minimum found
11	– – –	500	6 808.3	Rejected solution
12	– – –	500	6 660.3	Rejected solution
13	– – –	500	4 459.3	Rejected solution
14	– – –	500	4 453.7	Rejected solution
15	0.2516	249	9 984.2	Local minimum found
16	– – –	500	5 540.1	Rejected solution
17	– – –	500	4 567.0	Rejected solution
18	– – –	500	5 390.9	Rejected solution

19	– – –	500	5 290.9	Rejected solution
20	0.4892	8 313	71 808.3	Local minimum found
21	0.1559	401	3 652.5	Local minimum found
22	– – –	500	5 320.0	Rejected solution
23	– – –	500	4 655.1	Rejected solution
24	– – –	500	5 500.6	Rejected solution
25	– – –	500	6 979.1	Rejected solution
26	– – –	500	4 834.4	Rejected solution
27	– – –	500	6 582.9	Rejected solution
28	0.5384	4 378	45 324.3	Local minimum found
29	0.6959	1 943	21 614.9	Local minimum found
30	– – –	500	5 655.7	Rejected solution
31	0.1720	409	3 566.5	Local minimum found
32	– – –	500	4 251.5	Rejected solution
33	– – –	500	5 624.3	Rejected solution
34	– – –	500	5 395.8	Rejected solution
35	– – –	500	6 331.9	Rejected solution
36	0.6166	1 581	15 964.3	Local minimum found
37	– – –	500	6 172.3	Rejected solution
38	– – –	500	5 019.5	Rejected solution
39	0.6083	647	6 784.1	Local minimum found
40	– – –	500	4 460.7	Rejected solution
41	0.6533	4 161	23 144.9	Local minimum found
42	– – –	500	4 912.4	Rejected solution
43	– – –	500	4 555.2	Rejected solution
44	– – –	500	5 137.4	Rejected solution
45	0.6745	5 109	28 650.9	Local minimum found
46	– – –	500	4 833.7	Rejected solution
47	– – –	500	5 326.4	Rejected solution
48	– – –	500	3 996.4	Rejected solution
49	– – –	500	6 925.3	Rejected solution
50	– – –	500	4 728.3	Rejected solution
51	– – –	500	6 738.6	Rejected solution
52	– – –	500	5 377.4	Rejected solution
53	0.2534	223	2 231.8	Local minimum found
54	– – –	500	6 588.0	Rejected solution
55	– – –	500	4 726.0	Rejected solution

56	– – –	500	6 441.7	Rejected solution
57	– – –	500	4 954.7	Rejected solution
58	– – –	500	4 857.2	Rejected solution
59	– – –	500	6 690.3	Rejected solution
60	0.2860	638	6 655.5	Local minimum found
61	– – –	500	5 209.1	Rejected solution
62	– – –	500	6 148.9	Rejected solution
63	– – –	500	4 520.7	Rejected solution
64	0.9835	2 601	18 325.4	Local minimum found
65	– – –	500	6 209.1	Rejected solution
66	0.6203	4 018	22 354.7	Local minimum found
67	– – –	500	8 110.2	Rejected solution
68	– – –	500	5 620.1	Rejected solution
69	– – –	500	5 635.4	Rejected solution
70	0.4358	2 506	15 496.7	Local minimum found
71	– – –	500	5 131.2	Rejected solution
72	– – –	500	5 443.6	Rejected solution
73	– – –	500	4 755.6	Rejected solution
74	– – –	500	5 982.4	Rejected solution
75	0.2061	325	3 126.6	Local minimum found
76	– – –	500	4 564.6	Rejected solution
77	– – –	500	5 278.9	Rejected solution
78	0.3588	2 596	19 433.7	Local minimum found
79	– – –	500	5 332.0	Rejected solution
80	– – –	500	4 703.4	Rejected solution
81	0.7443	10 000	75 665.3	Maximum iterations reached
82	– – –	500	6 576.6	Rejected solution
83	– – –	500	6 105.3	Rejected solution
84	– – –	500	6 152.7	Rejected solution
85	– – –	500	6 486.7	Rejected solution
86	– – –	500	4 792.9	Rejected solution
87	– – –	500	5 247.7	Rejected solution
88	– – –	500	4 737.1	Rejected solution
89	0.1632	165	1 919.6	Local minimum found
90	– – –	500	6 080.9	Rejected solution
91	– – –	500	6 462.0	Rejected solution
92	– – –	500	5 618.4	Rejected solution

93	– – –	500	7 140.7	Rejected solution
94	– – –	500	6 567.3	Rejected solution
95	– – –	500	6 759.9	Rejected solution
96	0.1972	186	2 114.5	Local minimum found
97	– – –	500	5 046.6	Rejected solution
98	– – –	500	6 433.9	Rejected solution
99	– – –	500	4 738.8	Rejected solution
100 ($\star$)	1.0880	301	2 675.8	Local minimum found

Table 4.5 – Summary of the results obtained from the dimensional synthesis of an eight-cable seventeen-edge six-DoF CDPM.

From Tab. 4.5, notice that the best result—the global minimum over the hundred local minima—belongs to Trial 100, which is marked by a star. This result reports a CDPM geometry with a three-dimensional workspace in translation that can be illustrated by an ellipsoid $\mathcal{W}_e$ with $\kappa = 1.0880$ (see Eq. (4.2)). Our synthesis program ensures us that at minimum fourteen strategically distributed points lying on this ellipsoid's surface are included in the CDPM WCW, at least for the nine different evaluated end-effector orientations $\mathbf{Q}_k$. We also know that this workspace is free of cable-cable and cable-edge interferences for each orientation $\mathbf{Q}_k$. It is also interesting to note that over the hundred tested geometries, the synthesis program has produced twenty-five solutions for which a local minimum has been found or the maximum iterations limit was reached. Among them, twelve trials have a final $\kappa \geq 0.5$ and three of them are close to or higher than $\kappa = 0.9$.

As for the first numerical application, the reader will find in Appendix D.2, for the twelve best results generated from the hundred trials, the Cartesian coordinates of the randomly-selected architectures, the closest-feasible initial solutions and their corresponding geometries after optimization. Furthermore, a graphical representation of the initial geometry, the final geometry and its WCW are included. Over the twelve trials, three represent a "good" optimization since their final values are close to or higher than 0.9 (Trial 7 with $\kappa = 0.8942$, Trial 64 with $\kappa = 0.9835$ and Trial 100 with $\kappa = 1.0880$). For these given optimizations, three graphs are added in Appendix D.2 in order to facilitate the analysis of their final CDPM geometries from different views: XY, XZ, and YZ.

As for the analysis of these results, we decided to focus on the two best ones, i.e., Trial 64 and Trial 100. Figures 4.33a, 4.33c and 4.33e respectively illustrate the evolution of the objective function and step size values, the initial WCW with the prescribed ellipsoid and the final WCW with the final reachable ellipsoid for Trial 64 while Figs. 4.33b, 4.33d and 4.33f are for Trial 100. It can be observed that even if the proposed synthesis program starts from a quasi-random—closest-feasible solution from the random solution—initial solution, it is possible to

converge towards a suitable final solution that almost fully fulfills the prescribed requirements of the intended application with a κ value of 0.9835. As expected, from observations noted in Sub-section 4.3.1, when the initial solution is set by the designer, it normally leads to a smaller number of iterations required to reach a local minimum, as it can be seen with Trial 100. Both Trials 64 and 100 also show step sizes that decrease over time, which shows that the program converged towards minima in the two cases. Globally, from Fig. 4.33, it is easily noticed that the dimensional synthesis program drastically improved the WCW coverage of the prescribed ellipsoid if we compare the initial and final solutions for both trials. Trial 100 provided a slightly better solution than did Trial 64. It is also interesting to note that the resulting pattern for the position of the attachment points $\mathbf{a}_i$ is relatively similar for both trials.

In order to analyze these two trials with respect to the interference-free regions, Figs. 4.34-4.41 present the interference regions between two cables and between a cable and an end-effector edge for the nine end-effector attitudes, for the initial and final solutions of each trial. Figure 4.34 shows the cable-cable interference regions for the initial solution of Trial 64, while Fig. 4.35 shows the same results for its final solution. Figure 4.36 shows the cable-edge interference regions for the initial solution of Trial 64, and Fig. 4.37 shows the same results for its final solution. The interference regions between two cables for the initial solution of Trial 100 are shown in Fig. 4.38, while Fig. 4.39 shows the same results for its final solution. Finally, the interference regions between a cable and an end-effector edge for the initial solution of Trial 100 are presented in Fig. 4.40 and the same results for its final solution are shown in Fig. 4.41. It is noted here that no exhaustive analysis is presented on these results, since it would lead to similar conclusions than the analysis completed in Sub-section 4.3.1. In short, no mechanical contact occurs within the ellipsoid of the final solutions, at least for the nine evaluated end-effector attitudes.

However, even if no interference between two cables and between a cable and an end-effector edge are observed in those results, there is still a chance that a mechanical contact occurs within the final ellipsoid. This possibility is due to the set of nine discrete end-effector attitudes to cover the prescribed range of rotations $\mathcal{W}_{p,r}$. This method does not assess every possible end-effector attitude. Even if this strategically-selected set of orientations contains the vertices and centroid of the box representing $\mathcal{W}_{p,r}$, it cannot guarantee the absence of mechanical interferences between a pair of cables or between a cable and an end effector when passing from one orientation to the other. Finely-discretized trajectories could be used to further analyze the final geometry, or a higher number of end-effector attitudes could be used to cover $\mathcal{W}_{p,r}$, at the cost of a drastic increase of the required computation time.

In light of the results obtained with this example, we demonstrated that a suitable CDPM architecture can be found to perform simple image-guided biopsies inside the geometrically-constrained volume of a conventional MRI system. As stated at the beginning of this sub-section, we only optimized the architecture of the slave part of the intended eight-cable

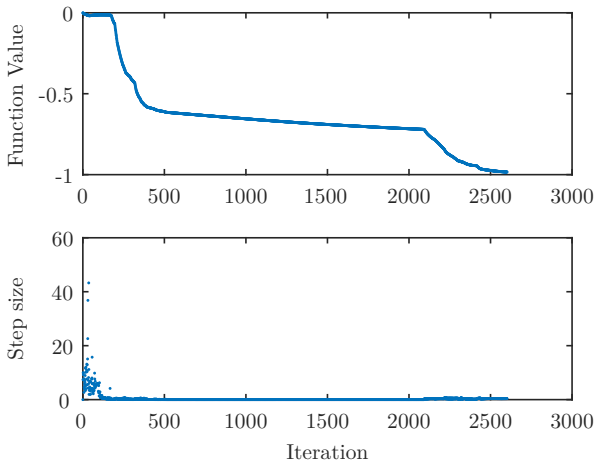

(a) Objective function and step size values for Trial 64 ($\kappa_{64,f} = 0.9835$)

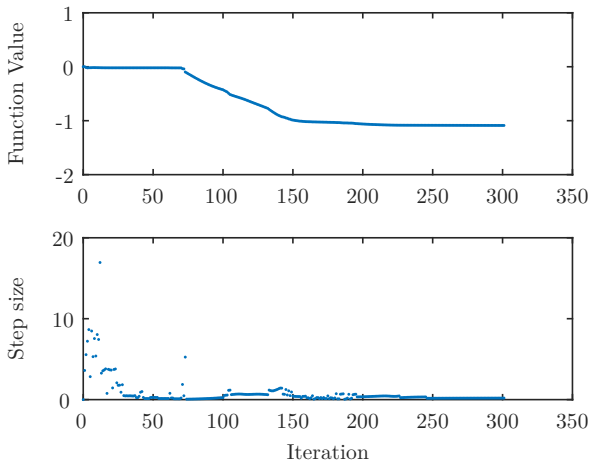

(b) Objective function and step size values for Trial 100 ($\kappa_{100,f} = 1.0880$)

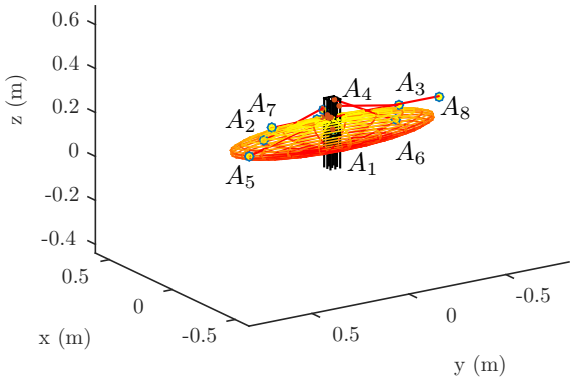

(c) Initial WCW and prescribed ellipsoid for Trial 64

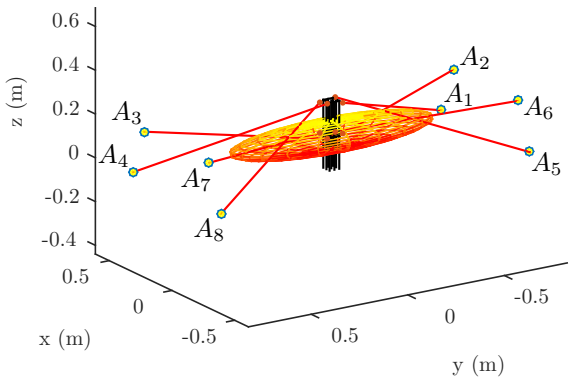

(d) Initial WCW and prescribed ellipsoid for Trial 100

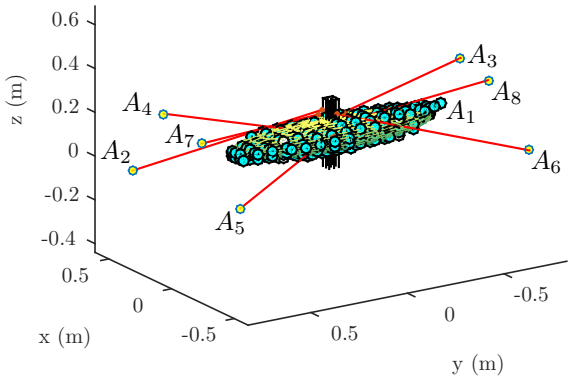

(e) Final WCW and final ellipsoid for Trial 64

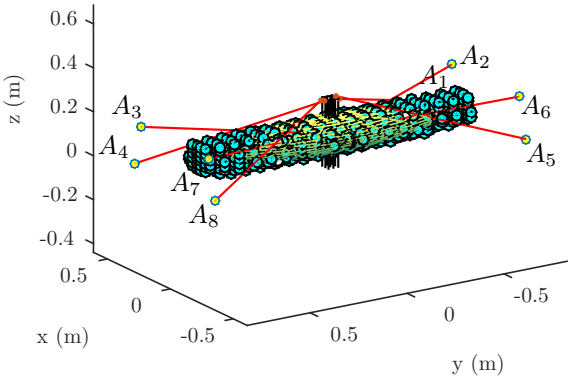

(f) Final WCW and final ellipsoid for Trial 100

Figure 4.33 – Illustration of the results obtained from the optimization of CDP's geometries corresponding to Trial 64 and Trial 100.

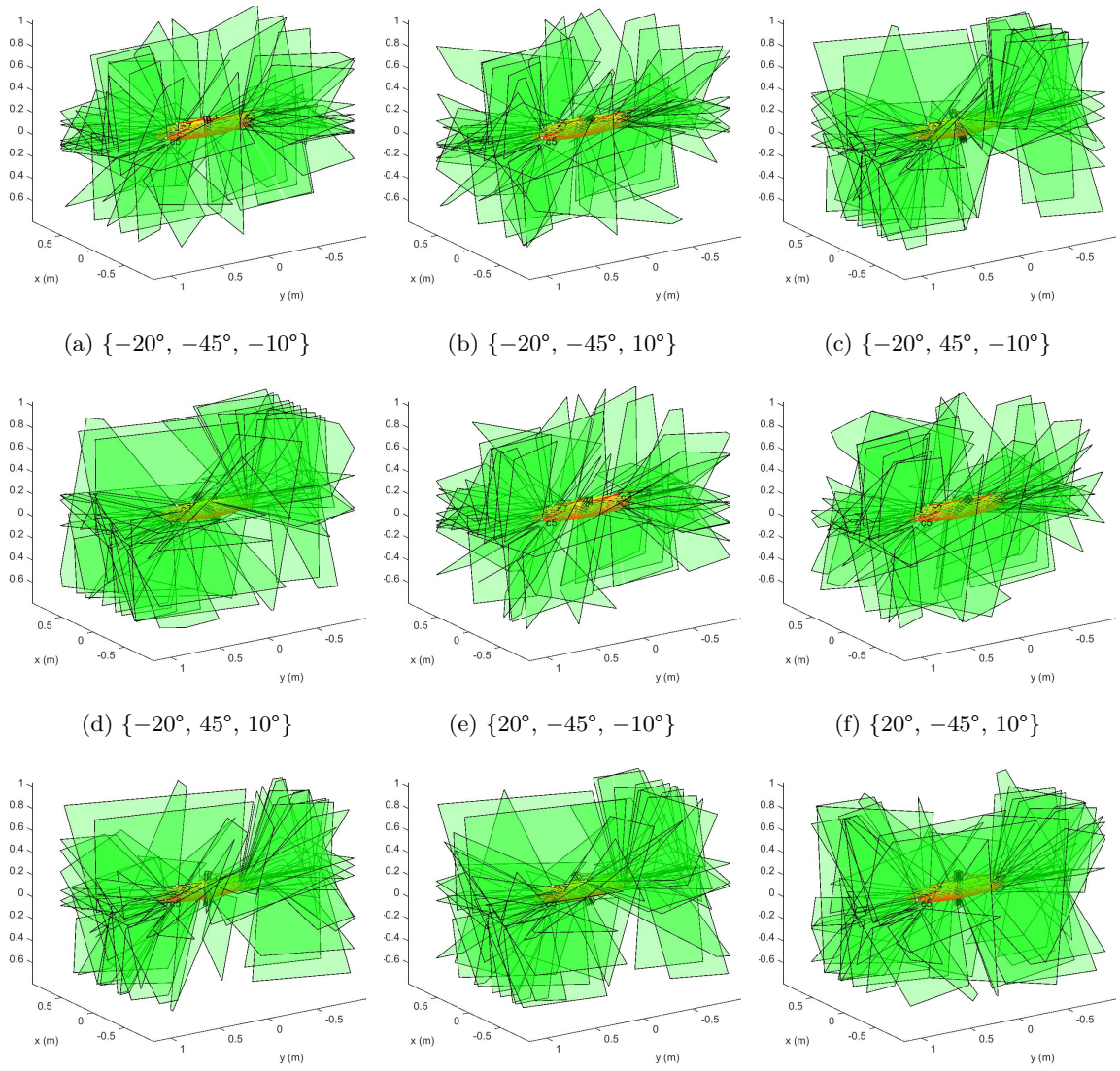

(a) {−20°, −45°, −10°} (b) {−20°, −45°, 10°} (c) {−20°, 45°, −10°}

(d) {−20°, 45°, 10°} (e) {20°, −45°, −10°} (f) {20°, −45°, 10°}

(g) {20°, 45°, −10°} (h) {20°, 45°, 10°} (i) {0°, 0°, 0°}

Figure 4.34 – Mechanical interference regions between two cables for the nine chosen attitudes $\{\theta_x, \theta_{y^{\mathrm{I}}}, \theta_{z^{\mathrm{II}}}\}$ of the end effector of the initial eight-cable seventeen-edge six-DoF CDP (Trial 64).

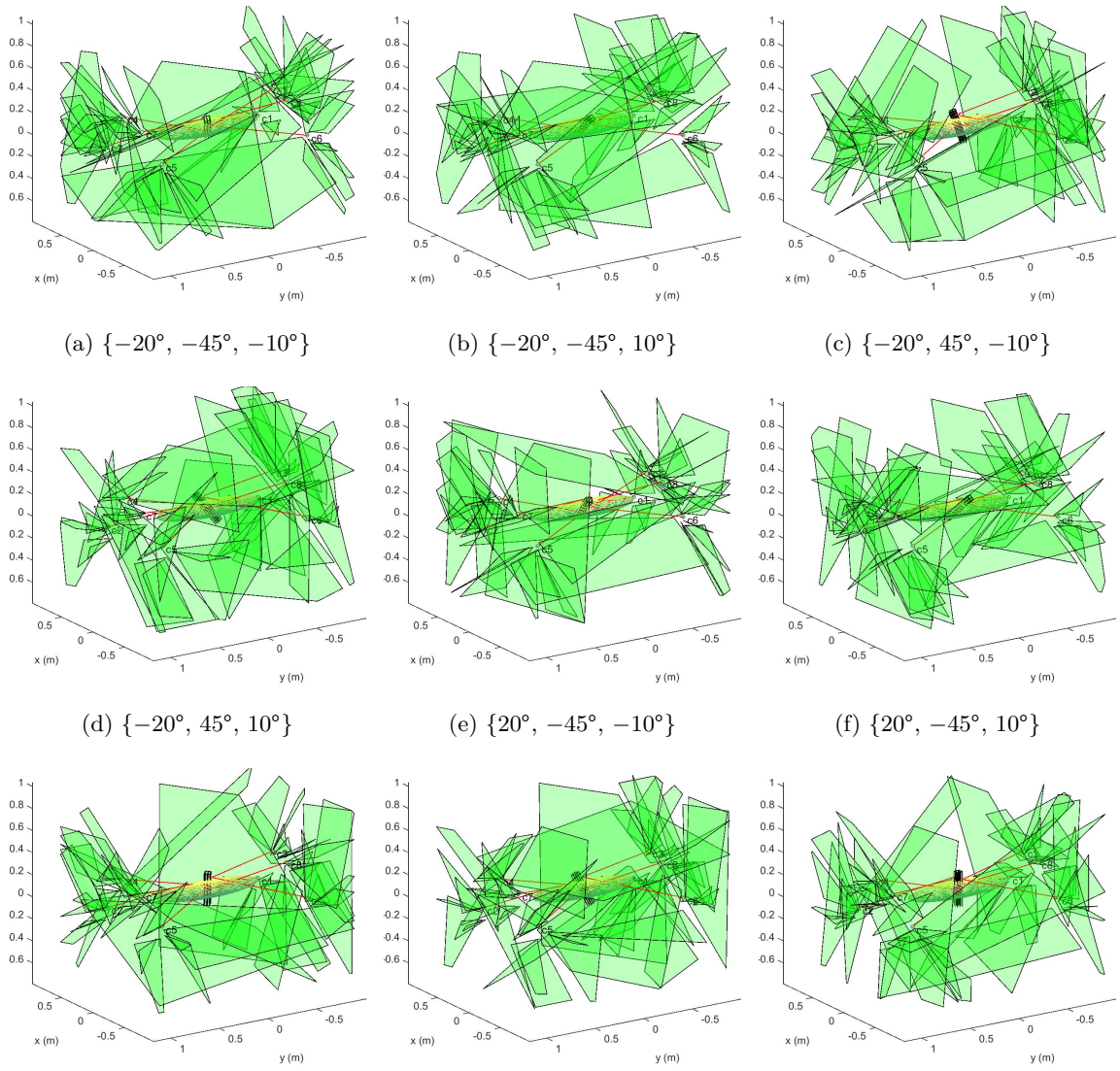

(a) $\{-20°, -45°, -10°\}$ (b) $\{-20°, -45°, 10°\}$ (c) $\{-20°, 45°, -10°\}$

(d) $\{-20°, 45°, 10°\}$ (e) $\{20°, -45°, -10°\}$ (f) $\{20°, -45°, 10°\}$

(g) $\{20°, 45°, -10°\}$ (h) $\{20°, 45°, 10°\}$ (i) $\{0°, 0°, 0°\}$

Figure 4.35 – Mechanical interference regions between two cables for the nine chosen attitudes $\{\theta_x, \theta_{y^{\mathrm{I}}}, \theta_{z^{\mathrm{II}}}\}$ of the end effector of the final eight-cable seventeen-edge six-DoF CDP (Trial 64).

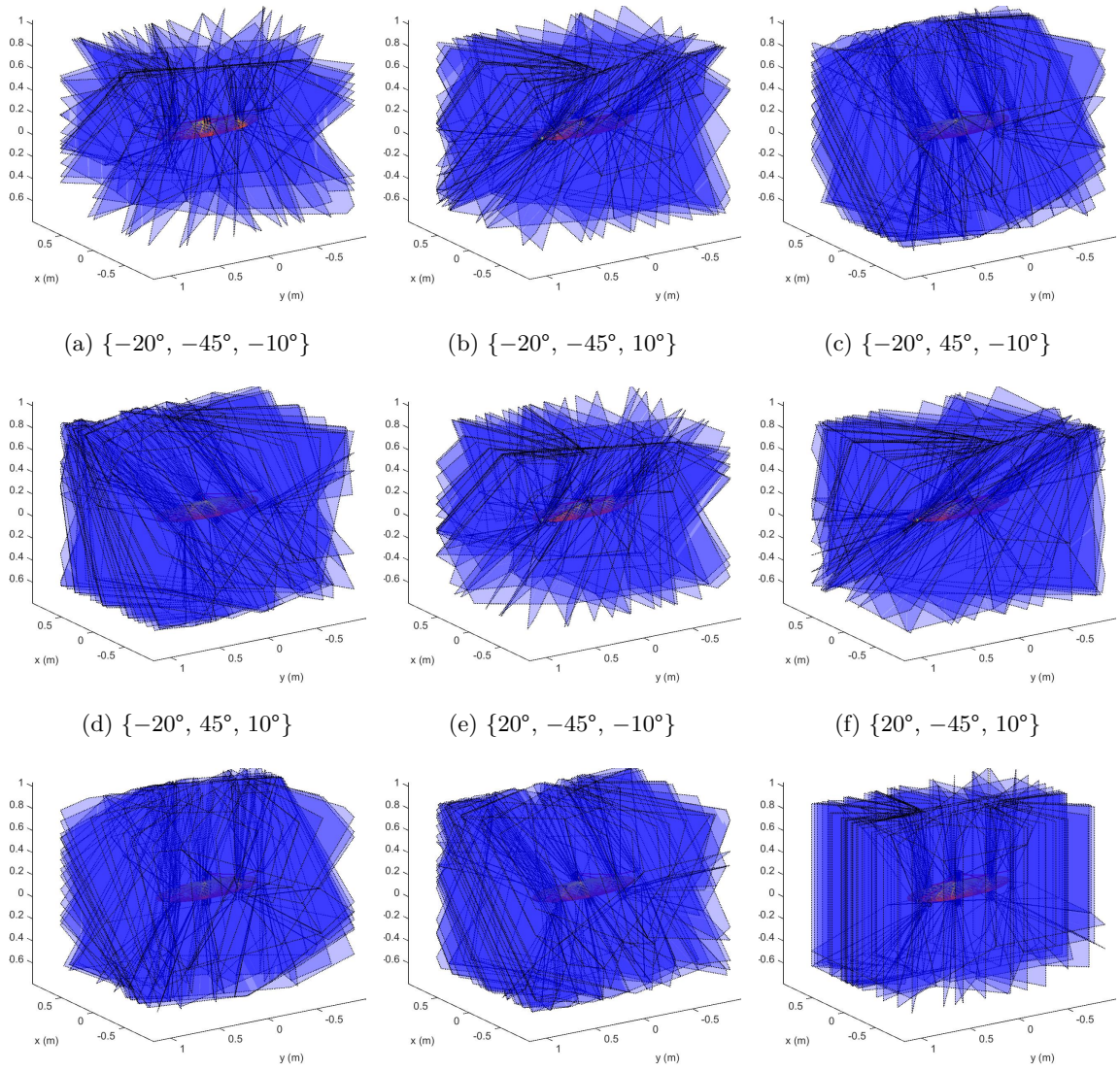

(a) $\{-20°, -45°, -10°\}$ (b) $\{-20°, -45°, 10°\}$ (c) $\{-20°, 45°, -10°\}$

(d) $\{-20°, 45°, 10°\}$ (e) $\{20°, -45°, -10°\}$ (f) $\{20°, -45°, 10°\}$

(g) $\{20°, 45°, -10°\}$ (h) $\{20°, 45°, 10°\}$ (i) $\{0°, 0°, 0°\}$

Figure 4.36 – Mechanical interference regions between a cable and an edge for the nine chosen attitudes $\{\theta_x, \theta_{y^{\mathrm{I}}}, \theta_{z^{\mathrm{II}}}\}$ of the end effector of the initial eight-cable seventeen-edge six-DoF CDP (Trial 64).

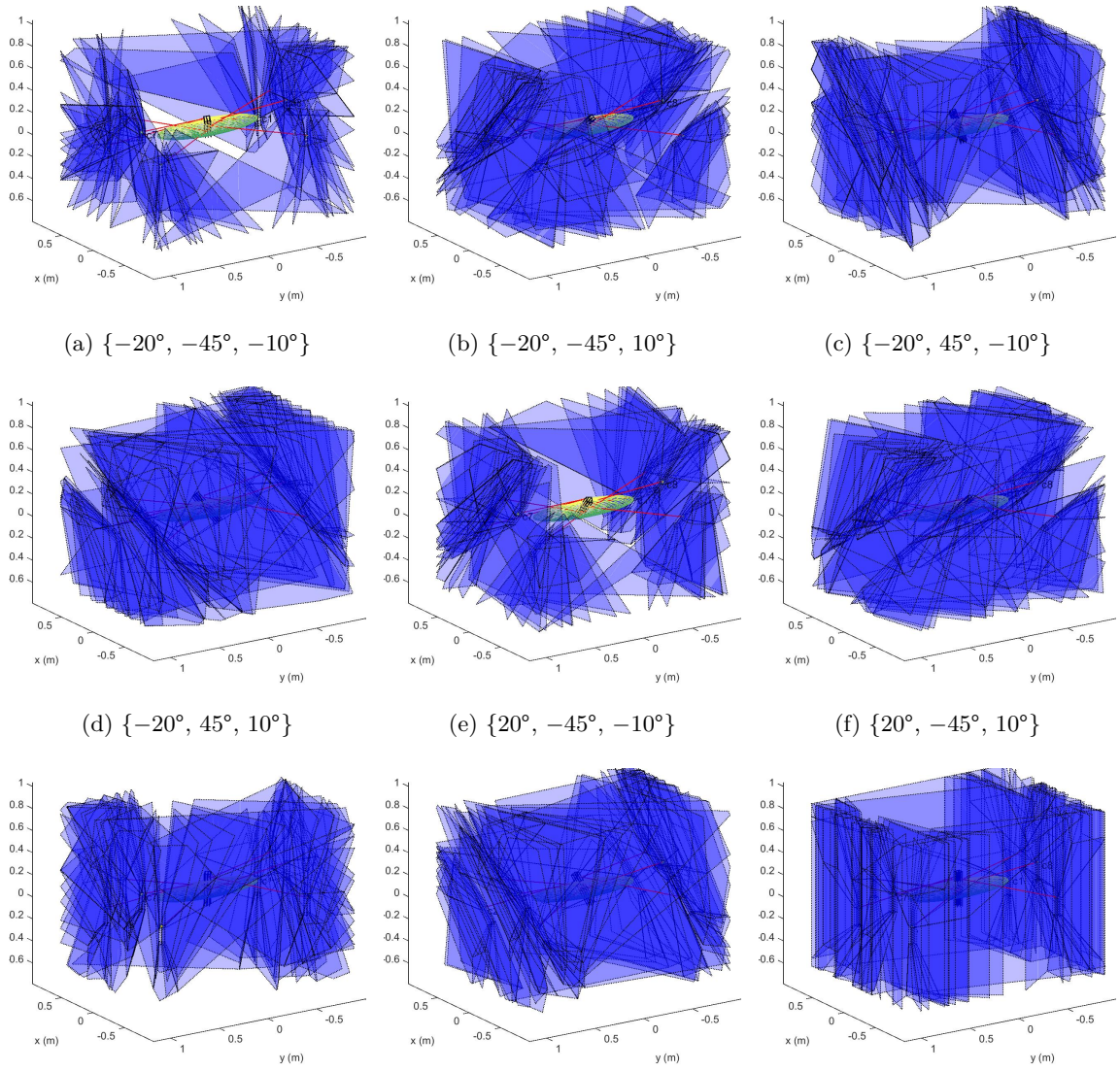

(a) $\{-20°, -45°, -10°\}$ (b) $\{-20°, -45°, 10°\}$ (c) $\{-20°, 45°, -10°\}$

(d) $\{-20°, 45°, 10°\}$ (e) $\{20°, -45°, -10°\}$ (f) $\{20°, -45°, 10°\}$

(g) $\{20°, 45°, -10°\}$ (h) $\{20°, 45°, 10°\}$ (i) $\{0°, 0°, 0°\}$

Figure 4.37 – Mechanical interference regions between a cable and an edge for the nine chosen attitudes $\{\theta_x,\ \theta_{y^{\mathrm{I}}},\ \theta_{z^{\mathrm{II}}}\}$ of the end effector of the final eight-cable seventeen-edge six-DoF CDP (Trial 64).

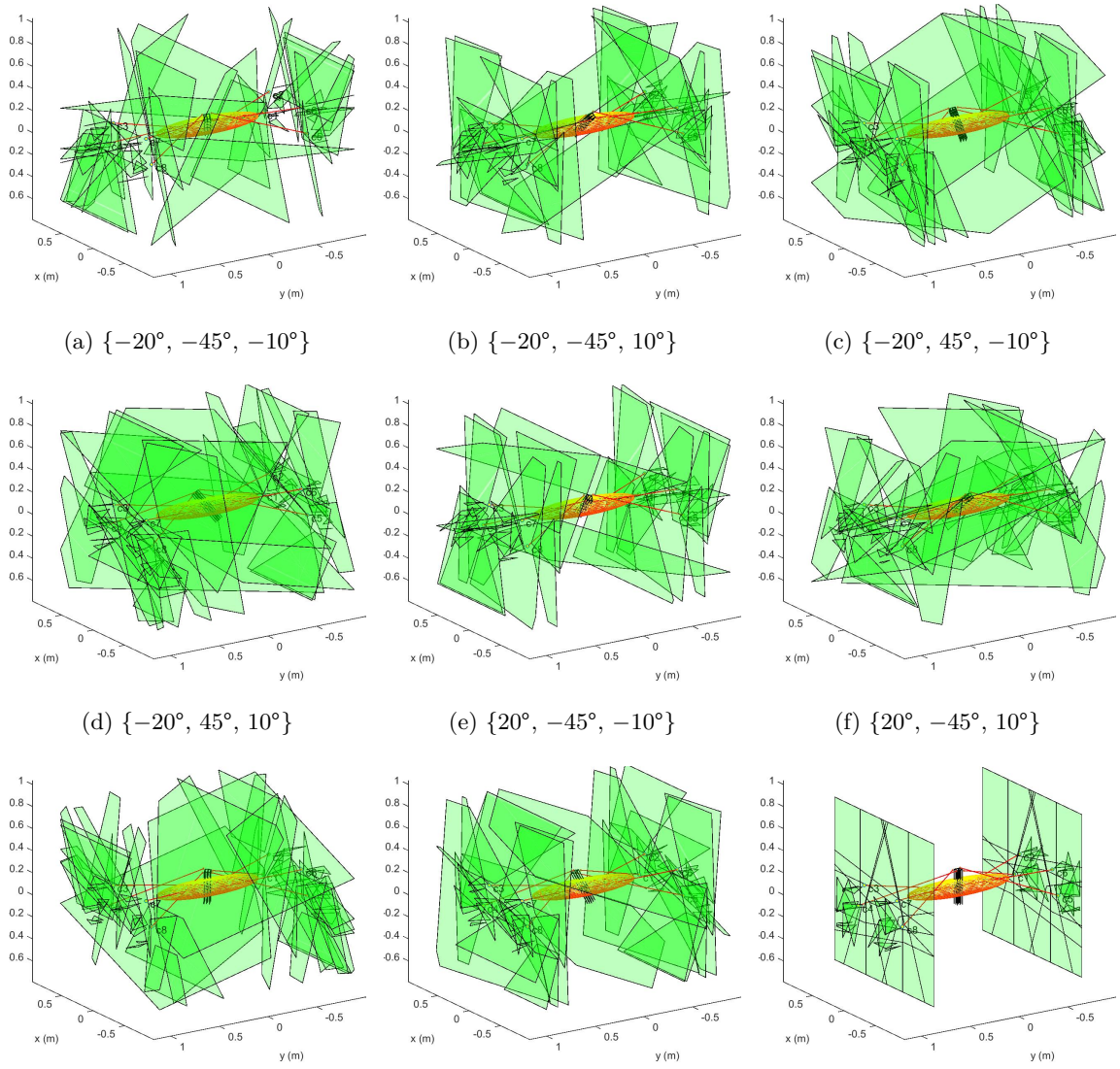

(a) {−20°, −45°, −10°} (b) {−20°, −45°, 10°} (c) {−20°, 45°, −10°}

(d) {−20°, 45°, 10°} (e) {20°, −45°, −10°} (f) {20°, −45°, 10°}

(g) {20°, 45°, −10°} (h) {20°, 45°, 10°} (i) {0°, 0°, 0°}

Figure 4.38 – Mechanical interference regions between two cables for the nine chosen attitudes $\{\theta_x, \theta_{y^{\mathrm{I}}}, \theta_{z^{\mathrm{II}}}\}$ of the end effector of the initial eight-cable seventeen-edge six-DoF CDP (Trial 100).

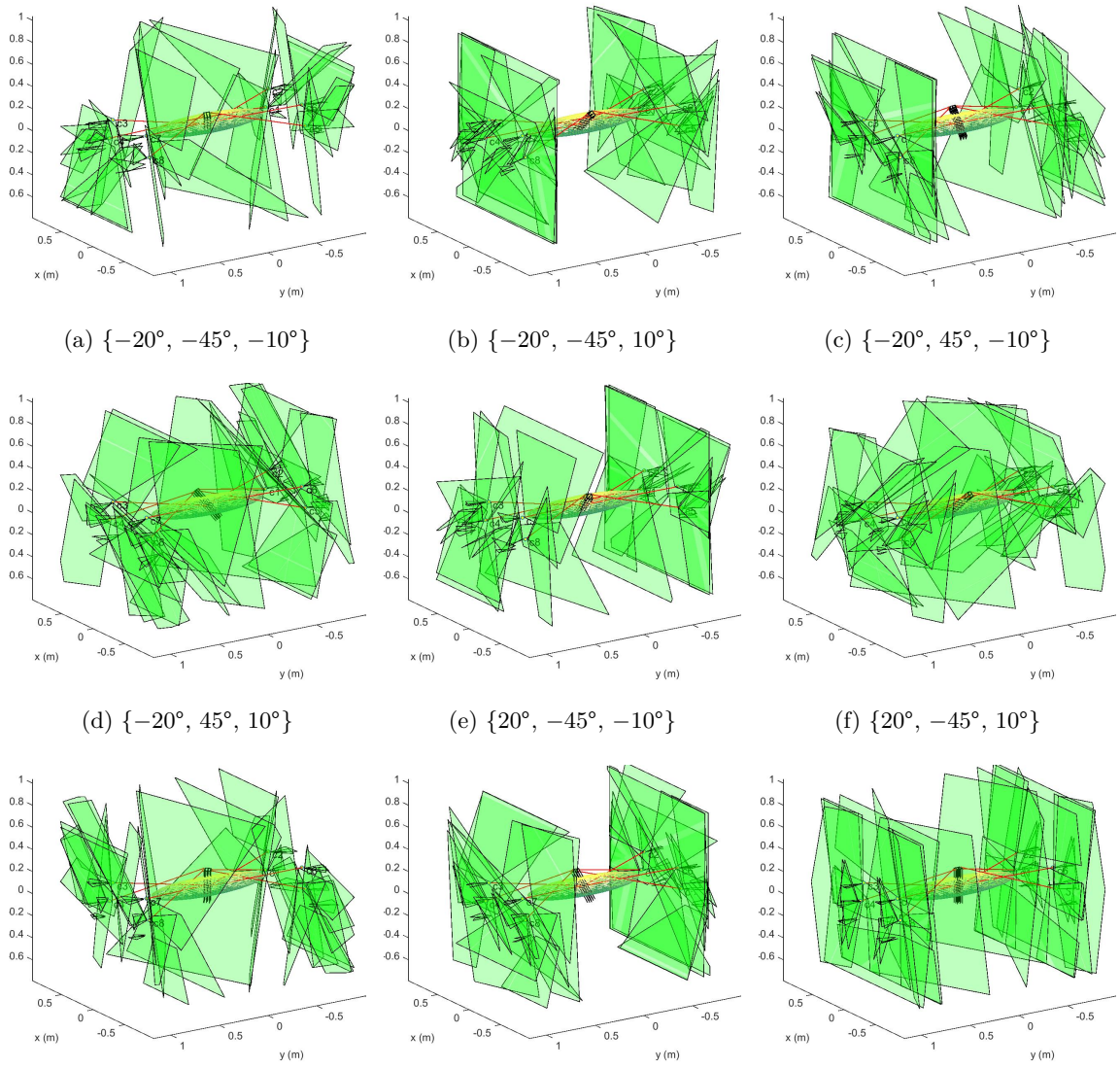

(a) {−20°, −45°, −10°} (b) {−20°, −45°, 10°} (c) {−20°, 45°, −10°}

(d) {−20°, 45°, 10°} (e) {20°, −45°, −10°} (f) {20°, −45°, 10°}

(g) {20°, 45°, −10°} (h) {20°, 45°, 10°} (i) {0°, 0°, 0°}

Figure 4.39 – Mechanical interference regions between two cables for the nine chosen attitudes $\{\theta_x, \theta_{y^{\mathrm{I}}}, \theta_{z^{\mathrm{II}}}\}$ of the end effector of the final eight-cable seventeen-edge six-DoF CDP (Trial 100).

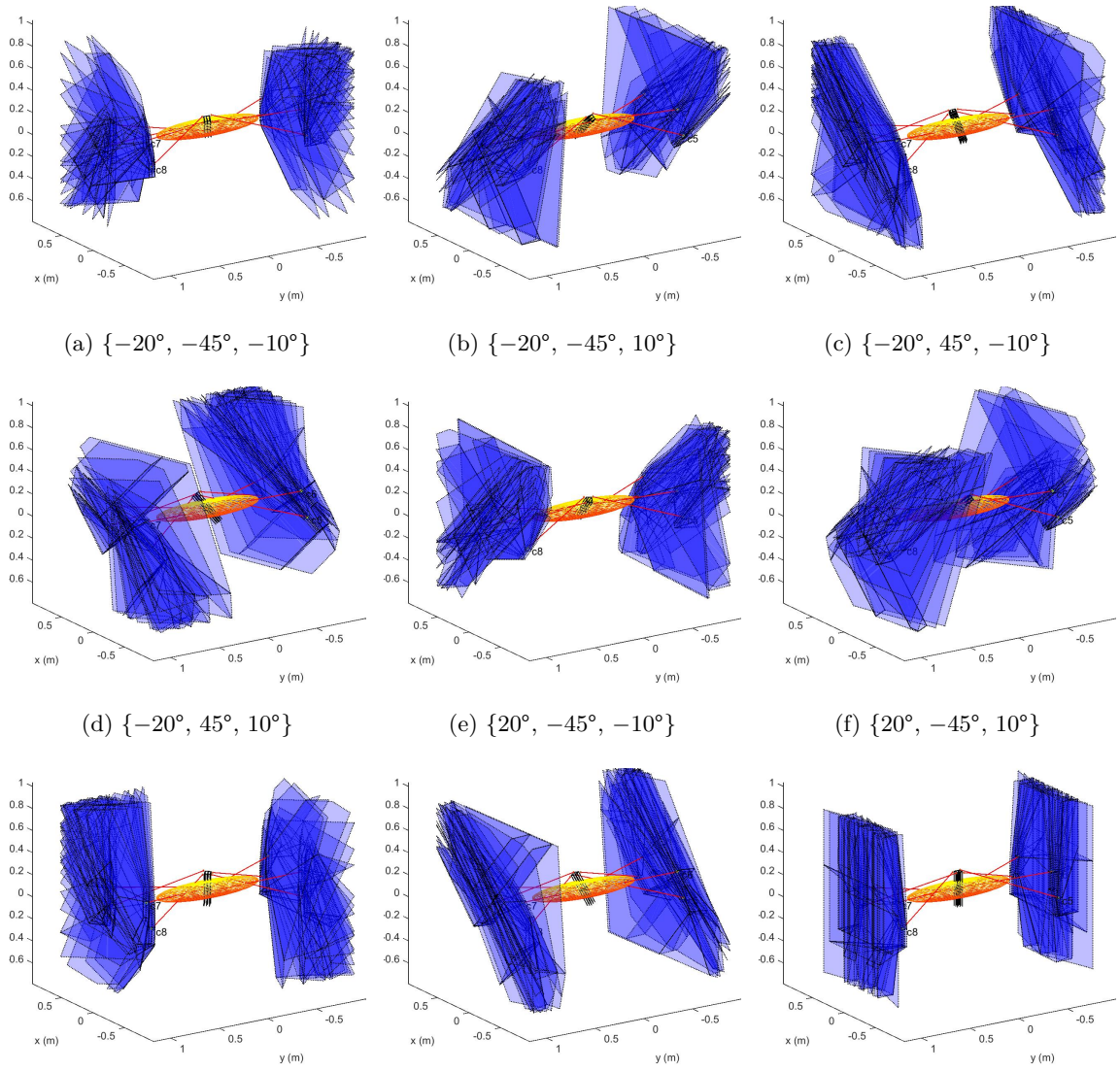

(a) {−20°, −45°, −10°} (b) {−20°, −45°, 10°} (c) {−20°, 45°, −10°}

(d) {−20°, 45°, 10°} (e) {20°, −45°, −10°} (f) {20°, −45°, 10°}

(g) {20°, 45°, −10°} (h) {20°, 45°, 10°} (i) {0°, 0°, 0°}

Figure 4.40 – Mechanical interference regions between a cable and an edge for the nine chosen attitudes $\{\theta_x, \theta_{y^{\mathrm{I}}}, \theta_{z^{\mathrm{II}}}\}$ of the end effector of the initial eight-cable seventeen-edge six-DoF CDP (Trial 100).

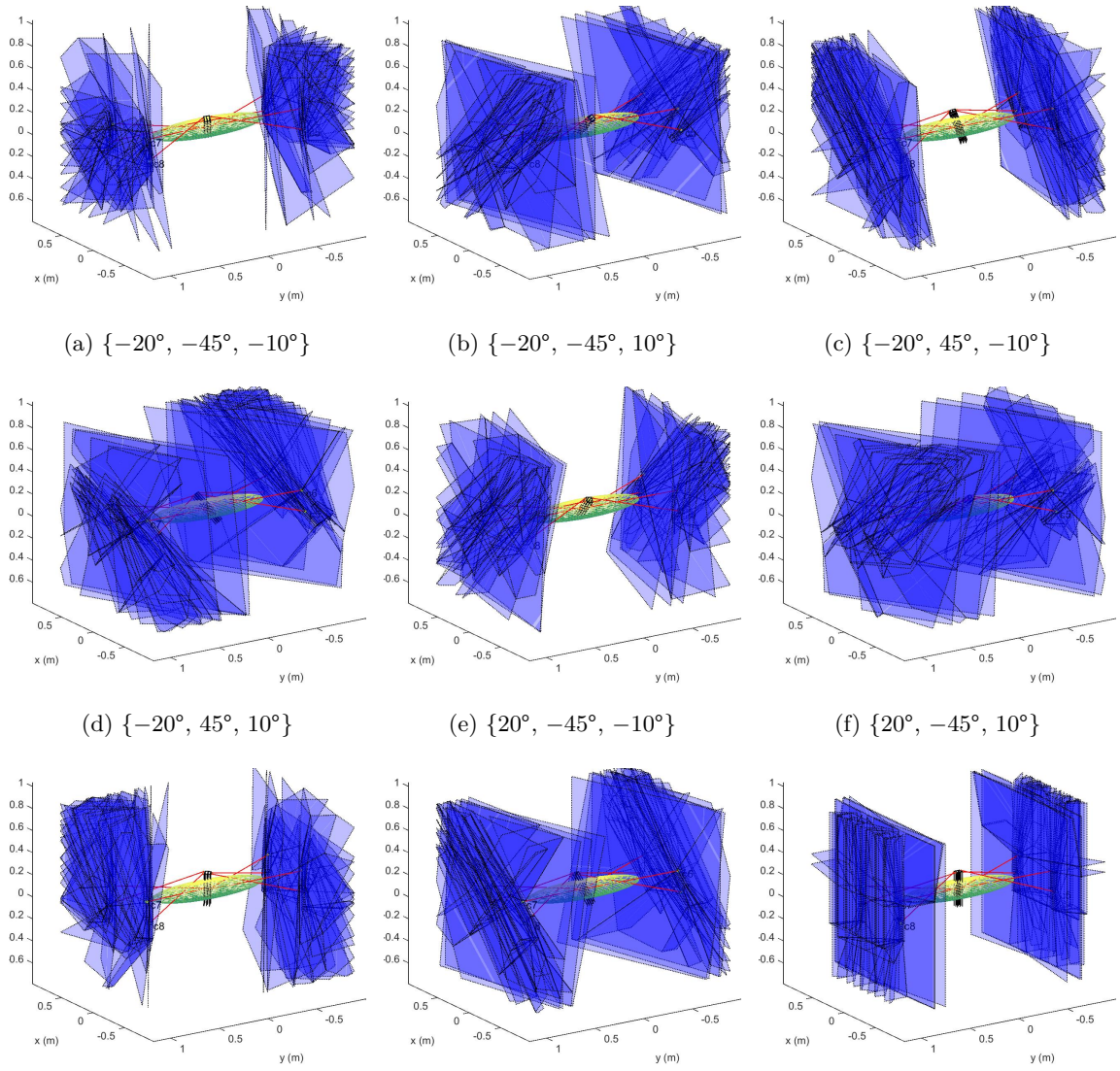

(a) $\{-20°, -45°, -10°\}$ (b) $\{-20°, -45°, 10°\}$ (c) $\{-20°, 45°, -10°\}$

(d) $\{-20°, 45°, 10°\}$ (e) $\{20°, -45°, -10°\}$ (f) $\{20°, -45°, 10°\}$

(g) $\{20°, 45°, -10°\}$ (h) $\{20°, 45°, 10°\}$ (i) $\{0°, 0°, 0°\}$

Figure 4.41 – Mechanical interference regions between a cable and an edge for the nine chosen attitudes $\{\theta_x,\ \theta_{y^{\mathrm{I}}},\ \theta_{z^{\mathrm{II}}}\}$ of the end effector of the final eight-cable seventeen-edge six-DoF CDP (Trial 100).

seventeen-edge six-DoF CDP. We know, however, from previous chapters, that the master part will have the same geometry as the slave part, up to a scaling factor κ_s. The selection of the optimal scaling factor is left for further work. Also, more analyses need to be completed in order to confirm that no mechanical interference can occur within its workspace and to determine a method, possibly based on the one presented in Chapter 2, to statically balance, in an approximate manner at least, this geometrically optimum CDP. Finally, a suitable selection of non-magnetic and non-conductive materials should be performed in order to manufacture such a mechanism, keeping in mind that ultimately it has to be MR-compatible.

4.4 Summary

The main purpose of this chapter is to present to the reader a new algorithm for the dimensional synthesis of cable-driven pantographs. Since the conceptual design of CDPs is based on the assembly of two fully-constrained CDPMs, this technique is inherently well suited for the dimensional synthesis of any CDPM, except those of the suspended type, which use the gravity effect to keep their cables under tension.

The first section served to survey the variety of tools available in the literature to solve the different types of optimization problems; which we divided into the two categories of local and global optimization techniques. It was also shown that each category can be sub-divided in two distinct branches, i.e., local optimization tools intended for unconstrained problems (for instance, Newton's method and the Gradient method) or for constrained problems (for instance, the Simplex methods, the Interior-Point methods and the SQP methods) and global optimization tools leading to guaranteed optimum (for instance, the Cutting Plane methods, the Branch and Bound methods and the Homotopy methods) or non-guaranteed optimum (for instance, the Simulated Annealing techniques, the Genetic Algorithms and the Multi-Start methods). The last part of this section provided an overview of published work specifically focusing on the application of optimization techniques to the synthesis of CDPMs. This review of literature has highlighted the fact that, to our best knowledge, no research group has yet combined an exact geometric interference index, which is not based on given trajectories, with a wrench workspace index, such as the wrench-closure workspace, into a single algorithm to optimize the full geometry—both attachment points of all cables—of a spatial CDPM for a prescribed workspace.

The second section described the new synthesis technique proposed to optimize the geometric parameters of spatial CDPs and spatial CDPMs. First of all, it was explained that the prescribed six-DoF workspace is divided in two parts: a three-DoF workspace in translation $\mathcal{W}_{p,t}$, and a three-DoF workspace in rotation $\mathcal{W}_{p,r}$. For simplicity reasons, it was decided to determine the required mathematical relations at discrete orientations of the CDPM end-effector in order to cover $\mathcal{W}_{p,r}$, which is common practice in the literature. For $\mathcal{W}_{p,t}$, however,

it was shown in Sub-section 4.2.1 that the prescribed workspace in translation is mapped to an ellipsoid instead of the box commonly used. This has the advantage of requiring a single relation to fully define the CDPM workspace in translation, as compared to the six relationships required for a box. The consequence of this choice was presented in the following sub-sections, where the three main criteria of the proposed algorithm were defined. In Sub-section 4.2.2, the constant-orientation wrench-closure workspace is presented as the first criterion. This workspace represents the set of end-effector positions where the CDPM is fully constrained by its cables for a given orientation. Its corresponding maximization problem is defined in Eq. (4.22). Sub-section 4.2.3 presented the second criterion which is the constant-orientation cable-cable interference. Its corresponding maximization problem, see Eq. (4.33), was derived by combining the ellipsoid relation with the mathematical definition of the interference regions between two cables obtained in Chapter 3. The last criterion was described in Sub-section 4.2.4 as the constant-orientation cable-edge interference. Its corresponding maximization problem is shown in Eq. (4.47) and it has been determined following the same process as that followed for the previous criterion. Finally, the complete problem describing the proposed dimensional synthesis algorithm was illustrated with Eq. (4.49). The main goal of this technique is to satisfy these three main criteria while optimizing the geometric parameters of the CDPM.

The following section focused on the numerical applications of the proposed algorithm. The initial part shows how the synthesis problem has been reformulated as a minimization problem, and solved using the MATLAB® *Optimization Toolbox*. In particular, the `fmincon` function was used, as it is suited for nonlinear constrained problem. The flowchart of the CDPM dimensional synthesis method was presented along with its constituting steps, which follow a Multi-Start approach. In Sub-section 4.3.1, the first numerical application of the algorithm was reported, i.e., the dimensional synthesis of an arbitrary seven-cable nine-edge six-DoF CDPM. This example was intended to show the behaviour of our proposed method. Among the fourteen trials that were launched during this first test (thirteen from random initial geometries and one from a human-reflected geometry), six resulted with a $\kappa \geq 1$ (κ being the negative of the objective function value) of which the best value was $\kappa^\star = 1.5192$. These results tend to prove that our proposed method can significantly improve the CDPM geometry while satisfying the three chosen criteria. A complete analysis was then performed in order to compare the initial geometry with the final ones among the most promising trials. These analyses easily demonstrated the superiority of the optimized solution. The set of fourteen trials of this first numerical example was fully computed in less than 24 hours.

Finally, in Sub-section 4.3.2, a second example was proposed to the reader, i.e., the dimensional synthesis of an eight-cable seventeen-edge six-DoF CDP intended for a medical application. The envisioned application was the manipulation of needles inside a MRI scanner in order to perform simple image-guided punctions or biopsies on patients. From the

three different types of existing MRI scanners, the cylindrical model was the one chosen in order to define the workspace limitations for the positioning of the attachment points of the cable-driven mechanism. This choice was based on the fact that the cylindrical MRI scanner model presents the strongest MR signal and best field homogeneity, which generate the best image quality compared to the C-shaped and double-donut configurations. A short review of the literature demonstrated that many devices have been designed by other researchers in order to perform tasks inside the gantry of these cylindrical imagers. A majority of them used ultrasonic motors, optical sensors, hydrostatic transmissions, hydrodynamic or pneumatic actuators in order to render their systems MR-compatible. In this work, we rather relied on a purely-mechanical cable-driven master-slave architecture, or, in other words, a CDP. Since the purpose of this chapter was to elaborate a dimensional synthesis program to synthesize the CDP, emphasis was put on the geometric constraints. Based on a recent model of a MRI system, i.e., the MAGNETOM® Skyra three-tesla by Siemens, and data provided in Refs. [298, 299], we defined the workspace requirements for the targeted application (see Figs. 4.28 and 4.29). We then added linear constraints to our problem in order to restrict the search to symmetric optimized geometries, which led to the formulation of the synthesis problem corresponding to this particular example with Eq. (4.91). Solving this new optimization program using the Multi-Start approach with a hundred initial guesses took 270.56 hours. Among the hundred trials (ninety-nine from random initial geometries and one from a human-reflected geometry), three resulted in a κ value close or higher than 0.9, the best result being that of Trial 100, with $\kappa^\star = 1.0880$. Because its objective value is greater than one, this local solution represents a suitable CDP geometry for the intended application. Indeed, its wrench-closure workspace includes the prescribed ellipsoid $\mathcal{W}_e$ and no cable-cable and cable-edge interferences occur within its final workspace, at least for the nine evaluated end-effector attitudes $\mathbf{Q}_k$, $k = 1, \ldots, 9$. Even if the results shown in this sub-section seem promising, the reader must be aware that further design work still needs to be completed, such as the determination of the best scaling factor κ_s between the master and the slave parts, for a prototype of this eight-cable seventeen-edge six-DoF CDP to be usable and MR-compatible.

Conclusion

"Life is pretty simple: You do some stuff. Most fails. Some works. You do more of what works. If it works big, others quickly copy it. Then you do something else. The trick is the doing something else."
- Leonardo da Vinci

This thesis presented the first steps towards the development of a new family of mechanisms, which we call *cable-driven pantographs* (CDPs). These mechanisms can be seen as of the telemanipulator or teleoperator type since they are based on a master-slave architecture. Both parts—the master and the slave—are represented by a single cable-driven parallel mechanism (CDPM) with identical geometries, except for a given scaling factor which is selected based on the requirements of the intended application. Force transmission within a CDP is ensured by the cables constraining the moving platforms and their corresponding nonlinear spring-loaded assemblies, which are specifically designed to generate the required tensions.

The main objective here was, as described in the Introduction, to develop relevant tools in order to assess and enhance CDP capabilities as well as to optimize their geometries for given applications. But more specifically, the initial idea that carries this work was to initiate the development of a low-cost, safe and reliable telemanipulator system that could be used within the bore of a magnetic-resonance imaging (MRI) scanner to remotely perform simple needle manipulations on patients, such as punctions and biopsies. From this application, a purely-mechanical design for the CDPs has been preferred to the conventional actuator-driven type to ultimately lead the device to be MRI-compatible.

From an academic perspective, the work presented in this thesis was intended to contribute to the scientific progress under five distinct topics. Firstly, the general objective was to develop and describe the new family of telemanipulators, i.e., the CDPs. Secondly, it was scheduled to elaborate their kinematic and kinetostatic models. Thirdly, the development and the evaluation of a methodology allowing to reach as close as possible the static equilibrium of a CDP over a given workspace was proposed. Fourthly, it was planned to develop a general method to geometrically determine the workspace regions where mechanical interferences involving the cables constraining the pose of the CDP end-effector occur. Lastly, a system-

atic approach was proposed to dimensionally synthesize the CDP geometry while satisfying geometric requirements based on the intended application.

This closing section summarizes for the reader the proposed methodologies and results described throughout this thesis while highlighting their main contributions. Then, with the objective of encouraging further research on CDPs, the author proposes ideas and guidelines for interested students to pursue and improve this work.

Summary and Contributions

In Chapter 1, the concept of cable-driven pantographs was unveiled as well as their working principle. Previous pantographs relied on rigid links, as it was the case for the planar two-dimensional pantograph reported in 1631 by Scheiner, or the more recent market-available three-dimensional devices designed for pure translations, or even the patented three-dimensional version that produces pure rotations. The work presented in this thesis innovates by using only cables—through a CDPM architecture—to transmit forces and fully constrain the pantograph motions within a six-dimensional workspace (three directions of translation and three axes of rotation).

The main advantages of CDPs over conventional telemanipulators are that they are purely mechanical and they are formed with CDPMs. Consequently, a CDP can be seen as a low-cost and reliable solution when no other sources of power is accessible or compatible with the working environment. The use of passive springs, which are directly linked to each cable-winding pulley, is found suitable to maintain the mechanism geometry over its workspace, i.e., to provide the minimum torques to keep the cables taut. Moreover, they exhibit advantages similar to those of CDPMs, such as lower inertia of the moving parts, potentially larger workspace and better portability.

This chapter also proposed a mathematical approach to derive the input-output displacement relationship, the input-output load relationship and the kinetostatic models for this new family of telemanipulators. As a result, the following rules were established. The geometry of the slave is proportional to that of the master through a constant scaling factor. The slave point-displacements are also in proportions with those of the master through the same scaling factor, and the slave rotations correspond exactly to those of the master. Moreover, if we consider that no friction acts on the cables connecting the master and slave moving platforms and that springs maintain a perfect equilibrium of the device over its workspace, we demonstrated that a given force at the slave end-effector would be balanced out by a force at the master end-effector in the opposite direction and proportional to the inverse of the scaling factor. On the other hand, a torque applied at the slave would be balanced by a torque equal in magnitude and opposite in direction at the master. The symbolic formulation for the kinetostatic model was also derived, for a two-cable one-DoF CDP and for a three-

cable two-DoF CDP. These equations were obtained using the assumption that a cable can slip without friction on its drum, so that the complete length of each cable undergoes deformation under a corresponding tension.

Preliminary validations of the CDP concept were completed in this chapter by building the first prototype of a three-cable two-DoF planar CDP using proportional-torque reel assemblies that link the master part to the slave one. The accuracy of input-output displacements between the master and the slave end-effectors was assessed and confirmed to be ≈ 0.49 and ≈ 0.50 along two orthogonal directions of the working plane, compared to the scaling factor of 0.5 that was chosen for this CDP. Also, using a force-torque sensor attached to the master end-effector, it was demonstrated that the force required from the user to statically hold the master end-effector in place was null only at the centre of the workspace. This result was expected since it is impossible to statically balance this system by using only springs at the drums. When moving the CDP end-effector over its workspace and away from this centre point, consequently, it was showed that the required forces were relatively high, even if slightly lower than the theoretical values. Indeed, the root mean square (RMS) value of the norm of the theoretical force over the CDP workspace was 24.7678 N and the experimental equivalent was $\approx$ 19.7 N. These differences were explained by the possible sources of errors involved in this type of measurements, such as assembly and measurement errors or the presence of friction within the mechanism. Overall, these preliminary experiments demonstrated the practicability of the CDP concept.

As it was clear from Chapter 1 that the devised CDP does not hold static equilibrium over its entire workspace, the focus of Chapter 2 was on the determination of a method to approximate as closely as possible the neutral equilibrium over the three-cable two-DoF CDP workspace. This novel approach relies on the design of passive nonlinear spring assemblies that are attached in parallel to the cables winding pulleys. These assemblies were formed by a four-bar linkage and a set of commercially-available constant-torque springs. They were designed to generate the required minimum cable tensions to preserve the system geometry and to minimize its potential energy fluctuations over the chosen CDP workspace.

The proposed method contains a series of four steps that must be completed to reach an optimum design of the passive nonlinear springs. Firstly, considering a given CDP geometry, the desired tension profile, which was shown as a function of the cable unwound length, has to be determined in order to minimize the norm of the resultant wrench acting at the master end-effector of the CDP. This tension profile was defined here as a polynomial of the Bernstein form, a linear combination of Bernstein bases, and it was obtained by solving a convex quadratic problem over the range of cable lengths. Secondly, knowing the kinematic model of a generic four-bar linkage, the determination of its prescribed behaviour was possible, i.e., the angular position of its output link as a function of the angular position of its input link, in order to produce the desired tension profile. Thirdly, a second convex quadratic problem

has to be solved to determine the best crank-rocker four-bar linkage system that can reproduce the prescribed input-output behaviour. Fourtly, a non-convex optimization problem has to be finally solved to completely define the remaining parameters of the nonlinear spring, i.e., the constant-torque values of the input and output links, their initial angular positions and the final angular position of the input link.

As a proof of concept, this new method was used to build the first prototype of a three-cable two-DoF CDP containing three passive nonlinear spring assemblies to maintain its geometry and to approximate a neutral equilibrium over its workspace. In order to determine a suitable solution for the design of the nonlinear springs, the suggested method was used to iterate over twenty different initial solutions and the best of all optimized solutions was kept. As in Chapter 1, a force-torque sensor was used to measure the forces that a user must apply at the end effector of the master to maintain a position. Experimental results demonstrated an improvement of approximately 50% compared to previous results where conventional proportional-torque springs were used. In theory, however, an improvement of approximately 75% was expected. This result, though still a significant step forward to the reach of the neutral equilibrium of CDPs, demonstrated that approximating a perfect static balancing using passive nonlinear springs can be, in practice, a difficult task due to all potential sources of errors. In light of the complexity of the nonlinear springs it involves, it is not clear whether such a balancing system would be of practical interest.

Since CDPs are formed with CDPMs, another problem needed to be addressed in this thesis, i.e., mechanical interferences between the moving parts of a CDPM. The technique proposed in this thesis distinguishes itself from others found in the literature, which rely on numerical methods to detect the occurrence of collisions between cables. In Chapter 3, the focus was rather on the development of a general method to geometrically determine in closed form the locus of mechanical interferences between all cables within the Cartesian workspace of a CDPM. Mechanical interferences in the planar case were first covered. Two examples of four-cable planar CDPMs were used to determine basic rules that can be applied when designing such a mechanism while aiming to keep the interference regions to a minimum. From the presented analysis, three basic rules were enumerated: First, minimize the number of cables used to constrain the CDPM. Second, minimize the number of attachment points at the base and at the end effector. Third, place the attachment points on the surface of a convex shape on the base and on the end effector.

The spatial case was then tackled in Chapter 3, which proved to be mathematically more involving. But as previously said, compared to other work found in the literature, the proposed method has the merit of taking advantage of the geometric properties of the phenomenon of mechanical interference in order to simplify the problem. As it was demonstrated in this chapter, for a mechanical interference to occur between a pair of cables, their attachment points must lie on the same plane in the CDPM workspace. This fact allows the simplification

of the problem from three dimensions to two dimensions, when the end-effector attitude of the CDPM is constant. It was also shown that this plane can be divided in nine distinct regions, only two of which involve a contact between the two cables considered. Then, an analogous mathematical derivation allowed to determine the interference region within the constant-orientation workspace between a cable and an edge of the end-effector. This derivation yielded similar results, except that the interference plane is now divided into seven regions and only one of them represents the locus where a collision occurs. Applying this method to each pair of cables of the CDPM and each combination of a cable and an edge of the end effector, for a given orientation, this approach proved to be a powerful tool to rapidly determine the locus of mechanical interferences for an arbitrary CDPM. Consequently, this tool can easily be used to design a CDPM or to plan Cartesian trajectories that avoid the interference regions within its workspace.

In order to validate the proposed methodology, two examples of application were presented to the reader. The first one was the analysis of the mechanical interference regions for a six-cable six-edge six-DoF CDPM and the second was the analysis of an eight-cable 31-edge six-DoF CDPM. These two examples were used to demonstrate the performances of the designed tool. With the first example, the set of regions containing the mechanical interference loci for all pairs of cables and all combinations of a cable and an end-effector edge were shown for nine different end-effector attitudes of the analyzed CDPM. The time required to compute and display the final results was less than a second, using a conventional computer, since the method is based on the exact geometry of the problem and does not need any iterative process or discretization. The second example was rather completed to compare the theoretical results obtained from the suggested method with experimental data measured on a CDPM prototype. In order to perform this experiment, a collision between two cables constraining the CDPM end-effector was generated within the mechanism workspace, for a given orientation, and the moving platform was moved while keeping the two cables in contact. The corresponding data was collected, i.e., the actuated-joint encoders of all cables, and compared, using the forward kinematic model, with the results obtained from the proposed methodology for the same pair of cables and the same end-effector attitude. This validation served as a proof of the efficiency of the geometric approach to predict the loci where the mechanical interferences between the two given cables occur since it was shown that the resulting interference planes—both experimental and theoretical—shared a similar normal vector and were almost passing through the same points in the CDPM workspace.

With the results obtained in Chapter 3, it was then clear that the suggested method to determine the mechanical interferences between the moving parts of a CDPM could be used as a tool to facilitate their synthesis. Consequently, the objective of Chapter 4 was the development of a global methodology to dimensionally synthesize the geometry of CDPMs, and inherently CDPs, that fulfill application-based requirements. First, an exhaustive overview of

the mathematical methods available in the literature to solve unconstrained and constrained local and global optimization problems was presented to the reader. Then a focus was set on the few researches that have been published on the synthesis of CDPMs, which, for the collision detection part, are mostly based on the use of Cartesian trajectories to determine the likelihood of moving-part collisions to occur. The innovation of the proposed synthesis method was to combine into the same optimization problem the exact geometry-based technique developed in Chapter 3 to detect mechanical interferences and a well-known index to design CDPMs, i.e., the wrench-closure workspace (WCW).

The approach suggested to dimensionally synthesize CDPMs, or CDPs, was based on the fact that the translational workspace is defined as an ellipsoid and the rotational workspace is discretized into a given number of constant end-effector attitudes. The choice of the ellipsoid was explained by the need of minimizing the required number of constraints to define the mechanism workspace, i.e., a single equation can be used to fully define the geometry of an ellipsoid compared to a set of equations for the definition of a box. Three different criteria were mathematically derived, and formulated as three distinct maximization problems, in order to present the bases of the global optimization algorithm: The constant-orientation wrench-closure workspace (COWCW), the constant-orientation cable-cable interference (COCCI), and the constant-orientation cable-edge interference (COCEI). Once combined, the global optimization problem was shown to be a minimization problem that aims at maximizing the size of the ellipsoid, where all constraints of the COWCW, the COCCI and the COCEI are fulfilled, for each given attitude of the CDPM end-effector, while modifying the attachment points of all cables. It was then proposed to solve this optimization problem by following a Multi-Start approach. In such a scheme, a classical descent method is ran several times from different initial guesses, leading to as many locally optimum solutions. The best of these local optima is retained and yields the synthesized CDPM geometry.

Finally, two examples of application for the proposed synthesis methodology were presented to the reader: The synthesis of an arbitrary seven-cable nine-edge six-DoF CDPM and the synthesis of an eight-cable seventeen-edge six-DoF CDP intended for a medical intervention. In the first example, the objective was to demonstrate the relevance and efficiency of this tool to optimize the geometry of a CDPM. The algorithm ran for slightly less than 24 hours, used a Multi-Start method with fourteen initial solutions, and a set of nine different end-effector attitudes to cover the prescribed workspace in rotation. Five of the fourteen optimizations ultimately converged to a final geometry that allows the ellipsoid to fulfill the prescribed workspace in translation. Then, an exhaustive analysis was proposed to the reader in order to validate the work accomplished by the synthesis program, i.e, for the best geometry among the fourteen trials, a comparison between the performances of the initial and the final solutions. From these results, it was clear that the optimization program allows to find the best compromise between the wrench-closure workspace, the cable-cable interference-free

workspace, and the cable-edge interference-free workspace, all at once, since significant improvements were observed between the initial and the optimized solutions. The same exercise was completed with the second example, which required to fulfill much more demanding constraints. The CDPM, which acts as the slave part of a CDP, has to be inserted inside the bore of a cylindrical MRI device to perform simple medical interventions. For this example, additional constraints were added in order to avoid any collision of the moving parts with the patient and with the internal wall of the MRI scanner. Using here a set of one hundred initial solutions for the Multi-Start method, and after slightly more than eleven days of computation, it was shown that three optimizations led to a geometry that fulfills more than 89% of the prescribed requirements, and among these three, one slightly exceeded the requirements at 108.8%. These results proved that the synthesis program proposed in this chapter is a relevant tool to dimensionally synthesize CDPMs, and, furthermore, that the design of a CDP that is intended to be used inside the gantry of a MRI device is possible.

The main goal of this thesis was to develop tools that aim to facilitate the work of designers when it comes to the synthesis of CDPs, and, by the same token, to the synthesis of single CDPMs. By the nature of this task, as the reader may imagine, many modifications could have been implemented as well as many different research directions could have been investigated in order improve this work. The next section summarizes potential ideas for such improvements.

Future Work and Research Directions

As any long-term project, it is relatively easy, once at the end, to make a list of tasks that could have been completed in order to improve its final outcomes. The objective of this section is, consequently, to present this list to those who may be interested in pursuing the work initiated in this thesis.

The following enumeration presents the proposed research avenues:

- A complete kinetostatic model for a generic n-DoF CDP should be explicitly defined. This model would involve, without any doubt, more demanding mathematical formulations than those presented in Sub-section 1.3.5, since it would include the end-effector orientations;
- In order to complete the validation of the kinetostatic model for linear and planar CDPs presented in Section 1.4, a prototype equipped with tension measuring instruments, e.g., load cells, should be designed and built. This experimental setup would allow the measurement of cable tensions while moving the master end-effector and applying different forces at the slave end-effector;
- In order to improve the experimental outcomes presented in Sub-section 2.2.4, regarding the level of neutral equilibrium reached at the CDP end-effector, one should equip the

bench test with load cells to measure the tension profile, as a function of the cable length, that each nonlinear spring assembly generates independently. The resulting tension profile should be compared with the prescribed tension profile and parameters should be adjusted towards a better tension profile generation. Once each nonlinear spring assembly is proven to produce the desired behaviour, a new evaluation of the level of neutral equilibrium should be made;

- The method proposed in Chapter 2 to approximate the static balancing of a planar CDP over its workspace should be extrapolated to the spatial case, at least for a constant-orientation end-effector pose. This application to the spatial case would involve the integration of a dimensionless scaling factor between the degrees of freedom in translation and those in rotation, since they do not contain the same units inside the optimization problems;

- In order to improve the performances of the passive nonlinear springs to approximate the neutral equilibrium within the CDP workspace, it would be interesting to evaluate a design based on the use of cams instead of a crank-rocker four-bar linkage. It would then be possible to reduce the overall dimensions of the nonlinear spring assembly;

- The method proposed to geometrically determine the interference-free regions of a CDP should be applied to the case of a mechanical interference between a cable or an end-effector edge with an edge of a static object lying inside the mechanism workspace. This object could represent an obstacle inside the CDP workspace such as the patient body or a third-party tool. This could become an additional criterion to be integrated within the algorithm to synthesize CDPM geometries in Chapter 4;

- In order to improve the geometric approach to determine mechanical interferences, it would be interesting to evaluate the possibility of detecting collision between a cable and a surface of the end effector rather than an edge. The use of edges in collision detection requires an approximate wireframe model of the end effector. This sometimes leads to false negatives because a cable passes through the end effector without touching any of its edges;

- An additional verification method should be developed and integrated to the analysis method in order to determine whether two entities cross each other between two different evaluated constant orientations of the CDP end-effector. The common perpendicular vector between two entities, e.g., a pair of cables, a cable and an end-effector edge, or a cable and a surface belonging to the end-effector geometry, could be used as the index, as its direction would change when the entity passes through the other;

- Also, the method proposed to detect the occurrence of mechanical interferences could be extended to take into account given ranges of CDP end-effector attitudes. The

resulting regions would line in the constant-point-position workspace, and, unlike the regions obtained in this thesis they would not be polygons;

- In Chapter 4, it would be useful to generalize the ellipsoid formulation of Eq. (4.1) in order to allow the definition of the prescribed workspace in translation with any orientation, and not be restricted to the orientation where the principal axes of the ellipsoid are parallel to those of the global frame;

- It would also be useful to replace the ellipsoid representing the workspace with a more conventional shape such as a box. This would add more constraints to the synthesis problem, but the workspace in translation would be more representative of the conventional application for CDPs;

- Instead of using the wrench-closure workspace as a criterion for the dimensional synthesis of CDPs, the integration of the wrench-feasible workspace (WFW) should be considered. This approach would add a level of complexity to the optimization problem, but the final solutions would be more practical, since a specific range for the cable tensions would be defined. The design of a CDP or CDPM would consequently be better tailored to a given set of tasks;

- With a generalized technique to approximate the neutral equilibrium over a CDP workspace, it would be interesting to include this criterion within the CDP synthesis problem in order to optimize the attachment points of each cable while reducing the fluctuations of the system potential energy for a given passive nonlinear spring. This tool, if found efficient regarding to the required computation time, would allow to directly synthesize CDPMs and CDPs with improved mechanical properties;

- A prototype of an eight-cable seventeen-edge six-DoF CDP should be designed and built in order to experimentally validate the practicability of the solution proposed for the intended medical application. This prototype could also serve as a test bench to evaluate different approaches to approximate a neutral equilibrium over the CDP workspace;

- With the objective of installing the CDP inside the bore of a cylindrical MRI scanner and perform medical interventions such as simple biopsies and punctures, one should be aware that many design steps still need to be completed first: To determine a set of MRI-compatible materials in order to build the CDP device (for example, non-magnetic and dielectric materials such as plastics, ceramics, and composites), to evaluate the best scaling factor between the master and the slave parts for the intended application, to design the end-effector tool that would allow the insertion and extraction of the needle, to evaluate the haptic capabilities of the spatial CDP, to evaluate the dynamic properties of the CDP device over a few metres, etc;

- In the case of a CDP application different from medical interventions inside the bore of a MRI scanner, the passive nonlinear springs could be used in parallel to electric actuators in order to correct for the deviation from the neutral equilibrium of the mechanism. This hybrid-type system would have the advantage of presenting a higher level of safety in case of a power failure, since the system would be in a quasi-static equilibrium due to the presence of the passive nonlinear springs. Thus, relatively small displacements of the end effector should be expected in such a situation, instead of a complete loss of control, which occurs when only electric actuators are used. In this way, only small contributions from the electric motors would be necessary to better approximate the static equilibrium;

- In a more general concept, it would be interesting to investigate the possibility of including the number of cables used to constrain the pose of the CDP end-effectors as a variable within the proposed synthesis problem. The pre-selected number of cables for the design of a CDP may not be optimal in regards of the intended application;

- Finally, it would be interesting to code the synthesis program with a more efficient programming language, such as C/C++, in order to decrease the computation time required to solve the optimization problem.

As the reader may notice, a wide variety of interesting topics could be investigated by those who are motivated to further understand and enhance the capabilities of this new type of telemanipulators, now known as *cable-driven pantographs*.

Fin.

Appendix A

Jacobian Matrix of Cable-Driven Parallel Mechanisms

This appendix presents the mathematical derivation leading to the determination of the Jacobian matrix corresponding to two different types of cable-driven parallel mechanisms (CDPMs). The Section A.1 shows the formulation of the Jacobian matrix associated to the planar m-cable three-DoF CDPMs and Section A.2 focuses on the general case, i.e., the spatial m-cable six-DoF CDPMs.

A.1 Planar Three-DoF Cable-Driven Parallel Mechanisms

Figure A.1 illustrates the kinematic model of a generic planar three-DoF CDPM. The vector $\mathbf{a}_i$ represents the position in two dimensions of the fixed-base eyelet A_i in the fixed frame $\mathcal{A}$, the vector $\mathbf{b}_i^{\mathcal{B}}$, expressed in frame $\mathcal{B}$ (attached to the moving platform), represents the position of the attachment point B_i of cable i on the moving platform, the vector $\mathbf{p}$, which is expressed in $\mathcal{A}$, represents the position of the reference point P on the moving platform with respect

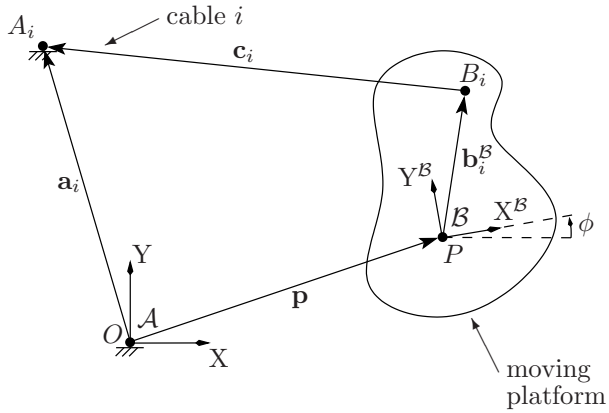

Figure A.1 – Kinematic modelling of a planar three-DoF CDPM.

to point O, and the vector $\mathbf{c}_i$ points from B_i to A_i, which represents the i^{th} cable, $i = 1, \ldots, m$, and where m is the total number of cables for the given CDPM. Finally, the following expression, which is commonly called the loop-closure equation, represents the length c_i of the cable i:

$$c_i = ||\mathbf{c}_i|| = \sqrt{(\mathbf{a}_i - \mathbf{p} - \mathbf{Q}\mathbf{b}_i^{\mathcal{B}})^T(\mathbf{a}_i - \mathbf{p} - \mathbf{Q}\mathbf{b}_i^{\mathcal{B}})}. \tag{A.1}$$

Moreover, we define the matrix $\mathbf{Q}$, that rotates frame $\mathcal{A}$ onto frame $\mathcal{B}$, as follows

$$\mathbf{Q} = \begin{bmatrix} \cos(\phi) & -\sin(\phi) \\ \sin(\phi) & \cos(\phi) \end{bmatrix}, \tag{A.2}$$

where ϕ is the variable representing the rotation motion of the PCDM's end-effector, following the right-hand method for its positive direction.

In order to derive the Jacobian matrix, we must first define the CDPM's velocity relations. We begin with the time derivative of the relation c_i^2, which is equivalent to $\mathbf{c}_i^T\mathbf{c}_i$ based on Eq. (A.1), that we express as follows:

$$c_i\dot{c}_i = (\mathbf{a}_i - \mathbf{p} - \mathbf{Q}\mathbf{b}_i^{\mathcal{B}})^T(-\dot{\mathbf{p}} - \dot{\mathbf{Q}}\mathbf{b}_i^{\mathcal{B}}), \tag{A.3}$$

where

$$\dot{\mathbf{Q}} = \mathbf{E}\mathbf{Q}\dot{\phi}, \tag{A.4}$$

and where $\dot{\phi}$ is the angular velocity component and $\mathbf{E}$ is the following matrix (a $\pi/2$ rad rotation matrix):

$$\mathbf{E} = \begin{bmatrix} 0 & -1 \\ 1 & 0 \end{bmatrix}. \tag{A.5}$$

Then, the velocity equation is given by

$$c_i\dot{c}_i = -(\mathbf{a}_i - \mathbf{p} - \mathbf{Q}\mathbf{b}_i^{\mathcal{B}})^T\dot{\mathbf{p}} - [(\mathbf{a}_i - \mathbf{p} - \mathbf{Q}\mathbf{b}_i^{\mathcal{B}})^T\mathbf{E}\mathbf{Q}\mathbf{b}_i^{\mathcal{B}}]\dot{\phi}. \tag{A.6}$$

This relation can be also expressed as follows:

$$\mathbf{J}\dot{\mathbf{s}} = \mathbf{K}\dot{\mathbf{c}}, \tag{A.7}$$

where matrix $\mathbf{J}$ is of dimension $m \times 3$, its i^{th} row being expressed as

$$\mathbf{j}_i = \begin{bmatrix} -(\mathbf{a}_i - \mathbf{p} - \mathbf{Q}\mathbf{b}_i^{\mathcal{B}})^T & -(\mathbf{a}_i - \mathbf{p} - \mathbf{Q}\mathbf{b}_i^{\mathcal{B}})^T\mathbf{E}\mathbf{Q}\mathbf{b}_i^{\mathcal{B}} \end{bmatrix}, \; i = 1, \ldots, m, \tag{A.8}$$

while matrix $\mathbf{K}$ is given by

$$\mathbf{K} = \begin{bmatrix} c_1 & 0 & 0 \\ 0 & \ddots & 0 \\ 0 & 0 & c_m \end{bmatrix}, \tag{A.9}$$

and $\dot{\mathbf{s}}$ and $\dot{\mathbf{c}}$ are the three-component Cartesian velocity vector and the m-component joint velocity vector, respectively. These two vectors can be written as follows:

$$\dot{\mathbf{s}} = \begin{bmatrix} \dot{\mathbf{p}}^T & \dot{\phi} \end{bmatrix}^T, \quad \text{and} \quad \dot{\mathbf{c}} = \begin{bmatrix} \dot{c}_1 & \cdots & \dot{c}_i & \cdots & \dot{c}_m \end{bmatrix}^T. \tag{A.10}$$

In summary, Eq. (A.7) represents the relationship between the Cartesian velocity and the joint velocity and it can be rearranged as

$$\dot{\mathbf{c}} = \mathbf{K}^{-1}\mathbf{J}\dot{\mathbf{s}}. \tag{A.11}$$

Then, using the principle of virtual work, we know that

$$-\mathbf{t}^T\delta\mathbf{c} + \mathbf{w}_p^T\delta\mathbf{s} = 0, \tag{A.12}$$

where $\delta\mathbf{c}$ and $\delta\mathbf{s}$ are the small virtual variations in the vector of cable lengths and in the vector of Cartesian coordinates $\{x,\ y,\ \phi\}$ of the end-effector pose, respectively. The vector $\mathbf{t}$ contains the magnitude of all cable tensions t_i and vector $\mathbf{w}_p$ represents the wrench exerted by the surrounding on the CDPM's end-effector, e.g., the gravity effect, the inertial effects and any additional external wrenches. The first part of this equation, i.e., $-\mathbf{t}^T\delta\mathbf{c}$, is the virtual work produced by the cable tensions on the moving platform (the negative sign results from the fact that the cable length c_i increases following the opposite direction of vector $\mathbf{c}_i$) while the second part, i.e., $\mathbf{w}_p^T\delta\mathbf{s}$, is the virtual work produced by the surrounding on the moving platform.

From Eq. (A.11), therefore, the following relationship can be established:

$$\delta\mathbf{c} = \mathbf{K}^{-1}\mathbf{J}\delta\mathbf{s}. \tag{A.13}$$

By substituting Eq. (A.13) into Eq. (A.12), we finally obtain the following equation:

$$\mathbf{W}\mathbf{t} = -\mathbf{w}_p, \tag{A.14}$$

where $\mathbf{W}$ is the Jacobian matrix of a planar m-cable three-DoF CDPM, a rectangular matrix of dimension $3 \times m$, which is defined as follows:

$$\mathbf{W} = -(\mathbf{K}^{-1}\mathbf{J})^T. \tag{A.15}$$

A.2 Spatial Six-DoF Cable-Driven Parallel Mechanisms

The determination of the Jacobian matrix corresponding to a spatial m-cable six-DoF CDPM can be easily obtained by following the same approach used in the previous section for the planar case.

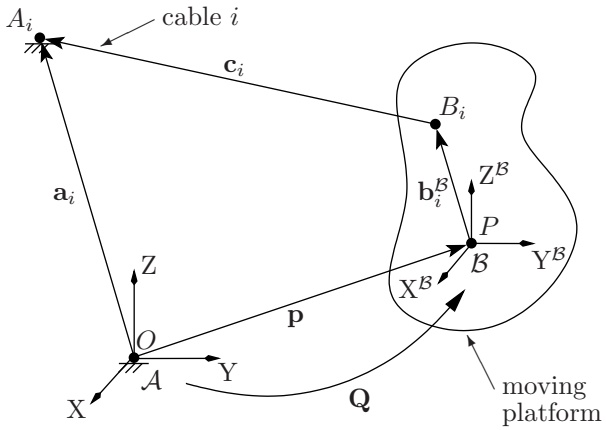

Figure A.2 – Kinematic modelling of a spatial six-DoF CDPM.

From Fig. A.2, which shows the kinematic model of a generic spatial six-DoF CDPM, we first express the length c_i of the i^{th} cable as

$$c_i = ||\mathbf{c}_i|| = \sqrt{(\mathbf{a}_i - \mathbf{p} - \mathbf{Q}\mathbf{b}_i^{\mathcal{B}})^T(\mathbf{a}_i - \mathbf{p} - \mathbf{Q}\mathbf{b}_i^{\mathcal{B}})}, \tag{A.16}$$

where the vector $\mathbf{a}_i$ represents the position in three dimensions of the fixed-base eyelet A_i in the fixed frame $\mathcal{A}$, the vector $\mathbf{b}_i^{\mathcal{B}}$, expressed in frame $\mathcal{B}$, represents the position of the attachment point B_i of cable i on the moving platform, the vector $\mathbf{p}$, which is expressed in $\mathcal{A}$, represents the position of the reference point P on the moving platform with respect to point O, and the vector $\mathbf{c}_i$ points from B_i to A_i. Moreover, let $\mathbf{Q}$ be the matrix that rotates frame $\mathcal{A}$ onto frame $\mathcal{B}$ and expressed as

$$\begin{aligned}\mathbf{Q} &= \mathbf{Q}_{z^{\text{II}}}\mathbf{Q}_{y^{\text{I}}}\mathbf{Q}_x, \\ &= \begin{bmatrix} c(\theta_x)c(\theta_{y^{\text{I}}}) & -s(\theta_x)c(\theta_{z^{\text{II}}}) + c(\theta_x)s(\theta_{y^{\text{I}}})s(\theta_{z^{\text{II}}}) & s(\theta_x)s(\theta_{z^{\text{II}}}) + c(\theta_x)s(\theta_{y^{\text{I}}})c(\theta_{z^{\text{II}}}) \\ s(\theta_x)c(\theta_{y^{\text{I}}}) & c(\theta_x)c(\theta_{z^{\text{II}}}) + s(\theta_x)s(\theta_{y^{\text{I}}})s(\theta_{z^{\text{II}}}) & -c(\theta_x)s(\theta_{z^{\text{II}}}) + s(\theta_x)s(\theta_{y^{\text{I}}})c(\theta_{z^{\text{II}}}) \\ -s(\theta_{y^{\text{I}}}) & c(\theta_{y^{\text{I}}})s(\theta_{z^{\text{II}}}) & c(\theta_{y^{\text{I}}})c(\theta_{z^{\text{II}}}) \end{bmatrix},\end{aligned} \tag{A.17}$$

where $c(\theta) \equiv \cos(\theta)$, $s(\theta) \equiv \sin(\theta)$, and variables $\{\theta_x,\ \theta_{y^{\text{I}}},\ \theta_{z^{\text{II}}}\}$ are the three components of the vector $\boldsymbol{\theta}$ defining the rotation motion of the CDPM end-effector, following the Euler angles convention XYZ (three successive pure rotations along the axes X ($X \equiv X^{\mathcal{B}}$), Y^{I} ($Y^{\text{I}} \equiv$ the new $Y^{\mathcal{B}}$), Z^{II} ($Z^{\text{II}} \equiv$ the new $Z^{\mathcal{B}}$), i.e., $\mathbf{Q}_x$, $\mathbf{Q}_{y^{\text{I}}}$, $\mathbf{Q}_{z^{\text{II}}}$, respectively. Note that Eq. (A.16), evaluated for $i = 1, \ldots, m$, where m is the total number of cables, is commonly called the loop-closure equations of the CDPM.

Then, in order to obtain the Jacobian matrix of a given CDPM, we must first define its velocity relations. In this purpose, we begin with the time derivative of the relation c_i^2, which is equivalent to $\mathbf{c}_i^T\mathbf{c}_i$ based on Eq. (A.16), that we express as follows:

$$c_i\dot{c}_i = (\mathbf{a}_i - \mathbf{p} - \mathbf{Q}\mathbf{b}_i^{\mathcal{B}})^T(-\dot{\mathbf{p}} - \dot{\mathbf{Q}}\mathbf{b}_i^{\mathcal{B}}), \tag{A.18}$$

where

$$\dot{\mathbf{Q}}\mathbf{b}_i^{\mathcal{B}} = \dot{\mathbf{Q}}\mathbf{Q}^T\mathbf{Q}\mathbf{b}_i^{\mathcal{B}}, \tag{A.19}$$

because $\mathbf{Q}^T\mathbf{Q} = \mathbf{1}_{3\times3}$ and where the matrix $\mathbf{1}_{3\times3}$ is the three-dimensional identity matrix. Moreover,

$$\dot{\mathbf{Q}}\mathbf{Q}^T = \boldsymbol{\Omega}, \tag{A.20}$$

where $\boldsymbol{\Omega}$ is commonly known as the angular velocity tensor. This matrix is defined as

$$\boldsymbol{\Omega} = \partial(\boldsymbol{\omega} \times \mathbf{x})/\partial\mathbf{x}, \tag{A.21}$$

where $\boldsymbol{\omega}$ is the angular velocity vector of the CDPM's end-effector, expressed in frame $\mathcal{A}$.

Then, the following equivalent relations can be obtained:

$$\dot{\mathbf{Q}}\mathbf{b}_i^{\mathcal{B}} = \boldsymbol{\Omega}\mathbf{Q}\mathbf{b}_i^{\mathcal{B}} = \boldsymbol{\omega} \times \mathbf{Q}\mathbf{b}_i^{\mathcal{B}}, \tag{A.22}$$

and the velocity equation is given by

$$c_i\dot{c}_i = -(\mathbf{a}_i - \mathbf{p} - \mathbf{Q}\mathbf{b}_i^{\mathcal{B}})^T\dot{\mathbf{p}} - [\mathbf{Q}\mathbf{b}_i^{\mathcal{B}} \times (\mathbf{a}_i - \mathbf{p} - \mathbf{Q}\mathbf{b}_i^{\mathcal{B}})]^T\boldsymbol{\omega}. \tag{A.23}$$

This relation can be also expressed as follows:

$$\mathbf{J}\dot{\mathbf{s}} = \mathbf{K}\dot{\mathbf{c}}, \tag{A.24}$$

where matrix $\mathbf{J}$ is of dimension $m \times 6$, its i^{th} row being expressed as

$$\mathbf{j}_i = \begin{bmatrix} -(\mathbf{a}_i - \mathbf{p} - \mathbf{Q}\mathbf{b}_i^{\mathcal{B}})^T & -[\mathbf{Q}\mathbf{b}_i^{\mathcal{B}} \times (\mathbf{a}_i - \mathbf{p} - \mathbf{Q}\mathbf{b}_i^{\mathcal{B}})]^T \end{bmatrix}, \ i = 1, \ldots, m, \tag{A.25}$$

while matrix $\mathbf{K}$ is given by

$$\mathbf{K} = \begin{bmatrix} c_1 & 0 & 0 \\ 0 & \ddots & 0 \\ 0 & 0 & c_m \end{bmatrix}, \tag{A.26}$$

and $\dot{\mathbf{s}}$ and $\dot{\mathbf{c}}$ are the six-component Cartesian velocity vector (a screw vector) and the m-component joint velocity vector, respectively. These two vectors can be written as follows:

$$\dot{\mathbf{s}} = \begin{bmatrix} \dot{\mathbf{p}}^T & \boldsymbol{\omega}^T \end{bmatrix}^T, \quad \text{and} \quad \dot{\mathbf{c}} = \begin{bmatrix} \dot{c}_1 & \cdots & \dot{c}_i & \cdots & \dot{c}_m \end{bmatrix}^T. \tag{A.27}$$

In summary, Eq. (A.24) represents the relationship between the Cartesian velocity and the joint velocity of the CDPM and it can be rearranged as

$$\dot{\mathbf{c}} = \mathbf{K}^{-1}\mathbf{J}\dot{\mathbf{s}}. \tag{A.28}$$

Then, using the principle of virtual work, we know that

$$-\mathbf{t}^T\delta\mathbf{c} + \mathbf{w}_p^T\delta\mathbf{s} = 0, \tag{A.29}$$

where $\delta\mathbf{c}$ and $\delta\mathbf{s}$ are the small virtual variations in the vector of cable lengths and in the vector of Cartesian coordinates of the end-effector pose, respectively. The vector $\mathbf{t}$ contains the magnitude of all cable tensions t_i and vector $\mathbf{w}_p$ represents the wrench exerted by the surrounding on the CDPM's end-effector, e.g., the gravity effect, the inertial effects and any additional external wrenches. The first part of this equation, i.e., $-\mathbf{t}^T\delta\mathbf{c}$, is the virtual work produced by the cable tensions on the moving platform (the negative sign results from the fact that the cable length c_i increases following the opposite direction of vector $\mathbf{c}_i$) and the second part, i.e., $\mathbf{w}_p^T\delta\mathbf{s}$, is the virtual work produced by the surrounding on the moving platform.

From Eq. (A.28), therefore, the following relationship can now be established:

$$\delta\mathbf{c} = \mathbf{K}^{-1}\mathbf{J}\delta\mathbf{s}, \tag{A.30}$$

and by substituting Eq. (A.30) into Eq. (A.29), we finally obtain the following equation:

$$\mathbf{W}\mathbf{t} = -\mathbf{w}_p, \tag{A.31}$$

where $\mathbf{W}$ is the Jacobian matrix of a spatial m-cable six-DoF CDPM, a rectangular matrix of dimensions $6 \times m$, which is defined as follows:

$$\mathbf{W} = -(\mathbf{K}^{-1}\mathbf{J})^T. \tag{A.32}$$

Appendix B

Dual Problems

This appendix contains the mathematical derivation of the dual problem associated to each criterion selected to form the basis of the proposed synthesis program presented in Chapter 4. The Section B.1 formulates the dual problem associated to the constant-orientation wrench-closure workspace (COWCW) criterion, Section B.2 focuses on the dual of the constant-orientation cable-cable interference (COCCI) problem and Section B.3 presents the dual of the constant-orientation cable-edge interference (COCEI) problem.

B.1 Dual of the Constant-Orientation Wrench-Closure Workspace Problem

Even though the primal of the constant-orientation wrench-closure workspace problem, formulated in Eq. (4.14), is sufficient to the computation of the proposed technique in Chapter 4 for the synthesis of CDPMs, its dual has been mathematically formulated during the preliminary tentatives to determine the ideal approach. Thus, for the sake of completeness, the dual problem associated to the COWCW is presented here.

In the case that it is relevant to determine if a pose of the CDPM's end-effector is outside the COWCW instead of inside—primal problem, the determination of its dual problem would be required. To do so, the Lagrangian duality principle [235] states that since our primal optimization constraints, i.e.,

$$\exists \mathbf{t} \geq \mathbf{0}_m | \mathbf{W}\mathbf{t} = \mathbf{0}_n, \mathbf{1}_m^T \mathbf{t} = 1, \tag{B.1}$$

can be expressed by the following minimization problem:

$$\begin{aligned} p_{\mathcal{W}}^{\star} = \underset{\mathbf{t}}{\text{minimize}} \quad & 0, \\ \text{subject to} \quad & -\mathbf{t} \leq \mathbf{0}_m, \\ & \begin{bmatrix} \mathbf{1}_m^T \\ \mathbf{W} \end{bmatrix} \mathbf{t} - \begin{bmatrix} 1 \\ \mathbf{0}_n \end{bmatrix} = \mathbf{0}_{n+1}, \end{aligned} \tag{B.2}$$

its corresponding dual problem can be then formulated as the following maximization problem:

$$\begin{aligned} d^{\star}_{\mathcal{W}} = \underset{\boldsymbol{\rho},\boldsymbol{\xi}}{\text{maximize}} \quad & g(\boldsymbol{\rho},\boldsymbol{\xi}), \\ \text{subject to} \quad & \boldsymbol{\rho} \geq \mathbf{0}_m, \end{aligned} \tag{B.3}$$

where

$$g(\boldsymbol{\rho},\boldsymbol{\xi}) = \underset{\mathbf{t}}{\text{infimum}}\ L(\mathbf{t},\boldsymbol{\rho},\boldsymbol{\xi}), \tag{B.4}$$

and where $L(\mathbf{t},\boldsymbol{\rho},\boldsymbol{\xi})$ is the Lagrangian of the primal problem (Eq. (B.2)) and it is defined as

$$L(\mathbf{t},\boldsymbol{\rho},\boldsymbol{\xi}) = -\boldsymbol{\rho}^T\mathbf{t} + \boldsymbol{\xi}^T\left(\begin{bmatrix} \mathbf{1}_m^T \\ \mathbf{W} \end{bmatrix}\mathbf{t} - \begin{bmatrix} 1 \\ \mathbf{0}_n \end{bmatrix}\right). \tag{B.5}$$

We know that the infimum occurs when the $\partial(L(\mathbf{t},\boldsymbol{\rho},\boldsymbol{\xi}))/\partial\mathbf{t} = \mathbf{0}_m$ and that the gradient of $L(\mathbf{t},\boldsymbol{\rho},\boldsymbol{\xi})$ is as follows:

$$\frac{\partial(L(\mathbf{t},\boldsymbol{\rho},\boldsymbol{\xi}))}{\partial\mathbf{t}} = -\boldsymbol{\rho} + \begin{bmatrix} \mathbf{1}_m^T \\ \mathbf{W} \end{bmatrix}^T\boldsymbol{\xi}. \tag{B.6}$$

Then, when solving it for $\boldsymbol{\rho}$, we obtain

$$\boldsymbol{\rho} = \begin{bmatrix} \mathbf{1}_m & \mathbf{W}^T \end{bmatrix}\boldsymbol{\xi}, \tag{B.7}$$

which is the value of $\boldsymbol{\rho}$ for the infimum of the Lagrangian $L(\mathbf{t},\boldsymbol{\rho},\boldsymbol{\xi})$ to be reached.

By substituting Eq. (B.7) into Eq. (B.5), the dual problem of the COWCW criterion is expressed as

$$\begin{aligned} d^{\star}_{\mathcal{W}} = \underset{\boldsymbol{\xi}}{\text{maximize}} \quad & g(\boldsymbol{\xi}) = -\boldsymbol{\xi}^T\begin{bmatrix} 1 \\ \mathbf{0}_n \end{bmatrix}, \\ \text{subject to} \quad & \begin{bmatrix} \mathbf{1}_m & \mathbf{W}^T \end{bmatrix}\boldsymbol{\xi} \geq \mathbf{0}_m. \end{aligned} \tag{B.8}$$

If we choose $\boldsymbol{\xi} = \begin{bmatrix} \delta s_0 & \delta\mathbf{s}^T \end{bmatrix}^T$, where δs_0 is an arbitrary constant and $\delta\mathbf{s}$ is, due to the nature of $\mathbf{W}$ and the principle of virtual work, the vector of the small virtual variations of the n Cartesian coordinates representing the pose of the CDPM's end-effector, we then obtain

$$\begin{aligned} d^{\star}_{\mathcal{W}} = \underset{\delta s_0,\delta\mathbf{s}}{\text{maximize}} \quad & -\delta s_0, \\ \text{subject to} \quad & \mathbf{W}^T\delta\mathbf{s} \geq -\mathbf{1}_m\delta s_0. \end{aligned} \tag{B.9}$$

Mathematically speaking, the problem of Eq. (B.9) has two possible solutions:

$$d^{\star}_{\mathcal{W}} = \begin{cases} 0 & \text{for} \quad \delta s_0 \geq 0, \\ \infty & \text{for} \quad \delta s_0 < 0. \end{cases} \tag{B.10}$$

Indeed, if $\delta s_0 \geq 0$, the maximum value of the objective function is reached when $d^{\star}_{\mathcal{W}} = 0$ and, inherently, the corresponding solution is $\delta s_0 = 0$ and $\delta\mathbf{s} = \mathbf{0}_n$. In this case, the dual problem

is bounded and the primal problem is feasible, which means that the CDPM's end-effector pose is inside the COWCW. However, if $\delta s_0 < 0$, the maximum is $d^\star_{\mathcal{W}} = \infty$ and this proves the dual problem to be unbounded and also that the primal problem is infeasible, i.e., the end-effector pose is outside the COWCW. This particular situation is in fact the information we want the dual problem to provide about the evaluated CDPM.

Finally, based on the previous statements, we can then formulate the following constraints in order to fully define the dual problem:

$$\exists \delta\mathbf{s} | \mathbf{W}^T \delta\mathbf{s} \geq \mathbf{0}_m,\ \mathbf{1}_m^T \mathbf{W}^T \delta\mathbf{s} = 1, \tag{B.11}$$

where the condition $\mathbf{1}_m^T \mathbf{W}^T \delta\mathbf{s} = 1$ ensures us that $\mathbf{W}^T \delta\mathbf{s} \neq \mathbf{0}_m$. Consequently, this means that $-\mathbf{1}_m \delta s_0 > \mathbf{0}_m$ and that, inherently, $\delta s_0 < 0$. As expected, here, we see that $\delta s_0 \geq 0$ is then discarded from the possible solutions as needed.

In summary, the primal problem of Eq. (B.1) says that for a given $\mathbf{t}$ such as $\mathbf{t} \geq \mathbf{0}_m$ and $\mathbf{1}^T\mathbf{t} = 1$, there must be at least one cable that can generate a wrench in the opposite direction of the resulting wrench from all other cables for an end-effector pose to be in the COWCW. In fact, this problem basically assesses the sum of all forces and torques applied on the moving platform by the cables.

On the other hand, the dual problem presented in Eq. (B.11) rather ensures that all work done on the moving platform by its surrounding is either null or positive, so that a given CDPM's end-effector pose is outside its COWCW. Note that to be inside the COWCW, there must be at least one cable that can generate a negative work on the moving platform. Here, for the need of the synthesis problem proposed in Chapter 4, the first approach is preferred.

B.2 Dual of the Constant-Orientation Cable-Cable Interference Problem

From the Lagrangian duality method (see [235]), when a primal problem can be expressed by a minimization problem such as the following (from Eq. (4.30) of Chapter 4):

$$\begin{aligned} p^\star_{\mathcal{C}} = \underset{\boldsymbol{\gamma}}{\text{minimize}} \quad & f(\boldsymbol{\gamma}) = \boldsymbol{\gamma}^T \mathbf{H}_{i,j,k} \boldsymbol{\gamma} + 2\mathbf{h}_{i,j,k}^T \boldsymbol{\gamma}, \\ \text{subject to} \quad & -\boldsymbol{\gamma} \leq \mathbf{0}_2, \end{aligned} \tag{B.12}$$

the dual problem can be determined by the following mathematical derivation. It should be noted here that Eq. (B.12) represents a quadratic problem, which is convex by nature, in regards to variables $\boldsymbol{\gamma}$ and, consequently, its global optimum is guaranteed.

First, the associated Lagrangian of Eq. (B.12) is:

$$L(\boldsymbol{\gamma}, \boldsymbol{\lambda}) = \boldsymbol{\gamma}^T \mathbf{H}_{i,j,k} \boldsymbol{\gamma} + 2\mathbf{h}_{i,j,k}^T \boldsymbol{\gamma} - \boldsymbol{\lambda}^T \boldsymbol{\gamma}, \tag{B.13}$$

and the corresponding dual problem can be formulated as the following maximization problem:

$$\begin{aligned} d^{\star}_{\mathcal{C}} = \underset{\boldsymbol{\lambda}}{\text{maximize}} \quad & g(\boldsymbol{\lambda}), \\ \text{subject to} \quad & \boldsymbol{\lambda} \geq \mathbf{0}_2, \end{aligned} \tag{B.14}$$

where

$$g(\boldsymbol{\lambda}) = \underset{\boldsymbol{\gamma}}{\text{infimum}}\ L(\boldsymbol{\gamma}, \boldsymbol{\lambda}). \tag{B.15}$$

We know that the infimum occurs when the $\partial(L(\boldsymbol{\gamma}, \boldsymbol{\lambda}))/\partial\boldsymbol{\gamma} = \mathbf{0}_2$ and that the gradient of $L(\boldsymbol{\gamma}, \boldsymbol{\lambda})$ is as follows:

$$\frac{\partial(L(\boldsymbol{\gamma}, \boldsymbol{\lambda}))}{\partial\boldsymbol{\gamma}} = 2\mathbf{H}_{i,j,k}\boldsymbol{\gamma} + 2\mathbf{h}_{i,j,k} - \boldsymbol{\lambda}. \tag{B.16}$$

Then, when solving it for $\boldsymbol{\gamma}$, we obtain

$$\boldsymbol{\gamma} = \frac{1}{2}\mathbf{H}^{-1}_{i,j,k}(\boldsymbol{\lambda} - 2\mathbf{h}_{i,j,k}), \tag{B.17}$$

which is the value of $\boldsymbol{\gamma}$ for the infimum of the Lagrangian $L(\boldsymbol{\gamma}, \boldsymbol{\lambda})$ to be reached.

Finally, by substituting Eq. (B.17) into Eq. (B.13), and after mathematical simplifications, the dual problem of the COCCI criterion is expressed as

$$\begin{aligned} d^{\star}_{\mathcal{C}} = \underset{\boldsymbol{\lambda}}{\text{maximize}} \quad & g(\boldsymbol{\lambda}) = -\frac{1}{4}\boldsymbol{\lambda}^T\mathbf{H}^{-1}_{i,j,k}\boldsymbol{\lambda} + \mathbf{h}^T_{i,j,k}\mathbf{H}^{-1}_{i,j,k}\boldsymbol{\lambda} - \mathbf{h}^T_{i,j,k}\mathbf{H}^{-1}_{i,j,k}\mathbf{h}_{i,j,k}, \\ \text{subject to} \quad & \boldsymbol{\lambda} \geq \mathbf{0}_2. \end{aligned} \tag{B.18}$$

In summary, the primal problem presented in Eq. (B.12), when $p^{\star}_{\mathcal{C}} \leq -h_{i,j,k}$, allows one to determine the minimum ellipsoid that limits the region where contacts between a pair of cables (i, j) occurs. In contrast, the dual problem showed in Eq. (B.18), when $d^{\star}_{\mathcal{C}} > -h_{i,j,k}$, allows one to determine the maximum ellipsoid that limits the region where no contact between the same pair of cables can occur. For the synthesis problem proposed in Chapter 4, the second approach is chosen.

B.3 Dual of the Constant-Orientation Cable-Edge Interference Problem

Similarly to Section B.2, when a primal problem can be expressed with a minimization problem such as the following (from Eq. (4.43) of Chapter 4):

$$\begin{aligned} p^{\star}_{\mathcal{E}} = \underset{\boldsymbol{\alpha}}{\text{minimize}} \quad & f(\boldsymbol{\alpha}) = \boldsymbol{\alpha}^T\mathbf{N}_{i,o,k}\boldsymbol{\alpha} + 2\mathbf{n}^T_{i,o,k}\boldsymbol{\alpha}, \\ \text{subject to} \quad & \mathbf{C}\boldsymbol{\alpha} + \mathbf{c} \leq \mathbf{0}_3, \end{aligned} \tag{B.19}$$

the dual problem can be determined as below. It should be also noted that Eq. (B.19) represents a quadratic problem, which is convex by nature, in regards to variables $\boldsymbol{\alpha}$ and, consequently, its global optimum is always guaranteed.

First, the associated Lagrangian of Eq. (B.19) is:

$$L(\boldsymbol{\alpha}, \boldsymbol{\phi}) = \boldsymbol{\alpha}^T \mathbf{N}_{i,o,k} \boldsymbol{\alpha} + 2\mathbf{n}_{i,o,k}^T \boldsymbol{\alpha} + (\mathbf{C}\boldsymbol{\alpha} + \mathbf{c})^T \boldsymbol{\phi}, \tag{B.20}$$

and the corresponding dual problem can be formulated as the following maximization problem:

$$\begin{aligned} d_{\mathcal{E}}^{\star} = \underset{\boldsymbol{\phi}}{\text{maximize}} \quad & g(\boldsymbol{\phi}), \\ \text{subject to} \quad & \boldsymbol{\phi} \geq \mathbf{0}_3, \end{aligned} \tag{B.21}$$

where

$$g(\boldsymbol{\phi}) = \underset{\boldsymbol{\alpha}}{\text{infimum}}\ L(\boldsymbol{\alpha}, \boldsymbol{\phi}). \tag{B.22}$$

We know that the infimum occurs when the $\partial(L(\boldsymbol{\alpha}, \boldsymbol{\phi}))/\partial\boldsymbol{\alpha} = \mathbf{0}_2$ and that the gradient of $L(\boldsymbol{\alpha}, \boldsymbol{\phi})$ is as follows:

$$\frac{\partial(L(\boldsymbol{\alpha}, \boldsymbol{\phi}))}{\partial \boldsymbol{\alpha}} = 2\mathbf{N}_{i,o,k}\boldsymbol{\alpha} + 2\mathbf{n}_{i,o,k} + \mathbf{C}^T\boldsymbol{\phi}. \tag{B.23}$$

Then, when solving it for $\boldsymbol{\alpha}$, we obtain

$$\boldsymbol{\alpha} = -\frac{1}{2}\mathbf{N}_{i,j,k}^{-1}(2\mathbf{n}_{i,o,k} + \mathbf{C}^T\boldsymbol{\phi}), \tag{B.24}$$

which is the value of $\boldsymbol{\alpha}$ for the infimum of the Lagrangian $L(\boldsymbol{\alpha}, \boldsymbol{\phi})$ to be reached.

Finally, by substituting Eq. (B.24) into Eq. (B.20), and after mathematical simplifications, the dual problem of the COCEI criterion is expressed as

$$\begin{aligned} d_{\mathcal{E}}^{\star} = \underset{\boldsymbol{\phi}}{\text{maximize}} \quad g(\boldsymbol{\phi}) = & -\frac{1}{4}\boldsymbol{\phi}^T\mathbf{C}\mathbf{N}_{i,o,k}^{-1}\mathbf{C}^T\boldsymbol{\phi} + (\mathbf{c}^T - \mathbf{n}_{i,o,k}^T\mathbf{N}_{i,o,k}^{-1}\mathbf{C}^T)\boldsymbol{\phi} \\ & - \mathbf{n}_{i,o,k}^T\mathbf{N}_{i,o,k}^{-1}\mathbf{n}_{i,o,k}, \\ \text{subject to} \quad & \boldsymbol{\phi} \geq \mathbf{0}_3. \end{aligned} \tag{B.25}$$

In summary, the primal problem presented in Eq. (B.19), when $p_{\mathcal{E}}^{\star} \leq -n_{i,k}$, allows one to determine the minimum ellipsoid that limits the region where contacts between a cable i and an edge o of a given geometry—CDPM's end-effector and its payload—occurs. In contrast, the dual problem showed in Eq. (B.25), when $d_{\mathcal{E}}^{\star} > -n_{i,k}$, allows one to determine the maximum ellipsoid that limits the region where no contact between a cable and an edge can occur. For the synthesis problem proposed in Chapter 4, the second approach is preferred.

Appendix C

Nonlinear Constraints of the Synthesis Program and their Derivatives

This appendix contains the details of the nonlinear inequality and equality constraints required to the programming of the problem of the dimensional synthesis of cable-driven parallel mechanisms (CDPMs), which is proposed in Chapter 4. Section C.1 presents each element that constitutes the mathematical expression of these nonlinear constraints while Section C.2 is dedicated to the formulation of the first-order derivatives of these constraints.

C.1 Nonlinear Constraints

In order to simplify the reading of the mathematical formulas included in Section 4.3 of this thesis, the presentation of the elements required to define the nonlinear constraints of the CDPM's synthesis problem are rather shown here. It should be noted that, by their nature, the nonlinear inequality constraints $\mathbf{c}_{\text{ineq}}(\mathbf{v})$ represent both the satisfactory conditions corresponding to the constant-orientation cable-cable interference criterion (see Sub-section 4.2.3) and those related to the constant-orientation cable-edge interference criterion (see Sub-section 4.2.4). We recall that these constraints depend on $\mathbf{v}$, which is the vector containing all of the variables of the synthesis problem, and must be always satisfied while optimizing a CDPM's geometry.

First, the nonlinear inequality constraints $\mathbf{c}_{\text{ineq}}(\mathbf{v})$ are given by:

$$\mathbf{c}_{\text{ineq}}(\mathbf{v}) \equiv \begin{bmatrix} \boldsymbol{\mu}_{aug}^{*}\mathbf{H}_{aug}^{a}\boldsymbol{\mu}_{aug} - 4\mathbf{H}_{aug}^{d}\mathbf{h}_{c,aug} \\ -\boldsymbol{\mu}_{aug} - 2\mathbf{h}_{aug} \\ \boldsymbol{\eta}_{aug}^{*}\mathbf{Z}_{aug}^{a}\boldsymbol{\eta}_{aug} - 4\mathbf{N}_{aug}^{d}(\mathbf{C}_{c,aug}\boldsymbol{\eta}_{aug} + \mathbf{n}_{c,aug}) \\ -\mathbf{D}_{aug}(\boldsymbol{\eta}_{aug} - 2\mathbf{z}_{aug}) \end{bmatrix}, \tag{C.1}$$

where

$$\boldsymbol{\mu}^*_{aug} \equiv \begin{bmatrix} \boldsymbol{\mu}^T_{2,1,1} & \cdots & \mathbf{0}^T_2 & \mathbf{0}^T_2 & \cdots & \mathbf{0}^T_2 \\ \vdots & \ddots & \vdots & \vdots & & \vdots \\ \mathbf{0}^T_2 & \cdots & \boldsymbol{\mu}^T_{m,1,1} & \mathbf{0}^T_2 & \cdots & \mathbf{0}^T_2 \\ \mathbf{0}^T_2 & \cdots & \mathbf{0}^T_2 & \boldsymbol{\mu}^T_{1,2,1} & \cdots & \mathbf{0}^T_2 \\ \vdots & & \vdots & \vdots & \ddots & \vdots \\ \mathbf{0}^T_2 & \cdots & \mathbf{0}^T_2 & \mathbf{0}^T_2 & \cdots & \boldsymbol{\mu}^T_{m-1,m,q} \end{bmatrix}, \tag{C.2}$$

$$\mathbf{H}^a_{aug} \equiv \begin{bmatrix} \mathrm{adj}(\mathbf{H}_{2,1,1}) & \cdots & \mathbf{0}_{2\times 2} & \mathbf{0}_{2\times 2} & \cdots & \mathbf{0}_{2\times 2} \\ \vdots & \ddots & \vdots & \vdots & & \vdots \\ \mathbf{0}_{2\times 2} & \cdots & \mathrm{adj}(\mathbf{H}_{m,1,1}) & \mathbf{0}_{2\times 2} & \cdots & \mathbf{0}_{2\times 2} \\ \mathbf{0}_{2\times 2} & \cdots & \mathbf{0}_{2\times 2} & \mathrm{adj}(\mathbf{H}_{1,2,1}) & \cdots & \mathbf{0}_{2\times 2} \\ \vdots & & \vdots & \vdots & \ddots & \vdots \\ \mathbf{0}_{2\times 2} & \cdots & \mathbf{0}_{2\times 2} & \mathbf{0}_{2\times 2} & \cdots & \mathrm{adj}(\mathbf{H}_{m-1,m,q}) \end{bmatrix}, \tag{C.3}$$

$$\mathbf{H}^d_{aug} \equiv \begin{bmatrix} \det(\mathbf{H}_{2,1,1}) & \cdots & 0 & 0 & \cdots & 0 \\ \vdots & \ddots & \vdots & \vdots & & \vdots \\ 0 & \cdots & \det(\mathbf{H}_{m,1,1}) & 0 & \cdots & 0 \\ 0 & \cdots & 0 & \det(\mathbf{H}_{1,2,1}) & \cdots & 0 \\ \vdots & & \vdots & \vdots & \ddots & \vdots \\ 0 & \cdots & 0 & 0 & \cdots & \det(\mathbf{H}_{m-1,m,q}) \end{bmatrix}, \tag{C.4}$$

$$\mathbf{h}_{aug} \equiv \begin{bmatrix} \mathbf{h}^T_{2,1,1} & \cdots & \mathbf{h}^T_{m,1,1} & \mathbf{h}^T_{1,2,1} & \cdots & \mathbf{h}^T_{m-1,m,q} \end{bmatrix}^T_{2(m^2-m)q}, \tag{C.5}$$

$$\mathbf{h}_{c,aug} \equiv \begin{bmatrix} h_{2,1,1} & \cdots & h_{m,1,1} & h_{1,2,1} & \cdots & h_{m-1,m,q} \end{bmatrix}^T_{(m^2-m)q}, \tag{C.6}$$

$$\boldsymbol{\eta}^*_{aug} \equiv \begin{bmatrix} \boldsymbol{\eta}^T_{1,1,1} & \cdots & \mathbf{0}^T_3 & \mathbf{0}^T_3 & \cdots & \mathbf{0}^T_3 \\ \vdots & \ddots & \vdots & \vdots & & \vdots \\ \mathbf{0}^T_3 & \cdots & \boldsymbol{\eta}^T_{1,f,1} & \mathbf{0}^T_3 & \cdots & \mathbf{0}^T_3 \\ \mathbf{0}^T_3 & \cdots & \mathbf{0}^T_3 & \boldsymbol{\eta}^T_{2,1,1} & \cdots & \mathbf{0}^T_3 \\ \vdots & & \vdots & \vdots & \ddots & \vdots \\ \mathbf{0}^T_3 & \cdots & \mathbf{0}^T_3 & \mathbf{0}^T_3 & \cdots & \boldsymbol{\eta}^T_{m,f,q} \end{bmatrix}, \tag{C.7}$$

$$\mathbf{Z}^a_{aug} \equiv \begin{bmatrix} \mathbf{Z}^a_{1,1,1} & \cdots & \mathbf{0}_{3\times 3} & \mathbf{0}_{3\times 3} & \cdots & \mathbf{0}_{3\times 3} \\ \vdots & \ddots & \vdots & \vdots & & \vdots \\ \mathbf{0}_{3\times 3} & \cdots & \mathbf{Z}^a_{1,f,1} & \mathbf{0}_{3\times 3} & \cdots & \mathbf{0}_{3\times 3} \\ \mathbf{0}_{3\times 3} & \cdots & \mathbf{0}_{3\times 3} & \mathbf{Z}^a_{2,1,1} & \cdots & \mathbf{0}_{3\times 3} \\ \vdots & & \vdots & \vdots & \ddots & \vdots \\ \mathbf{0}_{3\times 3} & \cdots & \mathbf{0}_{3\times 3} & \mathbf{0}_{3\times 3} & \cdots & \mathbf{Z}^a_{m,f,q} \end{bmatrix}, \tag{C.8}$$

$$\mathbf{N}_{aug}^{d} \equiv \begin{bmatrix} \det(\mathbf{N}_{1,1,1}) & \cdots & 0 & 0 & \cdots & 0 \\ \vdots & \ddots & \vdots & \vdots & & \vdots \\ 0 & \cdots & \det(\mathbf{N}_{1,f,1}) & 0 & \cdots & 0 \\ 0 & \cdots & 0 & \det(\mathbf{N}_{2,1,1}) & \cdots & 0 \\ \vdots & & \vdots & \vdots & \ddots & \vdots \\ 0 & \cdots & 0 & 0 & \cdots & \det(\mathbf{N}_{m,f,q}) \end{bmatrix}, \tag{C.9}$$

$$\mathbf{C}_{c,aug} \equiv \begin{bmatrix} \mathbf{c}^T & \cdots & \mathbf{0}_3^T \\ \vdots & \ddots & \vdots \\ \mathbf{0}_3^T & \cdots & \mathbf{c}^T \end{bmatrix}_{mfq \times 3mfq}, \tag{C.10}$$

$$\mathbf{D}_{aug} \equiv \begin{bmatrix} \mathbf{D}^{-1} & \cdots & \mathbf{0}_{3\times 3} \\ \vdots & \ddots & \vdots \\ \mathbf{0}_{3\times 3} & \cdots & \mathbf{D}^{-1} \end{bmatrix}_{3mfq \times 3mfq}, \tag{C.11}$$

$$\mathbf{z}_{aug} \equiv \begin{bmatrix} \mathbf{z}_{1,1,1}^T & \cdots & \mathbf{z}_{1,f,1}^T & \mathbf{z}_{2,1,1}^T & \cdots & \mathbf{z}_{m,f,q}^T \end{bmatrix}_{3mfq}^T, \tag{C.12}$$

$$\mathbf{n}_{c,aug} \equiv \begin{bmatrix} \mathbf{n}_{b,1}^T & \cdots & \mathbf{n}_{b,k}^T & \cdots & \mathbf{n}_{b,q}^T \end{bmatrix}_{mfq}^T, \tag{C.13}$$

$$\mathbf{n}_{b,k} \equiv \begin{bmatrix} \mathbf{n}_{a,k}^T & \cdots & \mathbf{n}_{a,k}^T & \cdots & \mathbf{n}_{a,k}^T \end{bmatrix}_{mf}^T, \tag{C.14}$$

$$\mathbf{n}_{a,k} \equiv \begin{bmatrix} n_{1,k} & \cdots & n_{i,k} & \cdots & n_{m,k} \end{bmatrix}_{m}^T, \tag{C.15}$$

and where,

$$\boldsymbol{\mu}_{aug}^{*} \in \mathbb{R}^{(m^2-m)q \times 2(m^2-m)q}, \tag{C.16}$$

$$\mathbf{H}_{aug}^{a} \in \mathbb{R}^{2(m^2-m)q \times 2(m^2-m)q}, \tag{C.17}$$

$$\mathbf{H}_{aug}^{d} \in \mathbb{R}^{(m^2-m)q \times (m^2-m)q}, \tag{C.18}$$

$$\boldsymbol{\eta}_{aug}^{*} \in \mathbb{R}^{mfq \times 3mfq}, \tag{C.19}$$

$$\mathbf{Z}_{aug}^{a} \in \mathbb{R}^{3mfq \times 3mfq}, \tag{C.20}$$

$$\mathbf{N}_{aug}^{d} \in \mathbb{R}^{mfq \times mfq}. \tag{C.21}$$

Finally, the nonlinear equality constraints $\mathbf{c}_{\text{eq}}(\mathbf{v})$, which represent the nonlinear satisfactory conditions corresponding to the constant-orientation wrench-closure workspace criterion (see Sub-section 4.2.2), are expressed as follows:

$$\mathbf{c}_{\text{eq}}(\mathbf{v}) \equiv \mathbf{W}_{aug}\mathbf{t}_{aug} = \begin{bmatrix} \mathbf{W}_{1,1} & \cdots & \mathbf{0}_{n\times m} & \cdots & \mathbf{0}_{n\times m} \\ \vdots & \ddots & \vdots & & \vdots \\ \mathbf{0}_{n\times m} & \cdots & \mathbf{W}_{q,1} & \cdots & \mathbf{0}_{n\times m} \\ \vdots & & \vdots & \ddots & \vdots \\ \mathbf{0}_{n\times m} & \cdots & \mathbf{0}_{n\times m} & \cdots & \mathbf{W}_{q,nb} \end{bmatrix} \mathbf{t}_{aug}, \tag{C.22}$$

where

$$\mathbf{W}_{aug} \in \mathbb{R}^{nqnb \times mqnb}. \tag{C.23}$$

C.2 Derivatives of the Nonlinear Constraints

The determination of the derivatives of nonlinear constraints can be required when the computing of a nonlinearly constrained optimization program is relatively time consuming and one desires to improve this aspect. In fact, if the resolving technique of an optimization program is based on the use of gradient-like methods, in general, providing an analytical formulation for the derivatives of the objective function and its associated constraints leads to decreasing the computation time required to perform a single function evaluation. With numerical tools such as the function `fmincon` from the *Optimization Toolbox* of the MATLAB® software, the internal algorithms normally need to numerically compute the gradients of the nonlinear problem in order to determine the direction of search for a given iteration. Consequently, when one knows the analytical formulation of these gradients, the computation time allocated to this sub-procedure can be dramatically reduced.

For the synthesis problem proposed in Chapter 4, for which the optimization function `fmincon` is solved using the *interior-point* algorithm, the determination of the derivatives of the nonlinear inequality and equality constraints in regards to $\mathbf{v}$, i.e., the gradients $\nabla \mathbf{c}_{\text{ineq}}(\mathbf{v})$ and $\nabla \mathbf{c}_{\text{eq}}(\mathbf{v})$, respectively, where the vector $\mathbf{v}$ contains all of the variables of the synthesis problem, is required since the optimization problem is strongly nonlinear and involves a large number of variables. The mathematical formulation of $\nabla \mathbf{c}_{\text{ineq}}(\mathbf{v})$ and $\nabla \mathbf{c}_{\text{eq}}(\mathbf{v})$ is then presented below. Note that the gradient of the objective function $f(\mathbf{v})$ is directly given in Chapter 4 with Eq. (4.74) because of its simplicity of formulation.

As previously shown in Section C.1, the nonlinear inequality and equality constraints are respectively expressed as follows:

$$\mathbf{c}_{\text{ineq}}(\mathbf{v}) \equiv \begin{bmatrix} \boldsymbol{\mu}_{aug}^{*}\mathbf{H}_{aug}^{a}\boldsymbol{\mu}_{aug} - 4\mathbf{H}_{aug}^{d}\mathbf{h}_{c,aug} \\ -\boldsymbol{\mu}_{aug} - 2\mathbf{h}_{aug} \\ \boldsymbol{\eta}_{aug}^{*}\mathbf{Z}_{aug}^{a}\boldsymbol{\eta}_{aug} - 4\mathbf{N}_{aug}^{d}(\mathbf{C}_{c,aug}\boldsymbol{\eta}_{aug} + \mathbf{n}_{c,aug}) \\ -\mathbf{D}_{aug}(\boldsymbol{\eta}_{aug} - 2\mathbf{z}_{aug}) \end{bmatrix}, \tag{C.24}$$

and

$$\mathbf{c}_{\text{eq}}(\mathbf{v}) \equiv \mathbf{W}_{aug}\mathbf{t}_{aug}. \tag{C.25}$$

Then, after applying the derivatives methods on the nonlinear inequality constraints $\mathbf{c}_{\text{ineq}}(\mathbf{v})$,

and after multiple formulation simplifications, we obtain:

$$\nabla \mathbf{c}_{\text{ineq}}(\mathbf{v}) =$$

$$\begin{bmatrix} 8\kappa(\mathbf{1}^T_{(m^2-m)q}\mathbf{H}^d_{aug}) & \mathbf{0}^T_{2(m^2-m)q} & 8\kappa(\mathbf{1}^T_{mfq}\mathbf{N}^d_{aug}) & \mathbf{0}^T_{3mfq} \\ \mathbf{I}^{a1c}_{aug} & \mathbf{I}^{a2c}_{aug} & \mathbf{I}^{a1e}_{aug} & \mathbf{I}^{a2e}_{aug} \\ \mathbf{I}^{b1c}_{aug} & \mathbf{I}^{b2c}_{aug} & \mathbf{I}^{b1e}_{aug} & \mathbf{I}^{b2e}_{aug} \\ \mathbf{0}_{3nb\times(m^2-m)q} & \mathbf{0}_{3nb\times 2(m^2-m)q} & \mathbf{0}_{3nb\times mfq} & \mathbf{0}_{3nb\times 3mfq} \\ \mathbf{0}_{mqnb\times(m^2-m)q} & \mathbf{0}_{mqnb\times 2(m^2-m)q} & \mathbf{0}_{mqnb\times mfq} & \mathbf{0}_{mqnb\times 3mfq} \\ 2(\boldsymbol{\mu}^*_{aug}\mathbf{H}^a_{aug})^T & -\mathbf{1}_{2(m^2-m)q\times 2(m^2-m)q} & \mathbf{0}_{2(m^2-m)q\times mfq} & \mathbf{0}_{2(m^2-m)q\times 3mfq} \\ \mathbf{0}_{3mfq\times(m^2-m)q} & \mathbf{0}_{3mfq\times 2(m^2-m)q} & \mathbf{Y}^T_{aug} & -\mathbf{D}^T_{aug} \end{bmatrix}, \tag{C.26}$$

where

$$\mathbf{Y}_{aug} \equiv \boldsymbol{\eta}^*_{aug}\mathbf{Z}^a_{aug} - 4\mathbf{C}_{c,aug}\mathbf{N}^d_{aug}, \tag{C.27}$$

and where the eight matrices noted $\mathbf{I}_{aug}$ are cell matrices and their dimensions are as follows:

$$\mathbf{I}^{a1c}_{aug},\ \mathbf{I}^{a2c}_{aug},\ \mathbf{I}^{b1c}_{aug},\ \mathbf{I}^{b2c}_{aug} \in \mathbb{R}^{m\times(m^2-m)q}, \tag{C.28}$$

$$\mathbf{I}^{a1e}_{aug},\ \mathbf{I}^{a2e}_{aug},\ \mathbf{I}^{b1e}_{aug},\ \mathbf{I}^{b2e}_{aug} \in \mathbb{R}^{m\times mfq}. \tag{C.29}$$

Note that each element of the cell matrices contains a sub-vector or a sub-matrix. Then, the purpose of the following is to define these sub-elements.

Here, matrices $\mathbf{I}_{aug}$ represent the partial derivatives of the nonlinear inequality constraints $\mathbf{c}_{\text{ineq}}(\mathbf{v})$ in regards to the geometric parameters $\mathbf{a}_i$ and $\mathbf{b}^{\mathcal{B}}_i$ of the CDPM. Since, in our dimensional synthesis program, each combination of two cables i and j and each combination of a cable i and an edge o are evaluated separately in a loop, i.e., one combination after the other, the structure of the cell matrices $\mathbf{I}_{aug}$ must be defined accordingly. Therefrom, for each evaluated pair of a cable i and a cable j, the structure of the matrices are:

$$\mathbf{I}^{a1c}_{aug}(row, col) \equiv \begin{cases} \mathbf{o}^{a1cj}_3 & \text{when} \quad row = j, \\ \mathbf{o}^{a1ci}_3 & \text{when} \quad row = i, \\ \mathbf{0}_3 & \text{otherwise}, \end{cases} \tag{C.30}$$

$$\mathbf{I}^{a2c}_{aug}(row, col) \equiv \begin{cases} \mathbf{O}^{a2cj}_{3\times 2} & \text{when} \quad row = j, \\ \mathbf{O}^{a2ci}_{3\times 2} & \text{when} \quad row = i, \\ \mathbf{0}_{3\times 2} & \text{otherwise}, \end{cases} \tag{C.31}$$

$$\mathbf{I}^{b1c}_{aug}(row, col) \equiv \begin{cases} \mathbf{o}^{b1cj}_3 & \text{when} \quad row = j, \\ \mathbf{o}^{b1ci}_3 & \text{when} \quad row = i, \\ \mathbf{0}_3 & \text{otherwise}, \end{cases} \tag{C.32}$$

$$\mathbf{I}^{b2c}_{aug}(row, col) \equiv \begin{cases} \mathbf{O}^{b2cj}_{3\times 2} & \text{when} \quad row = j, \\ \mathbf{O}^{b2ci}_{3\times 2} & \text{when} \quad row = i, \\ \mathbf{0}_{3\times 2} & \text{otherwise}, \end{cases} \tag{C.33}$$

where *col* represents each of all $(m^2 - m)q$ possible combinations of two cables, for each of the q orientations. Vectors $\mathbf{o}_3$ and matrices $\mathbf{O}_{3\times 2}$ are defined as follows:

$$\mathbf{o}_3^{a1cj} \equiv 2(\mathbf{i}^{aa} - 4\text{det}(\mathbf{H}_{i,j,k})(\mathbf{\Pi s}_{i,j,k} + \mathbf{f}) - 2h_{i,j,k}\mathbf{i}^{da}), \tag{C.34}$$

$$\mathbf{o}_3^{a1ci} \equiv -2(\mathbf{i}^{aa} - 2h_{i,j,k}\mathbf{i}^{da}), \tag{C.35}$$

$$\mathbf{O}_{3\times 2}^{a2cj} \equiv -2\left[\begin{array}{cc} (\mathbf{\Pi s}_{i,j,k} + \mathbf{\Pi s}_{i,j,k}^{\mathbf{S}_1} + \mathbf{f}) & \mathbf{\Pi s}_{i,j,k}^{\mathbf{S}_2} \end{array}\right], \tag{C.36}$$

$$\mathbf{O}_{3\times 2}^{a2ci} \equiv 2\left[\begin{array}{cc} (\mathbf{\Pi s}_{i,j,k} + \mathbf{f}) & \mathbf{0}_3 \end{array}\right], \tag{C.37}$$

$$\mathbf{o}_3^{b1cj} \equiv -2(\mathbf{i}^{ab} + 2h_{i,j,k}\mathbf{i}^{db}), \tag{C.38}$$

$$\mathbf{o}_3^{b1ci} \equiv 2(\mathbf{i}^{ab} + 4\text{det}(\mathbf{H}_{i,j,k})\mathbf{Q}_k^T(\mathbf{\Pi s}_{i,j,k} + \mathbf{f}) + 2h_{i,j,k}\mathbf{i}^{db}), \tag{C.39}$$

$$\mathbf{O}_{3\times 2}^{b2cj} \equiv -2\mathbf{Q}_k^T\left[\begin{array}{cc} \mathbf{0}_3 & (\mathbf{\Pi s}_{i,j,k} + \mathbf{f}) \end{array}\right], \tag{C.40}$$

$$\mathbf{O}_{3\times 2}^{b2ci} \equiv 2\mathbf{Q}_k^T\left[\begin{array}{cc} \mathbf{\Pi s}_{i,j,k}^{\mathbf{S}_1} & (\mathbf{\Pi s}_{i,j,k} + \mathbf{\Pi s}_{i,j,k}^{\mathbf{S}_2} + \mathbf{f}) \end{array}\right], \tag{C.41}$$

where $\mathbf{s}_{i,j,k}^{\mathbf{S}_1}$ and $\mathbf{s}_{i,j,k}^{\mathbf{S}_2}$ are defined from Eq. (4.24) as follows:

$$\mathbf{S}_{i,j,k} \equiv \left[\begin{array}{cc} \mathbf{s}_{i,j,k}^{\mathbf{S}_1} & \mathbf{s}_{i,j,k}^{\mathbf{S}_2} \end{array}\right], \tag{C.42}$$

and

$$\mathbf{s}_{i,j,k}^{\mathbf{S}_1} \equiv \mathbf{a}_j - \mathbf{a}_i, \tag{C.43}$$

$$\mathbf{s}_{i,j,k}^{\mathbf{S}_2} \equiv \mathbf{Q}_k(\mathbf{b}_j^{\mathcal{B}} - \mathbf{b}_i^{\mathcal{B}}), \tag{C.44}$$

and where $\mathbf{\Pi}$, $\mathbf{f}$ and $\mathbf{s}_{i,j,k}$ are defined by Eqs. (4.4), (4.6) and (4.25), respectively. Finally,

$$\mathbf{i}^{aa} \equiv \mu_{i,j,k,2}^2\mathbf{\Pi s}_{i,j,k}^{\mathbf{S}_1} - \mu_{i,j,k,1}\mu_{i,j,k,2}\mathbf{\Pi s}_{i,j,k}^{\mathbf{S}_2}, \tag{C.45}$$

$$\mathbf{i}^{da} \equiv \left[\begin{array}{cc} 2\mathbf{\Pi s}_{i,j,k}^{\mathbf{S}_1} & \mathbf{\Pi s}_{i,j,k}^{\mathbf{S}_2} \end{array}\right]\mathbf{E}_r^T\mathbf{h}_2 + \left[\begin{array}{cc} \mathbf{\Pi s}_{i,j,k}^{\mathbf{S}_2} & \mathbf{0}_3 \end{array}\right]\mathbf{E}_r\mathbf{h}_1, \tag{C.46}$$

$$\mathbf{i}^{ab} \equiv \mathbf{Q}_k^T(\mu_{i,j,k,1}\mu_{i,j,k,2}\mathbf{\Pi s}_{i,j,k}^{\mathbf{S}_1} - \mu_{i,j,k,1}^2\mathbf{\Pi s}_{i,j,k}^{\mathbf{S}_2}), \tag{C.47}$$

$$\mathbf{i}^{db} \equiv \mathbf{Q}_k^T(\left[\begin{array}{cc} \mathbf{0}_3 & \mathbf{\Pi s}_{i,j,k}^{\mathbf{S}_1} \end{array}\right]\mathbf{E}_r^T\mathbf{h}_2 + \left[\begin{array}{cc} \mathbf{\Pi s}_{i,j,k}^{\mathbf{S}_1} & 2\mathbf{\Pi s}_{i,j,k}^{\mathbf{S}_2} \end{array}\right]\mathbf{E}_r\mathbf{h}_1), \tag{C.48}$$

where $\mu_{i,j,k,1}$ and $\mu_{i,j,k,2}$ are the two components of the vector $\boldsymbol{\mu}_{i,j,k}$, vectors $\mathbf{h}_1$ and $\mathbf{h}_2$ represent the column of the matrix defined with Eq. (4.27), i.e.,

$$\mathbf{H}_{i,j,k} \equiv \left[\begin{array}{cc} \mathbf{h}_1 & \mathbf{h}_2 \end{array}\right], \tag{C.49}$$

and, finally, where matrix $\mathbf{E}_r$ is defined as follows:

$$\mathbf{E}_r \equiv \left[\begin{array}{cc} 0 & -1 \\ 1 & 0 \end{array}\right]. \tag{C.50}$$

Similarly, for each pair of a cable i and an edge o, the cells of the matrices from Eq. (C.29) are structured such as:

$$\mathbf{I}^{a1e}_{aug}(row, col) \equiv \begin{cases} \mathbf{o}_3^{a1ei} & \text{when} \quad row = i, \\ \mathbf{0}_3 & \text{otherwise}, \end{cases} \tag{C.51}$$

$$\mathbf{I}^{a2e}_{aug}(row, col) \equiv \begin{cases} \mathbf{O}_{3\times3}^{a2ei} & \text{when} \quad row = i, \\ \mathbf{0}_{3\times3} & \text{otherwise}, \end{cases} \tag{C.52}$$

$$\mathbf{I}^{b1e}_{aug}(row, col) \equiv \begin{cases} \mathbf{o}_3^{b1ei} & \text{when} \quad row = i, \\ \mathbf{0}_3 & \text{otherwise}, \end{cases} \tag{C.53}$$

$$\mathbf{I}^{b2e}_{aug}(row, col) \equiv \begin{cases} \mathbf{O}_{3\times3}^{b2ei} & \text{when} \quad row = i, \\ \mathbf{0}_{3\times3} & \text{otherwise}, \end{cases} \tag{C.54}$$

where *col* here represents each of all mfq possible combinations of a cable and an edge, for each of the q orientations. Also, vectors $\mathbf{o}_3$ and matrices $\mathbf{O}_{3\times3}$ are defined as follows:

$$\mathbf{o}_3^{a1ei} \equiv -8\det(\mathbf{N}_{i,o,k})(\mathbf{\Pi}\mathbf{r}_{i,k} + \mathbf{f}), \tag{C.55}$$

$$\mathbf{O}_{3\times3}^{a2ei} \equiv 2 \begin{bmatrix} \mathbf{0}_3 & \mathbf{\Pi}\mathbf{R}_{i,o,k} \end{bmatrix} \mathbf{D}^{-T}, \tag{C.56}$$

$$\mathbf{o}_3^{b1ei} \equiv \mathbf{Q}_k^T(2\mathbf{x}^{ab} + 4(\eta_{i,o,k,1} + n_{i,k})\mathbf{x}^{db} - \mathbf{o}_3^{a1ei}), \tag{C.57}$$

$$\mathbf{O}_{3\times3}^{b2ei} \equiv -2\mathbf{Q}_k^T \begin{bmatrix} \mathbf{0}_3 & (\mathbf{\Pi}\mathbf{r}_{i,k} + \mathbf{\Pi}\mathbf{r}_{i,o,k}^{\mathbf{R}_1} + \mathbf{f}) & (\mathbf{\Pi}\mathbf{r}_{i,k} + \mathbf{\Pi}\mathbf{r}_{i,o,k}^{\mathbf{R}_2} + \mathbf{f}) \end{bmatrix} \mathbf{D}^{-T}, \tag{C.58}$$

where $\mathbf{r}_{i,o,k}^{\mathbf{R}_1}$ and $\mathbf{r}_{i,o,k}^{\mathbf{R}_2}$ are defined from Eq. (4.35) as follows:

$$\mathbf{R}_{i,o,k} \equiv \begin{bmatrix} \mathbf{r}_{i,o,k}^{\mathbf{R}_1} & \mathbf{r}_{i,o,k}^{\mathbf{R}_2} \end{bmatrix}, \tag{C.59}$$

and

$$\mathbf{r}_{i,o,k}^{\mathbf{R}_1} \equiv \mathbf{a}_j - \mathbf{a}_i, \tag{C.60}$$

$$\mathbf{r}_{i,o,k}^{\mathbf{R}_2} \equiv \mathbf{Q}_k(\mathbf{b}_j^{\mathcal{B}} - \mathbf{b}_i^{\mathcal{B}}). \tag{C.61}$$

The elements $\mathbf{r}_{i,k}$ and $n_{i,k}$ are defined by Eqs. (4.36) and (4.40), respectively, and $\eta_{i,o,k,1}$ represents the first component of the vector $\boldsymbol{\eta}_{i,o,k}$. Finally,

$$\mathbf{x}^{ab} \equiv -\eta_{i,o,k,2}^2\mathbf{\Pi}\mathbf{r}_{i,o,k}^{\mathbf{R}_2} + \eta_{i,o,k,2}\eta_{i,o,k,3}\mathbf{\Pi}(\mathbf{r}_{i,o,k}^{\mathbf{R}_1} + \mathbf{r}_{i,o,k}^{\mathbf{R}_2}) - \eta_{i,o,k,3}^2\mathbf{\Pi}\mathbf{r}_{i,o,k}^{\mathbf{R}_1}, \tag{C.62}$$

$$\mathbf{x}^{db} \equiv \begin{bmatrix} 2\mathbf{\Pi}\mathbf{r}_{i,o,k}^{\mathbf{R}_1} & \mathbf{\Pi}(\mathbf{r}_{i,o,k}^{\mathbf{R}_1} + \mathbf{r}_{i,o,k}^{\mathbf{R}_2}) \end{bmatrix} \mathbf{E}_r^T\mathbf{n}_2 + \begin{bmatrix} \mathbf{\Pi}(\mathbf{r}_{i,o,k}^{\mathbf{R}_1} + \mathbf{r}_{i,o,k}^{\mathbf{R}_2}) & 2\mathbf{\Pi}\mathbf{r}_{i,o,k}^{\mathbf{R}_2} \end{bmatrix} \mathbf{E}_r\mathbf{n}_1, \tag{C.63}$$

where $\eta_{i,o,k,2}$ and $\eta_{i,o,k,3}$ are the second and the third components of the vector $\boldsymbol{\eta}_{i,o,k}$ and the vectors $\mathbf{n}_1$ and $\mathbf{n}_2$ represent the columns of the matrix defined with Eq. (4.38), i.e.,

$$\mathbf{N}_{i,o,k} \equiv \begin{bmatrix} \mathbf{n}_1 & \mathbf{n}_2 \end{bmatrix}. \tag{C.64}$$

On the other hand, the mathematical derivatives of the nonlinear equality constraints $\mathbf{c}_{\text{eq}}(\mathbf{v})$ lead to the following expressions:

$$\nabla \mathbf{c}_{\text{eq}}(\mathbf{v}) = \begin{bmatrix} \mathbf{0}_{nqnb}^T \\ \mathbf{W}_{aug}^a \\ \mathbf{W}_{aug}^b \\ \mathbf{W}_{aug}^p \\ \mathbf{W}_{aug}^T \\ \mathbf{0}_{(2(m^2-m)q+3mfq)\times nqnb} \end{bmatrix}, \tag{C.65}$$

where $\mathbf{W}_{aug}^{a,b}$ are cell matrices of dimensions $m \times qnb$ and are defined as

$$\mathbf{W}_{aug}^{a,b} = \begin{bmatrix} \mathbf{W}_{1,1,1}^{a,b} & \cdots & \mathbf{W}_{1,k,1}^{a,b} & \cdots & \mathbf{W}_{1,q,1}^{a,b} & \cdots & \mathbf{W}_{1,k,\epsilon}^{a,b} & \cdots & \mathbf{W}_{1,q,nb}^{a,b} \\ \vdots & & \vdots & & \vdots & & \vdots & & \vdots \\ \mathbf{W}_{i,1,1}^{a,b} & \cdots & \mathbf{W}_{i,k,1}^{a,b} & \cdots & \mathbf{W}_{i,q,1}^{a,b} & \cdots & \mathbf{W}_{i,k,\epsilon}^{a,b} & \cdots & \mathbf{W}_{i,q,nb}^{a,b} \\ \vdots & & \vdots & & \vdots & & \vdots & & \vdots \\ \mathbf{W}_{m,1,1}^{a,b} & \cdots & \mathbf{W}_{m,k,1}^{a,b} & \cdots & \mathbf{W}_{m,q,1}^{a,b} & \cdots & \mathbf{W}_{m,k,\epsilon}^{a,b} & \cdots & \mathbf{W}_{m,q,nb}^{a,b} \end{bmatrix}, \tag{C.66}$$

and where matrix $\mathbf{W}_{aug}^p$ is of dimensions $3nb \times nqnb$ and is expressed as follows:

$$\mathbf{W}_{aug}^p = \begin{bmatrix} \begin{bmatrix} \mathbf{W}_{1,1}^p & \cdots & \mathbf{W}_{q,1}^p \end{bmatrix} & \cdots & \mathbf{0}_{3\times nq} & \cdots & \mathbf{0}_{3\times nq} \\ \vdots & \ddots & \vdots & & \vdots \\ \mathbf{0}_{3\times nq} & \cdots & \begin{bmatrix} \mathbf{W}_{1,\epsilon}^p & \cdots & \mathbf{W}_{q,\epsilon}^p \end{bmatrix} & \cdots & \mathbf{0}_{3\times nq} \\ \vdots & & \vdots & \ddots & \vdots \\ \mathbf{0}_{3\times nq} & \cdots & \mathbf{0}_{3\times nq} & \cdots & \begin{bmatrix} \mathbf{W}_{1,nb}^p & \cdots & \mathbf{W}_{q,nb}^p \end{bmatrix} \end{bmatrix}. \tag{C.67}$$

Furthermore, for the case of a spatial six-DoF CDPM,

$$\mathbf{W}_{i,k,\epsilon}^a = t_{i,k,\epsilon} \begin{bmatrix} \mathbf{1}_{3\times 3} & (\text{cpm}(\mathbf{Q}_k \mathbf{b}_i^{\mathcal{B}}))^T \end{bmatrix}_{3\times n}, \tag{C.68}$$

$$\mathbf{W}_{i,k,\epsilon}^b = -\, t_{i,k,\epsilon} \begin{bmatrix} \mathbf{Q}_k^T & (\text{cpm}(\mathbf{a}_i - \mathbf{p}_\epsilon)\mathbf{Q}_k)^T \end{bmatrix}_{3\times n}, \tag{C.69}$$

$$\mathbf{W}_{k,\epsilon}^p = \begin{bmatrix} -(\mathbf{1}_m^T \mathbf{t}_{k,\epsilon})\mathbf{1}_{3\times 3} & -(\text{cpm}(\mathbf{Q}_k \mathbf{B} \mathbf{t}_{k,\epsilon}))^T \end{bmatrix}_{3\times n}, \tag{C.70}$$

where $n = 6$ and $\mathbf{B}$ has been defined with Eq. (4.18) in Chapter 4.

Appendix D

Geometric Parameters of the Cable-Driven Parallel Mechanisms

This appendix presents the geometric parameters, i.e., the attachment points $\mathbf{a}_i$ and $\mathbf{b}_i^{\mathcal{B}}$, $i = 1, \ldots, m$, of the m cables of the cable-driven parallel mechanisms (CDPMs), before and after their optimization with the dimensional synthesis program proposed in Section 4.3. From the CDPM's geometry optimizations contained in each sub-section of this appendix, all CDPMs are presented by the mean of three different tables, except for the last one. The first table shows the geometric parameters of the randomly-determined initial solution. The second table, also illustrated in a figure, contains the geometry of the closest-feasible initial solution, i.e., the projection of the randomized solution on the domain of the feasible solutions. The last table, and its corresponding figure, presents the optimized geometric parameters resulting from the dimensional synthesis problem. Finally, for the last trial of each sub-section, only two tables are displayed, the initial and the final geometric parameters (also illustrated in figures), since the initial solution is based on the designer's intuition and these initial geometric parameters are assumed to belong or to be close to the domain of the feasible solutions. Moreover, for each trial, the final wrench-closure workspace of the CDPM is shown with the final corresponding ellipsoid and, if $\kappa \gtrapprox 0.9$, three additional views are displayed for the final geometry in order to facilitate the analysis and comparison of the solutions that fulfill or approximately fulfill the prescribed requirements. Note that, in figures, each cable i is tagged with its associated number, for example, cable 1 is tagged by "$c1$".

The Section D.1 presents the data corresponding to the fourteen CDPM's geometries optimized for the first numerical application of the dimensional synthesis program, which is described in Sub-section 4.3.1. Then, Section D.2 shows the twelve best sets of geometric parameters over a total of a hundred CDPM's geometries generated for the envisioned medical application described in Sub-section 4.3.2.

D.1 Synthesis of Seven-Cable Nine-Edge Six-DoF Cable-Driven Parallel Mechanisms

Table D.1 and Fig. D.1 present and illustrate the geometric parameters and the final wrench-closure workspace (WCW) as well as the final ellipsoid $\mathcal{W}_t$ ($\kappa = 0.4798$) resulting from the dimensional synthesis (Trial 1) of the CDPM presented in Sub-section 4.3.1.

	$\mathbf{a}_{1,r}$	$\mathbf{a}_{2,r}$	$\mathbf{a}_{3,r}$	$\mathbf{a}_{4,r}$	$\mathbf{a}_{5,r}$	$\mathbf{a}_{6,r}$	$\mathbf{a}_{7,r}$
x (m)	0.9172	0.2858	0.7572	0.7537	0.3804	0.5678	0.0759
y (m)	0.0540	0.5308	0.7792	0.9340	0.1299	0.5688	0.4694
z (m)	0.0119	0.3371	0.1622	0.7943	0.3112	0.5285	0.1656
	$\mathbf{b}^{\mathcal{B}}_{1,r}$	$\mathbf{b}^{\mathcal{B}}_{2,r}$	$\mathbf{b}^{\mathcal{B}}_{3,r}$	$\mathbf{b}^{\mathcal{B}}_{4,r}$	$\mathbf{b}^{\mathcal{B}}_{5,r}$	$\mathbf{b}^{\mathcal{B}}_{6,r}$	$\mathbf{b}^{\mathcal{B}}_{7,r}$
$x^{\mathcal{B}}$ (m)	0.0204	−0.0474	0.0308	0.0378	0.0496	−0.0099	−0.0832
$y^{\mathcal{B}}$ (m)	−0.0542	0.0827	−0.0695	0.0652	0.0077	0.0992	−0.0844
$z^{\mathcal{B}}$ (m)	−0.0115	−0.0787	0.0924	−0.0991	0.0550	0.0635	0.0737

(a) Randomly-determined geometric parameters $\mathbf{a}_{i,r}$ and $\mathbf{b}^{\mathcal{B}}_{i,r}$

	$\mathbf{a}_{1,0}$	$\mathbf{a}_{2,0}$	$\mathbf{a}_{3,0}$	$\mathbf{a}_{4,0}$	$\mathbf{a}_{5,0}$	$\mathbf{a}_{6,0}$	$\mathbf{a}_{7,0}$
x (m)	0.9176	0.2808	0.7556	0.7388	0.3651	0.5629	0.0747
y (m)	0.0535	0.5342	0.7821	0.9320	0.1321	0.5918	0.4705
z (m)	0.0126	0.3401	0.1636	0.8071	0.3207	0.5253	0.1670
	$\mathbf{b}^{\mathcal{B}}_{1,0}$	$\mathbf{b}^{\mathcal{B}}_{2,0}$	$\mathbf{b}^{\mathcal{B}}_{3,0}$	$\mathbf{b}^{\mathcal{B}}_{4,0}$	$\mathbf{b}^{\mathcal{B}}_{5,0}$	$\mathbf{b}^{\mathcal{B}}_{6,0}$	$\mathbf{b}^{\mathcal{B}}_{7,0}$
$x^{\mathcal{B}}$ (m)	0.0143	−0.0303	0.0346	0.0441	0.0540	−0.0059	−0.0803
$y^{\mathcal{B}}$ (m)	−0.0508	0.0745	−0.0614	0.0122	0.0247	0.0914	−0.0855
$z^{\mathcal{B}}$ (m)	−0.0161	−0.0772	0.1000	−0.0380	−0.0198	0.0713	0.0733

(b) Closest-feasible initial geometric parameters $\mathbf{a}_{i,0}$ and $\mathbf{b}^{\mathcal{B}}_{i,0}$

	$\mathbf{a}_{1,f}$	$\mathbf{a}_{2,f}$	$\mathbf{a}_{3,f}$	$\mathbf{a}_{4,f}$	$\mathbf{a}_{5,f}$	$\mathbf{a}_{6,f}$	$\mathbf{a}_{7,f}$
x (m)	0.9995	0.0003	0.8224	0.5949	0.0006	0.9997	0.0896
y (m)	0.0007	0.9985	0.9997	0.6045	0.0002	0.7956	0.0512
z (m)	0.6276	0.5104	0.5740	0.9997	0.4457	0.7756	0.0003
	$\mathbf{b}^{\mathcal{B}}_{1,f}$	$\mathbf{b}^{\mathcal{B}}_{2,f}$	$\mathbf{b}^{\mathcal{B}}_{3,f}$	$\mathbf{b}^{\mathcal{B}}_{4,f}$	$\mathbf{b}^{\mathcal{B}}_{5,f}$	$\mathbf{b}^{\mathcal{B}}_{6,f}$	$\mathbf{b}^{\mathcal{B}}_{7,f}$
$x^{\mathcal{B}}$ (m)	0.0457	−0.0998	0.0999	0.0999	0.0996	−0.0995	−0.0697
$y^{\mathcal{B}}$ (m)	−0.0878	0.0719	−0.0998	0.0166	−0.0568	0.0999	−0.0512
$z^{\mathcal{B}}$ (m)	0.0337	0.0109	0.0999	−0.0836	−0.0785	0.0984	0.0881

(c) Final geometric parameters $\mathbf{a}_{i,f}$ and $\mathbf{b}^{\mathcal{B}}_{i,f}$

Table D.1 – Geometric parameters of the CDPM corresponding to the Trial 1 of the numerical application of the dimensional synthesis program presented in Sub-section 4.3.1.

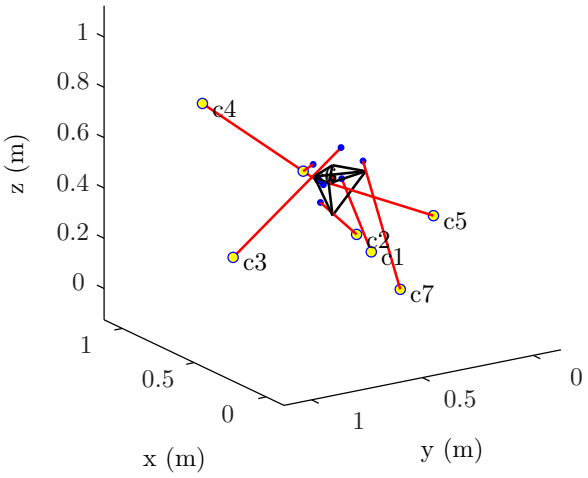

(a) The initial geometry of the CDPM

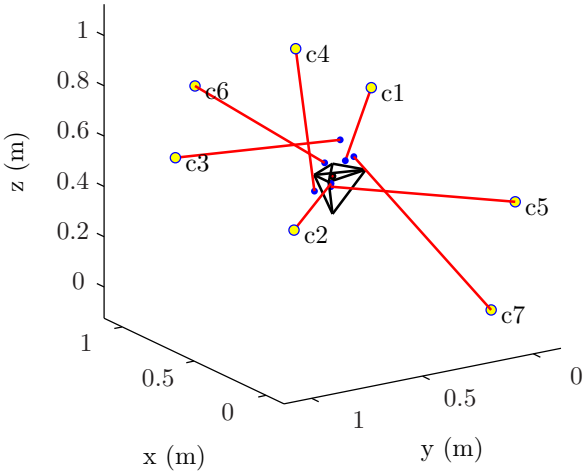

(b) The final geometry of the CDPM

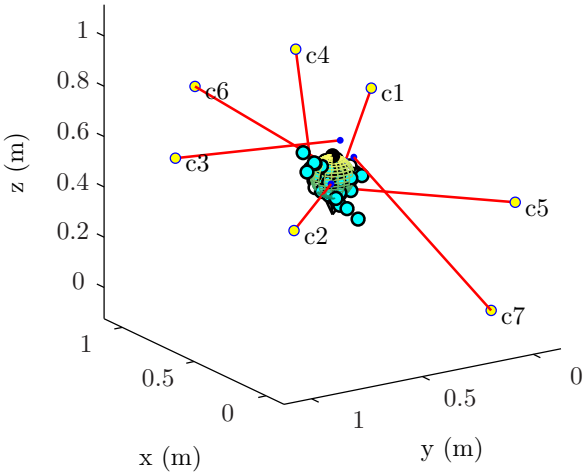

(c) The WCW of the final CDPM's geometry with the final $\mathcal{W}_t$ ($\kappa = 0.4798$)

Figure D.1 – Illustration of different results obtained from the optimization of a CDPM (Trial 1) for the numerical application of the dimensional synthesis program presented in Sub-section 4.3.1.

Table D.2 and Fig. D.2 present and illustrate the geometric parameters and the final wrench-closure workspace (WCW) as well as the final ellipsoid $\mathcal{W}_t$ ($\kappa = 0.7679$) resulting from the dimensional synthesis (Trial 2) of the CDPM presented in Sub-section 4.3.1.

	$\mathbf{a}_{1,r}$	$\mathbf{a}_{2,r}$	$\mathbf{a}_{3,r}$	$\mathbf{a}_{4,r}$	$\mathbf{a}_{5,r}$	$\mathbf{a}_{6,r}$	$\mathbf{a}_{7,r}$
x (m)	0.0844	0.3998	0.2599	0.8001	0.4314	0.9106	0.1818
y (m)	0.2638	0.1455	0.1361	0.8693	0.5797	0.5499	0.1450
z (m)	0.8530	0.6221	0.3510	0.5132	0.4018	0.0760	0.2399
	$\mathbf{b}^{\mathcal{B}}_{1,r}$	$\mathbf{b}^{\mathcal{B}}_{2,r}$	$\mathbf{b}^{\mathcal{B}}_{3,r}$	$\mathbf{b}^{\mathcal{B}}_{4,r}$	$\mathbf{b}^{\mathcal{B}}_{5,r}$	$\mathbf{b}^{\mathcal{B}}_{6,r}$	$\mathbf{b}^{\mathcal{B}}_{7,r}$
$x^{\mathcal{B}}$ (m)	−0.0753	−0.0632	−0.0520	−0.0165	−0.0901	0.0805	0.0890
$y^{\mathcal{B}}$ (m)	−0.0018	−0.0021	−0.0325	0.0800	−0.0262	−0.0778	0.0561
$z^{\mathcal{B}}$ (m)	−0.0221	−0.0517	−0.0192	−0.0807	−0.0736	0.0884	0.0912

(a) Randomly-determined geometric parameters $\mathbf{a}_{i,r}$ and $\mathbf{b}^{\mathcal{B}}_{i,r}$

	$\mathbf{a}_{1,0}$	$\mathbf{a}_{2,0}$	$\mathbf{a}_{3,0}$	$\mathbf{a}_{4,0}$	$\mathbf{a}_{5,0}$	$\mathbf{a}_{6,0}$	$\mathbf{a}_{7,0}$
x (m)	0.0875	0.4070	0.2602	0.7995	0.4643	0.9106	0.1823
y (m)	0.2660	0.1422	0.1362	0.8699	0.5844	0.5501	0.1450
z (m)	0.8572	0.6178	0.3499	0.5137	0.4054	0.0760	0.2394
	$\mathbf{b}^{\mathcal{B}}_{1,0}$	$\mathbf{b}^{\mathcal{B}}_{2,0}$	$\mathbf{b}^{\mathcal{B}}_{3,0}$	$\mathbf{b}^{\mathcal{B}}_{4,0}$	$\mathbf{b}^{\mathcal{B}}_{5,0}$	$\mathbf{b}^{\mathcal{B}}_{6,0}$	$\mathbf{b}^{\mathcal{B}}_{7,0}$
$x^{\mathcal{B}}$ (m)	−0.0719	−0.0836	−0.0686	−0.0132	−0.0757	0.0805	0.0898
$y^{\mathcal{B}}$ (m)	−0.0169	−0.0067	−0.0221	0.0739	−0.0160	−0.0771	0.0560
$z^{\mathcal{B}}$ (m)	−0.0413	−0.0648	−0.0191	−0.0829	−0.0425	0.0885	0.0903

(b) Closest-feasible initial geometric parameters $\mathbf{a}_{i,0}$ and $\mathbf{b}^{\mathcal{B}}_{i,0}$

	$\mathbf{a}_{1,f}$	$\mathbf{a}_{2,f}$	$\mathbf{a}_{3,f}$	$\mathbf{a}_{4,f}$	$\mathbf{a}_{5,f}$	$\mathbf{a}_{6,f}$	$\mathbf{a}_{7,f}$
x (m)	0.0043	0.0055	0.0002	0.9988	0.7419	0.9987	0.6675
y (m)	0.9983	0.0005	0.3560	0.9990	0.9998	0.0019	0.0007
z (m)	0.9989	0.4567	0.3006	0.9927	0.0000	0.0010	0.9990
	$\mathbf{b}^{\mathcal{B}}_{1,f}$	$\mathbf{b}^{\mathcal{B}}_{2,f}$	$\mathbf{b}^{\mathcal{B}}_{3,f}$	$\mathbf{b}^{\mathcal{B}}_{4,f}$	$\mathbf{b}^{\mathcal{B}}_{5,f}$	$\mathbf{b}^{\mathcal{B}}_{6,f}$	$\mathbf{b}^{\mathcal{B}}_{7,f}$
$x^{\mathcal{B}}$ (m)	−0.0998	−0.0986	−0.0671	0.0998	−0.0504	0.0998	0.0779
$y^{\mathcal{B}}$ (m)	0.0076	0.0996	−0.0996	−0.0615	0.0365	−0.0894	−0.0998
$z^{\mathcal{B}}$ (m)	0.0383	−0.0654	0.0995	0.0283	−0.0125	0.0895	0.0643

(c) Final geometric parameters $\mathbf{a}_{i,f}$ and $\mathbf{b}^{\mathcal{B}}_{i,f}$

Table D.2 – Geometric parameters of the CDPM corresponding to the Trial 2 of the numerical application of the dimensional synthesis program presented in Sub-section 4.3.1.

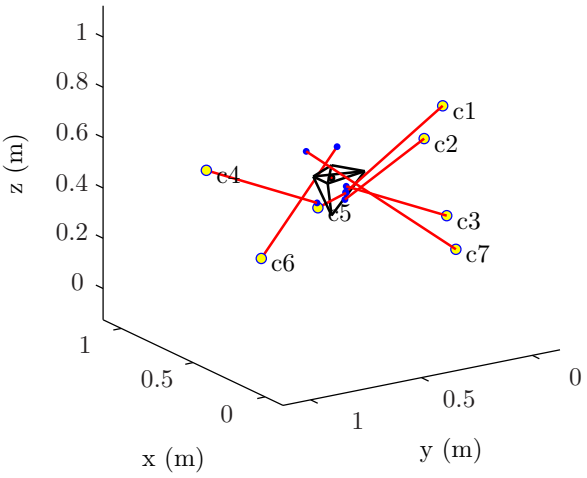

(a) The initial geometry of the CDPM

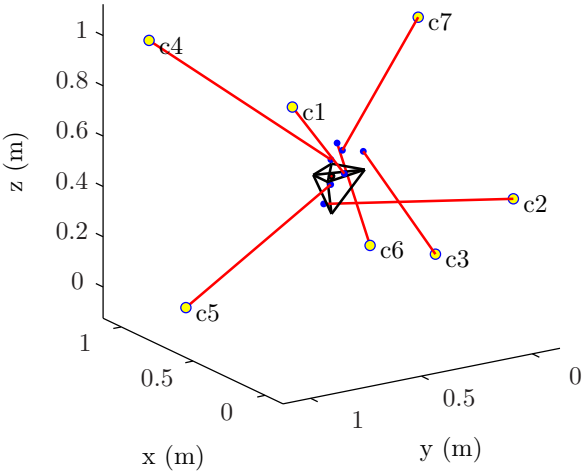

(b) The final geometry of the CDPM

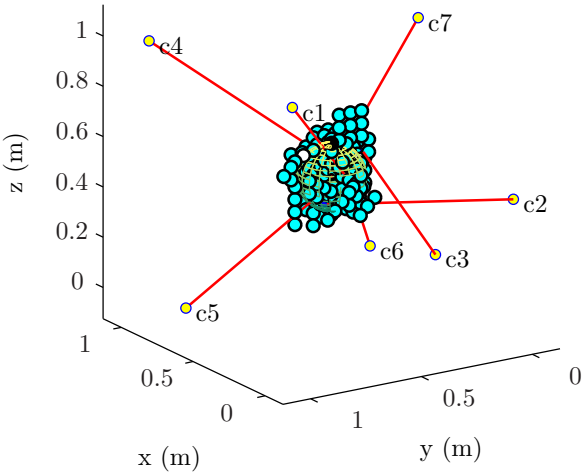

(c) The WCW of the final CDPM's geometry with the final $\mathcal{W}_t$ ($\kappa = 0.7679$)

Figure D.2 – Illustration of different results obtained from the optimization of a CDPM (Trial 2) for the numerical application of the dimensional synthesis program presented in Sub-section 4.3.1.

Table D.3 and Fig. D.3 present and illustrate the geometric parameters and the final wrench-closure workspace (WCW) as well as the final ellipsoid $\mathcal{W}_t$ ($\kappa = 0.4657$) resulting from the dimensional synthesis (Trial 3) of the CDPM presented in Sub-section 4.3.1.

	$\mathbf{a}_{1,r}$	$\mathbf{a}_{2,r}$	$\mathbf{a}_{3,r}$	$\mathbf{a}_{4,r}$	$\mathbf{a}_{5,r}$	$\mathbf{a}_{6,r}$	$\mathbf{a}_{7,r}$
x (m)	0.5752	0.0598	0.2348	0.3532	0.8212	0.0154	0.0430
y (m)	0.1690	0.6491	0.7317	0.6477	0.4509	0.5470	0.2963
z (m)	0.7447	0.1890	0.6868	0.1835	0.3685	0.6256	0.7802
	$\mathbf{b}^{\mathcal{B}}_{1,r}$	$\mathbf{b}^{\mathcal{B}}_{2,r}$	$\mathbf{b}^{\mathcal{B}}_{3,r}$	$\mathbf{b}^{\mathcal{B}}_{4,r}$	$\mathbf{b}^{\mathcal{B}}_{5,r}$	$\mathbf{b}^{\mathcal{B}}_{6,r}$	$\mathbf{b}^{\mathcal{B}}_{7,r}$
$x^{\mathcal{B}}$ (m)	−0.0838	0.0859	0.0551	−0.0026	−0.0128	−0.0106	−0.0387
$y^{\mathcal{B}}$ (m)	0.0017	0.0022	0.0635	0.0590	0.0289	−0.0243	0.0623
$z^{\mathcal{B}}$ (m)	0.0066	−0.0299	0.0878	0.0752	0.0100	0.0245	0.0174

(a) Randomly-determined geometric parameters $\mathbf{a}_{i,r}$ and $\mathbf{b}^{\mathcal{B}}_{i,r}$

	$\mathbf{a}_{1,0}$	$\mathbf{a}_{2,0}$	$\mathbf{a}_{3,0}$	$\mathbf{a}_{4,0}$	$\mathbf{a}_{5,0}$	$\mathbf{a}_{6,0}$	$\mathbf{a}_{7,0}$
x (m)	0.5758	0.0599	0.2357	0.3531	0.8283	0.0197	0.0436
y (m)	0.1705	0.6496	0.7321	0.6477	0.4702	0.5593	0.2971
z (m)	0.7465	0.1890	0.6887	0.1835	0.3839	0.6334	0.7818
	$\mathbf{b}^{\mathcal{B}}_{1,0}$	$\mathbf{b}^{\mathcal{B}}_{2,0}$	$\mathbf{b}^{\mathcal{B}}_{3,0}$	$\mathbf{b}^{\mathcal{B}}_{4,0}$	$\mathbf{b}^{\mathcal{B}}_{5,0}$	$\mathbf{b}^{\mathcal{B}}_{6,0}$	$\mathbf{b}^{\mathcal{B}}_{7,0}$
$x^{\mathcal{B}}$ (m)	−0.0857	0.0864	0.0530	−0.0032	−0.0079	−0.0162	−0.0333
$y^{\mathcal{B}}$ (m)	−0.0001	0.0018	0.0654	0.0587	−0.0020	−0.0227	0.0625
$z^{\mathcal{B}}$ (m)	0.0064	−0.0319	0.0824	0.0754	−0.0010	−0.0038	0.0254

(b) Closest-feasible initial geometric parameters $\mathbf{a}_{i,0}$ and $\mathbf{b}^{\mathcal{B}}_{i,0}$

	$\mathbf{a}_{1,f}$	$\mathbf{a}_{2,f}$	$\mathbf{a}_{3,f}$	$\mathbf{a}_{4,f}$	$\mathbf{a}_{5,f}$	$\mathbf{a}_{6,f}$	$\mathbf{a}_{7,f}$
x (m)	0.9983	0.2894	0.9987	0.0016	0.9979	0.0011	0.0453
y (m)	0.0013	0.8318	0.9975	0.9980	0.0016	0.9950	0.0023
z (m)	0.9969	0.0001	0.9976	0.0016	0.0013	0.9983	0.9989
	$\mathbf{b}^{\mathcal{B}}_{1,f}$	$\mathbf{b}^{\mathcal{B}}_{2,f}$	$\mathbf{b}^{\mathcal{B}}_{3,f}$	$\mathbf{b}^{\mathcal{B}}_{4,f}$	$\mathbf{b}^{\mathcal{B}}_{5,f}$	$\mathbf{b}^{\mathcal{B}}_{6,f}$	$\mathbf{b}^{\mathcal{B}}_{7,f}$
$x^{\mathcal{B}}$ (m)	−0.0699	0.0514	0.0997	−0.0996	0.0997	−0.0998	0.0435
$y^{\mathcal{B}}$ (m)	−0.0995	−0.0287	0.0996	0.0997	−0.0055	−0.0993	0.0993
$z^{\mathcal{B}}$ (m)	0.0997	−0.0845	0.0303	0.0947	−0.0964	0.0585	0.0998

(c) Final geometric parameters $\mathbf{a}_{i,f}$ and $\mathbf{b}^{\mathcal{B}}_{i,f}$

Table D.3 – Geometric parameters of the CDPM corresponding to the Trial 3 of the numerical application of the dimensional synthesis program presented in Sub-section 4.3.1.

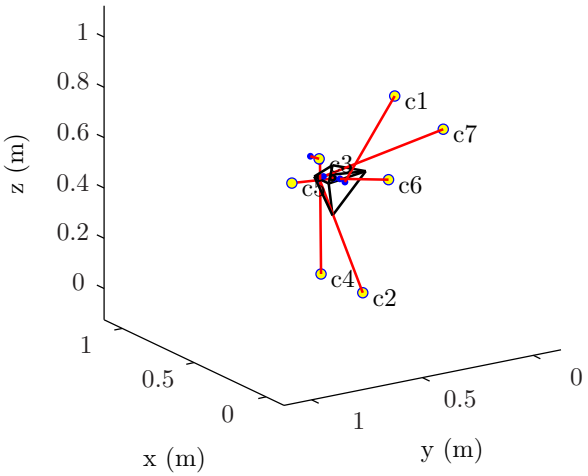

(a) The initial geometry of the CDPM

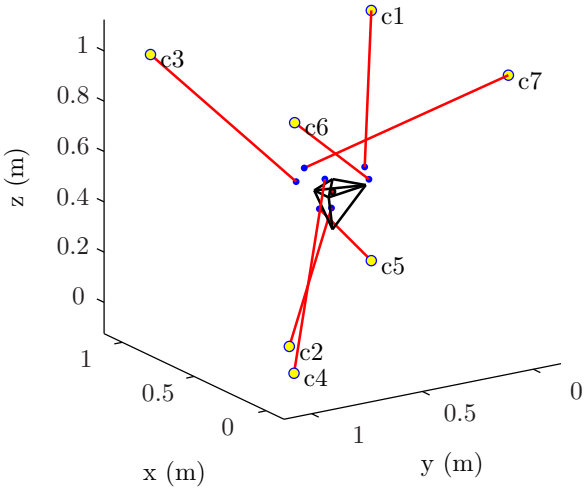

(b) The final geometry of the CDPM

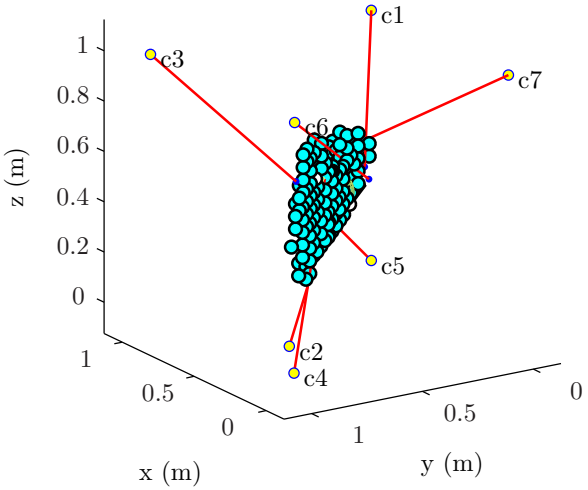

(c) The WCW of the final CDPM's geometry with the final $\mathcal{W}_t$ ($\kappa = 0.4657$)

Figure D.3 – Illustration of different results obtained from the optimization of a CDPM (Trial 3) for the numerical application of the dimensional synthesis program presented in Sub-section 4.3.1.

Table D.4 and Fig. D.4 present and illustrate the geometric parameters and the final wrench-closure workspace (WCW) as well as the final ellipsoid $\mathcal{W}_t$ ($\kappa = 0.3240$) resulting from the dimensional synthesis (Trial 4) of the CDPM presented in Sub-section 4.3.1.

	$\mathbf{a}_{1,r}$	$\mathbf{a}_{2,r}$	$\mathbf{a}_{3,r}$	$\mathbf{a}_{4,r}$	$\mathbf{a}_{5,r}$	$\mathbf{a}_{6,r}$	$\mathbf{a}_{7,r}$
x (m)	0.2077	0.3012	0.4709	0.2305	0.8443	0.1948	0.2259
y (m)	0.1707	0.2277	0.4357	0.3111	0.9234	0.4302	0.1848
z (m)	0.9049	0.9797	0.4389	0.1111	0.2581	0.4087	0.5949
	$\mathbf{b}^{\mathcal{B}}_{1,r}$	$\mathbf{b}^{\mathcal{B}}_{2,r}$	$\mathbf{b}^{\mathcal{B}}_{3,r}$	$\mathbf{b}^{\mathcal{B}}_{4,r}$	$\mathbf{b}^{\mathcal{B}}_{5,r}$	$\mathbf{b}^{\mathcal{B}}_{6,r}$	$\mathbf{b}^{\mathcal{B}}_{7,r}$
$x^{\mathcal{B}}$ (m)	−0.0476	0.0206	0.0422	−0.0557	−0.0765	−0.0407	−0.0362
$y^{\mathcal{B}}$ (m)	−0.0152	0.0016	−0.0829	−0.0475	0.0602	−0.0942	0.0858
$z^{\mathcal{B}}$ (m)	0.0461	−0.0023	0.0157	−0.0525	−0.0082	0.0926	0.0094

(a) Randomly-determined geometric parameters $\mathbf{a}_{i,r}$ and $\mathbf{b}^{\mathcal{B}}_{i,r}$

	$\mathbf{a}_{1,0}$	$\mathbf{a}_{2,0}$	$\mathbf{a}_{3,0}$	$\mathbf{a}_{4,0}$	$\mathbf{a}_{5,0}$	$\mathbf{a}_{6,0}$	$\mathbf{a}_{7,0}$
x (m)	0.2009	0.3004	0.4698	0.2284	0.8317	0.1938	0.2208
y (m)	0.1784	0.2284	0.4343	0.3118	0.9359	0.4339	0.1879
z (m)	0.9070	0.9797	0.4361	0.1121	0.2603	0.4097	0.5962
	$\mathbf{b}^{\mathcal{B}}_{1,0}$	$\mathbf{b}^{\mathcal{B}}_{2,0}$	$\mathbf{b}^{\mathcal{B}}_{3,0}$	$\mathbf{b}^{\mathcal{B}}_{4,0}$	$\mathbf{b}^{\mathcal{B}}_{5,0}$	$\mathbf{b}^{\mathcal{B}}_{6,0}$	$\mathbf{b}^{\mathcal{B}}_{7,0}$
$x^{\mathcal{B}}$ (m)	−0.0570	0.0135	0.0444	−0.0556	−0.0262	−0.0405	−0.0396
$y^{\mathcal{B}}$ (m)	−0.0193	−0.0009	−0.0806	−0.0402	0.0283	−0.0895	0.0913
$z^{\mathcal{B}}$ (m)	0.0263	−0.0136	0.0141	−0.0552	0.0069	0.0919	0.0011

(b) Closest-feasible initial geometric parameters $\mathbf{a}_{i,0}$ and $\mathbf{b}^{\mathcal{B}}_{i,0}$

	$\mathbf{a}_{1,f}$	$\mathbf{a}_{2,f}$	$\mathbf{a}_{3,f}$	$\mathbf{a}_{4,f}$	$\mathbf{a}_{5,f}$	$\mathbf{a}_{6,f}$	$\mathbf{a}_{7,f}$
x (m)	0.2534	0.2904	0.9992	0.8781	0.9989	0.0009	0.0012
y (m)	0.0003	0.0001	0.9983	0.0012	0.9992	0.9972	0.7343
z (m)	0.8841	0.8179	0.1857	0.0010	0.8307	0.0735	0.0007
	$\mathbf{b}^{\mathcal{B}}_{1,f}$	$\mathbf{b}^{\mathcal{B}}_{2,f}$	$\mathbf{b}^{\mathcal{B}}_{3,f}$	$\mathbf{b}^{\mathcal{B}}_{4,f}$	$\mathbf{b}^{\mathcal{B}}_{5,f}$	$\mathbf{b}^{\mathcal{B}}_{6,f}$	$\mathbf{b}^{\mathcal{B}}_{7,f}$
$x^{\mathcal{B}}$ (m)	−0.0995	0.0186	0.0753	0.0992	−0.0866	−0.0479	−0.0999
$y^{\mathcal{B}}$ (m)	−0.0996	0.0600	−0.0998	−0.0987	0.0985	−0.0256	0.0994
$z^{\mathcal{B}}$ (m)	0.0994	−0.0998	−0.0492	−0.0986	0.0250	−0.0996	0.0997

(c) Final geometric parameters $\mathbf{a}_{i,f}$ and $\mathbf{b}^{\mathcal{B}}_{i,f}$

Table D.4 – Geometric parameters of the CDPM corresponding to the Trial 4 of the numerical application of the dimensional synthesis program presented in Sub-section 4.3.1.

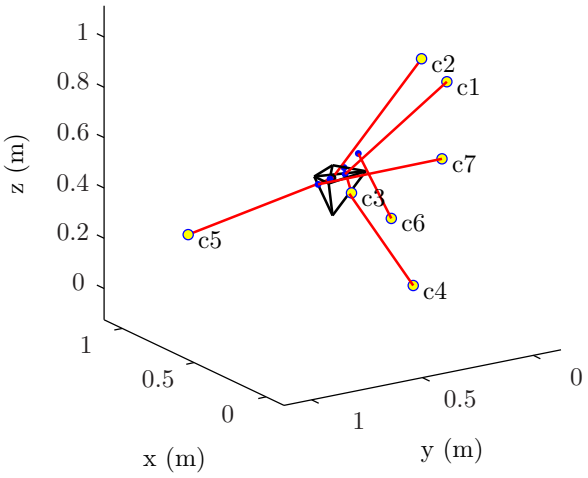

(a) The initial geometry of the CDPM

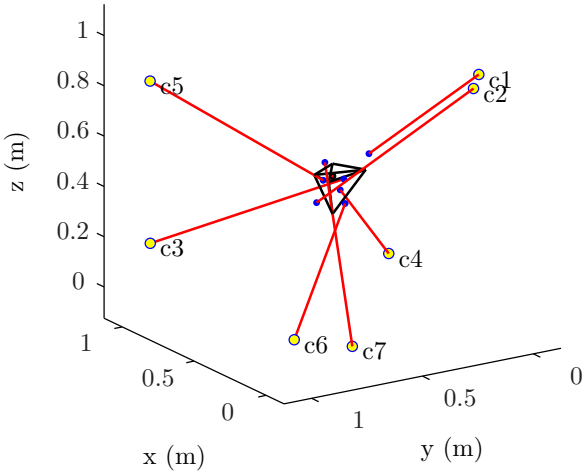

(b) The final geometry of the CDPM

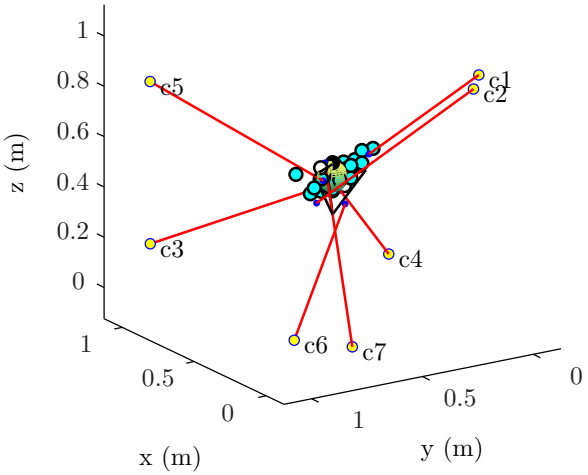

(c) The WCW of the final CDPM's geometry with the final $\mathcal{W}_t$ ($\kappa = 0.3240$)

Figure D.4 – Illustration of different results obtained from the optimization of a CDPM (Trial 4) for the numerical application of the dimensional synthesis program presented in Sub-section 4.3.1.

Table D.5 and Figs. D.5 and D.6 present and illustrate the geometric parameters and the final wrench-closure workspace (WCW) as well as the final ellipsoid $\mathcal{W}_t$ ($\kappa = 1.0306$) resulting from the dimensional synthesis (Trial 5) of the CDPM presented in Sub-section 4.3.1.

	$\mathbf{a}_{1,r}$	$\mathbf{a}_{2,r}$	$\mathbf{a}_{3,r}$	$\mathbf{a}_{4,r}$	$\mathbf{a}_{5,r}$	$\mathbf{a}_{6,r}$	$\mathbf{a}_{7,r}$
x (m)	0.5211	0.2316	0.4889	0.6241	0.6791	0.3955	0.3674
y (m)	0.9880	0.0377	0.8852	0.9133	0.7962	0.0987	0.2619
z (m)	0.3354	0.6797	0.1366	0.7212	0.1068	0.6538	0.4942
	$\mathbf{b}^{\mathcal{B}}_{1,r}$	$\mathbf{b}^{\mathcal{B}}_{2,r}$	$\mathbf{b}^{\mathcal{B}}_{3,r}$	$\mathbf{b}^{\mathcal{B}}_{4,r}$	$\mathbf{b}^{\mathcal{B}}_{5,r}$	$\mathbf{b}^{\mathcal{B}}_{6,r}$	$\mathbf{b}^{\mathcal{B}}_{7,r}$
$x^{\mathcal{B}}$ (m)	0.0558	0.0430	0.0807	0.0782	−0.0332	0.0397	−0.0604
$y^{\mathcal{B}}$ (m)	−0.0939	0.0488	0.0000	−0.0040	0.0809	0.0220	0.0235
$z^{\mathcal{B}}$ (m)	0.0719	0.0611	0.0153	−0.0634	−0.0520	0.0773	−0.0943

(a) Randomly-determined geometric parameters $\mathbf{a}_{i,r}$ and $\mathbf{b}^{\mathcal{B}}_{i,r}$

	$\mathbf{a}_{1,0}$	$\mathbf{a}_{2,0}$	$\mathbf{a}_{3,0}$	$\mathbf{a}_{4,0}$	$\mathbf{a}_{5,0}$	$\mathbf{a}_{6,0}$	$\mathbf{a}_{7,0}$
x (m)	0.5174	0.2328	0.4936	0.6296	0.6909	0.4177	0.3572
y (m)	0.9878	0.0369	0.8821	0.9118	0.7948	0.0927	0.2700
z (m)	0.3356	0.6796	0.1326	0.7223	0.1118	0.6504	0.5118
	$\mathbf{b}^{\mathcal{B}}_{1,0}$	$\mathbf{b}^{\mathcal{B}}_{2,0}$	$\mathbf{b}^{\mathcal{B}}_{3,0}$	$\mathbf{b}^{\mathcal{B}}_{4,0}$	$\mathbf{b}^{\mathcal{B}}_{5,0}$	$\mathbf{b}^{\mathcal{B}}_{6,0}$	$\mathbf{b}^{\mathcal{B}}_{7,0}$
$x^{\mathcal{B}}$ (m)	0.0452	0.0349	0.0873	0.0122	−0.0009	0.0469	−0.0534
$y^{\mathcal{B}}$ (m)	−0.0921	0.0538	0.0014	0.0148	0.0785	0.0090	0.0100
$z^{\mathcal{B}}$ (m)	0.0753	0.0652	0.0127	−0.0502	−0.0286	0.0722	−0.1000

(b) Closest-feasible initial geometric parameters $\mathbf{a}_{i,0}$ and $\mathbf{b}^{\mathcal{B}}_{i,0}$

	$\mathbf{a}_{1,f}$	$\mathbf{a}_{2,f}$	$\mathbf{a}_{3,f}$	$\mathbf{a}_{4,f}$	$\mathbf{a}_{5,f}$	$\mathbf{a}_{6,f}$	$\mathbf{a}_{7,f}$
x (m)	0.9970	0.0063	0.7629	0.9982	1.0000	0.0002	0.0002
y (m)	0.9995	0.0004	0.9998	0.9994	0.2402	0.2463	0.0615
z (m)	0.9778	0.8809	0.3282	0.9995	0.0826	0.6551	0.0002
	$\mathbf{b}^{\mathcal{B}}_{1,f}$	$\mathbf{b}^{\mathcal{B}}_{2,f}$	$\mathbf{b}^{\mathcal{B}}_{3,f}$	$\mathbf{b}^{\mathcal{B}}_{4,f}$	$\mathbf{b}^{\mathcal{B}}_{5,f}$	$\mathbf{b}^{\mathcal{B}}_{6,f}$	$\mathbf{b}^{\mathcal{B}}_{7,f}$
$x^{\mathcal{B}}$ (m)	0.0999	−0.0992	0.0619	−0.0924	0.0093	0.0997	0.0400
$y^{\mathcal{B}}$ (m)	−0.0999	0.0998	−0.0973	0.0597	0.0729	−0.0999	−0.0397
$z^{\mathcal{B}}$ (m)	0.0938	0.0997	−0.0999	0.0742	−0.0721	0.0999	−0.1000

(c) Final geometric parameters $\mathbf{a}_{i,f}$ and $\mathbf{b}^{\mathcal{B}}_{i,f}$

Table D.5 – Geometric parameters of the CDPM corresponding to the Trial 5 of the numerical application of the dimensional synthesis program presented in Sub-section 4.3.1.

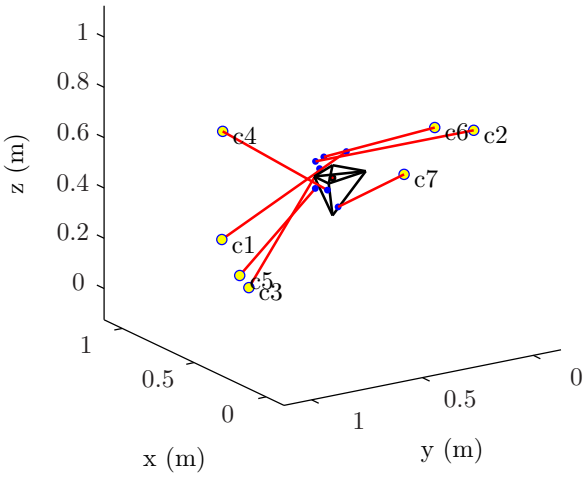

(a) The initial geometry of the CDPM

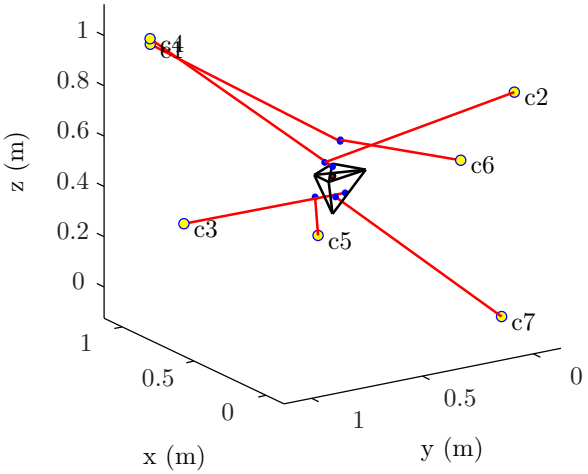

(b) The final geometry of the CDPM

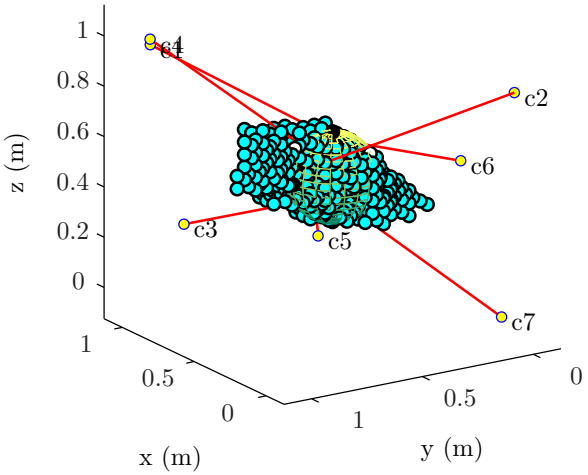

(c) The WCW of the final CDPM's geometry with the final $\mathcal{W}_t$ ($\kappa = 1.0306$)

Figure D.5 – Illustration of different results obtained from the optimization of a CDPM (Trial 5) for the numerical application of the dimensional synthesis program presented in Sub-section 4.3.1.

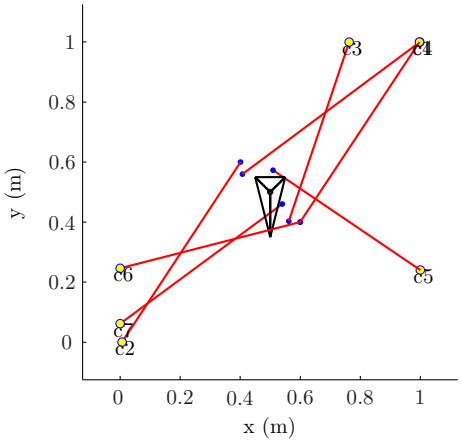

(a) An XY view of the final CDPM's geometry

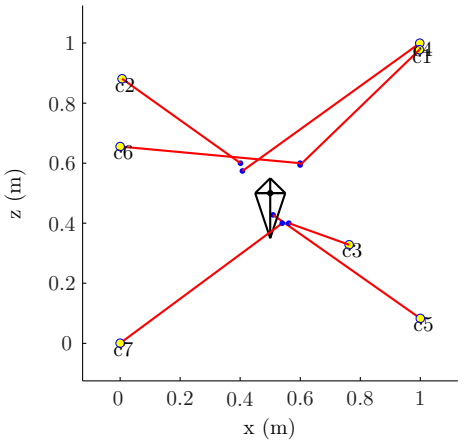

(b) An XZ view of the final CDPM's geometry

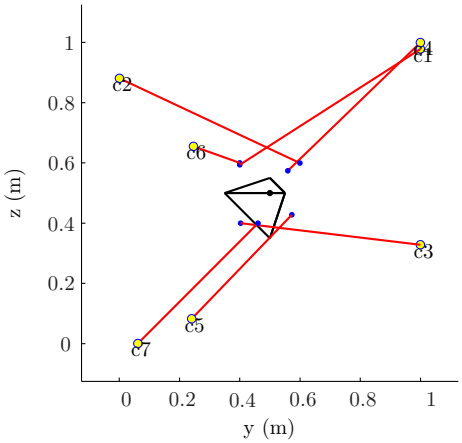

(c) An YZ view of the final CDPM's geometry

Figure D.6 – Three different two-dimensional points of view of the optimized CDPM's geometry (Trial 5) from the numerical application of the dimensional synthesis program presented in Sub-section 4.3.1 ($\kappa = 1.0306$).

Table D.6 and Fig. D.7 present and illustrate the geometric parameters and the final wrench-closure workspace (WCW) as well as the final ellipsoid $\mathcal{W}_t$ ($\kappa = 0.6066$) resulting from the dimensional synthesis (Trial 6) of the CDPM presented in Sub-section 4.3.1.

	$\mathbf{a}_{1,r}$	$\mathbf{a}_{2,r}$	$\mathbf{a}_{3,r}$	$\mathbf{a}_{4,r}$	$\mathbf{a}_{5,r}$	$\mathbf{a}_{6,r}$	$\mathbf{a}_{7,r}$
x (m)	0.4899	0.1679	0.9787	0.7127	0.5005	0.4711	0.0596
y (m)	0.6820	0.0424	0.0714	0.5216	0.0967	0.8181	0.8175
z (m)	0.7224	0.1499	0.6596	0.5186	0.9730	0.6490	0.8003
	$\mathbf{b}^{\mathcal{B}}_{1,r}$	$\mathbf{b}^{\mathcal{B}}_{2,r}$	$\mathbf{b}^{\mathcal{B}}_{3,r}$	$\mathbf{b}^{\mathcal{B}}_{4,r}$	$\mathbf{b}^{\mathcal{B}}_{5,r}$	$\mathbf{b}^{\mathcal{B}}_{6,r}$	$\mathbf{b}^{\mathcal{B}}_{7,r}$
$x^{\mathcal{B}}$ (m)	−0.0092	−0.0135	0.0651	−0.0833	−0.0734	−0.0653	−0.0218
$y^{\mathcal{B}}$ (m)	0.0663	0.0607	−0.0879	−0.0201	0.0054	−0.0166	0.0314
$z^{\mathcal{B}}$ (m)	0.0256	−0.0416	−0.0137	−0.0969	0.0968	−0.0666	−0.0788

(a) Randomly-determined geometric parameters $\mathbf{a}_{i,r}$ and $\mathbf{b}^{\mathcal{B}}_{i,r}$

	$\mathbf{a}_{1,0}$	$\mathbf{a}_{2,0}$	$\mathbf{a}_{3,0}$	$\mathbf{a}_{4,0}$	$\mathbf{a}_{5,0}$	$\mathbf{a}_{6,0}$	$\mathbf{a}_{7,0}$
x (m)	0.4976	0.1794	0.9797	0.7157	0.5029	0.4881	0.0604
y (m)	0.6828	0.0542	0.0728	0.5335	0.0960	0.8342	0.8178
z (m)	0.7196	0.1241	0.6598	0.5005	0.9715	0.6100	0.8009
	$\mathbf{b}^{\mathcal{B}}_{1,0}$	$\mathbf{b}^{\mathcal{B}}_{2,0}$	$\mathbf{b}^{\mathcal{B}}_{3,0}$	$\mathbf{b}^{\mathcal{B}}_{4,0}$	$\mathbf{b}^{\mathcal{B}}_{5,0}$	$\mathbf{b}^{\mathcal{B}}_{6,0}$	$\mathbf{b}^{\mathcal{B}}_{7,0}$
$x^{\mathcal{B}}$ (m)	−0.0230	−0.0314	0.0658	−0.0682	−0.0928	−0.0390	−0.0339
$y^{\mathcal{B}}$ (m)	0.0832	0.0163	−0.0900	0.0077	0.0044	−0.0076	0.0131
$z^{\mathcal{B}}$ (m)	0.0254	−0.0268	−0.0196	−0.0490	0.0992	−0.0270	−0.0774

(b) Closest-feasible initial geometric parameters $\mathbf{a}_{i,0}$ and $\mathbf{b}^{\mathcal{B}}_{i,0}$

	$\mathbf{a}_{1,f}$	$\mathbf{a}_{2,f}$	$\mathbf{a}_{3,f}$	$\mathbf{a}_{4,f}$	$\mathbf{a}_{5,f}$	$\mathbf{a}_{6,f}$	$\mathbf{a}_{7,f}$
x (m)	0.9995	0.0006	0.9992	0.9951	0.0025	0.0001	0.8922
y (m)	0.9015	0.0021	0.6027	0.0015	0.0027	0.9999	0.9987
z (m)	0.9833	0.2569	0.9981	0.0007	0.9982	0.0028	0.9989
	$\mathbf{b}^{\mathcal{B}}_{1,f}$	$\mathbf{b}^{\mathcal{B}}_{2,f}$	$\mathbf{b}^{\mathcal{B}}_{3,f}$	$\mathbf{b}^{\mathcal{B}}_{4,f}$	$\mathbf{b}^{\mathcal{B}}_{5,f}$	$\mathbf{b}^{\mathcal{B}}_{6,f}$	$\mathbf{b}^{\mathcal{B}}_{7,f}$
$x^{\mathcal{B}}$ (m)	0.0786	0.0128	0.0646	−0.0422	−0.0998	−0.0165	−0.0999
$y^{\mathcal{B}}$ (m)	0.0997	−0.0013	−0.0998	−0.0156	0.0994	0.0198	0.0783
$z^{\mathcal{B}}$ (m)	0.0997	−0.0819	−0.0998	−0.0883	0.0893	−0.0548	−0.0609

(c) Final geometric parameters $\mathbf{a}_{i,f}$ and $\mathbf{b}^{\mathcal{B}}_{i,f}$

Table D.6 – Geometric parameters of the CDPM corresponding to the Trial 6 of the numerical application of the dimensional synthesis program presented in Sub-section 4.3.1.

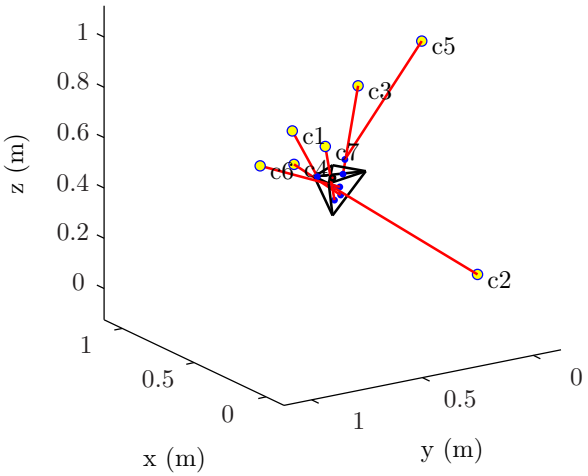

(a) The initial geometry of the CDPM

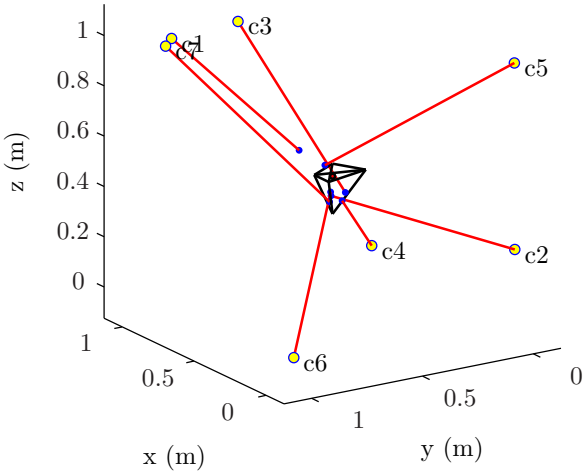

(b) The final geometry of the CDPM

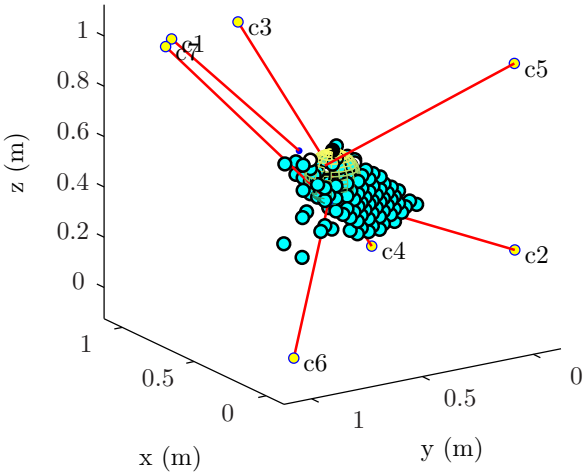

(c) The WCW of the final CDPM's geometry with the final $\mathcal{W}_t$ ($\kappa = 0.6066$)

Figure D.7 – Illustration of different results obtained from the optimization of a CDPM (Trial 6) for the numerical application of the dimensional synthesis program presented in Sub-section 4.3.1.

Table D.7 and Fig. D.8 present and illustrate the geometric parameters and the final wrench-closure workspace (WCW) as well as the final ellipsoid $\mathcal{W}_t$ ($\kappa = 0.6063$) resulting from the dimensional synthesis (Trial 7) of the CDPM presented in Sub-section 4.3.1.

	$\mathbf{a}_{1,r}$	$\mathbf{a}_{2,r}$	$\mathbf{a}_{3,r}$	$\mathbf{a}_{4,r}$	$\mathbf{a}_{5,r}$	$\mathbf{a}_{6,r}$	$\mathbf{a}_{7,r}$
x (m)	0.3724	0.1981	0.4897	0.3395	0.9516	0.9203	0.0527
y (m)	0.7379	0.2691	0.4228	0.5479	0.9427	0.4177	0.9831
z (m)	0.3015	0.7011	0.6663	0.5391	0.6981	0.6665	0.1781
	$\mathbf{b}^{\mathcal{B}}_{1,r}$	$\mathbf{b}^{\mathcal{B}}_{2,r}$	$\mathbf{b}^{\mathcal{B}}_{3,r}$	$\mathbf{b}^{\mathcal{B}}_{4,r}$	$\mathbf{b}^{\mathcal{B}}_{5,r}$	$\mathbf{b}^{\mathcal{B}}_{6,r}$	$\mathbf{b}^{\mathcal{B}}_{7,r}$
$x^{\mathcal{B}}$ (m)	−0.0744	0.0998	−0.0658	−0.0935	0.0122	0.0764	0.0338
$y^{\mathcal{B}}$ (m)	−0.0619	−0.0262	−0.0079	0.0963	−0.0687	0.0711	0.0290
$z^{\mathcal{B}}$ (m)	−0.0247	−0.0618	−0.0143	−0.0036	−0.0759	0.0179	−0.0548

(a) Randomly-determined geometric parameters $\mathbf{a}_{i,r}$ and $\mathbf{b}^{\mathcal{B}}_{i,r}$

	$\mathbf{a}_{1,0}$	$\mathbf{a}_{2,0}$	$\mathbf{a}_{3,0}$	$\mathbf{a}_{4,0}$	$\mathbf{a}_{5,0}$	$\mathbf{a}_{6,0}$	$\mathbf{a}_{7,0}$
x (m)	0.3729	0.1992	0.4868	0.3593	0.9523	0.9295	0.0559
y (m)	0.7360	0.2660	0.4162	0.5334	0.9418	0.4159	0.9791
z (m)	0.2984	0.7010	0.6640	0.4729	0.6990	0.6376	0.1676
	$\mathbf{b}^{\mathcal{B}}_{1,0}$	$\mathbf{b}^{\mathcal{B}}_{2,0}$	$\mathbf{b}^{\mathcal{B}}_{3,0}$	$\mathbf{b}^{\mathcal{B}}_{4,0}$	$\mathbf{b}^{\mathcal{B}}_{5,0}$	$\mathbf{b}^{\mathcal{B}}_{6,0}$	$\mathbf{b}^{\mathcal{B}}_{7,0}$
$x^{\mathcal{B}}$ (m)	−0.0730	0.0995	−0.0654	−0.0929	0.0138	0.0565	0.0409
$y^{\mathcal{B}}$ (m)	−0.0619	−0.0346	0.0102	0.0927	−0.0737	0.0529	0.0411
$z^{\mathcal{B}}$ (m)	−0.0139	−0.0738	−0.0070	0.0364	−0.0685	0.0245	−0.0101

(b) Closest-feasible initial geometric parameters $\mathbf{a}_{i,0}$ and $\mathbf{b}^{\mathcal{B}}_{i,0}$

	$\mathbf{a}_{1,f}$	$\mathbf{a}_{2,f}$	$\mathbf{a}_{3,f}$	$\mathbf{a}_{4,f}$	$\mathbf{a}_{5,f}$	$\mathbf{a}_{6,f}$	$\mathbf{a}_{7,f}$
x (m)	0.0048	0.0002	0.9988	0.0006	0.9992	0.9990	0.0055
y (m)	0.8958	0.0001	0.0018	0.4620	0.9980	0.0030	0.9993
z (m)	0.0015	0.5654	0.9976	0.2613	0.9979	0.0020	0.0011
	$\mathbf{b}^{\mathcal{B}}_{1,f}$	$\mathbf{b}^{\mathcal{B}}_{2,f}$	$\mathbf{b}^{\mathcal{B}}_{3,f}$	$\mathbf{b}^{\mathcal{B}}_{4,f}$	$\mathbf{b}^{\mathcal{B}}_{5,f}$	$\mathbf{b}^{\mathcal{B}}_{6,f}$	$\mathbf{b}^{\mathcal{B}}_{7,f}$
$x^{\mathcal{B}}$ (m)	−0.0996	0.0990	0.0025	−0.0997	0.0965	0.0997	0.0995
$y^{\mathcal{B}}$ (m)	−0.0994	−0.0681	−0.0561	0.0993	−0.0015	0.0162	0.0997
$z^{\mathcal{B}}$ (m)	−0.0996	−0.0858	0.0997	0.0995	−0.0630	−0.0994	−0.0996

(c) Final geometric parameters $\mathbf{a}_{i,f}$ and $\mathbf{b}^{\mathcal{B}}_{i,f}$

Table D.7 – Geometric parameters of the CDPM corresponding to the Trial 7 of the numerical application of the dimensional synthesis program presented in Sub-section 4.3.1.

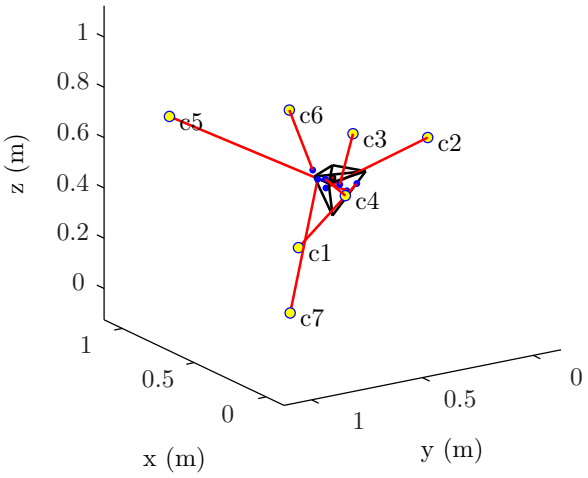

(a) The initial geometry of the CDPM

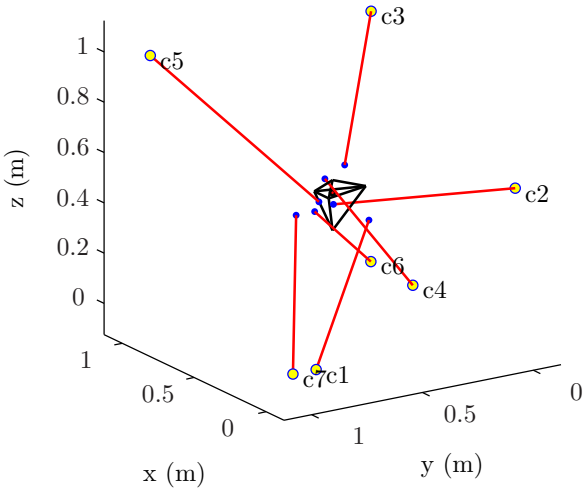

(b) The final geometry of the CDPM

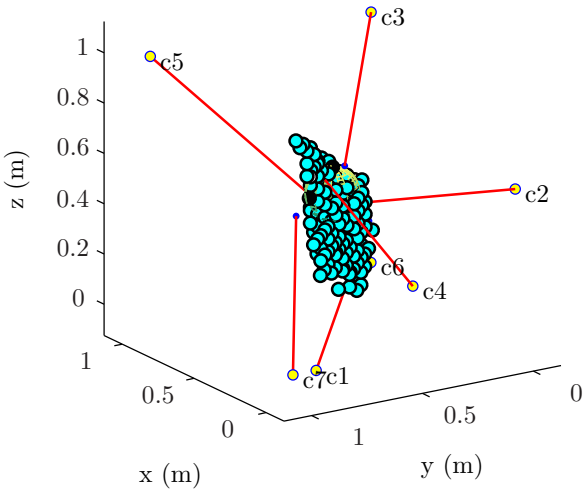

(c) The WCW of the final CDPM's geometry with the final $\mathcal{W}_t$ ($\kappa = 0.6063$)

Figure D.8 – Illustration of different results obtained from the optimization of a CDPM (Trial 7) for the numerical application of the dimensional synthesis program presented in Sub-section 4.3.1.

Table D.8 and Fig. D.9 present and illustrate the geometric parameters and the final wrench-closure workspace (WCW) as well as the final ellipsoid $\mathcal{W}_t$ ($\kappa = 0.6468$) resulting from the dimensional synthesis (Trial 8) of the CDPM presented in Sub-section 4.3.1.

	$\mathbf{a}_{1,r}$	$\mathbf{a}_{2,r}$	$\mathbf{a}_{3,r}$	$\mathbf{a}_{4,r}$	$\mathbf{a}_{5,r}$	$\mathbf{a}_{6,r}$	$\mathbf{a}_{7,r}$
x (m)	0.3846	0.5830	0.2518	0.2904	0.6171	0.2653	0.8244
y (m)	0.9827	0.7302	0.3439	0.5841	0.1078	0.9063	0.8797
z (m)	0.8178	0.2607	0.5944	0.0225	0.4253	0.3127	0.1615
	$\mathbf{b}^{\mathcal{B}}_{1,r}$	$\mathbf{b}^{\mathcal{B}}_{2,r}$	$\mathbf{b}^{\mathcal{B}}_{3,r}$	$\mathbf{b}^{\mathcal{B}}_{4,r}$	$\mathbf{b}^{\mathcal{B}}_{5,r}$	$\mathbf{b}^{\mathcal{B}}_{6,r}$	$\mathbf{b}^{\mathcal{B}}_{7,r}$
$x^{\mathcal{B}}$ (m)	−0.0642	−0.0154	−0.0812	0.0197	−0.0058	0.0392	0.0400
$y^{\mathcal{B}}$ (m)	0.0277	−0.0933	−0.0862	−0.0361	0.0062	0.0309	−0.0185
$z^{\mathcal{B}}$ (m)	0.0640	0.0437	0.0937	0.0063	−0.0350	−0.0789	0.0222

(a) Randomly-determined geometric parameters $\mathbf{a}_{i,r}$ and $\mathbf{b}^{\mathcal{B}}_{i,r}$

	$\mathbf{a}_{1,0}$	$\mathbf{a}_{2,0}$	$\mathbf{a}_{3,0}$	$\mathbf{a}_{4,0}$	$\mathbf{a}_{5,0}$	$\mathbf{a}_{6,0}$	$\mathbf{a}_{7,0}$
x (m)	0.3845	0.5890	0.2493	0.2857	0.6203	0.2692	0.8244
y (m)	0.9823	0.7308	0.3408	0.5815	0.1082	0.9114	0.8802
z (m)	0.8184	0.2646	0.5889	0.0240	0.4362	0.3197	0.1622
	$\mathbf{b}^{\mathcal{B}}_{1,0}$	$\mathbf{b}^{\mathcal{B}}_{2,0}$	$\mathbf{b}^{\mathcal{B}}_{3,0}$	$\mathbf{b}^{\mathcal{B}}_{4,0}$	$\mathbf{b}^{\mathcal{B}}_{5,0}$	$\mathbf{b}^{\mathcal{B}}_{6,0}$	$\mathbf{b}^{\mathcal{B}}_{7,0}$
$x^{\mathcal{B}}$ (m)	−0.0307	−0.0376	−0.0631	0.0169	−0.0230	0.0339	0.0346
$y^{\mathcal{B}}$ (m)	0.0105	−0.0887	−0.0862	−0.0294	0.0050	0.0436	0.0055
$z^{\mathcal{B}}$ (m)	0.0014	0.0399	0.0999	0.0138	−0.0245	−0.0851	0.0375

(b) Closest-feasible initial geometric parameters $\mathbf{a}_{i,0}$ and $\mathbf{b}^{\mathcal{B}}_{i,0}$

	$\mathbf{a}_{1,f}$	$\mathbf{a}_{2,f}$	$\mathbf{a}_{3,f}$	$\mathbf{a}_{4,f}$	$\mathbf{a}_{5,f}$	$\mathbf{a}_{6,f}$	$\mathbf{a}_{7,f}$
x (m)	0.0686	0.9806	0.0014	0.0155	0.9990	0.0005	0.9982
y (m)	0.4640	1.0000	0.0013	0.2928	0.0013	0.5052	0.9990
z (m)	0.9733	0.0000	0.9954	0.0004	0.0020	0.9996	0.8718
	$\mathbf{b}^{\mathcal{B}}_{1,f}$	$\mathbf{b}^{\mathcal{B}}_{2,f}$	$\mathbf{b}^{\mathcal{B}}_{3,f}$	$\mathbf{b}^{\mathcal{B}}_{4,f}$	$\mathbf{b}^{\mathcal{B}}_{5,f}$	$\mathbf{b}^{\mathcal{B}}_{6,f}$	$\mathbf{b}^{\mathcal{B}}_{7,f}$
$x^{\mathcal{B}}$ (m)	−0.1000	−0.0993	−0.0962	−0.0948	−0.0988	−0.0999	0.0997
$y^{\mathcal{B}}$ (m)	−0.0998	−0.0792	−0.0972	−0.0765	−0.0764	0.0996	0.0809
$z^{\mathcal{B}}$ (m)	−0.1000	−0.0983	0.0994	−0.1000	−0.0995	−0.0999	−0.0789

(c) Final geometric parameters $\mathbf{a}_{i,f}$ and $\mathbf{b}^{\mathcal{B}}_{i,f}$

Table D.8 – Geometric parameters of the CDPM corresponding to the Trial 8 of the numerical application of the dimensional synthesis program presented in Sub-section 4.3.1.

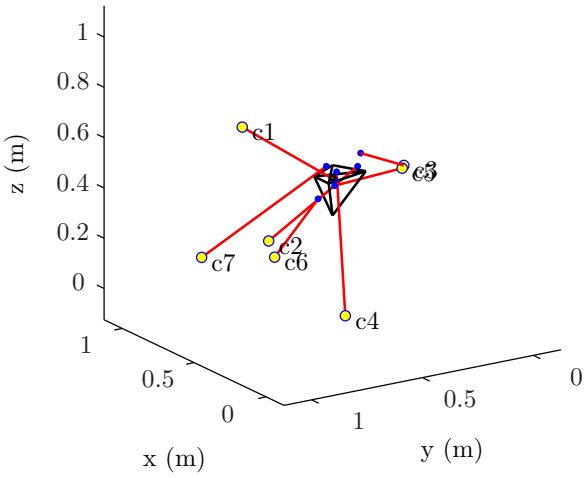

(a) The initial geometry of the CDPM

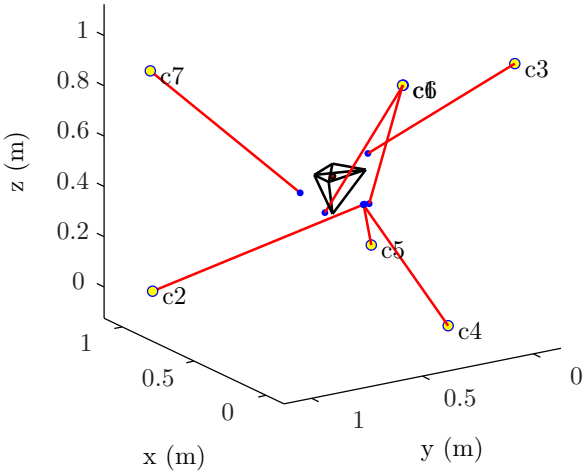

(b) The final geometry of the CDPM

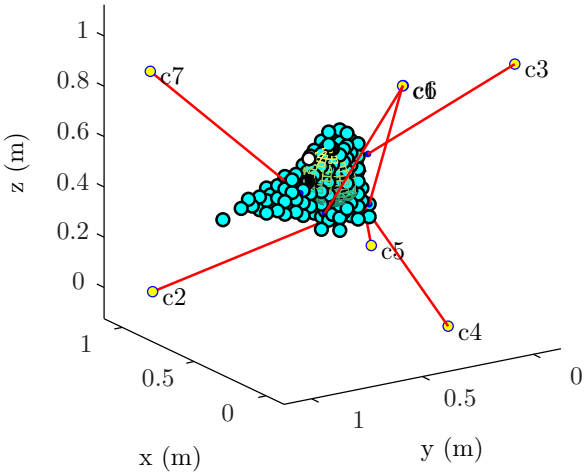

(c) The WCW of the final CDPM's geometry with the final $\mathcal{W}_t$ ($\kappa = 0.6468$)

Figure D.9 – Illustration of different results obtained from the optimization of a CDPM (Trial 8) for the numerical application of the dimensional synthesis program presented in Sub-section 4.3.1.

Table D.9 and Figs. D.10 and D.11 present and illustrate the geometric parameters and the final wrench-closure workspace (WCW) as well as the final ellipsoid $\mathcal{W}_t$ ($\kappa = 1.4468$) resulting from the dimensional synthesis (Trial 9) of the CDPM presented in Sub-section 4.3.1.

	$\mathbf{a}_{1,r}$	$\mathbf{a}_{2,r}$	$\mathbf{a}_{3,r}$	$\mathbf{a}_{4,r}$	$\mathbf{a}_{5,r}$	$\mathbf{a}_{6,r}$	$\mathbf{a}_{7,r}$
x (m)	0.7788	0.4235	0.0908	0.2665	0.1537	0.2810	0.4401
y (m)	0.5271	0.4574	0.8754	0.5181	0.9436	0.6377	0.9577
z (m)	0.2407	0.6761	0.2891	0.6718	0.6951	0.0680	0.2548
	$\mathbf{b}^{\mathcal{B}}_{1,r}$	$\mathbf{b}^{\mathcal{B}}_{2,r}$	$\mathbf{b}^{\mathcal{B}}_{3,r}$	$\mathbf{b}^{\mathcal{B}}_{4,r}$	$\mathbf{b}^{\mathcal{B}}_{5,r}$	$\mathbf{b}^{\mathcal{B}}_{6,r}$	$\mathbf{b}^{\mathcal{B}}_{7,r}$
$x^{\mathcal{B}}$ (m)	−0.0552	0.0336	0.0689	−0.0311	0.0561	0.0351	−0.0987
$y^{\mathcal{B}}$ (m)	0.0204	−0.0226	0.0832	−0.0998	−0.0075	−0.0151	−0.0078
$z^{\mathcal{B}}$ (m)	0.0540	−0.0355	0.0569	−0.0057	−0.0928	−0.0648	0.0444

(a) Randomly-determined geometric parameters $\mathbf{a}_{i,r}$ and $\mathbf{b}^{\mathcal{B}}_{i,r}$

	$\mathbf{a}_{1,0}$	$\mathbf{a}_{2,0}$	$\mathbf{a}_{3,0}$	$\mathbf{a}_{4,0}$	$\mathbf{a}_{5,0}$	$\mathbf{a}_{6,0}$	$\mathbf{a}_{7,0}$
x (m)	0.7796	0.4302	0.0911	0.2677	0.1544	0.2833	0.4388
y (m)	0.5178	0.4440	0.8762	0.5156	0.9444	0.6363	0.9568
z (m)	0.2410	0.6745	0.2900	0.6743	0.6948	0.0664	0.2534
	$\mathbf{b}^{\mathcal{B}}_{1,0}$	$\mathbf{b}^{\mathcal{B}}_{2,0}$	$\mathbf{b}^{\mathcal{B}}_{3,0}$	$\mathbf{b}^{\mathcal{B}}_{4,0}$	$\mathbf{b}^{\mathcal{B}}_{5,0}$	$\mathbf{b}^{\mathcal{B}}_{6,0}$	$\mathbf{b}^{\mathcal{B}}_{7,0}$
$x^{\mathcal{B}}$ (m)	−0.0225	0.0081	0.0687	−0.0376	0.0564	0.0328	−0.0996
$y^{\mathcal{B}}$ (m)	−0.0007	0.0035	0.0885	−0.0987	−0.0039	−0.0093	−0.0079
$z^{\mathcal{B}}$ (m)	0.0151	0.0107	0.0548	−0.0087	−0.0937	−0.0686	0.0420

(b) Closest-feasible initial geometric parameters $\mathbf{a}_{i,0}$ and $\mathbf{b}^{\mathcal{B}}_{i,0}$

	$\mathbf{a}_{1,f}$	$\mathbf{a}_{2,f}$	$\mathbf{a}_{3,f}$	$\mathbf{a}_{4,f}$	$\mathbf{a}_{5,f}$	$\mathbf{a}_{6,f}$	$\mathbf{a}_{7,f}$
x (m)	0.9993	0.2521	0.0002	0.9997	0.0004	0.9998	0.0164
y (m)	0.0004	0.0002	0.9775	0.9997	0.9997	0.0013	0.9997
z (m)	0.0376	0.9999	0.0797	0.9999	0.8584	0.0002	0.0008
	$\mathbf{b}^{\mathcal{B}}_{1,f}$	$\mathbf{b}^{\mathcal{B}}_{2,f}$	$\mathbf{b}^{\mathcal{B}}_{3,f}$	$\mathbf{b}^{\mathcal{B}}_{4,f}$	$\mathbf{b}^{\mathcal{B}}_{5,f}$	$\mathbf{b}^{\mathcal{B}}_{6,f}$	$\mathbf{b}^{\mathcal{B}}_{7,f}$
$x^{\mathcal{B}}$ (m)	−0.0999	0.0446	0.0379	0.0177	−0.0131	0.0759	−0.0747
$y^{\mathcal{B}}$ (m)	−0.0993	0.0154	0.0998	0.0132	0.0476	0.0148	−0.0033
$z^{\mathcal{B}}$ (m)	−0.0756	0.0626	0.0837	0.0834	−0.0999	0.0998	0.0996

(c) Final geometric parameters $\mathbf{a}_{i,f}$ and $\mathbf{b}^{\mathcal{B}}_{i,f}$

Table D.9 – Geometric parameters of the CDPM corresponding to the Trial 9 of the numerical application of the dimensional synthesis program presented in Sub-section 4.3.1.

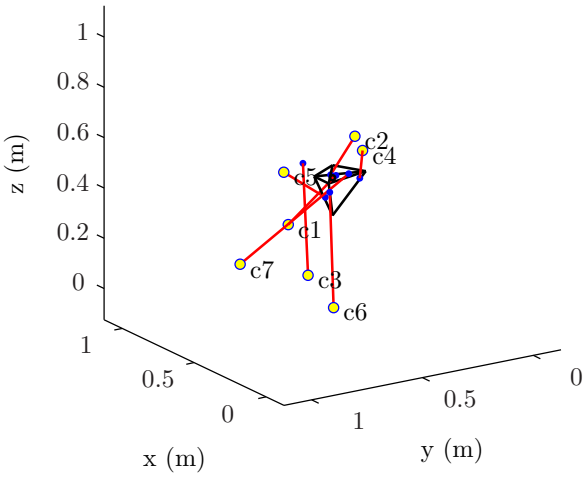

(a) The initial geometry of the CDPM

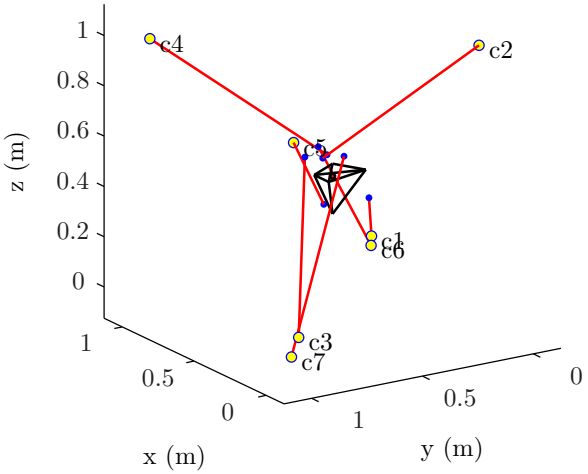

(b) The final geometry of the CDPM

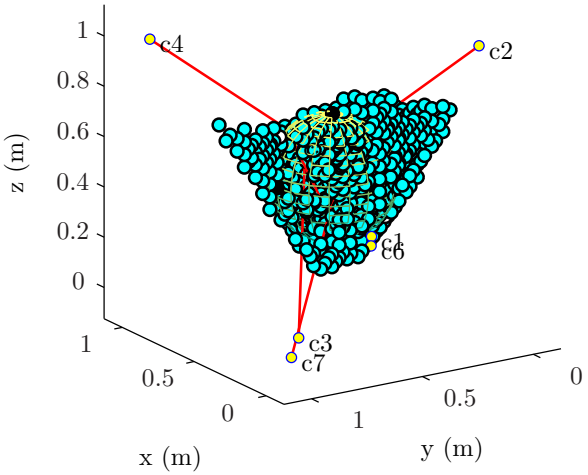

(c) The WCW of the final CDPM's geometry with the final $\mathcal{W}_t$ ($\kappa = 1.4468$)

Figure D.10 – Illustration of different results obtained from the optimization of a CDPM (Trial 9) for the numerical application of the dimensional synthesis program presented in Sub-section 4.3.1.

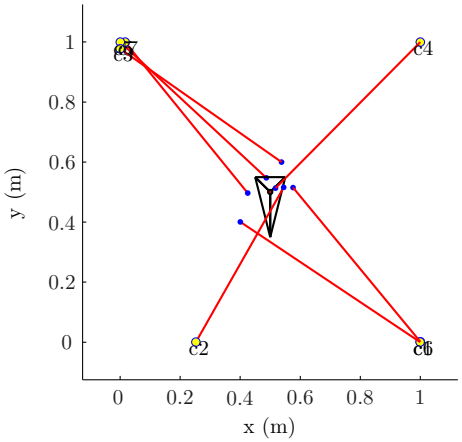

(a) An XY view of the final CDPM's geometry

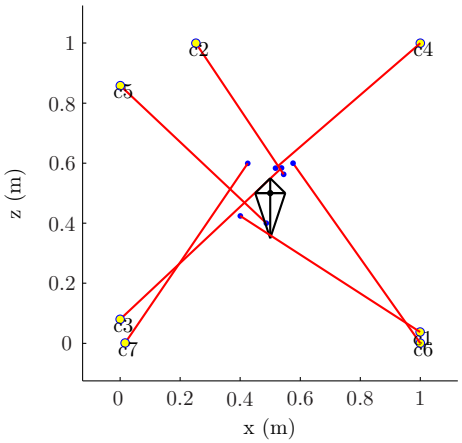

(b) An XZ view of the final CDPM's geometry

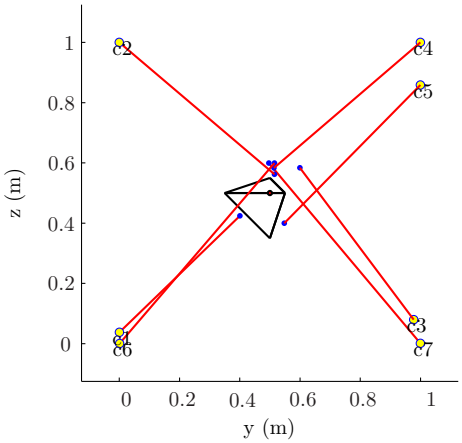

(c) An YZ view of the final CDPM's geometry

Figure D.11 – Three different two-dimensional points of view of the optimized CDPM's geometry (Trial 9) from the numerical application of the dimensional synthesis program presented in Sub-section 4.3.1 ($\kappa = 1.4468$).

Table D.10 and Figs. D.12 and D.13 present and illustrate the geometric parameters and the final wrench-closure workspace (WCW) as well as the final ellipsoid $\mathcal{W}_t$ ($\kappa = 1.4430$) resulting from the dimensional synthesis (Trial 10) of the CDPM presented in Sub-section 4.3.1.

	$\mathbf{a}_{1,r}$	$\mathbf{a}_{2,r}$	$\mathbf{a}_{3,r}$	$\mathbf{a}_{4,r}$	$\mathbf{a}_{5,r}$	$\mathbf{a}_{6,r}$	$\mathbf{a}_{7,r}$
x (m)	0.4735	0.1527	0.3411	0.6074	0.1917	0.7384	0.2428
y (m)	0.9174	0.2691	0.7655	0.1887	0.2875	0.0911	0.5762
z (m)	0.6834	0.5466	0.4257	0.6444	0.6476	0.6790	0.6358
	$\mathbf{b}^{\mathcal{B}}_{1,r}$	$\mathbf{b}^{\mathcal{B}}_{2,r}$	$\mathbf{b}^{\mathcal{B}}_{3,r}$	$\mathbf{b}^{\mathcal{B}}_{4,r}$	$\mathbf{b}^{\mathcal{B}}_{5,r}$	$\mathbf{b}^{\mathcal{B}}_{6,r}$	$\mathbf{b}^{\mathcal{B}}_{7,r}$
$x^{\mathcal{B}}$ (m)	0.0890	−0.0582	0.0419	−0.0528	−0.0761	0.0215	−0.0100
$y^{\mathcal{B}}$ (m)	−0.0083	0.0324	0.0541	−0.0300	0.0324	−0.0168	0.0684
$z^{\mathcal{B}}$ (m)	0.0666	−0.0487	0.0227	0.0164	0.0081	0.0740	−0.0470

(a) Randomly-determined geometric parameters $\mathbf{a}_{i,r}$ and $\mathbf{b}^{\mathcal{B}}_{i,r}$

	$\mathbf{a}_{1,0}$	$\mathbf{a}_{2,0}$	$\mathbf{a}_{3,0}$	$\mathbf{a}_{4,0}$	$\mathbf{a}_{5,0}$	$\mathbf{a}_{6,0}$	$\mathbf{a}_{7,0}$
x (m)	0.4683	0.1529	0.3750	0.6184	0.1907	0.7479	0.2438
y (m)	0.9156	0.2686	0.7760	0.1951	0.2854	0.0920	0.5772
z (m)	0.6857	0.5459	0.4061	0.6468	0.6419	0.6697	0.6369
	$\mathbf{b}^{\mathcal{B}}_{1,0}$	$\mathbf{b}^{\mathcal{B}}_{2,0}$	$\mathbf{b}^{\mathcal{B}}_{3,0}$	$\mathbf{b}^{\mathcal{B}}_{4,0}$	$\mathbf{b}^{\mathcal{B}}_{5,0}$	$\mathbf{b}^{\mathcal{B}}_{6,0}$	$\mathbf{b}^{\mathcal{B}}_{7,0}$
$x^{\mathcal{B}}$ (m)	0.0984	−0.0554	0.0064	−0.0607	−0.0625	0.0234	−0.0097
$y^{\mathcal{B}}$ (m)	−0.0036	0.0317	0.0080	−0.0269	0.0357	0.0112	0.0678
$z^{\mathcal{B}}$ (m)	0.0632	−0.0472	0.0190	0.0155	0.0318	0.0214	−0.0511

(b) Closest-feasible initial geometric parameters $\mathbf{a}_{i,0}$ and $\mathbf{b}^{\mathcal{B}}_{i,0}$

	$\mathbf{a}_{1,f}$	$\mathbf{a}_{2,f}$	$\mathbf{a}_{3,f}$	$\mathbf{a}_{4,f}$	$\mathbf{a}_{5,f}$	$\mathbf{a}_{6,f}$	$\mathbf{a}_{7,f}$
x (m)	0.0713	0.0005	0.9998	0.9998	0.0006	0.9997	0.5205
y (m)	0.9998	0.0004	0.9997	0.0919	0.0002	0.0005	0.9998
z (m)	0.9999	0.0765	0.0005	0.9998	0.1849	0.9995	0.0004
	$\mathbf{b}^{\mathcal{B}}_{1,f}$	$\mathbf{b}^{\mathcal{B}}_{2,f}$	$\mathbf{b}^{\mathcal{B}}_{3,f}$	$\mathbf{b}^{\mathcal{B}}_{4,f}$	$\mathbf{b}^{\mathcal{B}}_{5,f}$	$\mathbf{b}^{\mathcal{B}}_{6,f}$	$\mathbf{b}^{\mathcal{B}}_{7,f}$
$x^{\mathcal{B}}$ (m)	0.0179	0.0998	0.0341	−0.0998	−0.0997	0.0982	−0.0999
$y^{\mathcal{B}}$ (m)	0.0192	−0.0665	0.0588	0.0048	0.0223	0.0337	−0.0652
$z^{\mathcal{B}}$ (m)	0.0409	−0.0996	0.0891	0.0979	0.0901	−0.0995	−0.0999

(c) Final geometric parameters $\mathbf{a}_{i,f}$ and $\mathbf{b}^{\mathcal{B}}_{i,f}$

Table D.10 – Geometric parameters of the CDPM corresponding to the Trial 10 of the numerical application of the dimensional synthesis program presented in Sub-section 4.3.1.

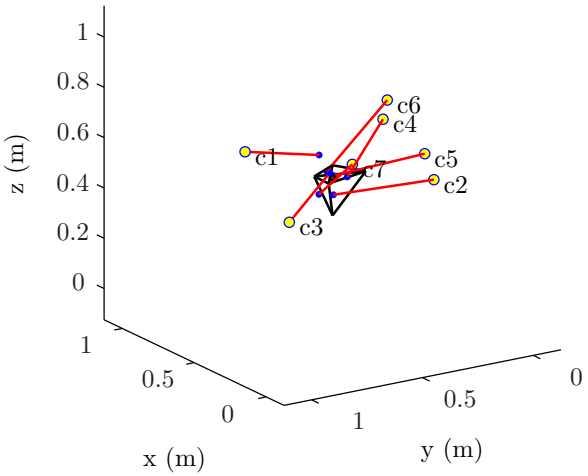

(a) The initial geometry of the CDPM

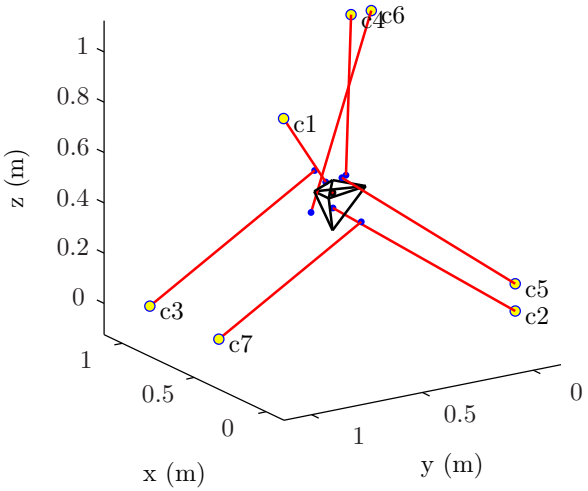

(b) The final geometry of the CDPM

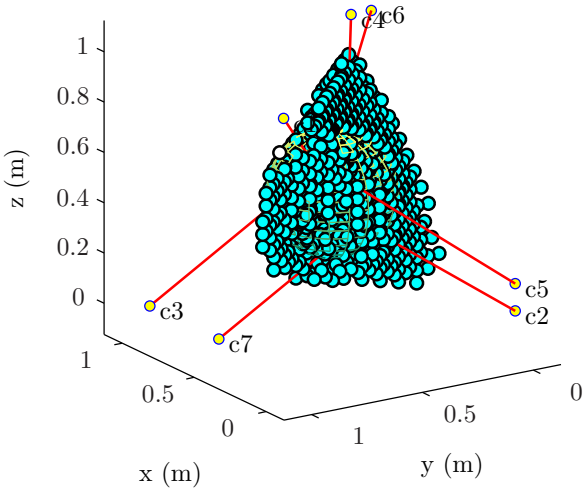

(c) The WCW of the final CDPM's geometry with the final $\mathcal{W}_t$ ($\kappa = 1.4430$)

Figure D.12 – Illustration of different results obtained from the optimization of a CDPM (Trial 10) for the numerical application of the dimensional synthesis program presented in Sub-section 4.3.1.

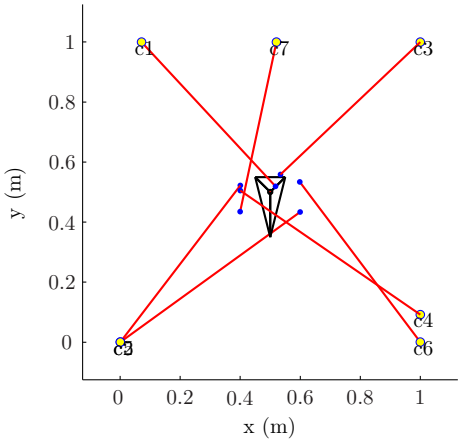

(a) An XY view of the final CDPM's geometry

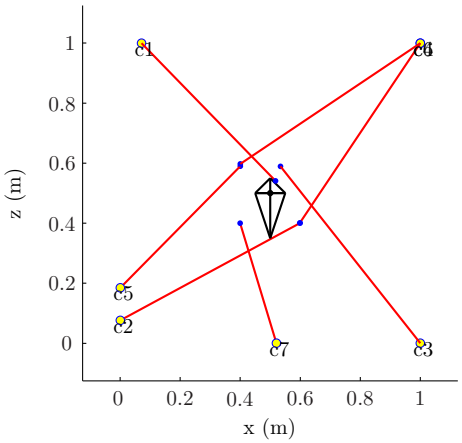

(b) An XZ view of the final CDPM's geometry

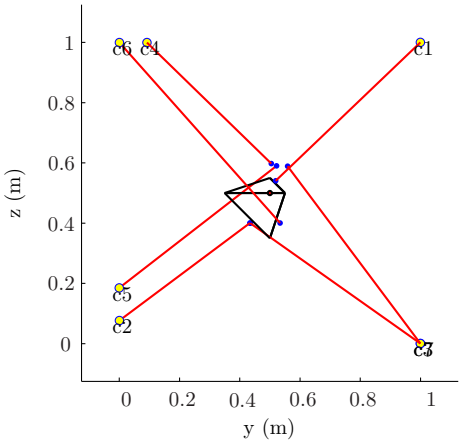

(c) An YZ view of the final CDPM's geometry

Figure D.13 – Three different two-dimensional points of view of the optimized CDPM's geometry (Trial 10) from the numerical application of the dimensional synthesis program presented in Sub-section 4.3.1 ($\kappa = 1.4430$).

Table D.11 and Fig. D.14 present and illustrate the geometric parameters and the final wrench-closure workspace (WCW) as well as the final ellipsoid $\mathcal{W}_t$ ($\kappa = 0.5408$) resulting from the dimensional synthesis (Trial 11) of the CDPM presented in Sub-section 4.3.1.

	$\mathbf{a}_{1,r}$	$\mathbf{a}_{2,r}$	$\mathbf{a}_{3,r}$	$\mathbf{a}_{4,r}$	$\mathbf{a}_{5,r}$	$\mathbf{a}_{6,r}$	$\mathbf{a}_{7,r}$
x (m)	0.3181	0.1192	0.9398	0.6456	0.4795	0.6393	0.5447
y (m)	0.6473	0.5439	0.7210	0.5225	0.9937	0.2187	0.1058
z (m)	0.1097	0.0636	0.4046	0.4484	0.3658	0.7635	0.6279
	$\mathbf{b}^{\mathcal{B}}_{1,r}$	$\mathbf{b}^{\mathcal{B}}_{2,r}$	$\mathbf{b}^{\mathcal{B}}_{3,r}$	$\mathbf{b}^{\mathcal{B}}_{4,r}$	$\mathbf{b}^{\mathcal{B}}_{5,r}$	$\mathbf{b}^{\mathcal{B}}_{6,r}$	$\mathbf{b}^{\mathcal{B}}_{7,r}$
$x^{\mathcal{B}}$ (m)	0.0544	0.0866	0.0945	−0.0616	−0.0722	0.0393	−0.0812
$y^{\mathcal{B}}$ (m)	0.0051	0.0061	0.0722	−0.0030	−0.0213	0.0343	0.0483
$z^{\mathcal{B}}$ (m)	0.0040	−0.0305	−0.0700	0.0172	−0.0476	−0.0911	0.0510

(a) Randomly-determined geometric parameters $\mathbf{a}_{i,r}$ and $\mathbf{b}^{\mathcal{B}}_{i,r}$

	$\mathbf{a}_{1,0}$	$\mathbf{a}_{2,0}$	$\mathbf{a}_{3,0}$	$\mathbf{a}_{4,0}$	$\mathbf{a}_{5,0}$	$\mathbf{a}_{6,0}$	$\mathbf{a}_{7,0}$
x (m)	0.3104	0.1086	0.9311	0.6482	0.4768	0.6261	0.5376
y (m)	0.6550	0.5604	0.7353	0.5249	0.9936	0.2401	0.1040
z (m)	0.1163	0.0797	0.4254	0.4625	0.3673	0.7827	0.6264
	$\mathbf{b}^{\mathcal{B}}_{1,0}$	$\mathbf{b}^{\mathcal{B}}_{2,0}$	$\mathbf{b}^{\mathcal{B}}_{3,0}$	$\mathbf{b}^{\mathcal{B}}_{4,0}$	$\mathbf{b}^{\mathcal{B}}_{5,0}$	$\mathbf{b}^{\mathcal{B}}_{6,0}$	$\mathbf{b}^{\mathcal{B}}_{7,0}$
$x^{\mathcal{B}}$ (m)	0.0418	0.0658	0.1000	−0.0541	−0.0392	0.0452	−0.0842
$y^{\mathcal{B}}$ (m)	0.0230	0.0086	0.0551	−0.0344	−0.0259	−0.0012	0.0452
$z^{\mathcal{B}}$ (m)	0.0038	−0.0579	−0.0805	0.0103	−0.0463	−0.0871	0.0525

(b) Closest-feasible initial geometric parameters $\mathbf{a}_{i,0}$ and $\mathbf{b}^{\mathcal{B}}_{i,0}$

	$\mathbf{a}_{1,f}$	$\mathbf{a}_{2,f}$	$\mathbf{a}_{3,f}$	$\mathbf{a}_{4,f}$	$\mathbf{a}_{5,f}$	$\mathbf{a}_{6,f}$	$\mathbf{a}_{7,f}$
x (m)	0.0704	0.0000	0.9999	0.9999	0.0000	0.9994	0.0679
y (m)	1.0000	0.7707	0.4249	1.0000	0.8143	0.0000	0.0000
z (m)	0.1297	0.1901	0.0003	0.7703	0.9864	0.9989	0.8254
	$\mathbf{b}^{\mathcal{B}}_{1,f}$	$\mathbf{b}^{\mathcal{B}}_{2,f}$	$\mathbf{b}^{\mathcal{B}}_{3,f}$	$\mathbf{b}^{\mathcal{B}}_{4,f}$	$\mathbf{b}^{\mathcal{B}}_{5,f}$	$\mathbf{b}^{\mathcal{B}}_{6,f}$	$\mathbf{b}^{\mathcal{B}}_{7,f}$
$x^{\mathcal{B}}$ (m)	−0.0481	0.0997	0.0971	0.0985	−0.0391	0.1000	−0.1000
$y^{\mathcal{B}}$ (m)	0.0482	0.0427	0.0411	0.0361	−0.0195	0.0414	−0.0300
$z^{\mathcal{B}}$ (m)	−0.0043	−0.0220	−0.0221	−0.0250	−0.1000	−0.0216	0.0652

(c) Final geometric parameters $\mathbf{a}_{i,f}$ and $\mathbf{b}^{\mathcal{B}}_{i,f}$

Table D.11 – Geometric parameters of the CDPM corresponding to the Trial 11 of the numerical application of the dimensional synthesis program presented in Sub-section 4.3.1.

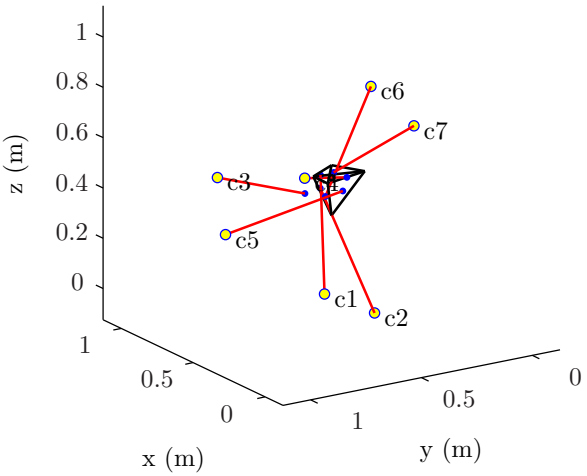

(a) The initial geometry of the CDPM

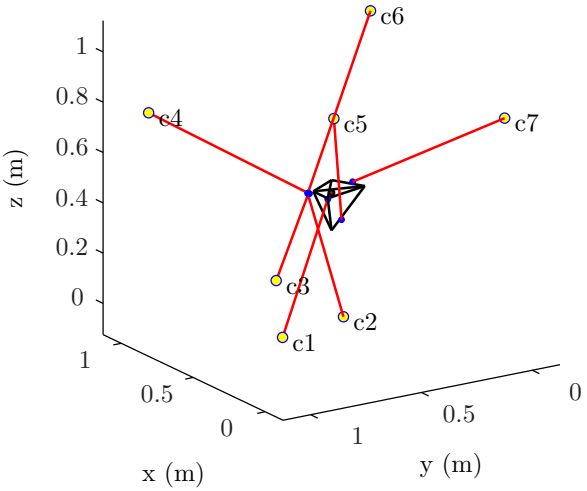

(b) The final geometry of the CDPM

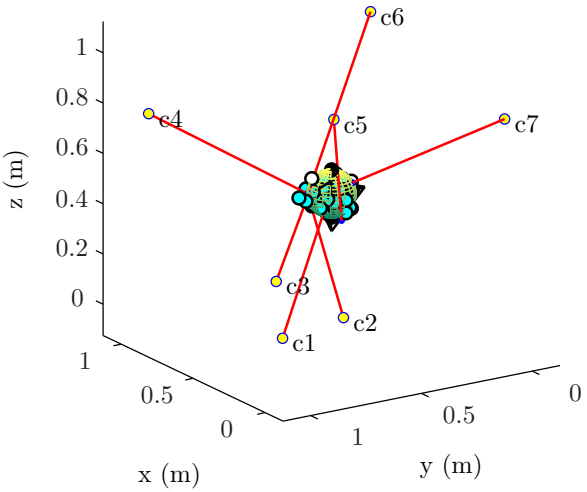

(c) The WCW of the final CDPM's geometry with the final $\mathcal{W}_t$ ($\kappa = 0.5408$)

Figure D.14 – Illustration of different results obtained from the optimization of a CDPM (Trial 11) for the numerical application of the dimensional synthesis program presented in Sub-section 4.3.1.

Table D.12 and Figs. D.15 and D.16 present and illustrate the geometric parameters and the final wrench-closure workspace (WCW) as well as the final ellipsoid $\mathcal{W}_t$ ($\kappa = 1.4457$) resulting from the dimensional synthesis (Trial 12) of the CDPM presented in Sub-section 4.3.1.

	$\mathbf{a}_{1,r}$	$\mathbf{a}_{2,r}$	$\mathbf{a}_{3,r}$	$\mathbf{a}_{4,r}$	$\mathbf{a}_{5,r}$	$\mathbf{a}_{6,r}$	$\mathbf{a}_{7,r}$
x (m)	0.2428	0.4424	0.6878	0.3592	0.7363	0.3947	0.6834
y (m)	0.7040	0.4423	0.0196	0.3309	0.4243	0.2703	0.1971
z (m)	0.8217	0.4299	0.8878	0.3912	0.7691	0.3968	0.8085
	$\mathbf{b}^{\mathcal{B}}_{1,r}$	$\mathbf{b}^{\mathcal{B}}_{2,r}$	$\mathbf{b}^{\mathcal{B}}_{3,r}$	$\mathbf{b}^{\mathcal{B}}_{4,r}$	$\mathbf{b}^{\mathcal{B}}_{5,r}$	$\mathbf{b}^{\mathcal{B}}_{6,r}$	$\mathbf{b}^{\mathcal{B}}_{7,r}$
$x^{\mathcal{B}}$ (m)	0.0510	−0.0245	−0.0568	0.0581	0.0899	−0.0345	0.0343
$y^{\mathcal{B}}$ (m)	−0.0123	0.0667	0.0538	−0.0665	0.0724	0.0980	0.0029
$z^{\mathcal{B}}$ (m)	0.0769	0.0176	−0.0690	−0.0600	−0.0186	0.0497	0.0651

(a) Randomly-determined geometric parameters $\mathbf{a}_{i,r}$ and $\mathbf{b}^{\mathcal{B}}_{i,r}$

	$\mathbf{a}_{1,0}$	$\mathbf{a}_{2,0}$	$\mathbf{a}_{3,0}$	$\mathbf{a}_{4,0}$	$\mathbf{a}_{5,0}$	$\mathbf{a}_{6,0}$	$\mathbf{a}_{7,0}$
x (m)	0.2435	0.4943	0.6883	0.3598	0.7366	0.3948	0.6843
y (m)	0.7047	0.5174	0.0218	0.3308	0.4242	0.2704	0.1976
z (m)	0.8219	0.4808	0.8904	0.3907	0.7689	0.3967	0.8086
	$\mathbf{b}^{\mathcal{B}}_{1,0}$	$\mathbf{b}^{\mathcal{B}}_{2,0}$	$\mathbf{b}^{\mathcal{B}}_{3,0}$	$\mathbf{b}^{\mathcal{B}}_{4,0}$	$\mathbf{b}^{\mathcal{B}}_{5,0}$	$\mathbf{b}^{\mathcal{B}}_{6,0}$	$\mathbf{b}^{\mathcal{B}}_{7,0}$
$x^{\mathcal{B}}$ (m)	0.0470	−0.0045	−0.0658	0.0593	0.0897	−0.0347	0.0321
$y^{\mathcal{B}}$ (m)	−0.0149	0.0027	0.0515	−0.0674	0.0724	0.0977	−0.0017
$z^{\mathcal{B}}$ (m)	0.0751	−0.0081	−0.0645	−0.0610	−0.0184	0.0496	0.0644

(b) Closest-feasible initial geometric parameters $\mathbf{a}_{i,0}$ and $\mathbf{b}^{\mathcal{B}}_{i,0}$

	$\mathbf{a}_{1,f}$	$\mathbf{a}_{2,f}$	$\mathbf{a}_{3,f}$	$\mathbf{a}_{4,f}$	$\mathbf{a}_{5,f}$	$\mathbf{a}_{6,f}$	$\mathbf{a}_{7,f}$
x (m)	0.0760	0.9998	0.0001	0.0003	0.5067	0.0011	0.9999
y (m)	0.9998	0.8442	0.0002	0.7069	0.9998	0.0701	0.0003
z (m)	0.0001	0.0003	0.6935	0.2855	0.9999	0.6539	0.7485
	$\mathbf{b}^{\mathcal{B}}_{1,f}$	$\mathbf{b}^{\mathcal{B}}_{2,f}$	$\mathbf{b}^{\mathcal{B}}_{3,f}$	$\mathbf{b}^{\mathcal{B}}_{4,f}$	$\mathbf{b}^{\mathcal{B}}_{5,f}$	$\mathbf{b}^{\mathcal{B}}_{6,f}$	$\mathbf{b}^{\mathcal{B}}_{7,f}$
$x^{\mathcal{B}}$ (m)	−0.0055	−0.0066	−0.0385	0.0014	−0.0024	0.0078	0.0009
$y^{\mathcal{B}}$ (m)	0.0998	0.0840	0.0911	−0.0999	0.0912	0.0926	0.0892
$z^{\mathcal{B}}$ (m)	0.0526	0.0479	−0.0865	−0.0998	0.0523	0.0999	0.0511

(c) Final geometric parameters $\mathbf{a}_{i,f}$ and $\mathbf{b}^{\mathcal{B}}_{i,f}$

Table D.12 – Geometric parameters of the CDPM corresponding to the Trial 12 of the numerical application of the dimensional synthesis program presented in Sub-section 4.3.1.

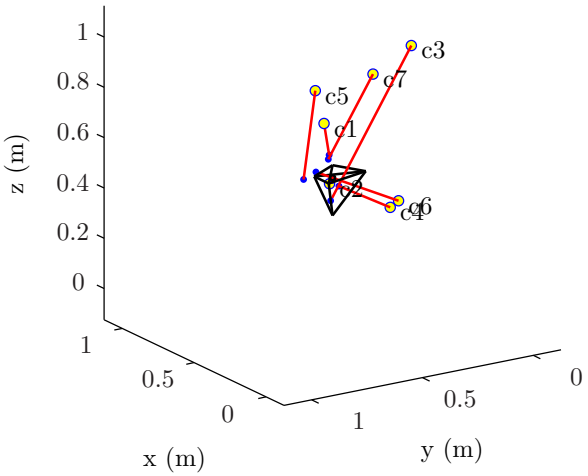

(a) The initial geometry of the CDPM

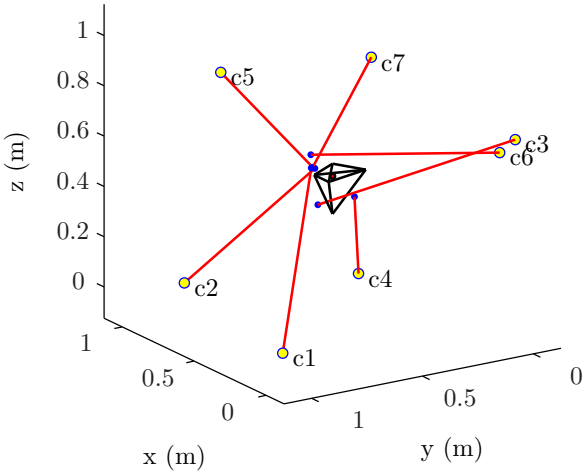

(b) The final geometry of the CDPM

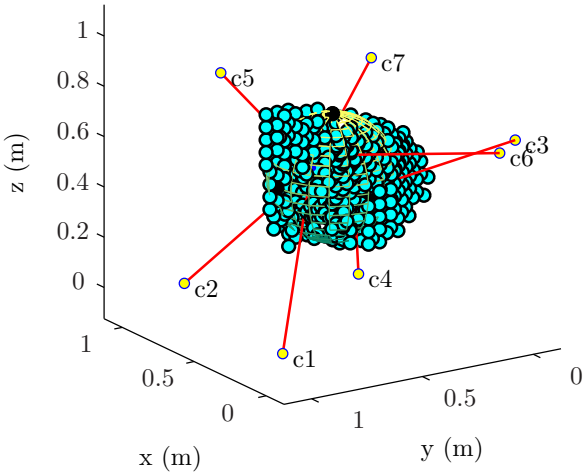

(c) The WCW of the final CDPM's geometry with the final $\mathcal{W}_t$ ($\kappa = 1.4457$)

Figure D.15 – Illustration of different results obtained from the optimization of a CDPM (Trial 12) for the numerical application of the dimensional synthesis program presented in Sub-section 4.3.1.

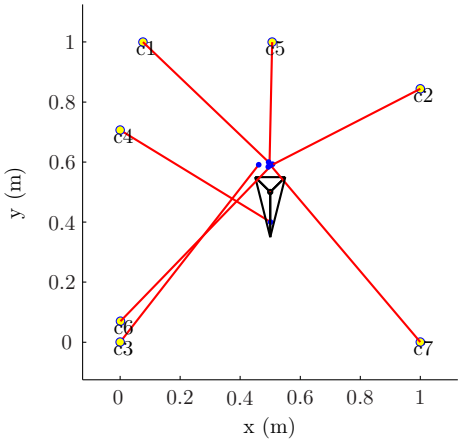

(a) An XY view of the final CDPM's geometry

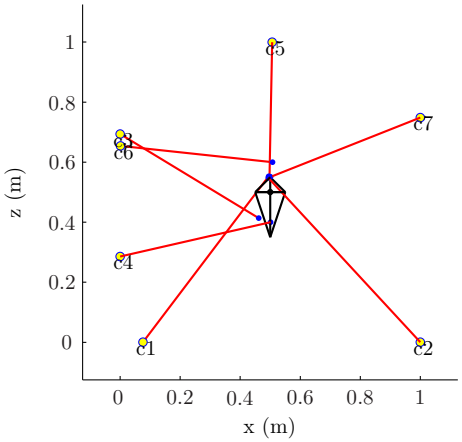

(b) An XZ view of the final CDPM's geometry

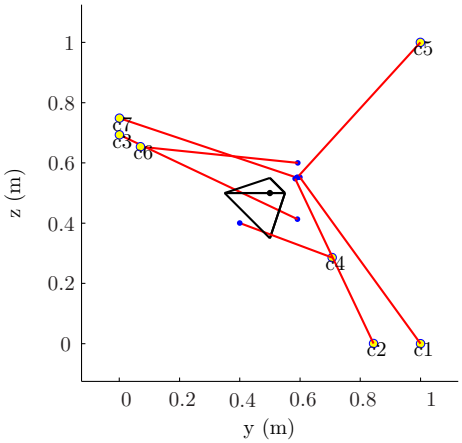

(c) An YZ view of the final CDPM's geometry

Figure D.16 – Three different two-dimensional points of view of the optimized CDPM's geometry (Trial 12) from the numerical application of the dimensional synthesis program presented in Sub-section 4.3.1 ($\kappa = 1.4457$).

Table D.13 and Figs. D.17 and D.18 present and illustrate the geometric parameters and the final wrench-closure workspace (WCW) as well as the final ellipsoid $\mathcal{W}_t$ ($\kappa = 1.3924$) resulting from the dimensional synthesis (Trial 13) of the CDPM presented in Sub-section 4.3.1.

	$\mathbf{a}_{1,r}$	$\mathbf{a}_{2,r}$	$\mathbf{a}_{3,r}$	$\mathbf{a}_{4,r}$	$\mathbf{a}_{5,r}$	$\mathbf{a}_{6,r}$	$\mathbf{a}_{7,r}$
x (m)	0.7900	0.3185	0.5341	0.0900	0.1117	0.1363	0.6787
y (m)	0.4952	0.1897	0.4950	0.1476	0.0550	0.8507	0.5606
z (m)	0.9296	0.6967	0.5828	0.8154	0.8790	0.9889	0.0005
	$\mathbf{b}^{\mathcal{B}}_{1,r}$	$\mathbf{b}^{\mathcal{B}}_{2,r}$	$\mathbf{b}^{\mathcal{B}}_{3,r}$	$\mathbf{b}^{\mathcal{B}}_{4,r}$	$\mathbf{b}^{\mathcal{B}}_{5,r}$	$\mathbf{b}^{\mathcal{B}}_{6,r}$	$\mathbf{b}^{\mathcal{B}}_{7,r}$
$x^{\mathcal{B}}$ (m)	0.0731	0.0225	0.0980	0.0055	−0.0041	0.0603	−0.0544
$y^{\mathcal{B}}$ (m)	−0.0004	0.0802	0.0149	0.0690	0.0477	0.0172	−0.0507
$z^{\mathcal{B}}$ (m)	0.0333	−0.0833	0.0252	0.0322	0.0460	0.0782	0.0965

(a) Randomly-determined geometric parameters $\mathbf{a}_{i,r}$ and $\mathbf{b}^{\mathcal{B}}_{i,r}$

	$\mathbf{a}_{1,0}$	$\mathbf{a}_{2,0}$	$\mathbf{a}_{3,0}$	$\mathbf{a}_{4,0}$	$\mathbf{a}_{5,0}$	$\mathbf{a}_{6,0}$	$\mathbf{a}_{7,0}$
x (m)	0.7923	0.3206	0.5282	0.0919	0.1127	0.1366	0.6826
y (m)	0.4904	0.1877	0.4861	0.1441	0.0558	0.8512	0.5585
z (m)	0.9278	0.6950	0.5847	0.8141	0.8815	0.9888	0.0017
	$\mathbf{b}^{\mathcal{B}}_{1,0}$	$\mathbf{b}^{\mathcal{B}}_{2,0}$	$\mathbf{b}^{\mathcal{B}}_{3,0}$	$\mathbf{b}^{\mathcal{B}}_{4,0}$	$\mathbf{b}^{\mathcal{B}}_{5,0}$	$\mathbf{b}^{\mathcal{B}}_{6,0}$	$\mathbf{b}^{\mathcal{B}}_{7,0}$
$x^{\mathcal{B}}$ (m)	0.0258	0.0249	0.0904	0.0376	−0.0040	0.0056	0.0046
$y^{\mathcal{B}}$ (m)	0.0181	0.0772	0.0069	0.0407	0.0548	−0.0063	0.0060
$z^{\mathcal{B}}$ (m)	0.0700	−0.0849	0.0162	0.0364	0.0611	0.0562	0.0721

(b) Closest-feasible initial geometric parameters $\mathbf{a}_{i,0}$ and $\mathbf{b}^{\mathcal{B}}_{i,0}$

	$\mathbf{a}_{1,f}$	$\mathbf{a}_{2,f}$	$\mathbf{a}_{3,f}$	$\mathbf{a}_{4,f}$	$\mathbf{a}_{5,f}$	$\mathbf{a}_{6,f}$	$\mathbf{a}_{7,f}$
x (m)	0.9999	0.2351	0.9999	0.0000	0.0095	0.0001	0.9998
y (m)	0.7469	0.0001	0.4921	0.0004	0.0688	0.9999	0.9999
z (m)	0.7075	0.0000	0.9997	0.3453	0.9997	0.8591	0.0000
	$\mathbf{b}^{\mathcal{B}}_{1,f}$	$\mathbf{b}^{\mathcal{B}}_{2,f}$	$\mathbf{b}^{\mathcal{B}}_{3,f}$	$\mathbf{b}^{\mathcal{B}}_{4,f}$	$\mathbf{b}^{\mathcal{B}}_{5,f}$	$\mathbf{b}^{\mathcal{B}}_{6,f}$	$\mathbf{b}^{\mathcal{B}}_{7,f}$
$x^{\mathcal{B}}$ (m)	−0.0905	−0.0498	0.0999	0.0257	−0.0998	−0.0386	0.0471
$y^{\mathcal{B}}$ (m)	0.1000	0.0273	−0.0999	−0.1000	0.0956	−0.0918	−0.0626
$z^{\mathcal{B}}$ (m)	0.0081	−0.0169	−0.0625	0.1000	−0.0448	0.0316	0.0083

(c) Final geometric parameters $\mathbf{a}_{i,f}$ and $\mathbf{b}^{\mathcal{B}}_{i,f}$

Table D.13 – Geometric parameters of the CDPM corresponding to the Trial 13 of the numerical application of the dimensional synthesis program presented in Sub-section 4.3.1.

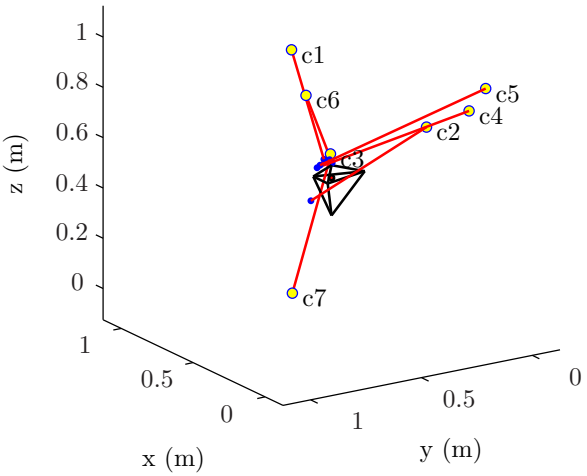

(a) The initial geometry of the CDPM

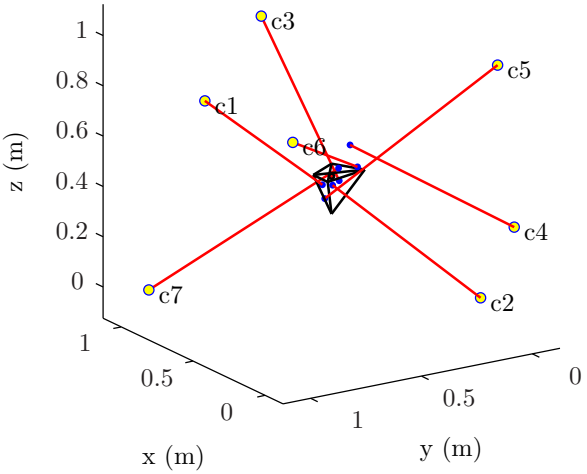

(b) The final geometry of the CDPM

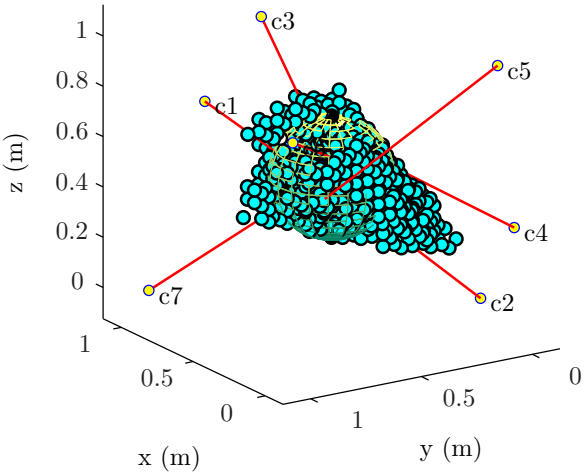

(c) The WCW of the final CDPM's geometry with the final $\mathcal{W}_t$ ($\kappa = 1.3924$)

Figure D.17 – Illustration of different results obtained from the optimization of a CDPM (Trial 13) for the numerical application of the dimensional synthesis program presented in Sub-section 4.3.1.

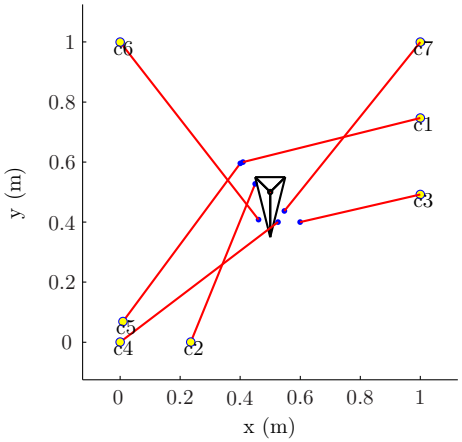

(a) An XY view of the final CDPM's geometry

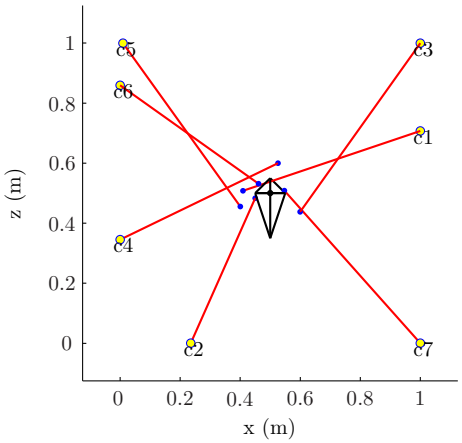

(b) An XZ view of the final CDPM's geometry

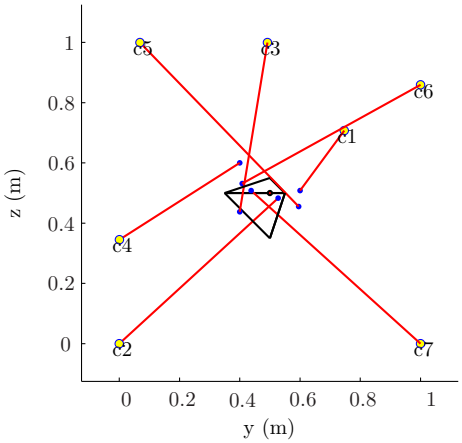

(c) An YZ view of the final CDPM's geometry

Figure D.18 – Three different two-dimensional points of view of the optimized CDPM's geometry (Trial 13) from the numerical application of the dimensional synthesis program presented in Sub-section 4.3.1 ($\kappa = 1.3924$).

Table D.14 and Figs. D.19 and D.20 present and illustrate the geometric parameters and the final wrench-closure workspace (WCW) as well as the final ellipsoid $\mathcal{W}_t$ ($\kappa = 1.5192$) resulting from the dimensional synthesis (Trial 14) of the CDPM presented in Sub-section 4.3.1.

In contrast with the first thirteen trials, the initial CDPM's geometry of Trial 14 was chosen based on author's intuition and experience[1]. These attachment points, i.e., $\mathbf{a}_{i,0}$ and $\mathbf{b}^{\mathcal{B}}_{i,0}$, have been selected to ensure that the CDPM presents a WCW while avoiding the occurrence of mechanical interferences between its moving parts.

	$\mathbf{a}_{1,0}$	$\mathbf{a}_{2,0}$	$\mathbf{a}_{3,0}$	$\mathbf{a}_{4,0}$	$\mathbf{a}_{5,0}$	$\mathbf{a}_{6,0}$	$\mathbf{a}_{7,0}$
x (m)	0.5000	0.0000	1.0000	0.0000	0.0000	1.0000	1.0000
y (m)	1.0000	1.0000	1.0000	0.0000	0.0000	0.0000	0.0000
z (m)	1.0000	0.0000	0.0000	0.0000	1.0000	0.0000	1.0000
	$\mathbf{b}^{\mathcal{B}}_{1,0}$	$\mathbf{b}^{\mathcal{B}}_{2,0}$	$\mathbf{b}^{\mathcal{B}}_{3,0}$	$\mathbf{b}^{\mathcal{B}}_{4,0}$	$\mathbf{b}^{\mathcal{B}}_{5,0}$	$\mathbf{b}^{\mathcal{B}}_{6,0}$	$\mathbf{b}^{\mathcal{B}}_{7,0}$
$x^{\mathcal{B}}$ (m)	0.0000	−0.0010	0.0010	−0.0500	−0.0500	0.0500	0.0500
$y^{\mathcal{B}}$ (m)	−0.1500	−0.1500	−0.1500	0.0500	0.0500	0.0500	0.0500
$z^{\mathcal{B}}$ (m)	0.0010	0.0000	0.0000	−0.0010	0.0010	−0.0010	0.0010

(a) Designer-intuition initial geometric parameters $\mathbf{a}_{i,0}$ and $\mathbf{b}^{\mathcal{B}}_{i,0}$

	$\mathbf{a}_{1,f}$	$\mathbf{a}_{2,f}$	$\mathbf{a}_{3,f}$	$\mathbf{a}_{4,f}$	$\mathbf{a}_{5,f}$	$\mathbf{a}_{6,f}$	$\mathbf{a}_{7,f}$
x (m)	0.8353	0.0001	0.9988	0.7744	0.0001	0.9964	0.9996
y (m)	0.9994	0.9972	0.9983	0.0001	0.0002	0.0004	0.9986
z (m)	0.9998	0.0003	0.0007	0.0002	0.9997	0.0004	0.9997
	$\mathbf{b}^{\mathcal{B}}_{1,f}$	$\mathbf{b}^{\mathcal{B}}_{2,f}$	$\mathbf{b}^{\mathcal{B}}_{3,f}$	$\mathbf{b}^{\mathcal{B}}_{4,f}$	$\mathbf{b}^{\mathcal{B}}_{5,f}$	$\mathbf{b}^{\mathcal{B}}_{6,f}$	$\mathbf{b}^{\mathcal{B}}_{7,f}$
$x^{\mathcal{B}}$ (m)	−0.0364	−0.0416	0.0538	−0.0999	−0.0422	0.0996	−0.0359
$y^{\mathcal{B}}$ (m)	−0.0998	0.0059	−0.0996	−0.0078	0.0175	0.0490	0.0996
$z^{\mathcal{B}}$ (m)	0.0996	−0.0234	−0.0758	−0.0999	−0.0229	0.0727	−0.0998

(b) Final geometric parameters $\mathbf{a}_{i,f}$ and $\mathbf{b}^{\mathcal{B}}_{i,f}$

Table D.14 – Geometric parameters of the CDPM corresponding to the Trial 14 of the numerical application of the dimensional synthesis program presented in Sub-section 4.3.1.

[1]Simple rules were followed to design this initial CDPM's geometry: In general, for maximizing the WCW, direct the m cables in a uniform-distributed manner around the moving platform in order to fully constrain the mechanism, at least at $\mathbf{p}_0$ and for $\mathbf{Q}_0$ (keep in mind that it must be possible to pull the end effector in all directions for each desired pose); Take advantage of the available space to position attachment points $\mathbf{a}_i$ on the base frame (for instances, at vertices); Position attachment points $\mathbf{b}_i$ in opposition to points $\mathbf{a}_i$, i.e., to cross cables, in order to increase the range of accessible end-effector attitudes. Then, to minimize the occurrence of mechanical interferences: Regroup attachment points together, which ensure that no other point along these cables can be in contact, unless the two cables are collinear; Similarly, position points $\mathbf{b}_i$ close to or on an end-effector edge; The two sets of attachment points $\mathbf{a}_i$ and $\mathbf{b}_i$ must normally form two convex shapes. When one follows these simple rules and find a "good" compromise, the resulting solution is generally close to or represents a feasible initial solution to start the optimization program from.

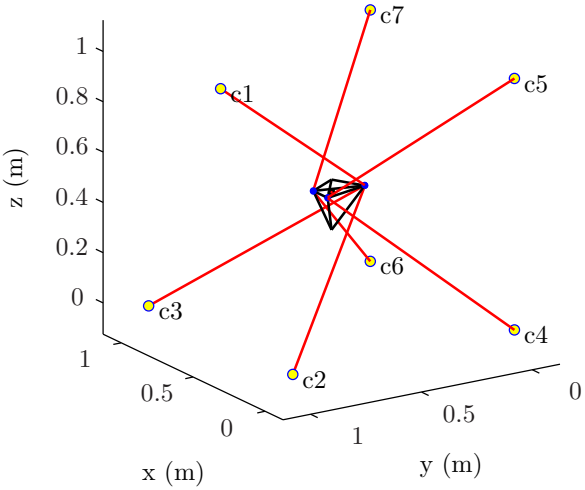

(a) The initial geometry of the CDPM

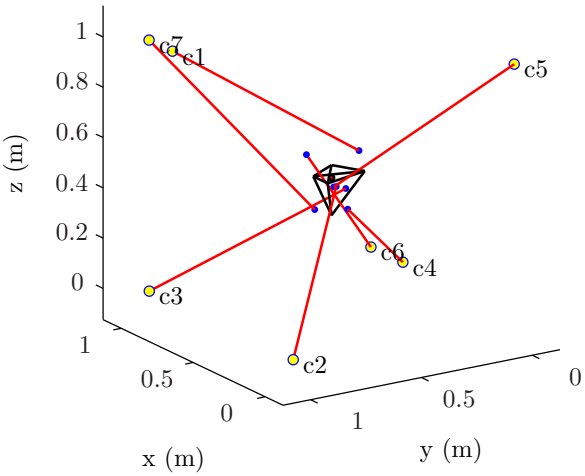

(b) The final geometry of the CDPM

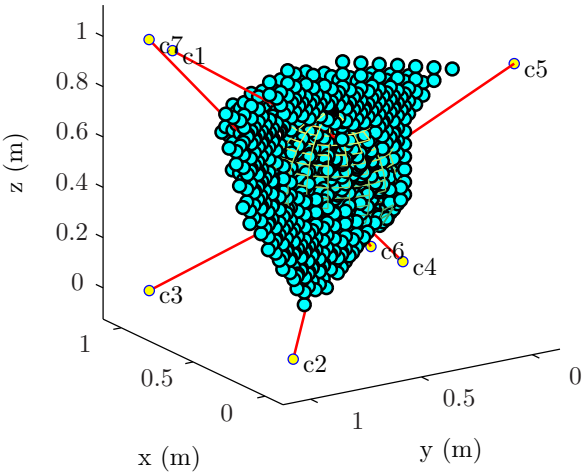

(c) The WCW of the final CDPM's geometry with the final $\mathcal{W}_t$ ($\kappa = 1.5192$)

Figure D.19 – Illustration of different results obtained from the optimization of a CDPM (Trial 14) for the numerical application of the dimensional synthesis program presented in Sub-section 4.3.1.

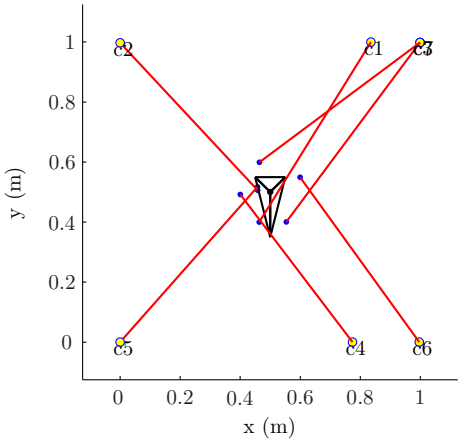

(a) An XY view of the final CDPM's geometry

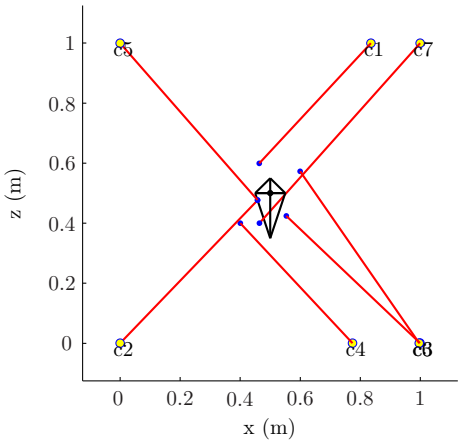

(b) An XZ view of the final CDPM's geometry

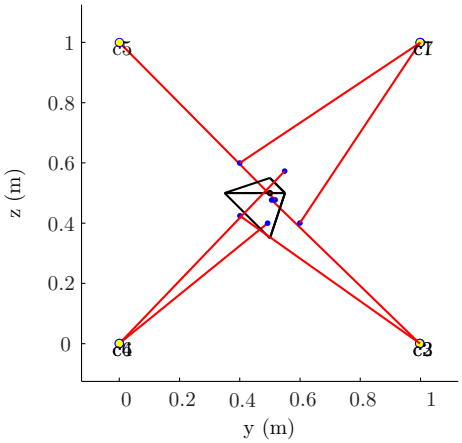

(c) An YZ view of the final CDPM's geometry

Figure D.20 – Three different two-dimensional points of view of the optimized CDPM's geometry (Trial 14) from the numerical application of the dimensional synthesis program presented in Sub-section 4.3.1 ($\kappa = 1.5192$).

D.2 Synthesis of Eight-Cable Seventeen-Edge Six-DoF Cable-Driven Parallel Mechanisms

Table D.15 and Fig. D.21 present and illustrate the geometric parameters and the final wrench-closure workspace (WCW) as well as the final ellipsoid $\mathcal{W}_t$ ($\kappa = 0.6913$) resulting from the dimensional synthesis (Trial 6) of the CDPM presented in Sub-section 4.3.2.

	$\mathbf{a}_{1,r}$	$\mathbf{a}_{2,r}$	$\mathbf{a}_{3,r}$	$\mathbf{a}_{4,r}$	$\mathbf{a}_{5,r}$	$\mathbf{a}_{6,r}$	$\mathbf{a}_{7,r}$	$\mathbf{a}_{8,r}$
x (m)	0.2892	0.1278	0.3127	−0.2806	0.0077	−0.2729	0.0317	0.1322
y (m)	−0.5641	0.4441	−0.1615	0.6373	−0.3087	−0.7023	−0.4488	−0.6675
z (m)	0.3326	0.0057	0.0401	0.0043	0.0757	0.0040	0.2249	0.1809
	$\mathbf{b}^{\mathcal{B}}_{1,r}$	$\mathbf{b}^{\mathcal{B}}_{2,r}$	$\mathbf{b}^{\mathcal{B}}_{3,r}$	$\mathbf{b}^{\mathcal{B}}_{4,r}$	$\mathbf{b}^{\mathcal{B}}_{5,r}$	$\mathbf{b}^{\mathcal{B}}_{6,r}$	$\mathbf{b}^{\mathcal{B}}_{7,r}$	$\mathbf{b}^{\mathcal{B}}_{8,r}$
$x^{\mathcal{B}}$ (m)	−0.0204	−0.0245	−0.0327	−0.0105	−0.0394	0.0082	−0.0017	−0.0154
$y^{\mathcal{B}}$ (m)	0.0196	0.0271	−0.0190	0.0011	−0.0043	−0.0127	0.0271	0.0386
$z^{\mathcal{B}}$ (m)	0.1002	0.0290	0.0197	0.0928	0.0526	0.0429	0.0880	0.0289

(a) Randomly-determined geometric parameters $\mathbf{a}_{i,r}$ and $\mathbf{b}^{\mathcal{B}}_{i,r}$

	$\mathbf{a}_{1,0}$	$\mathbf{a}_{2,0}$	$\mathbf{a}_{3,0}$	$\mathbf{a}_{4,0}$	$\mathbf{a}_{5,0}$	$\mathbf{a}_{6,0}$	$\mathbf{a}_{7,0}$	$\mathbf{a}_{8,0}$
x (m)	0.1391	0.2009	0.1416	−0.0480	−0.1391	−0.2009	−0.1416	0.0480
y (m)	−0.6007	0.3030	−0.3030	0.6007	0.1801	−0.1267	0.1267	−0.1801
z (m)	0.2072	0.0080	0.1342	0.2349	0.2072	0.0080	0.1342	0.2349
	$\mathbf{b}^{\mathcal{B}}_{1,0}$	$\mathbf{b}^{\mathcal{B}}_{2,0}$	$\mathbf{b}^{\mathcal{B}}_{3,0}$	$\mathbf{b}^{\mathcal{B}}_{4,0}$	$\mathbf{b}^{\mathcal{B}}_{5,0}$	$\mathbf{b}^{\mathcal{B}}_{6,0}$	$\mathbf{b}^{\mathcal{B}}_{7,0}$	$\mathbf{b}^{\mathcal{B}}_{8,0}$
$x^{\mathcal{B}}$ (m)	−0.0105	−0.0257	−0.0376	−0.0151	−0.0246	0.0098	−0.0009	−0.0164
$y^{\mathcal{B}}$ (m)	−0.0104	0.0243	−0.0215	0.0111	0.0111	−0.0153	0.0274	−0.0103
$z^{\mathcal{B}}$ (m)	0.1013	0.0300	0.0282	0.0917	0.0320	0.0410	0.0865	0.0280

(b) Closest-feasible initial geometric parameters $\mathbf{a}_{i,0}$ and $\mathbf{b}^{\mathcal{B}}_{i,0}$

	$\mathbf{a}_{1,f}$	$\mathbf{a}_{2,f}$	$\mathbf{a}_{3,f}$	$\mathbf{a}_{4,f}$	$\mathbf{a}_{5,f}$	$\mathbf{a}_{6,f}$	$\mathbf{a}_{7,f}$	$\mathbf{a}_{8,f}$
x (m)	0.0587	0.3497	0.3477	0.0067	−0.0587	−0.3497	−0.3477	−0.0067
y (m)	−0.7987	0.7974	−0.7974	0.7987	0.7998	−0.7534	0.7534	−0.7998
z (m)	0.3419	0.0006	0.0166	0.3477	0.3419	0.0006	0.0166	0.3477
	$\mathbf{b}^{\mathcal{B}}_{1,f}$	$\mathbf{b}^{\mathcal{B}}_{2,f}$	$\mathbf{b}^{\mathcal{B}}_{3,f}$	$\mathbf{b}^{\mathcal{B}}_{4,f}$	$\mathbf{b}^{\mathcal{B}}_{5,f}$	$\mathbf{b}^{\mathcal{B}}_{6,f}$	$\mathbf{b}^{\mathcal{B}}_{7,f}$	$\mathbf{b}^{\mathcal{B}}_{8,f}$
$x^{\mathcal{B}}$ (m)	−0.0066	−0.0399	−0.0399	−0.0398	−0.0400	0.0400	−0.0115	−0.0399
$y^{\mathcal{B}}$ (m)	−0.0388	0.0309	−0.0182	0.0260	0.0038	−0.0195	0.0228	−0.0199
$z^{\mathcal{B}}$ (m)	0.1600	0.0001	0.0467	0.1599	0.0155	0.0489	0.0608	0.0470

(c) Final geometric parameters $\mathbf{a}_{i,f}$ and $\mathbf{b}^{\mathcal{B}}_{i,f}$

Table D.15 – Geometric parameters of the CDPM corresponding to the Trial 6 of the numerical application of the dimensional synthesis program presented in Sub-section 4.3.2.

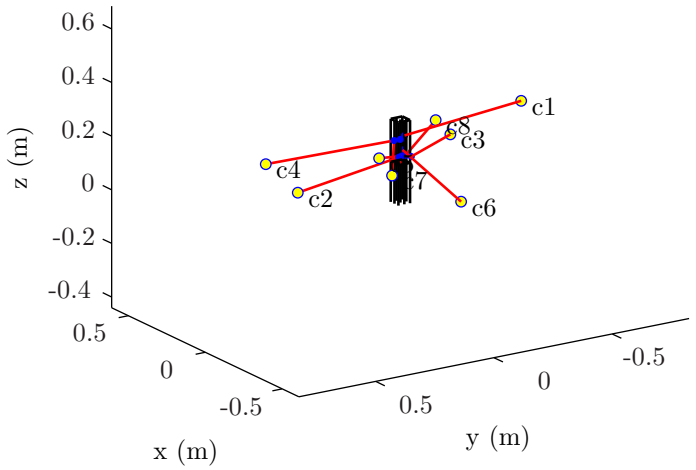

(a) The initial geometry of the CDPM

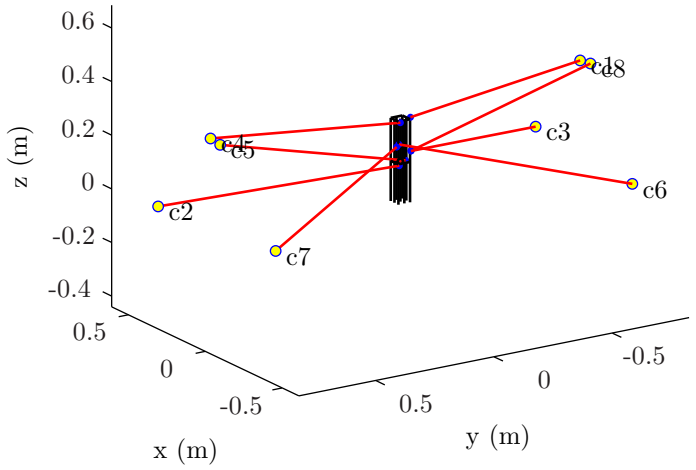

(b) The final geometry of the CDPM

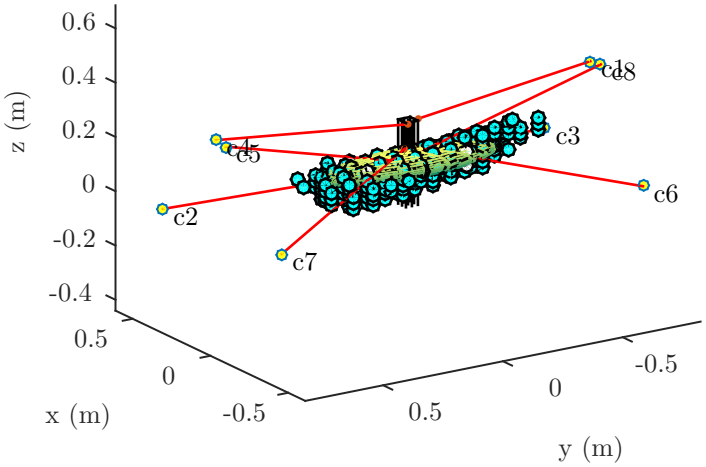

(c) The WCW of the final CDPM's geometry with the final $\mathcal{W}_t$ ($\kappa = 0.6913$)

Figure D.21 – Illustration of different results obtained from the optimization of a CDPM (Trial 6) for the numerical application of the dimensional synthesis program presented in Sub-section 4.3.2.

Table D.16 and Fig. D.22 present and illustrate the geometric parameters and the final wrench-closure workspace (WCW) as well as the final ellipsoid $\mathcal{W}_t$ ($\kappa = 0.8942$) resulting from the dimensional synthesis (Trial 7) of the CDPM presented in Sub-section 4.3.2.

	$\mathbf{a}_{1,r}$	$\mathbf{a}_{2,r}$	$\mathbf{a}_{3,r}$	$\mathbf{a}_{4,r}$	$\mathbf{a}_{5,r}$	$\mathbf{a}_{6,r}$	$\mathbf{a}_{7,r}$	$\mathbf{a}_{8,r}$
x (m)	0.1249	−0.3110	−0.3262	−0.1494	−0.2958	0.2804	0.2426	−0.0730
y (m)	−0.5293	−0.1113	−0.1341	0.3660	−0.1496	0.7229	0.6592	0.7223
z (m)	0.1211	0.1016	0.3103	0.0735	0.0458	0.1822	0.3169	0.1409
	$\mathbf{b}^{\mathcal{B}}_{1,r}$	$\mathbf{b}^{\mathcal{B}}_{2,r}$	$\mathbf{b}^{\mathcal{B}}_{3,r}$	$\mathbf{b}^{\mathcal{B}}_{4,r}$	$\mathbf{b}^{\mathcal{B}}_{5,r}$	$\mathbf{b}^{\mathcal{B}}_{6,r}$	$\mathbf{b}^{\mathcal{B}}_{7,r}$	$\mathbf{b}^{\mathcal{B}}_{8,r}$
$x^{\mathcal{B}}$ (m)	−0.0227	−0.0337	0.0346	0.0082	−0.0098	0.0132	0.0234	−0.0133
$y^{\mathcal{B}}$ (m)	0.0154	−0.0237	0.0367	0.0169	−0.0266	−0.0046	0.0106	0.0344
$z^{\mathcal{B}}$ (m)	0.0847	0.1002	0.1089	0.1477	0.0245	0.0649	0.0500	0.1110

(a) Randomly-determined geometric parameters $\mathbf{a}_{i,r}$ and $\mathbf{b}^{\mathcal{B}}_{i,r}$

	$\mathbf{a}_{1,0}$	$\mathbf{a}_{2,0}$	$\mathbf{a}_{3,0}$	$\mathbf{a}_{4,0}$	$\mathbf{a}_{5,0}$	$\mathbf{a}_{6,0}$	$\mathbf{a}_{7,0}$	$\mathbf{a}_{8,0}$
x (m)	0.2108	−0.1117	−0.1497	0.0276	−0.2108	0.1117	0.1497	−0.0276
y (m)	−0.4469	0.0203	−0.0203	0.4469	−0.4339	0.0366	−0.0366	0.4339
z (m)	0.0717	0.3068	0.3498	0.1496	0.0717	0.3068	0.3498	0.1496
	$\mathbf{b}^{\mathcal{B}}_{1,0}$	$\mathbf{b}^{\mathcal{B}}_{2,0}$	$\mathbf{b}^{\mathcal{B}}_{3,0}$	$\mathbf{b}^{\mathcal{B}}_{4,0}$	$\mathbf{b}^{\mathcal{B}}_{5,0}$	$\mathbf{b}^{\mathcal{B}}_{6,0}$	$\mathbf{b}^{\mathcal{B}}_{7,0}$	$\mathbf{b}^{\mathcal{B}}_{8,0}$
$x^{\mathcal{B}}$ (m)	−0.0168	−0.0277	0.0373	−0.0227	−0.0030	0.0187	0.0218	0.0024
$y^{\mathcal{B}}$ (m)	−0.0103	0.0132	−0.0105	0.0105	−0.0102	0.0108	−0.0210	0.0105
$z^{\mathcal{B}}$ (m)	0.1077	0.0700	0.1095	0.0993	0.0867	0.0873	0.0481	0.0951

(b) Closest-feasible initial geometric parameters $\mathbf{a}_{i,0}$ and $\mathbf{b}^{\mathcal{B}}_{i,0}$

	$\mathbf{a}_{1,f}$	$\mathbf{a}_{2,f}$	$\mathbf{a}_{3,f}$	$\mathbf{a}_{4,f}$	$\mathbf{a}_{5,f}$	$\mathbf{a}_{6,f}$	$\mathbf{a}_{7,f}$	$\mathbf{a}_{8,f}$
x (m)	0.3499	−0.1498	−0.0420	0.3471	−0.3499	0.1498	0.0420	−0.3471
y (m)	−0.7998	0.7999	−0.7999	0.7998	−0.6903	0.7999	−0.7999	0.6903
z (m)	0.0002	0.3499	0.3383	0.0215	0.0002	0.3499	0.3383	0.0215
	$\mathbf{b}^{\mathcal{B}}_{1,f}$	$\mathbf{b}^{\mathcal{B}}_{2,f}$	$\mathbf{b}^{\mathcal{B}}_{3,f}$	$\mathbf{b}^{\mathcal{B}}_{4,f}$	$\mathbf{b}^{\mathcal{B}}_{5,f}$	$\mathbf{b}^{\mathcal{B}}_{6,f}$	$\mathbf{b}^{\mathcal{B}}_{7,f}$	$\mathbf{b}^{\mathcal{B}}_{8,f}$
$x^{\mathcal{B}}$ (m)	−0.0226	−0.0400	0.0400	−0.0400	−0.0345	0.0400	0.0400	0.0368
$y^{\mathcal{B}}$ (m)	−0.0183	0.0156	−0.0124	0.0249	0.0194	0.0026	−0.0085	0.0251
$z^{\mathcal{B}}$ (m)	0.0695	0.0514	0.1280	0.0443	0.0226	0.0445	0.0000	0.0307

(c) Final geometric parameters $\mathbf{a}_{i,f}$ and $\mathbf{b}^{\mathcal{B}}_{i,f}$

Table D.16 – Geometric parameters of the CDPM corresponding to the Trial 7 of the numerical application of the dimensional synthesis program presented in Sub-section 4.3.2.

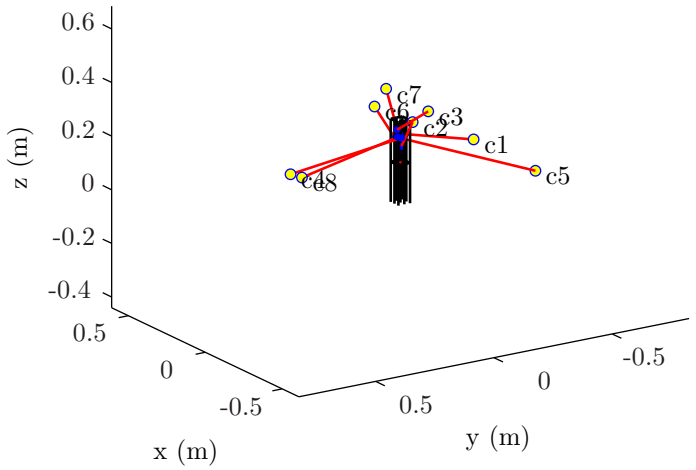

(a) The initial geometry of the CDPM

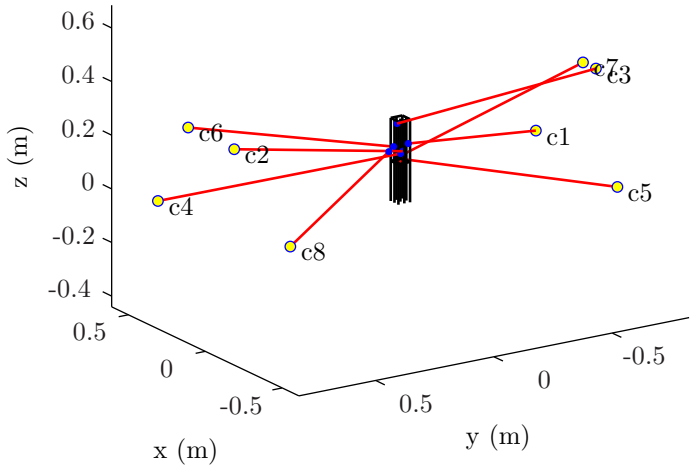

(b) The final geometry of the CDPM

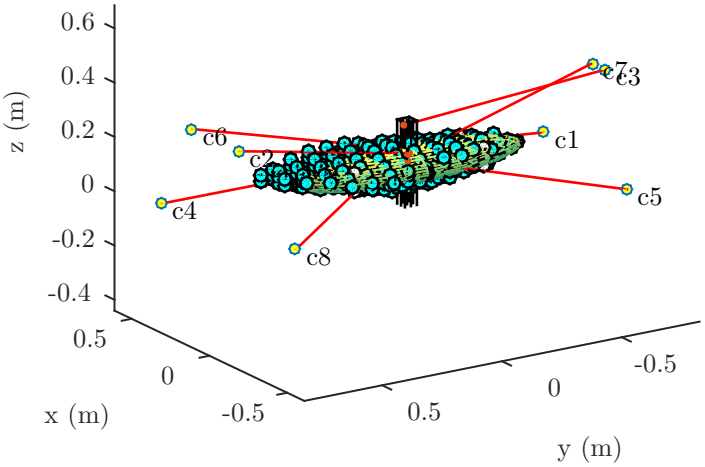

(c) The WCW of the final CDPM's geometry with the final $\mathcal{W}_t$ ($\kappa = 0.8942$)

Figure D.22 – Illustration of different results obtained from the optimization of a CDPM (Trial 7) for the numerical application of the dimensional synthesis program presented in Sub-section 4.3.2.

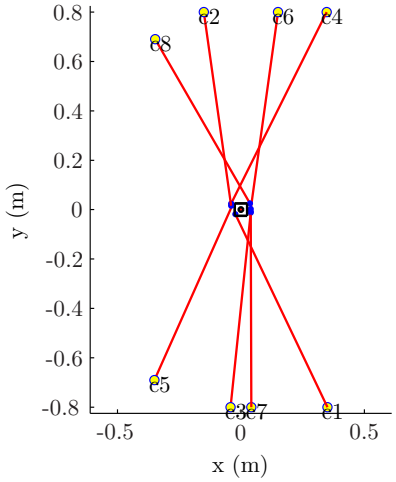

(a) An XY view of the final CDPM's geometry

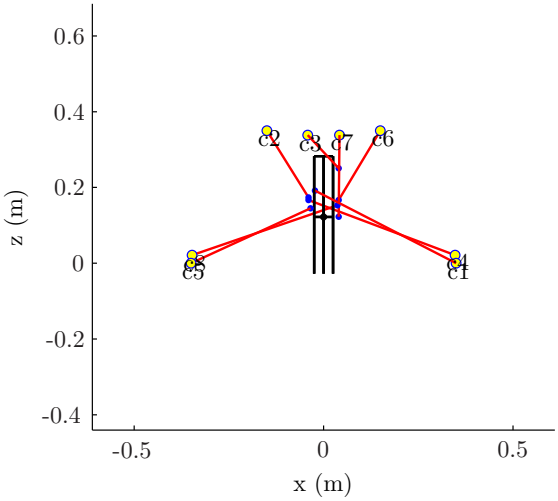

(b) An XZ view of the final CDPM's geometry

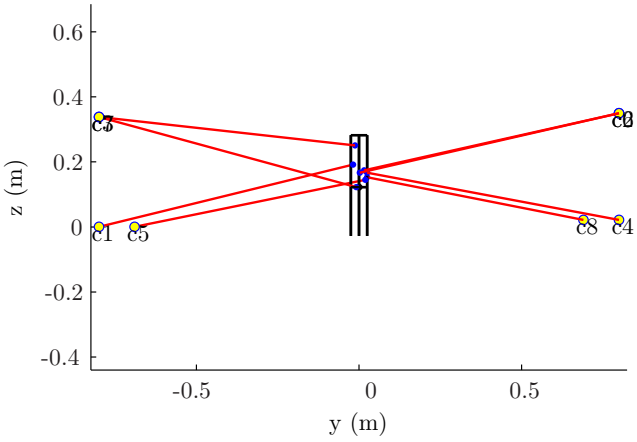

(c) An YZ view of the final CDPM's geometry

Figure D.23 – Three different two-dimensional points of view of the optimized CDPM's geometry (Trial 7) from the numerical application of the dimensional synthesis program presented in Sub-section 4.3.2 ($\kappa = 0.8942$).

Table D.17 and Fig. D.24 present and illustrate the geometric parameters and the final wrench-closure workspace (WCW) as well as the final ellipsoid $\mathcal{W}_t$ ($\kappa = 0.5384$) resulting from the dimensional synthesis (Trial 28) of the CDPM presented in Sub-section 4.3.2.

	$\mathbf{a}_{1,r}$	$\mathbf{a}_{2,r}$	$\mathbf{a}_{3,r}$	$\mathbf{a}_{4,r}$	$\mathbf{a}_{5,r}$	$\mathbf{a}_{6,r}$	$\mathbf{a}_{7,r}$	$\mathbf{a}_{8,r}$
x (m)	0.2138	0.0537	−0.2220	−0.1820	0.2706	−0.3299	−0.0071	−0.2325
y (m)	0.7659	0.3403	0.0008	−0.0463	−0.7046	0.2912	−0.7321	−0.6857
z (m)	0.1826	0.0339	0.2864	0.2861	0.2529	0.0525	0.2309	0.1815
	$\mathbf{b}^{\mathcal{B}}_{1,r}$	$\mathbf{b}^{\mathcal{B}}_{2,r}$	$\mathbf{b}^{\mathcal{B}}_{3,r}$	$\mathbf{b}^{\mathcal{B}}_{4,r}$	$\mathbf{b}^{\mathcal{B}}_{5,r}$	$\mathbf{b}^{\mathcal{B}}_{6,r}$	$\mathbf{b}^{\mathcal{B}}_{7,r}$	$\mathbf{b}^{\mathcal{B}}_{8,r}$
$x^{\mathcal{B}}$ (m)	0.0378	0.0119	0.0240	−0.0037	−0.0054	0.0260	−0.0333	−0.0293
$y^{\mathcal{B}}$ (m)	−0.0261	−0.0087	0.0265	0.0243	−0.0352	−0.0081	0.0022	−0.0067
$z^{\mathcal{B}}$ (m)	0.1051	0.1005	0.0467	0.0691	0.0025	0.1575	0.0267	0.0170

(a) Randomly-determined geometric parameters $\mathbf{a}_{i,r}$ and $\mathbf{b}^{\mathcal{B}}_{i,r}$

	$\mathbf{a}_{1,0}$	$\mathbf{a}_{2,0}$	$\mathbf{a}_{3,0}$	$\mathbf{a}_{4,0}$	$\mathbf{a}_{5,0}$	$\mathbf{a}_{6,0}$	$\mathbf{a}_{7,0}$	$\mathbf{a}_{8,0}$
x (m)	−0.0249	0.1926	−0.0841	0.0329	0.0249	−0.1926	0.0841	−0.0329
y (m)	0.4061	0.1721	−0.1721	−0.4061	−0.0162	0.5117	−0.5117	0.0162
z (m)	0.2169	0.0443	0.2762	0.2314	0.2169	0.0443	0.2762	0.2314
	$\mathbf{b}^{\mathcal{B}}_{1,0}$	$\mathbf{b}^{\mathcal{B}}_{2,0}$	$\mathbf{b}^{\mathcal{B}}_{3,0}$	$\mathbf{b}^{\mathcal{B}}_{4,0}$	$\mathbf{b}^{\mathcal{B}}_{5,0}$	$\mathbf{b}^{\mathcal{B}}_{6,0}$	$\mathbf{b}^{\mathcal{B}}_{7,0}$	$\mathbf{b}^{\mathcal{B}}_{8,0}$
$x^{\mathcal{B}}$ (m)	0.0167	0.0228	0.0333	0.0212	−0.0074	0.0206	−0.0377	−0.0281
$y^{\mathcal{B}}$ (m)	0.0104	0.0105	−0.0103	−0.0103	−0.0358	0.0103	−0.0111	0.0120
$z^{\mathcal{B}}$ (m)	0.1193	0.0664	0.0879	0.0913	0.0062	0.0774	0.0488	0.0252

(b) Closest-feasible initial geometric parameters $\mathbf{a}_{i,0}$ and $\mathbf{b}^{\mathcal{B}}_{i,0}$

	$\mathbf{a}_{1,f}$	$\mathbf{a}_{2,f}$	$\mathbf{a}_{3,f}$	$\mathbf{a}_{4,f}$	$\mathbf{a}_{5,f}$	$\mathbf{a}_{6,f}$	$\mathbf{a}_{7,f}$	$\mathbf{a}_{8,f}$
x (m)	−0.0087	0.3499	−0.1499	0.0185	0.0087	−0.3499	0.1499	−0.0185
y (m)	0.7998	0.3071	−0.3071	−0.7998	−0.7999	0.7995	−0.7995	0.7999
z (m)	0.2770	0.0000	0.3500	0.2756	0.2770	0.0000	0.3500	0.2756
	$\mathbf{b}^{\mathcal{B}}_{1,f}$	$\mathbf{b}^{\mathcal{B}}_{2,f}$	$\mathbf{b}^{\mathcal{B}}_{3,f}$	$\mathbf{b}^{\mathcal{B}}_{4,f}$	$\mathbf{b}^{\mathcal{B}}_{5,f}$	$\mathbf{b}^{\mathcal{B}}_{6,f}$	$\mathbf{b}^{\mathcal{B}}_{7,f}$	$\mathbf{b}^{\mathcal{B}}_{8,f}$
$x^{\mathcal{B}}$ (m)	0.0211	0.0259	0.0315	0.0257	0.0400	0.0231	−0.0400	−0.0400
$y^{\mathcal{B}}$ (m)	0.0188	0.0145	−0.0390	−0.0277	−0.0010	0.0105	−0.0172	0.0019
$z^{\mathcal{B}}$ (m)	0.1552	0.0934	0.1577	0.1598	0.0099	0.1104	0.1379	0.0582

(c) Final geometric parameters $\mathbf{a}_{i,f}$ and $\mathbf{b}^{\mathcal{B}}_{i,f}$

Table D.17 – Geometric parameters of the CDPM corresponding to the Trial 28 of the numerical application of the dimensional synthesis program presented in Sub-section 4.3.2.

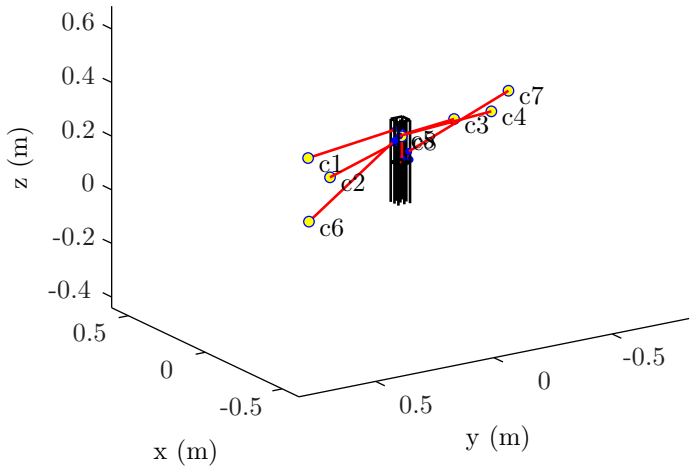

(a) The initial geometry of the CDPM

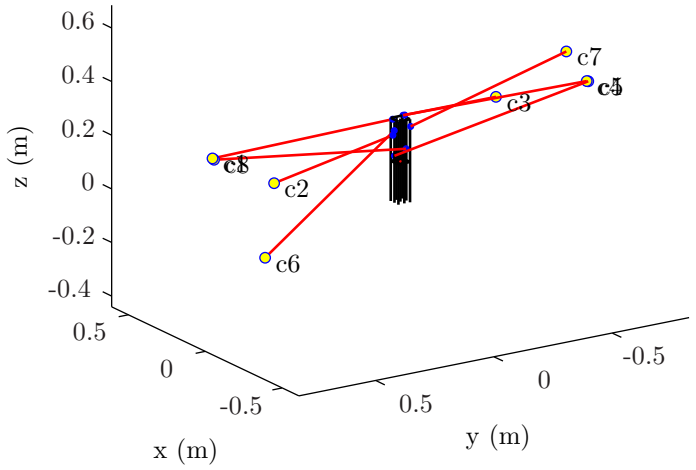

(b) The final geometry of the CDPM

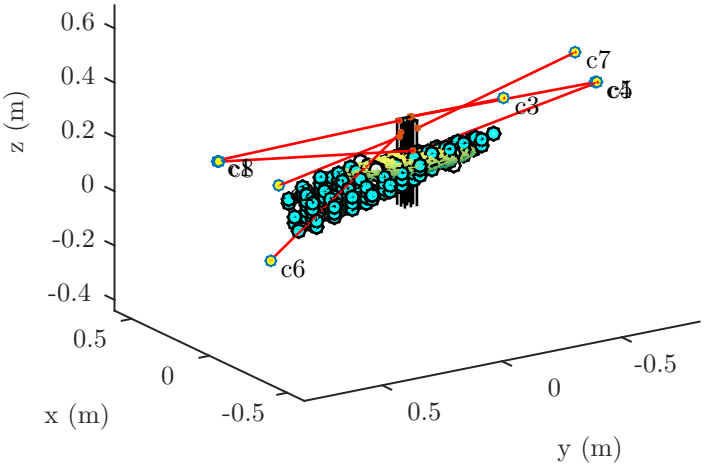

(c) The WCW of the final CDPM's geometry with the final $\mathcal{W}_t$ ($\kappa = 0.5384$)

Figure D.24 – Illustration of different results obtained from the optimization of a CDPM (Trial 28) for the numerical application of the dimensional synthesis program presented in Sub-section 4.3.2.

Table D.18 and Fig. D.25 present and illustrate the geometric parameters and the final wrench-closure workspace (WCW) as well as the final ellipsoid $\mathcal{W}_t$ ($\kappa = 0.6959$) resulting from the dimensional synthesis (Trial 29) of the CDPM presented in Sub-section 4.3.2.

	$\mathbf{a}_{1,r}$	$\mathbf{a}_{2,r}$	$\mathbf{a}_{3,r}$	$\mathbf{a}_{4,r}$	$\mathbf{a}_{5,r}$	$\mathbf{a}_{6,r}$	$\mathbf{a}_{7,r}$	$\mathbf{a}_{8,r}$
x (m)	0.2271	0.3379	0.1612	−0.1093	0.0588	−0.2746	0.2844	0.2658
y (m)	0.5084	−0.3828	0.1510	−0.7640	−0.1196	−0.2996	−0.5416	−0.5140
z (m)	0.1480	0.0330	0.2095	0.1648	0.2436	0.2450	0.2235	0.0118
	$\mathbf{b}^{\mathcal{B}}_{1,r}$	$\mathbf{b}^{\mathcal{B}}_{2,r}$	$\mathbf{b}^{\mathcal{B}}_{3,r}$	$\mathbf{b}^{\mathcal{B}}_{4,r}$	$\mathbf{b}^{\mathcal{B}}_{5,r}$	$\mathbf{b}^{\mathcal{B}}_{6,r}$	$\mathbf{b}^{\mathcal{B}}_{7,r}$	$\mathbf{b}^{\mathcal{B}}_{8,r}$
$x^{\mathcal{B}}$ (m)	−0.0345	−0.0144	0.0025	0.0124	−0.0074	0.0256	0.0175	0.0375
$y^{\mathcal{B}}$ (m)	0.0025	−0.0140	−0.0315	0.0089	0.0223	−0.0061	−0.0327	−0.0187
$z^{\mathcal{B}}$ (m)	0.0246	0.0450	0.0704	0.0843	0.0732	0.1401	0.0829	0.1510

(a) Randomly-determined geometric parameters $\mathbf{a}_{i,r}$ and $\mathbf{b}^{\mathcal{B}}_{i,r}$

	$\mathbf{a}_{1,0}$	$\mathbf{a}_{2,0}$	$\mathbf{a}_{3,0}$	$\mathbf{a}_{4,0}$	$\mathbf{a}_{5,0}$	$\mathbf{a}_{6,0}$	$\mathbf{a}_{7,0}$	$\mathbf{a}_{8,0}$
x (m)	0.0861	0.2996	−0.0380	−0.0374	−0.0861	−0.2996	0.0380	0.0374
y (m)	0.6361	−0.2694	0.2694	−0.6361	0.1960	−0.0100	0.0100	−0.1960
z (m)	0.1892	0.1310	0.2254	0.2231	0.1892	0.1310	0.2254	0.2232
	$\mathbf{b}^{\mathcal{B}}_{1,0}$	$\mathbf{b}^{\mathcal{B}}_{2,0}$	$\mathbf{b}^{\mathcal{B}}_{3,0}$	$\mathbf{b}^{\mathcal{B}}_{4,0}$	$\mathbf{b}^{\mathcal{B}}_{5,0}$	$\mathbf{b}^{\mathcal{B}}_{6,0}$	$\mathbf{b}^{\mathcal{B}}_{7,0}$	$\mathbf{b}^{\mathcal{B}}_{8,0}$
$x^{\mathcal{B}}$ (m)	−0.0329	−0.0185	0.0081	−0.0026	0.0139	0.0226	0.0123	0.0292
$y^{\mathcal{B}}$ (m)	0.0137	−0.0199	0.0074	−0.0100	0.0227	−0.0148	−0.0061	−0.0247
$z^{\mathcal{B}}$ (m)	0.0473	0.0647	0.1101	0.0589	0.0644	0.1026	0.0976	0.1511

(b) Closest-feasible initial geometric parameters $\mathbf{a}_{i,0}$ and $\mathbf{b}^{\mathcal{B}}_{i,0}$

	$\mathbf{a}_{1,f}$	$\mathbf{a}_{2,f}$	$\mathbf{a}_{3,f}$	$\mathbf{a}_{4,f}$	$\mathbf{a}_{5,f}$	$\mathbf{a}_{6,f}$	$\mathbf{a}_{7,f}$	$\mathbf{a}_{8,f}$
x (m)	0.3384	0.3497	0.1780	−0.1496	−0.3384	−0.3497	−0.1780	0.1496
y (m)	0.7996	−0.7997	0.7997	−0.7996	0.7983	0.2303	−0.2303	−0.7983
z (m)	0.0866	0.0001	0.3007	0.3497	0.0866	0.0001	0.3007	0.3497
	$\mathbf{b}^{\mathcal{B}}_{1,f}$	$\mathbf{b}^{\mathcal{B}}_{2,f}$	$\mathbf{b}^{\mathcal{B}}_{3,f}$	$\mathbf{b}^{\mathcal{B}}_{4,f}$	$\mathbf{b}^{\mathcal{B}}_{5,f}$	$\mathbf{b}^{\mathcal{B}}_{6,f}$	$\mathbf{b}^{\mathcal{B}}_{7,f}$	$\mathbf{b}^{\mathcal{B}}_{8,f}$
$x^{\mathcal{B}}$ (m)	−0.0329.	−0.0199	0.0400	0.0373	0.0400	−0.0362	−0.0399	0.0399
$y^{\mathcal{B}}$ (m)	0.0397	−0.0392	0.0028	−0.0368	0.0322	0.0022	−0.0394	−0.0389
$z^{\mathcal{B}}$ (m)	0.0263	0.0746	0.1431	0.0001	0.0284	0.0454	0.1600	0.1599

(c) Final geometric parameters $\mathbf{a}_{i,f}$ and $\mathbf{b}^{\mathcal{B}}_{i,f}$

Table D.18 – Geometric parameters of the CDPM corresponding to the Trial 29 of the numerical application of the dimensional synthesis program presented in Sub-section 4.3.2.

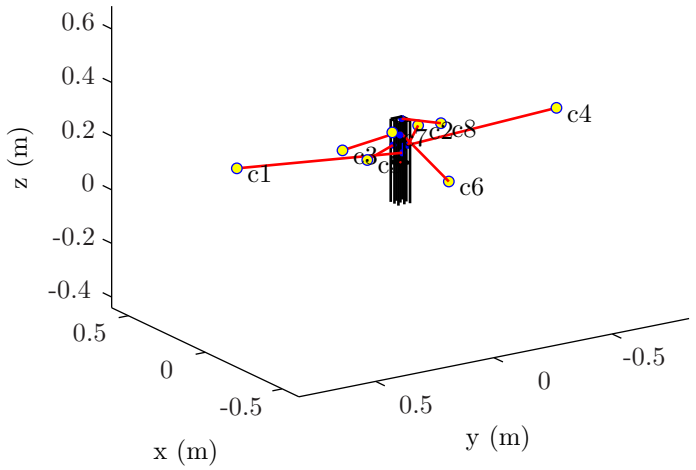

(a) The initial geometry of the CDPM

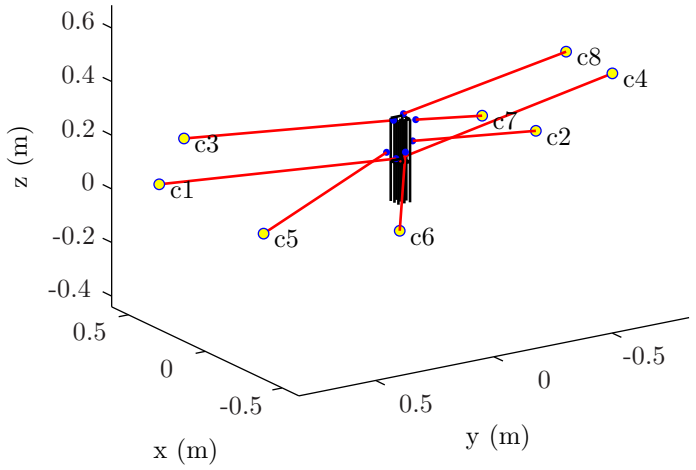

(b) The final geometry of the CDPM

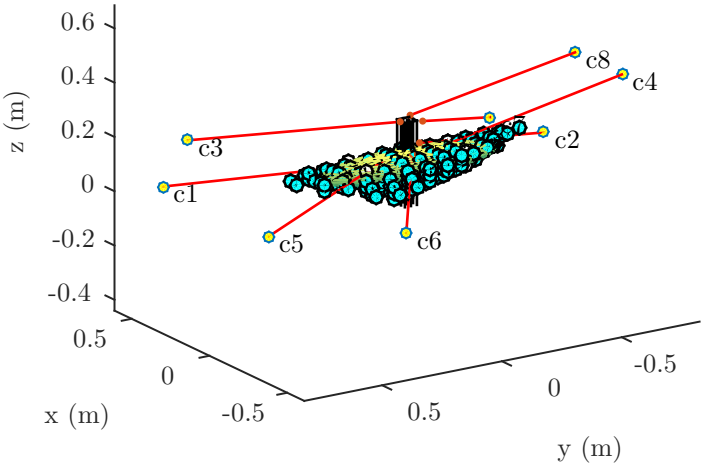

(c) The WCW of the final CDPM's geometry with the final $\mathcal{W}_t$ ($\kappa = 0.6959$)

Figure D.25 – Illustration of different results obtained from the optimization of a CDPM (Trial 29) for the numerical application of the dimensional synthesis program presented in Sub-section 4.3.2.

Table D.19 and Fig. D.26 present and illustrate the geometric parameters and the final wrench-closure workspace (WCW) as well as the final ellipsoid $\mathcal{W}_t$ ($\kappa = 0.6166$) resulting from the dimensional synthesis (Trial 36) of the CDPM presented in Sub-section 4.3.2.

	$\mathbf{a}_{1,r}$	$\mathbf{a}_{2,r}$	$\mathbf{a}_{3,r}$	$\mathbf{a}_{4,r}$	$\mathbf{a}_{5,r}$	$\mathbf{a}_{6,r}$	$\mathbf{a}_{7,r}$	$\mathbf{a}_{8,r}$
x (m)	−0.2253	−0.0983	−0.3103	0.0153	−0.1149	−0.2270	−0.2037	0.2836
y (m)	0.2806	−0.0505	0.6594	−0.6336	0.3929	0.3780	0.0990	−0.5053
z (m)	0.2090	0.1050	0.0469	0.0744	0.3132	0.0250	0.0849	0.0188
	$\mathbf{b}^{\mathcal{B}}_{1,r}$	$\mathbf{b}^{\mathcal{B}}_{2,r}$	$\mathbf{b}^{\mathcal{B}}_{3,r}$	$\mathbf{b}^{\mathcal{B}}_{4,r}$	$\mathbf{b}^{\mathcal{B}}_{5,r}$	$\mathbf{b}^{\mathcal{B}}_{6,r}$	$\mathbf{b}^{\mathcal{B}}_{7,r}$	$\mathbf{b}^{\mathcal{B}}_{8,r}$
$x^{\mathcal{B}}$ (m)	−0.0047	−0.0389	0.0318	−0.0243	−0.0325	−0.0154	−0.0035	−0.0319
$y^{\mathcal{B}}$ (m)	0.0396	−0.0134	−0.0162	−0.0350	−0.0161	−0.0363	0.0004	0.0209
$z^{\mathcal{B}}$ (m)	0.1010	0.0144	0.0129	0.1244	0.1448	0.0854	0.0175	0.1321

(a) Randomly-determined geometric parameters $\mathbf{a}_{i,r}$ and $\mathbf{b}^{\mathcal{B}}_{i,r}$

	$\mathbf{a}_{1,0}$	$\mathbf{a}_{2,0}$	$\mathbf{a}_{3,0}$	$\mathbf{a}_{4,0}$	$\mathbf{a}_{5,0}$	$\mathbf{a}_{6,0}$	$\mathbf{a}_{7,0}$	$\mathbf{a}_{8,0}$
x (m)	−0.0596	0.0873	0.0322	0.0087	0.0596	−0.0873	−0.0322	−0.0087
y (m)	0.4574	−0.3544	0.3544	−0.4574	0.4495	0.1394	−0.1394	−0.4495
z (m)	0.2606	0.0827	0.1445	0.1709	0.2606	0.0827	0.1445	0.1709
	$\mathbf{b}^{\mathcal{B}}_{1,0}$	$\mathbf{b}^{\mathcal{B}}_{2,0}$	$\mathbf{b}^{\mathcal{B}}_{3,0}$	$\mathbf{b}^{\mathcal{B}}_{4,0}$	$\mathbf{b}^{\mathcal{B}}_{5,0}$	$\mathbf{b}^{\mathcal{B}}_{6,0}$	$\mathbf{b}^{\mathcal{B}}_{7,0}$	$\mathbf{b}^{\mathcal{B}}_{8,0}$
$x^{\mathcal{B}}$ (m)	0.0075	−0.0293	−0.0065	−0.0097	−0.0387	−0.0090	0.0133	−0.0350
$y^{\mathcal{B}}$ (m)	0.0337	−0.0128	0.0105	−0.0313	0.0106	0.0105	−0.0118	−0.0106
$z^{\mathcal{B}}$ (m)	0.0929	0.0227	0.0026	0.1239	0.1372	0.0815	0.0024	0.1288

(b) Closest-feasible initial geometric parameters $\mathbf{a}_{i,0}$ and $\mathbf{b}^{\mathcal{B}}_{i,0}$

	$\mathbf{a}_{1,f}$	$\mathbf{a}_{2,f}$	$\mathbf{a}_{3,f}$	$\mathbf{a}_{4,f}$	$\mathbf{a}_{5,f}$	$\mathbf{a}_{6,f}$	$\mathbf{a}_{7,f}$	$\mathbf{a}_{8,f}$
x (m)	−0.0433	0.3480	0.2302	0.2597	0.0433	−0.3480	−0.2302	−0.2597
y (m)	0.7429	−0.8000	0.8000	−0.7429	0.7996	0.7993	−0.7993	−0.7996
z (m)	0.3498	0.0141	0.0824	0.2315	0.3498	0.0141	0.0824	0.2315
	$\mathbf{b}^{\mathcal{B}}_{1,f}$	$\mathbf{b}^{\mathcal{B}}_{2,f}$	$\mathbf{b}^{\mathcal{B}}_{3,f}$	$\mathbf{b}^{\mathcal{B}}_{4,f}$	$\mathbf{b}^{\mathcal{B}}_{5,f}$	$\mathbf{b}^{\mathcal{B}}_{6,f}$	$\mathbf{b}^{\mathcal{B}}_{7,f}$	$\mathbf{b}^{\mathcal{B}}_{8,f}$
$x^{\mathcal{B}}$ (m)	0.0398	−0.0400	−0.0039	0.0397	−0.0400	−0.0028	0.0400	−0.0351
$y^{\mathcal{B}}$ (m)	0.0129	−0.0219	0.0007	−0.0398	0.0109	0.0317	−0.0398	0.0074
$z^{\mathcal{B}}$ (m)	0.0346	0.0248	0.0000	0.1455	0.1176	0.0172	0.0000	0.1023

(c) Final geometric parameters $\mathbf{a}_{i,f}$ and $\mathbf{b}^{\mathcal{B}}_{i,f}$

Table D.19 – Geometric parameters of the CDPM corresponding to the Trial 36 of the numerical application of the dimensional synthesis program presented in Sub-section 4.3.2.

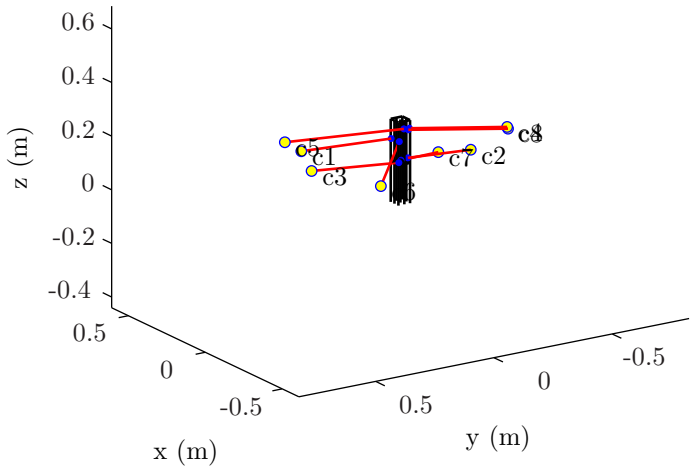

(a) The initial geometry of the CDPM

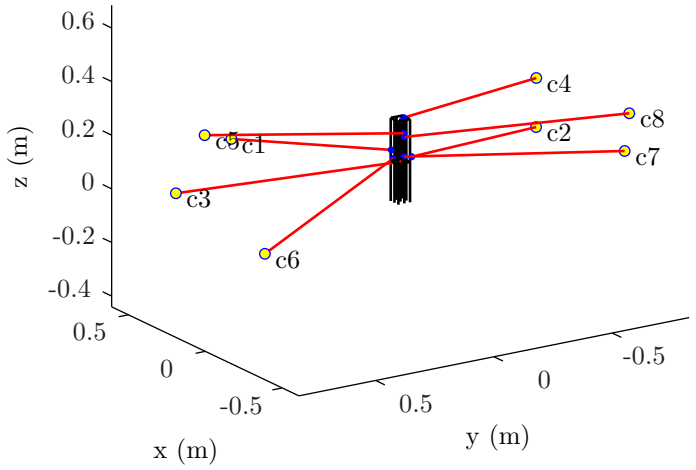

(b) The final geometry of the CDPM

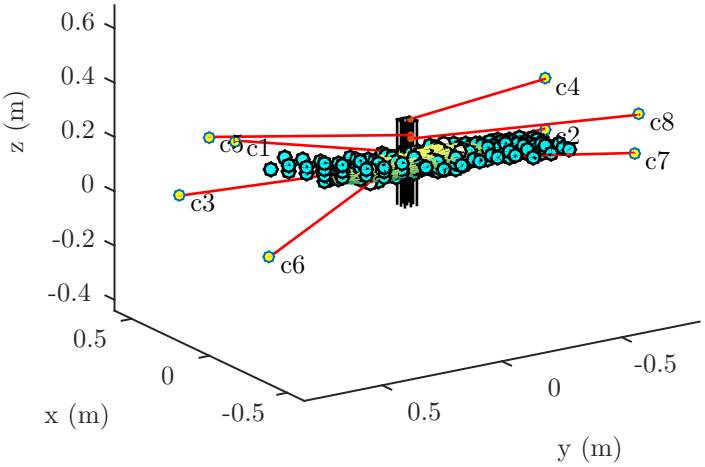

(c) The WCW of the final CDPM's geometry with the final $\mathcal{W}_t$ ($\kappa = 0.6166$)

Figure D.26 – Illustration of different results obtained from the optimization of a CDPM (Trial 36) for the numerical application of the dimensional synthesis program presented in Sub-section 4.3.2.

Table D.20 and Fig. D.27 present and illustrate the geometric parameters and the final wrench-closure workspace (WCW) as well as the final ellipsoid $\mathcal{W}_t$ ($\kappa = 0.6083$) resulting from the dimensional synthesis (Trial 39) of the CDPM presented in Sub-section 4.3.2.

	$\mathbf{a}_{1,r}$	$\mathbf{a}_{2,r}$	$\mathbf{a}_{3,r}$	$\mathbf{a}_{4,r}$	$\mathbf{a}_{5,r}$	$\mathbf{a}_{6,r}$	$\mathbf{a}_{7,r}$	$\mathbf{a}_{8,r}$
x (m)	−0.3084	−0.1289	0.1909	0.1375	−0.2623	−0.2589	−0.2854	−0.3445
y (m)	−0.1230	0.2489	0.3567	0.0499	−0.6259	0.2108	−0.5976	−0.5851
z (m)	0.0345	0.0497	0.0589	0.0687	0.1111	0.1108	0.0761	0.0879
	$\mathbf{b}^{\mathcal{B}}_{1,r}$	$\mathbf{b}^{\mathcal{B}}_{2,r}$	$\mathbf{b}^{\mathcal{B}}_{3,r}$	$\mathbf{b}^{\mathcal{B}}_{4,r}$	$\mathbf{b}^{\mathcal{B}}_{5,r}$	$\mathbf{b}^{\mathcal{B}}_{6,r}$	$\mathbf{b}^{\mathcal{B}}_{7,r}$	$\mathbf{b}^{\mathcal{B}}_{8,r}$
$x^{\mathcal{B}}$ (m)	0.0314	0.0163	0.0045	−0.0252	−0.0230	−0.0338	0.0331	0.0165
$y^{\mathcal{B}}$ (m)	0.0046	−0.0149	−0.0267	0.0098	0.0390	−0.0264	−0.0194	−0.0083
$z^{\mathcal{B}}$ (m)	0.0118	0.1095	0.0644	0.1573	0.0643	0.0993	0.0247	0.0610

(a) Randomly-determined geometric parameters $\mathbf{a}_{i,r}$ and $\mathbf{b}^{\mathcal{B}}_{i,r}$

	$\mathbf{a}_{1,0}$	$\mathbf{a}_{2,0}$	$\mathbf{a}_{3,0}$	$\mathbf{a}_{4,0}$	$\mathbf{a}_{5,0}$	$\mathbf{a}_{6,0}$	$\mathbf{a}_{7,0}$	$\mathbf{a}_{8,0}$
x (m)	0.0228	0.0760	0.2380	0.2412	−0.0228	−0.0759	−0.2380	−0.2412
y (m)	−0.0847	−0.0626	0.0626	0.0847	−0.0100	0.4043	−0.4043	0.0100
z (m)	0.1549	0.0961	0.0782	0.0807	0.1549	0.0961	0.0782	0.0806
	$\mathbf{b}^{\mathcal{B}}_{1,0}$	$\mathbf{b}^{\mathcal{B}}_{2,0}$	$\mathbf{b}^{\mathcal{B}}_{3,0}$	$\mathbf{b}^{\mathcal{B}}_{4,0}$	$\mathbf{b}^{\mathcal{B}}_{5,0}$	$\mathbf{b}^{\mathcal{B}}_{6,0}$	$\mathbf{b}^{\mathcal{B}}_{7,0}$	$\mathbf{b}^{\mathcal{B}}_{8,0}$
$x^{\mathcal{B}}$ (m)	0.0067	0.0116	0.0155	−0.0209	−0.0030	0.0083	0.0314	0.0212
$y^{\mathcal{B}}$ (m)	−0.0086	−0.0229	0.0065	0.0119	0.0081	0.0061	−0.0252	−0.0065
$z^{\mathcal{B}}$ (m)	0.0170	0.1108	0.0127	0.1545	0.0174	0.0385	0.0390	0.0510

(b) Closest-feasible initial geometric parameters $\mathbf{a}_{i,0}$ and $\mathbf{b}^{\mathcal{B}}_{i,0}$

	$\mathbf{a}_{1,f}$	$\mathbf{a}_{2,f}$	$\mathbf{a}_{3,f}$	$\mathbf{a}_{4,f}$	$\mathbf{a}_{5,f}$	$\mathbf{a}_{6,f}$	$\mathbf{a}_{7,f}$	$\mathbf{a}_{8,f}$
x (m)	0.2489	0.3454	0.2402	0.2715	−0.2489	−0.3454	−0.2402	−0.2715
y (m)	−0.7992	−0.7999	0.7999	0.7992	−0.3952	0.5046	−0.5046	0.3952
z (m)	0.2455	0.0341	0.1763	0.2160	0.2455	0.0341	0.1763	0.2160
	$\mathbf{b}^{\mathcal{B}}_{1,f}$	$\mathbf{b}^{\mathcal{B}}_{2,f}$	$\mathbf{b}^{\mathcal{B}}_{3,f}$	$\mathbf{b}^{\mathcal{B}}_{4,f}$	$\mathbf{b}^{\mathcal{B}}_{5,f}$	$\mathbf{b}^{\mathcal{B}}_{6,f}$	$\mathbf{b}^{\mathcal{B}}_{7,f}$	$\mathbf{b}^{\mathcal{B}}_{8,f}$
$x^{\mathcal{B}}$ (m)	0.0100	0.0399	0.0211	0.0399	−0.0400	0.0398	0.0400	−0.0399
$y^{\mathcal{B}}$ (m)	−0.0209	0.0310	−0.0020	0.0397	0.0233	0.0362	−0.0399	0.0030
$z^{\mathcal{B}}$ (m)	0.0219	0.0776	0.0000	0.1599	0.0415	0.0597	0.0282	0.1246

(c) Final geometric parameters $\mathbf{a}_{i,f}$ and $\mathbf{b}^{\mathcal{B}}_{i,f}$

Table D.20 – Geometric parameters of the CDPM corresponding to the Trial 39 of the numerical application of the dimensional synthesis program presented in Sub-section 4.3.2.

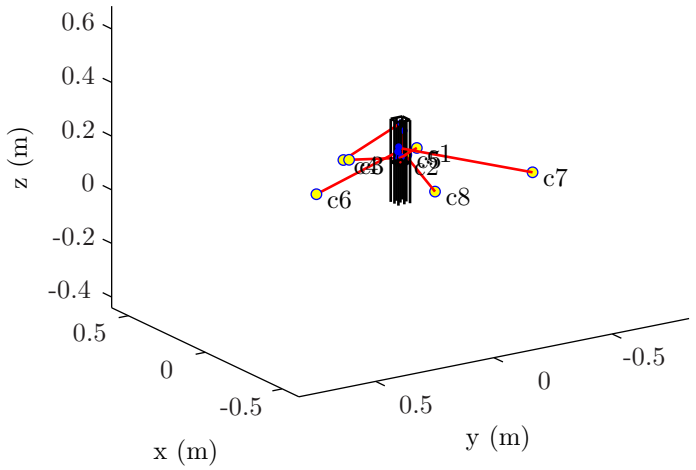

(a) The initial geometry of the CDPM

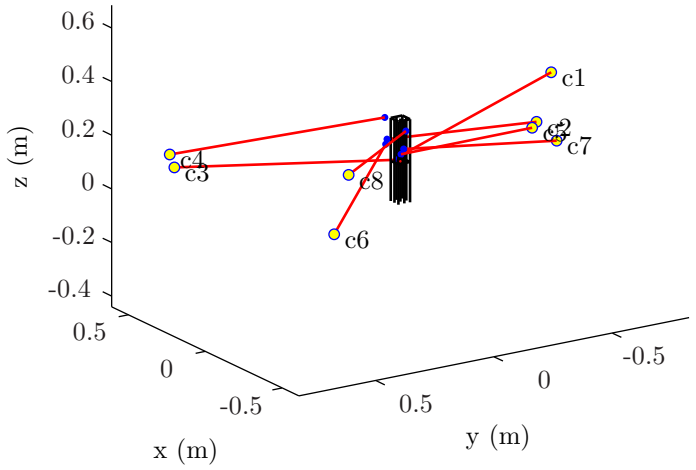

(b) The final geometry of the CDPM

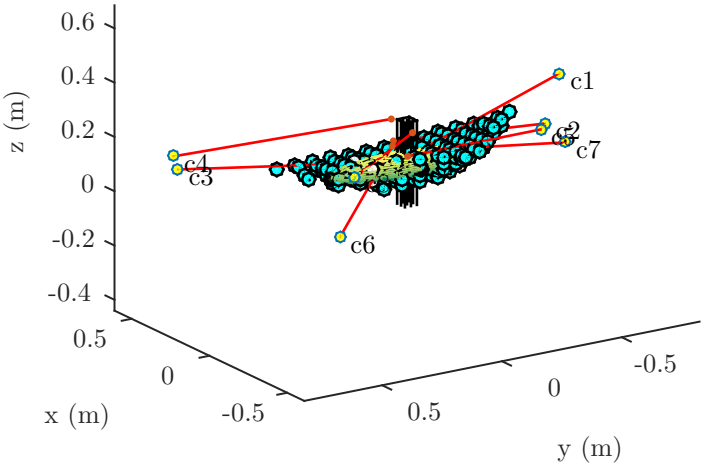

(c) The WCW of the final CDPM's geometry with the final $\mathcal{W}_t$ ($\kappa = 0.6083$)

Figure D.27 – Illustration of different results obtained from the optimization of a CDPM (Trial 39) for the numerical application of the dimensional synthesis program presented in Sub-section 4.3.2.

Table D.21 and Fig. D.28 present and illustrate the geometric parameters and the final wrench-closure workspace (WCW) as well as the final ellipsoid $\mathcal{W}_t$ ($\kappa = 0.6533$) resulting from the dimensional synthesis (Trial 41) of the CDPM presented in Sub-section 4.3.2.

	$\mathbf{a}_{1,r}$	$\mathbf{a}_{2,r}$	$\mathbf{a}_{3,r}$	$\mathbf{a}_{4,r}$	$\mathbf{a}_{5,r}$	$\mathbf{a}_{6,r}$	$\mathbf{a}_{7,r}$	$\mathbf{a}_{8,r}$
x (m)	0.2164	0.1740	−0.2659	0.0175	−0.1219	0.0325	−0.0708	−0.0594
y (m)	−0.5108	−0.3914	−0.7671	0.6779	0.2459	0.6922	−0.5384	0.6738
z (m)	0.2781	0.2021	0.1540	0.0902	0.2632	0.0800	0.0225	0.2686
	$\mathbf{b}^{\mathcal{B}}_{1,r}$	$\mathbf{b}^{\mathcal{B}}_{2,r}$	$\mathbf{b}^{\mathcal{B}}_{3,r}$	$\mathbf{b}^{\mathcal{B}}_{4,r}$	$\mathbf{b}^{\mathcal{B}}_{5,r}$	$\mathbf{b}^{\mathcal{B}}_{6,r}$	$\mathbf{b}^{\mathcal{B}}_{7,r}$	$\mathbf{b}^{\mathcal{B}}_{8,r}$
$x^{\mathcal{B}}$ (m)	0.0137	0.0172	0.0114	−0.0065	−0.0087	0.0253	−0.0146	0.0252
$y^{\mathcal{B}}$ (m)	0.0231	0.0282	0.0005	0.0109	0.0361	−0.0045	−0.0352	0.0293
$z^{\mathcal{B}}$ (m)	0.1010	0.0568	0.1595	0.0359	0.1044	0.0968	0.0620	0.0227

(a) Randomly-determined geometric parameters $\mathbf{a}_{i,r}$ and $\mathbf{b}^{\mathcal{B}}_{i,r}$

	$\mathbf{a}_{1,0}$	$\mathbf{a}_{2,0}$	$\mathbf{a}_{3,0}$	$\mathbf{a}_{4,0}$	$\mathbf{a}_{5,0}$	$\mathbf{a}_{6,0}$	$\mathbf{a}_{7,0}$	$\mathbf{a}_{8,0}$
x (m)	0.1740	0.0708	0.0052	0.0418	−0.1740	−0.0708	−0.0052	−0.0418
y (m)	−0.5941	0.1873	−0.1873	0.5941	−0.2138	0.6161	−0.6161	0.2138
z (m)	0.2650	0.1339	0.1750	0.1750	0.2650	0.1339	0.1750	0.1750
	$\mathbf{b}^{\mathcal{B}}_{1,0}$	$\mathbf{b}^{\mathcal{B}}_{2,0}$	$\mathbf{b}^{\mathcal{B}}_{3,0}$	$\mathbf{b}^{\mathcal{B}}_{4,0}$	$\mathbf{b}^{\mathcal{B}}_{5,0}$	$\mathbf{b}^{\mathcal{B}}_{6,0}$	$\mathbf{b}^{\mathcal{B}}_{7,0}$	$\mathbf{b}^{\mathcal{B}}_{8,0}$
$x^{\mathcal{B}}$ (m)	0.0014	0.0108	0.0203	−0.0272	0.0086	0.0038	−0.0110	0.0299
$y^{\mathcal{B}}$ (m)	−0.0104	0.0208	−0.0113	0.0131	−0.0104	0.0106	−0.0285	0.0297
$z^{\mathcal{B}}$ (m)	0.0911	0.0706	0.1552	0.0476	0.0870	0.1168	0.0520	0.0226

(b) Closest-feasible initial geometric parameters $\mathbf{a}_{i,0}$ and $\mathbf{b}^{\mathcal{B}}_{i,0}$

	$\mathbf{a}_{1,f}$	$\mathbf{a}_{2,f}$	$\mathbf{a}_{3,f}$	$\mathbf{a}_{4,f}$	$\mathbf{a}_{5,f}$	$\mathbf{a}_{6,f}$	$\mathbf{a}_{7,f}$	$\mathbf{a}_{8,f}$
x (m)	0.2168	0.3249	0.0720	0.2546	−0.2168	−0.3249	−0.0720	−0.2546
y (m)	−0.5340	0.5755	−0.5755	0.5340	−0.6941	0.8000	−0.8000	0.6941
z (m)	0.2710	0.0603	0.0994	0.2382	0.2710	0.0603	0.0994	0.2382
	$\mathbf{b}^{\mathcal{B}}_{1,f}$	$\mathbf{b}^{\mathcal{B}}_{2,f}$	$\mathbf{b}^{\mathcal{B}}_{3,f}$	$\mathbf{b}^{\mathcal{B}}_{4,f}$	$\mathbf{b}^{\mathcal{B}}_{5,f}$	$\mathbf{b}^{\mathcal{B}}_{6,f}$	$\mathbf{b}^{\mathcal{B}}_{7,f}$	$\mathbf{b}^{\mathcal{B}}_{8,f}$
$x^{\mathcal{B}}$ (m)	0.0384	0.0311	0.0338	−0.0400	0.0400	−0.0289	−0.0400	0.0280
$y^{\mathcal{B}}$ (m)	−0.0144	−0.0192	−0.0088	0.0238	−0.0169	0.0052	0.0135	0.0237
$z^{\mathcal{B}}$ (m)	0.0850	0.0413	0.1415	0.0506	0.0850	0.0839	0.0000	0.0364

(c) Final geometric parameters $\mathbf{a}_{i,f}$ and $\mathbf{b}^{\mathcal{B}}_{i,f}$

Table D.21 – Geometric parameters of the CDPM corresponding to the Trial 41 of the numerical application of the dimensional synthesis program presented in Sub-section 4.3.2.

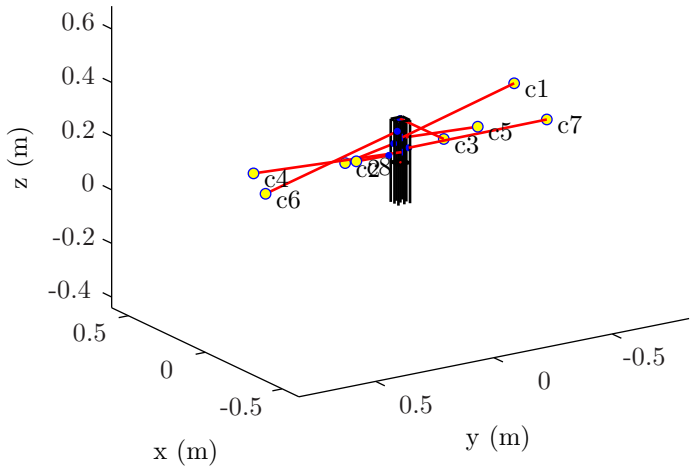

(a) The initial geometry of the CDPM

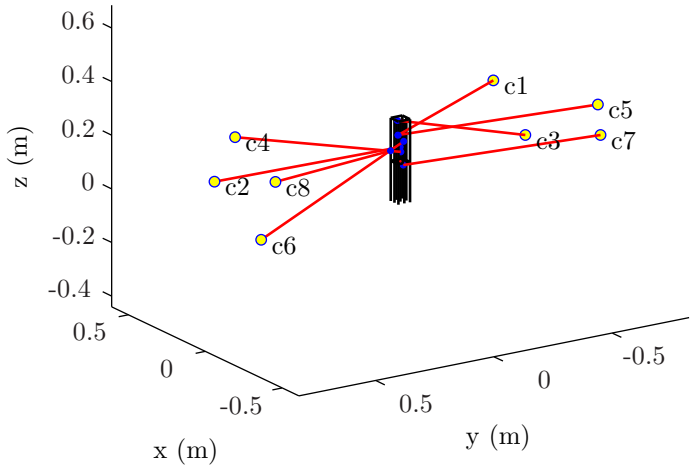

(b) The final geometry of the CDPM

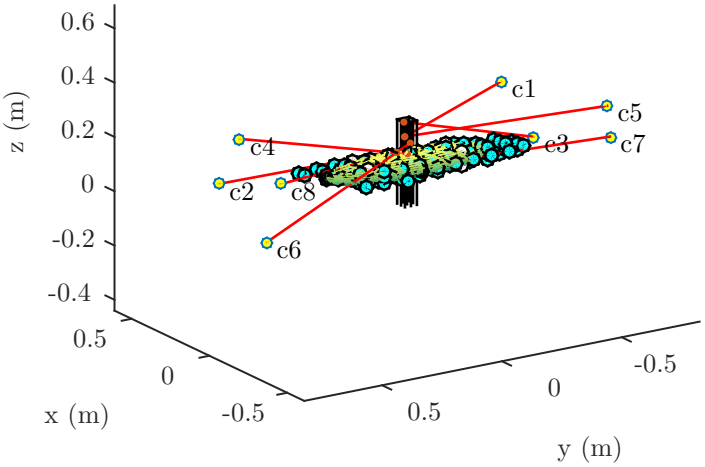

(c) The WCW of the final CDPM's geometry with the final $\mathcal{W}_t$ ($\kappa = 0.6533$)

Figure D.28 – Illustration of different results obtained from the optimization of a CDPM (Trial 41) for the numerical application of the dimensional synthesis program presented in Sub-section 4.3.2.

Table D.22 and Fig. D.29 present and illustrate the geometric parameters and the final wrench-closure workspace (WCW) as well as the final ellipsoid $\mathcal{W}_t$ ($\kappa = 0.6745$) resulting from the dimensional synthesis (Trial 45) of the CDPM presented in Sub-section 4.3.2.

	$\mathbf{a}_{1,r}$	$\mathbf{a}_{2,r}$	$\mathbf{a}_{3,r}$	$\mathbf{a}_{4,r}$	$\mathbf{a}_{5,r}$	$\mathbf{a}_{6,r}$	$\mathbf{a}_{7,r}$	$\mathbf{a}_{8,r}$
x (m)	−0.1097	0.3052	−0.2627	0.1614	0.1025	0.2332	−0.0712	0.1749
y (m)	0.5364	−0.2841	0.0836	0.7666	0.0789	−0.2713	0.1912	−0.2230
z (m)	0.2648	0.1449	0.1723	0.2432	0.3405	0.1147	0.2932	0.2587
	$\mathbf{b}^{\mathcal{B}}_{1,r}$	$\mathbf{b}^{\mathcal{B}}_{2,r}$	$\mathbf{b}^{\mathcal{B}}_{3,r}$	$\mathbf{b}^{\mathcal{B}}_{4,r}$	$\mathbf{b}^{\mathcal{B}}_{5,r}$	$\mathbf{b}^{\mathcal{B}}_{6,r}$	$\mathbf{b}^{\mathcal{B}}_{7,r}$	$\mathbf{b}^{\mathcal{B}}_{8,r}$
$x^{\mathcal{B}}$ (m)	0.0363	−0.0374	−0.0115	0.0130	−0.0175	−0.0216	0.0169	0.0100
$y^{\mathcal{B}}$ (m)	0.0072	0.0128	−0.0362	−0.0121	−0.0039	−0.0207	0.0172	0.0285
$z^{\mathcal{B}}$ (m)	0.0450	0.1170	0.0220	0.1339	0.0222	0.0941	0.0586	0.1291

(a) Randomly-determined geometric parameters $\mathbf{a}_{i,r}$ and $\mathbf{b}^{\mathcal{B}}_{i,r}$

	$\mathbf{a}_{1,0}$	$\mathbf{a}_{2,0}$	$\mathbf{a}_{3,0}$	$\mathbf{a}_{4,0}$	$\mathbf{a}_{5,0}$	$\mathbf{a}_{6,0}$	$\mathbf{a}_{7,0}$	$\mathbf{a}_{8,0}$
x (m)	−0.1110	0.0473	−0.0709	0.0569	0.1110	−0.0472	0.0709	−0.0568
y (m)	−0.0379	−0.0099	0.0099	0.0380	0.0836	−0.1842	0.1842	−0.0836
z (m)	0.3193	0.1272	0.2606	0.1333	0.3193	0.1273	0.2606	0.1333
	$\mathbf{b}^{\mathcal{B}}_{1,0}$	$\mathbf{b}^{\mathcal{B}}_{2,0}$	$\mathbf{b}^{\mathcal{B}}_{3,0}$	$\mathbf{b}^{\mathcal{B}}_{4,0}$	$\mathbf{b}^{\mathcal{B}}_{5,0}$	$\mathbf{b}^{\mathcal{B}}_{6,0}$	$\mathbf{b}^{\mathcal{B}}_{7,0}$	$\mathbf{b}^{\mathcal{B}}_{8,0}$
$x^{\mathcal{B}}$ (m)	0.0351	−0.0397	0.0236	0.0366	−0.0395	−0.0398	0.0398	0.0390
$y^{\mathcal{B}}$ (m)	−0.0255	−0.0067	−0.0051	0.0026	0.0071	−0.0154	0.0065	−0.0370
$z^{\mathcal{B}}$ (m)	0.0335	0.0428	0.0114	0.0562	0.1133	0.0790	0.1000	0.0808

(b) Closest-feasible initial geometric parameters $\mathbf{a}_{i,0}$ and $\mathbf{b}^{\mathcal{B}}_{i,0}$

	$\mathbf{a}_{1,f}$	$\mathbf{a}_{2,f}$	$\mathbf{a}_{3,f}$	$\mathbf{a}_{4,f}$	$\mathbf{a}_{5,f}$	$\mathbf{a}_{6,f}$	$\mathbf{a}_{7,f}$	$\mathbf{a}_{8,f}$
x (m)	−0.0648	0.3458	−0.0624	0.3498	0.0648	−0.3458	0.0624	−0.3498
y (m)	−0.7992	−0.7994	0.7994	0.7992	0.7967	−0.7998	0.7998	−0.7967
z (m)	0.3168	0.0002	0.2688	0.0004	0.3168	0.0002	0.2688	0.0004
	$\mathbf{b}^{\mathcal{B}}_{1,f}$	$\mathbf{b}^{\mathcal{B}}_{2,f}$	$\mathbf{b}^{\mathcal{B}}_{3,f}$	$\mathbf{b}^{\mathcal{B}}_{4,f}$	$\mathbf{b}^{\mathcal{B}}_{5,f}$	$\mathbf{b}^{\mathcal{B}}_{6,f}$	$\mathbf{b}^{\mathcal{B}}_{7,f}$	$\mathbf{b}^{\mathcal{B}}_{8,f}$
$x^{\mathcal{B}}$ (m)	0.0269	−0.0322	0.0159	0.0396	−0.0400	−0.0399	0.0400	0.0400
$y^{\mathcal{B}}$ (m)	−0.0389	−0.0219	−0.0204	−0.0192	0.0094	−0.0391	0.0057	−0.0399
$z^{\mathcal{B}}$ (m)	0.0405	0.0802	0.0341	0.0002	0.0991	0.0500	0.1559	0.0772

(c) Final geometric parameters $\mathbf{a}_{i,f}$ and $\mathbf{b}^{\mathcal{B}}_{i,f}$

Table D.22 – Geometric parameters of the CDPM corresponding to the Trial 45 of the numerical application of the dimensional synthesis program presented in Sub-section 4.3.2.

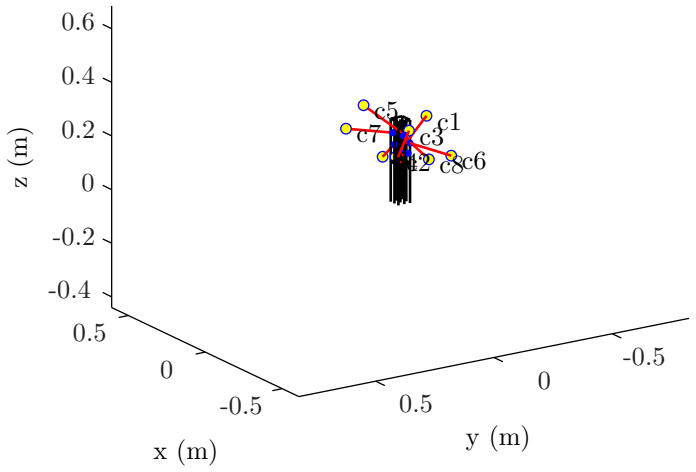

(a) The initial geometry of the CDPM

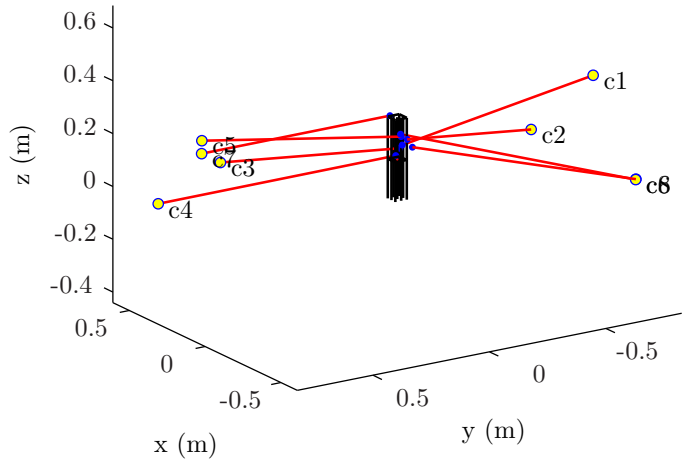

(b) The final geometry of the CDPM

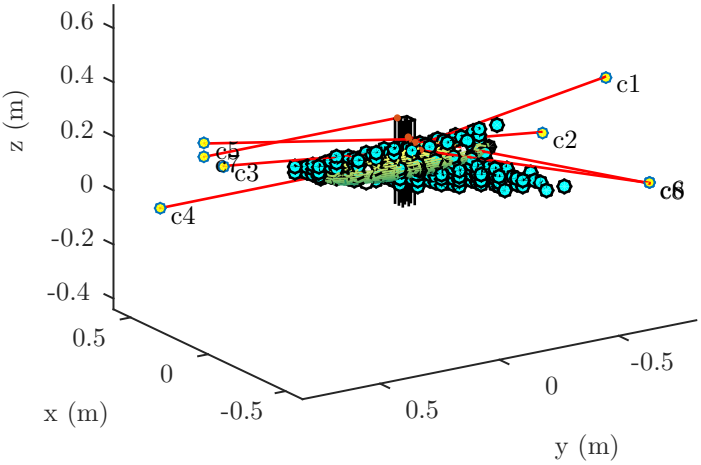

(c) The WCW of the final CDPM's geometry with the final $\mathcal{W}_t$ ($\kappa = 0.6745$)

Figure D.29 – Illustration of different results obtained from the optimization of a CDPM (Trial 45) for the numerical application of the dimensional synthesis program presented in Sub-section 4.3.2.

Table D.23 and Fig. D.30 present and illustrate the geometric parameters and the final wrench-closure workspace (WCW) as well as the final ellipsoid $\mathcal{W}_t$ ($\kappa = 0.9835$) resulting from the dimensional synthesis (Trial 64) of the CDPM presented in Sub-section 4.3.2.

	$\mathbf{a}_{1,r}$	$\mathbf{a}_{2,r}$	$\mathbf{a}_{3,r}$	$\mathbf{a}_{4,r}$	$\mathbf{a}_{5,r}$	$\mathbf{a}_{6,r}$	$\mathbf{a}_{7,r}$	$\mathbf{a}_{8,r}$
x (m)	0.3194	0.0511	0.2448	−0.1566	0.0856	0.0619	0.3244	−0.2899
y (m)	0.0008	0.0345	−0.6557	0.6475	0.6150	−0.0976	0.4508	−0.5625
z (m)	0.2169	0.0912	0.1560	0.2954	0.0687	0.1063	0.1692	0.1182
	$\mathbf{b}^{\mathcal{B}}_{1,r}$	$\mathbf{b}^{\mathcal{B}}_{2,r}$	$\mathbf{b}^{\mathcal{B}}_{3,r}$	$\mathbf{b}^{\mathcal{B}}_{4,r}$	$\mathbf{b}^{\mathcal{B}}_{5,r}$	$\mathbf{b}^{\mathcal{B}}_{6,r}$	$\mathbf{b}^{\mathcal{B}}_{7,r}$	$\mathbf{b}^{\mathcal{B}}_{8,r}$
$x^{\mathcal{B}}$ (m)	0.0239	0.0390	−0.0273	−0.0210	0.0162	−0.0100	0.0379	0.0378
$y^{\mathcal{B}}$ (m)	0.0115	0.0288	−0.0078	0.0106	0.0388	0.0048	0.0347	0.0176
$z^{\mathcal{B}}$ (m)	0.0774	0.1022	0.1420	0.0318	0.0633	0.1587	0.0644	0.1054

(a) Randomly-determined geometric parameters $\mathbf{a}_{i,r}$ and $\mathbf{b}^{\mathcal{B}}_{i,r}$

	$\mathbf{a}_{1,0}$	$\mathbf{a}_{2,0}$	$\mathbf{a}_{3,0}$	$\mathbf{a}_{4,0}$	$\mathbf{a}_{5,0}$	$\mathbf{a}_{6,0}$	$\mathbf{a}_{7,0}$	$\mathbf{a}_{8,0}$
x (m)	0.1367	0.0352	−0.0157	0.0554	−0.1367	−0.0352	0.0157	−0.0554
y (m)	−0.0100	0.3309	−0.3309	0.0100	0.5128	−0.3046	0.3046	−0.5128
z (m)	0.1500	0.1411	0.1987	0.2184	0.1500	0.1411	0.1987	0.2184
	$\mathbf{b}^{\mathcal{B}}_{1,0}$	$\mathbf{b}^{\mathcal{B}}_{2,0}$	$\mathbf{b}^{\mathcal{B}}_{3,0}$	$\mathbf{b}^{\mathcal{B}}_{4,0}$	$\mathbf{b}^{\mathcal{B}}_{5,0}$	$\mathbf{b}^{\mathcal{B}}_{6,0}$	$\mathbf{b}^{\mathcal{B}}_{7,0}$	$\mathbf{b}^{\mathcal{B}}_{8,0}$
$x^{\mathcal{B}}$ (m)	0.0258	0.0369	−0.0359	−0.0254	0.0092	−0.0016	0.0363	0.0232
$y^{\mathcal{B}}$ (m)	0.0076	0.0273	−0.0134	0.0136	0.0120	−0.0104	0.0299	−0.0089
$z^{\mathcal{B}}$ (m)	0.0802	0.1103	0.1350	0.0302	0.0722	0.1548	0.0713	0.0667

(b) Closest-feasible initial geometric parameters $\mathbf{a}_{i,0}$ and $\mathbf{b}^{\mathcal{B}}_{i,0}$

	$\mathbf{a}_{1,f}$	$\mathbf{a}_{2,f}$	$\mathbf{a}_{3,f}$	$\mathbf{a}_{4,f}$	$\mathbf{a}_{5,f}$	$\mathbf{a}_{6,f}$	$\mathbf{a}_{7,f}$	$\mathbf{a}_{8,f}$
x (m)	0.3499	0.3498	0.1988	0.1857	−0.3499	−0.3498	−0.1988	−0.1857
y (m)	−0.7441	0.7999	−0.7999	0.7441	0.6948	−0.7999	0.7999	−0.6948
z (m)	0.0000	0.0000	0.2725	0.2949	0.0000	0.0000	0.2725	0.2949
	$\mathbf{b}^{\mathcal{B}}_{1,f}$	$\mathbf{b}^{\mathcal{B}}_{2,f}$	$\mathbf{b}^{\mathcal{B}}_{3,f}$	$\mathbf{b}^{\mathcal{B}}_{4,f}$	$\mathbf{b}^{\mathcal{B}}_{5,f}$	$\mathbf{b}^{\mathcal{B}}_{6,f}$	$\mathbf{b}^{\mathcal{B}}_{7,f}$	$\mathbf{b}^{\mathcal{B}}_{8,f}$
$x^{\mathcal{B}}$ (m)	0.0307	0.0358	−0.0400	−0.0395	−0.0334	−0.0397	0.0398	0.0390
$y^{\mathcal{B}}$ (m)	−0.0004	0.0221	−0.0400	0.0203	−0.0118	−0.0061	0.0400	−0.0221
$z^{\mathcal{B}}$ (m)	0.0106	0.1033	0.1012	0.0105	0.0219	0.0998	0.0838	0.0202

(c) Final geometric parameters $\mathbf{a}_{i,f}$ and $\mathbf{b}^{\mathcal{B}}_{i,f}$

Table D.23 – Geometric parameters of the CDPM corresponding to the Trial 64 of the numerical application of the dimensional synthesis program presented in Sub-section 4.3.2.

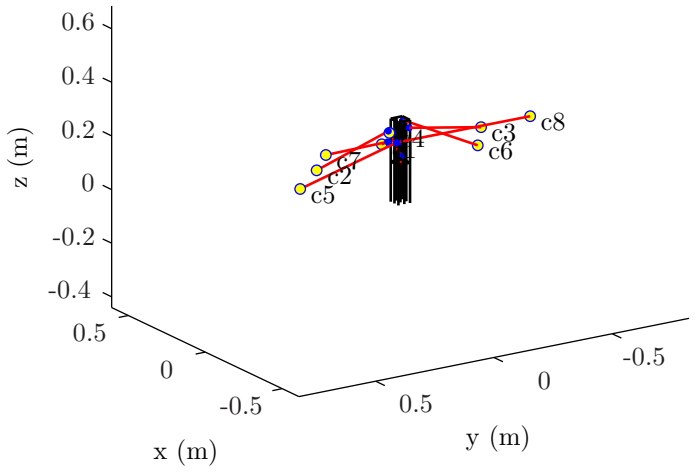

(a) The initial geometry of the CDPM

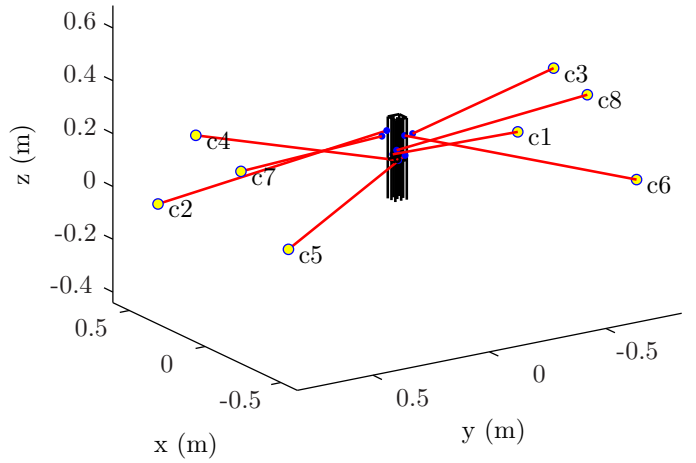

(b) The final geometry of the CDPM

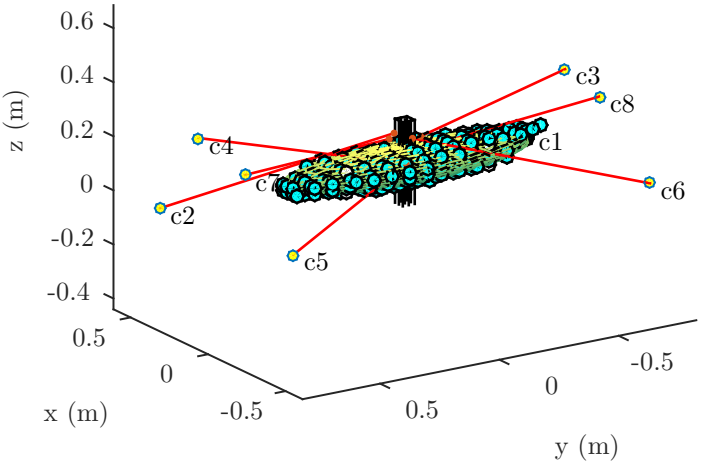

(c) The WCW of the final CDPM's geometry with the final $\mathcal{W}_t$ ($\kappa = 0.9835$)

Figure D.30 – Illustration of different results obtained from the optimization of a CDPM (Trial 64) for the numerical application of the dimensional synthesis program presented in Sub-section 4.3.2.

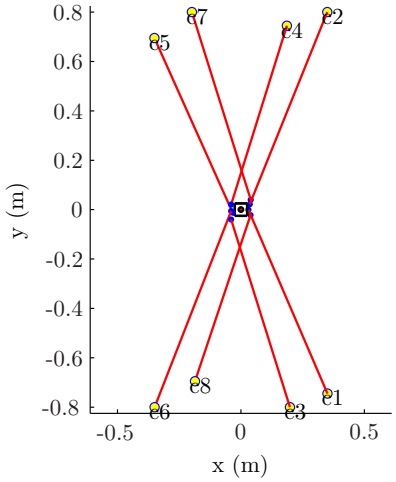

(a) An XY view of the final CDPM's geometry

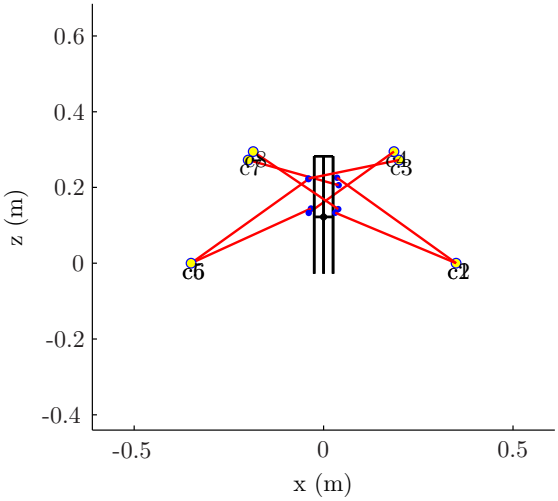

(b) An XZ view of the final CDPM's geometry

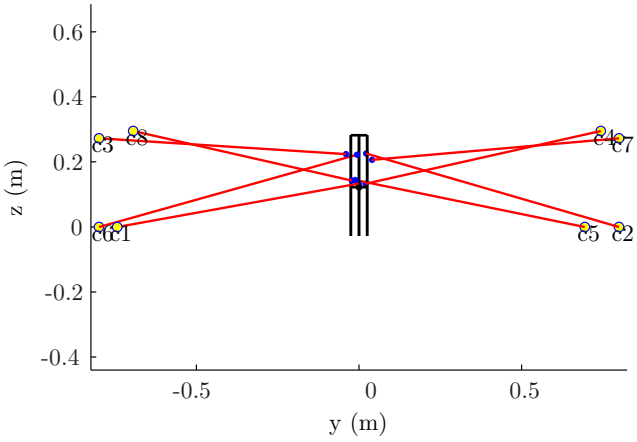

(c) An YZ view of the final CDPM's geometry

Figure D.31 – Three different two-dimensional points of view of the optimized CDPM's geometry (Trial 64) from the numerical application of the dimensional synthesis program presented in Sub-section 4.3.2 ($\kappa = 0.9835$).

Table D.24 and Fig. D.32 present and illustrate the geometric parameters and the final wrench-closure workspace (WCW) as well as the final ellipsoid $\mathcal{W}_t$ ($\kappa = 0.6203$) resulting from the dimensional synthesis (Trial 66) of the CDPM presented in Sub-section 4.3.2.

	$\mathbf{a}_{1,r}$	$\mathbf{a}_{2,r}$	$\mathbf{a}_{3,r}$	$\mathbf{a}_{4,r}$	$\mathbf{a}_{5,r}$	$\mathbf{a}_{6,r}$	$\mathbf{a}_{7,r}$	$\mathbf{a}_{8,r}$
x (m)	−0.2744	−0.0281	−0.0344	0.0358	0.2138	0.1406	0.2606	−0.3135
y (m)	−0.4485	−0.0646	0.7337	0.4641	−0.0770	−0.2665	−0.7054	0.3854
z (m)	0.1774	0.0700	0.1495	0.0590	0.2631	0.1289	0.3296	0.0060
	$\mathbf{b}^{\mathcal{B}}_{1,r}$	$\mathbf{b}^{\mathcal{B}}_{2,r}$	$\mathbf{b}^{\mathcal{B}}_{3,r}$	$\mathbf{b}^{\mathcal{B}}_{4,r}$	$\mathbf{b}^{\mathcal{B}}_{5,r}$	$\mathbf{b}^{\mathcal{B}}_{6,r}$	$\mathbf{b}^{\mathcal{B}}_{7,r}$	$\mathbf{b}^{\mathcal{B}}_{8,r}$
$x^{\mathcal{B}}$ (m)	0.0263	0.0101	0.0031	0.0120	0.0181	−0.0324	0.0302	−0.0389
$y^{\mathcal{B}}$ (m)	−0.0165	−0.0256	0.0341	−0.0345	0.0065	0.0110	0.0121	0.0292
$z^{\mathcal{B}}$ (m)	0.0090	0.1307	0.0846	0.1111	0.0340	0.0869	0.1124	0.1530

(a) Randomly-determined geometric parameters $\mathbf{a}_{i,r}$ and $\mathbf{b}^{\mathcal{B}}_{i,r}$

	$\mathbf{a}_{1,0}$	$\mathbf{a}_{2,0}$	$\mathbf{a}_{3,0}$	$\mathbf{a}_{4,0}$	$\mathbf{a}_{5,0}$	$\mathbf{a}_{6,0}$	$\mathbf{a}_{7,0}$	$\mathbf{a}_{8,0}$
x (m)	−0.1316	0.0190	−0.0957	0.2083	0.1316	−0.0190	0.0957	−0.2083
y (m)	−0.5663	−0.2917	0.2917	0.5663	−0.2668	0.0100	−0.0100	0.2668
z (m)	0.3293	0.1593	0.2889	0.0342	0.3293	0.1593	0.2889	0.0342
	$\mathbf{b}^{\mathcal{B}}_{1,0}$	$\mathbf{b}^{\mathcal{B}}_{2,0}$	$\mathbf{b}^{\mathcal{B}}_{3,0}$	$\mathbf{b}^{\mathcal{B}}_{4,0}$	$\mathbf{b}^{\mathcal{B}}_{5,0}$	$\mathbf{b}^{\mathcal{B}}_{6,0}$	$\mathbf{b}^{\mathcal{B}}_{7,0}$	$\mathbf{b}^{\mathcal{B}}_{8,0}$
$x^{\mathcal{B}}$ (m)	−0.0073	0.0278	0.0378	0.0228	0.0085	−0.0332	0.0228	−0.0299
$y^{\mathcal{B}}$ (m)	−0.0092	−0.0086	0.0166	0.0078	−0.0085	0.0235	0.0079	0.0099
$z^{\mathcal{B}}$ (m)	0.0249	0.1481	0.0584	0.0954	0.0373	0.0907	0.1114	0.0967

(b) Closest-feasible initial geometric parameters $\mathbf{a}_{i,0}$ and $\mathbf{b}^{\mathcal{B}}_{i,0}$

	$\mathbf{a}_{1,f}$	$\mathbf{a}_{2,f}$	$\mathbf{a}_{3,f}$	$\mathbf{a}_{4,f}$	$\mathbf{a}_{5,f}$	$\mathbf{a}_{6,f}$	$\mathbf{a}_{7,f}$	$\mathbf{a}_{8,f}$
x (m)	−0.1455	0.1601	−0.1471	0.3500	0.1455	−0.1601	0.1471	−0.3500
y (m)	−0.7999	−0.7999	0.7999	0.7999	−0.6237	0.7875	−0.7875	0.6237
z (m)	0.3497	0.0001	0.3468	0.0000	0.3497	0.0001	0.3468	0.0000
	$\mathbf{b}^{\mathcal{B}}_{1,f}$	$\mathbf{b}^{\mathcal{B}}_{2,f}$	$\mathbf{b}^{\mathcal{B}}_{3,f}$	$\mathbf{b}^{\mathcal{B}}_{4,f}$	$\mathbf{b}^{\mathcal{B}}_{5,f}$	$\mathbf{b}^{\mathcal{B}}_{6,f}$	$\mathbf{b}^{\mathcal{B}}_{7,f}$	$\mathbf{b}^{\mathcal{B}}_{8,f}$
$x^{\mathcal{B}}$ (m)	−0.0343	0.0333	0.0400	0.0302	0.0257	−0.0399	0.0384	−0.0018
$y^{\mathcal{B}}$ (m)	−0.0076	−0.0026	−0.0090	−0.0035	−0.0397	−0.0146	0.0266	0.0275
$z^{\mathcal{B}}$ (m)	0.0265	0.1368	0.0374	0.0735	0.0001	0.0000	0.1431	0.1402

(c) Final geometric parameters $\mathbf{a}_{i,f}$ and $\mathbf{b}^{\mathcal{B}}_{i,f}$

Table D.24 – Geometric parameters of the CDPM corresponding to the Trial 66 of the numerical application of the dimensional synthesis program presented in Sub-section 4.3.2.

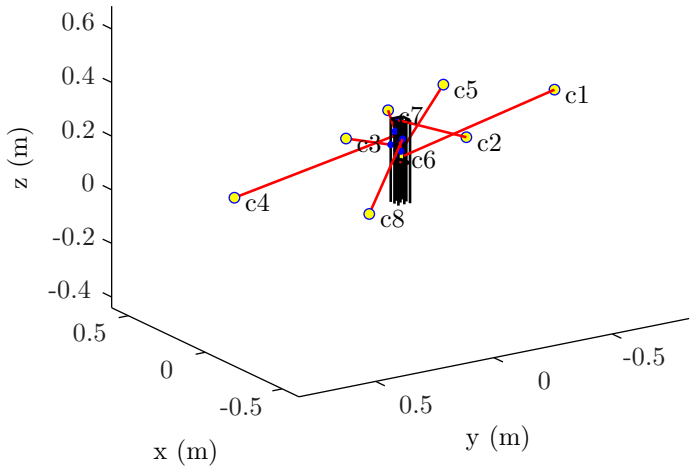

(a) The initial geometry of the CDPM

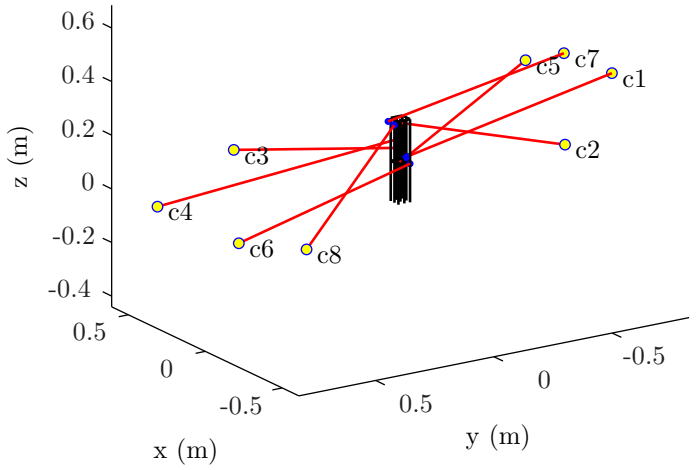

(b) The final geometry of the CDPM

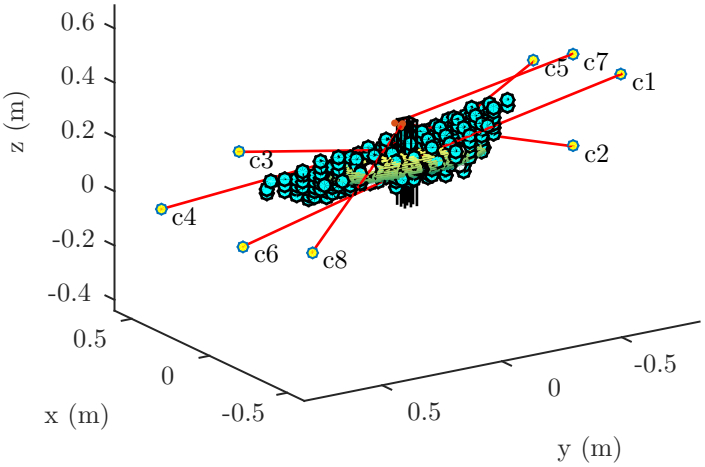

(c) The WCW of the final CDPM's geometry with the final $\mathcal{W}_t$ ($\kappa = 0.6203$)

Figure D.32 – Illustration of different results obtained from the optimization of a CDPM (Trial 66) for the numerical application of the dimensional synthesis program presented in Sub-section 4.3.2.

Table D.25 and Fig. D.33 present and illustrate the geometric parameters and the final wrench-closure workspace (WCW) as well as the final ellipsoid $\mathcal{W}_t$ ($\kappa = 0.7443$) resulting from the dimensional synthesis (Trial 81) of the CDPM presented in Sub-section 4.3.2.

	$\mathbf{a}_{1,r}$	$\mathbf{a}_{2,r}$	$\mathbf{a}_{3,r}$	$\mathbf{a}_{4,r}$	$\mathbf{a}_{5,r}$	$\mathbf{a}_{6,r}$	$\mathbf{a}_{7,r}$	$\mathbf{a}_{8,r}$
x (m)	0.2876	0.2697	0.2062	0.2981	−0.2248	0.0123	0.0889	0.2892
y (m)	0.2623	−0.1773	0.3840	0.5082	0.1606	−0.6640	0.6758	−0.7142
z (m)	0.1845	0.0416	0.1331	0.2845	0.0854	0.3095	0.2494	0.1324
	$\mathbf{b}^{\mathcal{B}}_{1,r}$	$\mathbf{b}^{\mathcal{B}}_{2,r}$	$\mathbf{b}^{\mathcal{B}}_{3,r}$	$\mathbf{b}^{\mathcal{B}}_{4,r}$	$\mathbf{b}^{\mathcal{B}}_{5,r}$	$\mathbf{b}^{\mathcal{B}}_{6,r}$	$\mathbf{b}^{\mathcal{B}}_{7,r}$	$\mathbf{b}^{\mathcal{B}}_{8,r}$
$x^{\mathcal{B}}$ (m)	−0.0201	−0.0198	0.0214	−0.0360	0.0148	0.0096	0.0197	0.0382
$y^{\mathcal{B}}$ (m)	−0.0093	−0.0192	0.0302	0.0245	−0.0031	−0.0327	0.0051	−0.0250
$z^{\mathcal{B}}$ (m)	0.0851	0.0568	0.0504	0.1163	0.0825	0.1265	0.0327	0.1085

(a) Randomly-determined geometric parameters $\mathbf{a}_{i,r}$ and $\mathbf{b}^{\mathcal{B}}_{i,r}$

	$\mathbf{a}_{1,0}$	$\mathbf{a}_{2,0}$	$\mathbf{a}_{3,0}$	$\mathbf{a}_{4,0}$	$\mathbf{a}_{5,0}$	$\mathbf{a}_{6,0}$	$\mathbf{a}_{7,0}$	$\mathbf{a}_{8,0}$
x (m)	0.2567	0.1282	0.0595	0.0086	−0.2567	−0.1282	−0.0595	−0.0086
y (m)	−0.1249	−0.2811	0.2811	0.1249	0.4372	−0.6698	0.6698	−0.4372
z (m)	0.1320	0.1771	0.1894	0.2127	0.1320	0.1771	0.1894	0.2127
	$\mathbf{b}^{\mathcal{B}}_{1,0}$	$\mathbf{b}^{\mathcal{B}}_{2,0}$	$\mathbf{b}^{\mathcal{B}}_{3,0}$	$\mathbf{b}^{\mathcal{B}}_{4,0}$	$\mathbf{b}^{\mathcal{B}}_{5,0}$	$\mathbf{b}^{\mathcal{B}}_{6,0}$	$\mathbf{b}^{\mathcal{B}}_{7,0}$	$\mathbf{b}^{\mathcal{B}}_{8,0}$
$x^{\mathcal{B}}$ (m)	−0.0091	−0.0156	0.0000	−0.0294	0.0175	0.0006	0.0384	0.0214
$y^{\mathcal{B}}$ (m)	−0.0124	−0.0195	0.0253	0.0209	0.0108	−0.0300	0.0119	−0.0142
$z^{\mathcal{B}}$ (m)	0.0935	0.0513	0.0528	0.1327	0.0744	0.1148	0.0548	0.0684

(b) Closest-feasible initial geometric parameters $\mathbf{a}_{i,0}$ and $\mathbf{b}^{\mathcal{B}}_{i,0}$

	$\mathbf{a}_{1,f}$	$\mathbf{a}_{2,f}$	$\mathbf{a}_{3,f}$	$\mathbf{a}_{4,f}$	$\mathbf{a}_{5,f}$	$\mathbf{a}_{6,f}$	$\mathbf{a}_{7,f}$	$\mathbf{a}_{8,f}$
x (m)	0.3498	0.3213	0.2487	0.0447	−0.3498	−0.3213	−0.2487	−0.0447
y (m)	−0.7999	−0.7659	0.7659	0.7999	0.7999	−0.7997	0.7997	−0.7999
z (m)	0.0000	0.0678	0.2458	0.3286	0.0000	0.0678	0.2458	0.3286
	$\mathbf{b}^{\mathcal{B}}_{1,f}$	$\mathbf{b}^{\mathcal{B}}_{2,f}$	$\mathbf{b}^{\mathcal{B}}_{3,f}$	$\mathbf{b}^{\mathcal{B}}_{4,f}$	$\mathbf{b}^{\mathcal{B}}_{5,f}$	$\mathbf{b}^{\mathcal{B}}_{6,f}$	$\mathbf{b}^{\mathcal{B}}_{7,f}$	$\mathbf{b}^{\mathcal{B}}_{8,f}$
$x^{\mathcal{B}}$ (m)	0.0387	−0.0383	−0.0400	0.0003	−0.0004	−0.0337	0.0400	0.0399
$y^{\mathcal{B}}$ (m)	0.0400	−0.0400	0.0334	0.0290	0.0228	−0.0253	0.0323	−0.0095
$z^{\mathcal{B}}$ (m)	0.0635	0.0626	0.0013	0.1600	0.0769	0.0761	0.0010	0.0667

(c) Final geometric parameters $\mathbf{a}_{i,f}$ and $\mathbf{b}^{\mathcal{B}}_{i,f}$

Table D.25 – Geometric parameters of the CDPM corresponding to the Trial 81 of the numerical application of the dimensional synthesis program presented in Sub-section 4.3.2.

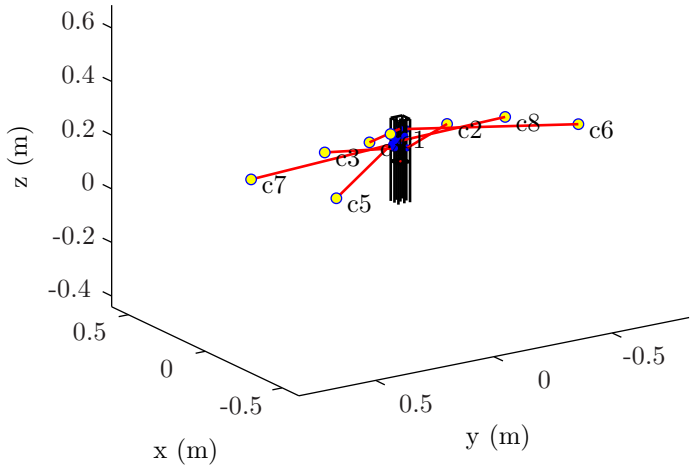

(a) The initial geometry of the CDPM

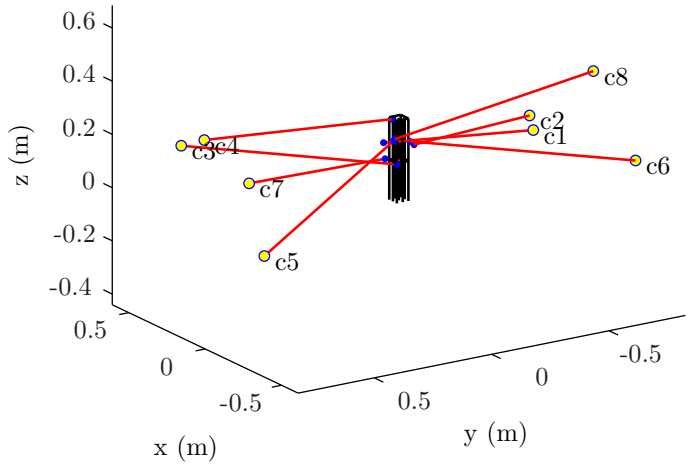

(b) The final geometry of the CDPM

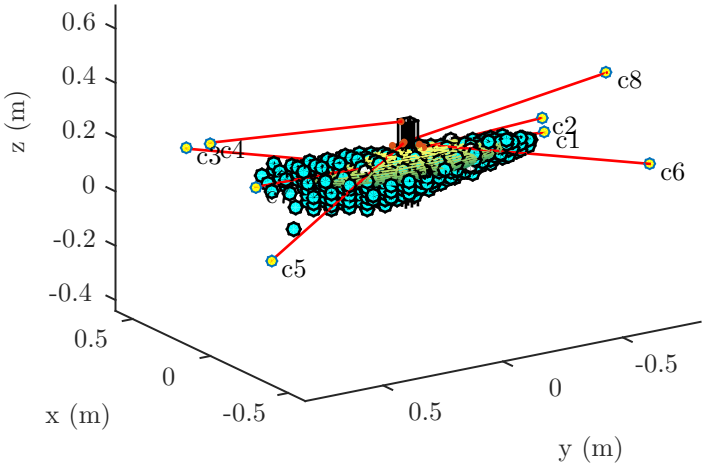

(c) The WCW of the final CDPM's geometry with the final $\mathcal{W}_t$ ($\kappa = 0.7443$)

Figure D.33 – Illustration of different results obtained from the optimization of a CDPM (Trial 81) for the numerical application of the dimensional synthesis program presented in Sub-section 4.3.2.

Table D.26 and Figs. D.34 and D.35 present and illustrate geometric parameters and the final wrench-closure workspace (WCW) as well as the final ellipsoid $\mathcal{W}_t$ ($\kappa = 1.0880$) resulting from the dimensional synthesis (Trial 100) of the CDPM presented in Sub-section 4.3.2.

Alike for previous Section D.1, here, the initial CDPM's geometry of Trial 100 was chosen based on author's intuition and experience[2]. These attachment points, i.e., $\mathbf{a}_{i,0}$ and $\mathbf{b}^{\mathcal{B}}_{i,0}$, have been selected to tend toward a CDPM that presents a WCW while avoiding the occurrence of mechanical interferences between its moving parts. However, one should note that this initial CDPM does not have a WCW, even at $\mathbf{p}_0$, because of its demanding geometrical constraints.

	$\mathbf{a}_{1,0}$	$\mathbf{a}_{2,0}$	$\mathbf{a}_{3,0}$	$\mathbf{a}_{4,0}$	$\mathbf{a}_{5,0}$	$\mathbf{a}_{6,0}$	$\mathbf{a}_{7,0}$	$\mathbf{a}_{8,0}$
x (m)	0.3500	0.2600	0.2600	0.3500	−0.3500	−0.2600	−0.2600	−0.3500
y (m)	−0.8000	−0.8000	0.8000	0.8000	−0.8000	−0.8000	0.8000	0.8000
z (m)	0.0000	0.2100	0.2100	0.0000	0.0000	0.2100	0.2100	0.0000
	$\mathbf{b}^{\mathcal{B}}_{1,0}$	$\mathbf{b}^{\mathcal{B}}_{2,0}$	$\mathbf{b}^{\mathcal{B}}_{3,0}$	$\mathbf{b}^{\mathcal{B}}_{4,0}$	$\mathbf{b}^{\mathcal{B}}_{5,0}$	$\mathbf{b}^{\mathcal{B}}_{6,0}$	$\mathbf{b}^{\mathcal{B}}_{7,0}$	$\mathbf{b}^{\mathcal{B}}_{8,0}$
$x^{\mathcal{B}}$ (m)	−0.0300	−0.0300	−0.0300	−0.0300	0.0300	0.0300	0.0300	0.0300
$y^{\mathcal{B}}$ (m)	−0.0400	−0.0400	0.0400	0.0400	−0.0400	−0.0400	0.0400	0.0400
$z^{\mathcal{B}}$ (m)	0.1500	0.0100	0.0000	0.1600	0.1600	0.0000	0.0100	0.1500

(a) Designer-intuition initial geometric parameters $\mathbf{a}_{i,0}$ and $\mathbf{b}^{\mathcal{B}}_{i,0}$

	$\mathbf{a}_{1,f}$	$\mathbf{a}_{2,f}$	$\mathbf{a}_{3,f}$	$\mathbf{a}_{4,f}$	$\mathbf{a}_{5,f}$	$\mathbf{a}_{6,f}$	$\mathbf{a}_{7,f}$	$\mathbf{a}_{8,f}$
x (m)	0.3154	0.2668	0.2668	0.3154	−0.3154	−0.2668	−0.2668	−0.3154
y (m)	−0.7999	−0.8000	0.8000	0.7999	−0.7999	−0.8000	0.8000	0.7999
z (m)	0.0412	0.2203	0.2202	0.0412	0.0412	0.2203	0.2202	0.0412
	$\mathbf{b}^{\mathcal{B}}_{1,f}$	$\mathbf{b}^{\mathcal{B}}_{2,f}$	$\mathbf{b}^{\mathcal{B}}_{3,f}$	$\mathbf{b}^{\mathcal{B}}_{4,f}$	$\mathbf{b}^{\mathcal{B}}_{5,f}$	$\mathbf{b}^{\mathcal{B}}_{6,f}$	$\mathbf{b}^{\mathcal{B}}_{7,f}$	$\mathbf{b}^{\mathcal{B}}_{8,f}$
$x^{\mathcal{B}}$ (m)	−0.0144	−0.0055	−0.0052	−0.0150	0.0150	0.0052	0.0055	0.0144
$y^{\mathcal{B}}$ (m)	−0.0384	−0.0241	0.0243	0.0391	−0.0391	−0.0243	0.0241	0.0384
$z^{\mathcal{B}}$ (m)	0.1531	0.0055	0.0038	0.1583	0.1583	0.0038	0.0055	0.1531

(b) Final geometric parameters $\mathbf{a}_{i,f}$ and $\mathbf{b}^{\mathcal{B}}_{i,f}$

Table D.26 – Geometric parameters of the CDPM corresponding to the Trial 100 of the numerical application of the dimensional synthesis program presented in Sub-section 4.3.2.

[2]Simple rules were followed to design this initial CDPM's geometry: In general, for maximizing the WCW, direct the m cables in a uniform-distributed manner around the moving platform in order to fully constrain the mechanism, at least at $\mathbf{p}_0$ and for $\mathbf{Q}_0$ (keep in mind that it must be possible to pull the end effector in all directions for each desired pose); Take advantage of the available space to position attachment points $\mathbf{a}_i$ on the base frame (for instances, at vertices); Position attachment points $\mathbf{b}_i$ in opposition to points $\mathbf{a}_i$, i.e., to cross cables, in order to increase the range of accessible end-effector attitudes. Then, to minimize the occurrence of mechanical interferences: Regroup attachment points together, which ensure that no other point along these cables can be in contact, unless the two cables are collinear; Similarly, position points $\mathbf{b}_i$ close to or on an end-effector edge; The two sets of attachment points $\mathbf{a}_i$ and $\mathbf{b}_i$ must normally form two convex shapes. When one follows these simple rules and find a "good" compromise, the resulting solution is generally close to or represents a feasible initial solution to start the optimization program from.

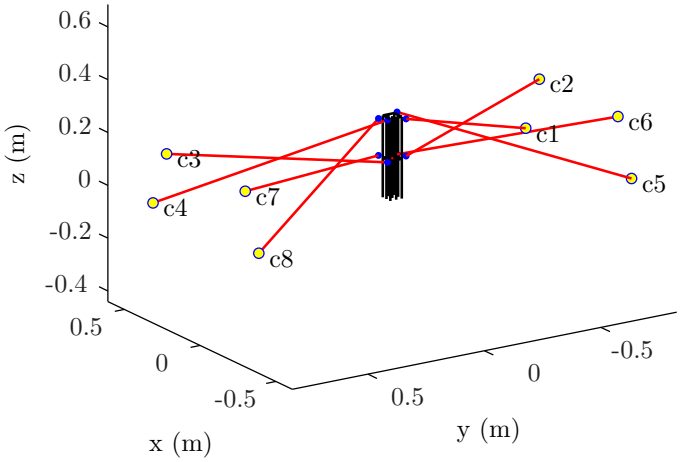

(a) The initial geometry of the CDPM

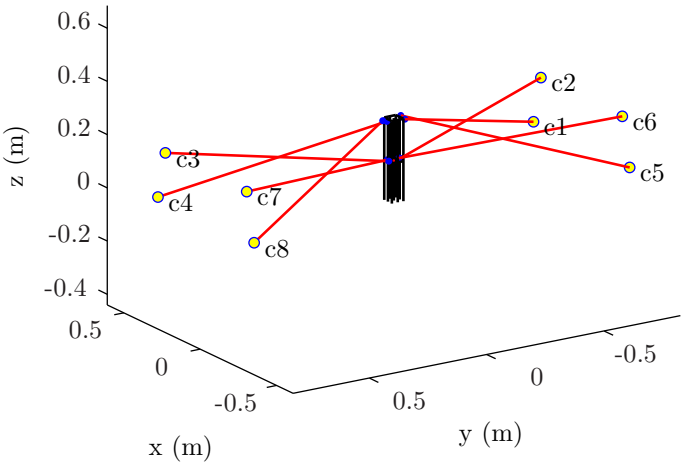

(b) The final geometry of the CDPM

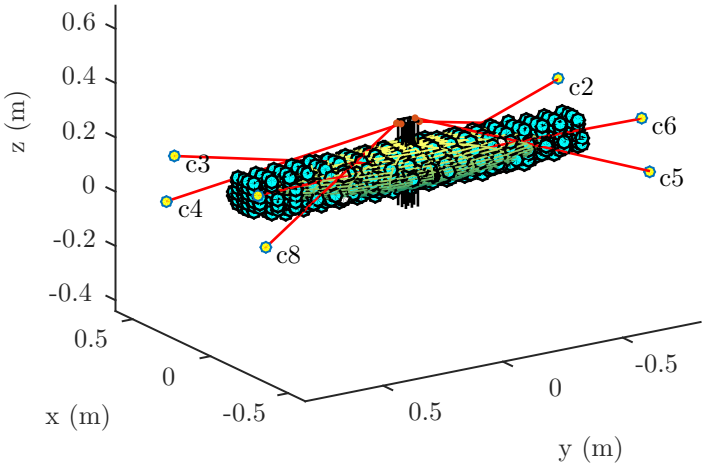

(c) The WCW of the final CDPM's geometry with the final $\mathcal{W}_t$ ($\kappa = 1.0880$)

Figure D.34 – Illustration of different results obtained from the optimization of a CDPM (Trial 100) for the numerical application of the dimensional synthesis program presented in Sub-section 4.3.2.

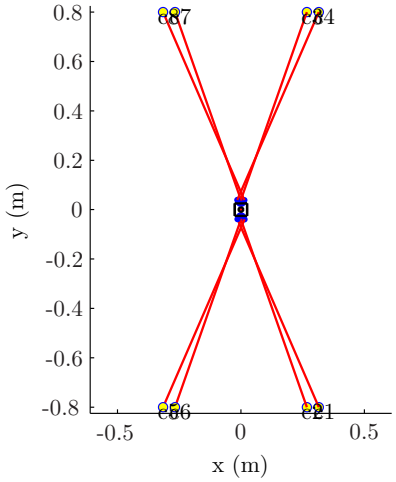

(a) An XY view of the final CDPM's geometry

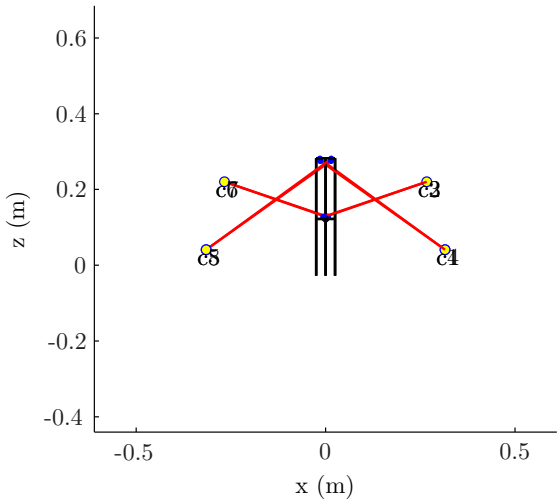

(b) An XZ view of the final CDPM's geometry

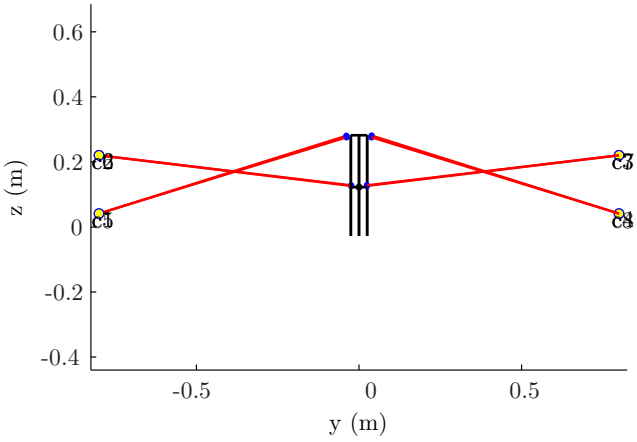

(c) An YZ view of the final CDPM's geometry

Figure D.35 – Three different two-dimensional points of view of the optimized CDPM's geometry (Trial 100) from the numerical application of the dimensional synthesis program presented in Sub-section 4.3.2 ($\kappa = 1.0880$).

Bibliography

[1] K. Capek. *Rossum's Universal Robots (R. U. R.)*. Theatrical manuscript, Prague, Czech Republic, January 1921.

[2] C. T. Rubin. Machine morality and human responsibility. *The New Atlantis*, 32:58–79, 2011.

[3] Oxford English Dictionary, www.oed.com/.

[4] G. C. Devol Jr. Programmed article transfer. Patent 2,988,237, United-States, 1961.

[5] T. Fukuda, R. Michelini, V. Potkonjak, S. Tzafestas, K. Valavanis, and M. Vukobratovic. How far away is "artificial man". *Robotics & Automation Magazine*, 8(1):66–73, 2001.

[6] S. A. Oke. A literature review on artificial intelligence. *International Journal of Information and Management Sciences*, 19(4):535–570, 2008.

[7] J. H. Payne Jr. Remote-control manipulator. Patent 2,476,249, United-States, 1949.

[8] R. C. Goertz. Fundamentals of general-purpose remote manipulators. *Nucleonics*, 10(11):36–42, 1952.

[9] R. C. Goertz. Remote-control manipulator. Patent 2,632,754, United-States, 1953.

[10] R. C. Goertz, R. G. Schmitt Jr., R. A. Olsen, and R. B. Wehrle. Remote-control manipulator. Patent 2,774,488, United-States, 1956.

[11] R. W. Wiesener. True motion miniature manipulator. Patent 3,650,410, United-States, 1972.

[12] J.-C. Germond, J.-P. Guilbaud, and J. Vertut. Articulated master-slave manipulator. Patent 3,664,517, United-States, 1972.

[13] D. François and C. Glachet. Master-slave mechanical manipulator with homothetic displacements. Patent 4,298,300, United-States, 1981.

[14] C. Glachet, D. François, J. Tentélier, and C. Frioux. Master-slave type telescopic telemanipulator. Patent 4,493,598, United-States, 1985.

[15] C. Reboulet. “Master-slave” remote manipulation apparatus having six degrees of freedom. Patent 6,026,701, United-States, 2000.

[16] R. C. Goertz, W. M. Thompson, and R. A. Olsen. Electronic master slave manipulator. Patent 2,846,084, United-States, 1958.

[17] P. S. Green. Teleoperator system and method with telepresence. Patent 2,632,123, Canada, 1993.

[18] D. L. Brock and W. Lee. Articulated apparatus for telemanipulator system. Patent 6,432,112, United-States, 2002.

[19] D. Stoianovici. Robotic surgery. *World Journal of Urology*, 18:289–295, 2000.

[20] K. Cleary and C. Nguyen. State of the art in surgical robotics: Clinical applications and technology challenges. *Computer Aided Surgery*, 6:312–328, 2001.

[21] R. H. Taylor and D. Stoianovici. Medical robotics in computer-integrated surgery. *IEEE Transactions on Robotics and Automation*, 19(5):765–781, 2003.

[22] A. R. Lanfranco, A. E. Castellanos, J. P. Desai, and W. C. Meyers. Robotic surgery: A current perspective. *Annals of Surgery*, 239(1):14–21, 2004.

[23] R. H. Taylor. A perspective on medical robotics. *Proceedings of the IEEE*, 94(9):1652–1664, 2006.

[24] J. Troccaz. La chirurgie urologique assistée par ordinateur et robot. *Progrès en Urologie*, 16:112–120, 2006.

[25] Neuromate® by Renishaw, www.renishaw.com/.

[26] U.S. Food and Drug Administration, www.fda.gov/.

[27] G. R. Sutherland, P. B. McBeth, and D. F. Louw. NeuroArm: an MR compatible robot for microsurgery. *International Congress Series 1256*, pages 504–508, 2003.

[28] P. B. McBeth, D. F. Louw, P. R. Rizun, and G. R. Sutherland. Robotics in neurosurgery. *The American Journal of Surgery*, 188:68S–75S, 2004.

[29] The neuroArm project, www.neuroarm.org/.

[30] SYMBIS Surgical System by IMRIS Inc., www.imris.com/.

[31] ROBODOC® by Curexo Technology Corporation, www.robodoc.com/.

[32] J. Pransky. Robodoc–surgical robot success story. *Industrial Robot*, 24(3):231–233, 1997.

[33] MAKOplasty® by MAKO Surgical Corporation, www.makosurgical.com/.

[34] M. Ghodoussi, S. E. Butner, and Y. Wang. Robotic surgery–the transatlantic case. In *Proceedings of the IEEE International Conference on Robotics and Automation*, Washington, DC, United-States, May 2002.

[35] da Vinci® Surgical System by Intuitive Surgical Inc., www.intuitivesurgical.com/.

[36] A. J. Madhani, G. Niemeyer, and J. K. Salisbury Jr. The black falcon: A teleoperated surgical instrument for minimally invasive surgery. In *Proceedings of the IEEE/RSJ International Conference on Intelligent Robots and Systems*, Vancouver, B.-C., Canada, October 1998.

[37] G. S. Guthart and J. K. Salisbury Jr. The intuitive™ telesurgery system: Overview and application. In *Proceedings of the IEEE International Conference on Robotics and Automation*, San Francisco, CA, United-States, April 2000.

[38] A. Tewari, J. Peabody, R. Sarle, G. Balakrishnan, A. Hemal, A. Shrivastava, and M. Menon. Technique of da Vinci robot-assisted anatomic radical prostatectomy. *Urology*, 60(4):569–572, 2002.

[39] CyberKnife® by Accuray Inc., www.cyberknife.com/.

[40] M. Bosc. *Contribution à la détection de changements dans des séquences IRM 3D multimodales*. PhD dissertation, Université Louis Pasteur - Strasbourg I, Strasbourg, France, 2003.

[41] H. Elhawary, A. Zivanovic, B. Davies, and M. Lampérth. A review of magnetic resonance imaging compatible manipulators in surgery. *Proceedings of the IMechE: Journal of Engineering in Medecine*, 220:413–424, 2006.

[42] K. Chinzei and K. Miller. Towards MRI guided surgical manipulator. *Medical Science Monitor*, 7(1):153–163, 2001.

[43] L. M. DeVita, J. S. Plante, and S. Dubowsky. The design of high precision parallel mechanisms using binary actuation and elastic averaging: With application to MRI cancer treatment. In *The 12th IFToMM World Congress*, Besançon, France, June 2007.

[44] E. G. Christoforou, A. Özcan, and N. V. Tsekos. Manipulator for magnetic resonance imaging guided interventions: Design, prototype and feasibility. In *Proceedings of the IEEE International Conference on Robotics and Automation*, Orlando, FL, United-States, May 2006.

[45] J. Izawa, T. Shimizu, T. Aodai, T. Kondo, H. Gomi, S. Toyama, and K. Ito. MR compatible manipulandum with ultrasonic motor for fMRI studies. In *Proceedings of*

the IEEE International Conference on Robotics and Automation, Orlando, FL, United-States, May 2006.

[46] D. Stoianovici, D. Song, D. Petrisor, D. Ursu, D. Mazilu, M. Mutener, M. Schar, and A. Patriciu. "MRI stealth" robot for prostate interventions. *Minimally Invasive Therapy*, 16(4):241–248, 2007.

[47] M. Muntener, A. Patriciu, D. Petrisor, D. Mazilu, H. Bagga, L. Kavoussi, K. Cleary, and D. Stoianovici. Magnetic resonance imaging compatible robotic system for fully automated brachytherapy seed placement. *Urology*, 68(6):1313–1317, 2006.

[48] M. Muntener, A. Patriciu, D. Petrisor, M. Schär, D. Ursu, D. Y. Song, and D. Stoianovici. Transperineal prostate intervention: Robot for fully automated MR imaging–system description and proof of principle in a canine model. *Radiology*, 247(2):543–549, 2008.

[49] E. G. Christoforou, N. V. Tsekos, and A. Özcan. Design and testing of a robotic system for MR image-guided interventions. *Journal of Intelligent and Robotic Systems*, 47(2):175–196, 2006.

[50] MAGNETOM® Skyra MRI system by Siemens Inc., www.siemens.com/.

[51] D. Chapuis, R. Gassert, G. Ganesh, E. Burdet, and H. Bleuler. Investigation of a cable transmission for the actuation of MR compatible haptic interfaces. In *Proceedings of the First IEEE/RAS-EMBS International Conference on Biomedical Robotics and Biomechatronics, BioRob 2006*, Pisa, Tuscany, Italy, February 2006.

[52] S. Abdelaziz, L. Esteveny, L. Barbé, P. Renaud, B. Bayle, and M. de Mathelin. Development of a MR-compatible cable-driven manipulator: Design and technological issues. In *Proceedings of the IEEE International Conference on Robotics and Automation*, Saint Paul, MN, United-States, May 2012.

[53] Bureau International des Poids et Mesures, www.bipm.org/en/si/.

[54] C. Scheiner. *Pantographice: seu ars delineandi res quaslibet per paralelogrammum lineare sen carum, mechanicum, mobil, libellis duobus explicata, demonstrutionibus geometricis illustrata.* Romae: Ex Typographia Ludouici Grignani, Rome, Italy, 1631.

[55] S. Plumley. Metal cutting pantograph. Patent 211,948, Canada, 1922.

[56] A. J. Plese. Pantograph. Patent 366,250, Canada, 1937.

[57] L. Valois. Pantograph. Patent 537,969, Canada, 1957.

[58] J.-P. Blain. Pantograph. Patent 1,115,943, Canada, 1982.

[59] F. Freudenstein and P. Calcaterra. Tracer-type instrument for changing scales in two mutually perpendicular directions. *The Review of Scientific Instruments*, 26(9):866–869, 1955.

[60] I. Artobolevsky. *Les Mécanismes dans la Technique Moderne: Tome 1: Mécanismes à Leviers*. MIR Publishers, 1975.

[61] A. J. Nielson and L. L. Howell. Compliant pantographs via the pseudo-rigid-body model. In *Proceedings of the ASME Design Engineering Technical Conference, DETC98/MECH-5930*, Atlanta, GA, United-States, September 1998.

[62] B. Cheverton, editor. *Repertory of Patent Inventions, and Other Discoveries and Improvements in Arts, Manufactures, and Agriculture*. Alexander Macintosh Printer, Great New-Street, London, 1844.

[63] E. T. Green. Engraving machine. Patent 2,627,658, United-States, 1953.

[64] A. A. Burry. Pantographic model-to-workpiece cutting-sculpturing system. Patent 1,126,943, Canada, 1982.

[65] Machine Tool Traders, www.master-machines.com/.

[66] C. Reboulet. Dispositif d'articulation à structure parallèle et appareils de transmission de mouvement à distance en faisant application. Patent 2,672,836, France, 1992.

[67] B. Allotta, L. Pugi, and F. Bartolini. Design and experimental results of an active suspension system for a high-speed pantograph. *IEEE/ASME Transactions on Mechatronics*, 13(5):548–557, 2008.

[68] S. D. Eppinger, D. N. O'Connor, W. P. Seering, and D. N. Wormley. Modeling and experimental evaluation of asymmetric pantograph dynamics. *Transactions of ASME Journal of Dynamic Systems, Measurement, and Controls*, 110(2):168–174, 1988.

[69] M. Lesser, L. Karlsson, and L. Drugge. An interactive model of a pantograph-catenary system. *Vehicle System Dynamics: International Journal of Vehicle Mechanics and Mobility*, 25(S1):397–412, 1996.

[70] A. S. K. Kwan and S. Pellegrino. A cable-rigidized 3D pantograph. In *Proceedings of the Fourth European Symposium on 'Space Mechanisms and Tribology'*, Cannes, France, September 1989.

[71] A. S. K. Kwan and S. Pellegrino. Matrix formulation of macro-elements for deployable structures. *Computers & Structures*, 50(2):237–254, 1994.

[72] Z. You and S. Pellegrino. Cable-stiffened pantographic deployable structures part 1: Triangular mast. *The American Institute of Aeronautics and Astronautics Journal*, 34(4):813–820, 1996.

[73] Z. You and S. Pellegrino. Cable-stiffened pantographic deployable structures part 2: Mesh reflector. *The American Institute of Aeronautics and Astronautics Journal*, 35(8):1348–1355, 1997.

[74] A. G. Cherniavsky, V. I. Gulyayev, V. V. Gaidaichuk, and A. I. Fedoseev. Large deployable space antennas based on usage of polygonal pantograph. *Journal ofAerospace Engineering*, 18(3):139–145, 2005.

[75] G. L. Long and C. L. Collins. A pantograph linkage parallel platform master hand controller for force-reflection. In *Proceedings of the IEEE International Conference on Robotics and Automation*, Nice, France, May 1992.

[76] G. Campion, Q. Wang, and V. Hayward. The pantograph Mk-II: A haptic instrument. In *Proceedings of the IEEE/RSJ International Conference on Intelligent Robots and Systems*, Edmonton, AB, Canada, August 2005.

[77] C. Gosselin. Cable-driven parallel mechanisms: State of the art and perspectives. *Mechanical Engineering Reviews*, 1(1):1–17, 2014.

[78] S. Bouchard and C. Gosselin. Workspace optimization of a very large cable-driven parallel mechanism for a radiotelescope application. In *Proceedings of ASME International Design Engineering Technical Conferences and Computers and Information in Engineering Conference, IDETC/CIE 2007*, Las Vegas, NV, United-States, September 2007.

[79] S. Bouchard. *Géométrie des Robots Parallèles entraînés par des Câbles*. PhD dissertation, Université Laval, Quebec City, QC, Canada, 2008.

[80] A. Alikhani, S. Behzadipour, S. A. Sadough Vanini, and A. Alasty. Workspace analysis of a three dof cable-driven mechanism. *Journal of Mechanisms and Robotics*, 1(4):041005, 2009.

[81] S. Behzadipour and A. Khajepour. Stiffness of cable-based parallel manipulators with application to stability analysis. *Journal of Mechanical Design*, 128(1):303–310, 2006.

[82] S. Kawamura and K. Ito. A new type of master for teleoperation using a radial wire drive system. In *Proceedings of the IEEE International Conference on Intelligent Robots and Systems*, Yokohama, Japan, July 1993.

[83] C. Bonivento, A. Eusebi, C. Melchiorri, M. Montanari, and G. Vassura. Wireman: A portable wire manipulator for touch-rendering of bas-relief virtual surfaces. In *Proceedings of the IEEE International Conference on Advanced Robotics*, Monterey, CA, United-States, July 1997.

[84] R. L. Williams II. Cable-suspended haptic interface. *International Journal of Virtual Reality*, 3(3):13–20, 1998.

[85] T. Morizono, K. Kurahashi, and S. Kawamura. Analysis and control of a force display system driven by parallel wire mechanism. *Robotica*, 16(5):551–563, 1998.

[86] R. L. Williams II. Planar cable-suspended haptic interface: Design for wrench exertion. In *Proceedings of the ASME Design Technical Conferences, 25th Design Automation Conference, DETC99/DAC-8639*, Las Vegas, NV, United-States, September 1999.

[87] S. Walairacht, Y. Koike, and M. Sato. String-based haptic interface device for multi-fingers. In *Proceedings of the IEEE International Conference on Virtual Reality*, New-Brunswick, NJ, United-States, March 2000.

[88] S. Kim, M. Ishii, Y. Koike, and M. Sato. Development of tension based haptic interface and possibility of its application to virtual reality. In *Proceedings of the ACM symposium on Virtual reality software and technology*, Seoul, Korea, October 2000.

[89] S. Tadokoro, T. Matsushima, Y. Murao, H. Kohkawa, and M. Hiller. A parallel cable-driven motion for virtual acceleration. In *Proceedings of the IEEE/RSJ International Conference on Intelligent Robots and Systems*, Maui, HI, United-States, October 2001.

[90] M. Sato. Development of string-based force display: SPIDAR. In *Proceedings of the International Conference on Virtual Systems and Multi-Media*, Gyeongju, Korea, September 2002.

[91] C. Ferraresi, M. Paoloni, and F. Pescarmona. A force-feedback six-degrees-of-freedom wire-actuated master for teleoperation: the WiRo-6.3. *Industrial Robot: An International Journal*, 34(3):195–200, 2007.

[92] C. Gosselin, R. Poulin, and D. Laurendeau. A planar parallel 3-dof cable-driven haptic interface. In *Proceedings of the 12th World Multi-Conference on Systemics, Cybernetics and Informatics*, Orlando, FL, United-States, June 2008.

[93] M. J.-D. Otis, V. Duchaine, G. Billette, S. Perreault, C. Gosselin, and D. Laurendeau. *Cartesian Control of a Cable-Driven Haptic Mechanism*, pages 75–101. Advances in Haptics. InTech, 2010.

[94] S. Fels, Y. Kinoshita, T.-P. G. Chen, Y. Takama, S. Yohanan, S. Takahashi, A. Gadd, and K. Funahashi. Swimming across the pacific: a VR swimming interface. *IEEE Journal on Computer Graphics and Applications*, 25(1):24–31, 2005.

[95] D. Mayhew, B. Bachrach, W. Z. Rymer, and R. F. Beer. Development of the MACARM – a novel cable robot for upper limb neurorehabilitation. In *Proceedings of the IEEE International Conference on Rehabilitation Robotics*, Chicago, IL, United-States, June 2005.

[96] D. Zanotto, G. Rosati, S. Minto, and A. Rossi. Sophia-3: A semiadaptive cable-driven rehabilitation device with a tilting working plane. *IEEE Transactons on Robotics*, 30(4):974–979, 2014.

[97] K. Homma, O. Fukuda, J. Sugawara, Y. Nagata, and M. Usuba. A wire-driven leg rehabilitation system: Development of a 4-dof experimental system. In *Proceedings of the IEEE/ASME International Conference on Advanced Intelligent Mechatronics*, Kobe, Japan, July 2003.

[98] K. Homma, O. Fukuda, Y. Nagata, and M. Usuba. Study of a wire-driven leg rehabilitation system. In *Proceedings of the IEEE/RSJ International Conference on Intelligent Robots and Systems*, Sendai, Japan, September 2004.

[99] S. Perreault. Conception mécanique d'une plate-forme de marche entraînée par câbles. Master's project, Université Laval, Quebec City, QC, Canada, 2007.

[100] S. Perreault and C. Gosselin. Cable-driven parallel mechanisms: Application to a locomotion interface. In *Proceedings of the ASME International Design Engineering Technical Conferences & Computers and Information in Engineering Conference*, Las Vegas, NV, United-States, September 2007.

[101] S. Perreault and C. Gosselin. Cable-driven parallel mechanisms: Application to a locomotion interface. *Journal of Mechanical Design*, 130(10):102301, 2008.

[102] M. Otis, T.-L. Nguyen-Dang, T. Laliberté, D. Ouellet, D. Laurendeau, and C. Gosselin. Cable tension control and analysis of reel transparency for 6-dof haptic foot platform on a cable-driven locomotion interface. *International Journal of Electrical, Computer, and Systems Engineering*, 3(1):16–29, 2009.

[103] M. J.-D. Otis, S. Perreault, T.-L. Nguyen-Dang, P. Lambert, M. Gouttefarde, D. Laurendeau, and C. Gosselin. Determination and management of cable interferences between two 6-dof foot platforms in a cable-driven locomotion interface. *IEEE Transactions on Systems, Man and Cybernetics, Part A: Systems and Humans*, 39(3):528–544, 2009.

[104] M. J.-D. Otis. *Analyse, commade et intégration d'un mécanisme parallèle entraîné par des câbles pour la réalisation d'une interface haptique comme métaphore de navigation dans un environnement virtuel*. PhD dissertation, Université Laval, Quebec City, QC, Canada, 2009.

[105] P. Lafourcade and M. Llibre. First steps toward a sketch-based design methodology for wire-driven manipulators. In *Proceedings of the IEEE/ASME International Conference on Advanced Intelligent Mechatronics*, Kobe, Japan, July 2003.

[106] P. Lafourcade. *Étude des manipulateurs parallèles à câbles, conception d'une suspension active pour soufflerie*. PhD dissertation, Ecole Nationale Supérieur de l'Aéronautique et de l'Espace, Toulouse, France, 2004.

[107] R. Verhoeven. *Analysis of the Workspace of Tendon-based Stewart Platforms*. PhD dissertation, University of Duisburg-Essen, Duisburg, Germany, 2004.

[108] K. Usher, G. Winstanley, P. Corke, D. Stauffacher, and R. Carnie. A cable-array robot for air vehicle simulation. In *Proceedings of the Australasian Conference on Robotics and Automation*, Canberra, Australia, December 2004.

[109] K. Usher, G. Winstanley, P. Corke, and D. Stauffacher. Air vehicle simulator: an application for a cable array robot. In *Proceedings of the IEEE International Conference on Robotics and Automation*, Barcelona, Spain, April 2005.

[110] S. Kawamura, M. Ida, T. Wada, and J.-L. Wu. Development of a virtual sports machine using a wire drive system: A trial of virtual tennis. In *Proceedings of the IEEE International Conference on Intelligent Robots and Systems*, Pittsburgh, PA, United-States, August 1995.

[111] J. P. Trevelyan. A suspended device for humanitarian demining. In *EUREL International Conference on The Detection of Abandoned Land Mines: A Humanitarian Imperative Seeking a Technical Solution*, Edinburgh, Scotland, October 1996.

[112] S. Tadokoro, R. Verhoeven, M. Hiller, and T. Takamori. A portable parallel manipulator for search and rescue at large-scale urban earthquakes and an identification algorithm for the installation in understructured environments. In *Proceedings of the IEEE International Conference on Intelligent Robots and Systems*, Kyongju, South Korea, October 1999.

[113] E. Ottaviano, M. Ceccarelli, A. Paone, and G. Carbone. A low-cost easy operation 4-cable driven parallel manipulator. In *Proceedings of the IEEE International Conference on Robotics and Automation*, Barcelona, Spain, April 2005.

[114] P. Bosscher, R. L. Williams II, and M. Tummino. A concept for rapidly-deployable cable robot search and rescue systems. In *Proceedings of the ASME International Design Engineering Technical Conferences and Computers and Information in Engineering Conference*, Long Beach, CA, United-States, September 2005.

[115] J.-D. Deschênes, P. Lambert, S. Perreault, N. Martel-Bisson, N. Zoso, A. Zaccarin, P. Hébert, S. Bouchard, and C. Gosselin. A cable-driven parallel mechanism for capturing object appearance from multiple viewpoints. In *Proceedings of the IEEE International Conference on 3-D Digital Imaging and Modeling*, Montreal, QC, Canada, August 2007.

[116] B. Peng, R. Nan, R. G. Strom, B. Duan, G. Ren, J. Zhai, Y. Qiu, S. Wu, Y. Su, L. Zhu, and C. Jin. The technical scheme for FAST. In *Workshop on Perspectives on Radio Astronomy: Science with Large Antenna Arrays*, Amsterdam, The Netherlands, April 1999.

[117] H. Le Coroller, J. Dejonghe, C. Arpesella, D. Vernet, and A. Labeyrie. Tests with a Carlina-type hypertelescope prototype I. Demonstration of star tracking and fringe acquisition with a balloon-suspended focal camera. *Astronomy and Astrophysics*, 426(2):721–728, 2004.

[118] K. Maeda, S. Tadokoro, T. Takamori, M. Hiller, and R. Verhoeven. On design of a redundant wire-driven parallel robot WARP manipulator. In *Proceedings of the IEEE International Conference on Robotics and Automation*, Detroit, MI, United-States, May 1999.

[119] S. Kawamura, H. Kino, and C. Won. High-speed manipulation by using parallel wire-driven robots. *Robotica*, 18(1):13–21, 2000.

[120] R. V. Bostelman, J. S. Albus, and R. E. Graham. RoboCrane and Emma applied to waste storage tank remediation. In *American Nuclear Society Seventh Topical Meeting on Robotics and Remote Systems*, Augusta, GA, United-States, April 1997.

[121] R. Bostelman, A. Jacoff, and R. Bunch. Delivery of an advanced double-hull ship welding system using robocrane. In *Third International Computer Science Conventions Symposia on Intelligent Industrial Automation and Soft Computing*, Genova, Italy, June 1999.

[122] A. Pott, H. Mütherich, W. Kraus, V. Schmidt, P. Miermeister, and A. Verl. IPAnema: A family of cable-driven parallel robots for industrial applications. In T. Bruckmann and A. Pott, editors, *Cable-Driven Parallel Robots*, volume 12 of *Mechanisms and Machine Science*, pages 119–134. Springer Berlin Heidelberg, 2013.

[123] S. Abdelaziz, L. Esteveny, P. Renaud, B. Bayle, L. Barbé, M. de Mathelin, and A. Gangi. Design considerations for a novel MRI compatible manipulator for prostate cryoablation. *International Journal of Computer Assisted Radiology and Surgery*, 6(6):811–819, 2011.

[124] S. Abdelaziz, L. Esteveny, P. Renaud, B. Bayle, and M. de Mathelin. Design and optimization of a novel MRI compatible wire-driven robot for prostate cryoablation. In *Proceedings of the ASME International Design Engineering Technical Conferences and Computers and Information in Engineering Conference*, Washington, DC, United-States, August 2011.

[125] SKYCAM, www.skycam.tv/.

[126] R. G. Roberts, T. Graham, and T. Lippitt. On the inverse kinematics, statics, and fault tolerance of cable-suspended robots. *Journal of Robotic Systems*, 15(10):581–597, 1998.

[127] J. W. Jeong, S. H. Kim, and Y. K. Kwak. Kinematics and workspace analysis of a parallel wire mechanism for measuring a robot pose. *Mechanism and Machine Theory*, 34(6):825–841, 1999.

[128] G. Barrette and C. Gosselin. Kinematic analysis and design of planar parallel mechanisms actuated with cables. In *Proceedings of the ASME Biennial Mechanisms and Robotics Conference*, Baltimore, MD, United-States, September 2000.

[129] R. L. Williams II and P. Gallina. Planar cable-direct-driven robots, Part 1: Kinematics and statics. In *Proceedings of the ASME International Design Engineering Technical Conferences*, Pittsburgh, PA, United-States, September 2001.

[130] C. Gosselin and J. Wang. Kinematic analysis and design of cable-driven spherical parallel mechanisms. In *Proceedings of the 15th CISM-IFToMM Symposium on Robot Design, Dynamics and Control*, Montreal, QC, Canada, June 2004.

[131] M. Hiller, S. Fang, S. Mielczarek, R. Verhoeven, and D. Franitza. Design, analysis and realization of tendon-based parallel manipulators. *Mechanism and Machine Theory*, 40(4):429–445, 2005.

[132] S. Bouchard and C. Gosselin. Kinematic sensitivity of a very large cable-driven parallel mechanism. In *Proceedings of the ASME International Design Engineering Technical Conferences and Computers and Information in Engineering Conference*, Philadelphia, PA, United-States, September 2006.

[133] R. Kurtz and V. Hayward. Dexterity measure for tendon actuated parallel mechanisms. In *Proceedings of the IEEE International Conference on Advanced Robotics*, Pisa, Italy, June 1991.

[134] E. Ottaviano, M. Ceccarelli, and F. Thomas. Singularity configurations of a 6-wire parallel architecture. In *Proceedings of the 12th International Workshop on Robotics in Alpe-Adria-Danube Region*, Cassino, Italy, May 2003.

[135] G. Yang, S. H. Yeo, and C. B. Pham. Kinematics and singularity analysis of a planar cable-driven parallel manipulator. In *Proceedings of the IEEE International Conference on Intelligent Robots and Systems*, Sendai, Japan, September 2004.

[136] X. Diao, O. Ma, and Q. Lu. Singularity analysis of planar cable-driven parallel robots. In *Proceedings of the IEEE International Conference on Robotics, Automation and Mechatronics*, Chengdu, China, September 2008.

[137] Y.-Q. Zheng and X.-W. Liu. Force transmission index based workspace analysis of a six dof wire-driven parallel manipulator. In *Proceedings of the ASME International Design Engineering Technical Conferences and Computers and Information in Engineering Conference*, Montreal, QC, Canada, September 2002.

[138] G. Côté and C. Gosselin. Frontières d'équilibre de mécanismes à câbles comprenant des liens passifs. In *Proceedings of the CCToMM Symposium on Mechanisms, Machines, and Mechatronics*, Saint-Hubert, QC, Canada, May 2003.

[139] E. Stump and V. Kumar. Workspace delineation of cable-actuated parallel manipulators. In *Proceedings of the ASME International Design Engineering Technical Conferences and Computers and Information in Engineering Conference*, Salt Lake City, UT, United-States, September 2004.

[140] G. Barrette and C. Gosselin. Determination of the dynamic workspace of cable-driven planar parallel mechanisms. *Journal of Mechanical Design*, 127(2):242–248, 2005.

[141] E. Stump and V. Kumar. Workspaces of cable-actuated parallel manipulators. *Journal of Mechanical Design*, 128(1):159–167, 2006.

[142] D. McColl and L. Notash. Configuration and workspace analysis of planar wire-actuated parallel manipulators. In *Proceedings of the 17th CISM-IFToMM Symposium on Robot Design, Dynamics, and Control*, Tokyo, Japan, July 2008.

[143] A. Ghasemi, M. Eghtesad, and M. Farid. Workspace analysis for planar and spatial redundant cable robots. In *Proceedings of the American Control Conference*, Seattle, WA, United-States, June 2008.

[144] A. Ghasemi, M. Eghtesad, and M. Farid. Workspace analysis for planar and spatial redundant cable robots. *Journal of Mechanisms and Robotics*, 1(4):044502, 2009.

[145] Y. Zhang, Y. Zhang, X. Dai, and Y. Yang. Workspace analysis of a novel 6-dof cable-driven parallel robot. In *Proceedings of the IEEE International Conference on Robotics and Biomimetics*, Guilin, China, December 2009.

[146] S. Bouchard, C. Gosselin, and B. Moore. On the ability of a cable-driven robot to generate a prescribed set of wrenches. *Journal of Mechanisms and Robotics*, 2(1):011010, 2010.

[147] M. Gouttefarde and C. Gosselin. Wrench-closure workspace of six-dof parallel mechanisms driven by 7 cables. *Transactions of the Canadian Society for Mechanical Engineering*, 29(4):541–552, 2005.

[148] M. Gouttefarde. *Analyse de l'Espace des Poses Polyvalentes des Mécanismes Parallèles entraînés par Câbles*. PhD dissertation, Université Laval, Quebec City, QC, Canada, 2005.

[149] M. Gouttefarde and C. Gosselin. Analysis of the wrench-closure workspace of planar parallel cable-driven mechanisms. *IEEE Transactions on Robotics*, 22(3):434–445, 2006.

[150] M. Arsenault. Optimization of the prestress stable wrench closure workspace of planar parallel three-degree-of-freedom cable-driven mechanisms with four cables. In *Proceedings of the IEEE International Conference on Robotics and Automation*, Anchorage, AK, United-States, May 2010.

[151] A. T. Riechel and I. Ebert-Uphoff. Force-feasible workspace analysis for underconstrained, point-mass cable robots. In *Proceedings of the IEEE International Conference on Robotics and Automation*, New Orleans, LA, United-States, April 2004.

[152] P. Bosscher and I. Ebert-Uphoff. Wrench-based analysis of cable-driven robots. In *Proceedings of the IEEE International Conference on Robotics and Automation*, New Orleans, LA, United-States, April 2004.

[153] P. Bosscher, A. T. Riechel, and I. Ebert-Uphoff. Wrench-feasible workspace generation for cable-driven robots. *IEEE Transactions on Robotics*, 22(5):890–902, 2006.

[154] M. Gouttefarde, J.-P. Merlet, and D. Daney. Wrench-feasible workspace of planar parallel cable-driven mechanisms. In *Proceedings of the IEEE International Conference on Robotics and Automation*, Roma, Italy, April 2007.

[155] R. G. Robert, T. Graham, and J. M. Trumpower. On the inverse kinematics and statics of cable-suspended robots. In *Proceedings of the IEEE International Conference on Systems, Man, and Cybernetics*, Orlando, FL, United-States, October 1997.

[156] R. G. Robert, T. Graham, and T. Lippitt. On the inverse kinematics, statics, and fault tolerance of cable-suspended robots. *Journal of Field Robotics*, 15(10):581–597, 1998.

[157] M. A. Rahimi, H. Hemami, and Y. F. Zheng. Experimental study of a cable-driven suspended platform. In *Proceedings of the IEEE International Conference on Robotics and Automation*, Detroit, MI, United-States, May 1999.

[158] T. Arai, S. Matsumura, Y. Yoshimura, and H. Osumi. A proposal for a wire suspended manipulator: A kinematic analysis. *Robotica*, 17(1):3–9, 1998.

[159] H. Osumi, Y. Utsugi, and M. Koshikawa. Development of a manipulator suspended by parallel wire structure. In *Proceedings of the IEEE/RSJ International Conference on Intelligent Robots and Systems*, Takamatsu, Japan, October 2000.

[160] M. Yamamoto and A. Mohri. Inverse kinematics analysis for incompletely restrained parallel wire mechanisms. In *Proceedings of the IEEE/RSJ International Conference on Intelligent Robots and Systems*, Takamatsu, Japan, October 2000.

[161] M. Carricato and J.-P. Merlet. *Geometrico-Static Analysis of Under-Constrained Cable-Driven Parallel Robots*, pages 309–319. Advances in Robot Kinematics: Motion in Man and Machine. Springer Publisher, 2010.

[162] C. Gosselin, S. Lefrançois, and N. Zoso. Underactuated cable-driven robots: Machine, control and suspended bodies. In *Proceedings of the CIM Symposium on Brain, Body and Machine*, Montreal, QC, Canada, November 2010.

[163] S. Krut, O. Company, and F. Pierrot. Force performance indexes for parallel mechanisms with actuation redundancy, especially for parallel wire-driven manipulators. In *Proceedings of the IEEE/RSJ International Conference on Intelligent Robots and Systems*, Sendai, Japan, September 2004.

[164] S.-R. Oh and S. K. Agrawal. Cable suspended planar robots with redundant cables: Controllers with positive tensions. *IEEE Transactions on Robotics*, 21(3):457–465, 2005.

[165] M. Hassan and A. Khajepour. Optimization of actuator forces in cable-based parallel manipulators using convex analysis. *IEEE Transactions on Robotics*, 24(3):736–740, 2008.

[166] C. Gosselin and M. Grenier. On the determination of the force distribution in overconstrained cable-driven parallel mechanisms. *Meccanica*, 46(1):3–15, 2011.

[167] A. M. Hay and J. A. Snyman. Analysis and optimisation tools for a reconfigurable tendon-driven manipulator. In *Proceedings of 2nd CIRP International Conference on Reconfigurable Manufacturing*, Ann Arbor, MI, United-States, August 2003.

[168] A. M. Hay and J. A. Snyman. Optimization of a planar tendon-driven parallel manipulator for a maximal dextrous workspace. *Engineering Optimization*, 37(3):217–236, 2005.

[169] X. Diao and O. Ma. Force-closure analysis of a 6-dof cable manipulators with seven or more cables. *Robotica*, 27(2):209–215, 2008.

[170] C. Leclerc and C. Gosselin. Algorithme génétique multicritériel pour l'optimisation de l'architecture des mécanismes entraînés par câbles — application à un simulateur de vol. In *Proceedings of the CCToMM Symposium on Mechanisms, Machines and Mechatronics*, Quebec City, QC, Canada, May 2009.

[171] J. M. McCarthy. 21st century kinematics—synthesis, compliance and tensegrity. *Journal of Mechanisms and Robotics*, 3(2):020201, 2011.

[172] D. Lau, K. Bhalerao, D. Oetomo, and S. K. Halgamuge. *On the Task Specific Evaluation and Optimisation of Cable-Driven Manipulators*, pages 707–716. Advances in Reconfigurable Mechanisms and Robots I. Springer-Verlag Publisher, 2012.

[173] K. Azizian and P. Cardou. The dimensional synthesis of planar parallel cable-driven mechanisms through convex relaxations. *Journal of Mechanisms and Robotics*, 4(3):031011, 2012.

[174] M. Yamamoto, N. Yanai, and A. Mohri. Inverse dynamics and control of crane-type manipulator. In *Proceedings of the IEEE/RSJ International Conference on Intelligent Robots and Systems*, Kyongju, South Korea, October 1999.

[175] W.-J. Shiang, D. Cannon, and J. Gorman. Dynamic analysis of the cable array robotic crane. In *Proceedings of the IEEE International Conference on Robotics and Automation*, Detroit, MI, United-States, May 1999.

[176] R. L. Williams II and P. Gallina. Planar cable-direct robot, Part II: Dynamics and control. In *Proceedings of the ASME International Design Engineering Technical Conferences*, Pittsburgh, PA, United-States, September 2001.

[177] N. Yanai, M. Yamamoto, and A. Mohri. Anti-sway control for wire-suspended mechanism based on dynamics compensation. In *Proceedings of the IEEE International Conference on Robotics and Automation*, Washington, DC, United-States, May 2002.

[178] J.-J. Lee and Y.-H. Lee. Dynamic analysis of tendon driven robotic mechanisms. *Journal of Robotic Systems*, 20(5):229–238, 2003.

[179] H. Kino. Principle of orthogonalization for completely restrained parallel wire driven robot. In *Proceedings of the IEEE/ASME International Conference on Advanced Intelligent Mechatronics*, Kobe, Japan, July 2003.

[180] Y.-H. Lee and J.-J. Lee. Modeling for the dynamics of tendon-driven robotic mechanisms with flexible tendons. *Mechanism and Machine Theory*, 38(12):1431–1447, 2003.

[181] M. Yamamoto, N. Yanai, and A. Mohri. Trajectory control of incompletely restrained parallel-wire-suspended mechanism based on inverse dynamics. *IEEE Transactions on Robotics*, 20(5):840–850, 2004.

[182] Y. X. Su, C. H. Zheng, and B. Y. Duan. Fuzzy learning tracking of a parallel cable manipulator for the square kilometre array. *Mechatronics*, 15(6):731–746, 2005.

[183] S.-R. Oh and S. K. Agrawal. A reference governor-based controller for a cable robot under input constraints. *IEEE Transactions on Control Systems Technology*, 13(4):639–645, 2005.

[184] J. Park, W.-K. Chung, and W. Moon. Wire-suspended dynamical system: Stability analysis by tension-closure. *IEEE Transactions on Robotics*, 21(3):298–308, 2005.

[185] X. Yin and A. P. Bowling. Dynamic performance limitations due to yielding in cable-driven robotic manipulators. *Journal of Mechanical Design*, 128(1):311–318, 2006.

[186] J. A. dit Sandretto, D. Daney, and M. Gouttefarde. Calibration of a fully-constrained parallel cable-driven robot. In *Proceedings of the 19th CISM-IFToMM Symposium on Robot Design, Dynamics, and Control*, Paris, France, June 2012.

[187] J.-P. Merlet. *Analysis of the Influence of Wires Interference on the Workspace of Wire Robots*, pages 211–218. On Advances in Robot Kinematics. Kluwer Academic Publishers, 2004.

[188] S. Perreault, P. Cardou, C. Gosselin, and M. J.-D. Otis. Geometric determination of the interference-free constant-orientation workspace of parallel cable-driven mechanisms. *Journal of Mechanisms and Robotics*, 2(3):031016, 2010.

[189] T. Kobayashi and Y. Takahashi. Vibration control for two dimensional wire driven positioning robot. In *Proceedings of the 37th SICE Annual Conference. International Session Papers*, Chiba, Japan, July 1998.

[190] S. Kawamura, W. Choe, S. Tanaka, and S. R. Pandian. Development of an ultrahigh speed robot Falcon using wire driven system. In *Proceedings of the IEEE International Conference on Robotics and Automation*, Nagoya, Japan, May 1995.

[191] J. Albus, R. Bostelman, and N. Dagalakis. The NIST RoboCrane. *The Journal of Robotic Systems*, 10(5):709–724, 1993.

[192] P. H. Borgstrom, B. L. Jordan, M. A. Batalin, G. S. Sukhatme, and W. J. Kaiser. Field-tests of a redundantly actuated cable-driven robot for environmental sampling applications. In *Proceedings of the IEEE International Conference on Automation Science and Engineering*, Bangalore, India, August 2009.

[193] H. Elhawary, Z. T. H. Tse, A. Hamed, M. Rea, B. L. Davies, and M. U. Lamperth. The case for MR-compatible robotics: A review of the state of the art. *The International Journal of Medical Robotics And Computer Assisted Surgery*, 4(2):105–113, 2008.

[194] R. Gassert, L. Dovat, O. Lambercy, Y. Ruffieux, D. Chapuis, G. Ganesh, E. Burdet, and H. Bleuler. A 2-dof fMRI compatible haptic interface to investigate the neural control of arm movements. In *Proceedings of the IEEE International Conference on Robotics and Automation*, Orlando, FL, United-States, May 2006.

[195] B. T. Larson, A. G. Erdman, N. V. Tsekos, E. Yacoub, P. V. Tsekos, and I. G. Koutlas. Design of a MRI-compatible robotic stereotactic device for minimally invasive interventions in the breast. *Transactions of the ASME Journal of Biomechanical Engineering*, 126(4):458–465, 2004.

[196] J. A. dit Sandretto, G. Trombettoni, and D. Daney. *Confirmation of Hypothesis on Cable Properties for Cable-Driven Robots*, pages 85–93. New Trends in Mechanism and Machine Science: Theory and Applications in Engineering. Springer Publisher, 2013.

[197] Stock Drive Products and Sterling Instrument, "Datasheets of Neg'ator Springs", www.sdp-si.com/.

[198] MSC Software: ADAMS®, www.mscsoftware.com/product/adams.

[199] Carl Stahl® Sava Industries, www.savacable.com/.

[200] ATI Industrial Automation, www.ati-ia.com/.

[201] MATLAB® from MathWorks®: Documentation Center, www.mathworks.com/help/index.html.

[202] R. H. Nathan. Constant force generator mechanism and adjustable seat constructed therewith. Patent 4,387,876, United-States, 1983.

[203] R. H. Nathan. A constant force generation mechanism. *Journal of Mechanical Design*, 107(4):508–512, 1985.

[204] V. Arakelian and S. Ghazaryan. Improvement of balancing accuracy of robotic systems: Application to leg orthosis for rehabilitation devices. *Mechanism and Machine Theory*, 43(5):565–575, 2008.

[205] P.-Y. Lin, W.-B. Shieh, and D.-Z. Chen. A theoretical study of weight-balanced mechanisms for design of spring assistive mobile arm support (MAS). *Mechanism and Machine Theory*, 61(0):156–167, 2013.

[206] J. L. Herder. *Energy-Free Systems: Theory, Conception and Design of Statically Balanced Spring Mechanisms*. PhD dissertation, Delft University of Technology, Delft, Netherlands, 2001.

[207] G. J. M. Tuijthof and J. L. Herder. Design, actuation and control of an anthropomorphic robot arm. *Mechanism and Machine Theory*, 35(7):945–962, 2000.

[208] D. A. Streit and E. Shin. Equilibrators for planar linkages. In *Proceedings of ASME Mechanisms Conference*, Chicago, IL, United-States, September 1990.

[209] E. Shin and D. A. Streit. Spring equilibrator theory for static balancing of planar pantograph linkages. *Mechanism and Machine Theory*, 26(7):645–657, 1991.

[210] T. Laliberté, C. Gosselin, and M. Jean. Static balancing of 3-dof planar parallel mechanisms. *IEEE/ASME Transactions on Mechatronics*, 4(4):363–377, 1999.

[211] S. R. Deepak and G. K. Ananthasuresh. Static balancing of a four-bar linkage and its cognates. *Mechanism and Machine Theory*, 48(0):62–80, 2012.

[212] D. A. Streit and B. J. Gilmore. "Perfect" spring equilibrators for rotatable bodies. *Journal of Mechanisms, Transmissions, and Automation in Design*, 111(4):451–458, 1989.

[213] G. J. Walsh, D. A. Streit, and B. J. Gilmore. Spatial spring equilibrator theory. *Mechanism and Machine Theory*, 26(2):155–170, 1991.

[214] I. Ebert-Uphoff, C. Gosselin, and T. Laliberté. Static balancing of spatial parallel platform mechanisms—revisited. *Journal of Mechanical Design*, 122(1):43–51, 2000.

[215] F. L. S. Riele, E. E. G. Hekman, and J. L. Herder. Planar and spatial gravity balancing with normal springs. In *Proceedings of the ASME International Design Engineering Technical Conferences and Computers and Information in Engineering Conference*, Salt Lake City, UT, United-States, September 2004.

[216] S. K. Agrawal and A. Fattah. Gravity-balancing of spatial robotic manipulators. *Mechanism and Machine Theory*, 39(12):1331–1344, 2004.

[217] P.-Y. Lin. Design of statically balanced spatial mechanisms with springs suspensions. *Journal of Mechanisms and Robotics*, 4(2):021015, 2012.

[218] S. Lessard, P. Bigras, and I. A. Bonev. A new medical parallel robot and its static balancing optimization. *Journal of Medical Devices*, 1(4):272–278, 2007.

[219] A. Russo, R. Sinatra, and F. Xi. Static balancing of parallel robots. *Mechanism and Machine Theory*, 40(2):191–202, 2005.

[220] C. Baradat, V. Arekelian, S. Briot, and S. Guegan. Design and prototyping of a new balancing mechanism for spatial parallel manipulators. *Journal of Mechanical Design*, 130:072305, 2008.

[221] M.-A. Lacasse, G. Lachance, J. Boisclair, J. Ouellet, and C. Gosselin. On the design of a statically balanced serial robot using remote counterweights. In *International Conference on Robotics and Automation*, Karlsruhe, Germany, May 2013.

[222] K. Fujikoshi. Balancing apparatus for jointed robot. Patent jp51-122254, Japan, 1976.

[223] W. S. Newman and H. Hogan. The optimal control of balanced manipulators. In *Proceedings of the Winter Annual Meeting of the ASME*, Anaheim, CA, United-States, December 1986.

[224] J. Wang and C. Gosselin. Static balancing of spatial three-degree-of-freedom parallel mechanisms. *Mechanism and Machine Theory*, 34(3):437–452, 1999.

[225] S. K. Agrawal and A. Fattah. Reactionless space and ground robots: Novel designs and concept studies. *Mechanism and Machine Theory*, 39(1):25–40, 2004.

[226] M. Idan and A. J. Grunwald. Analytical evaluation of a simple partial gravity balancing method for limited-power flight simulation. In *Proceedings of AIAA Modeling and Simulation Technologies Conference*, Portland, OR, United-States, August 1999.

[227] F. Wildenberg. Compensating system for a hexapod. Patent 6,474,915, United-States, 2002.

[228] Y. Segawa, M. Yamamoto, and A. Shimada. Parallel link mechanism. Patent jp2000120824, Japan, 2000.

[229] S. Huang and J. M. Schimmels. The bounds and realization of spatial stiffness achieved with simple springs connected in parallel. *IEEE Transactions on Robotics and Automation*, 14(3):466–475, 1998.

[230] S. Perreault, P. Cardou, and C. Gosselin. Towards parallel cable-driven pantographs. In *Proceedings of the ASME International Design Engineering Technical Conferences and Computers and Information in Engineering Conference*, Washington, DC, United-States, August 2011.

[231] R. T. Farouki. The bernstein polynomial basis: A centennial retrospective. *Computer Aided Geometric Design*, 29(6):379–419, 2012.

[232] S. Perreault and P. Cardou. Approximate static balancing of a planar parallel cable-driven mechanism. In *Proceedings of the CCToMM Symposium on Mechanisms, Machines, and Mechatronics*, Quebec City, Quebec, Canada, May 2009.

[233] P. J. Davis. *Interpolation & Approximation*. Dover Publications, Inc., 1975.

[234] R. T. Farouki and T. N. T. Goodman. On the optimal stability of the bernstein basis. *Mathematics of Computation*, 65(216):1553–1566, 1996.

[235] S. Boyd and L. Vendenberghe. *Convex Optimization*. Cambridge University Press, 2004.

[236] G. Strang. *Linear Algebra and its Application*. Brooks/Cole Thomson Learning Inc., third edition, 1988.

[237] F. Freudenstein. An analytical approach to the design of four-link mechanisms. *Transactions of the ASME*, 76(3):483–492, 1954.

[238] F. Freudenstein. Approximate synthesis of four-bar linkages. *Transactions of the ASME*, 77(8):853–861, 1955.

[239] F. Y. Chen. An analytical method for synthesizing the four-bar crank-rocker mechanism. *ASME Journal of Engineering for Industry*, 91B(1):45–54, 1969.

[240] A. K. Khare and R. K. Dave. Optimizing 4-bar crank-rocker mechanism. *Mechanism and Machine Theory*, 14(5):319–325, 1979.

[241] C. Gosselin. *Kinematic Analysis, Optimization and Programming of Parallel Robotic Manipulators*. PhD dissertation, McGill University, Montreal, QC, Canada, 1988.

[242] C. Gosselin and J. Angeles. Mobility analysis of planar and spherical linkages. *Computers in Mechanical Engineering*, 7(1):56–60, 1988.

[243] F. Dudita, D. Diaconescu, and G. Gogu. *Sinteza Mecanismului Patrulater Antiparalelogram Utilizat ca Mecanism de Prehensiune in Robotii Industriali*, pages 237–241. Mecanisme Articulate: Inventica si Cinematica in Abordare Filogenetica. Editura Tehnica, Bucuresti, Romania, 1989.

[244] T. D. Todorov. Synthesis of four-bar mechanisms by freudenstein-chebyshev. *Mechanism and Machine Theory*, 37(12):1505–1512, 2002.

[245] W. A. Harmening. Static mass balancing with a torsion spring and four-bar linkage. In *Proceedings of the ASME Design Engineering Technical Conference*, New York, NY, United-States, October 1974.

[246] I. Simionescu and L. Ciupitu. The static balancing of the industrial robot arms, Part I: Discrete balancing. *Mechanism and Machine Theory*, 35(9):1287–1298, 2000.

[247] C. E. Benedict, G. K. Matthew, and D. Tesar. Torque balancing of machines by sub-unit cam systems. In *Proceedings of the Second Applied Mechanism Conference*, Stillwater, OK, United-States, October 1971.

[248] N. Ulrich and V. Kumar. Passive mechanical gravity compensation for robot manipulators. In *Proceedings of the IEEE International Conference on Robotics and Automation*, Sacramento, CA, United-States, April 1991.

[249] I. Simionescu and L. Ciupitu. The static balancing of the industrial robot arms, Part II: Continuous balancing. *Mechanism and Machine Theory*, 35(9):1299–1311, 2000.

[250] Y. Wischnitzer, N. Shvalb, and M. Shoham. Wire-driven parallel robot: Permitting collisions between wires. *The International Journal of Robotics Research*, 27(9):1007–1026, 2008.

[251] M. J.-D. Otis, T.-L. Nguyen-Dang, D. Laurendeau, and C. Gosselin. Interference estimated time of arrival on a 6-dof cable-driven haptic foot platform. In *Proceedings of the IEEE International Conference on Intelligent Robots and Systems*, Kobe, Japan, May 2009.

[252] M. J.-D. Otis, S. Comtois, D. Laurendeau, and C. Gosselin. Human safety algorithms for a parallel cable-driven haptic interface. In *Proceedings of the CIM Symposium on Brain, Body and Machine*, Montreal, QC, Canada, November 2010.

[253] V. J. Lumelsky. On fast computation of distance between line segments. *Information Processing Letters*, 21(2):55–61, 1985.

[254] J. Andrade-Cetto and F. Thomas. A wire-based active tracker. *IEEE Transactions on Robotics*, 24(3):642–651, 2008.

[255] K. H. J. Voss, V. Van der Wijk, and J. L. Herder. Investigation of a cable-driven parallel mechanism for interaction with a variety of surfaces, applied to the cleaning of free-form buildings. In *Proceedings of the 13th IFToMM International Symposium on Advances in Robot Kinematics*, Innsbruck, Austria, June 2012.

[256] Y. Su, J. W. Mi, and Y. Y. Qiu. Interference determination for parallel cable-driven robots. *Advanced Materials Research*, 310:2013–2018, 2011.

[257] A. Pott, D. Franitza, and M. Hiller. Orientation workspace verification for parallel kinematic machines with constant leg length. In *Proceedings of Mechatronics and Robotics*, Aachen, Germany, September 2004.

[258] J. S. Ketchel and P. M. Larochelle. Self-collision detection in spatial closed chains. *Journal of Mechanical Design*, 130(9):89–97, 2008.

[259] J.-P. Merlet and D. Daney. Legs interference checking of parallel robots over a given workspace or trajectory. In *Proceedings of the IEEE International Conference on Robotics and Automation*, Orlando, FL, United-States, May 2006.

[260] E. H. Moore. On the reciprocal of the general algebraic matrix. *Bulletin of the American Mathematical Society*, 26(9):394–395, 1920.

[261] R. Penrose. A generalized inverse for matrices. *Mathematical Proceedings of the Cambridge Philosophical Society*, 51(3):406–413, 1955.

[262] R. Penrose. On best approximate solutions of linear matrix equations. *Mathematical Proceedings of the Cambridge Philosophical Society*, 52(1):17–19, 1956.

[263] Datasheets of the Flock of Birds™ by Ascension Technology Corporation, www.ascension-tech.com/.

[264] P. M. Pardalos and M. G. C. Resende. *Handbook of Applied Optimization*. Oxford University Press, 2002.

[265] H. H. Goldstine and A. Goldstine. The electronic numerical integrator and computer (ENIAC). *IEEE Annals of the History of Computing*, 18(1):10–16, 1996.

[266] D. P. Bertsekas. *Convex Analysis and Optimization*. Athena Scientific, 2003.

[267] J. J. Moré and D. C. Sorensen. Newton's method. In *Studies in Numerical Analysis*, The Mathematical Association of America: Studies in Mathematics, pages 29–82. G. H. Golub, Washington, DC, United-States, 1984.

[268] G. B. Dantzig. *Linear Programming and Extensions*. Princetown University Press, 1963.

[269] J. K. Lenstra, A. H. G. Rinnooy, and A. Schrijver. *History of Mathematical Programming: A Collection of Personal Reminiscences*. CWI, 1991.

[270] N. K. Karmarkar. A new polynomial-time algorithm for linear programming. *Combinatorica*, 4(4):373–395, 1984.

[271] R. J. Vanderbei and D. F. Shanno. An interior-point algorithm for nonconvex nonlinear programming. *Computational Optimization and Applications*, 13(1-3):231–252, 1999.

[272] R. B. Wilson. *A simplicial algorithm for concave programming*. PhD dissertation, Harvard University, Cambridge, MA, United-States, 1963.

[273] P. T. Boggs and J. W. Tolle. Sequential quadratic programming. *Acta Numerica*, 4(1):1–51, 1995.

[274] H. Tuy. *Cutting Plane Methods for Global Optimization*, pages 590–594. Encyclopedia of Optimization. Springer US, 2009.

[275] M. Andramonov, A. Rubinov, and B. Glover. Cutting angle methods in global optimization. *Applied Mathematics Letters*, 12(3):95–100, 1999.

[276] G. L. Nemhauser and L. A. Wolsey. *Integer and Combinatorial Optimization*. Wiley-Interscience, 1999.

[277] W. Forster. *Homotopy Methods*, pages 669–750. Handbook of Global Optimization. Springer US, 1995.

[278] P. M. Pardalos and H. E. Romeijn. *Handbook of Global Optimization - Volume* 2. Nonconvex Optimization and its Applications. Kluwer Academic Publishers, 2002.

[279] I. H. Osman and J. P. Kelly. *Meta-Heuristics: Theory and Applications*. Springer Science & Business Media, 1996.

[280] D. E. Goldberg. *Genetic Algorithms in Search, Optimization, and Machine Learning*. Addison-Wesley Professional, 1989.

[281] R. Marti. Multi-start methods. In *Handbook of Metaheuristics*, International Series in Operations Research & Management Science, pages 355–368. Springer US, 2003.

[282] J. Dattorro. *Convex Optimization & Euclidean Distance Geometry*. M$\epsilon\beta$oo Publishing, 2005.

[283] D. P. Bertsekas. *Convex Optimization Theory*. Athena Scientific, 2009.

[284] R. Horst, P. M. Pardalos, and N. V. Thoai. *Nonconvex Optimization and its Applications: Introduction to Global Optimization*. Kluwer Academic Publishers, 1995.

[285] K. Azizian and P. Cardou. The dimensional synthesis of spatial cable-driven parallel mechanisms through convex relaxations. *Journal of Mechanisms and Robotics*, 5(4):044502, 2013.

[286] S. Tadokoro, S. Nishioka, T. Kimura, M. Hattori, T. Takamori, and K. Maeda. On fundamental design of wire configurations of wire-driven parallel manipulators with redundancy. In *Proceedings of the 1996 Japan/USA Symposium on Flexible Automation*, Boston, MA, United-States, July 1996.

[287] S. Abdelaziz, L. Esteveny, L. Barbé, P. Renaud, B. Bayle, and M. de Mathelin. Design of an MRI-compatible cable-driven manipulator with new instrumentation and synthesis methods. *Journal of Mechanical Design*, 136(9):091006, 2013.

[288] K. Azizian and P. Cardou. *The constant-orientation dimensional synthesis of planar cable-driven parallel mechanisms through convex relaxations*, pages 215–230. Cable-Driven Parallel Robots. Springer, 2013.

[289] K. Azizian. *Optimum-synthesis methods for cable-driven parallel mechanisms*. PhD dissertation, Université Laval, Quebec City, QC, Canada, 2012.

[290] L. Gagliardini, S. Caro, M. Gouttefarde, P. Wenger, and A. Girin. Optimal design of cable-driven parallel robots for large industrial structures. In *Proceedings of the European Workshop on Applications of Parallel and Cable-Driven Robots*, Lyon, France, March 2014.

[291] L. Gagliardini, S. Caro, M. Gouttefarde, P. Wenger, and A. Girin. Optimal design of cable-driven parallel robots for large industrial structures. In *Proceedings of the IEEE International Conference on Robotics and Automation*, Hong Kong, China, June 2014.

[292] M. Gouttefarde, J.-F. Collard, N. Riehl, and C. Baradat. Geometry selection of a redundantly actuated cable-suspended parallel robot. *IEEE Transactions on Robotics*, 31(2):501–510, 2015.

[293] D. S. Watkins. *Fundamentals of Matrix Computations*. Wiley, third edition, 2010.

[294] J. R. Shewchuk. An introduction to the conjugate gradient method without the agonizing pain. Technical report, Carnegie Mellon University, Pitttsburgh, PA, United-States, 1994.

[295] U.S. Food and Drug Administration: Medical Devices - Device Regulation and Guidance, www.fda.gov/medicaldevices/deviceregulationandguidance/guidancedocuments/.

[296] J. F. Schenck. The role of magnetic susceptibility in magnetic resonance imaging: MRI magnetic compatibility of the first and second kinds. *Journal of Medical Physics*, 23(6):815–850, 1996.

[297] K. Chinzei, K. Yoshinaka, and T. Washio. Numerical simulations and lab tests for design of MR-compatible robots. In *Proceedings of the IEEE International Conference on Robotics and Automation*, Orlando, FL, United-States, May 2006.

[298] C. Keroglou, I. Seimenis, N. V. Tsekos, C. Pitris, E. Eracleous, and E. G. Christoforou. Consideration of geometric constraints regarding MR-compatible interventional robotic devices. In *Proceedings of the 3rd IEEE RAS & EMBS International Conference on Biomedical Robotics and Biomechatronics*, Tokyo, Japan, September 2010.

[299] E. G. Christoforou, I. Seimenis, E. Andreou, E. Eracleous, and N. V. Tsekos. A novel, general-purpose, MR-compatible, manually actuated robotic manipulation system for minimally invasive interventions under direct MRI guidance. *The International Journal of Medical Robotics and Computer Assisted Surgery*, 10(1):22–34, 2014.

[300] Online English dictionary by Merriam-Webster, www.merriam-webster.com/dictionary/.

[301] K. Masumane, E. Kobayashi, Y. Masutani, M. Suzuki, T. Dohi, H. Iseki, and K. Takakura. Development of an MRI-compatible needle insertion manipulator for stereotactic neurosurgery. *Journal of Image Guided Surgery*, 1(4):242–248, 1995.

[302] U. Spaelter, D. Chapuis, R. Gassert, R. Moser, and H. Bleuber. A versatile MRI/fMRI compatible spherical 2-dof haptic interface. In *Proceedings of the 1st IEEE RAS & EMBS International Conference on Biomedical Robotics and Biomechatronics*, Pisa, Italy, February 2006.

[303] S. A. Huettel, A. W. Song, and G. McCarthy. *Functional Magnetic Resonance Imaging*. Sinauer Associates, second edition, 2008.

[304] N. Yu, C. Hollnagel, A. Blickenstorfer, S. S. Kollias, and R. Riener. Comparison of MRI-compatible mechatronic systems with hydrodynamic and pneumatic actuation. *IEEE/ASME Transactions on Mechatronics*, 13(3):268–277, 2008.

[305] E. Taillant, J.-C. Avila-Vilchis, C. Allegrini, I. Bricault, and P. Cinquin. CT and MR compatible light puncture robot: Architectural design and first experiments. In C. Barillot, D. R. Haynor, and P. Hellier, editors, *Medical Image Computing and Computer-Assisted Intervention – MICCAI 2004*, volume 3217 of *Lecture Notes in Computer Science*, pages 145–152. Springer Berlin Heidelberg, 2004.

[306] A. Patriciu, D. Petrisor, M. Muntener, D. Mazilu, M. Schär, and D. Stoianovici. Automatic brachytherapy seed placement under MRI guidance. *IEEE Transactions on Biomedical Engineering*, 54(8):1499–1506, 2007.

[307] J. A. Cunha, I.-C. Hsu, J. Pouliot, M. Roach III, K. Shinohara, J. Kurhanewicz, G. Reed, and D. Stoianovici. Toward adaptive stereotactic robotic brachytherapy for prostate cancer: Demonstration of an adaptive workflow incorporating inverse planning and an MR stealth robot. *Minimally Invasive Therapy*, 19(4):189–202, 2010.

[308] G. S. Fischer, S. P. DiMaio, I. I. Iordachita, and G. Fichtinger. Robotic assistant for transperineal prostate interventions in 3T closed MRI. In N. Ayache, S. Ourselin, and A. Maeder, editors, *Medical Image Computing and Computer-Assisted Intervention – MICCAI 2007*, volume 4791 of *Lecture Notes in Computer Science*, pages 425–433. Springer Berlin Heidelberg, 2007.

[309] G. S. Fischer, I. Iordachita, C. Csoma, J. Tokuda, S. P. DiMaio, C. M. Tempany, N. Hata, and G. Fichtinger. MRI-compatible pneumatic robot for transperineal prostate needle placement. *IEEE/ASME Transactions on Mechatronics*, 13(3):295–305, 2008.

[310] A. Melzer, B. Gutmann, T. Remmele, R. Wolf, A. Lukoscheck, M. Bock, H. Bardenheuer, and H. Fischer. INNOMOTION for percutaneous image-guided interventions. *IEEE Engineering in Medecine and Biology Magazine*, 27(3):66–73, 2008.

[311] S.-E. Song, N. Cho, J. Tokuda, N. Hata, C. Tempany, G. Fichtinger, and I. Iordachita. Preliminary evaluation of a MRI-compatible modular robotic system for MRI-guided prostate interventions. In *Proceedings of the 3rd IEEE RAS & EMBS International Conference on Biomedical Robotics and Biomechatronics*, Tokyo, Japan, September 2010.

[312] N. V. Tsekos, E. Christoforou, and A. Özcan. A general-purpose MR-compatible robotic system. *IEEE Engineering in Medecine and Biology Magazine*, 27(3):51–58, 2008.

[313] A. Salimi, A. Ramezanifar, J. Mohammadpour, and K. M. Grigoriadis. Gain-scheduling control of a cable-driven MRI-compatible robotic platform for intracardiac interventions. In *Proceedings of the American Control Conference*, Washington, DC, United-States, June 2013.

[314] A. Salimi, A. Ramezanifar, and K. M. Grigoriadis. Control of a cable-driven platform in a master-slave robotic system: LPV approach. *ASME Journal of Dynamic Systems, Measurements, and Control*, 137(9):094502, 2015.

[315] D. Beyersdorff, A. Winkel, B. Hamm, S. Lenk, S. A. Loening, and M. Taupitz. MR imaging-guided prostate biopsy with a closed MR unit at 1.5 T: Initial results. *Radiology*, 234(2):576–581, 2005.

[316] E. G. Christoforou, I. Seimenis, E. Andreou, and N. V. Tsekos. Development and initial testing of a general-purpose, MR-compatible, manually-actuated manipulator for image-guided interventions. In *Proceedings of the 4th IEEE RAS & EMBS International Conference on Biomedical Robotics and Biomechatronics*, Roma, Italy, June 2012.